CISM International Centre for Mechanical Sciences 588
Courses and Lectures

Stefano Lenci · Giuseppe Rega *Editors*

Global Nonlinear Dynamics for Engineering Design and System Safety

International Centre
for Mechanical Sciences

Springer

CISM International Centre for Mechanical Sciences

Courses and Lectures

Volume 588

Managing Editor

Paolo Serafini, Udine, Italy

Series editors

Elisabeth Guazzelli, Marseille, France
Franz G. Rammerstorfer, Vienna, Austria
Wolfgang A. Wall, Munich, Germany
Bernhard Schrefler, Udine, Italy

المنارة للاستشارات

For more than 40 years the book series edited by CISM, “International Centre for Mechanical Sciences: Courses and Lectures”, has presented groundbreaking developments in mechanics and computational engineering methods. It covers such fields as solid and fluid mechanics, mechanics of materials, micro- and nanomechanics, biomechanics, and mechatronics. The papers are written by international authorities in the field. The books are at graduate level but may include some introductory material.

More information about this series at http://www.springer.com/series/76

المنارة للاستشارات

Stefano Lenci · Giuseppe Rega
Editors

Global Nonlinear Dynamics for Engineering Design and System Safety

Springer

المنارة للاستشارات

Editors
Stefano Lenci
Department of Civil, Building Engineering, and Architecture
Polytechnic University of Marche
Ancona, Italy

Giuseppe Rega
Department of Structural and Geotechnical Engineering
Sapienza University of Rome
Rome, Italy

ISSN 0254-1971 ISSN 2309-3706 (electronic)
CISM International Centre for Mechanical Sciences
ISBN 978-3-319-99709-4 ISBN 978-3-319-99710-0 (eBook)
https://doi.org/10.1007/978-3-319-99710-0

Library of Congress Control Number: 2018952871

© CISM International Centre for Mechanical Sciences 2019
This work is subject to copyright. All rights are reserved by the Publisher, whether the whole or part of the material is concerned, specifically the rights of translation, reprinting, reuse of illustrations, recitation, broadcasting, reproduction on microfilms or in any other physical way, and transmission or information storage and retrieval, electronic adaptation, computer software, or by similar or dissimilar methodology now known or hereafter developed.
The use of general descriptive names, registered names, trademarks, service marks, etc. in this publication does not imply, even in the absence of a specific statement, that such names are exempt from the relevant protective laws and regulations and therefore free for general use.
The publisher, the authors and the editors are safe to assume that the advice and information in this book are believed to be true and accurate at the date of publication. Neither the publisher nor the authors or the editors give a warranty, express or implied, with respect to the material contained herein or for any errors or omissions that may have been made. The publisher remains neutral with regard to jurisdictional claims in published maps and institutional affiliations.

This Springer imprint is published by the registered company Springer Nature Switzerland AG
The registered company address is: Gewerbestrasse 11, 6330 Cham, Switzerland

المنارة للاستشارات

Preface

In the last few decades, global nonlinear dynamics has been evolving in a revolutionary way, with applications to a wide variety of mechanical/structural systems made possible by the use of sophisticated analytical, geometrical, and computational techniques employing powerful concepts and tools of dynamical systems, bifurcation, and chaos theory, properly updated and complemented with a view to engineering aims and with meaningful experimental verifications.

The achievements occurred in the area entail a substantial change of perspective when dealing with vibration problems and are ready to meaningfully affect the analysis, control, and design of systems at different scales in applied mechanics and structural dynamics.

In this context, attention has to be paid, in particular, to the evolution and update of the classical concept of stability, as ensuing from consideration of global dynamical effects. Local and global dynamics, bifurcation and complexity, theoretical and practical stability play an extremely important—yet still generally overlooked—role as regards understanding and suitably controlling nonlinear phenomena, as well as reliably determining the load carrying capacity and safety of engineering systems.

Local stability and global stability have to be discussed by also considering the effects of imperfections or small, but finite, dynamical perturbations, along with variations of control parameters. All of them may arise in technical applications and experiments and are to be properly considered in the design stage in order to secure the system capability to sustain changes without modifying the desired outcome.

Robustness of solutions against variations of initial conditions or control parameters, and system dynamical integrity, are fundamental concepts in analysis and design. They have to be addressed in view of global phenomena occurring in the system, which may indeed entail the existence of merely residual levels of integrity, definitely unacceptable in technical applications. It is just this item that makes the concept of practical stability, and the associated global analysis, necessary.

المنارة للاستشارات

The overall transition from a local stability perspective to a global safety concept has also major implications as regards the feasibility and effectiveness of techniques aimed at controlling nonlinear dynamics. In fact, these may drastically change according to whether the goal is increasing the overall dynamical integrity of the system, or merely realizing and/or stabilizing a specific kind of response.

This volume presents a series of essays based on the lectures for the Advanced School on 'Global Nonlinear Dynamics for Engineering Design and System Safety,' held at the International Centre for Mechanical Sciences (CISM) in Udine, Italy, June 13–17, 2016, which provide a sound base and a theoretical framework for many applications.

All of the above-mentioned issues, which also permit to explain partial discrepancies between experimental and theoretical/numerical results based on merely local analyses, are addressed in the six volume chapters by referring to a number of systems of interest in applications, ranging from macro- to micro/nano-mechanics. Archetypal discrete systems and reduced-order models of continuous structures are considered. Specific phenomenological aspects are discussed, yet paying attention to the common or distinguishing nonlinear dynamical features which are expected to play a meaningful role in the analysis and design for engineering applications.

J. M. T. Thompson summarizes the progress of the key idea of dynamical integrity over the last three decades, overviewing some examples of how using it to cope with the erosion of basins of attraction. Dealing with the concept in more detail, G. Rega, S. Lenci, and L. Ruzziconi present various possible implementations of dynamical integrity as a tool to analyze global dynamics in terms of attractor robustness and basin erosion in phase space and control parameter space, by also dwelling on its expected potential for establishing a novel paradigm of safe, yet aware, engineering design. L. Ruzziconi, S. Lenci, and M. I. Younis discuss the role of dynamical integrity for interpreting and predicting experimental behavior, distinguishing between theoretical and practical existence of solutions, and wanted/unwanted attractors, in the presence of escape phenomena which are dynamical system representations of different failure mechanisms of physical systems. Dealing with the class of slender structures liable to interactive unstable buckling, P. B. Goncalves, D. Orlando, F. M. A. Silva, S. Lenci, and G. Rega analyze the influence of interactive buckling and coupled instabilities on the load carrying capacity of an archetypal discrete model, by also considering the effect of imperfections and the safety increase achievable by controlling global bifurcations; a reduced-order model of a continuous structure is also considered, dwelling on the influence of uncertainties and noise on dynamical integrity. V. Settimi and G. Rega present a general framework for studying local and global dynamics of mechanical systems in a safety perspective, along with their control with different objectives and consequences, taking as reference a reduced-order model of noncontact atomic force microscope, which can represent a large number of nonlinear models with some ensuing dynamic phenomena. Finally, F.-R. Xiong, Q. Han, L. Hong, and J.-Q. Sun review the cell mapping methods for global analysis of nonlinear systems with multiple steady-state responses, as applied to deterministic, stochastic, and fuzzy dynamical systems, and present several examples of recent applications.

المنارة للاستشارات

We wish to thank the former Rectors of the CISM Professors E. Guazzelli, F. Pfeiffer, and F. Rammerstorfer, the Secretary General Professor B. Schrefler, and all the staff for the warm hospitality and kind assistance during the course.

Ancona, Italy — Stefano Lenci
Rome, Italy — Giuseppe Rega

المنارة للاستشارات

Contents

المنارة للاستشارات

Dynamical Integrity: Three Decades of Progress from Macro to Nanomechanics

J. Michael T. Thompson

Abstract During the explosion of interest in applied nonlinear dynamics and chaos in the 1980s, a key concept was quickly seen to be the concept of dynamical integrity which was required to cope with, for example, the erosion of basins of attraction by fractal incursions. Articles by Thompson and Soliman laid down the fundamental ideas, but major contributions by Rega and Lenci established this integrity as a central issue in the design of (for example) structures in their inevitable dynamic environment. They extended and developed the various integrity measures and pioneered ways of controlling the basin erosion phenomenon, applying the ideas to a wide range of mechanical problems. The present paper offers a review of this progress, highlighting key conceptual ideas and some of the more interesting applications.

Keywords Dynamical integrity · MEMS · Nano-mechanics · Fractal basins

1 Introduction

During the explosion of interest in applied nonlinear dynamics and chaos in the 1980s, a key idea was quickly seen to be the concept of dynamical integrity which was required to cope with, for example, the erosion of basins of attraction by fractal incursions. Articles by Thompson and Soliman laid down the fundamental ideas, but major contributions by Rega and Lenci established this integrity as a central issue in the design of (for example) structures in their inevitable dynamic environment. They extended and developed the various integrity measures and pioneered ways of controlling the basin erosion phenomenon—and applied the ideas to a wide range of mechanical problems. The present paper offers a review of this progress, highlighting key conceptual ideas and some of the more interesting applications.

The technical concept of *integrity* relates to any dynamical system that is operating in a metastable state, namely, one which is stable against small disturbances but

J. M. T. Thompson (✉)
Department of Applied Maths and Theoretical Physics, University of Cambridge, Cambridge, UK
e-mail: J.M.T.Thompson@damtp.cam.ac.uk

© CISM International Centre for Mechanical Sciences 2019

S. Lenci and G. Rega (eds.), *Global Nonlinear Dynamics for Engineering Design and System Safety*, CISM International Centre for Mechanical Sciences 588,
https://doi.org/10.1007/978-3-319-99710-0_1

المنارة للاستشارات

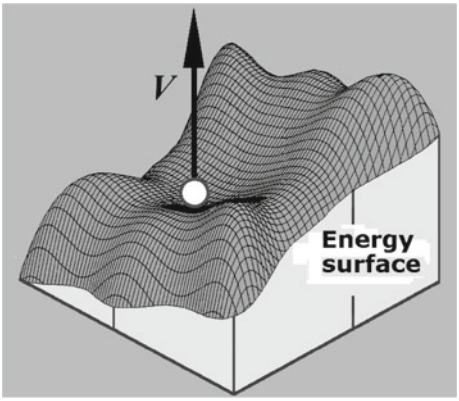

Fig. 1 A ball rolling on a total potential energy surface, illustrating a metastable state with several potential escape routes over mountain passes

unstable against large ones. As a concrete example, we might consider a ball rolling on the energy surface of Fig. 1.

Sitting in the well at a potential energy minimum it is stable, but could easily be knocked out of it, and roll away out of our region of interest. As a short-hand, we might say that it has *escaped* from the well, and jumped dynamically to *infinity*. Very often, an escaping jump will imply a serious malfunction or collapse, and we will for convenience usually speak in these terms. But in some circumstances, such a jump might be a desired outcome, as when a molecule is required to jump out of a potential well and away from a constraining protein to destroy a virus; or when the jump implies the required activation of a switch in an electronic circuit.

Usually, a dynamical system will be subjected to *controlled* static or dynamic changes under which it is expected to operate, and these will invariably change the shape of the potential well, and the height of the constraining energy barriers. Additionally, any real system will experience unwanted disturbances and shocks from its environment, which are often conveniently described as *noise*. Predicting escape or non-escape from such a metastable condition is the topic of this chapter, and it clearly requires a study of phase space and its conceptual safe basins of attraction. Under periodic excitation, these basins of attraction can suddenly shrink in size and become penetrated by fractal fingers, as we shall now describe.

In this chapter, we look at the new phenomena presented to engineers and applied scientists in the book by Thompson and Stewart (1986) and examine, in particular, the Thompson-Soliman treatment of fractal basin erosion in driven nonlinear oscillators, as quantified by Dover Cliff integrity curves (Thompson 1989; Soliman and Thompson 1989). After describing these original discoveries at University College London, we then follow the development over the next 27 years focusing particularly on the imaginative contributions of Giuseppe Rega and Stefano Lenci. These authors devised new integrity measures and the successful idea of controlling erosion by adding predicted super-harmonics to the basic sinusoidal forcing. We finally look at intriguing applications of integrity, including capsize of ships, the buckling of spherical and cylindrical shells; and developments in micro-electromechanical

المنارة للاستشارات

systems (MEMS) and nano-electromechanical systems (NEMS). Note that, in this paper, we write MEMS to embrace NEMS as well.

Applications in MEMS do indeed seem almost custom-made for the implementation of integrity ideas, especially since the electronic components can be tuned with great precision. They already impinge heavily on all our lives, as essential elements of accelerometers and pressure sensors in cars, radio-frequency switches and microphones in cell phones and inertia sensors in video games. This makes them a hot evolving area of science and technology driven by insatiable demands for sophisticated sensors and actuators, which should ideally be self-powered, self-calibrated and self-tested: and their mass production necessitates tight control and precision.

Most MEMS devices, including gyroscopes, micro-mirrors and thermal actuators, have moving parts that are often highly compliant with significant geometric nonlinearity. Actuation is often by parallel-plate electrostatic forces which are themselves inherently nonlinear, as is the new phenomenon of squeeze-film damping. So to meet all the design challenges, it has become essential to delve deeply into the dynamics, and in particular to explore the opportunities of operating micro-electromechanical systems (MEMS) in highly nonlinear regimes.

2 Fractal Erosion and the Dover Cliff

The escape of a particle (or ball) from a potential well is a recurrent problem throughout science and engineering. Very often, escape might represent some sort of failure or collapse, but of course, it could be the desired closing of a miniature MEMS switch. Examining the simplest case of a damped particle in a cubic well, subjected to sinusoidal forcing the significance of the fractal erosion process was first noted by Thompson (1989) working on the escape from a cubic potential well as illustrated in Fig. 2.

The equation, with damping and periodic forcing, is written as

$$x'' + \beta\, x' + x - x^2 = F\sin(\omega t) \tag{1}$$

and the total potential energy $V(x)$ has the form illustrated. With $F = 0$, before we introduce non-zero forcing, this nonlinear dynamical system has a two-dimensional phase space spanned by the displacement, x and its time (t) derivative x', giving the portrait displayed in the lower left diagram. In this, the basin of attraction of the asymptotically stable attractor at the bottom of the well is shown in grey, bounded by the smooth insets (stable manifolds) of the unstable hilltop saddle equilibrium.

Once the system is forced ($F \neq 0$), the phase space becomes three-dimensional spanned by (x, x', t) and we use stroboscopic sampling at the forcing-period, T, to obtain a two-dimensional mapping in the (x, x') Poincaré section. In this section, the hilltop solution is now a fixed point corresponding to a small unstable cycle of period T (called an $n = 1$ cycle). The discrete Poincaré mapping allows invariant manifolds

المنارة للاستشارات

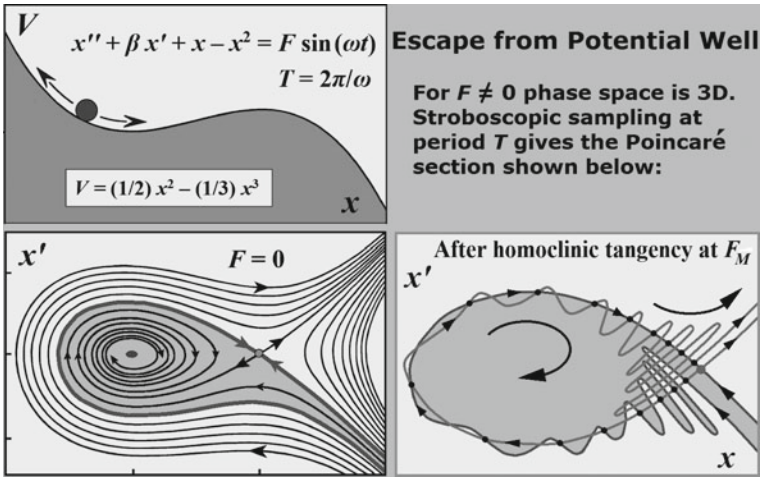

Fig. 2 Escape from a potential well under periodic forcing

to touch and then intersect, and this first happens at a homoclinic tangency at $F = F_M$ which can be predicted theoretically by a Melnikov analysis.

For $F > F_M$, there is a homoclinic tangle in which the inset and outset manifolds intersect each other an infinite number of times. This creates chaos and an infinity of periodic orbits with mapping points located close to the tangled manifolds. The basin of attraction of the constrained states within the well (of which there may be many, of different types) is shown in grey in the lower right diagram and is still bounded by the inset of the hilltop solution (now a small unstable cycle). Note, though, that the basin is now being effectively penetrated by an infinite number of fractal fingers.

It was soon established that this basin erosion process is common to a wide class of escape problems, under both direct and parametric loading (Stewart et al. 1991; Lansbury et al. 1992; Thompson et al. 1992). Figure 3 shows side-by-side the processes for the escape equation and the escape from one well to another in the double well oscillator. The latter can be written as

$$x'' + k\,x' - x + x^3 = A\,\sin(\omega t). \tag{2}$$

We continue this story in Fig. 4. Here, we have plotted the area, A, of the safe basin (within an appropriate phase-space window), against the magnitude of the forcing, F, which is here scaled to be unity at the final loss of stability of the central main-sequence attractor. Meanwhile, the area, A, is scaled to be unity at $F = 0$. The area stays roughly constant while its boundary is smooth and continues with very little discontinuity past the homoclinic tangency at F_M, where the boundary becomes fractal. Notice that at F_M there is still a central $n = 1$ periodic attractor, though its path does go through a hysteresis loop (as shown in the lower right-hand sketch of Fig. 4). Note carefully that at the homoclinic tangency there is no dramatic change

المنارة للاستشارات

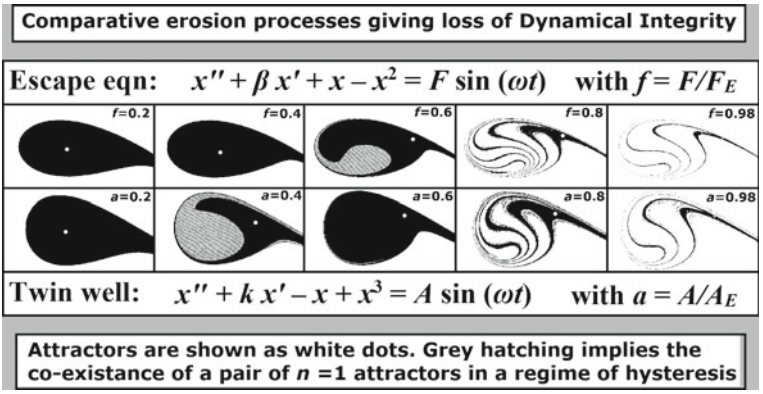

Fig. 3 Erosion processes for two different escape problems (Lansbury et al. 1992). Displayed are the well-known escape and twin-well equations

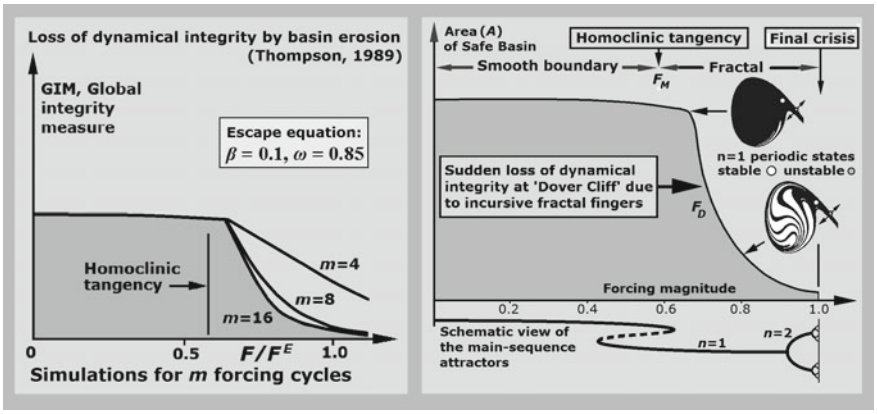

Fig. 4 Illustration of how the area of the safe basin within the well suddenly decreases, signifying a loss of integrity. **a** The first Dover Cliff graph obtained by Thompson (1989). **b** The same phenomenon is shown in a later more complete diagram

in the centre of the safe basin. Chaos and an infinity of periodic orbits exist close to the edge in the thin fractal zones, but this does not influence the main central sequence of attractors. Starts within the fractal zone lead to chaotic transients, which oscillate hesitatingly for an arbitrary and unpredictable length of time before either escaping or settling onto a safe attractor. But this phenomenon is not in itself serious or dangerous for so long as the fractal zone is confined to a thin layer around the edge of the basin, as it is just after F_M.

Some way beyond the tangency the fractal fingers suddenly become incursive and spread rapidly into the safe basin, with thick finger-like striations penetrating into the very heart of the central zone around the origin, giving in the graph what we might call a Dover Cliff at the somewhat arbitrary $F_D > F_M$. There is a sudden loss of the

المنارة للاستشارات

safe basin (which manifests itself in other ways besides just the loss of area) and we can say that the *dynamical integrity* of the central attractor is lost.

Being now inevitably close to its basin boundary, the central attractor will be very sensitive to the dynamic disturbances of an operational environment. As we increase F further, we observe that the $n = 1$ central periodic attractor finally undergoes a period doubling cascade to a chaotic attractor, which is destroyed at a global *crisis* bifurcation at $F = 1$, after which there are no (major) attractors. This final crisis is what a designer would traditionally have used as the failure criterion, but our argument is that the F_D at the Dover Cliff should be adopted in design work.

3 Thompson-Soliman Integrity Measures

Nonlinear oscillators with one degree of freedom, some form of periodic forcing (direct and/or parametric), some damping (linear or nonlinear), but with a wide variety of well shapes are all prone to the described type of basin erosion, which is best observed in a stroboscopic Poincaré section. For this reason, the simple integrity measure of the basin area used by Thompson (1989) was immediately re-examined and generalized by Soliman and Thompson (1989) who introduced the various measures of engineering integrity illustrated in Fig. 5. This figure also includes one later measure introduced by Lenci and Rega (2003) that we shall discuss in the following section.

The 1989 definitions are as follows:

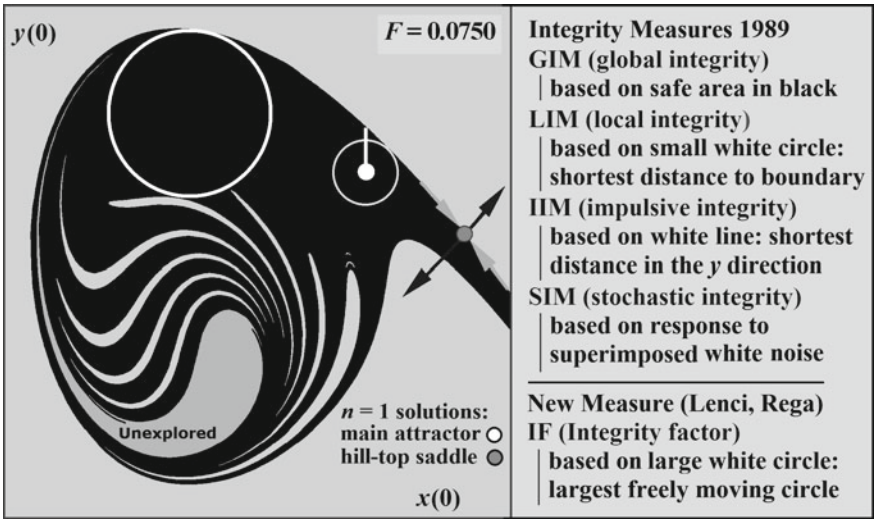

Fig. 5 Definition of various integrity measures illustrated on a basin (of the escape equation) which is already well eroded by fractal fingers. The grey 'unexplored' area has no significance here

المنارة للاستشارات

GIM. Following Thompson (1989), the simplest is based on the area of the safe basin within a prescribed window. This *global integrity measure* (*GIM*) is particularly easy to use and is conveniently independent of the (possibly unknown) finite attractors onto which the constrained motions settle.

LIM. For a given point attractor which has been located in the (x, x') Poincaré section, a particularly relevant measure of its integrity is the minimum distance, L, in any direction, from the attractor to its basin boundary. This gives us our second *local integrity measure* (*LIM*).

IIM. Our third measure, based on the concept that a mechanical oscillator might be subjected to an impulse, in which it could be thought to experience an instantaneous step change in velocity, involves the minimum distance in the direction of $+x'$ or $-x'$. The minimum distance in the Poincaré section from a point attractor to its boundary in the direction of positive x' is written as $I+$, and in the direction of negative x' as $I-$. With either a positive or negative sense, the value of I gives us the *impulsive integrity measure* (*IIM*).

SIM. A fourth, *stochastic integrity measure* (*SIM*) can be defined in terms of the mean escape time when the attractor is subjected to additive white noise excitation of prescribed intensity.

A useful comparison between three of these measures for the escape equation was made by Soliman and Thompson (1990) as illustrated in Fig. 6. Notice that the different starting heights of these curves have no particular significance; it is the following shape and position of the Dover Cliff that is of interest. The two marked values of the forcing amplitude show the homoclinic tangency (F_M) and the final crisis of the main-sequence steady-state attractors (F_C).

As well as looking at the fractal forms in phase space, it is useful for design purposes to look at the corresponding forms in control space (Thompson and Soliman 1990). One such diagram can be drawn in the (F, ω) control space for the ambient starting condition $(x = x' = 0)$, as shown in Fig. 7.

Here, the displayed forms of the bifurcation diagrams for (on the left) direct excitation and (on the right) parametric excitation are seen to be essentially similar in form, emphasizing the wide generality of fractal escape phenomena.

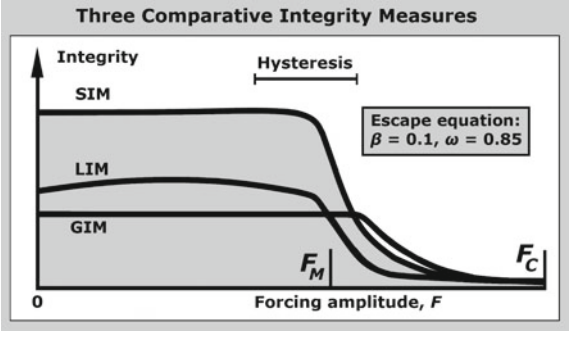

Fig. 6 Comparative Dover cliffs corresponding to the three different integrity measures, SIM, LIM and GIM

المنارة للاستشارات

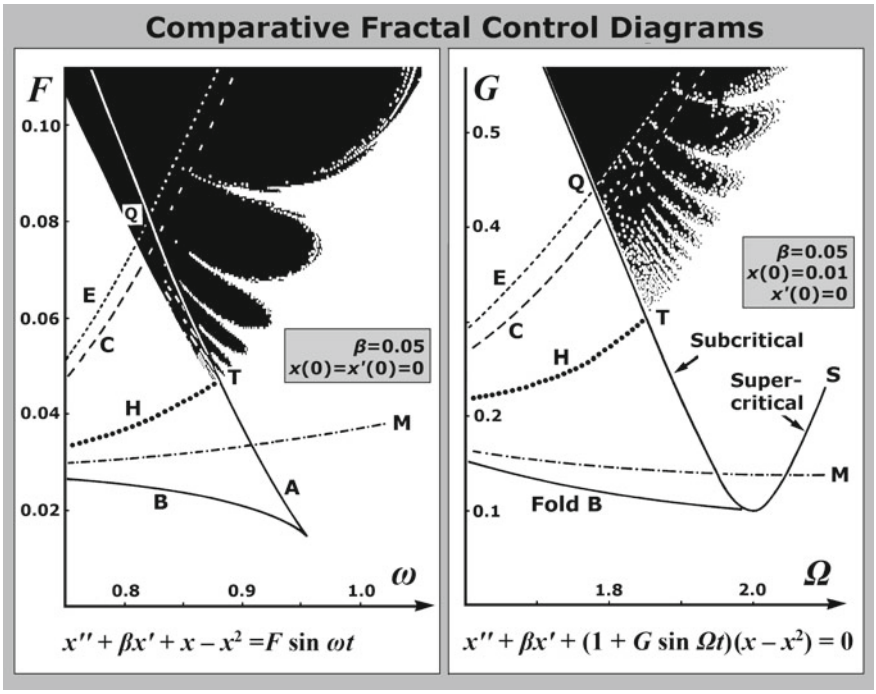

Fig. 7 Comparative fractal control diagrams (at the lower value of damping, $\beta = 0.05$)

4 Lenci-Rega Integrity Measures

Stefano Lenci and Giuseppe Rega have given a great deal of thought, over many years, to the integrity measures that can be most useful in assessing the extent of fractal basin erosion. A useful and comprehensive review of their work can be found in their contribution to my *Festschrift* (Lenci et al. 2013), where they consider in detail experiments on a rotating pendulum and a micro-electromechanical system. Two further sources are their overview of the subject in *Applied Mechanics Reviews* (Rega and Lenci 2015) and their broader perspective of global safety (Lenci and Rega 2011). Here, we shall look at three of their, particularly interesting ideas.

The first is that the phase of the forcing at which the stroboscopic section is taken might play a role (Rega and Lenci 2005). To take account of this, they define the 'true safe basin' as the smallest phase-independent set of initial conditions sharing the desired dynamical property (GIM, LIM, etc.). It is not immediately clear how important this might be.

The second is the introduction of a new measure (Lenci and Rega 2003) that they call the integrity factor (IF) which was displayed earlier in Fig. 4. This is based on the radius of the largest circle that lies entirely in the safe basin. Needing no knowledge of the relevant attractors, this is as computationally easy to use as GIM

المنارة للاستشارات

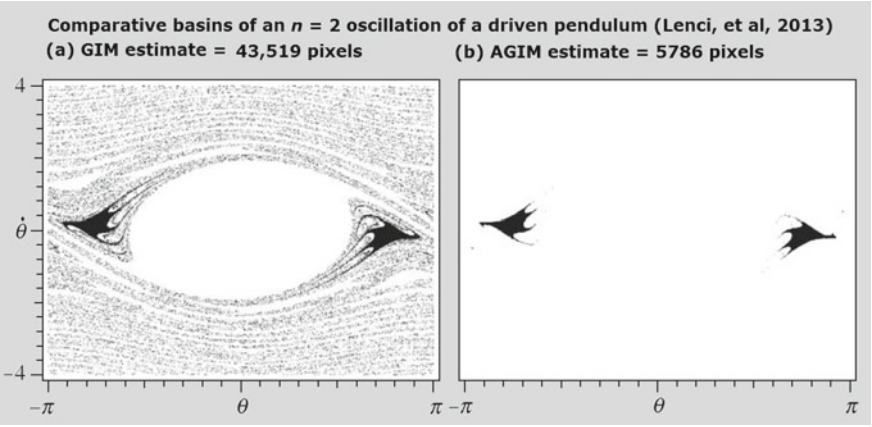

Fig. 8 Safe basins of attraction of the period 2 solution of a driven pendulum. Here **a** shows the 'nominal' basin of attraction, and **b** the 'actual' safe basin

and succeeds in eliminating all the potentially dangerous fractal regimes from the integrity evaluation. As we can see in the figure, it is a very useful measure of the compact part of the safe basin.

The third idea is directed towards improving GIM, which (unlike LIM and IF) tends to count as safe lots of fractal regimes of dubious reliability (Rega and Lenci 2005). They first note that, in practice, safe basins are always obtained in a discrete way, leading to the counting of a finite number of cells or pixels. Each cell can be supposed to have an identifying number (specifying the colour in a picture, for example) defining a distinctive property of interest, which we will here take to be either escape or non-escape. Then, when adding up the cells of a 'nominal' safe basin they propose to eliminate from the count all cells that are not surrounded by cells having the same identifying number. They call the result the 'actual' safe basin in which many of the thinnest fractal parts are no longer present. An extreme example of a 'nominal' safe basin and its associated 'actual' one is reproduced in Fig. 8, which clearly shows the elimination of the fractal parts. When used with GIM, as here, Lenci and Rega call this the 'actual global integrity measure' AGIM.

Examples of four integrity measures are considered and compared with each other by Lenci et al. (2013) for two experiments, a pendulum and a MEMS system.

5 Global Bifurcations of the Erosion Process

Before looking at applications, we devote this section to displaying the underlying mechanisms that are involved in the sharp basin erosion process, as illustrated in Fig. 9. We focus, in particular, on the escape equation (displayed at the foot of the figure) at the fixed damping level of $\beta = 0.1$, but this scenario is known to be common

المنارة للاستشارات

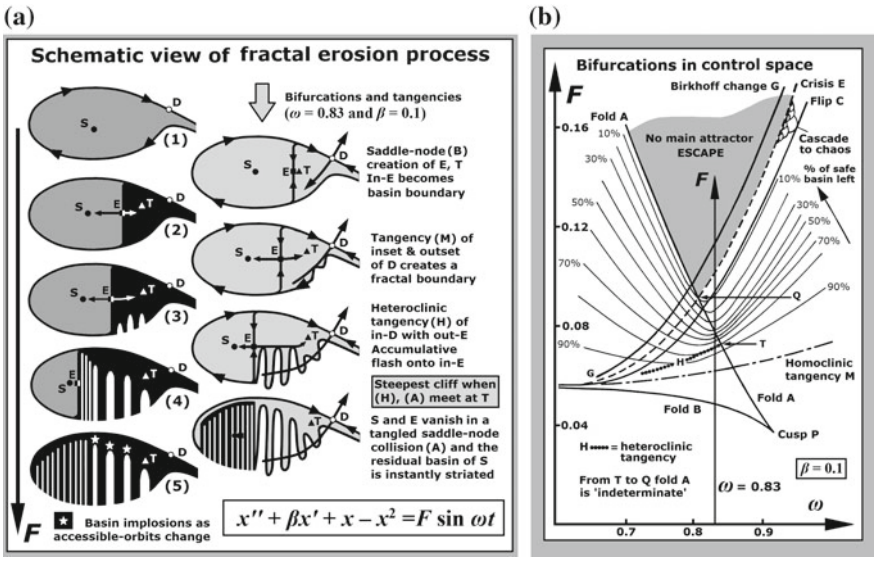

Fig. 9 **a** Mechanics of erosion: a schematic set of basins under increasing F. **b** Mechanics of erosion: various local and global bifurcation curves are displayed in the (F, ω) control space

to a wide variety of periodically driven damped oscillators which involve an escape from a potential well (Soliman and Thompson 1992).

In Fig. 9b is the control space of the forcing amplitude, F, against the forcing frequency ω. Curves in this space denote the various local and global bifurcations that we are obliged to consider if we wish to fully understand the Dover cliff erosion process. In this figure, there is a vertical line at $\omega = 0.83$, and we focus attention on the slow controlled increase of F along this line. The attractor–basin phase portraits that we observe under this sweep of F are displayed in the first column of Fig. 9a, and the bifurcations that trigger changes in these portraits are shown in the second column.

At low F, before we cross curve B in the bifurcation diagram, we have the phase portrait (1). Here, in the phase space of the starting conditions, we show the stroboscopic Poincaré mapping point of the unique non-resonant attractor, S, lying in its grey non-escaping basin of attraction whose boundary is formed by the stable manifold (inset) of the unstable hilltop saddle cycle, D. The constant negative divergence of the phase 'flow', a consequence of the constant positive damping coefficient, β, implies that the basin must have infinite area in the full Poincaré section, with a finite area in any finite window of interest.

The first bifurcation, on crossing curve B, is a local saddle-node fold which creates simultaneously a resonant unstable saddle E, and an adjacent resonant attracting node T. This is the beginning of the hysteresis regime of two competing stable $n = 1$ attractors. The negative divergence implies that T is born with a "residual" basin of (in)finite area. The basin structure after fold B is illustrated in portrait (2). The

المنارة للاستشارات

total non-escaping basin, still bounded by the inset of D, is now divided into two by the inset of the resonant saddle, E with the basin of S shown in grey and the basin of T shown in black. Because the inset of E is born heteroclinically tangled with the unstable manifold (outset) of D, the two bounded coexisting basins accumulate onto D. But the boundaries are still smooth and as yet there is no fractal structure.

This changes as we cross curve M, where the inset and outset of D exhibit a global homoclinic tangency which for low damping can be accurately located by a Melnikov perturbation analysis. Touching once, these two manifolds must touch an infinite number of times, generating at higher F a homoclinic tangle and a fractal basin boundary (Thompson and Stewart 1986). This tangle is displayed very schematically in portrait (3) where large incursive fractal fingers are starting to penetrate into the black resonant basin. However, they have not yet crossed the white line representing the outset of E directed towards T, and the rate of erosion of the safe basin, comprising the union of the basins of S and T, is still relatively low. This white line is crossed when we hit curve H representing a global heteroclinic tangency at which the inset of D touches (at an infinity of points) the outset of E. This triggers a major fractal incursion in which the escaping fractal fingers flash through the outset of E, and accumulate on the inset of E as shown in portrait (4). This generates the rapid rate of erosion of the safe area, under increasing F, at our fixed value of $\omega = 0.83$.

Referring back to the bifurcation diagram of Fig. 9b, we should notice the thin contours lines that show the percentage of the safe basin that remains at a given point in the (F, ω) control space. These show that the steepest Dover cliff can be expected at about the frequency, ω, where curve H hits curve A at the point marked T. This 'worst-case' frequency is close to, but just above the one that we are considering here ($\omega = 0.83$).

Since its creation with the attractor T, at fold B, the resonant saddle E, has been moving steadily across the portrait towards the non-resonant attractor S, and on reaching the fold on curve A, we witness their collision and annihilation. This marks the end of the hysteresis regime involving the two major coexisting harmonic attractors, S, and T. This fold A is, between T and Q, what has been called a 'tangled saddle-node' (Thompson and Soliman 1991) because under slowly increasing F it gives rise to an indeterminate dynamic jump to either the attractor T or completely out of the basin to the 'attractor at infinity'. Correspondingly, at this fold, the (in)finite residual basin of S is instantaneously striated by fine fingers. Under further increase of F, these fine striations thicken out, so that in the final portrait (5) the whole of the black basin of T is heavily eroded by relatively thick fingers. The erosion process continues as a sequence of basin implosions (marked by stars in the last portrait) associated with short-lived subharmonic cascades at the extremities of the major incursive fingers and related to changes in accessible saddle orbits.

Meanwhile, the resonant harmonic attractor, T, period-doubles to a subharmonic of order $n = 2$ with twice the period of the forcing function at curve C marking a local flip bifurcation. This is the start of a full period doubling cascade ending on curve E where the final chaotic attractor is annihilated in an end collision with the current accessible orbit. This global boundary crisis, E, marks the end of the main sequence of attractors after which there is no (major) attractor available to the system

المنارة للاستشارات

and (almost) all the transients lead to escape. These bracketed caveats are needed because there may indeed be small regimes of F containing bounded attractors but these usually have very small basins of attraction. A subsequent change of Birkhoff signature on curve G throws additional light on the escape process as demonstrated by McRobie (1992).

6 Experimental Studies by Lawrence Virgin

Having examined all these fairly intricate theoretical phenomena, based almost exclusively on numerical simulations of simple models, it is important to see to what extent they relate to the real world of the laboratory. A leading figure in the experimental side of nonlinear dynamics is Lawrence Virgin with his team at Duke University, who has published extensively on the subject. Lawrence's book, *Introduction to Experimental Nonlinear Dynamics* (Virgin 2000), is an excellent compendium of their contributions. This work makes extensive use of stochastic interrogation and we start by examining this in a little detail.

Stochastic interrogation applies a sequence of randomly chosen disturbances to an experimental system, thereby inducing transients which explore new areas of phase space, building up a fuller description of the intrinsic dynamics. In his excellent book on experimental dynamics, Virgin first describes how small perturbations from stable and unstable fixed points can be used to estimate their attractive and repulsive eigenvalues. He then describes how this was extended to large perturbations by Cusumano and his co-workers (Cusumano and Kimble 1995) to provide sets of randomly distributed initial conditions strong enough to induce jumps between basins of attraction.

To study basins in this way, a required large perturbation is achieved by imposing a short burst of randomly chosen forcing conditions, before switching back to the basic set of undisturbed forcing parameters. By carefully noting the initial transition through a stroboscopic Poincaré section, subsequent penetrations are tracked until the transient finally settles onto a particular steady-state solution. The coordinates of the initial transition, and all the subsequent penetrations can then be given the identifying colour for the basin of the particular steady state. This single interrogation can then be automated to run repeatedly, with constantly varying random perturbations, to build up a large collection of coloured points displaying the basins of attraction in the section.

The technique is illustrated in the schematic diagram of Fig. 10, reproduced from Waite et al. (2014), where we can see in the grey columns the periods of stochastic input: following which we can watch the transient settling onto a different attractor.

Using this approach Todd and Virgin (1997) made an experimental study of the bifurcations and basin boundary metamorphoses that give rise to the indeterminate jumps from a tangled saddle-node bifurcation. This was done with their gravity-loaded cart-and-track system designed to mimic the twin-well Duffing oscillator, in which the escape from one well to the other is known to exhibit the same generic

المنارة للاستشارات

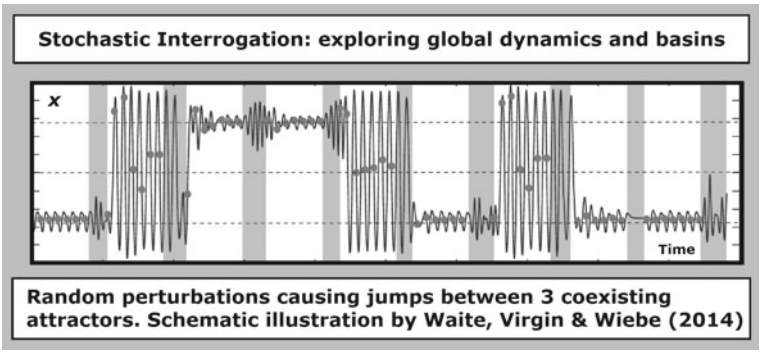

Fig. 10 Schematic illustration of the stochastic interrogation of a laboratory experiment

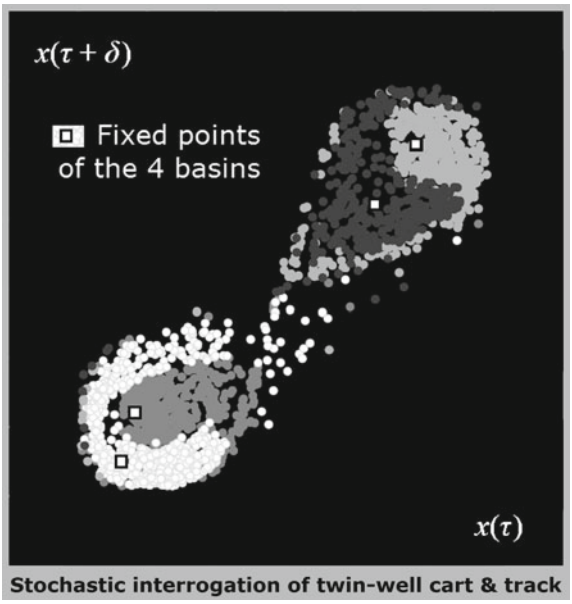

Fig. 11 An experimental phase portrait obtained by stochastic interrogation of a cart-and-track version of the twin-well Duffing oscillator. Fixed-points (squares) and shaded basins of four competing attractors can be seen

features as the single-well escape equation. We reproduce in Fig. 11 one of their attractor–basin portraits from this study, a colour copy of which forms the cover of the aforementioned book. This shows, in time-embedded coordinates, one of the phase-space portraits generated by stochastic interrogation.

The method worked so well that the authors were able to replicate experimentally the subtle global features responsible for the tangled saddle-node that had previously only been seen in numerical simulations. Note, in particular, that the experimental

المنارة للاستشارات

version of our Fig. 9b is presented in Fig. 14.12 of Virgin (2000). In further work Wiebe et al. (2015) made good progress in determining competing basins of attraction by stochastic interrogation for the tricky problem posed by a distributed system represented by a harmonically forced buckled beam.

7 Transient Capsize Diagram

One of the first applications of the integrity ideas was the proposal of a 'transient capsize test' for ships. A vessel excited harmonically by ocean waves coming from the beam can be described by an equation similar to that of our cubic well, with escape from the well now representing its capsize. Using the fact that at the Dover Cliff incursive fractals come sweeping across the centre of what was the safe basin, it was clear that to pin-point the cliff we do not need to use a massive grid of starts but can make just a small number of trial simulations (or model tests) in which a ship in relatively calm water suddenly encounters a train of large fixed-amplitude waves (Thompson et al. 1990; MacMaster and Thompson 1994; Thompson 1997). If the fixed height is below the level corresponding to the cliff the ship will remain upright; if it is above it, the ship will capsize repeatedly. Indeed, a trial simulation from the ambient state at the origin ($x = x' = 0$) will often be adequate to locate the cliff with sufficient precision for practical purposes. This is shown in Fig. 12.

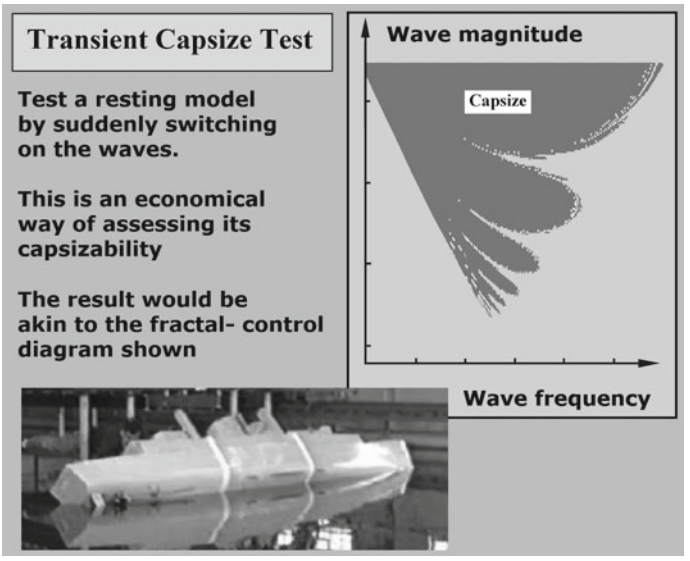

Fig. 12 The transient capsize test producing a plot akin to a fractal control diagram

المنارة للاستشارات

Careful studies showed that, despite the unpredictability of chaotic transients, simulations need only be continued for about 16 wave periods: at a pragmatic engineering level, if a boat does not capsize in 16 forcing cycles it is unlikely to capsize at all. Requiring, then, perhaps only a single simulation from an ambient start at each (F, ω) sea-state, we have a feasible approach for either computer studies or model testing in a wave tank, both of which can otherwise be expensive and time-consuming. This new approach offers distinct advantages over one based on the outdated and narrow concept of steady-state rolling motions.

One standard procedure for testing a small-scale model of a vessel in a wave tank has been to test for capsize in irregular waves of known spectrum, requiring very long experiments, which even then have frequently not produced any capsizes at all because sufficiently steep waves occur so rarely in standard sea spectra. But to make a rational assessment of capsizability in either computer simulations or model tests it is indeed necessary to induce a large number of capsizes. So the new transient capsize approach is seen to be both easier and more relevant than alternative procedures (Rainey and Thompson 1991).

8 Snap-Through of a Spherical Dome

A timely study by Soliman and Gonçalves (2003) examined the nonlinear elastic buckling and dynamics of a shallow spherical dome clamped at its edge and subjected to uniform external pressure, P, as shown in Fig. 13. Considering rotationally symmetric deflected states of the shell, within a one-degree-of-freedom Galerkin approximation, the load P was written as a constant part P_0 plus a time-varying sinusoidal part of amplitude A as shown. With $A = 0$ the static loading would yield snap-through buckling at a critical value of $P = P_C$. For their study, the authors fixed P at $P_0 < P_C$ chosen so that the unbuckled shell was in a metastable state with the potential energy taking the displayed form.

With P_0 and the frequency, ω, both fixed, the aim was to study the nonlinear dynamics under slowly increasing A to investigate the snap-through corresponding to escape from the metastable well. This is then our classical escape problem, yielding the expected safe basin erosion due to the sudden and rapid incursion of fractal fingers. This is quantified by the Dover Cliff of the GIM basin-area function shown in the lower centre picture. Once again, the well-defined cliff edge at A_D offers a better design criterion than the last stable state of the main-sequence attractors at A_S. The authors finally produce an escape boundary in control space of amplitude, A, versus frequency, ω, shown in the right-hand diagram, with the well-established features.

المنارة للاستشارات

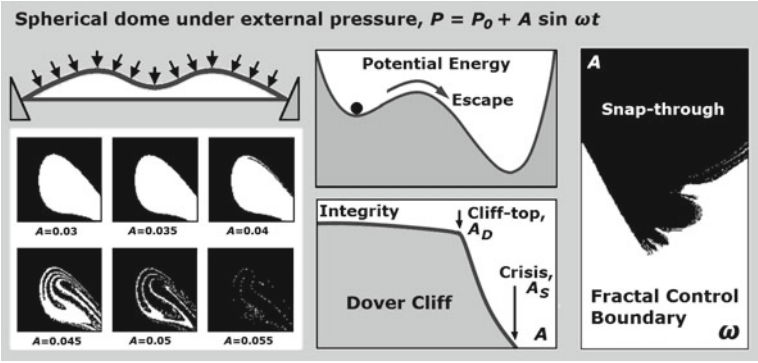

Fig. 13 Integrity study of the snap-through of a pressurized spherical dome

9 Parametrically Excited Cylindrical Shell

A recent paper by Gonçalves et al. (2011) studies the nonlinear dynamics of a long elastic cylindrical shell under uniform axial compression illustrated in Fig. 14. Akin to the spherical dome, the compression is taken to be the sum of a static pre-load and a time-dependent sinusoidal component. The pre-load is again less than the linear buckling load but greater than the static 'lower buckling load'. So the trivial unbuckled state of the shell is statically metastable and can be driven into parametric resonance by the sinusoidal dynamic component. This resonance can drive the shell to escape from its local potential-energy well, leading to its collapse and failure. Designing against this escape requires an examination of the basins of attraction and their fractal erosion, using the concepts of engineering integrity: which is the problem addressed by the authors.

Starting with Donnell's shallow shell theory, the authors use a Galerkin approach to reduce the dynamics to that of a two-degree-of-freedom oscillator, which their earlier studies had shown to be capable of describing qualitatively the complex nonlinear static and dynamic buckling behaviour of the shell. The normal deflection, W, is a function of the circumferential angle, θ, and the axial coordinate, x, and has the general form

$$W(\theta, x) = A_{11}\cos(n\theta)\sin(m\pi x/L) + A_{02}\cos(2m\pi\, x/L) \tag{3}$$

where n is the number of waves in the circumferential direction of the basic buckling or vibration mode, and m is the number of half waves in the axial direction. The potential energy of this oscillator (derived earlier by Popov et al. 1998) is show in Fig. 14, next to a purely notional buckling form of the shell.

With two degrees of freedom, the autonomous shell with no excitation has a 4D phase space, which must be examined in a Poincaré section once the time-dependent excitation is added. The inclusion of some damping in the formulation gives rise

المنارة للاستشارات

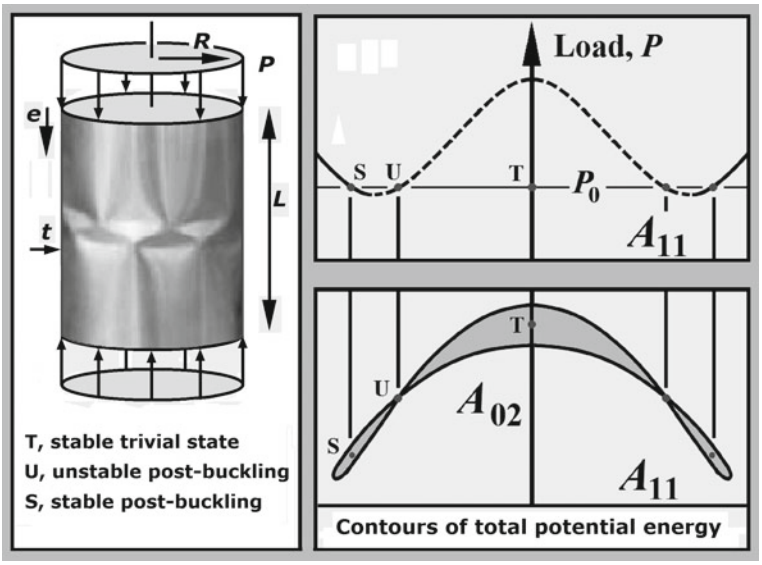

Fig. 14 Two-mode interactive post-buckling of a cylindrical shell

to attractors in these phase spaces, and it is the paths and basins of these attractors that are explored by the authors. Five different broad classes of solution are identified: (1) the trivial pre-buckling solution, (2) the non-trivial subharmonic of order two within the pre-buckling well, (3) the small-amplitude vibrations within each of the post-buckling wells, (4) the medium-amplitude cross-well solutions and (5) a very large-amplitude cross-well period three solution, which is robust in the whole excitation amplitude range. Periodic, quasi-periodic and chaotic solutions are all encountered. The concepts of safe basin and integrity measures are used to quantify the erosion profile of the various solutions. Two characteristic cases, one associated with a sub-critical parametric bifurcation and another with a super-critical parametric bifurcation, are considered in the analysis.

10 Integrity Issues in Atomic Force Microscopy

A new source of applications for the more sophisticated techniques of nonlinear dynamics and chaos has arisen relatively recently in the design of micro-electro-mechanical systems (MEMS) as described by a comprehensive overview in the book by Younis (2011). Here, for example, we find a wide variety of miniature cantilevers which are required to vibrate with great precision in the presence of highly nonlinear (Lennard-Jones) inter-atomic potentials. Among the applications described in this book is the atomic force microscope (AFM) in which a miniature flexible cantilever

المنارة للاستشارات

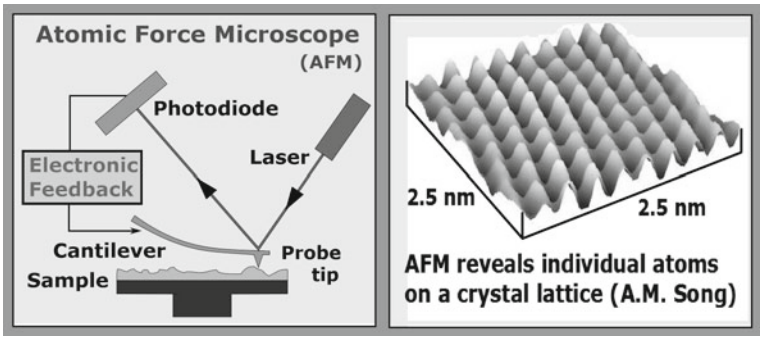

Fig. 15 The atomic force microscope and its view of individual atoms. The right-hand picture is displayed courtesy of Professor Aimin Song, School of Electrical and Electronic Engineering, University of Manchester

with a sharp tip at its free end is used to probe the surface of a sample or specimen. This is illustrated schematically in the left-hand diagram of Fig. 15.

Here a reflected laser beam is used to sense and measure the displacement of the tip perpendicular to the surface of the specimen. For control purposes, an electronic feedback is sometimes employed, but this will not be the case in the experiment that we describe here. On the right of Fig. 15 we show how individual atoms on a crystal lattice can be revealed by an AFM.

Now, in some forms of AFM, the cantilever tip may be designed to make contact with the surface (constantly or intermittently) but we shall focus here on the contact-free method. For this, the cantilever is driven into lateral vibration with the tip very close to, but (hopefully) not making contact with the fixed sample. This can be achieved by an actuator (piezoelectric, magnetic or electrostatic) driving the cantilever into resonance. This driving can be laterally (producing direct resonance of the cantilever) or axially along the cantilever as illustrated in Fig. 16 (producing parametric resonance).

Measurement of the surface profile depends on the fact that whenever the tip (stationary or vibrating) gets extremely close to the sample, it will experience interatomic attractive forces. The Lennard-Jones potential energy of this interaction will be added to the parabolic potential of the cantilever's strain energy, making the dynamic response of the cantilever significantly nonlinear: and in this instance equivalent to that of a ball rolling on the grey energy well of Fig. 16. The cantilever's response to these forces, sensed via the laser beam, can be analysed to supply the required topographical information about the surface of the sample.

Drawn underneath the well in Fig. 16 is the phase portrait of an *undamped* and *undriven* cantilever, with the homoclinic saddle connection clearly seen. Inside this homoclinic orbit, we have the desirable bounded motions, while outside are undesirable 'escaping' motions that result in the tip hitting the specimen. Given that the real cantilever will have damping, the parametric excitation now yields the classic scenario of the 'escape from a potential well'. For which we can expect fractal basin

المنارة للاستشارات

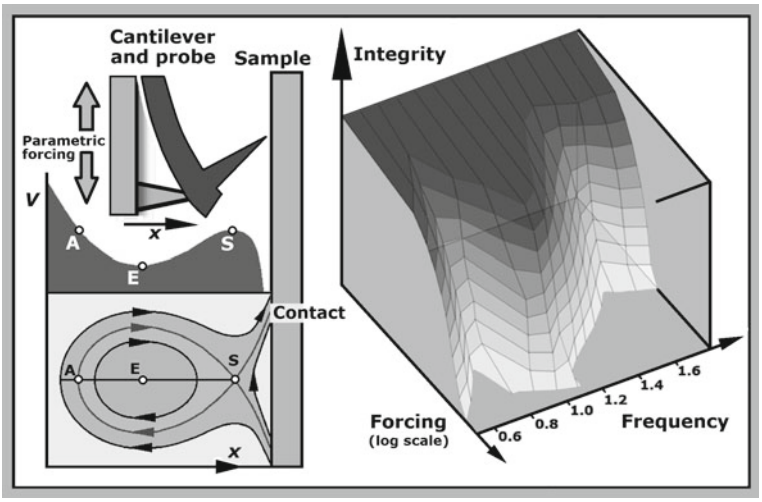

Fig. 16 Basin erosion and loss of integrity in atomic force microscopy (AFM)

boundaries giving basin erosion and loss of dynamical integrity. In this application, escape implies the undesirable 'jump-to-contact instability' resulting (for example) in damage to the tip and/or the specimen. A similar phenomenon described by Younis (2011) is the 'pull-in' instability that can damage miniature parallel-plate capacitors.

In the right-hand diagram of Fig. 16 we show the results of Rega and Settimi (2013) who made a detailed and skillful theoretical study of an AFM of this type. Their three-dimensional Dover Cliff quantifies the loss of dynamical integrity over the two-dimensional control space of the driving magnitude and the driving frequency. The possibility of controlling this loss of integrity is studied by Settimi et al. (2016) and Settimi and Rega (2016).

11 Control Ideas of Lenci and Rega

The most significant step in the extension and development of the integrity idea was made by Stefano Lenci and Giuseppe Rega, who sought to improve the integrity of a nonlinear system by controlling the mechanism of fractal incursion. This incursion was known to be triggered, under increasing harmonic forcing, F, by the first homoclinic tangling of the invariant manifolds (inset and outset) of the hilltop saddle cycle that evolves from the hilltop equilibrium solution. This homoclinic bifurcation at F_M can be located analytically for a lightly damped system by the Melnikov method. Their key idea was to add super-harmonic waveforms to the basic (direct or parametric) harmonic excitation, using the Melnikov theory to predict which of these super-harmonics had the desired (optimal) effect of increasing F_M.

المنارة للاستشارات

One of their first applications of this method was to the directly excited cubic escape equation, often called the Helmholtz oscillator (Lenci and Rega 2003). For this they investigated the mathematical Melnikov problem, to determine the theoretically optimal excitation that maximizes the distance between stable and unstable manifolds for fixed excitation amplitudes. The optimal excitations in the reduced case with a finite number of super-harmonic corrections were first determined, and the optimization problem with infinite super-harmonics was next solved under a constraint on the relevant amplitudes. The mixed case of a finite number of constrained super-harmonics was also considered. All the theoretical results were confirmed by numerical simulations, and the practical effectiveness of the control method was made dramatically visual with the basin erosion and Dover cliff features.

The increase achieved in the basins is displayed here in Fig. 17 where, under fixed conditions of damping, forcing magnitude and forcing frequency, we see the increases of safe basin achieved firstly by optimum control with one super-harmonic and secondly with two super-harmonics.

The comparable shift of the Dover cliff is shown in Fig. 18. This shows the optimally stabilized cliff with from 1 to 10 super-harmonics, and in particular the successful shift of the underlying homoclinic tangency.

Useful reviews of this work on the control of basin erosion, with reference to applications for the Helmholtz, the Duffing and rigid block oscillators is presented by Rega and Lenci (2005, 2008).

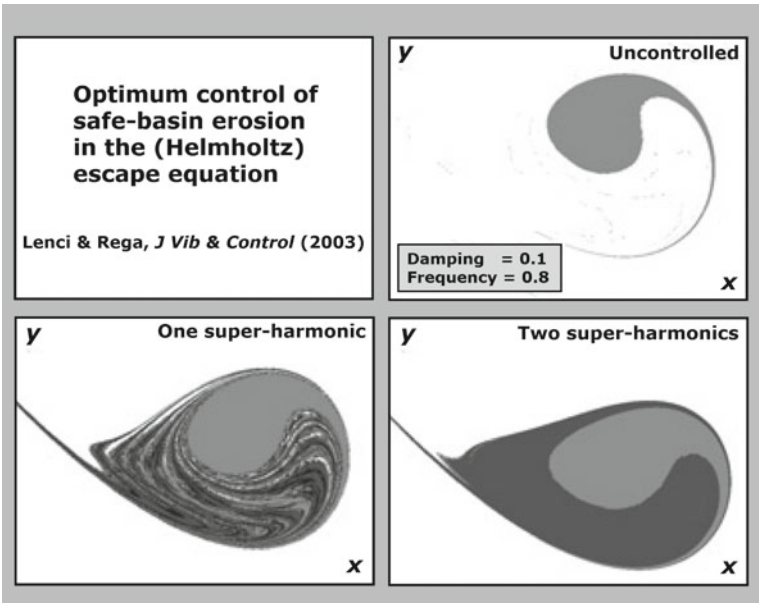

Fig. 17 Safe basin in phase-space enlarged in size by two forms of control

المنارة للاستشارات

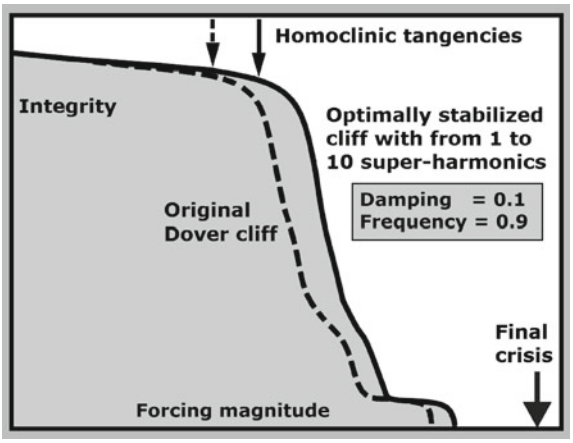

Fig. 18 Improvement in shifting the Dover cliff to higher forcing magnitude

12 Control of Pull-in for an Actuated Micro-beam

We conclude this survey of integrity and its control with a recent application to the dynamic pull-in of an electrically actuated micro-beam (Lenci and Rega 2006). Micro-beams are structural elements employed in the rapidly developing field of micro- and nano-electromechanical systems. Such a beam may be a component in a resonant sensor or an actuator and measured in microns, the order of magnitude of a beam's dimensions might be: length ~100, breadth ~10 and height ~1. In MEMS devices electrostatic and electrodynamic attraction might control displacements of the order of microns, while in NEMS devices, such as scanning probe microscopes, atomic interactions on sharp tips operate at nano-metric scales. Many unfamiliar phenomena come into play at these very small scales, including two forms of damping, namely squeeze-film damping dominant in air and coupled thermo-elastic damping dominant in an ultra-high vacuum. It is the latter that is needed in the present application, so we must say a few words about it. In a vibrating structure, the strain field causes a change in the internal energy such that a compressed region becomes hotter and a stretched region becomes cooler. Irreversible heat flow, driven by the associated temperature gradients, then results in the dissipation of energy underlying the thermo-elastic damping. To quantify this damping requires an analysis of the coupled strain and temperature fields throughout the structure.

The micro-beam in this reported application, in a vacuum with thermo-elastic damping, is required to oscillate freely between two electrodes, and its potential energy has the form illustrated in Fig. 19 where x is the downwards deflection of the centre of the beam.

The unwanted 'pull-in' event corresponds to escape from the well, which physically corresponds to the electrodes hitting one another causing potential damage. Numerical simulations show that, in the now-expected way, there exists fractal basin

المنارة للاستشارات

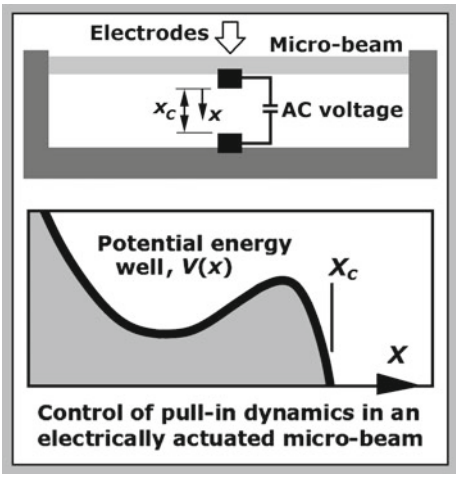

Fig. 19 Micro-beam oscillation in a high vacuum under excitation from the electrodes

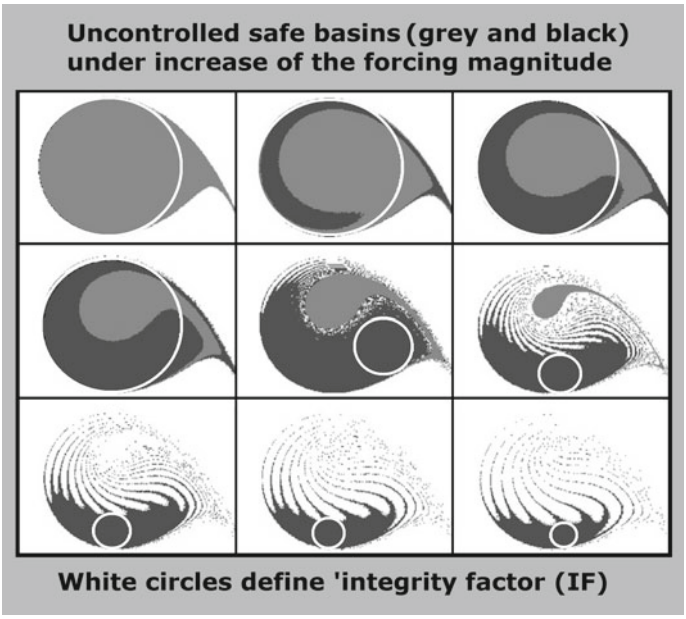

Fig. 20 Original uncontrolled basins of the periodically excited micro-beam

erosion before this pull-in, as illustrated in Fig. 20. Here the safe uncontrolled basins, being the union of the grey and black basins, are seen to be progressively eroded as the forcing magnitude increases.

المنارة للاستشارات

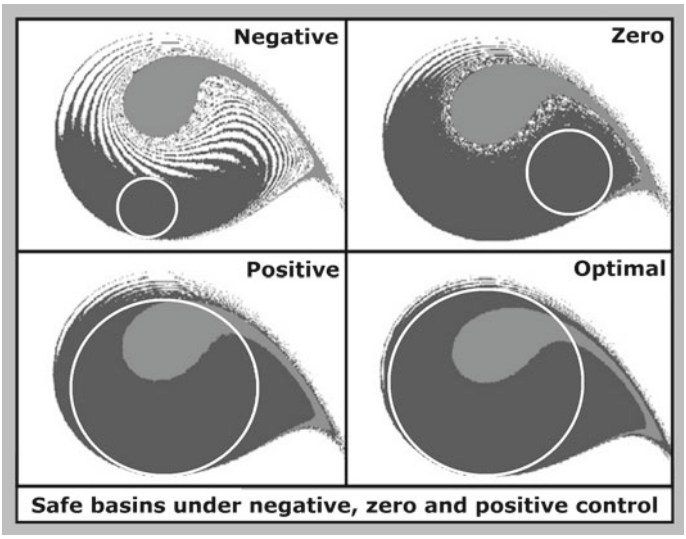

Fig. 21 Successful control of the safe basin of the micro-beam: **a** under negative control, **b** under zero control, **c** under positive control and **d** under optimal control

A significant feature of the paper by Lenci and Rega (2006) is its consideration of two different integrity measures: the global integrity measure (GIM), using the area of the safe basin, and the integrity factor (IF), based on the radius of the largest circle entirely contained in the safe basin as nicely displayed by the white circles in the figure. The authors claim that while the former is a natural and easy measure, it does not properly take into account the fractal tongues eroding the safe basin. The IF is their preferred choice, measuring as it does the 'compact' core of the safe basin, important in many practical applications.

For this study, the authors use a single-well softening model recently proposed by Gottlieb and Champneys (2005) and it is the homoclinic bifurcation, which triggers the safe basin erosion eventually leading to pull-in, that is taken as the undesired event. As in their earlier studies, the authors confirm that appropriate control of added super-harmonics is successful in shifting the tangency towards higher excitation amplitudes. The optimization problem is formulated, and excellent performances of the control method are demonstrated. Figure 21 shows this in terms of safe basins in the stroboscopic phase portrait.

Finally, Fig. 22 shows the shifting of the Dover Cliff for the two integrity measures IF and GIM. In each graph is plotted the response for the beam (1) uncontrolled, (2) under basic control and (3) under optimal control. Great improvements are seen, particularly in the integrity factor (IF) graph. More recent work, examining the response of an imperfect micro-beam, should be noted (Ruzziconi et al. 2013).

المنارة للاستشارات

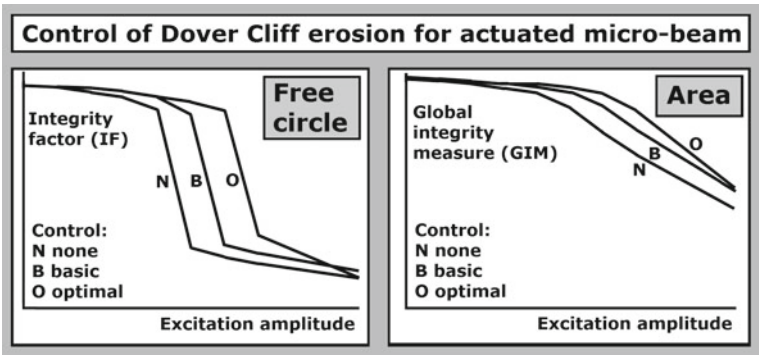

Fig. 22 Dover cliff erosion curves for dangerous pull-in of the actuated micro-beam

13 Concluding Remarks

We have seen in this chapter how the concept of dynamical integrity has been developed into a vital tool for assessing the robustness of driven oscillators to unpredictable finite disturbances, of either a static or dynamic nature. Over the same period, the concept has been used in a wide range of practical applications of mechanics and electro-mechanics. New developments and new applications can be confidently predicted in the years ahead, especially in the expanding arena of MEMS and NEMS.

References

Cusumano, J. P., & Kimble, B. W. (1995). A stochastic interrogation method for experimental measurements of global dynamics and basin evolution: Application to a two-well oscillator. *Nonlinear Dynamics, 8,* 213–235.

Gonçalves, P. B., Silva, F. M. A., Rega, G., & Lenci, S. (2011). Global dynamics and integrity of a two-dof model of a parametrically excited cylindrical shell. *Nonlinear Dynamics, 63,* 61–82.

Gottlieb, O., & Champneys, A. R. (2005). Global bifurcations of nonlinear thermo-elastic micro-beams subject to electrodynamic actuation. In G. Rega & F. Vestroni (Eds.), *IUTAM Symp. Chaotic Dynamics of Systems and Processes in Mechanics* (Vol. 122, pp. 47–57). Solid Mechanics and its Applications. Berlin: Springer.

Lansbury, A. N., Thompson, J. M. T., & Stewart, H. B. (1992). Basin erosion in the twin-well Duffing oscillator: Two distinct bifurcation scenarios. *International Journal of Bifurcation and Chaos, 2,* 505–532.

Lenci, S., & Rega, G. (2003). Optimal control of homoclinic bifurcation: Theoretical treatment and practical reduction of safe basin erosion in the Helmholtz oscillator. *Journal of Vibration and Control, 9,* 281–316.

Lenci, S., & Rega, G. (2006). Control of pull-in dynamics in a nonlinear thermos-elastic electrically actuated micro-beam. *Journal of Micromechanics and Microengineering, 16,* 390–401.

Lenci, S., & Rega, G. (2011). Load carrying capacity of systems within a global safety perspective. Parts I and II. *International Journal of Non-Linear Mechanics*, *46*, 1232–1239 and 1240–1251.

المنارة للاستشارات

Lenci, S., Rega, G., & Ruzziconi, L. (2013). The dynamical integrity concept for interpreting/predicting experimental behaviour: From macro- to nano-mechanics. *Philosophical Transactions of the Royal Society A, 371,* 20120423.

MacMaster, A. G., & Thompson, J. M. T. (1994). Wave tank testing and the capsizability of hulls. *Proceedings of the Royal Society of London, Series A: Mathematical and Physical Sciences, 446,* 217–232.

McRobie, F. A. (1992). Birkhoff signature change: A criterion for the instability of chaotic resonance. *Philosophical Transactions of the Royal Society A, 338,* 557–568.

Popov, A. A., Thompson, J. M. T., & McRobie, F. A. (1998). Low dimensional models of shell vibrations: Parametrically excited vibrations of cylindrical shells. *Journal of Sound and Vibration, 209,* 163–186.

Rainey, R. C. T., & Thompson, J. M. T. (1991). The transient capsize diagram: A new method of quantifying stability in waves. *Journal of Ship Research, 35,* 58–62.

Rega, G., & Lenci, S. (2005). Identifying, evaluating, and controlling dynamical integrity measures in nonlinear mechanical oscillators. *Nonlinear Analysis, 63,* 902–914.

Rega, G., & Lenci, S. (2008). Dynamical integrity and control of non-linear mechanical oscillators. *Journal of Vibration and Control, 14,* 159–179.

Rega, G., & Lenci, S. (2015). A global dynamics perspective for system safety from macro to nano-mechanics: Analysis, control and design engineering. *Applied Mechanics Reviews, 67,* 050802.

Rega, G., & Settimi, V. (2013). Bifurcation, response scenarios and dynamic integrity in a single-mode model of noncontact atomic force microscopy. *Nonlinear Dynamics, 73,* 101–123.

Ruzziconi, L., Younis, M. I., & Lenci, S. (2013). An electrically actuated imperfect microbeam: Dynamical integrity for interpreting and predicting the device response. *Meccanica, 48,* 1761–1775.

Settimi, V., & Rega, G. (2016). Exploiting global dynamics of a noncontact atomic force microcantilever to enhance its dynamical robustness via numerical control. *International Journal of Bifurcation and Chaos, 26,* 1630018.

Settimi, V., Rega, G., & Lenci, S. (2016). Analytical control of homoclinic bifurcation of the hilltop saddle in a noncontact atomic force micro-cantilever. IUTAM Symposium on Analytical Methods in Nonlinear Dynamics. *Procedia IUTAM, 19,* 19–26.

Soliman, M. S., & Gonçalves, P. B. (2003). Chaotic behaviour resulting in transient and steady state instabilities of pressure-loaded shallow spherical shells. *Journal of Sound and Vibration, 259,* 497–512.

Soliman, M. S., & Thompson, J. M. T. (1989). Integrity measures quantifying the erosion of smooth and fractal basins of attraction. *Journal of Sound and Vibration, 135,* 453–475.

Soliman, M. S., & Thompson, J. M. T. (1990). Stochastic penetration of smooth and fractal basin boundaries under noise excitation. *Dynamics and Stability of Systems, 5,* 281–298.

Soliman, M. S., & Thompson, J. M. T. (1992). Global dynamics underlying sharp basin erosion in nonlinear driven oscillators. *Physical Review A, 45,* 3425–3431.

Stewart, H. B., Thompson, J. M. T., Lansbury, A. N., & Ueda, Y. (1991). Generic patterns of bifurcation governing escape from potential wells. *International Journal of Bifurcation and Chaos, 1,* 265–267.

Thompson, J. M. T. (1989). Chaotic phenomena triggering the escape from a potential well. *Proceedings of the Royal Society of London, Series A: Mathematical and Physical Sciences, 421,* 195–225.

Thompson, J. M. T. (1997). Designing against capsize in beam seas: Recent advances and new insights. *Applied Mechanics Reviews, 50,* 307–325.

Thompson, J. M. T., Rainey, R. C. T., & Soliman, M. S. (1990). Ship stability criteria based on chaotic transients from incursive fractals. *Philosophical Transactions of the Royal Society A, 332,* 149–167.

Thompson, J. M. T., Rainey, R. C. T., & Soliman, M. S. (1992). Mechanics of ship capsize under direct and parametric wave excitation. *Philosophical Transactions of the Royal Society A, 338,* 471–490.

المنارة للاستشارات

Thompson, J. M. T., & Soliman, M. S. (1990). Fractal control boundaries of driven oscillators and their relevance to safe engineering design. *Proceedings of the Royal Society of London, Series A: Mathematical and Physical Sciences, 428,* 1–13.

Thompson, J. M. T., & Soliman, M. S. (1991). Indeterminate jumps to resonance from a tangled saddle-node bifurcation. *Proceedings of the Royal Society of London, Series A: Mathematical and Physical Sciences, 432,* 101–111.

Thompson, J. M. T., & Stewart, H. B. (1986). *Nonlinear dynamics and chaos.* Chichester: Wiley (second extended edition, 2002).

Todd, M. D., & Virgin, L. N. (1997). An experimental verification of basin metamorphoses in a nonlinear mechanical system. *International Journal of Bifurcation and Chaos, 7,* 1337–1357.

Virgin, L. N. (2000). *Introduction to experimental nonlinear dynamics*. Cambridge: Cambridge University Press.

Waite, J. J., Virgin, L. N., & Wiebe, R. (2014). Competing responses in a discrete mechanical system. *International Journal of Bifurcation and Chaos, 24,* 1430003.

Wiebe, R., Virgin, L. N., & Spottswood, S. M. (2015). Stochastic interrogation of competing responses in a nonlinear distributed system. *Nonlinear Dynamics, 79,* 607–615.

Younis, M. I. (2011). *MEMS linear and nonlinear statics and dynamics*. New York: Springer.

المنارة للاستشارات

Dynamical Integrity: A Novel Paradigm for Evaluating Load Carrying Capacity

Giuseppe Rega, Stefano Lenci and Laura Ruzziconi

Abstract The chapter offers an overview of the effects of the research advancements in nonlinear dynamics on the evaluation of system safety. The achievements developed over the last 30 years entailed a substantial change of perspective. After recalling the outstanding contributions due to Euler and Koiter, we focus on Thompson's intuition of global safety. This concept represents a paramount enhancement, full of theoretical and practical implications. Its relevance as a novel paradigm for evaluating the load carrying capacity of a system is highlighted. Making reference to a variety of different case studies, we emphasize that global safety has induced a deep development in the analysis, control, and design of mechanical and structural systems. Recent results are presented, and the possibility to implement effective dedicated control procedures based on global safety concepts is explored. We stress the importance of global safety for valorizing all the potential of the system and guaranteeing superior targets. The very general character of the dynamical integrity approach to design is highlighted.

Keywords Global safety · Dynamical integrity · Load carrying capacity · Novel paradigm

G. Rega (✉)
Department of Structural and Geotechnical Engineering,
Sapienza University of Rome, Rome, Italy
e-mail: giuseppe.rega@uniroma1.it

S. Lenci
Department of Civil and Building Engineering and Architecture,
Polytechnic University of Marche, Ancona, Italy
e-mail: lenci@univpm.it

L. Ruzziconi
Faculty of Engineering, eCampus University, Novedrate, Italy
e-mail: laura.ruzziconi@uniecampus.it

© CISM International Centre for Mechanical Sciences 2019

S. Lenci and G. Rega (eds.), *Global Nonlinear Dynamics for Engineering Design and System Safety*, CISM International Centre for Mechanical Sciences 588,
https://doi.org/10.1007/978-3-319-99710-0_2

المنارة للاستشارات

1 Introduction

Determining the load carrying capacity is essential in the engineering design to operate the system with the desired outcome. Outstanding contributions were due to Euler (1744) and Koiter (1945), who laid the foundation for studying this issue. Initially, the analysis was performed in the framework of the local stability theory. Successively, the problem was reconsidered by Thompson (1989), who realized that the local stability may be not enough. This is because disturbances inevitably exist in real-world applications. They give uncertainties to the operating initial conditions. If the system is not sufficiently "robust" to tolerate them, they may lead in practice to an outcome completely different from what theoretically predicted by local achievements. For this reason, we need to perform additional investigations and complement the analysis by studying the system also from a global safety perspective (Thompson and Stewart 2002; Thompson 2018).

This basic idea was clearly formulated in the first pioneering papers. Thompson (1989) fully identified the global safety issue. He emphasized that from a practical point of view, the rapid erosion of the basin boundary represents a dramatic loss of engineering integrity for any system, which may be easily destroyed in a noisy real-world environment. To deeply investigate this aspect, he introduced engineering dynamical integrity diagrams, which neatly summarize the progressive loss of the basin area. Soliman and Thompson (1989) attempted to properly quantify the dynamical integrity. They realized that the robustness of the system's response usually needs to be addressed from a variety of different perspectives. They proposed four alternative dynamical integrity measures, each one of which is focused on a specific aspect in order to estimate properly the system's structural safety according to the requirements arising in the engineering design. Specifically, they introduced the Global Integrity Measure (*GIM*), the Local Integrity Measure (*LIM*), the Impulsive Integrity Measure (*IIM*), and the Stochastic Integrity Measure (*SIM*). Lansbury et al. (1992) discussed the need of an appropriate definition of safe basin, i.e., of the set of initial conditions which may be considered as "safe" for the system.

The relevance of the global analysis for a safe engineering design was clear since the outset. Investigating the capsizing of a ship (Thompson et al. 1990; Soliman and Thompson 1991; Rainey and Thompson 1991; Thompson 1997), it has been observed that the safe basin is eroded quite suddenly, which implies that the wave height at capsizing is significantly smaller than the height where the final steady-state motion loses stability. This analysis offered a new approach to the quantification of ship stability in waves. Analyzing driven oscillators (Soliman and Thompson 1992), the mechanism of basin erosion has been described and its occurrence in a wide class of nonlinear systems has been highlighted. The rate of erosion is intrinsically dependent upon the manifolds organization, which to a large extent is determined by the global events following the homoclinic tangency. Dynamical integrity diagrams have been performed to examine the loss of engineering integrity due to the rapid erosion of the non-escaping basin, when varying the driving parameters. Dealing with the erosion phenomenon (Thompson and Soliman 1990), the incursive escaping fingers

المنارة للاستشارات

have been shown to sweep across the center of the safe basin in correspondence of the fall of dynamical integrity. This yields the characteristic "Dover Cliff" profile. Abstracting from the particular case study, a deep discussion about the issue of global safety in a mechanical system has been developed. In the stochastic framework (Soliman and Thompson 1990), the stochastic penetration of smooth and fractal basin boundaries under noise excitation has been examined and the effect of external noise on a steady-state attractor has been investigated using a dynamical integrity measure suitably defined for the stochastic case.

Starting from these seminal works, global safety concepts and tools have been further developed. Additional definitions of safe basin have been considered. For instance, Lenci and Rega (2004a, d) investigated the True Safe Basin, which attempts to extend the analysis to the special case where phase-independent arguments are required, e.g., in impacting systems. Focusing on the nontrivial issue of assessing properly the dynamical integrity, other measures have been suggested. Lenci and Rega (2003a, b) proposed the Integrity Factor (*IF*), which is able to catch and combine the main aspects of both the *GIM* and the *LIM*. Lenci et al. (2013) introduced the Actual Global Integrity Measure (*AGIM*), where a different theoretical approach is assumed to focus only on the sole compact part of the safe basin. Belardinelli et al. (2018) refer to the Anisotropic Local Integrity Measure (*ALIM*) and the Anisotropic Integrity Factor (*AIF*), which generalize, respectively, the *LIM* and the *IF* to account for inhomogeneous sensitivities of the state-space variables to perturbations. Furthermore, the protection thickness has been proposed by Sun (1994), the ratio of safe initial points by Gan and He (2007), the maximum speed of erosion by de Souza Jr. and Rodrigues (2002), etc. The principal definitions of safe basins and the principal definitions of dynamical integrity measures are compared by Rega and Lenci (2005, 2008), with also a view to control aspects, highlighting their distinctive features and main characteristics.

The global safety analysis has been observed to properly interpret and predict the experimental data (Ruzziconi et al. 2018). In a pendulum parametrically excited by wave motion, Lenci and Rega (2011a) found that rotations exist experimentally only where the dynamical integrity is large enough, so that the system can support experimental imperfections leading to changes in the initial conditions. In a capacitive accelerometer, Ruzziconi et al. (2013d) and Alsaleem et al. (2010) noticed that the experimental vulnerability to dynamic pull-in develops well before the theoretical inevitable escape. Impressive are the reported results. The experimental pull-in bands deviate considerably from the classical theoretical simulations based on the Lyapunov stability theory, whereas they approach closely the dynamical iso-integrity curves. In a microbeam-based microelectromechanical system (MEMS), Ruzziconi et al. (2013a, c, f) explored the possibility to apply the global safety analysis for addressing different issues commonly encountered in the engineering design. This analysis proved effective to identify the unknown parameters, which is essential to formulate a reliable mechanical model. Also, it was applied to determine the range of applicability of the model, after which the theoretical results start decreasing their accuracy with respect to the experimental data. As highlighted by Lenci et al. (2013), all the aforementioned experimental studies differ not only for being both in

المنارة للاستشارات

the macro- and microscales, but, more importantly, for their dynamical characteristics. They may be considered as complementary examples, which implicitly confirm the general value of the global safety analysis.

Global safety investigations have been the subject of renewed interest in view of their applications to many different structures (Gonçalves et al. 2018). In the Augusti's model, Orlando et al. (2011) analyzed the influence of nonlinear modal interactions on the dynamical behavior and examined the basins evolution due to variation of the system's parameters. Erosion profiles have been performed, which illustrate the loss of safety of the structure due to penetration of eroding fractal tongues into the safe basin. In a MEMS device with bistable static configuration, Ruzziconi et al. (2012, 2013b) examined the development of considerable versatility of behavior, which may be desirable in applications. Due to the complexity of the system's response, the dynamical integrity analysis is called not only to address the classical problem of the disappearance of an attractor but also to predict the practical final behavior. In noncontact Atomic Force Microscopy (AFM), Rega and Settimi (2013) identified the overall stability boundary in the excitation parameter space and analyzed the erosion profiles of the bounded attractors. The need to identify the practical escape thresholds was discussed, in order to ensure an a priori design safety target. In an excited cylindrical shell (Gonçalves and Del Prado 2002, 2005; Gonçalves et al. 2007), Gonçalves et al. (2011) focused on the parametric instability and escape boundaries. They were the first to address the dynamical integrity issue in dimensions higher than one. They examined the changes of the basins of attraction in the four-dimensional phase space and developed integrity profiles to measure the magnitude of the safe basin of the various solutions.

The global safety analysis has been increasingly referred in control issues. A controller has been designed by Lenci and Rega, which aims at controlling the overall system dynamics. This method was initially formulated for the optimal control of chaos in discontinuous mechanical systems and successively generalized to continuous nonlinear oscillators. It has been applied, for instance, to control the chaotic response region in a simple inverted pendulum with rigid unilateral constraints (Lenci and Rega 1998a), the nonlinear dynamics in a two-well impact system (Lenci and Rega 1998b, c), the single-well to cross-well chaos transition (Lenci and Rega 2003c), the final behavior in asymmetric oscillators (Lenci and Rega 2004c), etc. In this respect, the global safety analysis plays a key role since is essential to investigate in detail the effectiveness of the control technique from a global viewpoint and verify its performances. In the Helmholtz oscillator (Lenci and Rega 2003a), the controller excitations have been shown to be able to increase the homoclinic bifurcation threshold, i.e., to defer the beginning of the erosion, thus preserving for larger parameter ranges the integrity of the system. In a Duffing oscillator (Lenci and Rega 2003b), the influence of the control on the reduction of the erosion was examined by comparing the erosion profiles at different excitations, which aims at reducing the sensitivity to initial conditions. In a thermoelastic electrically actuated microbeam (Lenci and Rega 2006b), by relying on the results achieved in the dynamical integrity analysis, the controller was able to avert the pull-in threshold and shift it toward higher excitation amplitudes. In both the Augusti's model and in an inverted guyed

المنارة للاستشارات

pendulum (Lenci et al. 2012b), the dynamical integrity was decreased by the complex nonlinear phenomena, while the controller was proven to increase their safety in a dynamic environment. A unified control framework of the nonregular dynamics was presented in Rega and Lenci (2003) and in Lenci and Rega (2004b). For comprehensive overview of recent advances in control, we refer to Rega and Lenci (2009) and Rega et al. (2010).

Local versus global perspective in both dynamics and control has been widely analyzed by Settimi and Rega (2018). Focusing on a noncontact AFM microbeam, the issue of adopting an effective control method has been explored in order to keep the system response in an operationally suitable regime, which is necessary for a reliable measurement of the sample surface. Initially, an external feedback control technique was applied (Settimi et al. 2015; Settimi and Rega 2016c). Extensive simulations were performed, and the stability regions were detected to evaluate both the effectiveness of the control actuation and the possible criticalities on the overall response. Developing systematic dynamical integrity simulations (Settimi and Rega 2016b), the considered control technique was demonstrated to work well for the "local" purpose for which it is specifically designed. Nevertheless, some meaningful drawbacks arise. A worsening of the system's practical stability has been noticed especially in the very sensitive region around the resonance frequencies, where, instead, the system global behavior has to be more strictly taken under control in practical applications. For this reason, a different control technique has been assumed (Settimi and Rega 2016a), which was developed along the same line proposed by Rega and Lenci (2009). This global control method was based on exploiting the global dynamical features and aimed at obtaining an enlargement of the system's safe region in parameters space. It allowed detecting the value of the optimal superharmonic to be added for shifting the global bifurcation to a higher value of forcing amplitude, and succeeded in delaying the drop down of the erosion profile, thus increasing the overall robustness of the AFM system.

Global safety predictions have been recently accounted in the stochastic framework. In an archetypal model of a structure liable to post-buckling behavior, Gonçalves and Santee (2008) showed that uncertainties in parameters or small random perturbations of the applied load generally lower the system's load carrying capacity with respect to the unperturbed ideal case. However, the scatter of results is well above the Melnikov threshold. In this respect, the iso-integrity curves have been suggested as reliable, but not conservative, lower bounds of safety. Further developing these results in different systems, Silva et al. (2013) and Silva and Gonçalves (2015) observed the influence of inherent uncertainties and random noise on the attractor-basins organization. Their non-negligible effects in terms of global safety have been analyzed by resorting to different dynamical integrity measures. When dealing with structures liable to instability, these effects must be carefully taken into account to state a proper definition of safety factors.

In addition to the theoretical aspects, also the computational techniques have been examined. The cell-to-cell mapping method introduced by Hsu (1987) has been widely referred in the literature, and several variants have been proposed to improve the computational efficiency. They have been applied in many engineering

المنارة للاستشارات

applications (Hong and Sun 2006; Sun 2013). Efforts have been made to extend this method in case of systems with many degrees-of-freedom (van Campen et al. 1995; Kreuzer and Lagemann 1996; Eason and Dick 2014). Implementation with parallel routines for investigating domain's topology has been suggested (Belardinelli and Lenci 2016a, b). For a complete and detailed overview of recent advancements in this field, we refer to Xiong et al. (2018) and references therein.

Overall, nonlinear dynamics is a valuable source. They have "*the potential to significantly enhance performance, effectiveness, reliability and safety of physical systems as well as offering novel technologies and designs*" (Wiercigroch and Rega 2013), and "*it is time to develop basic technologies to take advantage of the natural richness of behavior offered by nonlinear systems*" (Wiercigroch and Pavlovskaia 2008). The global safety theory exactly points in this direction. This concept allows establishing a novel paradigm to evaluate accurately and properly the load carrying capacity of a system. This is fundamental to enhance its safety and valorize all its potential in engineering applications.

For all these reasons, in the nonlinear dynamics community, the introduction of global safety has entailed a substantial change of perspective (Rega and Lenci 2015), which meaningfully affects analysis, control, and design of mechanical and structural systems. This chapter aims at highlighting, discussing, and reviewing the main aspects. Dwelling on various case studies coming from different fields, major achievements are presented and recent results are reported. Both common and more specific problems are examined. Additional case studies can be found in the forthcoming chapters of the present book, where further selected models are considered, which are extracted from a magnitude of different contexts of interest.

The chapter is organized as follows. In Sect. 2, the global safety perspective is introduced, by presenting the basic idea and shading light on the main aspects. In Sect. 3, the dynamical integrity tools are examined (safe basin, alternative dynamical integrity measures, and dynamical integrity diagrams), showing the importance of the dynamical integrity as a novel criterion for evaluating the load carrying capacity of a system. Sections 4–6 investigate the use of global safety concepts in the analysis (Sect. 4), control (Sect. 5), and design (Sect. 6); reference is made to different systems and/or models of interest in applied mechanics. In Sect. 7, the main conclusions are summarized.

2 Achieving the Load Carrying Capacity

In this section, we introduce Thompson's notion of global safety (1989). After briefly recalling the historical background, the basic underlying idea is presented. This represents a valuable advancement for the research community, both from a theoretical and from a practical viewpoint. We emphasize the fundamental role of the dynamical integrity to develop a novel paradigm for a reliable estimation of the actual load carrying capacity of a system. By means of an archetypal model, the principal aspects of global safety are illustrated. The Euler, Koiter, and Thompson load carrying capacity

المنارة للاستشارات

are evaluated, compared, and discussed. The aim of the reported case study is that of giving a preliminary overview of the importance of global safety for engineers and designers, while leaving a deep insight on the specific issues for the forthcoming sections.

2.1 *Three Outstanding Contributions: Euler, Koiter, and Thompson*

Achieving the load carrying capacity of a dynamical system and keeping it when varying some design parameter is a very sensitive item, full of theoretical relevance and practical implications, which has been increasingly attracting the attention of researchers since the past. This topic is intrinsically associated with the concept of loss of stability. It was a long history of successes and defeats of scientists, which, in the authors' opinion, still extends over the present time. In the following, we focus on the major historical contributions due to Euler, Koiter, and Thompson.

The earliest outstanding study was due to Euler (1707–1783). He was the first to discover the *loss of stability* of an equilibrium configuration. In his original work (Euler 1744), he considered a column subjected to compressive axial load. When increasing the axial load, he realized that there is a threshold beyond which the system exhibits buckling behavior. He determined the famous Euler buckling load of a column and obtained a pitchfork bifurcation, i.e., a bifurcation of the branching type. Talking in modern language, the loss of load carrying capacity was identified with the system instability occurring at the local bifurcation point of an equilibrium path, when varying a driving parameter. Note that Euler was referring to perfect structures, i.e., structures without model imperfections. The concept of stability was not developed at that time; nevertheless, it is felt that the main idea of loss of stability was already lurking in Euler's background, although in a substantially static framework.

The concept of *stability* was formulated in a rigorous way only much later, with the major contribution, among others, of Lyapunov (1857–1918) (Lyapunov 1892). We quote Leine (2010) for an interesting historical overview of the development of the stability concepts. The mathematical definition of Lyapunov (or classical) local stability roughly states that under infinitesimal changes in the initial conditions, the system must keep the reference response. Thus, the definition of stability was formulated in terms of sensitivity of the system's behavior to changes in the initial conditions. This formulation is more dynamically oriented.

The introduction of the stability concept was and is a very important advancement in research, for instance, it plays a major role in the solution of a variety of engineering problems ensuing from modern technological development.

Within this context, the second outstanding contribution to the load carrying capacity issue was due to Koiter (1914–1997). He was the first to discover that the load carrying capacity of a system is sensitive to *static* perturbations, which are always present in nature and technology (Koiter 1945). In fact, under realistic conditions, the system is inevitably subjected to model imperfections (perturbations of

المنارة للاستشارات

static nature). They may strongly influence the load carrying capacity of the system and they may seriously lower its critical load. As an example, due to the imperfections, the branching point of an equilibrium path becomes a snap point, which, in the dangerous cases, corresponds to a meaningfully lower load threshold. Thus, static perturbations have to be taken into account carefully for a safe engineering design.

This idea and its successive developments were so important that investigation in this direction continues up to date (e.g., Mang et al. 2009). In some sense, Koiter was a precursor—in the mechanical community—of the unfolding concept of the bifurcation theory, as well as of the associated structural stability issue.

Indeed, later on, the bifurcation theory provided a mathematical background (Guckenheimer and Holmes 1983; Wiggins 1990; Troger and Steindl 1991; Kustnezov 1995; Nayfeh and Balachandran 1995) to this engineering intuition, with the development of the *structural stability* concept, which studies the perturbations of the system with respect to the parameters and not with respect to the initial conditions, as in classical local stability. Although the idea is simple, the general theorems are very complex and abstract. Among the major achievements, we recall, for instance, that it has been rigorously shown that both transcritical and pitchfork bifurcations (responsible for branching) are structurally unstable events, i.e., they are unobservable in the real world, unless their occurrence is forced by some constraint (e.g., symmetry). In fact, when adding perturbations in the system (imperfections in mechanical language), both of them are proven to become saddle-node bifurcations (responsible for snap).

Structural stability is part of the more general *catastrophe theory* (Thom 1972; Zeeman 1977). Yet, when applied to engineering problems in classical mechanics (such as buckling), structural stability has still a substantially local character.

Although at Koiter's time it was clear that stability is a dynamical concept (Budiansky and Hutchinson 1964), the major initial contributions were concerned with a "static" stability approach (Pignataro et al. 1990; van der Heijden 2009). Successively, "flutter" or "galloping" came to the attention of researchers (see Thompson (1982) for a theoretical approach and Novak (1969) for a practical approach). In the bifurcation theory language, the Hopf bifurcation was "discovered" to exist in practice, according to the fact that it is a structurally stable event. It was actually seen to occur, e.g., in the dramatic failure of the Tacoma Bridge or in other aero-elastically induced collapses of structures. Hereafter, dynamics definitely entered the problem of loss of stability. However, only *local* bifurcational events were concerned, indeed.

All this background is the framework of the third outstanding contribution on the load carrying capacity issue, which was due to Thompson (1989). Around the 90s, he realized that *engineering* perturbations can have a *dynamic* nature and not only a static one, as in Koiter's vision, and mostly that they can be of *finite* magnitude. Indeed, in real-world applications, the system is inevitably subjected not only to model imperfections but also to possibly meaningful disturbances in the initial conditions. Their effects on the response may be dramatic. To take them into account, Thompson understood that, in addition to the classical local stability analysis, the system's load carrying capacity has to be investigated also from a *global safety* perspective. In these regards, he introduced the notion of *dynamical integrity*.

المنارة للاستشارات

Thus, the concept of global safety updates and broadens the classical concept of stability, by complementing its solely local theoretical character with a global practical one. For all these reasons, in spite of its conceptual simplicity, Thompson's intuition represents a paramount enhancement, full of new items and important consequences.

2.2 Global Safety Perspective: The Basic Idea

According to the classical stability theory, small changes in the initial conditions do not affect substantially the system's response. However, how small have to be perturbations? From a mathematical point of view, the magnitude of perturbations is not important (e.g., 10^{-50} is ok). From a practical point of view, instead, this point is far from being indifferent. In fact, disturbances in the initial conditions are unavoidable in real-world applications. They inevitably have a *finite* magnitude, although small, and not an *infinitesimal* one. This may induce serious effects on the final behavior of the system. Quoting from Gonçalves et al. (2007), "*small perturbations not exceeding the stability threshold usually have a transient character and are followed by the full recovery of the desired regime,*" but "*large ones can cause deviations out of the stability domain and may potentially lead to irreversible system breakdown.*" Considering only infinitesimal changes in the initial conditions, which makes sense from the mathematical viewpoint, appears weak from a mechanical and/or practical one.

That is to say, the (Lyapunov) classical stability analysis is indispensable for studying a system, since it enables to detect the attractors, determine the parameter ranges where they "theoretically" exist, explore their bifurcational events, illustrate their unique characteristics in terms of periodic and/or chaotic behavior, etc. All this investigation is essential, and we cannot prescind from it. Nevertheless, this is not enough for practical applications, since does not inform whether these theoretical predictions are actually robust against disturbances in the initial conditions. Because of them, in the parameter range where the "theoretical stability" according to the classical local viewpoint is guaranteed, the "practical stability" may be not automatically ensured.

This aspect is not trivial. To address it, we need to investigate the system also from the (Thompson) global safety perspective, i.e., the results obtained via the classical local stability theory have to be further developed and combined with the results achieved by analyzing the safety from a global viewpoint. The former detects the range of theoretical existence of the desired behavior; the latter starts from these results and detects the practical subset of this parameter range where the desired behavior may effectively sustain relatively large perturbations in the initial conditions without changing the final outcome, namely, where the classical theoretical predictions may be effectively observed in practice.

Thus, to investigate the classical stability a *local* analysis is sufficient, whereas to investigate the global safety a *global* analysis is required. In fact, assessing the

المنارة للاستشارات

robustness of a given solution against disturbances in the initial conditions naturally involves attractor-basins investigations. From their observation, Thompson had a double intuition and realized the following two main points:

(i) If the safe basin of a given, desirable, solution is not "*large*" enough, even if the solution is stable there will be no hope to observe it in real-world applications (seeing that, as previously observed, classical local stability refers to infinitesimal changes in initial conditions, while global safety refers to finite changes in initial conditions). This was his first fundamental understanding. In other words, safe basins must have a large enough magnitude.
(ii) A second fundamental requirement for actual global safety is that the safe basin must be topologically "uncorrupted" or "*dynamically integer*" (e.g., non-fractal). More precisely, for a reliable estimation of the load carrying capacity, we have to trust only on the compact part of the safe basin, ruling out fractality, squeezing, and other topological effects which reduce safety without appreciably affecting the magnitude of the safe basin.

Accordingly, global safety highlights that only the behaviors equipped with sufficient dynamical integrity can be actually expected under realistic conditions. The others are too vulnerable to disturbances and in practice cannot be observed in experiments and applications. This consideration paves the way to the introduction of a novel criterion for evaluating the load carrying capacity of a system, which is based on the results coming from dynamical integrity investigation. This enables the designer to widen the traditional range of applicability of the system and best use all its potential, while keeping ensuring adequate safety targets.

2.3 An Archetypal Model: Stability Perspective

Referring to an archetypal mechanical system (Fig. 1), the major historical contributions due to Euler, Koiter, and Thompson are reviewed and illustrated. The principal aspects involved in the three estimations of the critical load are highlighted. The simplicity of the model permits an analytical investigation, even for several points of the global analysis requested in the Thompson approach. This allows a deep understanding of the system's safety. As Koiter lowers the buckling load prediction of Euler, Thompson lowers the buckling load prediction of Koiter, $p^{crit}_{Euler} \geq p^{crit}_{Koiter} \geq p^{crit}_{Thompson}$. The Thompson global safety is observed to be necessary for a reliable estimation of the load carrying capacity of the system under realistic conditions.

Both the stability and the dynamical perspectives are investigated, respectively, in the present section (Sect. 2.3) and in the forthcoming one (Sect. 2.4). More details can be found in Lenci and Rega (2011c, d).

Asymmetrically constrained inverted pendulum. We analyze the single degree-of-freedom mechanical system depicted in Fig. 1, which represents an inverted pendulum with an asymmetric elastic constraint, subjected to an axial load P and a lateral

المنارة للاستشارات

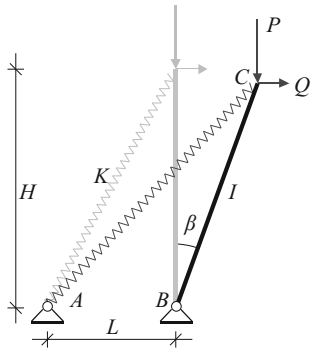

Fig. 1 The asymmetrically constrained inverted pendulum under coexisting axial load P and lateral excitation Q

excitation Q. The latter is supposed to be a static load simulating a model imperfection. The present archetype has been traditionally used in the technical literature to investigate the post-buckling behavior and imperfection sensitivity of structural systems liable to unstable bucking (Bazant and Cedolin 1991). In the schematic, H is the length of the rigid beam, L is the horizontal distance between the hinge B and the extreme point of the spring A, β is the angle of rotation which describes the system configuration, I is the moment of inertia of the beam with respect to the hinge B, and K is the stiffness of the linear spring.

The dimensionless time $t = \hat{t}\sqrt{KLH/I}$, vertical load $p = P/KL$, and horizontal load $q = Q/KL$ are assumed, and the dimensionless parameter $\alpha = 2LH/(L^2 + H^2)$ is introduced, which satisfies $0 < \alpha \leq 1$ and $\alpha = 1$ if and only if $L = H$. As an example, in the following, we suppose $\alpha = 0.8$.

The potential is

$$V(\beta) = \frac{[1 - \sqrt{1 + \alpha \sin(\beta)}]^2}{\alpha} - p[1 - \cos(\beta)] - q\sin(\beta) \tag{1}$$

and the dimensionless equation of motion is

$$\ddot{\beta} - p\sin(\beta) + \left[1 - \frac{1}{\sqrt{1 + \alpha\sin(\beta)}} - q\right]\cos(\beta) = 0 \tag{2}$$

where the dot means derivative with respect to the dimensionless time.

We investigate the potential. The case without imperfection is examined in Fig. 2, where the wells are reported for increasing values of the axial load p. The system has a 2π periodicity with respect to β. Various stable and unstable equilibrium points exist. Our focus mainly dwells on the rest position, $\beta = 0$. As far as a small p is applied, this configuration is a stable equilibrium. Raising p, instead, the right potential barrier surrounding this point gradually lowers and finally makes it unstable in the clockwise direction. Adding a small (non-null and constant) lateral excitation, i.e., adding a small imperfection, the stable equilibrium no longer coincides with the

المنارة للاستشارات

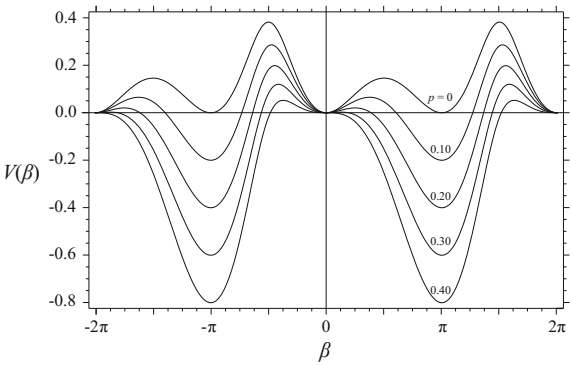

Fig. 2 Potential $V(\beta)$ in the perfect case ($q = 0$), at different values of vertical load p

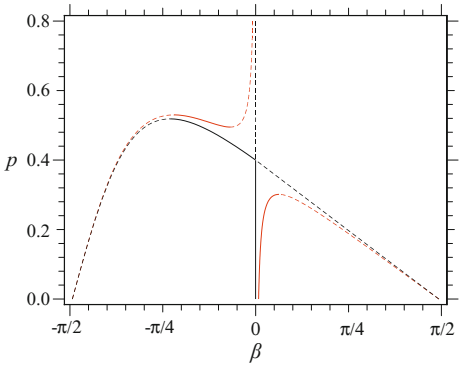

Fig. 3 Bifurcation diagram in a neighborhood of the considered bifurcation point, in the perfect case in black line ($q = 0$) and in the imperfect one in red line ($q = 0.01$). Stable and unstable branches are denoted by solid and dashed lines, respectively

rest position, but is slightly shifted (not shown in the figure); similarly occurs for the other stable and unstable points.

Recalling the bifurcation theory, the equilibrium points are given by

$$p\sin(\beta) = \left[1 - \frac{1}{\sqrt{1+\alpha\sin(\beta)}} - q\right]\cos(\beta) \tag{3}$$

The associated bifurcation diagram zoomed in the region of interest for the present analysis is reported in Fig. 3. The perfect case and the imperfect one are overlapped with each other, respectively, in black and red lines. In the perfect case, a static transcritical bifurcation occurs, with the two meeting branches exchanging their stability.

Adding the imperfection, the transcritical bifurcation is perturbed and replaced by two saddle-node bifurcations, one involving the branches at p lower than the unperturbed transcritical bifurcation point and the other one involving the branches beyond it. This outcome is in conformity with the structural stability theory. The value of p corresponding to the first saddle-node bifurcation is well below the transcritical bifurcation point, i.e., although the imperfection is small, it is able to lower considerably the threshold corresponding to the first bifurcational event.

المنارة للاستشارات

Here, we can clearly note the difference between the Euler and the Koiter critical loads.

Euler critical load. To detect the Euler critical load p_E, we consider the case without static imperfection ($q = 0$), which exhibits the transcritical bifurcation in Fig. 3. Once assumed the perfect case, the Euler critical load p_E is the load in correspondence of the bifurcation point. To evaluate it, we can resort, for instance, to the classical asymptotic development method, which yields

$$p_E = \frac{\alpha}{2} \tag{4}$$

As an example, at $\alpha = 0.8$, we obtain $p_E = 0.4$.

Koiter critical load. To detect the Koiter critical load p_K, we consider the case *with* static imperfection ($q \neq 0$), which exhibits the perturbed transcritical bifurcation consisting of two saddle nodes, Fig. 3. Once assumed the imperfect case, the Koiter critical load p_K is the load in correspondence of the first saddle-node bifurcation point. Similarly to the Euler critical load, also the Koiter one can be evaluated by resorting to the asymptotic development method, which allows approximating it for small values of q, i.e., for small values of β. This yields

$$p_k = \frac{\alpha}{2} - \alpha \frac{\sqrt{6}}{2} \sqrt{q} \tag{5}$$

At $\alpha = 0.8$, we have $p_E - p_K \cong 0.98 \sqrt{q}$.

Note that the difference between the Euler and the Koiter critical loads depends on the square root of the imperfection. This is well known in the literature (see, for instance, Thompson and Hunt 1973, p. 21) and is at the base of the sensitive dependence of the critical load on the imperfections.

As an example, at $\alpha = 0.8$ and $q = 0.01$, we obtain $p_K = 0.302$. This estimation is very accurate, since by numerically solving without approximations we have $p_K = 0.3014$. Thus, in this case, the Koiter critical load is the 75% of the Euler prediction, i.e., substantially lower despite the smallness of the considered imperfection.

Thompson critical load. In the previous subsections, we have analyzed the effects of adding a *static* imperfection parameter q (Koiter). Here, we analyze the effects of adding a *dynamical* imperfection, i.e., *finite* changes in the initial conditions (Thompson). To perform this analysis, we need to operate in the phase space. We initially focus on the case without q, and then extend the results to the more general situation where q exists and has to be taken into account. As an example, we refer to $p = 0.05$.

The phase portrait is drawn in Fig. 4. Five different types of solution can be detected, which, for increasing values of energy, are as follows:

1. in-well periodic orbits, both in the well around $\beta = 0$ (left well) and in the well around $\beta = \pi$ (right well);

المنارة للاستشارات

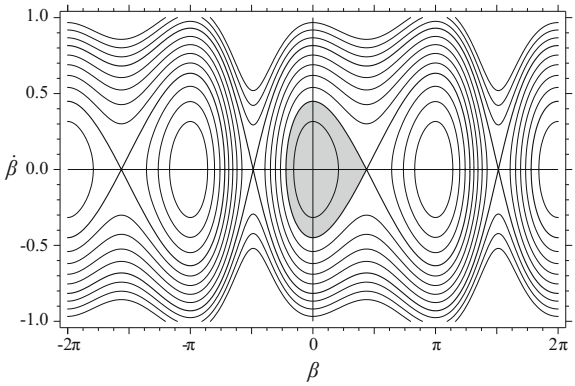

Fig. 4 Phase portrait in the perfect case ($q = 0$), at $p = 0.05$. Thick lines denote homoclinic and heteroclinic orbits. The safe region related to the equilibrium $\beta = 0$ is shaded in gray

2. two orbits homoclinic to the inner hilltop saddle, at $\beta_s = 1.375$, one on the right of the saddle and surrounding the right potential well, and the other one on the left and surrounding the left potential well;
3. cross-well periodic oscillations, turning around the two potential wells;
4. two heteroclinic orbits of the outer hilltop saddle at $\beta = 4.672$, one in the lower part of the phase space implying anticlockwise rotation, and the other one in the upper part of the phase space implying clockwise rotation;
5. clockwise and anticlockwise rotations, encompassing all wells.

Since we are focusing on the equilibrium configuration $\beta = 0$ (perfect case), to analyze it from a global viewpoint, we consider the left potential well containing it and the associated homoclinic orbit. This area is shaded in gray in the phase portrait in Fig. 4. It represents the safe region of the equilibrium position (it will become its "basin of attraction," if adding an infinitesimal damping).

To investigate this area for increasing values of the axial load p, we examine the homoclinic loop delimiting it, Fig. 5. The dots denote the saddle points for each loop. As p is far from the Euler critical load, the safe region is wide. Conversely, as p approaches the Euler threshold, the safe region shrinks and "rapidly" becomes residual. This is dangerous in practice. In fact, the larger is the safe area, the larger is the ability of the equilibrium position to support finite changes in the initial conditions. As the axial load increases, the safe area decreases, reducing dramatically the actual safety of the system. For example, at $p = 0.35$, the area is so narrow that the solution is actually unsafe for practical applications.

Note that as far as the equilibrium point is stable, the safe area may shrink up to become infinitesimal, but it is not null, in agreement with the fact that the solution is stable from a mathematical viewpoint. This observation clarifies the difference between the classical local stability and the Thompson global safety. The classical stability detects the parameter range where the configuration becomes unstable; along its stability range, no attention is drawn on the wideness of its safe area, thus

المنارة للاستشارات

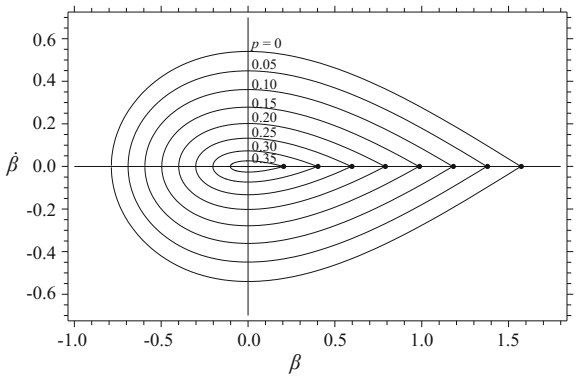

Fig. 5 Homoclinic loops in the perfect case ($q = 0$), at different values of p. The Euler critical load is $p_E = 0.4$. The dots denote the saddle points β_s for each loop

accounting as safe also the infinitesimal one. The Thompson global safety, instead, starts from the results achieved in the classical stability analysis and develops them further. Focusing on the parameter range where the classical stability is ensured, it investigates the wideness of the safe area and alerts that the safeness of the system is guaranteed under realistic conditions only in the region where this area is not too reduced, i.e., where it is able to support finite (and not only infinitesimal) changes in the initial conditions.

To have an idea of the deterioration of the system's safety, it is useful to draw the function $A(p)$, which represents the safe area A inside the homoclinic loop as the axial load p is varied. This area can be computed analytically (Lenci and Rega 2011c). To enhance generality, we normalize it with respect to the analogous area at the unloaded case, which is assumed as reference, i.e., we plot $A(p)/A(0)$, where $A(0) = 1.720792$ for $\alpha = 0.8$. The resulting diagram is shown in Fig. 6, where we report both the limiting perfect condition where q is absent, which is denoted by a thicker line, and several examples at different constant values of q.

These profiles provide a dimensionless measure of the percentage reduction—with respect to the reference unloaded condition—of the magnitude of the safe region while increasing the axial load. As better observed in the forthcoming Sect. 3, in the Thompson's dynamical integrity perspective, this diagram represents a Global Integrity Measure (*GIM*) profile. Yet, herein it plays the simpler role of a measure of the *robustness* of the stable equilibrium position under finite size perturbations.

In the perfect case, increasing the axial load p, the *GIM* decreases up to finally vanishing in correspondence of the Euler critical load p_E, where the safe area is infinitesimal. However, the safe region becomes merely residual—and thus actually unreliable—well below p_E. For example, if we assume that the 10% of the initial area is still acceptable (and this is of course a very low value in practice), then we have that the Thompson critical load is $p_T = 0.238$, i.e., the 59% of the Euler prediction.

المنارة للاستشارات

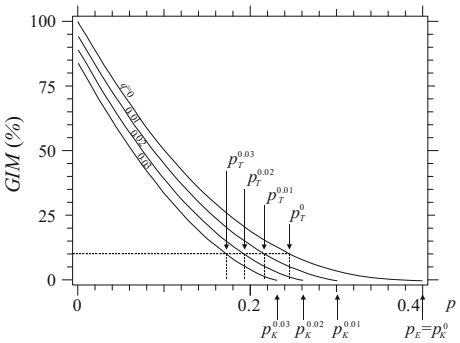

Fig. 6 *GIM* profile representing the normalized area inside the homoclinic loops as a function of the axial load p. The perfect case ($q=0$) and examples of imperfect ones ($q\neq 0$) at different increasing values of q. The Euler, Koiter, and Thompson critical loads are denoted as p_E, p_K, and p_T, respectively. The horizontal dashed line at $GIM=10\%$ schematically shows how to compute the associated Thompson critical loads

Adding the imperfection q, the general picture delineated for the perfect system does not meaningfully change in terms of shape but considerably differs in terms of critical load. In fact, the resulting curves are nearly parallel to each other and shift toward lower values of *GIM* of a quantity which is roughly independent of p, and is instead proportional to q. As expected, when *GIM* is null, each curve meets its corresponding Koiter critical load.

These profiles clearly show that, as the *static* imperfection parameter q (Koiter) reduces the extent of the safe range of the stable equilibrium under consideration, the *dynamical* imperfection (Thompson) further decreases this safe range. For example, in the present case, the Euler critical load is $p_E=0.4$; supposing a static imperfection $q=0.02$, the Koiter critical load lowers down to $p_K^{0.02}=0.261$; supposing also a dynamical imperfection corresponding to $GIM=10\%$, the Thompson critical load drops to $p_T^{0.02}=0.187$. Thus, the Koiter critical load is significantly lower than the Euler prediction, and the Thompson critical load is significantly lower than the Koiter (and Euler) one. This means that the bifurcation (Euler or Koiter) threshold overestimates the actual critical load in the presence of (even transient) dynamical imperfections.

The Euler, Koiter, and Thompson critical loads are reported in Table 1, in order to appreciate quantitatively the percentage reduction due to the Koiter static imperfection and, independently, the percentage reduction due to the Thompson dynamical imperfections, where all of them are evaluated with respect to the Euler critical threshold (perfect case). We can observe that in the absence of the static imperfection, the dynamical one considerably decreases the critical load. As the former is added and increased, instead, the reduction due to the latter becomes progressively less important. Nevertheless, meaningful additional decrements are still produced, which further lower the critical load with respect to the one entailed by the sole static imperfection.

المنارة للاستشارات

Table 1 The Koiter and the Thompson critical loads at different increasing values of q. In parentheses, there is the percentage with respect to the Euler critical load p_E, reported in italic. The column $GIM = 10\%$ is illustrated in Fig. 6

q	Koiter load	Thompson load		
		$GIM = 5\%$	$GIM = 10\%$	$GIM = 20\%$
0.00	*0.4 (100%)*	0.277 (67%)	0.238 (59%)	0.184 (46%)
0.01	0.301 (75%)	0.242 (61%)	0.210 (52%)	0.163 (41%)
0.02	0.261 (65%)	0.215 (54%)	0.187 (47%)	0.145 (36%)
0.03	0.230 (57%)	0.192 (48%)	0.167 (42%)	0.128 (32%)

Before concluding this subsection, it is worth noting that, while the Koiter critical load can be quantitatively determined upon fixing the value of the static imperfection q, the Thompson critical load can be determined only upon choosing the admissible residual safe region, i.e., after fixing the acceptable GIM, as clearly illustrated in Table 1. This corresponds to fix the maximum allowed *dynamical* imperfections (change in initial conditions), which can be safely supported by the system. In this respect, both Koiter and Thompson theories share the property of being practically determinable with the exact knowledge (or an estimation) of the static (q) and dynamical imperfection (which affects GIM), respectively. However, this issue is not easily achieved in practice, since their magnitude is usually unknown and, moreover, has a large statistical dispersion.

2.4 An Archetypal Model: Dynamical Perspective

Further referring to the archetypal model in Sect. 2.3, the present study aims at complementing and completing the companion one, by fully accounting for the effects of actual dynamic excitations on the load carrying capacity of a mechanical system. In fact, when dynamic excitations are added, the whole response picture is quite different, more complex indeed. Accordingly, the global safety issue becomes more involved, from both a theoretical and a practical point of view. Robustness and erosion profiles are built, respectively, for varying axial load and dynamic excitation amplitude, showing that they permit appreciating the practical reduction of the system load carrying capacity.

The Koiter load carrying capacity. We keep analyzing the archetypal system in Fig. 1. We assume that the lateral force, i.e., the "imperfection" in our model, is constituted by a harmonic excitation of amplitude q_1 and given frequency ω added to the static force q (only this last term, instead, was considered in Sect. 2.3). This is of course a simplification of real excitations, but it is sufficient for our purposes. Furthermore, to simulate realistic situations, we suppose damping term acting on the structure.

المنارة للاستشارات

The equation of motion becomes

$$\ddot{\beta} + c\dot{\beta} - p\sin(\beta) + \left[1 - \frac{1}{\sqrt{1+\alpha\sin(\beta)}} - (q + q_1\sin(\omega t))\right]\cos(\beta) = 0 \quad (6)$$

To avoid the further complexity related to the resonance, in the following, we consider the dynamics far from its activation, at $\omega = 0.8$ (in correspondence of the resonance, additional phenomena are certainly expected).

We investigate the effects of the dynamic excitation on the system's load carrying capacity. Initially, we develop the analysis in the framework of the Koiter perspective. Accordingly, we focus on the attractors (mainly the periodic ones) and their range of existence and stability, highlighting how this is affected by the dynamic excitation. We analyze the bifurcations entailing the disappearance of the attractors, since they play the role of Koiter critical thresholds.

The path following of periodic solutions is reported in Fig. 7a. For a very small excitation amplitude ($q_1 = 0.005$), the path is similar (and practically can be superimposed) to the static one reported in Fig. 3. Increasing q_1, the path maintains its general shape, but a period-doubling (*PD*) bifurcation appears (point *A*) determining a temporary loss of stability of the main path, which then regains stability by an inverse *PD* bifurcation (point *B*) before undergoing the final saddle-node (*SN*) bifurcation (point *C*). For example, at $q_1 = 0.05$, these points occur, respectively, at $p = 0.1813$, $p = 0.2278$, and $p = 0.2962$. The unstable (red) interval becomes larger when increasing q_1 and eventually it reaches $p = 0$, meaning that due to dynamic excitation the system is unable to carry any axial load. However, this latter case occurs for very large values of q_1 (e.g., at $q_1 = 0.176$), which can no longer be considered as irremovable "imperfections" and thus are out of interest here.

To have a complete description, the loci of the *PD* bifurcations and of the upper *SN* bifurcation are reported in the parameters space (q_1, p), Fig. 7b. Note that the *PD* bifurcations exist for $q_1 > 0.007$.

The zone below the lower (thicker) curve PD_{low} is the region of stability of the period-1 solution, which can be considered as the region of "Koiter" dynamic admissibility. This identification could appear rough and too conservative at a first glance, because above PD_{low} periodic solutions do exist. In particular, for low values of q_1, above PD_{low} there are period-2 attractors, while above PD_{up} the main period-1 attractor regains stability. However, the period-2 solution cannot always be considered as a safe (e.g., acceptable) solution, while the upper period-1 solution is not always reachable by increasing p. This means that PD_{low} is really the Koiter critical threshold in the presence of dynamic excitations.

The interaction between the static (p) and dynamic (q_1) causes of loss of load carrying capacity can be summarized as follows. For $q_1 < 0.007$, the dynamic excitation has practically no effect and the system fails at about the *SN* obtained in Sect. 2.3, since in this range the dynamic excitation lowers this threshold only slightly. At $q_1 = 0.007$, there is a sudden fall down of the critical load, which then continues to decrease smoothly for increasing values of q_1. Moreover (not shown in the figures), if the static (Koiter) imperfection q is also increased, the overall pattern of the thresh-

المنارة للاستشارات

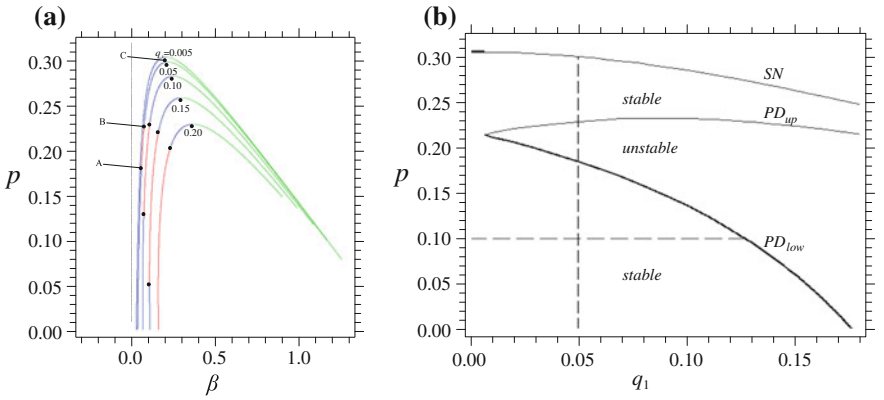

Fig. 7 **a** Path following of periodic solutions; blue = attractor, green/red = regular/flip saddles. **b** The curves of *SN*, upper and lower *PD* bifurcations in the (q_1, p) parameter plane. The thick line corresponds to the (discontinuous) Koiter threshold in the presence of dynamic excitation. The dashed lines correspond to p and q_1 values, along which we build the integrity profiles of the forthcoming Figs. 10 and 11. In (**a**) and (**b**), $c = 0.01$, $\alpha = 0.8$, $q = 0.01$, and $\omega = 0.8$

old curves remains substantially unchanged from the qualitative viewpoint, but the regions of stable periodic solutions become lower and lower.

Overall, in the presence of dynamic excitations, the response becomes much more complex than the static one, also for external frequencies out of the resonance interval. These phenomena strongly reduce the Koiter load carrying capacity of the system, even in the case of relatively small excitation amplitudes, so that considering only static imperfections can be very unsafe. Note that, despite the presence of dynamic excitations, the Koiter load carrying capacity is still determined by *local* bifurcations. This is a peculiarity of the "Koiter approach." On the contrary, the "Thompson approach" involves a *global* analysis.

Axial load versus dynamic excitation. We investigate the influence of the presence of axial load and external dynamic excitation by analyzing the metamorphoses induced on the organization of the attractor-basins phase portraits. To better appreciate the effects of each contribution, we consider the scenario when each one is varied while the other is kept fixed and only slightly perturbed.

We start by focusing on the effects of the *axial load*. To analyze them, we report attractor-basins phase portraits at increasing values of p, specifically at $p = 0.00$ and $p = 0.15$, Fig. 8. To deviate only slightly from the unforced case, we assume a small dynamic excitation, $q_1 = 0.05$.

Respectively, the basins of attraction of the period-1 oscillation around $\beta = 0$ (which is the attractor of interest in the present analysis) and of the period-1 oscillation around $\beta = \pi$ are white and red; the basins of the clockwise ($\dot{\beta} > 0$) and the anticlockwise ($\dot{\beta} < 0$) rotations are blue and cyan; the basins of the period-3 oscillations around $\beta = 0$ and $\beta = \pi$ are gray and green.

المنارة للاستشارات

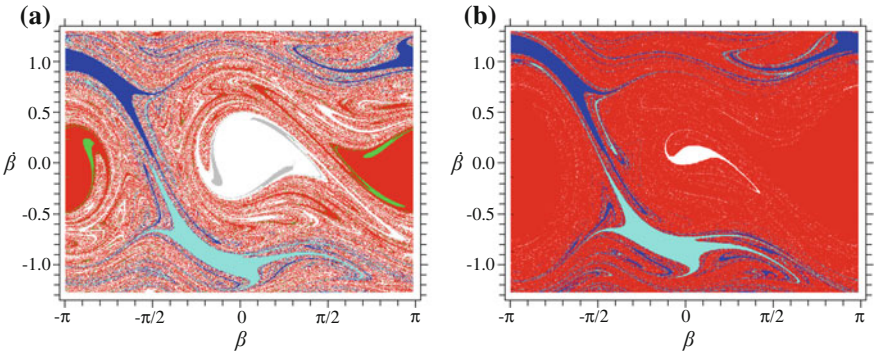

Fig. 8 Attractor-basins phase portraits at $c = 0.01$, $\alpha = 0.8$, $q = 0.01$, $q_1 = 0.05$, and $\omega = 0.8$ for increasing values of the axial load p, specifically **a** $p = 0.00$, **b** $p = 0.15$. The phase space window is $-\pi < \beta < \pi$ and $-1.3 < \dot{\beta} < 1.3$ in every picture

We can clearly observe the main features related to p. For a comprehensive understanding, it is worth comparing the obtained attractor-basins phase portraits in Fig. 8 with the potential previously investigated in Fig. 2. As seen in the latter, if there is no axial load, the reference well and the adjacent one have the same depth. Roughly speaking, they have the same "degree of attractivity." As p is added, instead, an "unbalanced potential effect" arises. The reference well becomes flatter in favor of the adjacent one, which, conversely, becomes deeper and larger, and thus much more "attractive". This is more and more pronounced as ramping the axial load up.

This feature is properly reflected in the attractor-basins phase portraits in Fig. 8. At $p = 0.0$, the reference basin is wide and presents a large compact part inside the well. Similarly occurs for the adjacent one. At $p = 0.15$, instead, the compact area leading to the reference attractor progressively shrinks, whereas the other one expands increasingly. Successively, the reference basin becomes residual and finally disappears (not shown in the figures).

Thus, the axial load is observed to strongly affect the *robustness* of the wells.

Next, we focus on the effects of the *dynamic excitation*. Although both q_1 and ω are parameters of interest, for simplicity we investigate only the effects of q_1 and keep considering $\omega = 0.8$, i.e., far from resonance. The attractor-basins phase portraits at $q_1 = 0.00$ and $q_1 = 0.05$ are reported in Fig. 9. To deviate only slightly from the case without axial load, we assume $p = 0.05$.

At $q_1 = 0.00$, each center in the unforced undamped case becomes an attractor. Both of them present a wide compact area inside its own well. The reference one is slightly smaller due to the small axial load. Thin tongues are spiraling around the compact parts.

Raising q_1, the attractor-basins phase portraits become increasingly complex, with the coexistence of a number of attractors. At $q_1 = 0.05$, five different basins occur, as already visible in Fig. 8a for $p = 0$. In addition to the reference solution and the adjacent one, clockwise and anticlockwise rotations appear and exist for a wide

المنارة للاستشارات

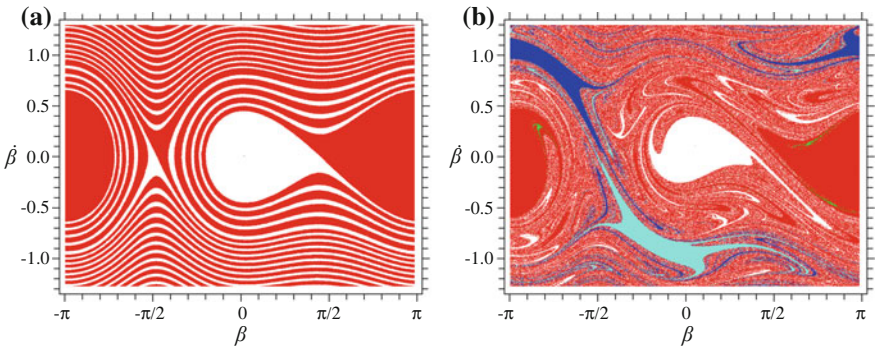

Fig. 9 Attractor-basins phase portraits at $c = 0.01$, $\alpha = 0.8$, $q = 0.01$, $p = 0.05$, and $\omega = 0.8$, for increasing values of the dynamic excitation q_1, specifically **a** $q_1 = 0.00$, **b** $q_1 = 0.05$. The phase space window is $-\pi < \beta < \pi$ and $-1.3 < \dot{\beta} < 1.3$ in every picture

parameter range, both with a wide compact area surrounding the attractor. Also, a period-3 oscillation emerges, although this is a minor attractor existing in a small parameter range and equipped with a very narrow basin.

An important aspect related to the existing dynamic excitation is the erosion of the basins of attraction (and their consequent reduction of dynamical integrity), again visible already in Fig. 8a. This point deserves special attention. Focusing on the attractor of interest, we can note that its basin is subjected to a distributed fractalization due to the basins of other attractors (in particular of the adjacent one). This phenomenon is triggered by the global bifurcation of the homoclinic orbit surrounding the reference potential well, which allows the penetration of the eroding out-of-well fractal tongues into the basin of the in-well attractor; then, secondary homoclinic and heteroclinic bifurcations further accelerate the process.

The effects of the erosion are clearly apparent. The compact area surrounding the considered attractor has been somehow reduced by fractality. Nevertheless, at the present parameter values, this safe compact area is still rather wide, which guarantees the attractor not to be extremely vulnerable against dynamical perturbations constituted by changes in the initial conditions. Further increasing the excitation amplitude (not reported in the figures), instead, the safe outline disappears and the reference basin is widely eroded, making its safe compact region practically residual, i.e., smaller perturbations (with respect to the unexcited case) are sufficient to lead to another attractor.

Thus, the dynamic excitation is observed to strongly affect the *erosion* of the attractor-basins phase portraits (in addition to influencing the appearance of coexisting different attractors).

The Thompson load carrying capacity. Robustness profiles: increasing axial load at fixed dynamic excitation. We replay the analysis of Sect. 2.3, i.e., we investigate how the global safety decreases when increasing the axial load, but now considering the effects of the dynamic excitation.

المنارة للاستشارات

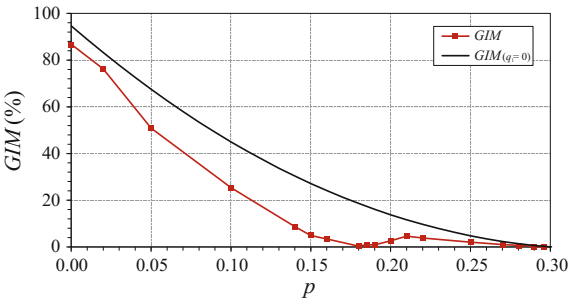

Fig. 10 *Robustness* profile of *GIM*, at $c = 0.01$, $q = 0.01$, $\alpha = 0.8$, $q_1 = 0.05$, and $\omega = 0.8$. The *GIM* curve for the case without dynamic excitation ($q_1 = 0$) is reported for comparison

We still focus on the reference potential well. Accordingly, we consider as safe basin the union of the basins of all attractors belonging to the well under investigation; in the present case, this is mainly constituted by the basin of the reference attractor (except for a small range where also a minor attractor appears inside the well). To measure the robustness of the well, we resort to the *GIM*, where we assume as normalizing condition the case at $p = 0$ and $q_1 = 0$.

The profiles are built by constructing several attractor-basins phase portraits at increasing values of p, and by measuring the *GIM*. An example is shown in Fig. 10, which illustrates the *GIM* curve at $q_1 = 0.05$; the *GIM* curve for the unexcited case is reported for comparison. Like the curve in the absence of dynamic excitation ($q_1 = 0$), also the curve in the presence of it ($q_1 \neq 0$) basically represents a profile of robustness of the well; a difference is in the role possibly played by the fractal erosion, which is, however, herein, a substantially localized phenomenon, as somehow expectable given the actual non-evolutionary, static indeed, character of the considered driving parameter (axial load).

As anticipated in the attractor-basins phase portraits, the well is and remains wide as far as a small axial load is applied. The existence of a safe region is well documented by the *GIM* curve, which assumes very high values, close to the 100% (slightly smaller because of the presence of damping). Increasing p, the *GIM* properly accounts for the progressive reduction of robustness in favor of the adjacent well. The profile gradually deteriorates and reaches the PD_{low} by a practically horizontal slope. This entails (and indeed is the root of the) sensitivity to dynamical perturbations. After the interval between the two *PD* bifurcations, the attractor recovers a small fraction of its stability and integrity, but subsequently it definitely disappears through *SN*.

To have a quantitative idea of the decrement of the practical safety, let us suppose that the admissible *GIM* is the 20%, which is quite a small value, indeed. We obtain that the "dynamic" Thompson practical stability threshold is equal to $p_T(q_1 = 0.05) = 0.116$, which is the 64% of the practical (i.e., "dynamic") Koiter threshold $p_K(q_1 = 0.05) \cong 0.18$ corresponding to the first period-doubling PD_{low}, and the 39% of the theoretical (i.e., nearly "static") Koiter threshold $p_K(q_1 = 0.05) = 0.296$ corresponding to the final *SN* bifurcation of the path.

Thus, the *GIM* profile properly provides a quantitative estimation of the practical *robustness* of the well. It clearly alerts that this is robust in practice only in the initial

المنارة للاستشارات

range, which corresponds to the lower stable part of the local bifurcation path of the attractor. The final range, instead, is actually unreliable, since too vulnerable under realistic conditions. More in general, the robustness profile in the presence of dynamic excitation shows that the practical Thompson critical threshold is lower, and possibly much lower, than the Koiter one, thus extending to the "dynamic" case the general conclusion drawn in Sect. 2.3 in terms of robustness of the stable equilibria solely occurring in the absence of dynamic excitation.

Furthermore, the *GIM* profiles are able to show some effects associated with the topological erosion of the reference potential well. In fact, by comparing the scenarios at $q_1 = 0.0$ and $q_1 = 0.05$, we can observe that the two curves share a similar qualitative behavior, but the profile in the presence of dynamic excitation is systematically below the corresponding one in the absence of it. Still supposing that the admissible *GIM* is the 20%, we obtain that the "dynamic" practical stability (Thompson) threshold, which is equal to $p_T(q_1 = 0.05) = 0.116$, is the 66% of the "static" one, which is equal to $p_T(q_1 = 0) = 0.175$, namely, the dynamic excitation almost halves the "static" practical stability (Thompson) threshold.

Thus, the dynamic excitation—though being rather small in the present example—entails a strong reduction of the actual robustness, i.e., a strong reduction of the structural performance of the system. This point will be analyzed more in depth in the forthcoming subsection.

The Thompson load carrying capacity. Erosion profiles: increasing dynamic excitation at fixed axial load. We analyze the meaningful effects of the dynamic excitation in reducing/eroding the safety of the well. Accordingly, we further consider the previous definition of safe basin. The *GIM* curves at increasing excitation amplitude are reported in Fig. 11, showing the case at $p = 0.1$ and, for comparison, in the absence of axial load. Note that these curves substantially represent profiles of actual *erosion* of the well.

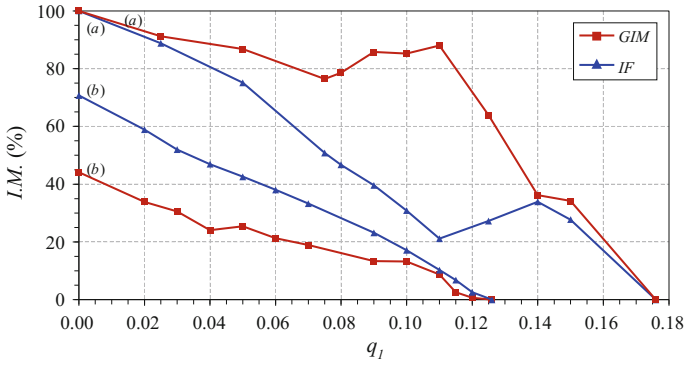

Fig. 11 *Erosion* profiles of *GIM* (red) and *IF* (cyan), at $c = 0.01$, $q = 0.01$, $\alpha = 0.8$, $\omega = 0.8$, and **a** $p = 0$ (without axial load), **b** $p = 0.1$

المنارة للاستشارات

At $p = 0.0$, the curve starts from $GIM = 100\%$, due to the normalization, and ends where the last attractor disappears at the "limiting" (i.e., purely dynamic) Koiter load carrying capacity $q_{1,K} \cong 0.177$. Raising the excitation amplitude, the erosion is triggered and gradually proceeds. There is a deep fall in correspondence of $q_1 \cong 0.140$, after which the integrity is practically residual until disappearance. This confirms that the practical Thompson critical threshold is lower, and possibly much lower than the Koiter one. This depends of course on the admissible value of residual integrity (and on the employed dynamical integrity measure). For example, if we admit that the 40% of the initial integrity is still acceptable, we have $q_{1,T}^{GIM} = 0.14$, corresponding to the 79% of the Koiter threshold. If, instead, one needs a practically uneroded situation, e.g., 80% of the initial value, then $q_{1,T}^{GIM} = 0.115$, corresponding to the 65% of the Koiter threshold.

By comparing the curves at $p = 0$ and $p = 0.1$, we can note that in the latter the erosion profile starts at a lower value of GIM (at about $GIM \cong 44\%$). In fact, the reference well is less robust, since the adjacent one has captured part of its safe basin (as previously observed in the robustness profiles in Fig. 10, in the potential in Fig. 2, and in the attractor-basins phase portraits in Figs. 8 and 9). The fractalization of course proceeds anyway. The well is gradually eroded, as shown by the profile progressively decreasing up to the final disappearance of the last in-well attractor. Thus, at $p = 0.1$, the entire curve settles at very low values of GIM, i.e., the well is always very sensitive to disturbances.

It is worth observing that for a reliable estimation of the load carrying capacity we have to trust only in the compact part of the safe basin and not in the fractal one. This is a very important aspect for safe engineering design. For this reason, in addition to the Global Integrity Measure (GIM), we consider also the Integrity Factor (IF) proposed by Lenci and Rega (2003b), which is defined as the normalized radius of the largest hyper-sphere belonging to the safe basin and is thus able to investigate only its compact core (see Sect. 3.1 forward).

In Fig. 11, the IF curves are overlapped to the GIM ones. For $p = 0$, the central part of the two curves shows a quite distinct behavior. In particular, IF is lower than GIM, sometimes much lower, meaning that there is a large fractal part of the basin which does not contribute to the dynamical integrity. This is an example in which using GIM would lead to unsafe conclusions, and IF is absolutely needed for a reliable integrity evaluation. For $p = 0.1$, instead, IF is always higher than GIM. In fact, the potential well around $\beta = \pi$ is much deeper and "attractive" than the reference one; so attractive, evidently, to capture the area of the safe basin from this last one for whatever q_1 value, thus entailing an overall reduced value of its GIM.

Thus, the erosion profiles highlight that the dynamical integrity of the system close to the Koiter load carrying capacity is merely residual and, to have a safe behavior, a lower, and possibly much lower, practical Thompson load carrying capacity must be considered in applications. Also, in the presence of fractality, it may be necessary to resort to dynamical integrity measures that are able to investigate only the compact part of the safe basin.

In Fig. 12, we summarize the dynamical integrity profiles obtained using the GIM, which provide a measure either of the reduction of robustness (for varying p)

المنارة للاستشارات

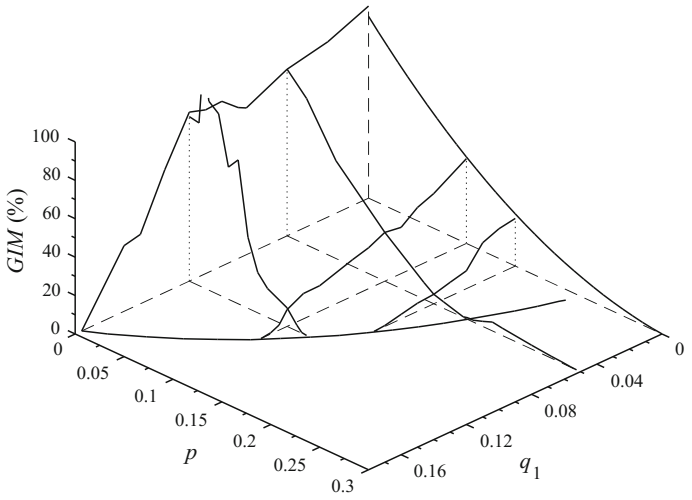

Fig. 12 A tridimensional view of the *robustness–erosion* profiles, at $c = 0.01$, $q = 0.01$, $\alpha = 0.8$, and $\omega = 0.8$

or of the extent of basin erosion (for varying q_1). This figure offers a comprehensive overview of the coupling effects entailed on the system's load carrying capacity by the coexistence of axial load and lateral dynamic excitation. The overall result is that both robustness and integrity may become dangerously residual well before the disappearance of the last in-well attractor by local bifurcations. It is this issue that makes the concept of practical stability, and the associated global analysis, necessary in applications for a safe system design.

3 Assessing the Dynamical Integrity

In the present section, the specific tools for assessing the dynamical integrity are introduced and their relevance to establish a novel paradigm of load carrying capacity is presented. Namely, we highlight that disturbances are always present in the real world and are non-necessarily small. To be in safe conditions, a system is called to sustain them in both the initial conditions (phase space) and in the control parameters (control space), without changing the desired outcome. To investigate the robustness of the system in the phase space, it is necessary to define the safe basin and detect the appropriate measure of dynamical integrity; to investigate the robustness of the system in the control space, it is necessary to draw dynamical integrity profiles and charts. Only if the system is robust both in the phase space and in the control space, its load carrying capacity is ensured. Thus, the dynamical integrity analysis can be assumed as a novel and valuable criterion for assessing the load carrying capacity of a system.

المنارة للاستشارات

3.1 Robustness in the Phase Space

Safe basin. The starting point of the dynamical integrity analysis is the definition of the safe basin. The safe basin denotes the set of initial conditions which lead to a safe outcome for the system, as opposed to all the other conditions which lead to a non-safe one. Thus, defining the safe basin is a very critical point, since entails choosing what is considered as dynamically acceptable. This is inherently linked to the engineering problem to be addressed and may significantly vary from case to case. That is why there is not a single definition of safe basin, but several ones have been formulated in the literature according to which safe condition is wished to be analyzed.

To remain as general as possible, we can state that *the safe basin is the set of initial conditions sharing a common dynamical property*, where the shared "common dynamical property" is specified based on the case study under investigation. Being very general, this definition covers a variety of different scenarios, which may be, for instance, the non-escape from a potential well in a (locally or globally) softening system, the convergence in time toward one (or more) attractor(s), the non-sensitivity to the initial conditions, etc. Here, we report the main properties referred to in the (often implicit) definitions of safe basin commonly encountered in the literature.

POTENTIAL WELL. There are engineering applications where it is important considering the in-well attractors all together (and not each one individually), namely, where we need to analyze the robustness of a given potential well. In this case, we can define the safe basin as *the set of all initial conditions approaching the bounded attractors belonging to a given potential well as* $t \to \infty$, or in other words, *the union of the basins of attraction of all bounded attractors belonging to a given potential well*. Thus, the safe condition is represented by the basins of attraction of all the attractors leading at steady state to the desired well, whereas the unsafe condition is represented by all the other outcomes (whether they be, e.g., dynamics inside another well, dynamics spanning different wells, escape to the "unbounded" attractor, etc.). This is probably the most intuitive definition of safe basin.

BOUNDED BEHAVIOR. When dealing with softening systems, we frequently need to analyze the robustness of all the bounded attractors (regardless which is the well they belong to) and avoid the region leading to the escape solution. In this case, we can define *the safe basin as the union of the basins of attraction of all the bounded attractors*, i.e., the safe condition is represented by all the initial conditions leading to a bounded motion, and the unsafe one by the escape.

INDIVIDUAL ATTRACTOR. Another common item in engineering is that of analyzing each one of the individual attractors arising inside the potential wells, e.g., for detecting the range of parameters where they can be actually observed in experiments and applications. To find a safe basin appropriate for this kind of problems, we need to resort to a definition where the attention is focused on the basin of attraction of each single attractor. In particular, *the safe basin is the set of initial conditions leading to a given attractor as* $t \to \infty$, *i.e., the basin of attraction of a given attractor*. The safe condition is represented by all the initial conditions that at steady dynamics lead

المنارة للاستشارات

to the attractor under consideration (thus, the safe basin coincides with the basin of the analyzed attractor) and the unsafe one by all the other dynamics (both bounded and unbounded).

In the aforementioned cases, the safe basin consists of a given basin of attraction or unions of them. However, other issues of practical importance may be of interest in applications, where "*improved*" definitions of safe basin may be required. Here, we report some of them.

TRANSIENT SAFE BASIN. From the safe engineering viewpoint, an important element consists of differentiating between steady or transient dynamics, i.e., between long-term or short-term behavior. In fact, the (temporary) escape from a potential well (or, more generally, from a safe given region of technical interest) during the transient response may be unimportant in some situations, while it must be avoided in other situations. Looking at the system response all along the time (i.e., from $t = 0$ to $t \to \infty$) and not only for $t \to \infty$ as done for classical (steady) safe basin, *the transient safe basin of a bounded attractor is defined as the conservative subset of the corresponding steady safe basin, obtained by considering only the initial conditions whose transient trajectories remain all the time within the chosen safe region of the phase space* (Rega and Lenci 2005; Gonçalves et al. 2007), e.g., within the desired potential well. Yet, one can also be interested in what happens to the system response in a finite time and alternatively define a transient safe basin as the *set of starting points whose trajectories do not escape within a maximum finite number of forcing cycles* (Soliman and Thompson 1989; Thompson and Soliman 1990; Soliman and Gonçalves 2003). Nevertheless, these definitions require time-consuming ad hoc algorithms for the safe basin evaluation due to the online continuous check on the state of the system. Also, additional information is usually needed to make operative the statement of their definition, since, e.g., in the dynamical case, the boundary of a potential well is not as clearly defined as in the static one.

TRUE SAFE BASIN. The phase of periodic excitations plays an important role in determining the system response and, accordingly, its integrity. As an example, this has been highlighted in the problem of overturning of rigid blocks. In similar case studies, we have to look for phase-independent arguments to correctly measure the loss of integrity of the system. For this reason, the *True Safe Basin* has been introduced, which is defined as *the intersection of all safe basins when the phase ranges over the period of the excitation* (Lenci and Rega 2004a, d), i.e., this is the smallest phase-independent set of initial conditions leading to "safe" dynamics, in appropriate sense.

It is worth noting that, when the safe basin coincides with a (union of) classical basin(s) of attraction, the basin boundaries—which play a major role in the system's dynamics—are stable manifolds of given saddles and have a clear dynamical meaning and well-defined properties, so that their evolution can be studied in terms of dynamical systems theory. This feature is not shared by the other safe basin definitions.

Apart from few cases, safe basins can be determined only numerically, and to date this is still computationally onerous for systems with more than, say, two mechanical degrees-of-freedom.

المنارة للاستشارات

Overall, the definition of safe basin depends on the "safe" condition that is wished to be analyzed. Of course, by simply changing the definition of safe basin, different characteristics of the system response may be investigated.

It is also worth noting that, in all of the above definitions, no attention is paid to the actual topology of the considered safe basin. In particular, nothing is said about its shape and its possible fractality or, conversely, the extent of its compact part. The matter is addressed in the next subsection and pertains to the distinction between "nominal" safe basins, herein introduced, and "actual" ones.

Dynamical integrity measures. Once selected the safe basin, we can consider it as practically stable if it is "large enough." This correlation is correct, but the meaning of "large enough" is not trivial and needs to be properly defined. To this purpose, several different dynamical integrity measures have been introduced by the research community. This is because not only choosing the safe basin but also choosing the appropriate dynamical integrity measure strongly depends on the problem at hand. Here comes the need of considering different dynamical integrity measures to provide a complete overview in assessing the robustness of a system. In the following, we dwell on the dynamical integrity measures proposed in the literature.

The *Global Integrity Measure* (*GIM*) is probably the most intuitive and easy dynamical integrity measure. It was introduced by Soliman and Thompson (1989) and can be defined as *the normalized geometrical hyper-volume (area in 2D cases) of the safe basin*. The *GIM* is a dimensionless number, usually written in percentage. The reference value is not denoted a priori, which permits choosing the most suitable normalizing condition. It is worth highlighting two important characteristics of the *GIM*. The first one is that the *GIM* refers only to the *safe basin* (whatever it be), without distinguishing among the individual attractors existing inside it; for this reason, it is particularly suitable for the estimation of the dynamical integrity of a potential well. The second one is that the *GIM* measures only the *size* (*magnitude*) of the analyzed safe basin, i.e., is actually measuring the *probability* of catching the safe basin. Unfortunately, this last point may be a limitation, since in many engineering applications the probabilistic estimate of the safe basin is not fully satisfactory. In fact, this means that the *GIM* is not able to provide information about the shape and nature of the safe basin. Mainly, no distinction is made between fractal and compact regions. From an engineering point of view, instead, this difference is extremely relevant. Compact areas represent a safe outcome, since in these regions small uncertainties in the considered initial conditions do not affect the final result; conversely, fractal areas are generally not safe, since in these regions small uncertainties may lead to a completely different response, which may be potentially dangerous. As the *GIM* is not able to differentiate between them, the *GIM* information is valuable, but generally incomplete.

In addition to the *GIM*, in their original work, Soliman and Thompson (1989) proposed also the *Local Integrity Measure* (*LIM*), which aims at investigating exactly the dynamical integrity aspects not accounted by the *GIM*, in primis whether the basin is smooth or fractal. The *LIM* is defined as *the normalized maximum radius of the hyper-sphere (circle in 2D cases) entirely belonging to the safe basin and centered at*

المنارة للاستشارات

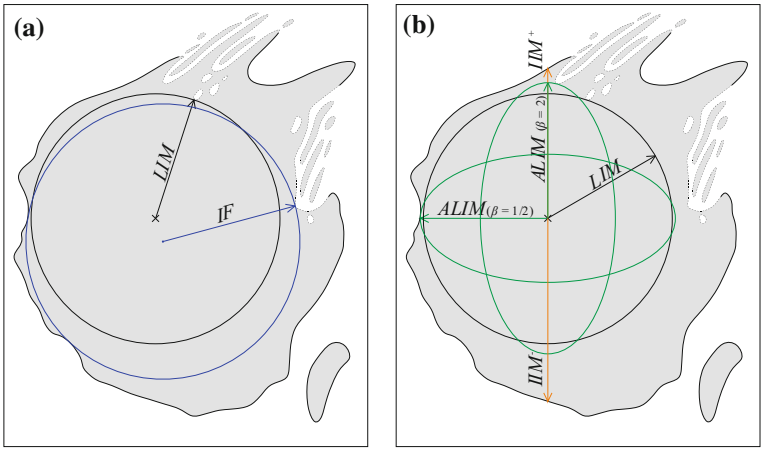

Fig. 13 Dynamical integrity measures illustrated for a hypothetical 2D safe basin (gray area) with period-1 attractor (cross). Assuming unitary reference value, **a** circles used in the evaluation of *LIM* (black) and *IF* (blue); **b** circles used in the evaluation of *ALIM* (green) in the cases of anisotropic parameter equal to $\beta = 1/2$ and $\beta = 2$; distance used in the evaluation of IIM^- and IIM^+ (orange)

the attractor. A schematic example is reported in Fig. 13a. Since the circle used for the evaluation of the *LIM* has to be entirely belonging to the safe basin, only the compact parts may enter the calculation. Thus, the *LIM* is able to measure the *compact*—or actually *safe*—part of the nominally safe basin, ruling out the fractal one, i.e., it is a more *conservative* estimate, which is safer from an engineering point of view. The *LIM* analyzes *each single attractor*, *one by one*, *separately*. In fact, we require the circle used for its evaluation to be centered at the attractor. This characteristic may be desirable when we need to investigate the robustness of each individual long-term behavior. Nevertheless, it cannot be used when we need to analyze the robustness of an entire potential well, where different competing attractors may coexist. The *LIM* is not always *computationally* easy, and may be numerically onerous, especially in the case of chaotic attractors.

Another fundamental dynamical integrity measure is the *Integrity Factor* (*IF*), which was introduced by Lenci and Rega (2003a, b). Their aim was that of overcoming the drawbacks of both the *GIM* and the *LIM*, without losing the advantages of them both, specifically: (i) on the one hand, being able to investigate not only the attractors but also the potential well, while remaining computationally easy (similarly to the *GIM*); (ii) on the other hand, accounting for the only compact part of the safe basin, ruling out the fractal one (similarly to the *LIM*). The Integrity Factor (*IF*) is defined as *the normalized radius of the largest hyper-sphere (circle in 2D cases) entirely belonging to the safe basin* (Fig. 13a). Note that the definition of the *IF* is exactly equal to the first part of the definition of the *LIM*. The only difference is at the end of the statement. In the *LIM,* it is further specified that the hyper-sphere has to be "centered at the attractor," whereas in the *IF* these final words are not present.

المنارة للاستشارات

This difference is not a mere detail, but is the main novelty of the *IF* criterion. Here comes its distinctive feature. In fact, we can observe that the *IF* fully meets the requirements it was intended for. Similarly to the *GIM*, the *IF* is not referred to a particular attractor but only to the *safe basin*; thus it may be used to focus on the entire potential well without distinguishing between different in-well dynamics, or, conversely, to distinguish among them, depending on the need. Similarly to the *LIM*, as the circle is completely inside the safe basin, the fractality intertwining this area with other regions does not enter the *IF* evaluation; thus, the *IF* considers only the compact "*core*" of the safe basin.

Other distance-based measures of dynamical integrity have been proposed in the literature. The *Protection Thickness* of a period-K attractor with K disjoint subsets of cells in the state space is defined as the minimum of the K distances between each subset and the set of multidomicile cells (Sun 1994); though being formulated in the generalized cell mapping terminology (Hsu 1987; Hsu and Chiu 1987) and with also a view to the effect of random disturbances (Sun and Hsu 1991), the protection thickness is nearly identical to the *LIM*. In the stochastic framework, specific indicators have been proposed. The *Stochastic Integrity Measure* (*SIM*) (Soliman and Thompson 1989, 1990) quantifies the effects of a noise excitation superimposed to a basic deterministic (harmonic) excitation, by correlating them with the geometric changes experienced by the deterministic basin of attraction. The *Ratio of Safe Initial Points* (Gan and He 2007) estimates the probability that the system works satisfactorily in a given limited domain within a specified time interval. The *Maximum Speed of Erosion* (σ) (de Souza Jr. and Rodrigues 2002) is an indicator of loss of global safety which quantifies the swiftness with which safe basins are lost as the excitation amplitude is increased, thus accounting mostly for the system robustness in the control space (see Sect. 3.2 forward).

No one of the aforementioned measures relying on distance-based criteria accounts for possible inhomogeneous sensitivities of the state-space variables to perturbations. Yet, in practical applications, a system could be primarily affected by perturbations in one of its characteristic quantities (velocity or position). The *Impulsive Integrity Measure* (*IIM*) (Soliman and Thompson 1989), defined as the *distance between the attractor and the nearest boundary of the basin along the direction of the velocity coordinate* (Fig. 13b), was developed to deal with impulsive problems just in this perspective. It aims at accounting for the sensitivity of an attractor subjected to impact loading, in order to get information about the size of the impulse that could be safely sustained.

More generally, *non-equidistant* measures can better account for *inhomogeneous sensitivities* of the state-space variables to perturbations, thus allowing a more confident and targeted identification of the safe regions. With reference to the 2D case, anisometric integrity measures have recently been introduced as improvement and generalization of the *LIM* and the *IF* (Belardinelli et al. 2018). The *Anisometric Local Integrity Measure* (*ALIM*) is defined as *the maximum of the two semi-axes of an ellipse centered in the safe attractor and totally contained in the largest compact (i.e., safe) portion of the basin* (Fig. 13b), and is thus non-equidistant in the state-space coordinates. It requires fixing a priori the ratio β (anisometric parame-

المنارة للاستشارات

ter) between the axes of the ellipse along the velocity and displacement directions, which reflects the different sensibility along the two directions. Analogously, the *Anisometric Integrity Factor* (*AIF*) corresponds to the *maximum of the two semi-axes of the biggest ellipse totally contained in the safe basin*: as in the *IF*, its center is not constrained in the basin attractor, and thus is "free" to move within the basin to accommodate jagged surfaces.

A substantially different theoretical approach to identify a reliable measure of the sole compact part of the safe basin excluding fractality from the calculation was suggested by Lenci et al. (2013). The idea is that of (i) keeping using the dynamical integrity measures already existing in the literature, but (ii) modifying properly the definition of the safe basin, so that fractal parts are eliminated (or strongly reduced). Hence, the concept of *Actual Safe Basin*, which is obtained *by eliminating from the nominal safe basin all the cells which are not surrounded by cells of initial conditions leading to the same safe basin.* Accordingly, fractal parts are no longer present (just some minimal fragments may subsist, which are effectively inessential) and the actual safe basin has a substantially compact shape (however, it may be disconnected). Once preliminarily eliminated (reduced) the fractal parts, we no longer need to pay attention to the definition of the dynamical integrity measure. For instance, we can take the *GIM* (which is the easiest one). To remember that we are considering the actual safe basin, we name it *Actual Global Integrity Measure* (*AGIM*), i.e., the *GIM* is referred to the "nominal" safe basin, whereas the *AGIM* to the "actual" one.

In summary, as highlighted, all the reported dynamical integrity measures are conceptually different from each other, since each one has been proposed to investigate a specific issue. Of course, other dynamical integrity measures relying on alternative criteria could be introduced, and further generalizations could be made. The former, e.g., by making reference to mechanical (energy-based) concepts instead of geometrical ones; the latter, e.g., by extending the 2D anisometric measures to higher dimensional systems, upon fixing the ratios between all the N-axes of the hyper-ellipsoid in the N-dimensional phase space, or by implementing an automatic search of the bounding ellipse (or other geometrical figures) giving rise to the "worst" dynamical integrity evaluation. More generally, it stands to the designer selecting the most appropriate measure according to the information needed.

3.2 Robustness in the Control Space

Dynamical integrity profiles. To have a comprehensive overview of the global safety of a system, we usually need to investigate in detail the evolution of its dynamical integrity when varying one or more parameters of interest. This is essential to detect the range where the desired outcome can be effectively observed in experiments and practice. In this regard, an engineering integrity diagram quantifying the reduction of the safe basin when increasing the driving parameter under consideration was proposed seemingly for the first time in Thompson and Ueda (1989), together with Thompson (1989).

المنارة للاستشارات

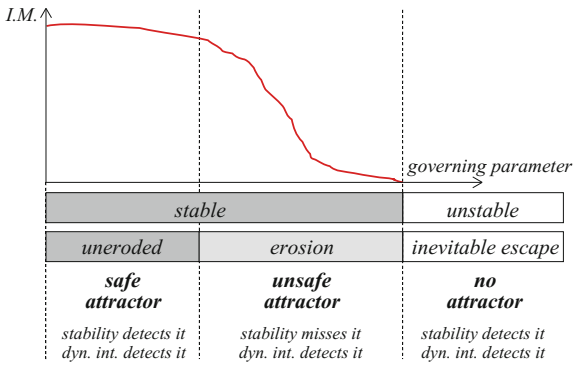

Fig. 14 Schematic dynamical integrity profile

The dynamical integrity profile is obtained by plotting the dynamical integrity measure as a function of the driving parameter, i.e., it offers a complete description of the global effects of a one-parameter variation in the control space. Many different outlines may arise. A schematic is illustrated in Fig. 14, which represents a common case of interest in a safety perspective, wherein the dynamical integrity decreases as increasing the parameter values. Three basically different parameter regions can be observed, which are typically encountered in systems, although with different shapes and extents. We analyze them, highlighting where we can rely on the sole outcomes of the classical local stability theory and where, instead, we have to investigate further and develop a deep insight into the global safety concepts.

In the first region (left side of the profile), both the theoretical and the practical stability are ensured. The desired solution theoretically exists and presents an elevated dynamical integrity (about the 100%), which enables to absorb the disturbances inevitably encountered in real-world applications. The structure can safely operate under realistic conditions. In a region of this kind, the local stability analysis is sufficient and a detailed global safety analysis can be omitted. This observation confirms and supports the fact that the latter is commonly not performed in many systems (e.g., in the case of weak nonlinearities). In fact, if the a priori calculation of a reference basin of attraction guarantees that elevated dynamical integrity properties are regularly achieved in the range of system operating conditions, the system is automatically in a safe situation without any need of further global investigations.

In the second region (middle part of the profile), even if the theoretical stability is ensured, the practical stability may be not guaranteed. Although the desired solution theoretically exists, it is paralleled with a varying dynamical integrity, which may rise up to elevated values as well as drop down to residual ones. As a consequence, the range(s) of practical existence of the desired solution may be smaller, and sometimes considerably smaller, than the one of theoretical existence. Thus, there is no need to avoid from scratch this region, since it offers the possibility to have one or more subsets of parameter values where we can safely operate the system; nevertheless, we need to reliably detect them. In a region of this kind, the local stability analysis

المنارة للاستشارات

has to be *complemented* by the global safety investigation, in order to assess where safe conditions are guaranteed with adequate safety targets.

In the third region (right side of the profile), the desired solution does no longer theoretically exist. To detect the boundary of theoretical disappearance, the local stability analysis is sufficient and there is no need to resort to the assessment of global safety, which is expected to confirm the results of the former.

We further focus on the intermediate region, since it is the one where a detailed global safety analysis is necessary. We can qualitatively distinguish between two different subregions, one on the left-hand side, where the dynamical integrity remains elevated although being slightly reduced, and the other on the right-hand side, where the dynamical integrity is practically residual and further decreases down to the theoretical disappearance of the desired behavior. Note that, depending on the system, the transition from one subregion to the other may be sudden or gradual, which affects the relevant extents.

The first subregion is still robust against disturbances, since it has lost only a small percentage of dynamical integrity, i.e., we can continue to safely operate the system in this range. The second subregion, instead, has critically lowered its dynamical integrity. While the classical stability analysis indicates a certain final response, the global safety analysis clearly alerts that this is completely vulnerable to disturbances, i.e., in practice the system is not able to exhibit it but will switch to another more robust response. It is worth highlighting that this dangerous reduction of dynamical integrity is not forewarned, since there are no features in the system's behavior that may raise the suspect of this dramatic fall of structural safety; we can anticipate it only by resorting to the global safety analysis. Thus, for all these reasons, the second subregion is unsafe and the designer is called upon to avoid working there, where the coefficients of safety are insufficient.

Bifurcations entailing reductions of dynamical integrity. The reduction of system global safety is commonly due to the occurrence of topological mechanisms, usually global bifurcations. These phenomena are central for understanding the system's dynamics under realistic conditions and also for their control. We recall some of them.

Drastic changes of dynamical integrity are typically related to homo/heteroclinic bifurcations of some saddles and to the *erosion* phenomena associated with them. In fact, when a homo/heteroclinic bifurcation takes place, it triggers the erosion of the involved basin. The basins of the surrounding attractors start entering inside it with incursive fractal tongues and reducing its magnitude. Then, the erosion proceeds with different mechanisms, which are usually extremely complex and may involve secondary homo/heteroclinic bifurcations. The erosion ends with the complete destruction of the involved basin, i.e., with the disappearance of the corresponding attractor, which leads to the onset of other dynamical regimes.

Particularly concerning, and indeed quite common, is the case of the homo/heteroclinic bifurcation of a hilltop saddle, which triggers the erosion of the entire potential well. In fact, the hilltop saddle is the globally organizing saddle which governs the whole system dynamics (or most of them). Its invariant manifolds

المنارة للاستشارات

(homo/heteroclinic orbits) delimit the potential well and constitute a barrier against the penetration of trajectories from the out-of-well attractors. Once this protecting barrier has been broken by the global homo/heteroclinic bifurcation, the well starts to be eroded by them, which finally fill it. This may be dangerous, especially in systems of the softening type, where the eroding out-of-well attractor is the escape, and the erosion process finally leads to the failure of the structure.

Yet, the hilltop saddle is not always the one whose invariant manifolds tangency and following intersection are actually responsible for the possibly sharp fall down of the erosion profile. Other saddles relevant to competing basins of attraction within the potential well may also play this role, with some ensuing difficulties as regards both their reliable detection and a possible control aimed at preventing/delaying the manifolds intersection, which has to be implemented in purely numerical terms (see Sect. 4 of Settimi and Rega (2018) in this book), contrary to the hilltop saddle case where an analytical Melnikov-based procedure is also possible (see Sect. 5 forward).

The dynamical integrity may be reduced not only by the erosion but also by the shrinkage of the basin with respect to a competing one, which corresponds to a reduction of *robustness* of the relevant attractor. This typically occurs in the neighborhood of the saddle-node local bifurcations marking the transition from a bistable (coexisting resonant and nonresonant solutions) dynamic regime to a monostable (resonant or nonresonant) regime within a safe potential well. Their global effects consist of the progressive contraction of the basin of the previously dominant attractor down to its final disappearance, and of the parallel expansion of the basin of the competing attractor which ends up remaining the sole one in the well.

In this context, another unsafe and potentially dramatic dynamical situation is represented by the boundary crisis (Grebogi et al. 1983; Nayfeh and Balachandran 1995), which is the global bifurcation event entailing the sudden disappearance of a chaotic attractor when it collides with the saddle point whose stable manifold delimits its basin. Below the bifurcation threshold, the state of the system is definitely safe, with an uncorrupted basin of attraction, if it is guaranteed that the system parameters undergo only small changes. At the bifurcation point, instead, the chaotic attractor suddenly vanishes and its former basin is captured by another, possibly unwanted, coexisting attractor (e.g., an in-well chaotic attractor is replaced by a cross-well one), with a variety of possible topological patterns.

3.3 A Novel Criterion for Load Carrying Capacity

A novel paradigm. We have observed that the effects of the (non-necessarily small) imperfections always present in the real world must be considered in general terms by referring to perturbations either of the initial conditions in the phase space or of the system parameters in the control space. The former may directly drive the response out of the safe basin toward a different, more robust, attractor (bounded or unbounded), when the basin itself is too small and/or too eroded; the latter may indirectly prevent from the possibility to actually realize the desired response, owing

المنارة للاستشارات

to the associated meaningful, and possibly sudden, reduction of dynamical integrity entailed by also small parameter variations.

Accordingly, the load carrying capacity is robustly achieved if the system is able to sustain changes in both the initial conditions and in the control parameters without changing the desired outcome, i.e., provided that:

(i) the solution/attractor of interest is practically stable, namely, it is characterized by a nonresidually integer (i.e., a suitably large and compact) basin, which allows to sustain the effects of finite changes in the initial conditions;
(ii) such a nonresidually integer basin is robust with respect to small changes in the control parameters values.

The combination of both these conditions allows detecting all the parameter ranges where the system is effectively reliable under the expected magnitude of disturbances. A further safety step consists of verifying whether such a minimum acceptable value of generalized dynamical integrity—which governs the practical stability of a solution/attractor—is actually kept when varying other control parameters in such a way to guarantee a satisfactorily uniform system safety.

Thus, the dynamical integrity offers a *novel paradigm* for evaluating the load carrying capacity of a system. This point will be extensively resumed in Sect. 6, which is entirely focused on the dynamical integrity approach in the design stage, in view of safely making use in applications of all the potential of the system.

Overall, as far as the problem of practical stability of structures is concerned, it is the authors' opinion that upon assuming the Thompson global safety perspective the issue of system load carrying capacity can be considered as definitely understood from a theoretical point of view, although much work is still needed in the direction of practical applications of the underlying ideas.

System's dynamical integrity scenario. Before proceeding with the dynamical integrity investigation in different case studies, it is worth briefly dwelling on the erosion of the potential well. The well reflects the mechanical and mathematical characters of a system, and its analysis is fundamental for a comprehensive knowledge. As observed in the previous section, when the homo/heteroclinic bifurcation of the manifolds of the hilltop saddle(s) occurs, it triggers the erosion of the well, which then increasingly proceeds. All this scenario has very important consequences in terms of both dynamics and dynamical integrity.

Specifically, depending on the out-of-well attractor onto which the system settles down after exceeding the potential barrier, we can distinguish between softening and hardening systems.

Softening systems. The system dynamics escape to "infinity." This is the case where, after the escape, the motion is theoretically *unbounded*. In fact, after the escape, there are no more mechanical resources to keep the dynamics bounded out of the well and the response is forced to inevitably diverge to infinity. The "infinity" attractor is the eroding attractor. We observe an increasing mutual tangling of its basin of attraction with the basin of attraction of one or more bounded attractors. The "infinity" attractor penetrates with fractal tongues inside the potential well and increasingly erodes the safe bounded area up to the total destruction of the well.

المنارة للاستشارات

This scenario where the trajectories rapidly approach infinity physically corresponds to the actual failure of the system, which is definitive and immediate. This outcome is usually destructive. Mechanical situations of reference in this respect are the capsizing of a rolling ship in ocean waves (Thompson et al. 1990), the overturning of a rocking rigid block under periodic acceleration of its basement (Lenci and Rega 2005), etc. However, there are technical situations wherein realizing a regime nominally "at infinity" is, on the contrary, highly desirable. For example, in a MEMS device (Younis 2011), the escape has the physical meaning of pull-in phenomenon, i.e., the collapse of the device onto the electrically charged substrate. When the MEMS is designed to be used as a resonator or sensor device, we are called to avoid the pull-in behavior; conversely, when it is designed to be used as a switch device, we are called to look for it.

Thus, in a softening system, the erosion is typically dangerous (usually much more dangerous than in a hardening system), even if of course this strongly depends on the specific problem at hand.

Hardening systems. The overall system dynamics still remains *bounded*, although being no more restricted within the reference well. This is the case where, after the escape, the motion develops entirely within a neighboring bounded well or it wanders around, e.g., two wells (the reference and a neighboring one). In fact, after the escape, the dynamics cannot go to infinity due to the system positive stiffness for whatever large displacements. The erosion of the analyzed well is due to the interpenetration of basins from adjacent wells, which basically do not change in magnitude but simply become tangled. The eroding attractor(s) is (are) that (those) of the neighboring potential well and vice versa.

Despite the tangling between the wells, only (safe) bounded behaviors can be expected. There are several classes of motion pertaining to such after-escape non-destructive regimes. The out-of-well phenomenon that typically sets on after the escape consists in chaotic attractors scattered between adjacent wells (the so-called cross-well chaos), although regular scattered attractors may also arise. They are quite common in systems. Scenarios of this kind may be observed for instance in a two-well Duffing-type oscillator (Lenci and Rega 2003b).

Depending on the application, such kinds of dynamics may need to be avoided or somehow controlled. However, technical situations can be devised wherein realizing alternating dynamic regimes between the reference well and an adjacent one can even be desirable. For example, the shift between oscillating (in-well) and rotating (out-of-well) regimes in a planar pendulum subjected to vertical harmonic excitation of its support has been advised for application in energy extraction (Wiercigroch 2010; Lenci and Rega 2011a).

Thus, in the hardening case, the out-of-well phenomenon is often unpleasant from the application viewpoint. However, it does not usually destroy the structure (immediately).

Both in softening and hardening systems, to study the detrimental effects of the erosion, the typical approach is that of deepening the dynamical integrity analysis progressively step by step, starting from the potential well, and then, depending on the obtained outcome, proceeding further with additional investigation.

المنارة للاستشارات

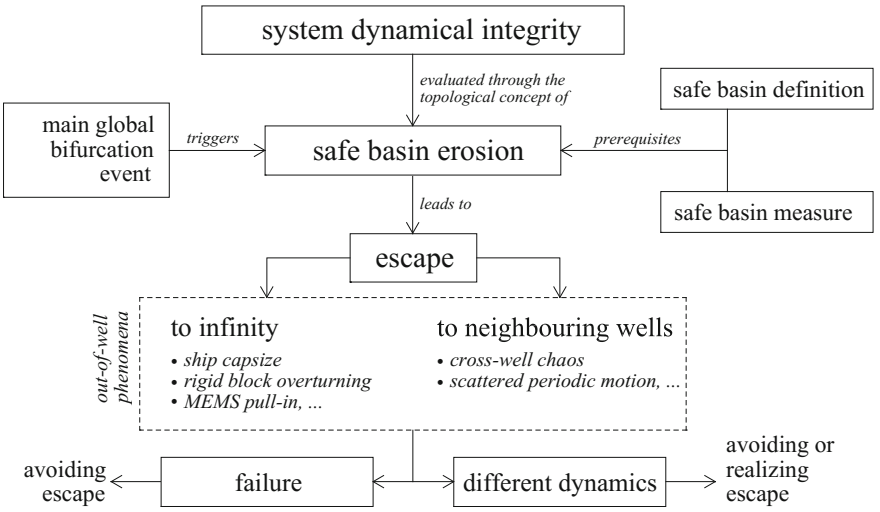

Fig. 15 System's dynamical integrity scenario

In fact, if the dynamical integrity of the well is elevated, there is the possibility to effectively operate the system within the desired well; in this case, exploring in depth the in-well dynamics may be worthy, e.g., by analyzing the individual in-well attractors. On the contrary, if the dynamical integrity of the well is residual, there is no possibility to effectively operate in these conditions; in this case, refining in depth the simulation is not so worthy, since each individual attractor will certainly be more vulnerable than the well containing it.

Of course, we would better refer to a dynamical integrity measure or another depending on the objective of the study, i.e., for a comprehensive knowledge, we need to combine the achievements coming from different dynamical integrity viewpoints. A schematic flowchart of the overall system's dynamical integrity scenario is shown in Fig. 15.

3.4 GIM, LIM, *and* IF*: A Comparative Study*

In the following, we report a case study where the system's dynamics are particularly rich. To address this complex behavior, we need to analyze its structural safety from different *perspectives*. Accordingly, different definitions of safe basin and different dynamical integrity measurements are considered. The combined use of different dynamical integrity tools is essential to raise the analysis to *advanced* levels of knowledge. This investigation is extracted from Ruzziconi et al. (2013e), which we refer to for more details.

المنارة للاستشارات

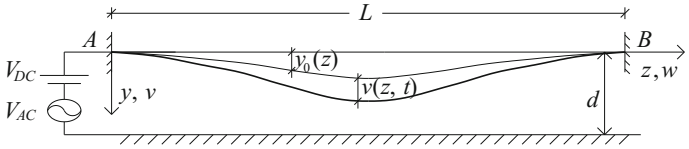

Fig. 16 A schematic of the slacked CNT

A slacked carbon nanotube electrically actuated. Nanoelectromechanical systems (NEMS) are a growing area of research, which extends the microelectromechanical systems (MEMS) technology to the nanoscale (Younis 2011). We examine a NEMS constituted by an electrically actuated single-walled slacked carbon nanotube (CNT). The electrode is placed directly underneath the CNT, at a certain distance d, which shrinks along the length of the nanotube due to the slacked configuration, Fig. 16.

We investigate the nonlinear behavior in a neighborhood of the first symmetric resonance frequency. The considered single-mode reduced-order model of the system's response is (Ruzziconi et al. 2013e)

$$\ddot{x} + 0.01\dot{x} + 1390.2x - 11570.8x^2 + 36392x^3 - \frac{0.26577}{(0.56866 - x)^2}(V_{DC} + V_{AC}\cos(\Omega t))^2 = 0 \tag{7}$$

where $x(t)$ is the modal coordinate amplitude, V_{DC} is the electrostatic voltage load (in the following assumed as fixed and equal to $V_{DC} = 1$ V), and $V_{AC}\cos(\Omega t)$ is the electrodynamic excitation with voltage V_{AC} and frequency Ω. The analysis is performed as the last two driving parameters are varied. The system has a single potential well with escape direction. In the present case, escaping means dynamic pull-in, which is completely unsafe and dangerous from a practical viewpoint since it leads to the failure of the device.

Thanks to the inherent nonlinearities, several principal attractors with different characteristics exist and compete in robustness, which may be desirable in CNT applications (Xu et al. 2017). They are named for convenience A, B, C, and D. An example of this multistability is depicted in the frequency response diagram in Fig. 17, where (i) A and B are the nonresonant and the resonant branches, respectively, overall exhibiting bending toward lower frequencies; (ii) C enlarges its oscillations at increasing frequency values and exists for a wide range, which exceeds the window shown in the figure; and (iii) D performs very large motion. Additionally, various minor attractors are observed which, differently from the principal ones, rapidly appear and disappear surviving only in narrow parameter ranges.

We focus on the attractor-basins phase portraits at $\Omega = 33$ when increasing V_{AC}, Fig. 18. The basins of B and C are, respectively, orange and green, the basins of the minor attractors are in the grayscale, and the escape is white. At $V_{AC} = 2$ V in Fig. 18a, there are only B and C. The compact regions of their basins are close to

المنارة للاستشارات

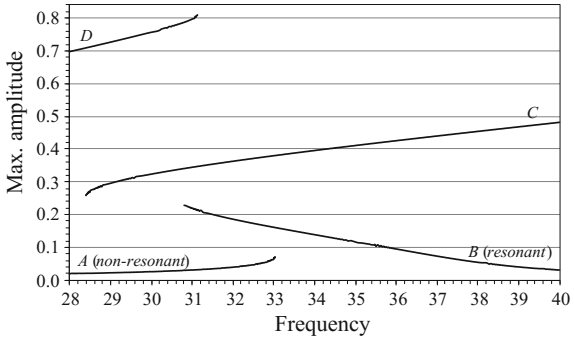

Fig. 17 Frequency response diagram showing the principal attractors at $V_{AC} = 3$ V

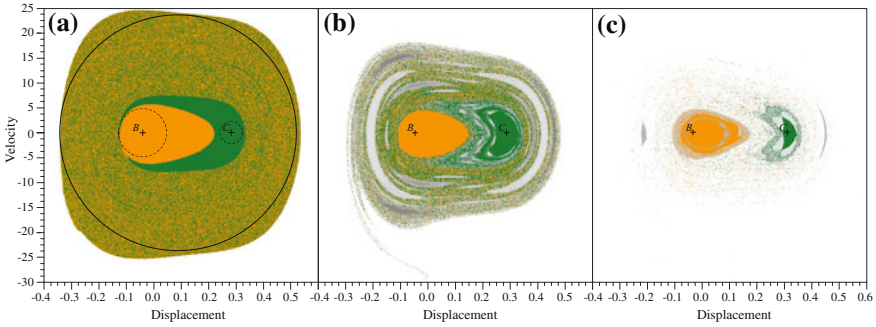

Fig. 18 Attractor-basins phase portraits at $\Omega = 33$ and (from left to right) **a** $V_{AC} = 2$ V, **b** $V_{AC} = 5$ V, **c** $V_{AC} = 6.4$ V, with examples of the circles used for the evaluation of the *IF* dynamical integrity for the potential well (solid line), and of the *LIM* dynamical integrity for the practical disappearance of each attractor (dashed line)

each other. They are large, but not so extensive with respect to the whole potential well. Fractality amply broadens, surrounding these compact cores.

At $V_{AC} = 5$ V in Fig. 18b, some minor attractors emerge. Each basin is small and mainly fractal, but all of them are able to cover substantial parts of the phase space, which considerably increases the probability to catch them in applications. They contribute to further expand fractality at the expense of the safe compact areas of the principal basins. Up to this voltage, the escape is located outside the fractal region, but slightly increasing V_{AC} the scenario suddenly changes.

At $V_{AC} = 6.4$ V in Fig. 18c, the escape enters the potential well, completely erodes the extensive fractal region, strongly reduces the basins of B and C, and separates them from each other. This produces an increasing vulnerability to dynamic pull-in. Other minor attractors appear and definitely deteriorate the integrity of the principal ones. Thus, the CNT is unsafe actually well before the inevitable escape, which occurs at about $V_{AC} \cong 9.2$ V.

المنارة للاستشارات

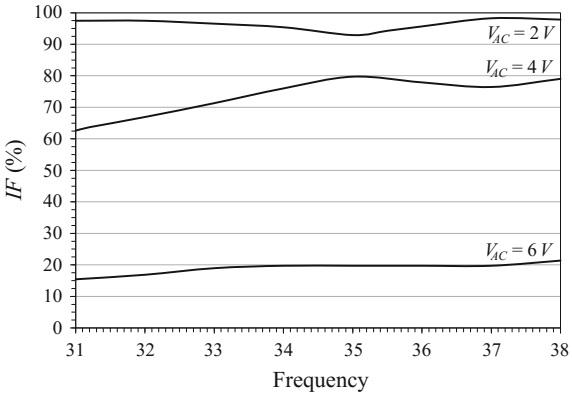

Fig. 19 Dynamical integrity profiles of *IF* for the potential well

The potential well (IF). We examine the system's dynamical integrity. We start the investigation by analyzing the potential well, i.e., all the bounded attractors taken together. Our aim is that of understanding the parameter ranges where the well remains wide enough, in order to tolerate disturbances in the initial conditions and avoid the escape (dynamic pull-in). Since we focus on the potential well, the safe condition is represented by all the initial conditions leading to a bounded motion, whereas the unsafe condition is represented by the escape solution. Hence, we consider as safe basin the union of the basins of all the bounded attractors.

To measure its dynamical integrity, we resort to the *IF* (an example of the circles is reported in Fig. 18a in solid line). In fact, since the circle does not refer (is not centered) at a particular attractor, this measurement is able to investigate in general and easily the entire potential well. Also, it allows considering only the compact "core" of the safe basin, ruling out its unsafe fractal tongues with the escape. Note that when the escape enters the well, it separates the compact area of bounded motion into several smaller parts, e.g., in Fig. 18c. According to the considered definition of safe basin, the *IF* has to be computed in the largest of these parts. This is in agreement with our purposes, since we wish to examine if at least the largest bounded area is still robust. As normalizing condition, it is assumed the case at $V_{AC} = 0.005$ V, i.e., next to the unforced dynamics where the well approximately achieves its maximum extent.

To analyze the changes in the well's dynamical integrity, we build the integrity profiles, where we calculate the *IF* as a function of the frequency, at a certain fixed V_{AC} value. Some of the curves are shown in Fig. 19. They are obtained by performing several attractor-basins phase portraits, evaluating the *IF*, and plotting the profile.

In this parameter range, the *IF* is nearly independent of Ω, but depends on the value of V_{AC}. When the voltage is small, e.g., at $V_{AC} = 2$ V, the well has an elevated dynamical integrity ($IF \cong 95\%$), which suggests the possibility to operate the nanostructure in safe conditions, far from the danger of pull-in. This safe region continues to exist for a wide parameter range. At $V_{AC} = 4$ V, the well is still robust, since the *IF* reduces, but remains very high, mainly over the 75%. At $V_{AC} = 6$ V, instead, the

المنارة للاستشارات

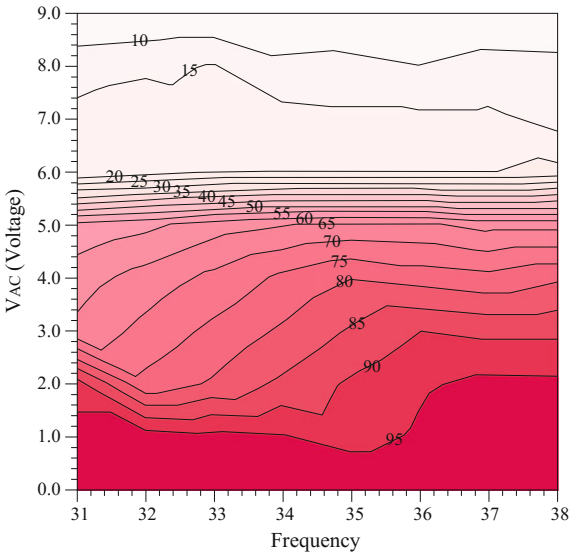

Fig. 20 Dynamical integrity chart of *IF* for the potential well

integrity of the well completely drops and becomes nearly residual, with $IF \cong 20\%$, i.e., the danger of dynamic pull-in increases considerably and arises much before the theoretical inevitable escape.

To describe the overall dynamics when both the frequency and the voltage are varied, we draw the integrity chart reported in Fig. 20. It illustrates the curves of constant percentage of *IF*. They are obtained as a contour plot of several integrity profiles, where a sampling grid of $\Omega \leq 1$ and $V_{AC} \leq 1$ V or less has been used. We can identify three parameter ranges with three different behaviors. The first range is $V_{AC} = [0; 5]$ V, where we can find safe conditions. In fact, the contour curves are distanced between each other, i.e., the deterioration of the dynamical integrity is rather small, slow, and approximately gradual. This range is worth for a further analysis, in order to understand which attractor may be expected to effectively operate the device.

The second range is $V_{AC} = [5; 6]$ V. Here, the contour curves are close to each other, and the system quickly switches from $IF > 55\%$, where it is able to tolerate considerable disturbances in safe conditions, to $IF < 20\%$, where it is totally vulnerable. This clearly detects the voltage range where the penetration of the escape destroys the well and alerts that the deterioration occurs suddenly, within a very small interval. To protect the nanostructure, we are required to assume in the design adequate coefficients of safety, which are able to keep any application far from this threshold.

The third range is $V_{AC} = [6; 9.2]$ V. In this last case, the dynamical integrity never exceeds $IF = 20\%$ and keeps slowly decreasing up to the inevitable escape. The well has lost much of its robustness. Disturbances typically encountered in experiments and in practice likely will lead to dynamic pull-in. This range is not worthy to further

المنارة للاستشارات

refine the simulations in order to detect the behavior of specific attractors, since they are equally or even more vulnerable than the entire well.

The probability of the attractors (GIM). We further investigate the range $V_{AC} = [0; 6]$ V where the well is robust, in order to explore the dynamical integrity properties of the in-well attractors. Initially, we consider each single attractor separately and analyze if it is paralleled with a wide basin of attraction. If its magnitude is very narrow, from a practical point of view the corresponding attractor does not exist; otherwise, it may effectively operate the device and may deserve further investigations.

The safe basin is the basin of attraction of each considered attractor, i.e., the safe condition consists of the initial conditions leading to the attractor under investigation. We measure the dynamical integrity of each safe basin using the *GIM* which includes both the steady dynamics (compact area around the attractor) and the transient (e.g., thin fractal and/or smooth tongues). This indicates that the *GIM* is able to provide information on the probability to catch each single attractor. From a computational point of view, the rest of the analysis is similar to the one developed in the previous subsection.

In Fig. 21, we report the integrity profile of *GIM* for *A* (blue), *B* (orange), *C* (green), and *D* (violet). For comparison, we show also the *GIM* of the whole potential well (all the bounded attractors together, black), and the *GIM* of the minor attractors (all of them together, gray). At $V_{AC} = 2$ V in Fig. 21a, the magnitude of the well is practically maximum. It is mainly covered by both *B* and *C*, which may reach and overcome $GIM = 40\%$ (except at $\Omega < 34$ in *B*). The integrity of *A* is usually smaller, $GIM \cong 10$–20%, and becomes residual both at $\Omega \cong 32$, where the extent of the already fractal part of its basin reduces noticeably, and in a neighborhood of the disappearance of the attractor. Similarly, *D* never exceeds $GIM = 20\%$. Minor attractors appear only at $\Omega \cong 31$–32, and actually they do not exist under realistic conditions because their *GIM* is too small.

Increasing V_{AC}, instead, the profile is completely different. At $V_{AC} = 6$ V in Fig. 21b, the total wideness of the potential well reduces ($GIM \cong 20$–30%). We can note that when the escape basin penetrates, it not only destroys the compact areas of the well (as observed by analyzing the *IF*) but also strongly reduces the probability to catch a bounded motion. A part of the well consists of the basin of *B* and *C*. The other part, instead, is due to the basins of minor attractors. At this voltage, they exist along all the analyzed Ω-range and the magnitude of their basins is non-trivially larger. Their *GIM* recurrently overcomes the *GIM* of the principal ones (even if each one of them, taken separately, has a small basin). They can be no longer neglected to the aim of identifying the actual dynamical outcome.

The general outline is described in more detail in the integrity charts in Fig. 22. Despite the extensive fractality and the multistability, this analysis is able to indicate which attractors can be effectively observed. Their number is smaller than the number of theoretical attractors.

At $V_{AC} = [0; 4]$ V, attractor *B* can practically appear in all the analyzed range, except in the trapezoidal region ranging from $V_{AC} = 1$ V and $\Omega \cong 31$–32 to $V_{AC} = 4$ V and $\Omega \cong 31$–35, where the *GIM* is residual, Fig. 22a. Similarly, the *GIM* of attractor

المنارة للاستشارات

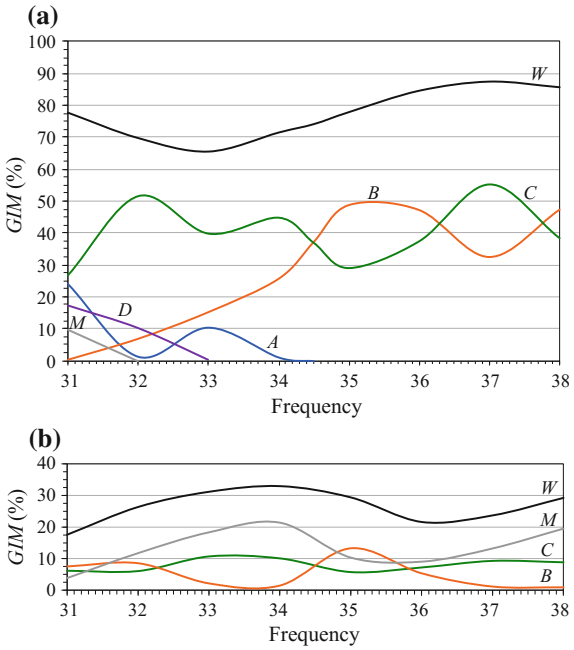

Fig. 21 Dynamical integrity profiles of *GIM* for the probability of the attractors at **a** $V_{AC} = 2$ V; **b** $V_{AC} = 6$ V. Attractor *A*, *B*, *C*, *D,* and minor attractors *M* are, respectively, blue, orange, green, violet, and gray. The potential well *W* is black

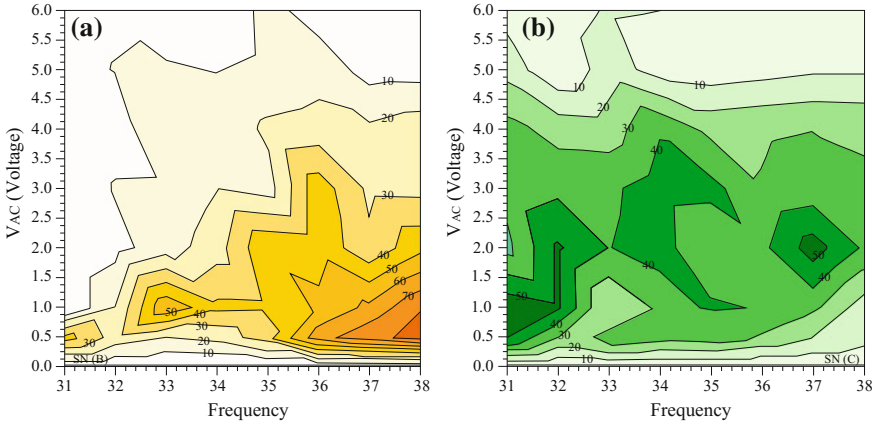

Fig. 22 Dynamical integrity charts of *GIM* for the probability of occurrence of **a** attractor *B* and **b** attractor *C*

C is fair up to $V_{AC} = 4$ V, except for a tiny range close to its saddle-node bifurcation, Fig. 22b. At $V_{AC} = [4; 6]$ V, the dynamical integrity of *B* and *C* drops, whereas the

المنارة للاستشارات

GIM of all the minor attractors increases; moreover, their basins of attraction usually develop close to the escape, as shown in Fig. 18. This confirms and underlines the increasing danger of behavior at higher V_{AC} values, as alerted in the *IF* dynamical integrity analysis of the potential well (previous subsection).

The practical disappearance of the attractors (LIM). As previously observed, the principal attractors (especially *B* and *C*) are by far more likely to occur. Nevertheless, a high probability does not guarantee to operate the system with them. This is because in many parameter ranges these attractors are paralleled with a small compact part of their basins of attraction, which may be not robust enough to tolerate the inevitable uncertainties in the initial conditions. Consequently, the attractor may practically disappear, e.g., it may jump to one of the highly probable coexisting motions.

To have a more detailed description, we consider the attractors that have large probability of occurrence and we examine their practical disappearance, in order to have information about the range where each one of them can be reliably observed under realistic conditions. Operatively, we focus on each attractor, consider as safe basin its own basin of attraction, and measure the dynamical integrity via the *LIM*, which provides a good estimate of the integrity also in case the attractor is eccentric with respect to the safe basin. Examples of the circles for the *LIM* evaluation are reported in Fig. 18a in dashed line.

The *LIM* is not very wide for all the attractors. At $V_{AC} = 2$ V in Fig. 23a, the resonant *B* shows *LIM* $\cong 8\%$ in $\Omega \cong [31; 34]$, then a sudden increment at $\Omega \cong 34.5$, which is related to the disappearance of *A*, and finally *LIM* $\cong 20$–30% in $\Omega \cong [35; 38]$. Attractors *A*, *C*, and *D* never exceed *LIM* $= 12\%$, i.e., they practically exist only if very small disturbances are ensured. Increasing V_{AC}, the *LIM* further reduces. At $V_{AC} = 6$ V in Fig. 23b, both *B* and *C* are equipped with a very small integrity, with *LIM* $\cong 7$–12%, which drops at $\Omega \cong 32$, where both basins are affected by minor attractors.

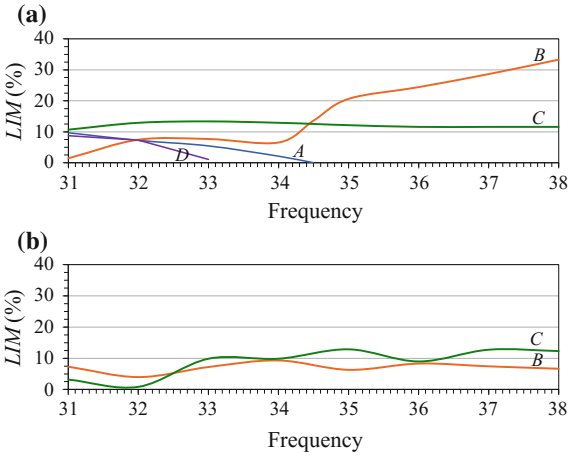

Fig. 23 Dynamical integrity profiles of *LIM* for the practical disappearance of the attractors at **a** $V_{AC} = 2$ V; **b** $V_{AC} = 6$ V. Attractor *A*, *B*, *C*, *D*, and minor attractors *M* are, respectively, blue, orange, green, and violet

المنارة للاستشارات

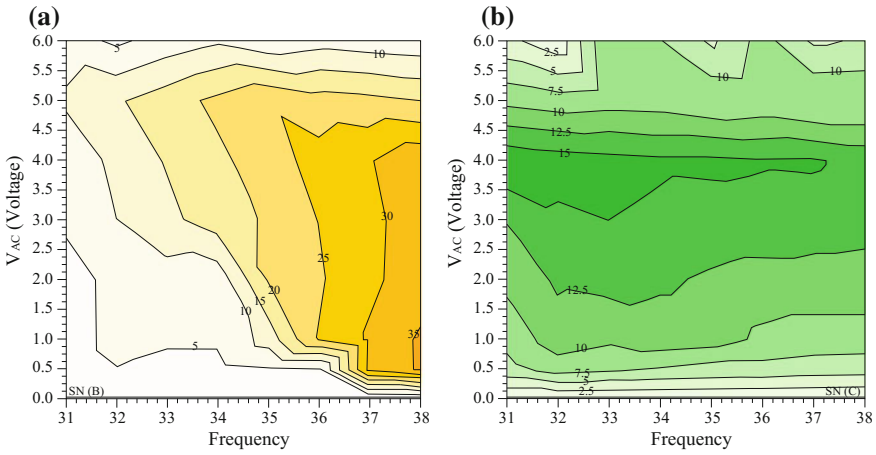

Fig. 24 Dynamical integrity charts of *LIM* for the practical disappearance of **a** attractor *B* and **b** attractor *C*

In Fig. 24, we show the integrity charts for *B* and *C*. They confirm that there are ranges where these attractors may be vulnerable to disturbances, despite the relatively large magnitude (*GIM*) of their basins. For *B* in Fig. 24a, the major *LIM* occurs at $\Omega > 33$ and becomes wide at $\Omega > 35$, where *LIM* $\cong$ 20–35%, which may guarantee to safely observe this motion also in case of large disturbances. For *C* in Fig. 24b, the *LIM* has maximum percentage at about $V_{AC} = [2.5; 4]$ V, but never reaches elevated values.

Therefore, there are many parameter ranges where the attractors are equipped with a meaningful *GIM* and a very small *LIM*, e.g., *C* has *GIM* = 30–40% and *LIM* = 10–12.5% at $V_{AC} = 1.5$ V. This means that there is a good probability to catch the attractor, but we cannot ensure to keep operating the device with this motion (also at small V_{AC} values), since disturbances may make it disappear in favor of switching to another attractor. Further deepening the analysis, we may need to understand (where possible) if this disappearance will lead to a safe jump to another bounded motion or to dynamic pull-in. For this additional dynamical integrity investigation, we refer to Ruzziconi et al. (2013e).

Overall, despite the complexity of the system's behavior, the combined use of both the *IF* and the *GIM* narrows it down to a small effective parameter range and to a few operating attractors; the *LIM* highlights the actual possibility to operate with a desired attractor, due to the topological sensitivity of its basin to inevitable uncertainties.

Therefore, the present case study illustrates a *synergic* combination among different dynamical integrity tools.

المنارة للاستشارات

4 Dynamical Integrity: Analysis

In the present section, we focus on the analysis of the overall evolution of the global safety, in view of a safe engineering "use" of the system. Two different case studies are presented, specifically a pendulum parametrically excited (Sect. 4.1) and a rigid block (Sect. 4.2).

The pendulum parametrically excited offers a complex nonlinear behavior. The dynamical integrity analysis is seen to provide valuable information about the robustness of competing solutions of different interest from an applicative viewpoint. Evident effects on the global safety are induced by dynamical events, which are analyzed by combining results from different complementary measures.

The rigid block represents a nonclassical problem. Here, we address the issue of extending the dynamical integrity tools in order to investigate properly its distinctive features. Two aspects of the dynamical analysis are emphasized, which typically do not arise in classical systems, i.e., (i) the interest toward the outcome of a specific initial condition of mechanical interest, instead of the whole dynamics, and (ii) the introduction of an alternative—and more reliable for the present case (and similar ones)—definition of safe basin, which accounts for the effect of the phase excitation.

Additional models will be considered in the forthcoming sections.

4.1 The Parametrically Excited Pendulum

The pendulum parametrically excited was extensively analyzed in the literature, e.g., the main nonlinear dynamical features have been examined in depth by Szemplińska-Stupnicka et al. (2000). We start with recalling the nonlinear response, to be successively referred to for understanding integrity and erosion features. The pendulum's dynamical integrity is shown to be strongly related to the dynamical properties of the system. The interaction among competing dynamic solutions (oscillations and rotations) is explored as part of a broader project aimed at developing advanced technologies for the extraction of energy from sea waves (Wiercigroch 2010; Xu et al. 2005, 2007; Xu and Wiercigroch 2007; Lenci and Rega 2011a; Lenci et al. 2012a, 2013; Das and Wahi 2016; etc.). The main singularities along the integrity profiles are associated with the occurrence of topologically meaningful dynamical events. Further details may be found in Lenci and Rega (2008).

Mechanical model and principal dynamical features. The nonlinear dynamics of the parametrically excited pendulum in Fig. 25a are governed by the dimensionless equation of motion

$$\ddot{x} + h\dot{x} + [1 + p\cos(\omega t)]\sin(x) = 0 \tag{8}$$

where h is the viscous damping, and p and ω are the amplitude and frequency of the vertical oscillation of the pivot, respectively. To take advantage of the results

المنارة للاستشارات

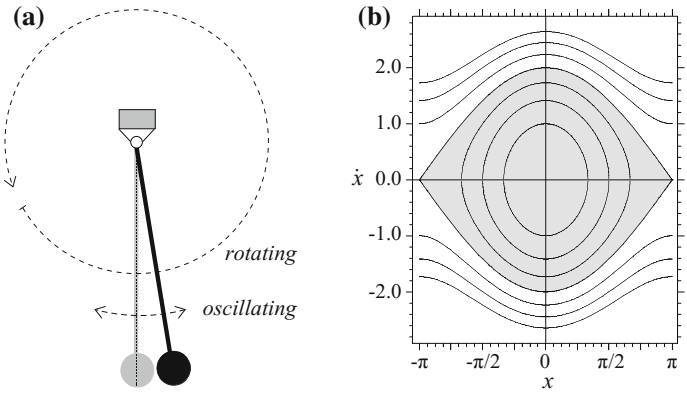

Fig. 25 **a** Parametrically excited pendulum. **b** Undamped unforced phase portrait

in Szemplińska-Stupnicka et al. (2000), we consider $h = 0.1$, which is the damping assumed in that paper; of course, the general findings are expected to hold also for a different value. We investigate the pendulum in correspondence of the principal parametric resonance, $\omega = 2$.

The phase portrait of the undamped unforced system is depicted in Fig. 25b. There are "small" amplitude (in-well) oscillations around the rest position $x_r = 0$ and "large" amplitude (out-of-well) rotating solutions. They are divided by the homoclinic orbits of the hilltop saddle $x_s = \pi$ (or $x_s = -\pi$, since they coincide due to the periodicity of the system), which separate the rotating from the oscillating regions in the phase space.

Adding damping and excitation, dynamics increase their complexity. We report the bifurcation diagram at $p \in [0, 2]$, Fig. 26. There are four competing attractors. The first one is the rest position, which turns into the inverse saddle (Ir) through a Hopf (*H*) bifurcation at $p \cong 0.196$. The stability is captured by the self-symmetric oscillating period-2 solution (O2), which is born simultaneously. O2 is stable up to $p \cong 1.260$, where it becomes a saddle through a pitchfork (*PF*) bifurcation. Upon a period-doubling (*PD*) cascade to chaos starting at $p \cong 1.332$ and ending at $p \cong 1.342$ by a boundary crisis (*CR*), the last oscillating attractors definitely disappear.

There are two rotating attractors (R1), which are born at $p \cong 0.418$ through a saddle-node (*SN*) bifurcation, along with the associated direct saddles (DR1). One is clockwise; the other is anticlockwise and symmetric with respect to the first (only one is reported in the figure). R1 are stable up to $p \cong 1.349$, where they become inverse saddles (IR1). Here, a classical *PD* cascade is triggered, definitely ending at $p \cong 1.809$ by a *CR* after which the tumbling chaos becomes the unique attractor (Bishop and Clifford 1996).

In addition to the previous principal attractors, there are other secondary motions. We can see the couple (one clockwise and one anticlockwise) of period-3 rotations R3 (again, only one is reported in the figure), born at $p \cong 0.888$ by a *SN* bifurcation

المنارة للاستشارات

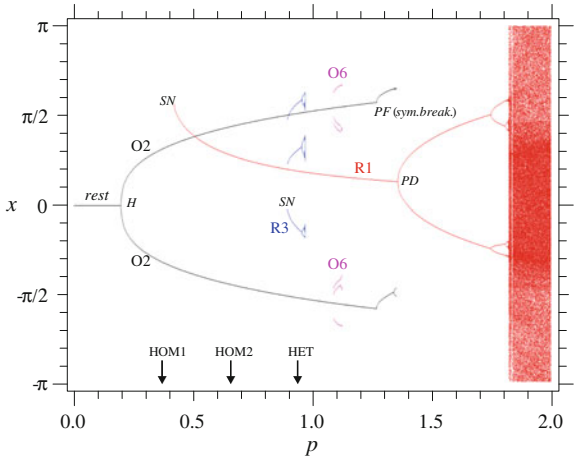

Fig. 26 Bifurcation diagram of the attractors at $\omega = 2$. HOM1, HOM2, and HET are the thresholds for homoclinic bifurcation of the hilltop saddle, homoclinic bifurcation of DR1, and heteroclinic bifurcation of DR1 and Ir, respectively

together with the corresponding saddle, and undergoing a *PD* cascade ending by a *CR* at $p \cong 0.961$, where R3 disappear. A self-symmetric oscillating attractor O6 of period-6 appears at $p \cong 1.082$ by a *SN* bifurcation, loses stability by a *PF* bifurcation to two O6 solutions at $p \cong 1.111$, which undergo a *PD* cascade ending by a *CR* at $p \cong 1.118$, after which O6 disappear.

Thus, in the range $p \in [0.418, 1.342]$, the in-well oscillating O2 and the out-of-well rotating R1 solutions coexist and compete with each other; in the range $p \in [0.888, 0.961]$, two further competing attractors R3 are present.

Three main global bifurcations can be observed. The first one is the homoclinic bifurcation of the hilltop saddle (HOM1) occurring for $p \cong 0.367$. This is the solely global event which can be approximated analytically by means of the Melnikov method (Guckenheimer and Holmes 1983; Koch and Leven 1985; Wiggins 1990). While being theoretically very important because it breaks the barrier between oscillating and rotating solutions, and thus permits mutual interferences, in the present case it has no direct and observable consequences in terms of dynamical integrity, basically because it occurs when the rotating attractors are not yet born (they appear slightly later, for $p \cong 0.418$).

The second global bifurcation is the homoclinic bifurcation of DR1 (HOM2) at $p \cong 0.655$. This has instead important practical consequences, since (not shown in the figures) the unstable manifold W_1^u, which belongs to the basin of O2, becomes tangent to the stable manifold W_1^s, which is the boundary of the basin of R1. Due to this global bifurcation, the boundary between the basins of the rotating and oscillating solutions becomes fractal, as clearly visible in Fig. 27b. The basin of oscillation O2 is gray, the basins of rotations R1 are blue (clockwise) and red (anticlockwise), and the basins of rotations R3 are dark blue (clockwise) and dark red (anticlockwise). By

المنارة للاستشارات

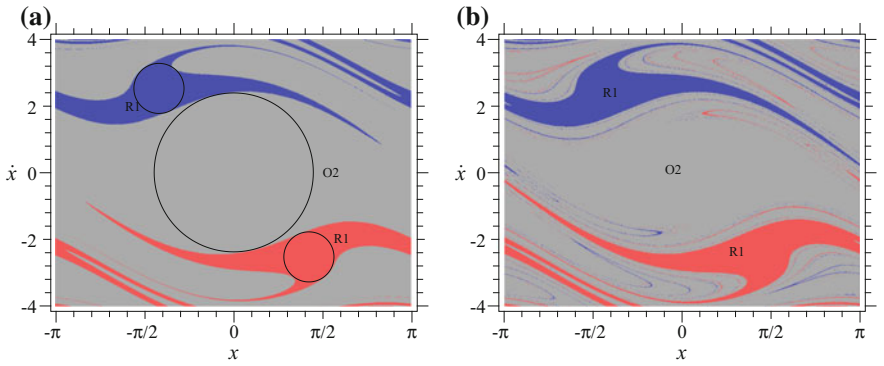

Fig. 27 Attractor-basins phase portraits at **a** $p = 0.65$, **b** $p = 0.70$. In (**a**), examples of the circles involved in the definition of the *IF* are reported

comparing Fig. 27a and b, we can observe that the basins of rotation and oscillation solutions start to tangle with each other and a mutual erosion through fractal tongues is triggered. Also, since the unstable manifold W_2^u belonging to the basin of R1 is still disjoined from the stable manifold W_2^s (not shown in the figures), the tongues of the basin of the rotating solutions penetrate the basin of the oscillating solution, but not vice versa, Fig. 27b. Thus, the rotating solutions are, roughly speaking, more robust and somehow dominating. As better observed next, this has significance in terms of dynamical integrity.

Note that the fractalization of the potential well of the oscillating solution starts from the outer part (it is possible because the homoclinic bifurcation of the hilltop saddle happened earlier). Initially, it tends "slowly" toward the central part of the potential well (compare Figs. 27b and 28a). Then, the penetration undergoes an instantaneous acceleration (compare Fig. 28a and b). This is due to the heteroclinic bifurcation of DR1 and Ir (HET), at $p \cong 0.935$, which is the third global bifurcation observed in Fig. 26. This suddenly drives the fractality around the rest position, i.e., in the central part of the potential well. The period-2 oscillation survives in a basin whose compact part is tightened around the corresponding two sinks in the stroboscopic Poincaré map (Fig. 28b).

In Fig. 28a, b, the basins of attraction of the secondary attractor R3 are also visible. R3 appear just inside the basins of attraction of R1, and thus they are basically antagonists of R1 and not of O2. In Fig. 28a, the basins of R3 have their maximum extent; then they rapidly decrease, Fig. 28b, until they disappear, which occurs for $p \cong 0.961$, i.e., just "after" Fig. 28b. Successively, after the disappearance of O2, only R1 solutions (clockwise and anticlockwise) remain, but the attractor-basins scenario is dominated by an extended fractality, which covers all the phase space except for a very small compact part surrounding each attractor [not shown in the figures, see Lenci and Rega (2008)].

المنارة للاستشارات

Integrity profiles. We investigate the dynamical integrity of the attractors previously identified. Since we are interested only in the steady dynamics, we consider as safe basin the classical basin of attraction of each attractor. Both *IF* and *GIM* are analyzed, as they provide complementary information and their combined use permits a comprehensive understanding of the overall evolution of the integrity scenario.

We focus on the phase space window $x \in [-\pi, \pi]$ and $\dot{x} \in [-4, 4]$, which contains the compact part of each attractor involved in the analysis, as in Figs. 27 and 28. To compute the *GIM*, the magnitude of the area of each safe basin is divided by the area of the window, so that the following equality holds: $GIM(\mathrm{O2}) + GIM(\mathrm{O6}) + 2GIM(\mathrm{R1}) + 2GIM(\mathrm{R3}) = 1$. The *IF*, on the other hand, is normalized so that $IF(\mathrm{O2})(p = 0.42) = 1$.

Many attractor-basins phase portraits have been built for increasing values of p, and for each of them both *IF* and *GIM* have been computed. This provides the integrity profiles, namely, the curves $IF(p)$ and $GIM(p)$ of the various attractors, which are reported, respectively, in Fig. 29a and 29b.

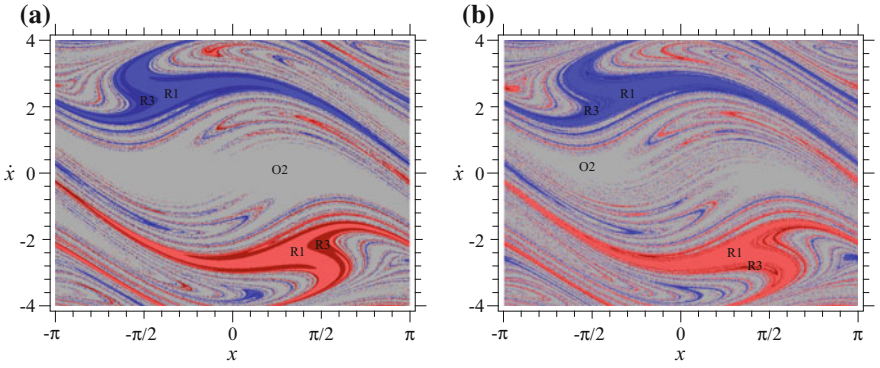

Fig. 28 Attractor-basins phase portraits at **a** $p = 0.90$, **b** $p = 0.96$

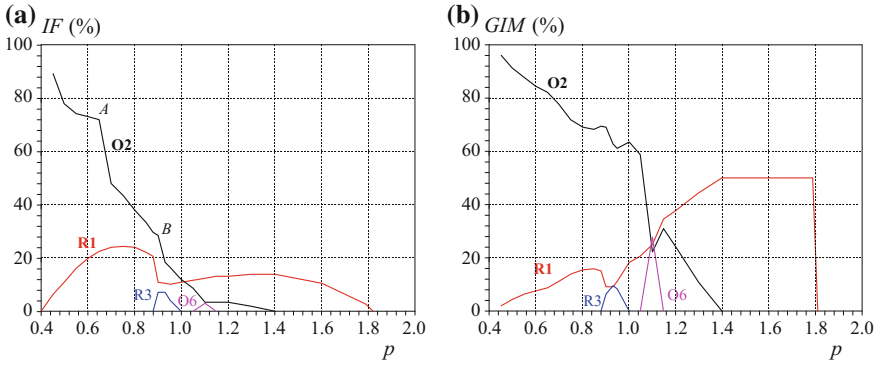

Fig. 29 Integrity profiles of **a** *IF* and **b** *GIM*

المنارة للاستشارات

We can observe the competition between the in-well (oscillating) and the out-of-well (rotating) attractors. The R1 basins grow up against the O2 basin, whose integrity is reduced up to its disappearance. This phenomenon is described by both the *IF* and the *GIM*, although to a different extent. The integrity curves of O2 have the classical qualitative behavior of the so-called "Dover Cliff" erosion curves (Thompson 1989). Starting from the uneroded case, they decrease quite rapidly, meaning that the integrity of the oscillation is suddenly reduced, and, after various phenomena, it vanishes in correspondence with the final crisis where O2 is destroyed.

Various localized effects are recognizable along the overall "smooth" erosion profile of O2, which is related to continuous modifications of the relevant basin boundaries. Such effects entail "instantaneous" reductions in the O2 integrity, as highlighted by sharp falls in the profile. The most evident ones are marked by *A* and *B*. They occur along the *IF* but *not* along the *GIM* curves, which means that *GIM* is unable (or less effective) to keep trace of the underlying dynamical events triggering instantaneous reductions in integrity.

The sharp fall labeled *A* in Fig. 29a occurs at $p \cong 0.655$ and is related to the homoclinic bifurcation of DR1, previously illustrated in Fig. 27a, b. These figures show that the area of the O2 basin is almost unchanged (this is why *GIM* practically does not record this event), while the penetration of the tongues strongly reduces the radius of the circle which measures the magnitude of the compact part of the basin. Also, in conformity with the manifold tangencies, this event erodes O2 and not R1.

The sharp fall labeled *B*, which is the second less-pronounced sharp fall in Fig. 29a, is a consequence of the heteroclinic bifurcation of DR1 and Ir at $p \cong 0.935$, as previously illustrated in Fig. 28a, b. From the comparison of these figures, the drastic reduction in the compact core of the safe basin of O2 is clearly revealed. This event is hardly recognizable in the *GIM* profile, likely for being somehow hidden by the almost simultaneous appearance of R3, which is the next meaningful event.

Note that the *IF* and *GIM* erosion profiles of O2 are similar from a qualitative point of view, but they exhibit important quantitative differences mostly in the final part of the curves. In fact, the *GIM* approaches zero with a nearly constant average slope, and it is significantly larger than the *IF*. Thus, it overestimates the integrity, which is instead only residual. Conversely, this fact is captured by the *IF*, which has a final plateau on which $IF \cong 3.5\%$, confirming that from a practical point of view the integrity of O2 actually ends with the appearance of O6, i.e., at $p = 1.082$ instead of at $p = 1.342$.

Particularly interesting are the integrity curves of R1, whose behavior is different from classical erosion curves starting from a value around 100% (uneroded basin) and decreasing, suddenly or slowly, up to 0 (disappearance of the attractor), just as it occurs herein for O2. In contrast, R1 exhibit more involved profiles since they start from zero, initially grow up against other pre-existing attractors (O2 in this case), and then evolve according to their specific features, which, of course, include the erosion of basins integrity up to their disappearance.

With reference to Fig. 29, it is worth highlighting how R1 change the "status" for growing values of *p*. Initially, they actively erode other (passive) attractors. Then,

المنارة للاستشارات

they are eroded by the secondary attractors, and finally they disappear by a process of reciprocal (self-)erosion at about $p = 1.8$.

The differences between the *IF* and the *GIM* of R1 are much more marked than the corresponding ones of O2. In fact, while the *GIM* is overall increasing up to the value of 0.5, the *IF* initially increases, reaches a maximum around $p \cong 0.75$, and then starts an overall dull decrement (apart from a sudden fall in correspondence of the existence of the secondary period-3 rotations R3). This is a clear example of how *IF* and *GIM* can also be qualitatively different. In particular, it appears that *GIM* is basically a measure of attractor robustness, whereas *IF* is actually a measure of basin integrity (or *safety*). From this latter viewpoint, *GIM* may lose important information. In fact, from the circumstance of being $GIM(\mathrm{R1})(p > 1.342) = 50\%$, one could entail that R1 are relatively safe in this range, which is actually not true, since their safe basin is completely fractal, as previously described but not shown in the figures. Thus, the stability of an attractor is not sufficient for practical purposes. In fact, no designer would operate in the relevant situation, although the two rotations are stable, because even small real perturbations would lead to transient tumbling chaos and possibly to a different motion, e.g., to reverse the sense of rotation. The information about the definite loss of integrity is instead correctly captured by *IF*, where $IF(\mathrm{R1})(p > 1.342) < 15\%$. This confirms that *IF* is a much more reliable measure of integrity from a topological viewpoint, as well as a more conservative and useful indicator for practical purposes.

The *IF* profile of R1 has not only a theoretical meaning. In fact, we infer that the optimal operating condition for R1 is in correspondence with its maximum, where $IF(\mathrm{R1})(p \cong 0.75) \cong 25\%$. For this value, however, O2 is still robust, as $IF(\mathrm{O2})(p \cong 0.75) \cong 50\%$. Thus, one can consider the possibility of increasing p, for example, up to $p \cong 0.85$, where $IF(\mathrm{R1})(p = 0.85) \cong 22\%$ has decreased only slightly, while $IF(\mathrm{O2})(p = 0.85) \cong 33\%$ has been strongly reduced (although it is still on the left of point *B*). This information may be of practical importance if one is interested in exploiting rotating solutions (Xu et al. 2007). The same reasoning does not hold for O2, because the curve $IF(\mathrm{O2})$ has no maximum.

Overall, we note that R1 undergo a "flat" *IF* erosion in the final part of their diagram, although starting from a limited basin extent, while the underlying O2 undergoes the classical sharp fall (Thompson 1989). In view of applications, the former behavior is safer, while the second is dangerous because the "failure" occurs abruptly. The coexistence of sharp and flat erosion profiles is an interesting characteristic of the considered mechanical system.

4.2 Rigid Block

The overturning behavior of rocking rigid blocks is an old and fascinating topic, which has been attracting interest of researchers for a long time. It was originally introduced for estimating magnitudes of earthquakes from observations of the response of columns to seismic excitations (Milne 1881; Perry 1881; Kirkpatrick

المنارة للاستشارات

1927), and was later dealt with to investigate the stability under ground motion of free-standing structures, like water towers, nuclear fuel rods (Koh 1986), ancient monuments (Oppenheim 1992), furniture in civil apartments (Winkler et al. 1995), etc. It has an intrinsic theoretical interest due to the growing attention toward non-smooth applications, which exhibit nonlinear features with no counterpart in smooth systems (Awrejcewicz and Lamarque 2003).

In the following, this problem is reconsidered in terms of dynamical systems theory. The overall response markedly depends on the excitation phase, which can induce different final behaviors, well beyond common sense expectation. Dramatic effects can be entailed in case the phase is free or unknown, as in seismic excitations. For this reason, we need to look for phase-independent results. The topic presentation is divided into two main parts. The first is concerned with the detection of upper and lower bounds of excitation threshold for overturning, while the second is focused on the dynamical integrity analysis based on the definition of the "true" safe basin. These points are correlated.

Deep insights can be found in Lenci and Rega (2004a, d, 2005, 2006a, c) and in Rega and Lenci (2005, 2008), where also additional analyses dealing with the effects of control and anti-control are discussed.

The rocking rigid block model. We consider a slender homogeneous rigid block rocking around base corners in a constant gravitational field, Fig. 30. Two major simplifications, commonly used in the literature, are employed: (i) the so-called Housner model (Housner 1963), according to which the block can only rock without sliding and up-lifting and (ii) piecewise linear equations of motion. The former is accurate if the block-foundation dry friction is sufficiently high or the block is inserted in a nick, and the block is heavy enough; the latter are accurate in the case of slender blocks.

Fig. 30 Rocking rigid block

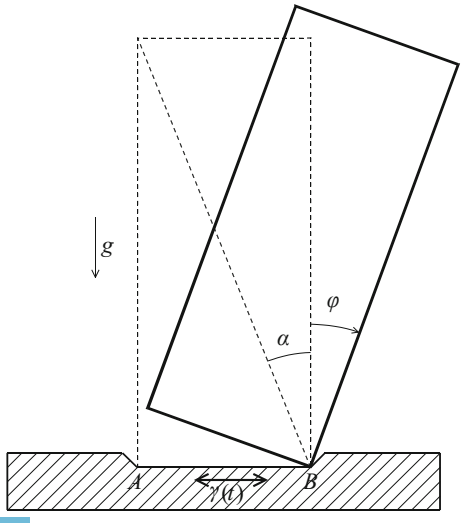

المنارة للاستشارات

Based on these assumptions, the governing dimensionless equations of planar motion are (Plaut et al. 1996)

$$\ddot{\varphi} + \delta\dot{\varphi} - \varphi + \alpha + \gamma(t) = 0 \qquad \varphi > 0 \tag{9a}$$

$$\ddot{\varphi} + \delta\dot{\varphi} - \varphi - \alpha + \gamma(t) = 0 \qquad \varphi < 0 \tag{9b}$$

$$\dot{\varphi}(t^+) = r\dot{\varphi}(t^-) \qquad \varphi = 0 \tag{9c}$$

where Eqs. (9a)–(9b) describe the rotation around point B and A, respectively; Eq. (9c) is the Newton restitution law at the impact, which is supposed to be instantaneous. The angle φ characterizes the state of the system and is measured with respect to the vertical direction; the angle α is the block shape parameter; $\delta > 0$ is the viscous damping coefficient; $r \in [0, 1]$ is the constant coefficient of restitution measuring the dissipation at impacts; $\gamma(t) = \sum_{j=1}^{N} \gamma_j \cos(j\omega t + \Psi_j)$ is the generic $(2\pi/\omega)$-periodic external excitation representing the dimensionless horizontal acceleration of the rigid foundation. In the forthcoming analysis, we consider only the case of harmonic excitation ($N = 1$).

For $\delta = 0$, $\gamma = 0$, and $r = 1$, the system is conservative. The potential and the associated phase portrait are depicted in Fig. 31. There is a unique potential well. This is developed around the rest position $\varphi = 0$ (which is a degenerate stable point) and is delimited by two symmetric hilltop saddles $\varphi_{1,2} = \pm\alpha$. The overturned positions $\varphi = \pm\pi/2$ represent the practical failure of the system (not reported in the figure). We can observe two different kinds of behavior, namely, small non-smooth oscillations around the rest position and large motions leading to overturning. These two classes are divided by the heteroclinic loop connecting the two hilltop saddles.

Lower and upper thresholds for overturning. This section is aimed at obtaining lower and upper bounds for overturning. Specifically, we detect the thresholds for the stability of the rest position (γ^{stat}), for the heteroclinic bifurcation (γ^{het}), and for the immediate overturning (γ^{imm}). All these curves are reported in Fig. 32.

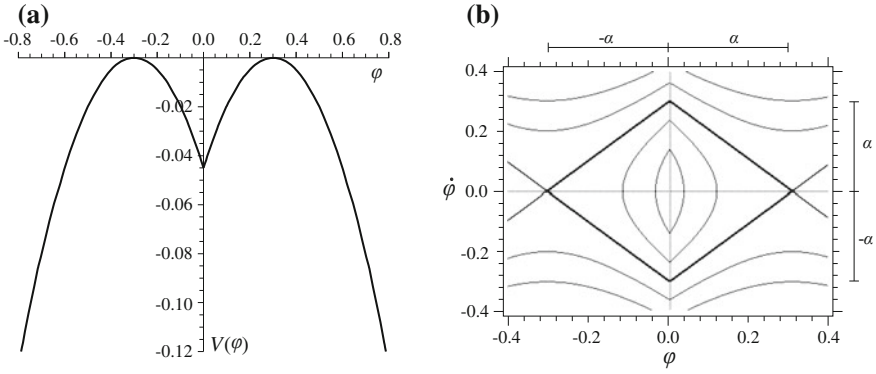

Fig. 31 **a** The potential and **b** the conservative phase portrait, at $\alpha = 0.3$

المنارة للاستشارات

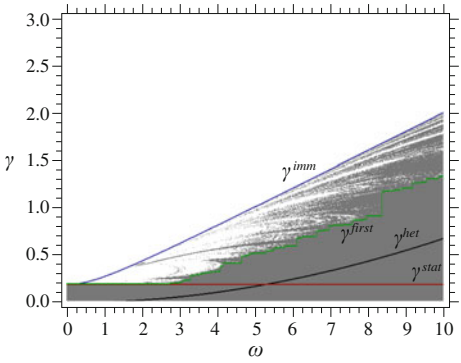

Fig. 32 The overturning chart of the rest position in the case of harmonic excitation, at $\delta = 0.02$, $r = 0.95$, $\alpha = 0.2$, $\psi = \pi + \text{atan}(\omega/\lambda) - \text{atan}[\delta\omega/(1+\omega^2)]$, $\lambda = [-\delta - \sqrt{(\delta^2+4)}]/2$ (this implies that the overturning is toward the right). The thresholds for the stability of the rest position (γ^{stat}), for the heteroclinic bifurcation (γ^{het}), for the immediate overturning (γ^{imm}), and for the first overturning (γ^{first}) are reported, respectively, in red, black, blue, and green line

Stability of the rest position (γ^{stat}). If the excitation amplitude is sufficiently small, then the external force is lesser than the gravitational force and is not able to move the body; accordingly, the rest position is certainly stable. This threshold can be determined analytically (Lenci and Rega 2006a). We obtain $\gamma^{stat} = \alpha$, which is the well-known West's formula (Kirkpatrick 1927). Owing to its physical meaning (no motion), γ^{stat} does not depend on damping, impact, and excitation frequency. Of course, the region $\gamma \leq \gamma^{stat}$ is safe from overturning of the rest position, i.e., γ^{stat} is a lower bound for overturning. For $\gamma \leq \gamma^{stat}$, the rest position is stable, although not globally attracting as some other attractors may, and actually do, coexist.

Heteroclinic bifurcation of the hilltop saddles (γ^{het}). This is a very important dynamical event. Below γ^{het}, the erosion of the safe basin is prevented, so the rest position is safe from overturning, even if it may lose stability and change into safe, in-well, periodic, and even chaotic small oscillations. Above γ^{het}, instead, the erosion of the safe (in-well) basins of attraction starts and, after an involved series of dynamical phenomena, finally leads to their complete destruction; of course, this entails also the overturning of the rest position.

To illustrate these facts, we report the attractor-basins phase portraits for an excitation amplitude just below and above γ^{het}, Fig. 33. In the former, the white-grays (i.e., out-well versus in-well) boundary is regular, although there are four safe basins of attraction, corresponding to four coexisting periodic attractors, with in-well fractality owing to the homo/heteroclinic intersection of other, non-hilltop, saddle manifolds. In the latter, the erosion of the safe bounded area is increasing, as shown by the penetration of fractal white tongues from the out-of-well solution within the gray basins. Touching of the white with the point (0, 0) corresponds to actual overturning of the rest position, while complete disappearance of the gray basins marks the end of confined dynamics.

المنارة للاستشارات

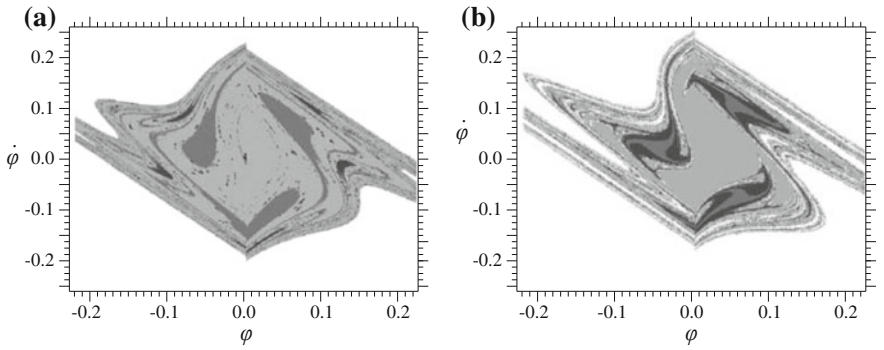

Fig. 33 Attractor-basins phase portraits at $\delta = 0.02$, $r = 0.95$, $\alpha = 0.2$, $\omega = 5$, $\psi = 1.76628$, $\gamma^{het} = 0.1838$ and **a** $\gamma = 0.18$, **b** $\gamma = 0.45$

Thus, the heteroclinic bifurcation represents a threshold above which overturning certainly occurs for some given excitation phase. In fact, above γ^{het}, the distance between toppling (white) basin and rest position decreases more or less quickly, so that the incidental overturning due to imponderable events is more and more likely. The γ^{het} threshold can be computed analytically and it can be proven that it depends on the restitution coefficient r, while it does not depend on the excitation phase (Lenci and Rega 2006a).

More in general, γ^{het} is another lower bound for overturning, determined through invariant manifolds arguments.

Immediate overturning threshold (γ^{imm}). This threshold detects the excitation amplitude above which there exists an excitation phase such that the rest position topples down without transient oscillations in the potential well. Therefore, by definition, γ^{imm} provides an upper bound for overturning.

An example is reported in Fig. 34a, which shows how the solution leaves the rest position, oscillates around the right hilltop saddle, and then escapes without impacts, i.e., without going back to the line $\varphi = 0$. On the other hand, below γ^{imm}, the solution may not overturn at all, Fig. 34b, or may overturn after transient in-well oscillations, Fig. 34c, this alternative being very sensitive to system parameter values, as confirmed by the closeness of γ in Fig. 34b, c.

We can analytically obtain γ^{imm} (Lenci and Rega 2006a). According to its definition, it does not depend on the excitation phase. Also, it does not depend on r, because there are no rebounds during immediate overturning.

Overturning chart of the rest position. We investigate the overturning behavior in the excitation frequency/amplitude parameters space (ω, γ). The analytical curves show that the combination of γ^{stat} and γ^{het} provides a unique threshold γ^*, which overall bounds the overturning from below. Specifically, $\gamma^* = \gamma^{stat}$ for $\omega < \omega^*$ and $\gamma^* = \gamma^{het}$ for $\omega > \omega^*$, where ω^* is the frequency where $\gamma^{stat} = \gamma^{het}$, which depends only on δ and r. For example, for $\delta = 0.02$, $r = 0.95$ we have $\omega^* = 5.2264$. Thus, the analytical curves individuate three different regions:

المنارة للاستشارات

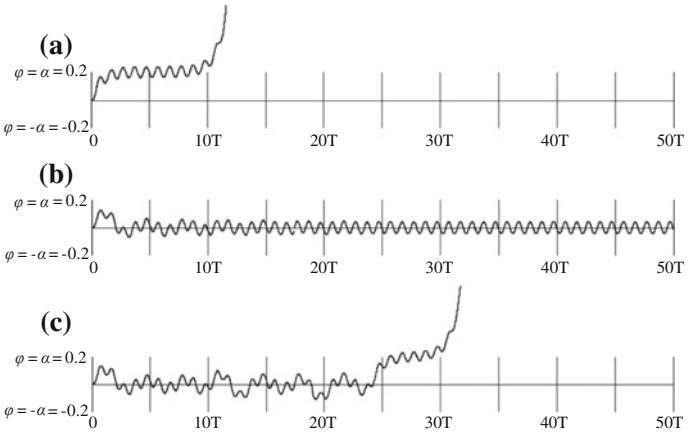

Fig. 34 Time history starting from the rest position at $\delta = 0.02$, $r = 0.95$, $\alpha = 0.2$, $\omega = 5$, $\psi = 1.76628$, $\gamma^{imm} = 1.029$ and **a** $\gamma = 1.02921$, **b** $\gamma = 0.9$, **c** $\gamma = 0.9011$

(1) $\gamma < \gamma^*$, where the block does not overturn (gray), and if the amplitude is very small, not even rocks;
(2) $\gamma^* < \gamma < \gamma^{imm}$, where overturning may or may not occur, with a possibly bounded transient. This is the intermediate transition region, which exhibits fractal features;
(3) $\gamma > \gamma^{imm}$, where the block directly topples (white), without transient oscillations in the safe potential well.

The extent of these regions does not depend on the excitation phase (though being strongly dependent on all the other system parameters), since both γ^* and γ^{imm} are independent of ψ.

To confirm the previous "three regions" scenario, we construct the overturning chart of the rest position, which is obtained by numerically integrating the equation of motion and drawing a white (gray) point, if the block is toppled (untoppled). This chart is overlapped with the analytical curves, Fig. 32. Perfect agreement is observed.

First Overturning Threshold. In the intermediate region, there certainly exists an overturning threshold such that, by increasing the excitation amplitude for each fixed excitation frequency, the block topples down for the first time. This threshold is important from an engineering viewpoint. In fact, below it no overturning occurs so that the structure is safe, although with a variable degree of reliability; on the other hand, above it there may be alternation of overturning and non-overturning zones in the parameters space, with a possibly fractal nature.

To investigate this point, we introduce the first overturning threshold (γ^{first}). This is defined as the excitation amplitude above which there exists an excitation phase ψ such that the block finally topples, irrespective of the length of the transient and of the number of oscillations in the potential well. In spite of its simplicity and relevance, this definition entails that only numerical evaluations of γ^{first} are possible, although

المنارة للاستشارات

the inequalities $\gamma^* < \gamma^{first} < \gamma^{imm}$ provide useful analytical estimates. The curve γ^{first} is also reported in Fig. 32, where we have slightly approximated it as illustrated in Lenci and Rega (2006a).

Hence, the intermediate region can be divided into two subregions, whose magnitude may considerably vary with the system parameters:

(1) $\gamma^* < \gamma < \gamma^{first}$, which is certainly protected against overturning, but with a variable degree of confidence, and thus can be named region of impending overturning. Here, a detailed dynamical integrity analysis is required to assess reliability. Note that the gap between γ^{first} and γ^{het} is due to the fact that γ^{het} represents just the triggering of penetration of unsafe tongues into the safe basin; a somewhat greater excitation amplitude is needed to enhance penetration and allow the tongues reaching the rest position, thus giving rise to a sequence of complex topological events ending with overturning;
(2) $\gamma^{first} < \gamma < \gamma^{imm}$, which presents fractal behavior; here, toppling is highly sensitive to small parameter variations (as well as to initial conditions).

The Excitation Phase. It can be shown that the overturning chart is strongly influenced by the excitation phase. This is able to produce different—sometimes considerably different—final behaviors. In fact, it can, and actually does, occur that for a given phase the block does not overturn, while it topples for a different one. Thus, if the excitation phase is free or unknown (e.g., in the earthquake), dramatic effects may arise. In such a case, there is a clear need of referring to phase-independent results.

"True" safe basin and erosion profiles. To assess the vulnerability of the system from overturning, we perform a dynamical integrity investigation. Contrary to other case studies examined in this chapter, for the rigid block there is no resonance frequency around which focusing numerical analyses, i.e., there are no preferred values of the excitation frequency, and, as an example, we choose $\omega = 3.5$.

Particularly demanding is the choice of the safe basin. Since we are analyzing the overturning, we are focusing on the in-well dynamics; in fact, when growing the excitation, the erosion of the potential well is the triggering phenomenon for toppling. Accordingly, we can consider as safe basin all the in-well bounded motions (union of the classical basins of attraction of all the in-well attractors).

Nevertheless, as previously observed, in the problem of overturning we typically have to look for results that are independent of the phase. The previous "classical" definition of safe basin, instead, is referred to a fixed ψ. For this reason, this definition is not expected to provide adequate information in the present case study. To overcome this limitation, the "true" safe basin is introduced. This is defined as the intersection of all classical safe basins when ψ ranges over the period. In particular, in the present case it corresponds to the smallest phase-independent set of initial conditions which do not entail overturning (note that this definition of "true" safe basin holds in general, i.e., for whatever classical safe basin it is referred to, not just for the in-well dynamics considered in the present analysis).

An example comparing the "classical" and the corresponding "true" in-well safe basin is reported in Fig. 35, which corresponds to the last point of the forthcoming

المنارة للاستشارات

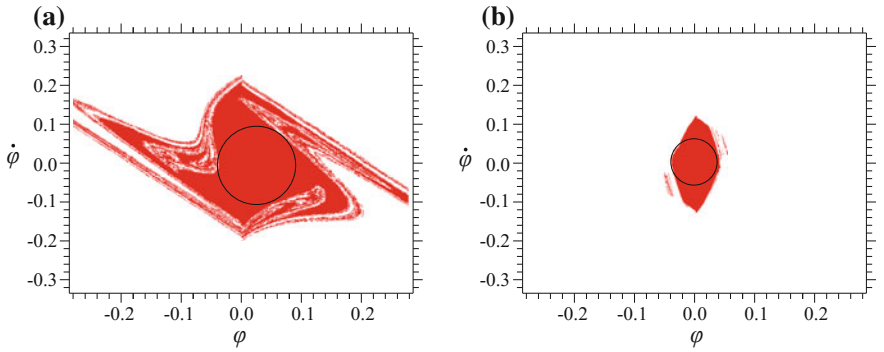

Fig. 35 **a** Classical safe basin and **b** "true" safe basin at $\gamma = 0.20$, $\omega = 3.5$, $\delta = 0.02$, $r = 0.95$, and $\alpha = 0.2$. The circles for evaluating the Integrity Factor are also reported

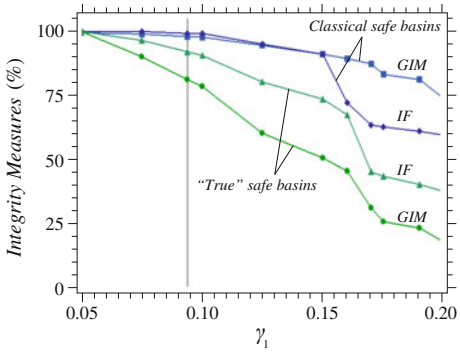

Fig. 36 Erosion profiles of *GIM* and *IF* for both classical and "true" safe basin, at $\omega = 3.5$, $\delta = 0.02$, $r = 0.95$, and $\alpha = 0.2$

erosion profiles, $\gamma = 0.20$. Not only the magnitudes are strongly different, but the degree of fractality is also much reduced in the "true" safe basin. Moreover, the "true" safe basin is "closer" to the interior circle involved in the definition of the *IF*, which is also reported.

In Fig. 36, the erosion profiles are shown, where both the "classical" and the "true" safe basin are investigated, by resorting both to the *GIM* and to the *IF*. The curves are normalized with respect to their values at $\gamma = 0.05$.

Overall, all the profiles behave qualitatively in the same way. As the excitation amplitude is increased, all the curves denote a decrement of dynamical integrity, especially after the heteroclinic bifurcation threshold at $\gamma = 0.094$; all curves have a sort of well visible step at about $\gamma = 0.165$, which is likely related to a secondary global bifurcation—possibly a heteroclinic connection between the hilltop and a relevant in-well saddle—which further promotes the penetration of eroding tongues. Thus, all the profiles are able to capture correctly the main global phenomena. Nevertheless, very different degrees of confidence are suggested.

We focus on the classical safe basin. As far as a small dynamic excitation is assumed, both *IF* and *GIM* basically coincide. Then, at about $\gamma \cong 0.15$, i.e., in

المنارة للاستشارات

correspondence of the previously mentioned secondary bifurcation, they suddenly diverge. For the *GIM* this step, while present, is not so evident; on the contrary, for the *IF* it is really apparent. This clearly denotes that the erosion has reduced abruptly the compactness of the safe bounded area, dropping it to smaller values, although not to totally vulnerable ones. The fractality still broadens for an extensive part of the phase space (in fact the *GIM* remains elevated); nevertheless, we cannot count on this fractal area, since it may be seriously dangerous.

Focusing on the "true" safe basin, instead, the reliability of the system is strongly reduced, both for the *GIM* and for the *IF*. The erosion is observed to produce considerable effects also at small dynamic excitations. In correspondence of the secondary heteroclinic bifurcation, the *GIM* has already more than halved its initial value. Similarly occurs for the *IF* soon after the heteroclinic event. At $\gamma = 0.20$, the system drops down to $IF \cong 35\%$ and $GIM \cong 15\%$, i.e., both *IF* and *GIM* clearly alert that the system is dangerously vulnerable.

Overall, when looking for phase-independent results, the classical safe basin seriously underestimates the erosion, since it suggests the system to be robust, though definitely it is not. The differences are dramatic when the excitation amplitude increases. The "true" safe basin, instead, appears more satisfactory for this kind of problems.

5 Dynamical Integrity: Control

The present section is devoted to investigate the benefits of the global safety approach in control issues. This analysis enables to check the actual performances of the assumed control technique, assessing the parameter ranges where they may be effectively exhibited under realistic conditions.

In the following, a convenient control method is introduced, which was proposed by Lenci and Rega (1998a). The intent of the considered control technique is really challenging, since it is aimed at controlling the overall global dynamics. Initially, we describe the main steps of the control procedure, which is based on shifting the homo/heteroclinic bifurcation of the saddle taken into account toward higher excitation amplitudes. Successively, we assess the actual effects of the control method, by resorting to the dynamic integrity analysis. Based on the obtained profiles, the proposed control technique is ascertained to effectively increase the engineering safety of a system in terms of global dynamics.

The control method is illustrated with reference to two classical archetypal oscillators, Helmholtz (Sect. 5.1) and Duffing (Sect. 5.2). An assessment of the effects of the same control technique in the nonlinear dynamics of reduced models of structures in macro- or micro-mechanics is presented in Gonçalves et al. (2018) and Settimi and Rega (2018) of this book, respectively.

المنارة للاستشارات

5.1 Helmholtz Oscillator

In the case of the softening Helmholtz oscillator, special attention is focused on the escape phenomenon, which constitutes the most dangerous aspect of the analyzed system. Due to the importance of this event, the effectiveness of the control method is investigated in detail and the global dynamical effects in terms of overall safety are discussed. The method is shown to be able to shift the homoclinic bifurcation triggering the erosion of the potential well, as per the theoretical predictions, and also to delay its actual strong occurrence, thus preserving the integrity of the system. For more details, we refer to Lenci and Rega (2003a, c, 2004b, c), Rega and Lenci (2003, 2005, 2008, 2009), and Rega et al. (2010).

The homoclinic bifurcation threshold. We consider the dimensionless softening Helmholtz equation (Lenci and Rega 2003a, 2004b; Rega and Lenci 2005)

$$\ddot{x} + \varepsilon\delta\dot{x} - x + x^2 = \varepsilon\gamma(\omega t) = \varepsilon\gamma_1 \sum_{j=1}^{\infty} \frac{\gamma_j}{\gamma_1} \sin\left(j\omega t + \Psi_j\right) \tag{10}$$

where $\varepsilon\delta$ is the damping coefficient and $\varepsilon\gamma(\omega t)$ is the generic $2\pi/\omega$-periodic external excitation given by a basic harmonic plus controlling superharmonics, which are optimally determined by the control technique. Specifically, $\varepsilon\gamma_1$ is the amplitude of the basic harmonic, $\varepsilon\gamma_j$ are the amplitudes of the controlling superharmonics, and Ψ_j are the phases.

To better observe the improvements provided by the control method, we write the excitation as reported in the right-hand side of Eq. (10), where $\varepsilon\gamma_1$ represents the overall amplitude of the excitation and γ_j/γ_1 represent the superharmonic corrections with respect to the basic harmonic assumed as reference. The dimensionless parameter ε is introduced to emphasize the smallness of damping and excitation, which indeed are considered as perturbations of the conservative case.

The potential and the unforced undamped phase portraits are depicted in Fig. 37. The equilibrium points are $x_1 = 0$, which is the hilltop saddle, and $x_2 = 1$, which is a center belonging to the unique potential well. There are two different classes of oscillations, namely, bounded periodic nonlinear cycles within the potential well and unbounded nonperiodic solutions which tend to $-\infty$ when $t \to \pm\infty$. They are separated by the unique homoclinic orbit of the hilltop saddle, $x_{hom}(t) = (3/2)(1/\cosh^2(t/2))$.

When perturbations (damping and forcing) are added, the stable and unstable manifolds split and, for sufficiently large values of excitation amplitude, they intersect. The first excitation giving tangencies of manifolds corresponds to the homoclinic bifurcation. This threshold can be computed analytically via the Melnikov's method (Guckenheimer and Holmes 1983; Wiggins 1990).

In the present case, the Melnikov function measuring the first-order (in ε) distance between the perturbed stable and unstable manifolds is

المنارة للاستشارات

$$\mathcal{M}(m) = -\frac{6}{5}\delta\left[1 + \frac{\gamma_1}{\gamma_{1,cr}^h(\omega)}h(m)\right] \tag{11}$$

with

$$h(m) = \sum_{j=1}^{\infty} h_j \cos(jm + \Psi_j) \quad h_j = \frac{\gamma_j}{\gamma_1}\frac{j^2 \sinh(\omega\pi)}{\sinh(j\omega\pi)} \tag{12}$$

where $\gamma_{1,cr}^h(\omega) = \delta\sinh(\omega\pi)/(5\pi\omega^2)$ is the critical curve of homoclinic bifurcation for the reference case of harmonic excitation. In (11)–(12), the argument m is given by $m = \omega t_0 + \phi_0$, where (t_0, ϕ_0) is a parametrization of the two-dimensional manifolds (in the three-dimensional space $(x,\dot{x},t)$). Note that $h_1 = 1$, that $h(m)$ is 2π-periodic and has zero mean value, and that the effects of superharmonic corrections in the Melnikov function are governed by the parameters $h_j, j > 1$.

Expression (11) is schematically illustrated in Fig. 38. It shows that the distance is made of a constant part plus an oscillating part, the first being proportional to the damping and the second to the excitation amplitude. We note that, (i) if γ_1 and ω are fixed, the (minimum) distance between the manifolds, which is attained at the minimum of $h(m)$, increases by increasing the minimum of $h(m)$, i.e., the larger is the minimum of $h(m)$, the larger is the distance; (ii) for a fixed ω, the larger is the minimum of $h(m)$, the larger is the multiplier $\gamma_{1,cr}$ needed to realize zero distance, namely, the excitation amplitude for homoclinic bifurcation. Accordingly, if we compare two given $\mathcal{M}^A(m)$ and $\mathcal{M}^B(m)$ for a fixed value of ω but varying γ_1, since the minimum of $h^B(m)$ is greater than the minimum of $h^A(m)$, the homoclinic bifurcation threshold is larger in case B than in case A, i.e., $\gamma_{1,cr}^B > \gamma_{1,cr}^A$.

The condition $\mathcal{M}(m) = 0$ for some $m[0, 2\pi]$ guaranteeing the homoclinic intersection of the stable and unstable manifolds occurs in the region of the parameter space defined by

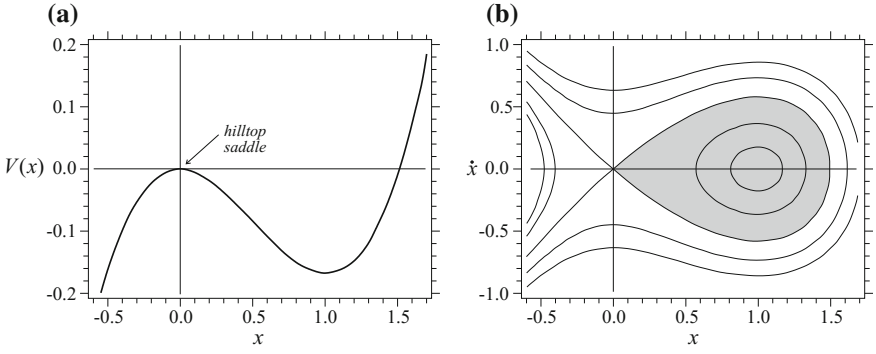

Fig. 37 **a** The potential $V(x)$ and **b** the unforced undamped phase portrait

المنارة للاستشارات

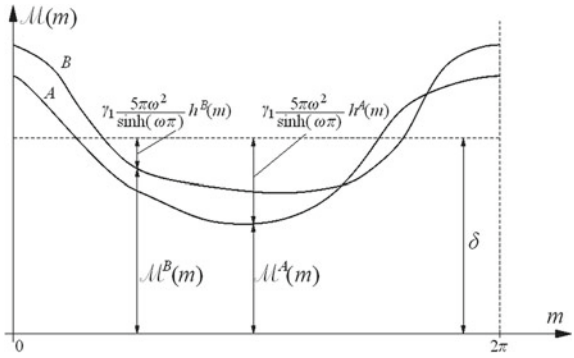

Fig. 38 A schematic diagram of the Melnikov distance between stable and unstable manifolds

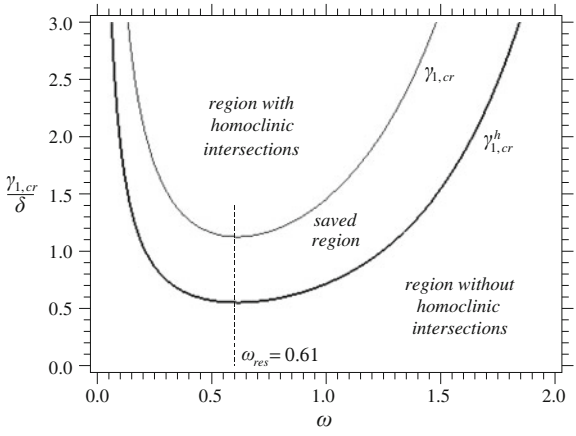

Fig. 39 The curves $\gamma^h_{1,cr}(\omega)$ (harmonic excitation) and $\gamma_{1,cr}$ for $M = 0.5$ (corresponding to the mathematical optimal solution), in the space of governing parameters (ω, γ_1)

$$\gamma_1 > \gamma_{1,\,cr}(\omega) = \gamma^h_{1,\,cr}(\omega)\frac{1}{M} \tag{13}$$

with

$$M = -\min_{m\in[0,\,2\pi]}\{h(m)\} = \max_{m\in[0,\,2\pi]}\{-h(m)\} \tag{14}$$

where M is a positive number accounting for the shape of the excitation.

As can be observed in Fig. 39, in the case of generic excitation, the curve $\gamma_{1,cr}(\omega)$ separates the zone where homoclinic intersections do not occur (below the critical curve) from the zone where homoclinic intersections do occur (above the critical curve). The same holds for $\gamma^h_{1,cr}(\omega)$ in the case of harmonic excitation.

These curves differ by a factor $1/M$. The strip above $\gamma^h_{1,cr}(\omega)$, where there is homoclinic intersection with harmonic excitation, and below $\gamma_{1,cr}(\omega)$, where there is no intersection with unharmonic excitation, is called *saved region* and represents the zone where unharmonic excitation is theoretically effective. Its (maximum) enlargement constitutes the objective of the control method.

المنارة للاستشارات

Optimal control and optimization problems. The central idea of the control method is to reduce the region of homoclinic intersection by varying the shape of the excitation. This entails increasing $\gamma_{1,cr}$ as much as possible by varying the Fourier coefficients h_j and Ψ_j of $\gamma(\omega t)$. Mathematically, it can be expressed by the following optimization problem:

$$\text{Maximizing } G \text{ by varying } h_j \text{ and } \Psi_j,\ j \geq 2,\ \text{of } h(m) \tag{15}$$

where G is the *gain*, which is defined as the ratio

$$G = \frac{\gamma_{1,cr}}{\gamma^h_{1,cr}} = \frac{1}{M} \tag{16}$$

thus, the smaller being M, the smaller being the upper region in the parameter space.

The (optimal) solution $h(m)$ is a positive Dirac delta of amplitude π at $m = 0$ plus the constant function $-1/2$. The Fourier coefficients are $h_j = 1$, $\Psi_j = 0$, and the optimal gain is $G = 2$, i.e., the critical amplitude is doubled in principle. Unfortunately, this mathematical optimal solution is not acceptable from a physical viewpoint, because the corresponding excitation would be a divergent series; this is not a pathological property of the Helmholtz oscillator but holds in general (Lenci and Rega 2004b).

To take into account the physical admissibility of the searched optimal excitation, some further constraint should be added to problem (15). This may be done in different ways. In any case, due to the new constraint, the physically admissible best gain is reduced, and the value $G = 2$ remains as a (hypothetically optimal) value of comparison (indeed, it is an upper bound) for the actual optimal problems. The more the constrained optimal is close to $G = 2$, the more the associated optimal excitation is effective, at least from a theoretical point of view.

Among various possibilities, we consider the (optimal) solution obtained by assuming only a *finite* number N of superharmonics, so that the question of the optimal excitation divergence automatically disappears. Results are reported in Table 2. Note that these *reduced-order* solutions are very satisfactory from a practical point of view, since they are easy to reproduce in experiments and/or applications and, moreover, they provide a high gain, which is quite close to the upper bound corresponding to the physically inadmissible mathematical solution.

Delaying the erosion of the potential well. To illustrate the practical performances of the control method, in the following, some numerical simulations are reported. They are focused on a neighborhood of the vertex of the escape region in the excitation parameters plane (Lenci and Rega 2003a), i.e., on the range corresponding to the most dangerous frequencies (the ones for which the escape occurs for the lowest value of excitation amplitude), where even small improvements are very useful.

We can clearly observe that the present control method is able to shift the beginning of the erosion of the potential well toward higher excitation amplitudes, Fig. 40. The

المنارة للاستشارات

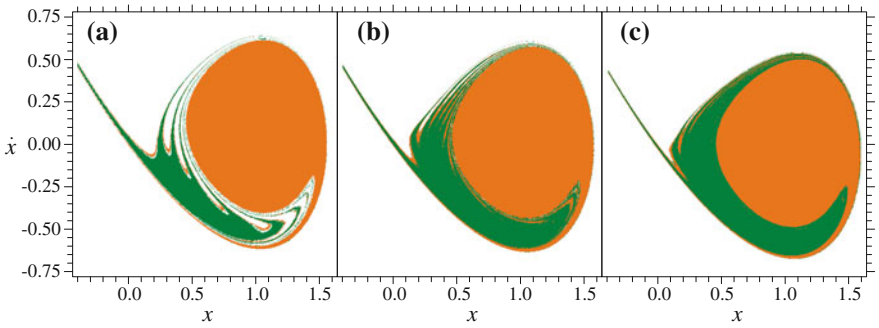

Fig. 40 Basins of attraction at $\omega = 0.8$ and $\varepsilon\gamma_1 = 1.8\ \varepsilon\gamma^h_{1,cr} = 0.02195$, for different excitations: **a** harmonic; **b** optimal excitation with one superharmonic; **c** optimal excitation with two superharmonics

basins of attraction of the nonresonant branch and of the resonant one are orange and green, respectively; the escape is white.

As an example, we refer to the frequency $\omega = 0.80$ and the excitation amplitude $\varepsilon\gamma_1 = 1.8\ \varepsilon\gamma^h_{1,cr} = 0.02195$. Since the assumed $\varepsilon\gamma_1$ is above $\varepsilon\gamma^h_{1,cr}$, at harmonic excitation fractal basin boundaries are observed, Fig. 40a. Fractal tongues of escape penetrate the potential well separating the basins of the nonresonant and the resonant branch. At optimal excitation with one superharmonic, fractal basin boundaries are still visible, Fig. 40b. This is in agreement with the fact that also for this excitation we are above the critical threshold, which is given by $\gamma_{1,\,cr} = 1.4142\ \gamma^h_{1,cr}$. However, the extent of the fractal region is reduced, since the fractalization of the boundaries starts later, and the erosion is less developed, although the two basins are still separated. At the optimal excitation with two superharmonic corrections, the fractalization has almost disappeared, Fig. 40c. In fact, the amplitude is still above the relevant critical value, which is now given by $\gamma_{1,\,cr} = 1.6180\ \gamma^h_{1,cr}$, but, differently from the previous cases, it is not so higher. Accordingly, the erosion takes place, but it involves only a

Table 2 The numerical results of various optimization problems with an increasing finite number of superharmonics

N	G_N	M_N	h_2	h_3	h_4	h_5	h_6	h_7
2	1.4142	0.7071	0.353553					
3	1.618	0.6180	0.552756	0.170789				
4	1.7321	0.5773	0.673525	0.333274	0.096175			
5	1.8019	0.5550	0.751654	0.462136	0.215156	0.059632		
6	1.8476	0.5412	0.807624	0.567084	0.334898	0.153043	0.042422	
7	1.8794	0.5321	0.842528	0.635867	0.422667	0.237873	0.103775	0.027323
…	…	…	…	…	…	…	…	…
∞	2	0.5	1	1	1	1	1	1

المنارة للاستشارات

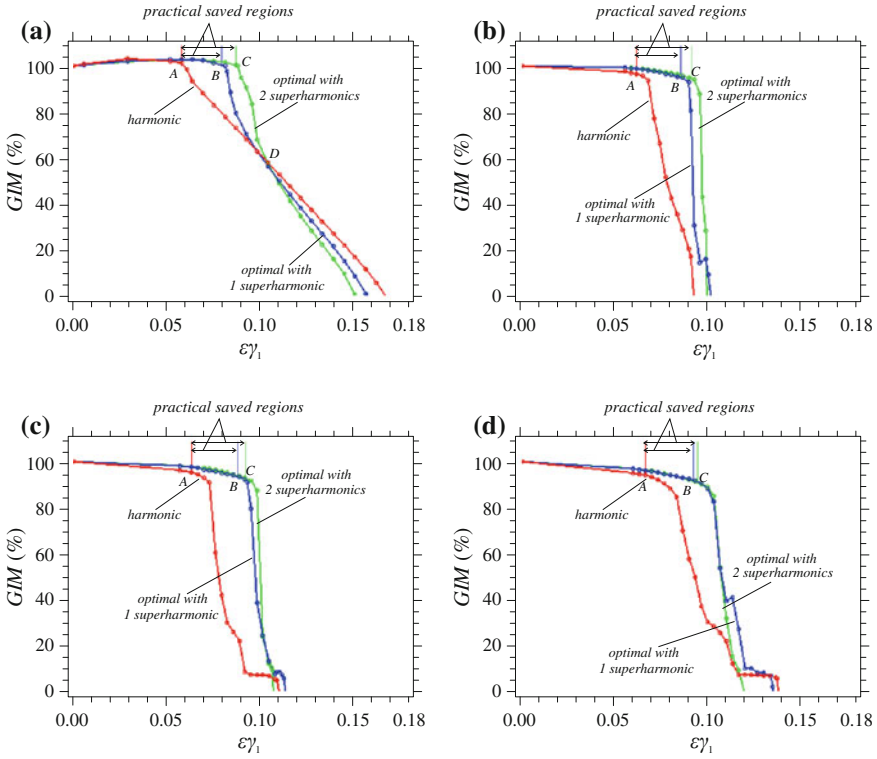

Fig. 41 Erosion profiles of *GIM* versus excitation amplitude γ_1, in the case of (i) harmonic excitation (red), (ii) optimal excitation with one controlling superharmonic (blue), and (iii) optimal excitation with two controlling superharmonics (green). The vertical segments denote the numerical homoclinic bifurcation. **a** $\omega = 0.70$, **b** $\omega = 0.81$, **c** $\omega = 0.85$, **d** $\omega = 0.90$. Specifically, in (**a**) we have at (ii) $\gamma_2/\gamma_1 = 0.8068$, at (iii) $\gamma_2/\gamma_1 = 1.2614$, $\gamma_3/\gamma_1 = 1.5621$; in (**b**) at (ii) $\gamma_2/\gamma_1 = 1.1329$, at (iii) $\gamma_2/\gamma_1 = 1.7713$, $\gamma_3/\gamma_1 = 3.0988$; in (**c**) at (ii) $\gamma_2/\gamma_1 = 1.2829$, at (iii) $\gamma_2/\gamma_1 = 2.0057$, $\gamma_3/\gamma_1 = 3.9787$; in (**d**) at (ii) $\gamma_2/\gamma_1 = 1.4992$, at (iii) $\gamma_2/\gamma_1 = 2.3438$, $\gamma_3/\gamma_1 = 5.4402$

narrow outer part of the basin of the resonant attractor, while the central core of the potential well remains uncorrupted.

To have a quantitative measure of the effects of the control method in reducing the erosion of the potential well, erosion profiles at increasing excitation amplitude are reported in Fig. 41. Since we are focusing on the potential well, we assume as safe basin the union of the classical basins of attraction of all the bounded attractors; we measure its dynamical integrity by the *GIM*, where the status in the absence of excitation is chosen as normalizing condition. We analyze the outcome at harmonic excitation, at optimal excitation with one controlling superharmonic, and at optimal excitation with two controlling superharmonics. As examples, we consider the excitation frequencies $\omega = 0.70$ (before the vertex of the escape region), $\omega = 0.81$ and $\omega = 0.85$ (in a neighborhood of the vertex), and $\omega = 0.90$ (after the vertex).

المنارة للاستشارات

We can clearly observe that the optimal control excitations are able to delay the homoclinic bifurcations (marked by vertical segments). This affects favorably the erosion profiles, whose sharp fall down turns out to be meaningfully shifted toward higher excitation amplitudes. Also, this shift is substantially independent of the frequency, showing the robustness of the control method. Thus, up to the shifted homoclinic bifurcations, the erosion is clearly reduced, which is beneficial to the overall system safety.

It is worth emphasizing that the control method is effective in shifting the *starting* point of the erosion (as somehow expected, if the controlled homoclinic bifurcation is the one actually responsible for the phenomenon, as in the present case), while there are no theoretical predictions on its ability to shift the *ending* point, too. Accordingly, there is not an expected outcome both as regards the development of the erosion profile and as regards its last part, but they may vary depending on the assumed excitations and at different frequency values. This can be clearly observed in the diagrams.

After the beginning of the erosion, the profiles corresponding to the controlled excitations are generally sharper than the one corresponding to the reference harmonic excitation—at least as regards the after-the-homoclinic bifurcation narrow fall of the *GIM*—and rapidly tend to it. In some cases, there is also a shift of the critical threshold of escape toward higher excitation amplitudes (i.e., a delay of the inevitable failure of the structure), which goes well beyond what theoretically expected by the proposed control method; in other cases, instead, this feature does not occur.

Specifically, at $\omega = 0.70$ in Fig. 41a, i.e., for "low" frequencies, the curves overlap nearly at a unique point (denoted by D), after which the *GIM* corresponding to the controlled excitations is lower than the one corresponding to the basic harmonic. Thus, in this parameter range, the control is effective in the saved region, while it is ineffective above this strip. This property holds also for $\omega < 0.70$, as shown by other, not reported, numerical simulations.

At $\omega = 0.81$ in Fig. 41b and at $\omega = 0.85$ in Fig. 41c, i.e., in a neighborhood of the vertex of the escape V-shaped region, the erosion curves do not overlap (apart from a few minor exceptions). The escape in case of controlled excitations occurs for slightly larger values of excitation amplitudes with respect to the uncontrolled case. Nevertheless, the profile of the controlled system is very sharp and there is an "instantaneous" fall toward the escape. While the robust increase of the beginning of the erosion and the possible increase of the escape excitation threshold are important practical performances of the control method, the sharpness of the profile may be dangerous in practical applications. In fact, a small increase of excitation around the points B and C of Fig. 41b may suddenly lead to the escape.

At $\omega = 0.90$ in Fig. 41d, i.e., for "large" frequencies, the very last part of the profile in the case of control with one superharmonic recovers the harmonic one, while in the case of control with two superharmonics it rapidly tends to zero (escape). This is due to the fact that in this range the relative amplitudes γ_2/γ_1 and γ_3/γ_1 of the added superharmonics are very large (see the caption of Fig. 41). This seems to confirm that also for large frequencies the control is effective in the saved region, as theoretically

المنارة للاستشارات

expected, while it is substantially ineffective above. However, better results (in terms of escape) can be achieved, for instance, by resorting to other optimal excitations, as observed in Lenci and Rega (2004b).

On the basis of the previous considerations, it is possible to individuate a well-defined *erosion reduction region*, which is the zone where the controlled profiles are above the harmonic profile and which can be approximated by the strip in between the harmonic and controlled homoclinic bifurcations in the parameters plane. In this region, effectiveness of control is always observed. The obtained gain appears to be considerable.

5.2 *Duffing Oscillator*

We consider the hardening Duffing oscillator with a two-well symmetric potential. The presence of two simultaneous homoclinic orbits is the new aspect of the present system. This has important consequences in terms of control. In particular, there is the possibility to develop two different control strategies, namely, "*one-side*" control and "*global*" control. Their effects on the global dynamics of the system are analyzed and compared. It is highlighted that the former is able to provide high gain but control of only a part of the phase space, and the latter low gain but control of the whole phase space. More details can be found in Lenci and Rega (2003b, c, 2004b, c, 2011b), Rega and Lenci (2003, 2005, 2008, 2009), and Rega et al. (2010).

Global control versus one-side control. We consider the dimensionless hardening Duffing equation (Lenci and Rega 2003b, 2004b; Rega and Lenci 2005)

$$\ddot{x} + \varepsilon\delta\dot{x} - \frac{x}{2} + \frac{x^3}{2} = \varepsilon\gamma(\omega t) = \varepsilon\gamma_1 \sum_{j=1}^{\infty} \frac{\gamma_j}{\gamma_1} \sin\left(j\omega t + \Psi_j\right) \tag{17}$$

where, as in Eq. (10), $\varepsilon\delta$ is the damping coefficient, $\varepsilon\gamma(\omega t)$ is the generic $2\pi/\omega$-periodic external excitation given by a basic harmonic plus controlling superharmonics, $\varepsilon\gamma_1$ is the overall amplitude, and γ_j/γ_1 and Ψ_j are the excitation shape parameters.

The associated potential and the unforced undamped phase portrait are depicted in Fig. 42. This is a symmetric two-well potential system. The dynamics are characterized by the presence of two centers ($x_{0,2} = \mp 1$) and a unique hilltop saddle ($x_1 = 0$), which has two symmetric homoclinic loops, one on the right and one on the left of the phase space, $x_{hom}^{l,r}(t) = \mp\sqrt{2}/\cosh(t/\sqrt{2})$.

Since there are two homoclinic orbits, there are two different Melnikov's functions, which can be written in the form

$$\mathcal{M}^{l,r}(m) = -\delta\frac{2\sqrt{2}}{3}\left[1 \mp \frac{\gamma_1}{\gamma_{1,\,cr}^{h}(\omega)} h(m)\right] \tag{18}$$

المنارة للاستشارات

with

$$h(m) = \sum_{j=1}^{\infty} h_j \cos(j\omega t + \Psi_j) \quad h_j = \frac{\gamma_j}{\gamma_1} \frac{j \cosh\left(\frac{\omega\pi}{\sqrt{2}}\right)}{\cosh\left(\frac{j\omega\pi}{\sqrt{2}}\right)} \tag{19}$$

where $\gamma^h_{1,cr}(\omega) = \delta\sqrt{2}\cosh(\omega\pi/\sqrt{2})/(3\pi\omega)$.

The condition $\mathcal{M}^l(m) = 0$ for some $m[0, 2\pi]$ guaranteeing the homoclinic intersection of the *left* stable and unstable manifolds occurs in the region of the parameter space defined by

$$\gamma_1 > \gamma^l_{1,\,cr}(\omega) = \gamma^h_{1,\,cr}(\omega)\frac{1}{M^l} \quad \text{with} \quad M^l = \max_{m\in[0,\,2\pi]}\{h(m)\} \tag{20}$$

Similarly, the condition $\mathcal{M}^r(m) = 0$ for some $m[0, 2\pi]$ guaranteeing the homoclinic intersection of the *right* stable and unstable manifolds occurs in the region of the parameter space defined by

$$\gamma_1 > \gamma^r_{1,\,cr}(\omega) = \gamma^h_{1,\,cr}(\omega)\frac{1}{M^r} \quad \text{with} \quad M^r = -\min_{m\in[0,\,2\pi]}\{h(m)\} \tag{21}$$

Note that M^l and M^r are positive numbers accounting for the shape of the excitation.

For a given generic excitation, the curves $\gamma^l_{1,cr}(\omega)$ and $\gamma^r_{1,cr}(\omega)$ represent the loci of the left and right homoclinic bifurcations, respectively, Fig. 43. In general, these two curves are distinct from each other. They coincide only for the class of excitations satisfying $\max\{h(m)\} = -\min\{h(m)\}$, which occurs, for example, in the case of harmonic excitation, where $h(m) = \cos(\omega t + \Psi_1)$ and $M^l = M^r = 1$, i.e., in the case of harmonic excitation the curve $\gamma^h_{1,cr}(\omega)$ represents the (coinciding) left and right

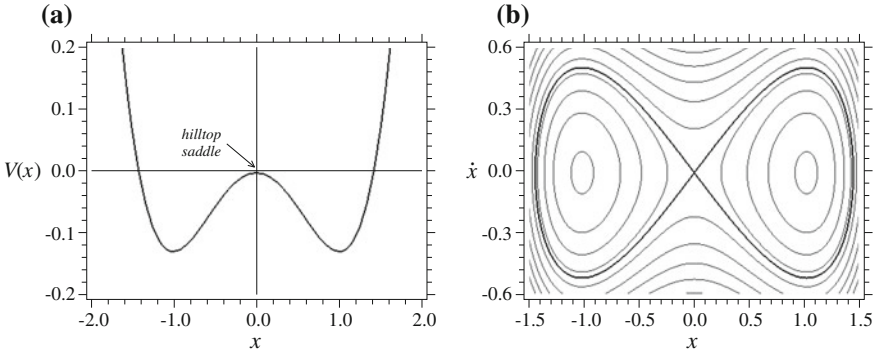

Fig. 42 **a** The potential $V(x)$ and **b** the unforced undamped phase portrait

المنارة للاستشارات

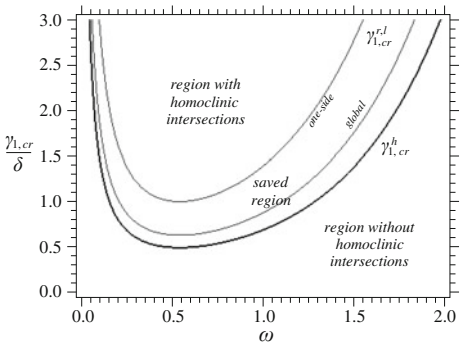

Fig. 43 The curves $\gamma^{h}_{1,cr}(\omega)$ and $\gamma^{l,r}_{1,cr}(\omega)$ for $G^{l,r} = 4/\pi$ (mathematical solution of global control) and for $G^{l,r} = 2$ (mathematical solution of one-side control)

homoclinic bifurcations. Thus, the *saved region* is represented by the strip located above $\gamma^{h}_{1,cr}(\omega)$ and below $\gamma^{l}_{1,cr}(\omega)$ and/or $\gamma^{r}_{1,cr}(\omega)$.

Here appears the peculiarity of the present oscillator. In fact, the presence of two homoclinic orbits permits choosing among different control strategies. Indeed, we can control *only* the right (left) homoclinic bifurcation, irrespective of what happens in the left (right) potential well, or we can try to control *simultaneously* the right and the left homoclinic bifurcations.

This question is important from the application viewpoint, since the first approach is aimed at obtaining a topologically "localized" control, whereas the second approach is aimed at controlling, on average, the "whole" phase space. Thus, three different cases can be investigated separately, specifically:

(ia) *"One-side" control on the right well (right control)*. It is aimed at reducing the region of the right homoclinic intersection by varying the shape of the excitation, which mathematically requires solving the optimization problem

$$\text{Maximizing } G^r \text{ by varying } h_j \text{ and } \Psi_j,\ j \geq 2,\ \text{of } h(m) \tag{22}$$

(ib) *"One-side" control on the left well (left control)*. It is aimed at reducing the region of the left homoclinic intersection by varying the shape of the excitation, which mathematically requires solving the optimization problem

$$\text{Maximizing } G^l \text{ by varying } h_j \text{ and } \Psi_j,\ j \geq 2,\ \text{of } h(m) \tag{23}$$

(ii) *"Global" control*. It is aimed at controlling *simultaneously* the right and the left homoclinic intersections, i.e., it is based on the simultaneous increasing of the two critical thresholds for homoclinic bifurcations. Since

$$\gamma^{l}_{1,cr} = \gamma^{r}_{1,cr} \Leftrightarrow G^l = G^r \Leftrightarrow \max\{h(m)\} = -\min\{h(m)\} \tag{24}$$

this entails solving

المنارة للاستشارات

$$\text{Maximizing } G = \left(G^l = G^r\right) \text{ by varying } h_j \text{ and } \Psi_j,\ j \geq 2,\ \text{of } h(m),$$
$$\text{under the } constraint - \min\{h(m)\} = \max\{h(m)\} \tag{25}$$

Note that in (ia), (ib), and (ii), G^l and G^r are the gains

$$G^l = \frac{\gamma^l_{1,\,cr}(\omega)}{\gamma^h_{1,\,cr}(\omega)} = \frac{1}{M^l} \qquad G^r = \frac{\gamma^r_{1,\,cr}(\omega)}{\gamma^h_{1,\,cr}(\omega)} = \frac{1}{M^r} \tag{26}$$

Thus, the "one-side" control considers only one homoclinic bifurcation, i.e., in this case we are able to control only one part of the phase space, while having to accept a possible worsening on the other part. Conversely, the global control permits controlling the entire phase space. Yet, the optimal gain in the global control is lesser than in the one-side controls, i.e., the global control is theoretically less performant (in fact, problem (25) is clearly a constrained version of (22)–(23)). These considerations show that the two approaches are complementary and not competing.

Similarly to the Helmholtz system, also in the present case study, the mathematical solutions are physically inadmissible because the corresponding excitations would be divergent. To overcome this drawback, in the following, we consider (optimal) reduced-order solutions obtained with a finite number N of superharmonics. Results are reported in Table 3, both for the right (or left) one-side control and for the global control. Note that both solutions provide gains which are quite close to the upper bounds, respectively, 2 and $4/\pi$, which correspond to the physically inadmissible mathematical solutions.

Control of the whole phase space versus control of a single potential well. In the following, we compare the different behaviors of global and one-side controls at $\omega = 0.80$, i.e., in the neighborhood of the vertex (most dangerous frequencies) of the V-shaped region of cross-well chaos (where the erosion ends up) in the excitation parameters plane (Szemplińska-Stupnicka and Rudowski 1993). Their effects on the attractor-basins phase portraits are analyzed in Fig. 44, where the cases of harmonic excitation, of global optimal excitation with one superharmonic, and of right one-side optimal excitation with one superharmonic are reported. The basins are, respectively, light pink and pink for the nonresonant and the resonant attractor in the left well, and light blue and blue for the ones in the right well.

As an example, we refer to $\varepsilon\gamma_1 = 0.0650$. Overall, we can note that the regularization of fractal basin boundaries is an important result, which is expected both in the global and in the one-side control. It is worth highlighting that only fractality between different wells can be eliminated by controlling the homoclinic bifurcation of the hilltop saddle, while the in-well fractality between coexisting confined attractors (e.g., resonant and nonresonant oscillations) is likely due to other homoclinic bifurcations; thus, it is not addressed in the present case study, though being also somehow favorably affected by the applied controls [in any case, it can be purposely controlled by the same method applied to the involved—non-hilltop—saddle (Lenci and Rega 2003c)].

المنارة للاستشارات

الخليج للاستشارات

Table 3 The reduced optimal solutions in the case of right (or left) one-side control (left part of the table) and in the case of global control (right part of the table). Note that the optimal solutions of the global control, which is aimed at being "symmetric," have no even superharmonics

N	G_N	h_2	h_3	h_4	N	G_N	h_3	h_5	h_7
2	1.4142	0.353553			3	1.1547	−0.166667		
3	1.6180	0.552756	0.170789		5	1.2071	−0.232259	0.060987	
4	1.7321	0.673525	0.333274	0.096175	7	1.2310	−0.264943	0.100220	−0.028897
…	…	…	…	…	…	…	…	…	…
∞	2	1	1	1	∞	1.2732	−0.333333	0.200000	−0.142857

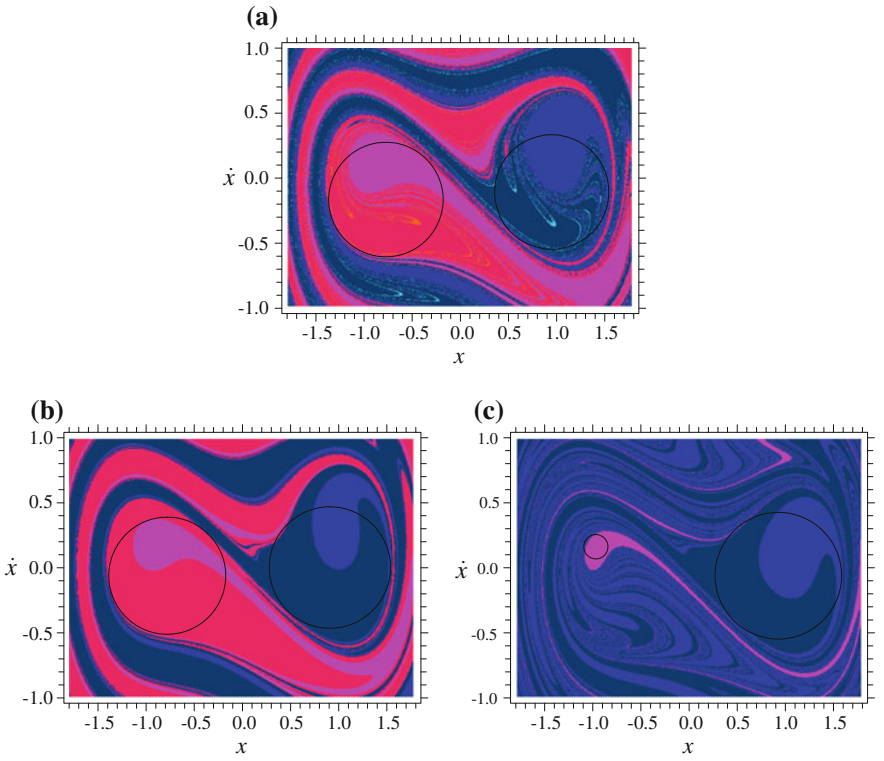

Fig. 44 Basins of attractions at $\varepsilon\gamma_1 = 0.065$ and $\omega = 0.80$, for **a** harmonic excitation, **b** global optimal excitation with one superharmonic, **c** right one-side optimal excitation with one superharmonic. Examples of the circles used in the evaluation of the *IF* are reported

The considered excitation amplitude is larger than $\varepsilon\gamma^h_{1,cr}(\omega) = 0.0570$, and accordingly under harmonic excitation we observe fractal basin boundaries between the right and left attractors, Fig. 44a. The (left-light pink and pink/right-light blue and blue) fractality is modest, due to closeness of the considered excitation to the homoclinic bifurcation threshold, and the behavior is "symmetric" according to the nature of the excitation.

The "symmetry" is maintained by the global control in Fig. 44b, which indeed entails no fractal basin boundaries, according to the fact that the homoclinic bifurcation for this excitation occurs for a (slightly) larger value of the amplitude ($\varepsilon\gamma_{1,cr|\,N=3} = 0.0659$). In the case of (right) one-side control, the "symmetry" is lost, Fig. 44c. In fact, for $\varepsilon\gamma_1 = 0.065$, we have homoclinic intersection of the left manifolds (being $\varepsilon\gamma^l_{1,cr} = 0.0421$) and no intersection of the right manifolds (being $\varepsilon\gamma^r_{1,cr} = 0.0807$). Thus, we observe (left-light pink/right-light blue and blue) fractal basins of attraction on the left and regular basins on the right. Furthermore, the (left-light pink/right-light blue and blue) fractality is rather extended on the left due to the considerable distance

المنارة للاستشارات

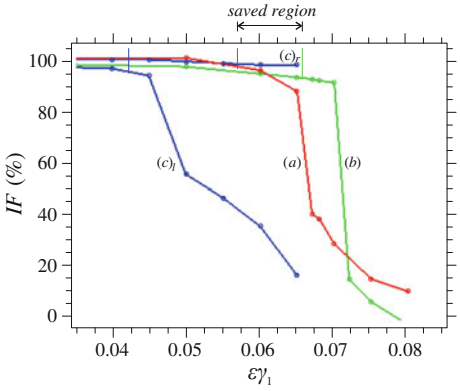

Fig. 45 The basins erosion curves at $\omega = 0.80$ and **a** harmonic excitation, **b** global optimal excitation with one superharmonic, **c** right one-side optimal excitation with one superharmonic

of the excitation value from the left homoclinic bifurcation threshold in parameter space.

Hence, the global control permits a limited reduction of cross-well fractality (related to the low theoretical gain) on the whole phase space, while the one-side control gives a strong reduction of fractality in the controlled potential well (related to the high theoretical gain), but extended fractality in the uncontrolled well, namely, a localized control in the phase space. A different extension of the fractal zones with harmonic and one-side optimal excitations is due to the different distances from the relevant homoclinic bifurcations triggering the fractalization.

The erosion profiles corresponding to harmonic, "one-side" and "global" controls with a single controlling superharmonic are reported in Fig. 45. As an example, we consider $\omega = 0.80$. The safe basin is assumed as the union of the basins of attraction of all the attractors belonging to a certain (left or right) potential well, and the dynamical integrity is measured by the Integrity Factor (*IF*).

In the case of global control, the global optimal excitation (curve (*b*)) is able to shift toward larger amplitudes the erosion curve with respect to the harmonic excitation (curve (*a*)), namely, it is effective in reducing the erosion. The controlled excitation profile is sharper than the one of the reference excitation, and after the fall the *IF* is smaller. This agrees with similar characteristics observed in Sect. 5.1 for the case of the Helmholtz oscillator and proves that there is a well-defined interval (approximately, the vertical segments in between curves (*a*) and (*b*)) where the control is effective.

The case of (right) one-side control has different properties. In fact, due to the asymmetry of this excitation, the left and right wells have a different behavior. According to the theoretical predictions, the erosion curve $(c)_l$ of the left uncontrolled potential well is much lower than curve (*a*), namely, there is a strong fractalization in the uncontrolled (left) potential well and even a strong reduction of the extent of the basin of the left attractor(s). In the right-controlled potential well, on the other hand, basically there is no erosion at all (curve $(c)_r$), in very good agreement with the theoretical predictions.

المنارة للاستشارات

The one-side erosion curves end at $\varepsilon\gamma_1 \cong 0.066$, where the last attractor belonging to the left potential well disappears by a saddle-node bifurcation. For $\varepsilon\gamma_1 > 0.066$—and up to $\varepsilon\gamma_1 < 0.0951$, where a cross-well chaotic attractor is established (Lenci and Rega 2003b)—there are only confined attractors in the controlled potential well, so that the question of cross-well fractalization of the basins makes no more sense. Note that the curve $(c)_r$ does not fall down. This agrees with the fact that the right homoclinic bifurcation occurs at $\varepsilon\gamma_{1,cr}^r = 0.0807$, a value well above the point where the curve disappears.

6 Dynamical Integrity: Design

After highlighting the relevance of the global safety for analyzing the nonlinear phenomena arising in a system and for controlling them, in the present section we dwell on its potential for getting hints in the design stage. We compare the conventional approach traditionally used in the literature and based on large safety factors, with the novel global safety approach based on dynamical integrity results.

6.1 Conventional Approach Versus Dynamical Integrity Approach

As extensively remarked along the chapter, because of the unavoidable presence of real-world disturbances, there is a discrepancy between the *theoretical* range of existence of the desired solution predicted by the local stability theory and the *practical* range of existence actually observable under realistic conditions, being the latter a subset of the former. This discrepancy is regularly experienced and the ensuing reduction of the operational range may be considerable.

An example is shown in Fig. 46, which illustrates a schematic (but very close to real) of the dynamics in a neighborhood of the resonance frequency, in the case of a softening-type behavior. The two-parameter safety chart is reported, as the excitation amplitude and the excitation frequency are varied. The backbone detects the resonance frequency, with the characteristic softening bending. The stability bifurcation threshold representing the bifurcation points is symbolically sketched. This is the boundary of the "stability region" (grayscale), beyond which there is the inevitable escape (white). In a neighborhood of the resonance frequency, the characteristic incursive vertex occurs, which denotes a fall in the stability region. Since this area is very sensitive, it needs to be carefully taken into account in the design. Overall, when ramping up the excitation amplitude, the chart highlights that the stability region becomes increasingly varied, rich, and complex especially in a neighborhood of the resonance, where the practical region is generally reduced more than the theoretical one.

المنارة للاستشارات

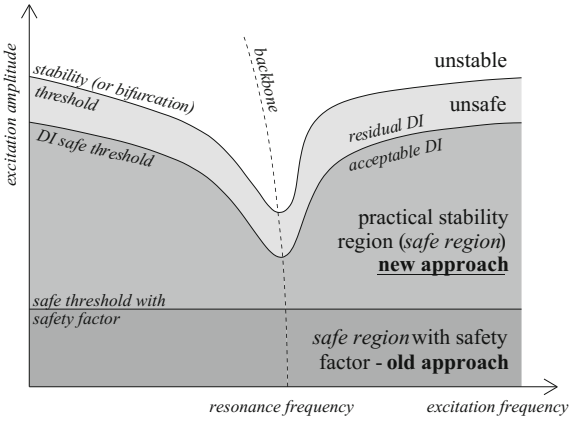

Fig. 46 Schematic safety chart for a system subjected to a harmonic excitation

To guarantee safe conditions in this scenario, the conventional approach regularly assumed by the technical community consists of relying only on the part of the parameter space where the nonlinear phenomena are not experienced. In fact, these phenomena generally require an advanced analysis and, if not properly investigated, they may have dramatically dangerous effects. The conventional approach is firmly intended to prevent them from scratch. The system, instead, is designed to operate only in the linear (or very close to linear) regime, which is the sole one to be considered as fully reliable. This is achieved by establishing large safety factors in the design stage, which are able to set a very cautious distance far from the nonlinear features, i.e., a safe threshold which has not to be overcome.

In Fig. 46, we report a typical safe region detected via the large safety factors (dark gray). The theoretical bounded dynamics occur also for elevated values of excitation amplitude; the dynamics allowed by the large safety factors, instead, stand well below. This enables to avoid the incursive vertex due to the resonance. This threshold is generally constant as the parameters are varied, i.e., it is not raised up when the system is kept in the safer regions spanning away from resonance.

As evinced by the example, the conventional approach is very simple. By means of large safety factors, a safe boundary is detected, which is deliberately very low; this enables the system to be certainly in safe conditions. Yet, a very low safe boundary means restricting the operational life of the system to a narrow parameter range; all the dynamics developing beyond it are intentionally overlooked, generally they are not even investigated. Thus, the conventional approach is safe, but very conservative.

This is the reason why it may be not fully satisfactory. In fact, the system is reliable in practice well above the area allowed by the large safety factors, as proven by experiments in various different fields (Lenci et al. 2013). Here, the dynamics exceed the linear regime, increase their complexity, and need a deeper investigation; nevertheless, they are non-necessarily dangerous. They may be safely operated in practice in a wider region of the parameters space, although smaller than the one of theoretical stability. If we overlook this aspect, we lose large part of the potential

المنارة للاستشارات

of the system. In fact, as emphasized in various circumstances (Wiercigroch and Pavlovskaia 2008; Wiercigroch and Rega 2013), there is a growing need to take advantage of the variety of nonlinear features to design and fabricate systems with superior performances and higher safety characteristics. Hence, the conventional approach is too restrictive for an ambitious engineering design.

This technically driven weakness is well known in the scientific literature. Various attempts have been made, and different thresholds have been suggested to widen the system operational range, while keeping safe conditions. We recall the Melnikov curve (Guckenheimer and Holmes 1983; Wiggins 1990), which is developed in the framework of the perturbation technique and detects the homo/heteroclinic bifurcation of the hilltop saddle. Resorting to this curve allows raising the safe boundary, but only slightly; also, this curve is not able to perceive the occurrence of some important features, e.g., the resonance phenomenon. Another curve referred in the literature is based on the Moon–Chirikov overlap criterion (Moon 1980), but even this curve remains rather low. For an overview, we refer to Moon (1987, 1992) and Szemplińska-Stupnicka (1995).

In this context, the introduction of the global safety concept paves the way for a novel approach to detect a safe threshold for the engineering design, such to be both reliable and able to valorize the full potential of the system.

In Fig. 46, we consider an admissible level of perturbations representing the magnitude of the disturbances expected in the structure, i.e., we consider an acceptable residual dynamical integrity (DI safe threshold). Below the selected iso-integrity curve, there is the region of the parameters space which can be safely allowed in the design. It includes the area detected by the conventional approach (dark gray) and broadens further (gray), which clearly states that large part of the complex nonlinear behavior can be consciously and safely operated. Above this whole range, the solution theoretically continues to exist up to its stability boundary, but is no more able to support the expected disturbances, thus being unsafe from a practical viewpoint (light gray). Further above, the escape is inevitable (white).

We emphasize the accuracy of the iso-integrity curve to face with the dynamics in a neighborhood of the resonance frequency; it permits no longer excluding them and thoroughly delineates the largest range where they can be safely taken into account in the design. Note that Fig. 46 is only a schematic; for an impressive real case study, we refer to Ruzziconi et al. (2018) in this book.

The example clearly shows the dynamical integrity approach. The designer is called to fix the minimum value of dynamical integrity which can be assumed as acceptable when varying a control parameter, i.e., the maximum allowed change of initial conditions which can be safely supported by the system with respect to the desired solution. In traditional terms, this corresponds to fixing a kind of safety factor with respect to the unwanted (static or dynamical) event, under given values of the other control parameters; but the context is now totally different with respect to the conventional approach, since it is based on the clear identification, comprehensive knowledge, and controllability of the elements governing the system behavior. This allows widening the range of applicability of the system and fully exploiting the

المنارة للاستشارات

whole safe region in parameters space, i.e., the dynamical integrity approach is safe but not too conservative.

Furthermore, the dynamic integrity chart reports a multiplicity of iso-integrity curves, each one corresponding to a different level of dynamic integrity (not shown in the figure). This enables to understand how the range of practical existence is increased or reduced by decreasing or increasing perturbations (and vice versa). In this sense, worthy information can be obtained about a variety of possible scenarios ensuing from consideration of different disturbances, thus going ahead with respect to the specific case study analyzed.

Thus, dynamical integrity is able to offer a very deep insight of the expected behavior of a system, which allows establishing a *novel paradigm* for a safe and aware engineering design.

6.2 Safe and Aware Engineering Design

As evinced in the recent literature, there is an increased interest of the research community toward exploiting nonlinear and global dynamics modeling and analysis for designing and controlling engineering systems. Of course, passing from simple models to actual engineered systems is quite involved. Yet, a novel design philosophy should stand in investigating conditions that optimize the behavior of naturally nonlinear systems in such a way to possibly generate favorable operation. Nonlinearities may arise as inherent characteristics of the system or may be artificially created. Properly taking them into account should radically influence current design, control, and exploitation paradigms of technological systems, within a magnitude of contexts. In this respect, global safety offers a valuable advancement.

Note that the dynamical integrity also allows performing the system reliability analysis without, or with a limited use of, stochastic arguments, see Gonçalves et al. (2018) in this book. These are only needed to determine the average amplitude of the expected perturbations (due to various environmental sources), which represent the admissible ones to be considered in the dynamical integrity approach to safety. It could be said that dynamical integrity is a way of dealing with imperfections in a substantially deterministic framework, owing to the increased level of knowledge and understanding of system behavior that it provides. These are challenging and unconventional aspects, which may be expected to influence the risk assessment and to meaningfully affect the awareness of practitioners of mechanics about the importance of a global analysis for an improved and modern use of systems and structures in engineering.

In a longer term perspective, this is expected to meaningfully pave the way to the possible introduction of technical recommendations fully accounting for, and possibly exploiting, the nonlinear and global behavior of systems within a new generation of standards and code regulations.

Widening the range of applicability and reliability of engineering dynamical systems entails an improved and aware use of existing structures/devices in larger ranges

المنارة للاستشارات

of parameters, as well as the design of new structures/devices, with the expected technological improvements ranging from the increase of performance or the cost reduction of existing systems up to the conception and development of novel systems.

7 Summary and Conclusions

In the present chapter, we have overviewed some recent advancements attained in the study of nonlinear dynamics. These achievements offer to the research community the possibility to raise the level of the knowledge on the system's behavior, with desirable advantages for the engineering design. After recalling some outstanding historical contributions to theoretical stability, we have focused on the role played by the global safety concept. The basic underlying idea has been presented. We have emphasized the need of analyzing the system's safety not only via the local perspective traditionally assumed but also from a global viewpoint.

Based on dynamical integrity results, a novel criterion can be established for evaluating the load carrying capacity of a system, which allows defining reliable but not too conservative lower bounds of safety to be referred in the design stage. In these regards, the main steps for assessing the dynamical integrity have been illustrated. Various definitions of safe basin and various alternative dynamical integrity measures have been considered and compared with each other. Dynamical integrity profiles have been introduced. We have shown that the multiplicity of different aspects commonly arising in systems calls for combining the achievements coming from different dynamical integrity tools. We have recalled a number of recurrent critical features leading to a dynamical integrity reduction. Among them, special attention has been drawn to the erosion of the potential well, which is particularly dangerous in systems of the softening type.

Analysis, control, and design of systems are strongly influenced by the introduction of the global safety approach. Results coming from different case studies have been reported, selecting them in such a way to cover the main mechanical and/or dynamical features typically arising in engineering.

Regarding the analysis, a pendulum parametrically excited has been explored from different dynamical integrity perspectives, which are needed to jointly concur for a deep insight. The nonclassical problem of a rigid block has been considered. It presents some characteristics commonly not encountered in classical systems, highlighting that the dynamical integrity definitions typically assumed are not completely satisfactory to face its inherent peculiarities; thus, we have discussed the need of introducing ad hoc definitions, which are capable to properly reflect the special nature of the system.

The problem of control has been addressed. Dealing with the homo/heteroclinic bifurcation of the hilltop saddle triggering the erosion of the potential well, a relevant control technique has been assumed, which is based on shifting the bifurcation threshold toward higher excitation amplitudes. The aim is that of controlling globally the overall system's dynamics. Making reference to both the Helmholtz oscillator

المنارة للاستشارات

and the Duffing one, we have probed the potentialities of the control method and focused on the importance of the global safety investigation to assess and confirm its effectiveness under realistic conditions.

The valuable contribution of the dynamical integrity in the design stage of a system has been highlighted. We have compared the conventional approach to system safety with the novel dynamical integrity one. The former completely overlooks the dynamics behind the problem and does not provide the designer with a capability to cleverly overcome it and go beyond the practical barrier. In contrast, the latter allows the designer to understand and govern the whole matter, giving hints toward a completely different, knowledge-based, criterion for system design, with the beneficial consequence of taking advantage of the system resources in a much more effective way.

Concluding, in the present chapter, we have emphasized the novelty of the global safety perspective. Although many issues remain open, this basic idea is decisive for a higher comprehensive understanding of the system. Impressive is its potential for increasing the practical usability of systems via a safe and aware engineering design.

References

Alsaleem, F. M., Younis, M. I., & Ruzziconi, L. (2010). An experimental and theoretical investigation of dynamic pull-in in MEMS resonators actuated electrostatically. *Journal of Microelectromechanical Systems, 19*(4), 794–806.

Awrejcewicz, J., & Lamarque, C.-H. (2003). *Bifurcation and chaos in nonsmooth mechanical systems*. Singapore: World Scientific.

Bazant, Z., & Cedolin, L. (1991). *Stability of structures*. New York: Oxford University Press.

Belardinelli, P., & Lenci, S. (2016a). A first parallel programming approach in basins of attraction computation. *International Journal of Non-Linear Mechanics, 80,* 76–81.

Belardinelli, P., & Lenci, S. (2016b). An efficient parallel implementation of cell mapping methods for MDOF systems. *Nonlinear Dynamics, 86*(4), 2279–2290.

Belardinelli, P., Lenci, S., & Rega, G. (2018). Seamless variation of isometric and anisometric dynamical integrity measures in basins' erosion. *Communications in Nonlinear Science and Numerical Simulation, 56,* 499–507.

Bishop, S. R., & Clifford, M. J. (1996). Zones of chaotic behavior in the parametrically excited pendulum. *Journal of Sound and Vibration, 189,* 142–147.

Budiansky, B., & Hutchinson, J. W. (1964). Dynamics buckling of imperfection-sensitive structures. In *Proceedings of the Eleventh International Congress of Applied Mechanics*, Munich, Germany (pp. 636–651).

Das, S., & Wahi, P. (2016). Initiation and directional control of period-1 rotation for parametric pendulum. *Proceedings of the Royal Society of London A, 472,* 20160719.

de Souza Jr, J. R., & Rodrigues, M. L. (2002). An investigation into mechanisms of loss of safe basins in a 2 D.O.F. nonlinear oscillator. *Journal of the Brazilian Society of Mechanical Sciences, 24,* 93–98.

Eason, R., & Dick, A. J. (2014). A parallelized multi-degrees-of-freedom cell map method. *Nonlinear Dynamics, 77*(3), 467–479.

Euler, L. (1744). *Methodus Inveniendi Lineas Curvas Maximi Minimive Proprietate Gaudentes, Sive Solutio Problematis Isoperimetrici Latissimo Sensu Accepti, Addentamentum 1: de Curvis Elasticis.* Laussanae et Genevae, Apud Marcum-Michaelem, Bousquet et Socios.

المنارة للاستشارات

Gan, C. B., & He, S. M. (2007). Studies on structural safety in stochastically excited Duffing oscillator with double potential wells. *Acta Mechanica Sinica, 23*(5), 577–583.

Gonçalves, P. B., & Del Prado, Z. J. G. N. (2002). Nonlinear oscillations and stability of parametrically excited cylindrical shells. *Meccanica, 37,* 569–597.

Gonçalves, P. B., & Del Prado, Z. J. G. N. (2005). Low-dimensional Galerkin models for nonlinear vibration and instability analysis of cylindrical shells. *Nonlinear Dynamics, 41,* 129–145.

Gonçalves, P. B., Orlando, D., Lenci, S., & Rega, G. (2018). Nonlinear dynamics, safety and control of structures liable to interactive unstable buckling. In S. Lenci & G. Rega (Eds.), *Global nonlinear dynamics for engineering design and system safety* (Vol. 588, pp. 167–228). CISM Courses and Lectures. Cham: Springer.

Gonçalves, P. B., & Santee, D. (2008). Influence of uncertainties on the dynamic buckling loads of structures liable to asymmetric post-buckling behavior. *Mathematical Problems in Engineering*, *2008*, 490137-1–490137-24.

Gonçalves, P. B., Silva, F. M. A., & Del Prado, Z. J. G. N. (2007). Global stability analysis of parametrically excited cylindrical shells through the evolution of basin boundaries. *Nonlinear Dynamics, 50,* 121–145.

Gonçalves, P. B., Silva, F. M. A., Rega, G., & Lenci, S. (2011). Global dynamics and integrity of a two-dof model of a parametrically excited cylindrical shell. *Nonlinear Dynamics, 63,* 61–82.

Grebogi, C., Ott, E., & Yorke, J. A. (1983). Crises, sudden changes in chaotic attractors and transient chaos. *Physica D: Nonlinear Phenomena, 7,* 181–200.

Guckenheimer, J., & Holmes, P. J. (1983). *Nonlinear oscillations, dynamical systems and bifurcation of vector fields*. New York: Springer.

Hong, L., & Sun, J. (2006). Bifurcations of a forced Duffing oscillator in the presence of fuzzy noise by the generalized cell mapping method. *International Journal of Bifurcation and Chaos, 16*(10), 3043–3051.

Housner, G. W. (1963). The behaviour of inverted pendulum structures during earthquakes. *Bulletin of the Seismological Society of America, 53*(2), 403–417.

Hsu, C. S. (1987). *Cell to cell mapping: A method of global analysis for nonlinear system*. New York: Springer.

Hsu, C. S., & Chiu, H. M. (1987). Global analysis of a system with multiple responses including a strange attractor. *Journal of Sound and Vibration, 114*(2), 203–218.

Kirkpatrick, P. (1927). Seismic measurements by the overthrow of columns. *Bulletin of the Seismological Society of America, 17,* 95–109.

Koch, B. P., & Leven, R. W. (1985). Subharmonic and homoclinic bifurcations in a parametrically forced pendulum. *Physica D: Nonlinear Phenomena, 16,* 1–13.

Koh, A. S. (1986). Rocking of rigid blocks on randomly shaking foundations. *Nuclear Engineering and Design, 97,* 269–276.

Koiter, W. T. (1945). *Over de Stabiliteit van het Elastisch Evenwicht*. Ph.D. Thesis, Delft University, Delft, The Netherlands. English translation: Koiter, W. T. (1967). *On the stability of elastic equilibrium*. NASA technical translation F-10, 833, Clearinghouse, US Department of Commerce/National Bureau of Standards N67–25033.

Kreuzer, E., & Lagemann, B. (1996). Cell mapping for multi-degree-of-freedom-systems parallel computing in nonlinear dynamics. *Chaos, Solitons & Fractals, 7*(10), 1683–1691.

Kustnezov, Y. A. (1995). *Elements of applied bifurcation theory*. New York: Springer.

Lansbury, A. N., Thompson, J. M. T., & Stewart, H. B. (1992). Basin erosion in the twin-well Duffing oscillator: Two distinct bifurcation scenarios. *International Journal of Bifurcation and Chaos, 2,* 505–532.

Leine, R. I. (2010). The historical development of classical stability concepts: Lagrange, Poisson and Lyapunov stability. *Nonlinear Dynamics, 59,* 173–182.

Lenci, S., Brocchini, M., & Lorenzoni, C. (2012a). Experimental rotations of a pendulum on water waves. *ASME Journal of Computational and Nonlinear Dynamics*, *7*(1), 011007-1–011007-9.

Lenci, S., Orlando, D., Rega, G., & Gonçalves, P. B. (2012b). Controlling practical stability and safety of mechanical systems by exploiting chaos properties. *Chaos*, *22*(4), 047502-1–047502-15.

المنارة للاستشارات

Lenci, S., & Rega, G. (1998a). A procedure for reducing the chaotic response region in an impact mechanical system. *Nonlinear Dynamics, 15,* 391–409.
Lenci, S., & Rega, G. (1998b). Controlling nonlinear dynamics in a two-well impact system. Part I. Attractors and bifurcation scenario under symmetric excitations. *International Journal of Bifurcation and Chaos, 8,* 2387–2408.
Lenci, S., & Rega, G. (1998c). Controlling nonlinear dynamics in a two-well impact system. Part II. Attractors and bifurcation scenario under unsymmetric optimal excitations. *International Journal of Bifurcation and Chaos, 8,* 2409–2424.
Lenci, S., & Rega, G. (2003a). Optimal control of homoclinic bifurcation: Theoretical treatment and practical reduction of safe basin erosion in the Helmholtz oscillator. *Journal of Vibration and Control, 9,* 281–315.
Lenci, S., & Rega, G. (2003b). Optimal control of nonregular dynamics in a Duffing oscillator. *Nonlinear Dynamics, 33,* 71–86.
Lenci, S., & Rega, G. (2003c). Optimal numerical control of single-well to cross-well chaos transition in mechanical systems. *Chaos, Solitons & Fractals, 15,* 173–186.
Lenci, S., & Rega, G. (2004a). A dynamical systems analysis of the overturning of rigid blocks. In *CD-Rom Proceedings of the XXI International Conference of Theoretical and Applied Mechanics*, IPPT PAN, Warsaw, Poland, 15–21 August 2004. ISBN 83-89687-01-1.
Lenci, S., & Rega, G. (2004b). A unified control framework of the nonregular dynamics of mechanical oscillators. *Journal of Sound and Vibration, 278*(4–5), 1051–1080.
Lenci, S., & Rega, G. (2004c). Global optimal control and system-dependent solutions in the hardening Helmholtz-Duffing oscillator. *Chaos, Solitons & Fractals, 21,* 1031–1046.
Lenci, S., & Rega, G. (2004d). Numerical aspects in the optimal control and anti-control of rigid block dynamics. In *Proceedings of the Sixth World Conference on Computational Mechanics*, WCCM VI, Beijing, China, 5–10 September 2004.
Lenci, S., & Rega, G. (2005). Heteroclinic bifurcations and optimal control in the nonlinear rocking dynamics of generic and slender rigid blocks. *International Journal of Bifurcation and Chaos, 15*(6), 1901–1918.
Lenci, S., & Rega, G. (2006a). A dynamical systems approach to the overturning of rocking blocks. *Chaos, Solitons & Fractals, 28,* 527–542.
Lenci, S., & Rega, G. (2006b). Control of pull-in dynamics in a nonlinear thermoelastic electrically actuated microbeam. *Journal of Micromechanics and Microengineering, 16,* 390–401.
Lenci, S., & Rega, G. (2006c). Optimal control and anti-control of the nonlinear dynamics of a rigid block. *Philosophical Transactions of the Royal Society A, 364,* 2353–2381.
Lenci, S., & Rega, G. (2008). Competing dynamic solutions in a parametrically excited pendulum: Attractor robustness and basin integrity. *ASME Journal of Computational and Nonlinear Dynamics*, *3*, 041010-1–041010-9.
Lenci, S., & Rega, G. (2011a). Experimental versus theoretical robustness of rotating solutions in a parametrically excited pendulum: A dynamical integrity perspective. *Physica D: Nonlinear Phenomena, 240,* 814–824.
Lenci, S., & Rega, G. (2011b). Forced harmonic vibration in a Duffing oscillator with negative linear stiffness and linear viscous damping. In I. Kovacic & M. J. Brennan (Eds.), *The Duffing equation: Nonlinear oscillators and their behaviour* (pp. 219–276). Wiley.
Lenci, S., & Rega, G. (2011c). Load carrying capacity of systems within a global safety perspective. Part I. Robustness of stable equilibria under imperfections. *International Journal of Nonlinear Mechanics*, *46*, 1232–1239.
Lenci, S., & Rega, G. (2011d). Load carrying capacity of systems within a global safety perspective. Part II. Attractor/basin integrity under dynamic excitations. *International Journal of Nonlinear Mechanics*, *46*, 1240–1251.
Lenci, S., Rega, G., & Ruzziconi, L. (2013). Dynamical integrity as a conceptual and operating tool for interpreting/predicting experimental behavior. *Philosophical Transactions of the Royal Society of London A*, *371*(1993), 20120423-1–20120423-19.

المنارة للاستشارات

Lyapunov, A. M. (1892). *The general problem of the stability of motion*. Ph.D. Thesis, Moscow University, Moscow, Russia. English translation: Lyapunov, A. M. (1992). *The general problem of the stability of motion*. London: Taylor & Francis.

Mang, H. A., Jia, X., & Hoenger, G. (2009). Hilltop buckling as the A and Ω in sensitivity analysis of the initial postbuckling behavior of elastic structures. *Journal of Civil Engineering and Management, 15,* 35–46.

Milne, J. (1881). Experiments in observational seismology. *Transactions of the Seismological Society of Japan, 3,* 12–64.

Moon, F. C. (1980). Experiments on chaotic motions of a forced nonlinear oscillator: Strange attractors. *Journal of Applied Mechanics, 47*(3), 638–644.

Moon, F. C. (1987). *Chaotic vibrations*. New York: Wiley.

Moon, F. C. (1992). *Chaotic and fractal dynamics. An introduction for applied scientists and engineers*. New York: Wiley.

Nayfeh, A. H., & Balachandran, B. (1995). *Applied nonlinear dynamics*. New York: Wiley.

Novak, M. (1969). Aeroelastic galloping of prismatic bodies. *ASCE Journal of the Engineering Mechanics Division, 95*(1), 115–142.

Oppenheim, I. J. (1992). The masonry arch as a four-link mechanism under base motion. *Earthquake Engineering and Structural Dynamics, 21,* 1005–1017.

Orlando, D., Gonçalves, P. B., Rega, G., & Lenci, S. (2011). Influence of modal coupling on the nonlinear dynamics of Augusti's model. *ASME Journal of Computational and Nonlinear Dynamics*, *6*, 041014-1–041014-11.

Perry, J. (1881). Note on the rocking of a column. *Transactions of the Seismological Society of Japan, 3,* 103–106.

Pignataro, M., Rizzi, N., & Luongo, A. (1990). *Stability, bifurcation and postcritical behaviour of elastic structures*. Amsterdam: Elsevier Science Publishers.

Plaut, R. H., Fielder, W. T., & Virgin, L. N. (1996). Fractal behaviour of an asymmetric rigid block overturning due to harmonic motion of a tilted foundation. *Chaos, Solitons & Fractals, 7,* 177–196.

Rainey, R. C. T., & Thompson, J. M. T. (1991). The transient capsize diagram—A new method of quantifying stability in waves. *Journal of Ship Research, 35*(1), 58–62.

Rega, G., & Lenci, S. (2003). Bifurcations and chaos in single-d.o.f. mechanical systems: Exploiting nonlinear dynamics for their control. In A. Luongo (Ed.), *Recent research development in structural dynamics* (pp. 331–369). Kerala: Research Signpost.

Rega, G., & Lenci, S. (2005). Identifying, evaluating, and controlling dynamical integrity measures in nonlinear mechanical oscillators. *Nonlinear Analysis, 63,* 902–914.

Rega, G., & Lenci, S. (2008). Dynamical integrity and control of nonlinear mechanical oscillators. *Journal of Vibration and Control*, *14*, 159–179, 2008.

Rega, G., & Lenci, S. (2009). Recent advances in control of complex dynamics in mechanical and structural systems. In M. A. F. Sanjuan & C. Grebogi (Eds.), *Recent progress in controlling chaos* (pp. 189–237). Singapore: World Scientific.

Rega, G., & Lenci, S. (2015). A global dynamics perspective for system safety from macro- to nanomechanics: Analysis, control, and design engineering. *Applied Mechanics Reviews*, *67*, 050802-1–050802-19.

Rega, G., Lenci, S., & Thompson, J. M. T. (2010). Controlling chaos: The OGY method, its use in mechanics, and an alternative unified framework for control of non-regular dynamics. In M. Thiel, J. Kurths, M. C. Romano, G. Károlyi, & A. Moura (Eds.), *Nonlinear dynamics and chaos: Advances and perspectives* (pp. 211–269). Berlin, Heidelberg: Springer.

Rega, G., & Settimi, V. (2013). Bifurcation, response scenarios and dynamic integrity in a single-mode model of noncontact atomic force microscopy. *Nonlinear Dynamics, 73*(1–2), 101–123.

Ruzziconi, L., Bataineh, A. M., Younis, M. I., Cui, W., & Lenci, S. (2013a). Nonlinear dynamics of an electrically actuated imperfect microbeam resonator: Experimental investigation and reduced-order modeling. *Journal of Micromechanics and Microengineering*, *23*(7), 075012-1–075012-14.

المنارة للاستشارات

Ruzziconi, L., Lenci, S., & Younis, M. I. (2013b). An imperfect microbeam under an axial load and electric excitation: Nonlinear phenomena and dynamical integrity. *International Journal of Bifurcation and Chaos*, *23*(2), 1350026-1–1350026-17.

Ruzziconi, L., Lenci, S., & Younis, M. I. (2018). Interpreting and predicting experimental responses of micro and nano devices via dynamical integrity. In S. Lenci & G. Rega (Eds.), *Global nonlinear dynamics for engineering design and system safety* (Vol. 588, pp. 113–166). CISM Courses and Lectures. Cham: Springer.

Ruzziconi, L., Younis, M. I., & Lenci, S. (2012). An efficient reduced-order model to investigate the behavior of an imperfect microbeam under axial load and electric excitation. *ASME Journal of Computational and Nonlinear Dynamics*, *8*, 011014-1–011014-9.

Ruzziconi, L., Younis, M. I., & Lenci, S. (2013c). An electrically actuated imperfect microbeam: Dynamical integrity for interpreting and predicting the device response. *Meccanica, 48*(7), 1761–1775.

Ruzziconi, L., Younis, M. I., & Lenci, S. (2013d). Dynamical integrity for interpreting experimental data and ensuring safety in electrostatic MEMS. In M. Wiercigroch, & G. Rega (Eds.), *IUTAM Symposium on Nonlinear Dynamics for Advanced Technologies and Engineering Design* (Vol. 32, pp. 249–261). IUTAM Bookseries. Springer.

Ruzziconi, L., Younis, M. I., & Lenci, S. (2013e). Multistability in an electrically actuated carbon nanotube: a dynamical integrity perspective. *Nonlinear Dynamics, 74*(3), 533–549.

Ruzziconi, L., Younis, M. I., & Lenci, S. (2013f). Parameter identification of an electrically actuated imperfect microbeam. *International Journal of Non-Linear Mechanics, 57,* 208–219.

Settimi, V., Gottlieb, O., & Rega, G. (2015). Asymptotic analysis of a noncontact AFM microcantilever sensor with external feedback control. *Nonlinear Dynamics, 79*(4), 2675–2698.

Settimi, V., & Rega, G. (2016a). Exploiting global dynamics of a noncontact atomic force microcantilever to enhance its dynamical robustness via numerical control. *International Journal of Bifurcation and Chaos*, *26*, 1630018-1–1630018-17.

Settimi, V., & Rega, G. (2016b). Global dynamics and integrity in noncontacting atomic force microscopy with feedback control. *Nonlinear Dynamics, 86*(4), 2261–2277.

Settimi, V., & Rega, G. (2016c). Influence of a locally-tailored external feedback control on the overall dynamics of a non-contact AFM model. *International Journal of Non-Linear Mechanics, 80,* 144–159.

Settimi, V., & Rega, G. (2018). Local versus global dynamics and control of an AFM model in a safety perspective. In S. Lenci & G. Rega (Eds.), *Global nonlinear dynamics for engineering design and system safety* (Vol. 588, pp. 229–286). CISM Courses and Lectures. Cham: Springer.

Silva, F. M. A., & Gonçalves, P. B. (2015). The influence of uncertainties and random noise on the dynamic integrity analysis of a system liable to unstable buckling. *Nonlinear Dynamics, 81*(1–2), 707–724.

Silva, F. M. A., Gonçalves, P. B., & Del Prado, Z. J. G. N. (2013). Influence of physical and geometrical system parameters uncertainties on the nonlinear oscillations of cylindrical shells. *Journal of the Brazilian Society of Mechanical Sciences and Engineering, 34,* 622–632.

Soliman, M. S., & Gonçalves, P. B. (2003). Chaotic behavior resulting in transient and steady state instabilities of pressure-loaded shallow spherical shells. *Journal of Sound and Vibration, 259*(3), 497–512.

Soliman, M. S., & Thompson, J. M. T. (1989). Integrity measures quantifying the erosion of smooth and fractal basins of attraction. *Journal of Sound and Vibration, 135,* 453–475.

Soliman, M. S., & Thompson, J. M. T. (1990). Stochastic penetration of smooth and fractal basin boundaries under noise excitation. *Dynamics and Stability of Systems, 5*(4), 281–298.

Soliman, M. S., & Thompson, J. M. T. (1991). Transient and steady state analysis of capsize phenomena. *Applied Ocean Research, 13*(2), 82–92.

Soliman, M. S., & Thompson, J. M. T. (1992). Global dynamics underlying sharp basin erosion in nonlinear driven oscillators. *Physical Review A, 45*(6), 3425–3431.

المنارة للاستشارات

Sun, J. Q. (1994). Effect of small random disturbance on the 'Protection Thickness' of attractors of nonlinear dynamic systems. In J. M. T. Thompson & S. R. Bishop (Eds.), *Nonlinearity and chaos in engineering dynamics* (pp. 435–437). Chichester: Wiley.

Sun, J. Q. (2013). Control of nonlinear dynamic systems with the cell mapping method. In O. Schütze, C. A. Coello Coello, A.-A. Tantar, E. Tantar, P. Bouvry, & P. Del Moral (Eds.), *EVOLVE—A bridge between probability, set oriented numerics, and evolutionary computation II. Advances in intelligent systems and computing* (pp. 3–18). Berlin, Heidelberg: Springer.

Xiong, F. R., Han, Q., Hong, L., & Sun, J. Q. (2018). Global analysis of nonlinear dynamical systems. In S. Lenci & G. Rega (Eds.), *Global nonlinear dynamics for engineering design and system safety* (Vol. 588, pp. 287–318). CISM Courses and Lectures. Cham: Springer.

Sun, J. Q., & Hsu, C. S. (1991). Effects of small random uncertainties on the non-linear systems studied by the generalized cell mapping methods. *Journal of Sound and Vibration, 147*(2), 185–201.

Szemplińska-Stupnicka, W. (1995). The analytical predictive criteria for chaos and escape in nonlinear oscillators: A survey. *Nonlinear Dynamics, 7*(2), 129–147.

Szemplińska-Stupnicka, W., & Rudowski, J. (1993). Steady state in the twin-well potential oscillator: Computer simulations and approximate analytical studies. *Chaos, 3,* 375–385.

Szemplińska-Stupnicka, W., Tyrkiel, E., & Zubrzycki, A. (2000). The global bifurcations that lead to transient tumbling chaos in a parametrically driven pendulum. *International Journal of Bifurcation and Chaos, 10,* 2161–2175.

Thom, R. (1972). *Structural stability and morphogenesis*. Massachusetts: W.A. Benjamin Inc.

Thompson, J. M. T. (1982). *Instability and catastrophe in science and engineering*. Wiley.

Thompson, J. M. T. (1989). Chaotic phenomena triggering the escape from a potential well. *Proceedings of the Royal Society of London A, 421,* 195–225.

Thompson, J. M. T. (1997). Designing against capsize in beam seas: Recent advances and new insights. *Applied Mechanics Reviews, 50*(5), 307–325.

Thompson, J. M. T. (2018). Dynamical integrity: Three decades of progress from macro to nano mechanics. In S. Lenci & G. Rega (Eds.), *Global nonlinear dynamics for engineering design and system safety* (Vol. 588, pp. 1–26). CISM Courses and Lectures. Cham: Springer.

Thompson, J. M. T., & Hunt, G. W. (1973). *A general theory of elastic stability*. London: Wiley.

Thompson, J. M. T., Rainey, R. C. T., & Soliman, M. S. (1990). Ship stability criteria based on chaotic transients from incursive fractals. *Philosophical Transactions of the Royal Society of London A, 332*(1624), 149–167.

Thompson, J. M. T., & Soliman, M. S. (1990). Fractal control boundaries of driven oscillators and their relevance to safe engineering design. *Proceedings of the Royal Society of London A, 428*(1874), 1–13.

Thompson, J. M. T., & Stewart, H. B. (1986). *Nonlinear dynamics and chaos*. Chichester: Wiley (second extended edition, 2002).

Thompson, J. M. T., & Ueda, Y. (1989). Basin boundary metamorphoses in the canonical escape equation. *Dynamics and Stability of Systems, 4*(3–4), 285–294.

Troger, H., & Steindl, A. (1991). *Nonlinear stability and bifurcation theory*. Wien: Springer.

van Campen, D. H., van de Vorst, E. L. B., van der Spek, J. A. W., & de Kraker, A. (1995). Dynamics of a multi-DOF beam system with discontinuous support. *Nonlinear Dynamics, 8*(4), 453–466.

van der Heijden, A. M. A. (ed.). (2009). *W. T. Koiter's elastic stability of solids and structures*. Cambridge University Press.

Wiercigroch, M. (2010). *A new concept for energy extraction from waves via parametric pendulor*. UK Patent Application.

Wiercigroch, M., & Pavlovskaia, E. (2008). Non-linear dynamics of engineering systems. *International Journal of Non-Linear Mechanics, 43*(6), 459–461.

Wiercigroch, M., & Rega, G. (2013). Introduction to *N*DATED. In M. Wiercigroch & G. Rega (Eds.), *IUTAM Symposium on Nonlinear Dynamics for Advanced Technologies and Engineering Design* (Vol. 32, pp. v–viii). IUTAM Bookseries. Springer.

المنارة للاستشارات

Wiggins, S. (1990). *Introduction to applied nonlinear dynamical systems and chaos*. New York, Heidelberg, Berlin: Springer.
Winkler, T., Meguro, K., & Yamazaki, F. (1995). Response of rigid body assemblies to dynamic excitation. *Earthquake Engineering and Structural Dynamics, 24,* 1389–1408.
Xu, T., Ruzziconi, L., & Younis, M. I. (2017). Global investigation of the nonlinear dynamics of carbon nanotubes. *Acta Mechanica, 228*(3), 1029–1043.
Xu, X., Pavlovskaia, E., Wiercigroch, M., Romeo, R., & Lenci, S. (2007). Dynamic interactions between parametric pendulum and electrodynamical shaker. *ZAMM—Journal of Applied Mathematics and Mechanics, 87,* 172–186.
Xu, X., & Wiercigroch, M. (2007). Approximate analytical solutions for oscillatory and rotational motion of a parametric pendulum. *Nonlinear Dynamics, 47,* 311–320.
Xu, X., Wiercigroch, M., & Cartmell, M. P. (2005). Rotating orbits of a parametrically excited pendulum. *Chaos, Solitons & Fractals, 23,* 1537–1548.
Younis, M. I. (2011). *MEMS linear and nonlinear statics and dynamics*. New York: Springer.
Zeeman, E. C. (1977). *Catastrophe theory: Selected papers, 1972–1977*. Oxford, England: Addison-Wesley.

المنارة للاستشارات

Interpreting and Predicting Experimental Responses of Micro- and Nano-Devices via Dynamical Integrity

Laura Ruzziconi, Stefano Lenci and Mohammad I. Younis

Abstract The present chapter highlights the importance of the dynamical integrity theory for micro and nanoapplications. Three case-studies of devices at different scales are presented (a capacitive accelerometer, a microbeam-based micro-electro-mechanical system, and a single-walled slacked carbon nanotube) and different issues commonly addressed in the engineering design are examined via dynamical integrity concepts. The iso-integrity curves are observed to follow exactly the experimental data. They are able to detect the parameter range where each attractor can be reliably observed in practice and where, instead, becomes vulnerable. Also, they may be used to simulate and predict the expected dynamics under different (smaller or larger) experimental disturbances. While referring to particular case-studies, we show the relevance of the dynamical integrity analysis for the engineering design of a mechanical system, in order to operate it in safe conditions, according to the desired outcome and depending on the expected disturbances.

Keywords Micro- and nano-devices · Experiments vs theory · Nonlinear dynamics · Dynamical integrity

L. Ruzziconi (✉)
Faculty of Engineering, eCampus University, Novedrate, Italy
e-mail: laura.ruzziconi@uniecampus.it

S. Lenci
Department of Civil and Building Engineering and Architecture, Polytechnic University of Marche, Ancona, Italy
e-mail: lenci@univpm.it

M. I. Younis
Physical Science and Engineering Division, King Abdullah University of Science and Technology (KAUST), Thuwal, Kingdom of Saudi Arabia
e-mail: Mohammad.Younis@kaust.edu.sa; myounis@binghamton.edu

M. I. Younis
Department of Mechanical Engineering, Binghamton University, State University of New York (SUNY), Binghamton, NY, USA

© CISM International Centre for Mechanical Sciences 2019

S. Lenci and G. Rega (eds.), *Global Nonlinear Dynamics for Engineering Design and System Safety*, CISM International Centre for Mechanical Sciences 588,
https://doi.org/10.1007/978-3-319-99710-0_3

المنارة للاستشارات

1 Introduction

Micro-electromechanical systems (MEMS) are currently actively applied in a wide spectrum of engineering fields, ranging from industrial, domestic, and commercial uses up to energy harvesting, communications, and bioengineering. MEMS are inherently nonlinear and multiphysical. Many studies investigate mechanical and dynamical aspects to design, optimize, and invent devices with distinctive features, unique characteristics, and superior performances. Multistability, jumps, chaotic motions, snap-through, escapes, and many other complex nonlinear features arising in the devices responses have been reported. New sophisticated devices deliberately operating in the nonlinear regime are emerging in a variety of different applications (Younis 2011; Senturia 2001).

Several nonlinear phenomena may arise in MEMS. Focusing on electrically actuated microbeams, Younis and Nayfeh (2003) investigated the effect of the design parameters on the dynamic response. Nonlinearities may lead to either softening or hardening behavior, depending on the dominance of the electric excitation, the mid-plane stretching, and the axial load. Nayfeh et al. (2007) analyzed the pull-in instability, showing similarities and differences between the static and the dynamic pull-in phenomenon. Distinct mechanisms leading to dynamic pull-in have been observed and the possibility to take advantage of it in the design of radio frequency MEMS (RF-MEMS) switches to lower the high driving voltage requirement has been explored. Abdel-Rahman et al. (2002) discussed the effects of the design parameters for tuning the device and widening the operational range of DC polarization. Nayfeh and Younis (2005) examined the dynamics under secondary resonance excitations. At subharmonic resonance, the frequency response is characterized by a sharp roll-off from pass-band to stop-band, both at hardening and softening behavior. This is promising for designing high-sensitive band-pass RF filters of improved characteristics.

Special attention has been devoted to the problem formulation, with the aim of balancing the need of enough fidelity in the model against the need of numerical efficiency for its practical use (Younis et al. 2003; Nayfeh et al. 2005; Rega and Troger 2005; Ruzziconi et al. 2012; Belardinelli et al. 2014).

Extensive experimental tests have been performed. Alsaleem et al. (2009) experimentally investigated nonlinear dynamic phenomena in a MEMS capacitive accelerometer, which are induced by exciting the microstructure with a nonlinear forcing composed of a DC electrostatic load superimposed on an AC harmonic one, rising up to large excitations. Many experimentally measured frequency-response curves have been reported, showing the primary resonance, the activation of various superharmonic and subharmonic resonances, the softening-spring behavior with bending toward lower frequency values, the pull-in instability, etc. Alsaleem et al. (2010) further developed the experimental investigation focusing on the pull-in bands. Several experimental data have been presented, illustrating regimes of AC forcing amplitude versus AC frequency, where a resonator is forced to pull-in. The effect of varying the electrostatic excitation has been examined. Different MEMS

المنارة للاستشارات

devices have been tested. Data are shown both for primary and for secondary resonance. Younis and Alsaleem (2009) presented an exploratory research on the possibility to make use of the escape and the jump phenomena to realize new concepts for mass sensing and detection and design novel devices of improved characteristics.

Many nonlinear features may arise. Exploring a particular MEMS oscillator, Rhoads et al. (2006a) investigated a device under pure parametric electrostatic excitation. The frequency-dynamic voltage behavior chart underlines the complexity of the dynamics, exhibiting Arnold tongues and saddle-node bifurcations and confirming a strong correlation with the experimental data. In parametrically excited resonant microbeam systems (Rhoads et al. 2006b), a multiplicity of topologically different dynamical behaviors has been noticed. The tunable nature of the system's response has been highlighted. Sample design charts for predicting transitions between qualitatively distinct parameter regions have been developed. This inherent flexibility may contribute to a general improvement in sensitivity, stop-band attenuation, and noise rejection. Similar highly nonlinear dynamics have been analyzed in electromagnetically actuated microbeams (Rhoads et al. 2013). In a MEMS resonator, Mestrom et al. (2008) theoretically and experimentally investigated the softening bending and related jumps between non-resonant and resonant branches. In a neighborhood of the fundamental resonance, the cyclic fold bifurcations have been experimentally measured and reported in the frequency-dynamic voltage behavior chart. In a clamped—clamped microbeam-based MEMS resonator (Mestrom et al. 2010), both softening and hardening behaviors have been experimentally and theoretically detected, depending on the excitation parameters. An extensive analysis has been developed, which enabled parameter study and design optimization of microsystems with respect to nonlinear dynamic features.

The possibility of devices with bistable behavior has deeply fascinated the MEMS and NEMS research community. Krylov et al. (2008) investigated shallow-arched microbeams electrically actuated. They are fabricated from silicon on insulator (SOI) wafer using deep reactive ion etching and in-plane responses are characterized by means of optical and scanning electron microscopy. Many experimental data and theoretical simulations have been developed, highlighting that the microstructure may exhibit numerous nonlinear phenomena, as sequential snap-through buckling and pull-in instability. Krylov and Dick (2010) further theoretically examined these features, detecting the boundaries of the bistability region and shedding light on the role of generic nonlinearities as well as on the influence of the device parameters. As demonstrated through a series of simulations (Krylov et al. 2011), bistability may occur also when actuated by fringing electrostatic fields. Medina et al. (2012) extensively examined the buckling problem of initially curved bell-shaped stress-free microbeams under a distributed electrostatic force. Symmetric and asymmetric snap-through, release and pull-in bifurcation points are compared, exploring the influence of the design parameters on the stability of the device. The phenomenon of symmetry breaking has been analyzed in depth and non-symmetric buckling criteria have been established. Significant results are reported by Medina et al. (2014), where experimental bifurcation maps built in terms of the critical snap-through, release and pull-in deflections of the microbeams have been developed, showing the location of

المنارة للاستشارات

the critical points and confirming experimentally the complex nonlinear behavior theoretically predicted. Furthermore, bistable behavior is feasible to be operated in curved microplates of realistic dimensions, under attainable voltages (Medina et al. 2016).

Along the same line, Ruzziconi et al. (2013b) theoretically investigated the nonlinear dynamics of an imperfect microbeam-based MEMS device with axial load deliberately added in order to have a bistable static configuration. Several competing attractors exist, including both in-well and cross-well oscillations, which may lead to a considerable versatility of behavior. The vulnerability of each attractor under realistic conditions has been discussed. Ramini et al. (2016a, c) experimentally examined the rich complex dynamics arising in an in-plane silicon micromachined arch. When the excitation is close to the first resonance frequency, a softening-spring behavior has been noticed. Conversely, when the excitation is close to the third (second symmetric) resonance frequency, a hardening spring behavior arises. Moreover, at the primary resonance with high voltage excitations, dynamic snap-through motion occurs, which exhibits hardening behavior. The snap-through frequency band is increased when increasing the voltage load. Hajjaj et al. (2017) experimentally tuned the resonance frequencies and their ratios via electrothermal modulation. An electrothermal voltage has been applied between the anchors of an arched microbeam generating a current that controls the axial stress caused by thermal expansion. The sensitivity of the frequency values to the variation of the electrothermal load has been explored, promoting the arches as wide-range tunable resonators. Ramini et al. (2016b) further developed this experimental investigation, showing that several modal interactions among the vibration modes can be activated. Between the first and third bending modes of vibrations, 2:1 internal resonance, 3:1 internal resonance, and mode veering (near crossing) have been observed, which may enhance the MEMS design with higher sensitive and less noisy responses.

As highlighted by Sumali et al. (2008), NEMS, natural "extension" of MEMS, is drawing increasing interest in the research community for their complex nonlinear features. Sazonova et al. (2004) and Üstünel et al. (2005) experimentally tested slacked clamped–clamped CNT to a DC and AC load and characterized their free vibration response. They underlined that the frequencies of vibration are extremely sensitive to the level of slack. Motivated by these experimental data, Ouakad and Younis (2012) theoretically investigated slacked carbon nanotubes electrically actuated. Mode crossing and mode veering are experienced. Along the veering line, the shape of the first mode is transferred into the different odd modes, from the lower to the higher modes, depending on the level of slack. Odd frequencies intersect the even ones, offering many possibilities of internal resonances and exchange of energy among higher and lower order modes. Ouakad and Younis (2011) proved the level of slack to significantly influence stability, natural frequencies, and pull-in voltages of the carbon nanotube. Slack makes the softening effect in the dynamics dominate any hardening effect from mid-plane stretching making the possibility of hardening-type resonance of slacked CNTs very hard. Cho et al. (2010) fabricated a nanomechanical resonator based on a doubly clamped carbon nanotube incorporating intrinsically geometric nonlinearity. They operated the device in a highly nonlinear

المنارة للاستشارات

regime. Extreme broadband resonance has been observed. Both tunability over a broad frequency range and enhanced sensitivity to external perturbations have been explored.

Moreover, Ouakad and Younis (2010) and Younis et al. (2010) simulated the dynamic behavior of MEMS arched resonators actuated electrically, emphasizing the potential of making use of them as band-pass filters and low-powered switches. Das and Batra (2009a, b) investigated sequential snap-through buckling and pull-in, detecting critical parameter values to delineate different regions of instability. Kacem and Hentz (2009) and Kacem et al. (2011) theoretically and experimentally analyzed the nonlinear dynamics of MEMS in order to enhance the performance of resonant sensors. In a close-loop electrostatic MEMS resonator, Seleim et al. (2012) discovered steady-state chaotic attractors and detected regions of large dynamic amplification, where the resonator can be used as an efficient long-stroke actuator. In a microaccelerometer, Tusset et al. (2012) found a chaotic response and applied control strategies, which proved effective in controlling the trajectory of the system and robust in presence of parametric errors. Cho et al. (2012) designed a nonlinear micromechanical cantilever system with intentionally integrated geometric nonlinearity realized through a nanotube coupling. In a system of microcantilevers connected by a geometrically nonlinear tunable nanomembrane, Jeong et al. (2014) explored the rich nonlinear dynamics, including the coexistence of softening and hardening behavior. Taking advantage of the complex multistability possibly arising in micro- and nano-electromechanical systems, Nguyen et al. (2015) presented an alternative mass-sensing technique and proposed strategies for detection, quantification, and localization of an added mass.

Nonlinear dynamics in MEMS and NEMS have been deeply analyzed also from a physical point of view. In microcantilevers, Venstra et al. (2010) demonstrated mechanical stiffening of the frequency response at large amplitudes, showing the bistable regime as a function of the drive frequency and amplitude. Focusing on intermodal coupling between the flexural vibration modes, Westra et al. (2010) illustrated theoretical and experimental diagrams of frequency–frequency response, where for example the amplitude of the nonlinear first mode is plotted versus the driving frequencies of the first and third mode. Castellanos-Gomez et al. (2012) explored the nonlinear interaction between two different eigenmodes in freely suspended carbon nanotube resonators. They may undergo mode softening and mode stiffening behavior. In a nanowired-based mechanical resonator, Kozinsky et al. (2007) systematically probed experimental and theoretical attractor–basins phase portraits. Despite an excellent matching, the separatrix defining the boundary of the basins is smooth in the theoretical simulations while blurred in the experiment, which is likely due to environmental noise affecting the system. In two elastically coupled nanomechanical resonators driven independently near their resonance frequencies, Karabalin et al. (2009) showed intricate nonlinear dynamics, including period-doubling transitions and chaos. Villanueva et al. (2013) experimentally measured the nonlinear response of nanomechanical cantilevers. In a micromechanical oscillator, Zhang et al. (2002) described a wide range of qualitatively varying frequency responses, which can be tuned to function like a low-pass, high-pass or band-pass filter. In an electrome-

المنارة للاستشارات

chanical resonator, Mahboob et al. (2016) investigated Hopf and period-doubling bifurcations. An extensive overview on ongoing developments in the application of nonlinear dynamic features in MEMS and NEMS devices is reported in Rhoads et al. (2010).

The present chapter is motivated by the increasing attention toward the nonlinear phenomena arising in MEMS/NEMS. Three different case-studies are presented, with focus on the experimental investigation and its interpretation. Our aim is that of capturing the overall scenario of the systems' complex experimental behavior, which is essential for proper design, performance analysis, and calibration. Systematic numerical simulations are developed along the guidelines of classical seminal works, as for instance Rega et al. (1995), Rega and Salvatori (1996), Szemplińska-Stupnicka (1992), Szemplińska-Stupnicka and Tyrkiel (1997), Nayfeh and Balachandran (1995), etc.

As observed in the pioneering studies of Thompson (1989), the theoretical existence, and stability (in the classical sense) of a certain behavior does not guarantee that we can actually observe it under realistic conditions, i.e., does not mean "safety" from a practical viewpoint. This is because in experiments and practice disturbances exist and are unavoidable. They give uncertainties to the operating initial conditions. If the system is not sufficiently "robust" to tolerate them, the actual response may be completely different from what theoretically predicted. Here comes the need of the dynamical integrity analysis. We refer to Rega and Lenci (2005, 2015), to Lenci and Rega (2011b, c), and to other chapters of this book, for an extensive discussion of this topic.

This basic idea has been extensively developed through a series of papers, where dynamical integrity concepts have been investigated in depth, as the issue of a reliable dynamical integrity measure (Soliman and Thompson 1989; Lenci and Rega 2003; Lenci et al. 2013) and the definition of safe basins (Lansbury et al. 1992). The dynamical integrity analysis has been performed in many different fields, as for instance ships to analyze their stability against capsizing (Thompson et al. 1990), archetypal nonlinear oscillators (Rega and Lenci 2008), Augusti's model (Orlando et al. 2011), and parametrically excited cylindrical shells (Gonçalves et al. 2011). Dynamical integrity has been considered to design a controller aimed at controlling the system's behavior from a global viewpoint. This control technique is based on shifting the homoclinic bifurcation toward higher excitation amplitudes and has been implemented in many different mechanical systems (Lenci and Rega 2004), including MEMS (Lenci and Rega 2006). Dynamical integrity has been applied for analyzing the experimental behavior, e.g., the experimental rotating oscillations in a pendulum parametrically excited by wave motion (Lenci and Rega 2011a).

The dynamical integrity analysis has been widely used in atomic force microscopy (AFM). As proved in Hornstein and Gottlieb (2008), complex nonlinear features may arise in AFM. The global dynamical behavior has been deeply investigated and the theoretical bounds of inevitable escape limiting the noncontacting mode of operation have been detected. Via the Melnikov's perturbation theory, they analytically approximated the homoclinic bifurcation triggering the erosion of the potential well. However, they indicated the possibility of safe bounded dynamics well above this

المنارة للاستشارات

threshold. Starting from these results, Rega and Settimi (2013) further improved the analysis with the aim of detecting the parameter ranges where attractors may actually lose their robustness under realistic conditions, i.e., of detecting the practical escape region. In this context, extensive dynamical integrity simulations have been developed and many erosion profiles have been performed, in order to ensure targets of acceptable safety, according to the required performances. To keep the AFM response within an operational regime, Settimi et al. (2015) and Settimi and Rega (2016b, c) examined the possibility of inserting a control system. Integrity charts providing curves with constant residual integrity have been presented and compared with the results obtained for the uncontrolled system. This allows evaluating the effectiveness of the control technique on the overall dynamical behavior in practical applications and realizing of the possible criticalities that may emerge. Moreover, taking into account the results of dynamical integrity simulations, Settimi and Rega (2016a) applied a global control technique, which has been formulated under the frame of the global control method proposed by Lenci and Rega (2004). This is aimed at achieving an enlargement of the system's safe region in the parameters space and delaying the drop down of the erosion profile, offering a considerable increment of the overall robustness of the AFM system during operating conditions.

Similarly to the atomic force microscopy, MEMS and NEMS have been largely subjected to dynamical integrity investigations. The present study surveys recent findings in the field (Ruzziconi et al. 2013a–f; Xu et al. 2017). Extensive dynamical integrity analyses are performed for different devices and their relevance in the engineering design is emphasized.

The chapter is organized as follows. Three different case-studies of devices at the micro- and nanoscales are presented, which are respectively focused on a capacitive accelerometer in Sect. 2, a microbeam-based MEMS device in Sect. 3, and a slacked carbon nanotube in Sect. 4. Their complex dynamics are deeply investigated. We dwell on the dynamical integrity charts, since they are valuable to achieve a comprehensive understanding of the actual behavior of a mechanical system, in view of its safe operation in practice. Though we refer to specific devices, the very general character of the global safety analysis is highlighted. The main conclusions are summarized in Sect. 5.

2 A Capacitive Accelerometer

The first device considered in the present chapter is an electrically actuated capacitive accelerometer. This study starts from the experimental data of dynamic pull-in (escape) systematically acquired via a frequency-sweeping process. Extensive numerical simulations of the system's nonlinear dynamics are developed, which are based on the classical Lyapunov local stability theory. General good matching is achieved. Nevertheless, these theoretical predictions are not completely fulfilled in some aspects. In particular, the actual range of existence of each attractor is a subset of its stability domain, and, consequently, the theoretical inevitable escape zone is

المنارة للاستشارات

not able to forewarn the experimental pull-in bands. This discrepancy is related to the presence of disturbances. The present study aims at finding a theoretical justification of the experimental evidence. This calls for further investigation, where dynamical integrity concepts are taken into account and provide the answer to the problem.

More details related to the experimental exploration of the capacitive accelerometer can be found in Alsaleem et al. (2010), and to the dynamical integrity analysis in Ruzziconi et al. (2013d).

2.1 Device and Experimental Setup

The device under investigation is a commercial capacitive accelerometer fabricated by Sensata Technologies (2017), Fig. 1. It consists of a proof mass suspended by two cantilever beams. The upper electrode is formed by the proof mass, which has a rectangular shape, with length 9 mm, width 5.32 mm, and thickness 150 μm. The lower electrode is placed directly underneath the proof mass on a silicon substrate. It has the same length, but a slightly smaller width, 4.4 mm. The separation gap between the two electrodes is 42 μm.

The lower electrode provides both electrostatic and electrodynamic actuation. When electrically excited, the proof mass oscillates in the out-of-plane direction, i.e., out of the plane of the substrate. Although some dimensions are in millimeters, the system has the same main characteristics of a MEMS device, since gap and thickness are in the micro-range and the structure is actuated electrically.

The lower electrode is a ceramic-based material and the upper electrode is a metal-based material, which helps the survivability of the device against stiction and failure due to the repetition of the pull-in event and due to the heat generated by it. Also, in case of pull-in, the value of the current passing through is lowered by a large resistor, which is added in series.

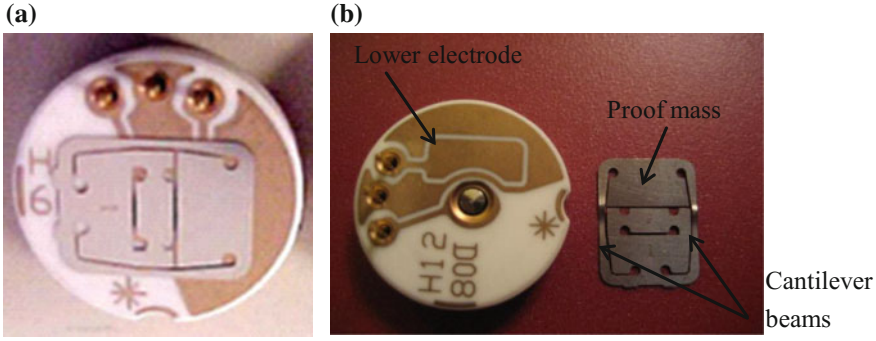

Fig. 1 The capacitive accelerometer, fabricated by Sensata Technologies (2017). **a** Assembled. **b** Taken-apart

المنارة للاستشارات

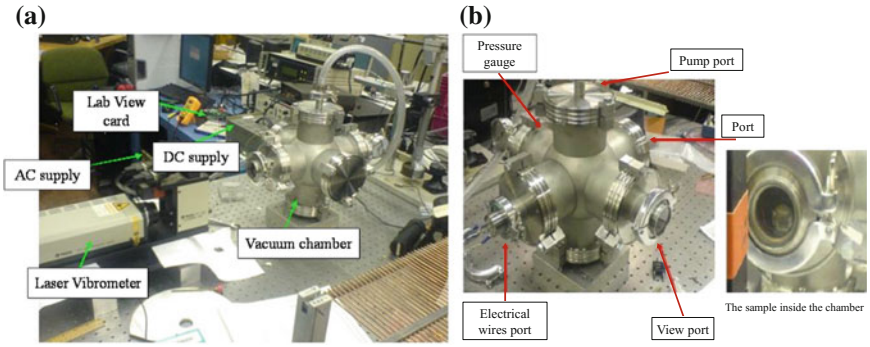

Fig. 2 **a** A picture of the experimental setup used for testing the capacitive accelerometer, showing the laser Doppler vibrometer, the vacuum chamber placed on an isolation table, the Lab View card, DC and AC supply. **b** The vacuum chamber and a zoom of the sample inside the chamber

We have tested extensively the device. According to our experience, it maintains the same characteristics and it is able to guarantee repeatable results even after a large number of tests. Thus, differently from other micro-electromechanical systems, the analyzed capacitive accelerometer has the advantage of being more likely to survive the repetitive failures due to pull-in, which allows a deep experimental investigation.

The experimental setup used for testing the device is represented in Fig. 2. There are a laser Doppler vibrometer, a Lab View data acquisition system, AC and DC power sources, a vacuum chamber, and a high vacuum pump. The device is inserted inside the vacuum chamber, which is placed directly underneath the laser Doppler vibrometer, such that it can measure the deflection of the proof mass.

The chamber is equipped with a viewport window, located on top and made of quartz glass, and with some ports, located in the lateral sides. The viewport window enables the laser to penetrate without any distortion. The lateral ports serve to supply pressure gauge and electrical connection. They are used to hook the chamber up to the high vacuum pump and to apply the AC and DC power sources, which are provided via the Lab View data acquisition system.

The signal is generated via a data acquisition (DAQ) card and applied on the outer pins shown in Fig. 1. When necessary, a power amplifier is used to amplify the signal.

2.2 Model Formulation and Parameters Extraction

We focus on the oscillations in the vicinity of the fundamental natural frequency of the device (primary resonance). To describe the response in this range, a nonlinear single degree-of-freedom lumped spring-mass model is considered, which is schematically illustrated in Fig. 3. The capacitive sensor is modeled as a parallel plate capacitor with two rigid plates, where the upper one is movable. The lumped mass represents

المنارة للاستشارات

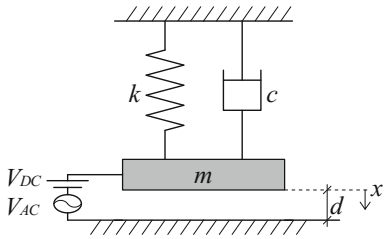

Fig. 3 The single d.o.f. mechanical model used to model the capacitive sensor

the proof mass and the spring represents the two cantilever beams. The resulting governing equation of motion is:

$$m\ddot{x} + c\dot{x} + kx = \varepsilon_0 \varepsilon_r A \frac{[V_{DC} + V_{AC}\cos(\Omega t)]^2}{2(d-x)^2}, \tag{1}$$

where $x(t)$ is the deflection of the proof mass, t is the physical time, the superscript dot denotes the time derivative, m is the effective mass of the proof mass, c is the viscous damping coefficient due to the squeeze-film effect, k is the linear effective stiffness of the cantilever beams, ε_0 is the dielectric constant in the free space ($\varepsilon_0 = 8.8542 \times 10^{-12}$ F/m), ε_r is the relative permittivity of the gap space medium (air) with respect to the free space ($\varepsilon_r = 1$), A is the lower electrode area, d is the capacitor gap width including the static effect of the mass weight, V_{DC} and V_{AC} are, respectively, the electrostatic and electrodynamic voltage, Ω is the electrodynamic voltage frequency. Since the size of the proof mass is much larger compared to the gap width underneath, it is safe to assume negligible fringing and suppose straight lines electric field.

The unknown parameters in Eq. (1) are k, m, and c. To extract them, experimental characterization of the device has been conducted. We follow the procedure outlined in Alsaleem et al. (2009, 2010). Here, we report the main steps.

The stiffness coefficient k is extracted by resorting to the static bifurcation diagram and matching the experimental and theoretical predictions. Specifically, we bias the microstructure with ramping V_{DC} inputs and measure the stable static deflection of the proof mass using the laser Doppler vibrometer, up to the static pull-in phenomenon. According to the measurements, the static pull-in voltage is observed at $V_{DC\_pull\text{-}in} \cong 115.3$ V. Focusing on the spring-mass model in Eq. (1) in the static case, from simple computations and recalling that $V_{DC\_pull\text{-}in}$ occurs at the saddle-node bifurcation point, it can be shown that the stiffness coefficient is $k = \varepsilon_0 \varepsilon_r A (V_{DC\_pull\text{-}in})^2/(2d^3(4/27))$, from which we identify $k = 215$ N/m.

To determine the effective mass m of the proof mass, we focus on the first natural frequency, which is experimentally measured at low electrostatic voltage and is observed to occur at about 192.5 Hz. As $m = k/\omega^2$, the effective mass of the proof mass is estimated to be $m = 0.147$ g.

Regarding the damping, various mechanisms of energy dissipation may affect the device. Among them, squeeze-film damping contribution dominates in MEMS and

المنارة للاستشارات

may be considered the main source of energy loss. In our device, this is even more pronounced since the proof is very large compared to the gap width, and hence it pumps and sucks considerable air in and out (rubbing against the walls of the plate causing energy loss). Hence, it is safe to assume that the only damping is coming from squeeze-film damping. The damping coefficient c is computed by means of the Blech model, which analytically solves the linearized Reynolds equation with trivial pressure boundary conditions. We consider only the first term in the series of the Blech model, since higher order terms do not affect the damping value too much because the pressure is very low and the air is not trapped underneath the movable mass. This yields $c = (768\eta_{eff}A^2)/(\pi^6(d-x)^3)(2/(4+\sigma^2/\pi^4))$ with $\sigma = (12A\omega\eta_{eff})/(Pa(d-x)^2)$ and $\eta_{eff} = \eta_0/(1+9.638Kn^{1.159})$, where Pa is the ambient pressure, i.e., the pressure value of the device during its operation, which in this case is 153 mTorr, Kn is the Knudsen number, $\eta_0 = 1.82 \times 10^{-5}$ N s/m^2 is the viscosity coefficient of air, η_{eff} is the effective viscosity coefficient of air, which in this case is $\eta_{eff} = 1.786 \times 10^{-7}$ N s/m^2. About the gap space between the two electrodes, this is varying with the proof mass motion. To slightly simplify the model, in the damping coefficient c we assume it to be constant and equal to d, i.e., in this term (and only in it) we drop its dependence on x. This is sufficiently accurate for our purposes, as proven experimentally in various previous publications on the same device (Alsaleem et al. 2009, 2010). We obtain $c = 1.5 \times 10^{-3}$ (N s)/m.

For convenience, we divide Eq. (1) by the extrapolated value of m. The resulting governing equation of the nonlinear dynamics of the device becomes

$$\ddot{x} + 10.1\dot{x} + 1.4629 \times 10^6 x = 1.2 \times 10^{-12} \frac{[V_{DC} + V_{AC}\cos(\Omega t)]^2}{(42 \times 10^{-6} - x)^2} \tag{2}$$

where x is expressed in micron. Equation (2) is the single d.o.f. model used in all the forthcoming investigation of the capacitive accelerometer.

In the following, the numerical simulations are based on the direct integration of the ordinary differential equation by using the Runge–Kutta method. All of them are obtained by self-developed codes implemented in Mathematica and Matlab, with the exception of the attractor–basins phase portraits, which are computed by resorting to the software package *Dynamics* (Nusse and Yorke 1998) and checked by self-developed codes via a lot of episodic investigations.

2.3 Experimental Response at Large AC Excitations

A deep experimental investigation is conducted. Many experimental frequency response diagrams are obtained. These data come from a frequency-sweeping process, where the electrodynamic voltage is kept constant and the frequency is increased (forward sweep) and/or decreased (backward sweep) slowly, i.e., quasi-statically. Both of them are necessary to catch the complete extent of the attractors. All the experiments are attained close to an ultra-high vacuum environment, at about the

المنارة للاستشارات

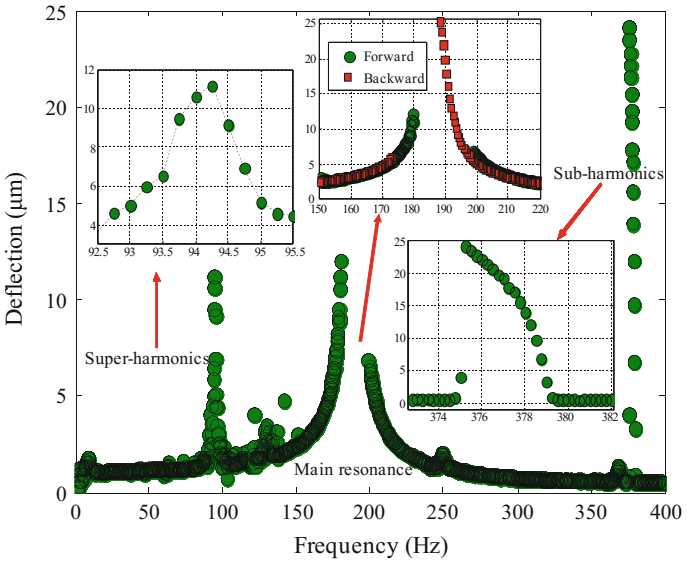

Fig. 4 Experimentally measured frequency response diagram at $V_{DC} = 40.1$ V and $V_{AC} = 18.4$ V. Forward and backward sweeps are in green dots and red squares, respectively. During the experimental test, the sampling rate is 0.5 Hz/s and the pressure is 153 mTorr. The enlargements show a neighborhood of the primary resonance, of the subharmonic resonance of order one-half, of the superharmonic resonance of order two

same low constant (as far as possible) pressure, 153 mTorr. The frequency step is 0.5 Hz and the time step is 1 s, i.e., the sampling rate is 0.5 Hz/s, which guarantees the steady-state condition at the end of each step, where the sweeps are recorded.

At low electric excitation, the capacitive accelerometer responds linearly (not shown in the figures). Raising the level of the voltage load, instead, nonlinear phenomena appear. As an example, we report the experimental frequency response diagram at $V_{DC} = 40.1$ V and $V_{AC} = 18.4$ V (almost half of the electrostatic voltage), Fig. 4. The sweep test is carried out over a wide parameter range, $\Omega = [0, 400]$ Hz.

Forward and backward sweeps are represented in green dots and red squares, respectively. Since the electrostatic load is rather elevated in the present case, the system's natural frequency (as expected) is slightly shifted toward a smaller frequency value with respect to what experimentally measured in the device characterization, which was assessed at low electrostatic voltage.

We focus on the response at primary resonance. This is so large that covers an extended part of the diagram. A zoom is reported in the top of the figure. Both the non-resonant branch (at left) and the resonant one (at right) are observed. Each one exists for a wide Ω-range, where it can safely operate the device. For a small (very small) portion we can see the characteristic bending of the two attractors toward lower frequencies, which is typical of a softening oscillator. Note that at these parameter values the device is able to offer large safe areas where it can be reliably actuated

المنارة للاستشارات

in safe conditions. This occurs despite the high electric excitation and despite the resonance phenomenon.

Approaching the main resonance from both sides, each attractor crosses its own safe region and disappears, leading to dynamic pull-in. In the present case, this takes place when the maximum amplitude starts increasing and both the attractors are terminated with slopes which seem to tend to infinity. The frequency response opens up. In addition to regular oscillations, non-regular dynamics occur. The final result is a broad frequency range, where none of the bounded attractors survives but only dynamic pull-in is experienced, $\Omega \cong [179.4, 188.6]$ Hz. As expected, this dynamic pull-in phenomenon is triggered at a voltage load much lower than the static pull-in threshold. This is an example of frequency response with a pull-in band.

Not only the primary resonance is activated, but also the superharmonic resonance of order two, near half the fundamental natural frequency, and the subharmonic resonance of order one-half, near twice the fundamental natural frequency. Each one of them involves a narrow interval, zoomed, respectively in the left and in the right-hand side of the figure. At the superharmonic resonance, no particular dynamical features are observed at this voltage excitation, except oscillations becoming higher. At the subharmonic resonance, instead, the experimental response presents softening behavior. The amplitude of the non-resonant branch is and remains tiny all along its range of existence. On the contrary, the resonant attractor exhibits a sudden amplification, undergoing a small vibration before the activation of subharmonic resonance and rising to a large one upon it. This feature may be beneficial, e.g., for designing sensitive sensors.

In the following, we consider the primary resonance and investigate the experimental pull-in bands.

2.4 Experimental Versus Theoretical Pull-in Dynamics

We analyze a neighborhood of the device natural frequency, Fig. 5. Simulations are overlapped with the experiments, in order to appreciate similarities and differences.

From a theoretical point of view, we can clearly observe the softening bending. Increasing the frequency, the non-resonant branch slightly increases its maximum amplitude eventually vanishing through a saddle-node bifurcation, at $\Omega \cong 180.1$ Hz. Similarly, decreasing the frequency the resonant branch performs wider and wider oscillations (considerably larger than in the non-resonant case) and finally experiences a period-doubling cascade of flip bifurcations running through subharmonics of infinitely high order, ultimately followed by chaotic motion and boundary crisis, at $\Omega \cong 176.2$ Hz. This last sequence of events is little perceived in the figure since is confined to a very short parameter range.

Very good matching is achieved with the experimental data. The model is able to detect the value where the natural frequency occurs, to catch the softening-spring behavior arising in a neighborhood of the primary resonance (although this phenomenon is only slightly sketched in the experiments), to properly simulate the sep-

المنارة للاستشارات

aration width between the non-resonant and the resonant branch. Thus, all the main dynamical features are adequately represented. This concurrence of results confirms our confidence in the model, which is essential to develop any further investigation.

Nevertheless, despite the satisfactory agreement, discrepancies arise in the length of each branch. The experimental curves of disappearance are systematically shifted from the theoretical ones and occur in the region where each attractor is theoretically expected to exist. The difference is minimal in the non-resonant case but really apparent in the resonant one. While the data show a pull-in band with no bounded motions, the simulations, instead, not only predict at least one bounded solution but also a narrow interval where both the branches coexist.

Hence, the last part of each theoretical attractor (including the bifurcational events) does not have an experimental counterpart. A similar difference between data and numerical predictions has been observed by Lenci and Rega (2011a) in a parametric pendulum, where, even in this case, the range of theoretical existence of rotations is wider than the actual one. This mismatching is likely related to the presence of disturbances, which are inevitably encountered under realistic conditions.

To have more complete information about the device behavior, additional simulated frequency response diagrams are reported in Fig. 6. At $V_{AC} = 10$ V, the attractors coexist for a wide Ω-range; rising the voltage, this interval progressively reduces, e.g., at $V_{AC} = 20$ V; finally, it disappears and a widening pull-in band expands, e.g., at $V_{AC} = 30$ V. Comparing the diagrams in Figs. 5 and 6, we can note that the pull-in bands in the experiments are critically shifted toward lower voltage excitations with respect to the theoretical escape zone.

For a comprehensive overview of the main dynamical events, we develop the theoretical behavior chart in Fig. 7, which illustrates the overall scenario when both the electrodynamic voltage and the frequency are varied. The chart describes where

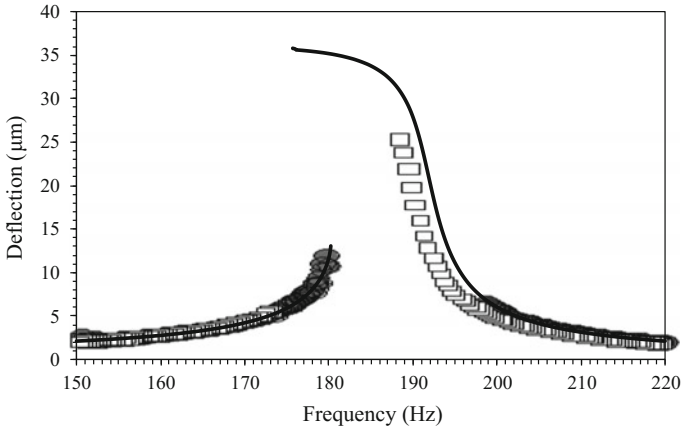

Fig. 5 Comparison between the experimental and the theoretical frequency response diagram, at $V_{DC} = 40.1$ V and $V_{AC} = 18.4$ V. The forward and backward sweeps are represented in grey dots and white squares, respectively. The numerical simulations are in black solid line

المنارة للاستشارات

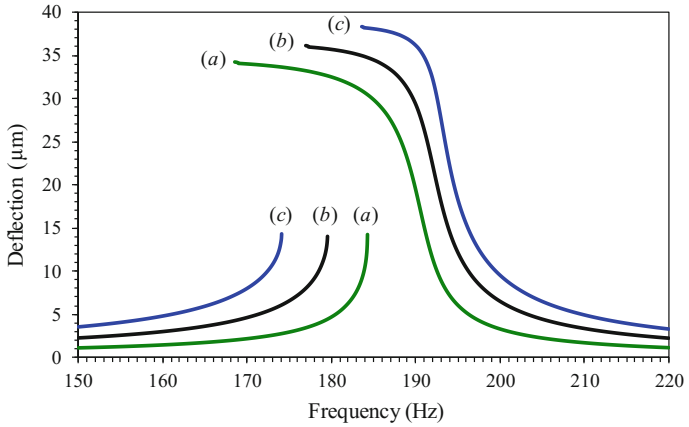

Fig. 6 The theoretical frequency response diagram at (a) V_{AC} = 10 V, (b) V_{AC} = 20 V and (c) V_{AC} = 30 V, respectively in green, black and blue line

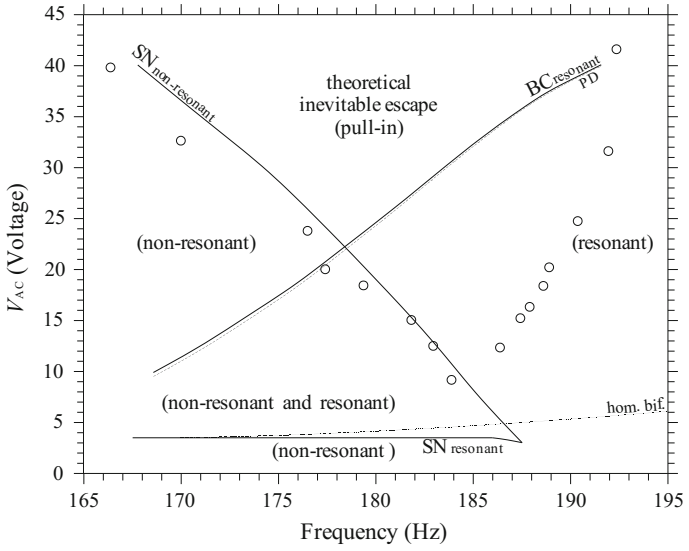

Fig. 7 Frequency-electrodynamic voltage behavior chart of the capacitive accelerometer with harmonic excitation close to the primary resonance Ω_{res} = 192.5 Hz. The curves of theoretical appearance and/or disappearance of the non-resonant and the resonant attractor are represented in solid line. The first period-doubling in the resonant branch is in dashed line. The homoclinic bifurcation threshold detected by the Melnikov method is in dotted line. The dots denote the experimental pull-in data

a bifurcation occurs and generates an attractor, detects which kind of bifurcation it is, e.g., a saddle-node (SN) or a boundary crisis (BC), and bounds where each attractor exists. Operatively, the chart is obtained by performing many theoretical frequency

المنارة للاستشارات

response diagrams, like the ones in Fig. 6, by detecting the frequency Ω and the voltage V_{AC} where each attractor theoretically disappears, and by reporting these coordinates in the (Ω, V_{AC}) space.

The device shares the same main qualitative features of other softening oscillators investigated in depth in the literature (Szemplińska-Stupnicka 1992; Soliman and Thompson 1992). In a neighborhood of the primary resonance, at (Ω; V_{AC}) approximately equal to (187.4; 3), we can observe the degenerate cusp bifurcation point where the non-resonant and the resonant attractor separate. Below this threshold, the response of the system presents only one branch (the non-resonant one), whereas, beyond it, it splits into the non-resonant and the resonant oscillations and both of them need to be examined.

Their curves of appearance and/or disappearance denote their theoretical bounds of existence. The region where the non-resonant attractor exists is located at the left-hand side of the chart, from the unforced dynamics to its saddle-node bifurcation (SN non-res). The resonant one, instead, appears at its saddle-node (SN res) and widely extends its range of existence beyond this line, throughout all the right-hand side of the chart. It performs the first period-doubling flip bifurcation (PD res) where the period doubles to a subharmonic of order 2. As observed in the frequency response diagram, this is followed by the infinite cascade of the flip bifurcations (not shown in the figure), leading to chaotic long-term behavior and finally vanishing through boundary crisis (BC res).

We can observe the Δ-shaped region, where both the non-resonant and the resonant dynamics coexist, which is bounded by the SN of the non-resonant branch and by the SN and the BC of the resonant one, i.e., at low forcing loads there are two competing attractors and each one of them may oscillate the device exhibiting its own characteristics.

There is the V-shaped region where the two attractors disappear. No bounded motions may occur in this parameter range and the escape (i.e., the dynamic pull-in) is inevitable. The higher the electrodynamic voltage is, the wider this band of frequency becomes. This V-shaped region has vertex at about (Ω; V_{AC}) equal to (187.4; 22.1) and is bordered on the left by the SN of the non-resonant branch and on the right by the BC of the resonant one. This feature is typically encountered in electrically actuated microstructures with softening behavior.

In addition to the theoretical results, the chart reports the experimental dynamic pull-in data, which are represented by dots. They are extracted from the experimental frequency response diagrams by repeating the same procedure used to provide the theoretical curves. In order to compare the sweeps among them, they are acquired by adopting the same experimental conditions; specifically, we refer to the same electrostatic voltage, pressure and sampling steps previously described.

Similarly to the theoretical predictions, the experimental pull-in data clearly presents an instability zone indicating the parameter values wherein the capacitive accelerometer is experimentally forced to dynamic pull-in (the reader is referred to Alsaleem et al. (2010) for further experimental data showing similar V-zones in various different MEMS devices). The chart highlights the same discrepancies detected in the frequency response diagrams. The experimental escape region is much wider

المنارة للاستشارات

than the theoretical one. The major differences are related to the resonant branch, especially at low voltages. The experimental vertex occurs at about $(\Omega; V_{AC})$ equal to (183.9; 9), i.e., the voltage load actually triggering the pull-in band is smaller than the theoretical one and is shifted at higher frequency values, closer to the system's natural frequency.

2.5 Mechanical Properties of the Governing Equation

We focus on the Hamiltonian unforced undamped system. The associated potential is

$$V(x) = \frac{1}{m}\left(k\frac{x^2}{2} - \frac{\varepsilon A V_{DC}^2}{2(d-x)}\right) \tag{3}$$

The potential function and the corresponding phase portrait are illustrated in Fig. 8. There is a single potential well with escape barrier, which is located at right

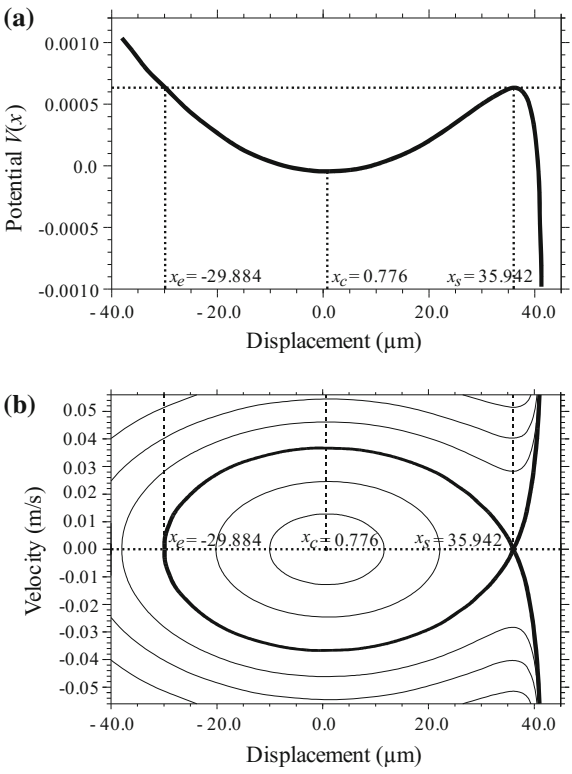

Fig. 8 **a** The cubic energy potential $V(x)$ with single well, hill-top saddle and escape barrier. **b** The phase portrait of the unforced undamped system, with center at $x_c = 0.776$ μm, saddle at $x_s = 35.942$ μm and homoclinic loop separating bounded and unbounded dynamics

المنارة للاستشارات

(toward the substrate). This asymmetry is in accordance with the asymmetry of the device since the considered capacitive accelerometer is excited on only one side. In conformity with the potential, the phase portrait presents two physical equilibrium points: the elliptic center at $x_c = 0.776$ μm, which is slightly shifted from zero due to the contribution of the electrostatic load, and the hill-top saddle at $x_s = 35.942$ μm.

Two different classes of oscillations can be observed: the bounded nonlinear periodic orbits within the potential well, corresponding to safe regular oscillatory motion of the device; the unbounded non-periodic solutions which tend to—∞ when $t \to \pm\infty$, corresponding to the pull-in phenomenon. In-well oscillations and out-of-well trajectories are separated by the homoclinic loop. Note its central role in organizing the whole system dynamics. It represents a barrier for confined motions.

Implicitly, the homoclinic orbit can be defined by

$$t(x) = \pm \int_{x_e}^{x} \frac{dr}{\sqrt{2[V(x_s) - V(r)]}} \tag{4}$$

where $x_e = -29.884$ μm is the intersection of the orbit with the horizontal axis. Equation (4) is an even function of the time t and can be computed only numerically. This expression will be used in the Melnikov analysis.

2.6 Melnikov Homoclinic Bifurcation Threshold

Adding perturbations to the Hamiltonian system, the stable and unstable manifolds of the hill-top saddle x_s split. At some parameter values, they become tangent. The tangency corresponds to the homoclinic bifurcation threshold. This is the phenomenon that triggers the erosion of the potential well. It signals the beginning of the penetration via fractal tongues of the out-of-well attractor (escape) inside the safe bounded area of the potential well. Further increasing the electric load, the erosion progressively develops, until for sufficiently high excitation amplitude it totally destroys the well.

Thus, the homoclinic bifurcation represents a very important and critical event. Its analytical prediction can be obtained via the Melnikov perturbation theory. A similar analysis was carried out by Gottlieb and Champneys (2005) and by Lenci and Rega (2006) for the case of a thermoelastic electrically actuated MEMS device. The perturbed system is deduced by assuming both the damping and the electrodynamic force as small perturbations to the Hamiltonian case. Comparable smallness is supposed.

The first-order distance between perturbed stable and unstable manifolds is proportional to the Melinkov function $M(t_0)$, which has the standard form (Guckenheimer and Holmes 1983):

$$M(t_0) = I_1 + I_2 \sin(\Omega t_0) \tag{5}$$

المنارة للاستشارات

where I_1 depends on the damping and I_2 depends on the excitation frequency and amplitude. The values of damping, frequency, and amplitude where $M(t_0)$ has a quadratic zero are the homoclinic bifurcation values, which satisfy the equation $|I_1| = |I_2|$. The Melnikov curve for the analyzed capacitive accelerometer is reported in dotted line in Fig. 7.

The dynamic pull-in bands are considerably far from the Melnikov curve, i.e., the device continues being in safe conditions well above the homoclinic bifurcation, although, as previously observed, not along all the range of theoretical existence of the attractors.

Hence, the Melnikov curve represents a very important theoretical (and also analytical) result; nevertheless, it is impractical to limit the excitation of the device to the Melnikov threshold, since it is too conservative. For this reason, we perform a dynamical integrity analysis, in order to have a criterion to detect the experimental pull-in bands and enable the designer to make use in safe conditions of all the range of practical existence of each attractor.

2.7 *Erosion of the Potential Well*

To understand the discrepancies between the experimental data and the theoretical predictions, we investigate the system within the framework of the escape from potential well theory. The device response is analyzed not only *locally*, by studying each single attractor, but also *globally*, by focusing on the phase space metamorphoses. Many attractor–basins phase portraits are performed when varying the electrodynamic voltage and frequency. Examples are reported in Fig. 9. Each row corresponds to a fixed V_{AC}, which is ramping from the bottom to the top of the set of figures, respectively at $V_{AC} = 4$ V, $V_{AC} = 8$ V and $V_{AC} = 18.4$ V. Along each row, the outline is shown when increasing the frequency excitation. The basins of attraction of the non-resonant branch and of the resonant one are orange and green, respectively; the escape is white, which corresponds to the system experiencing dynamic pull-in; the attractors are denoted with a cross.

At $V_{AC} = 4$ V, both the non-resonant and the resonant attractor exist and compete in robustness. At lower frequencies, this parameter range is just above the homoclinic bifurcation threshold detected by the Melnikov curve. We can see the onset of the erosion of the well. The degree of fractality is very low and concerns a minimal portion of the phase space, where the infinitely fine recurrent structure of a Cantor set can be observed. At $\Omega = 180$ Hz (Fig. 9a) the system is far from resonance. The basin of the non-resonant branch is wide and covers almost all the bounded part of the phase space. The basin of the resonant one, instead, is rather narrow and is located close to the escape area, spiraling around the other basin. Fractal parts are not so advanced and form only a thin layer around the edge of the bounded region. At $\Omega = 184$ Hz (Fig. 9b) and $\Omega = 186$ Hz (Fig. 9c) the two attractors progressively reverse the dominance. In fact, approaching the resonance, the basin of the resonant attractor becomes wider and wider, at the expense of the non-resonant one, which

المنارة للاستشارات

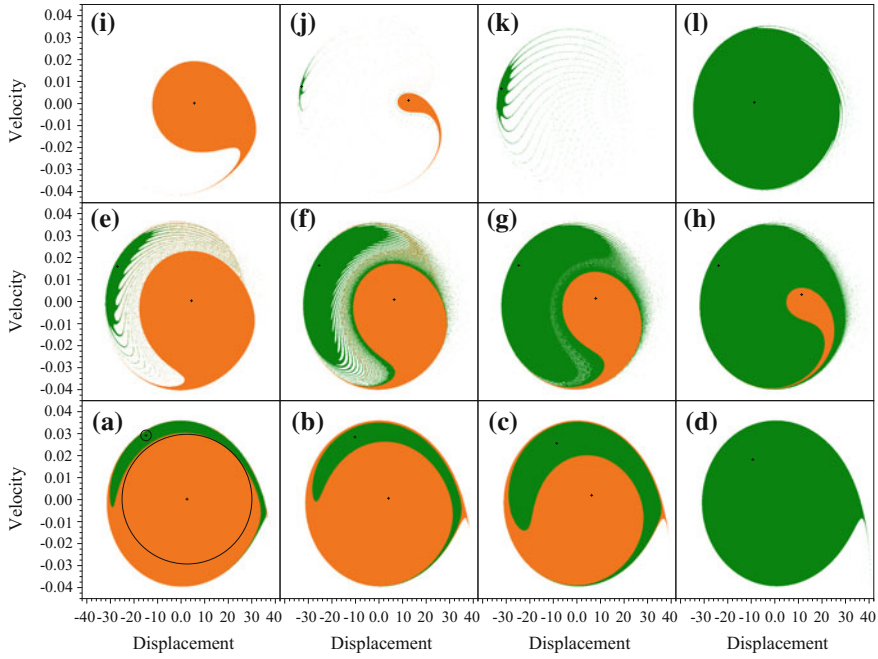

Fig. 9 Attractor–basins phase portraits at (from bottom left to top right): V_{AC} = 4 V and **a** Ω = 180 Hz, **b** Ω = 184 Hz, **c** Ω = 186 Hz, **d** Ω = 188 Hz; V_{AC} = 8 V and **e** Ω = 180 Hz, **f** Ω = 183 Hz, **g** Ω = 184 Hz, **h** Ω = 185 Hz; V_{AC} = 18.4 V and **i** Ω = 172 Hz, **j** Ω = 180 Hz, **k** Ω = 184 Hz, **l** Ω = 196 Hz. Examples of circles for the evaluation of the LIM are reported in (**a**) in solid line

gradually shrinks in size, up to vanishing. At Ω = 188 Hz (Fig. 9d) only the resonant oscillations exist and have an extensive basin, which is mainly uneroded. Slightly above the system's natural frequency, this attractor is eccentric with respect to its basin. Further increasing the frequency (not shown in the figure) the eccentricity reduces and turns less evident. Overall, at this level of voltage, the two basins remain close to each other and form a large and compact safe region. The escape is located outside this safe zone. Unfortunately, we did not record experimental data at these parameter values.

Rising the voltage, the fractal structure becomes increasingly clear. At V_{AC} = 8 V, the fractal (white) tongues of the out-of-well attractor start developing more rapidly, and, remarkably, they become incursive, they invade the basin of the resonant attractor and, through it, they penetrate inside the central core of the potential well. The escape becomes really dangerous, since not only enters the well but also separates the basins of the two attractors. The separation is clearly defined at the left of the system's natural frequency, whereas decreases and annihilates as approaching it. For example, at Ω = 180 Hz (Fig. 9e) the basins are separated; at Ω = 183 Hz (Fig. 9f), a part of the basin of the resonant attractor continues surrounding the basin of the non-resonant one, even if with fractal tongues; at Ω = 184 Hz (Fig. 9g), the surrounding part is

المنارة للاستشارات

larger; at $\Omega = 185$ Hz (Fig. 9h) the two basins are close to each other, which forms the safe compact core of the well, and fractality develops outside. Further increasing the voltage, the closeness quickly disappears all along the considered frequency range and the two basins settle far from each other, which prevents any safe jump between them.

At $V_{AC} = 18.4$ V, pull-in data are available to be compared with the theoretical predictions. The experimental disappearance of each attractor occurs exactly when the compact area of its basin of attraction becomes too much reduced. We focus on the resonant branch, since this is the case where the major discrepancies arise, and we investigate it as the frequency is decreased.

At $\Omega = 196$ Hz (Fig. 9l) only the resonant attractor exists and its basin is large and mainly compact. Some sporadic fractal points are spreading around, especially in a neighborhood of the hill-top saddle; however, their impact is negligible. At this excitation level, the resonant attractor is plainly observed in the experiments and can safely actuate the device. At $\Omega = 184$ Hz (Fig. 9k), instead, its basin has been increasingly eroded by the escape. Fractality outlines a few tiny curves, which develop as well-spaced nearly parallel fingers and span all the area previously belonging to the basin of the resonant branch. They further narrow as approaching the hill-top saddle. These thin lines are organized to surround but not to enter the area successively hold by the basin of the non-resonant branch since at these parameter values this area remains accounted for by only the escape. All that is left of the extensive compact basin of the resonant branch is only a residual part at the left-hand side of the phase space, in correspondence of the attractor. The escape is the main feature at this stage. The experimental disappearance of the resonant branch exactly occurs at $\Omega \cong 188.6$ Hz, i.e., in the interval between Fig. 9l and k, where the compactness of its basin becomes too small, which severely increases its sensitivity to disturbance. Further decreasing the frequency, this basin is more and more consumed by fractality, as can be observed in Fig. 9j, although it theoretically survives up to $\Omega \cong 176.2$ Hz.

A wide compact part around the attractor is very important to reliably operate the device. In fact, disturbances inevitably give uncertainties to the operating initial conditions. A wide compact area is essential to tolerate them since all the initial conditions in this area reach the same long-term behavior at steady dynamics. Conversely, the non-compact region is sensitive to disturbances, because a small shift in the initial conditions may lead to a different outcome. For this reason, the resonant attractor vanishes in practice when it is far from its theoretical boundary crisis, i.e., there is a large discrepancy between its practical and theoretical disappearance.

Similar aspects occur for the non-resonant branch. We analyze it when increasing the frequency. At $\Omega = 172$ Hz (Fig. 9i), its basin is robust and the attractor exists in the experiments. At $\Omega = 180$ Hz (Fig. 9j), instead, the basin maintains smooth basin boundaries but shrinks in size. The non-resonant branch experimentally disappears at $\Omega = 179.4$ Hz, which is in-between Fig. 9i and j, where it becomes too much vulnerable to disturbances.

Overall, increasing the voltage excitation, safe conditions for the resonant branch are shifted at higher and higher values of frequency, whereas for the non-resonant

المنارة للاستشارات

one at lower and lower levels. Accordingly, the gap subjected in practice to the escape progressively enlarges, reducing the range for safely operating each single branch.

Also note that, when an attractor disappears in practice if its basin is located inside the escape area, it is replaced by the escape and not by the basin of the other attractor, even if this one exists and is still robust. This explains why in the present case-study we have only data of dynamic pull-in and not examples of jump between the attractors.

2.8 Dynamical Integrity Analysis

The classical theoretical analysis based on the Lyapunov stability theory is essential to describe the dynamics that the system may exhibit; nevertheless, it is not able to judge on their robustness, i.e., is not able to take disturbances into account. For this reason, to detect the expected behavior under realistic conditions, we cannot restrict ourselves to the classical simulations; on the contrary, starting from them, we need to further improve the analysis via dynamical integrity. This is the aspect of global analysis which illustrates if a system is sufficiently robust to disturbances.

Tools of analysis. To guarantee the accuracy of the investigation, we select the dynamical integrity tools of safe basin and dynamical integrity measure in order to ensure compliance with the experimental frequency sweeps.

Our objective is that of detecting the parameter ranges where each branch may *practically* (and not theoretically) vanish because of the presence of disturbances. Therefore, we use the dynamical integrity analysis to investigate the phenomenon of disappearance of each attractor (and not other phenomena, as the discerning of jump or dynamic pull-in). Accordingly, we consider both the non-resonant branch and the resonant one and investigate each one of them, one by one, separately.

The safe basin is the set, in the phase space, of all the initial conditions sharing a certain property. Many different definitions of safe basin have been considered in the literature (Rega and Lenci 2015), according to which safe condition is desired to be investigated. In the present case-study, since we focus on the existence and/or disappearance of each single attractor, the safe condition is represented by having at steady-state the motion under consideration, whereas the unsafe condition is represented by having at steady-state all the other motions, both the bounded (in this case, the other branch) and the unbounded (escape) ones. Hence, for each attractor, we assume as safe basin its own basin of attraction.

We measure the dynamical integrity by using the Local Integrity Measure (LIM) introduced by Soliman and Thompson (1989). The LIM is the normalized minimum distance from the attractor to the boundary of the safe basin, i.e., the radius of the largest circle entirely belonging to the safe basin and centered at the attractor. Examples of circles used in the definition of LIM are reported in Fig. 9a in solid line. We normalize each radius with the analogous radius drawn for the non-resonant

المنارة للاستشارات

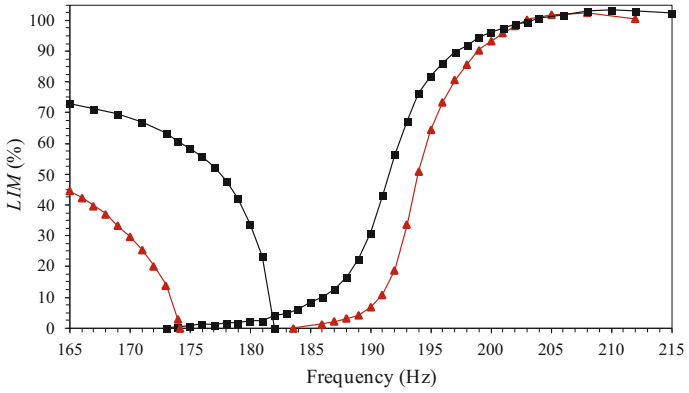

Fig. 10 LIM dynamical integrity profiles to analyze the practical disappearance of the non-resonant branch (at left) and of the resonant one (at right), at V_{AC} = 15 V and V_{AC} = 30 V, respectively in black and red solid line

branch at $V_{AC} = 0.1$ V and $\Omega = 180$ Hz, i.e., next to the unforced dynamics (however, other different normalizing conditions may be considered; results will be just scaled).

The LIM is an appropriate measure for our case-study. It takes into account the steady-state regime (since the circle used in the computation is centered at the attractor); it considers only the compact "core" of the safe basin surrounding the attractor, which we are interested in; it is able to rule out the non-compact regions, which are dangerous in practice. For all these reasons, the LIM is suitable for the analysis of the present experimental data, which are coming from a sweeping process, where at the end of each step the system is in steady-state conditions. Nevertheless, seeing the shape of the considered attractors, also other dynamical integrity measures could be accurate, as for instance the Integrity Factor proposed by Lenci and Rega (2003).

Dynamical integrity profiles. For the analysis of the structural safety of the device, we build dynamical integrity profiles, where we report the LIM as a function of the frequency, at a certain fixed V_{AC} value. Operatively, once fixed V_{AC}, each integrity profile is obtained by performing many attractor–basins phase portraits at different values of Ω, by computing the LIM (normalized radius) for both the non-resonant and the resonant branch, and by plotting LIM versus frequency. The integrity profiles at V_{AC} = 15 V and V_{AC} = 30 V are reported in Fig. 10 in the range $\Omega = [165; 215]$ Hz.

We focus on the case at V_{AC} = 15 V and analyze the resonant attractor. We can clearly distinguish three different parameter regions. (i) Above the natural frequency, the LIM dynamical integrity is really elevated. There is a nearly constant plateau, where LIM reaches and overcomes LIM = 90%, i.e., the resonant branch is very robust against disturbances. This is due to the large basin of attraction of the attractor. Experimentally, the resonant oscillations are clearly visible in practice all along this Ω-range, despite the presence of disturbances. (ii) Approaching the resonance, a sudden fall occurs, which develops in a very small interval. The LIM dynamical

المنارة للاستشارات

integrity drops abruptly from LIM = 80% at about $\Omega = 195$ Hz down to LIM = 10% at about $\Omega = 185$ Hz, i.e., becomes practically residual. From an attractor–basins point of view, this is related to fractality, which enters the potential well and increasingly erodes the basin of attraction of the resonant branch, decreasing dramatically the safe area and producing a strong deterioration in the reliability of the system. Due to this fall, the attractor loses robustness and becomes exposed to disturbances. Experimental dynamic pull-in appears precisely in this range. (iii) Further decreasing the frequency, the LIM additionally reduces, but the drop turns from sharp to more gradual and slowly leads to the complete disappearance of the attractor. The basin of attraction is almost completely fractal and its magnitude is actually trivial. We are not able to catch the resonant branch in this interval.

The non-resonant attractor has a similar behavior. Far from resonance, the LIM reaches elevated values, over LIM = 50%. Approaching the resonance, instead, the LIM completely drops, as in the resonant branch, except that in this case the fall straight leads to the disappearance of the attractor, without the extended region with a tiny LIM.

Varying the electrodynamic voltage, the main features characterizing the integrity profiles do not qualitatively change, both in the non-resonant and in the resonant attractor. However, they are progressively shifted. Increasing V_{AC}, e.g., at $V_{AC} = 30$ V, they appear at higher values of frequency in the resonant branch and at lower ones in the non-resonant one. This widens increasingly the gap between the pull-in bands. Also, comparing the integrity profiles at $V_{AC} = 15$ V and $V_{AC} = 30$ V, we can see that in the resonant attractor the range with a very narrow basin lengthens extensively at low electrodynamic voltages, amplifying the discrepancy between the theoretical curve of boundary crisis and the dynamic pull-in data; conversely, this is by far more reduced at higher excitations.

In Fig. 11 we report the frequency response diagrams and the integrity profiles, at $V_{AC} = 30$ V. They are overlapped to each other (in the latter, the sampled points are denoted with a black square). Regarding the resonant branch, only vibrations of small amplitude are equipped with a large structural safety. Increasing the amplitude, the robustness drops. Vulnerability critically amplifies. The wide final range, where the amplitude of oscillations is very high ending with period-doubling cascade and possibly chaotic motion, is associated with an extremely small and fractal safe basin. The LIM is irrelevant in this interval. From a practical point of view, these phenomena cannot be caught in practice. Similarly occurs in the non-resonant branch, where the range close to the saddle-node bifurcation is actually vulnerable.

Dynamical integrity chart. A comprehensive description of the device dynamical integrity when both the frequency and the electrodynamic voltage are varied can be achieved by computing the LIM dynamical integrity chart, Fig. 12. This is obtained by performing several integrity profiles at different values of V_{AC} and plotting the curves of constant percentage of LIM. They summarize the overall scenario of structural safety. We can observe that the experimental pull-in bands *follow* exactly the integrity curves.

المنارة للاستشارات

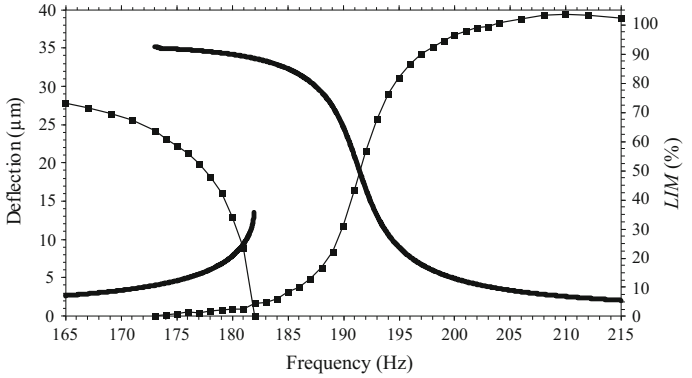

Fig. 11 Frequency response diagram and dynamical integrity profile (the sampled points are denoted with a black square), at V_{AC} = 30 V

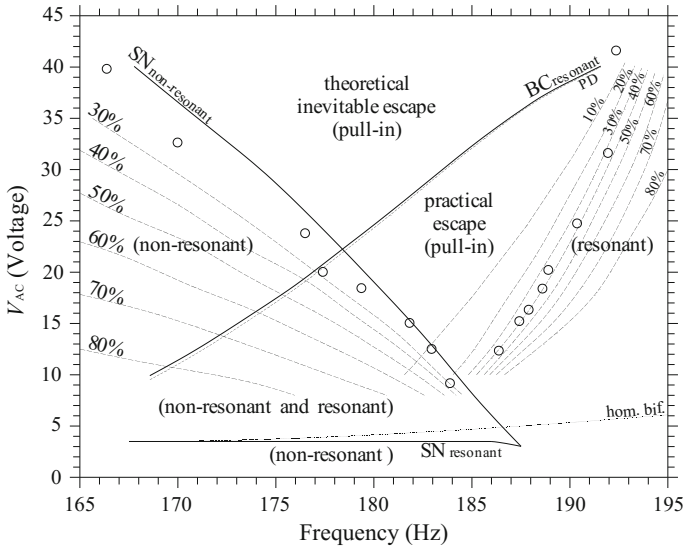

Fig. 12 LIM frequency-electrodynamic voltage integrity chart for the practical disappearance of the attractors. The curves of theoretical appearance and/or disappearance of the non-resonant and the resonant attractor are represented in solid line. The iso-LIM curves are in dashed line. The dots denote the experimental pull-in data

We focus on the resonant branch. Here the matching is really *astonishing*. We can clearly distinguish the three parameter ranges detected in the integrity profiles. (i) Beyond the natural frequency, there is the range with elevated LIM, which consists of a wide interval with slow development of integrity curves. In the profiles, this reflects the region of nearly constant plateau with high dynamical integrity, which is the safe area where the attractor exists and can be used safely. (ii) Decreasing

المنارة للاستشارات

the frequency, we can observe a small range characterized by a rapid occurrence of many integrity curves, where the attractor completely loses its robustness, switching from being able to tolerate considerable disturbances in safe conditions to being totally vulnerable. This is related to the sudden fall in the LIM integrity profiles. This region is in very good agreement with the experimental resonant pull-in band, which settles exactly at LIM = 30–40%, i.e., develops in a precise and very narrow interval of dynamical integrity. The smallness of the narrow interval is in agreement with the experiments, since all the data are acquired under (approximately) the same experimental conditions (e.g., with the same sampling steps, at practically constant pressure, etc.), and therefore, the attractor is expected to disappear at about the same level of dynamical integrity along all the voltage loads. Note that for the considered experimental conditions, this narrow strip leading to the practical pull-in seriously shortens the range of existence of the attractor than what predicted by the theoretical threshold of boundary crisis (LIM = 0%). (iii) For even lower frequency values, there is a large region where the integrity curves develop gradually and progressively lead to the curve of theoretical disappearance. This corresponds to the residual integrity in the profiles.

It is worth analyzing the outline of the iso-LIM curves. Moving far from the boundary crisis, they progressively modify their shape and finally largely differ from it. Specifically, the curve of boundary crisis is nearly straight and moderately inclined; the iso-LIM contour plots, instead, gradually increase their inclination tending to be vertical and progressively develop a configuration slightly concaved up. This is because, before disappearing, the resonant branch presents a very long part with an extremely narrow basin of attraction. The experimental pull-in data actually share the same shape experienced by the dynamical integrity curves, whereas the theoretical curve of boundary crisis is completely disregarded.

Similar features are observed in the non-resonant branch. In this case, the iso-LIM curves evolve practically in parallel with the saddle-node bifurcation threshold, keeping approximately the same shape and inclination. Far from it, they decrease slowly and develop at about constant steps with a wide distance between each other, i.e., the deterioration (or the increment) of the dynamical integrity is rather slow. Approaching the saddle-node bifurcation, instead, there is a sudden fall in dynamical integrity, where the integrity curves become closer and closer and drop abruptly to disappearance. The experimental non-resonant pull-in band occurs at LIM = 0–30%.

Therefore, for each attractor, the integrity curves divide the region of its theoretical existence into two different zones, namely the area of practical existence and the area of practical disappearance. In the range of practical existence, the attractor can be reliably observed in practice. In the range of practical disappearance, the attractor exists in the theoretical predictions but cannot be used in practice because is actually vulnerable. To operate the device in safe conditions with a certain final motion, this last region has to be avoided. This area may be quite narrow, as for the non-resonant attractor, or wide, as for the resonant one. In fact, we can rely on the non-resonant branch along almost all its range of theoretical existence; conversely, we can rely on the resonant one only in a really smaller interval. Thus, this case-study highlights that the practical disappearance can be considerably far from the theoretical one.

المنارة للاستشارات

Since the iso-LIM curves are able to properly detect the range where an attractor effectively vanishes in practice, the dynamical integrity chart can be used to provide a valuable theoretical tool to *interpret* the experimental behavior. This theoretically justifies the experimental evidence. Moreover, each integrity chart sketches not only the curves detecting the range of experimental disappearance of the corresponding attractor, but also many other curves at different levels of constant percentage of LIM. Accordingly, the chart is able to abstract from the particular case-study and examine a more general scenario, where different disturbances are assumed. It illustrates that the wideness of the range where each attractor practically exists may be enlarged (reduced) by decreasing (increasing) the disturbances, i.e., the chart may be used also to *predict* the expected boundaries of disappearance of each attractor.

The obtained results validate the use of the dynamical integrity analysis as an indicator of the amount of uncertainty in the operating initial conditions and in the model. The chart may serve as a guideline for the engineering design, since, depending on the magnitude of the expected disturbances, it can be used to establish safety factors in order to operate the device in safe conditions with the desired behavior.

The loss of structural safety in the analyzed mechanical system is summarized in Fig. 13 with a schematic dynamical integrity chart, where safe and unsafe parameter regimes are illustrated. Three basically different regions are detected, i.e., (i) the safe no-escape area, where at least one of the two attractors exist in practice (dark grey); (ii) the practical escape area, whose wideness depends on the magnitude of disturbances, where both the non-resonant branch and the resonant one disappear in practice (light grey); (iii) the theoretical inevitable escape, where no bounded attractors are expected to exist (white).

3 A Microbeam-Based MEMS Device

The second case-study deals with an electrically actuated microbeam-based MEMS device. The microbeam has non-negligible imperfections in the geometry, which are related to the microfabrication process. Although a deep experimental characterization is conducted, various parameters of the device remain unknown and/or uncertain, as often occurs in practice.

Many experimental tests are performed in the range where both the non-resonant and the resonant attractors exist and exhibit safe jump between each other. A theoretical model is introduced, where the unknowns are identified based on the experimental response. Referring to this model, a dynamical integrity analysis is developed. Similarly to the capacitive accelerometer, this analysis is able to properly interpret and predict the experimental data.

In the present case-study, we can clearly observe the importance of the dynamical integrity investigation to detect the range of applicability of the model. In fact, this analysis is able to distinguish the parameter range where the model can be reliably applied and to alert the parameter range where, conversely, its accuracy is decreased

المنارة للاستشارات

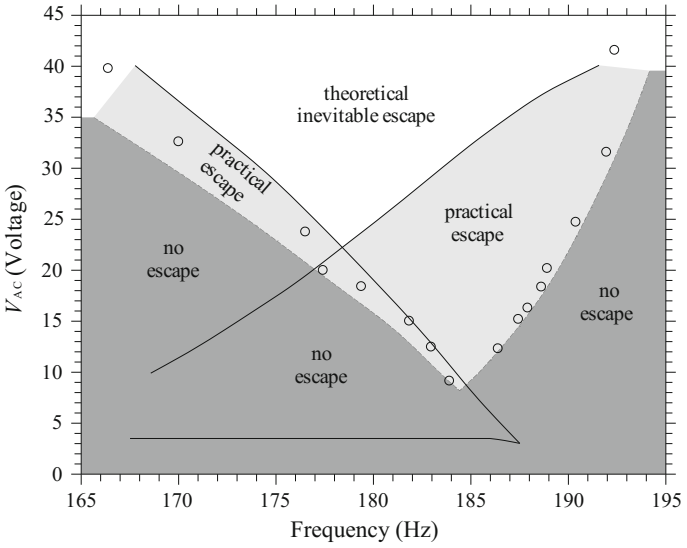

Fig. 13 Schematic dynamical integrity chart. The *dark grey* region corresponds to the no-escape area; the *light grey* region to the practical escape; the *white* region to the theoretical inevitable escape

and may actually become unsatisfactory. This suggests the application of dynamical integrity arguments in the identification process.

The experimental campaign on the microbeam-based MEMS device is performed in Ruzziconi et al. (2013a), the identification process is reported in Ruzziconi et al. (2013f), and the dynamical integrity analysis is developed in Ruzziconi et al. (2013c).

3.1 The MEMS Device and Its Experimental Natural Frequencies

The considered MEMS device consists of a polysilicon microbeam actuated by an electrode, placed directly underneath it on a substrate, Fig. 14. The electrode provides both an electrostatic and an electrodynamic load, where V_{DC} is the electrostatic voltage and $V_{AC}\cos(\hat{\Omega}\hat{t})$ is the electrodynamic excitation, with voltage V_{AC} and frequency $\hat{\Omega}$. The microbeam, although designed to be straight, is curled up of few microns, which is a typical imperfection due to the microfabrication process. Other small imperfections arise at the boundary conditions, where some portions of the pads next to the edges are vibrating as if the effective length were slightly longer than what actually measured (at about 20–30 μm longer at each edge).

Some dimensions of the device are directly attained via the experimental characterization. Nevertheless, no precise information is supplied about various parameters, since they cannot be detected via the available experimental setup. Some of them

المنارة للاستشارات

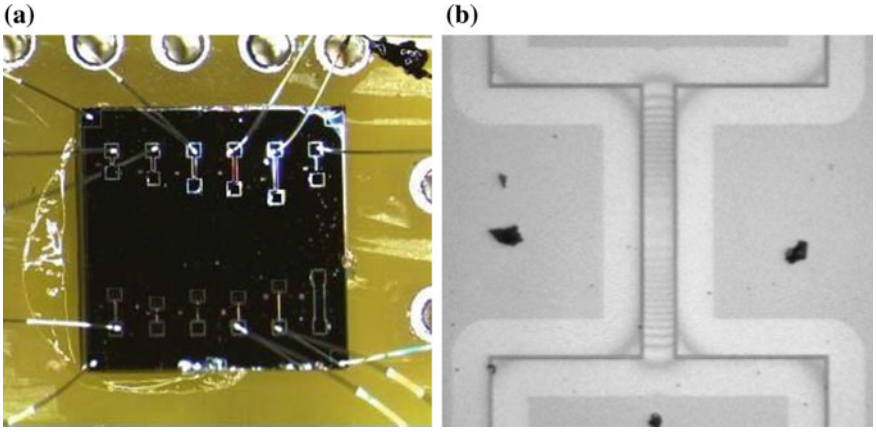

Fig. 14 **a** A general view of the MEMS chip. **b** A top-view picture of the analyzed MEMS device

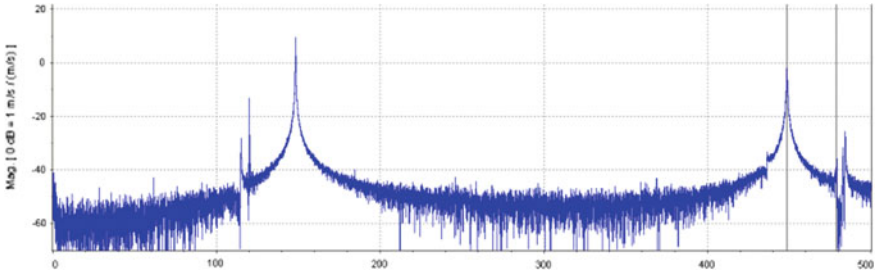

Fig. 15 Experimental frequency response at white noise and low pressure, with $V_{DC} = 1$ V and $V_{AC} = 1$ V. The first four measured natural frequencies occur at $\hat{\Omega} = 114.96$ kHz (first antisymmetric), $\hat{\Omega} = 148.32$ kHz (first symmetric), $\hat{\Omega} = 436.30$ kHz (second antisymmetric), and $\hat{\Omega} = 448.63$ kHz (second symmetric)

are completely unknown (e.g., the contribution of the arched shape and the contribution of the residual stresses); some others, instead, are known only via their nominal value, which is certainly a valuable reference, but it may somewhat differ from the actual measurement (e.g., the gap and the thickness).

An extensive experimental investigation is performed. We experimentally measure the first four natural frequencies. The resulting frequency response is reported in Fig. 15, which shows the velocity versus the frequency along all the desired $\hat{\Omega}$-range. This is acquired by exciting the microstructure with white noise of $V_{DC} = 1$ V and $V_{AC} = 1$ V. The first four natural frequencies are detected at about $\hat{\Omega} = 114.96$ kHz (first antisymmetric), $\hat{\Omega} = 148.32$ kHz (first symmetric), $\hat{\Omega} = 436.30$ kHz (second antisymmetric) and $\hat{\Omega} = 448.63$ kHz (second symmetric). They are expected not to significantly vary at a small V_{DC}, i.e., they may be considered representative of the device first four natural frequencies within the assumption of a small electrostatic load.

المنارة للاستشارات

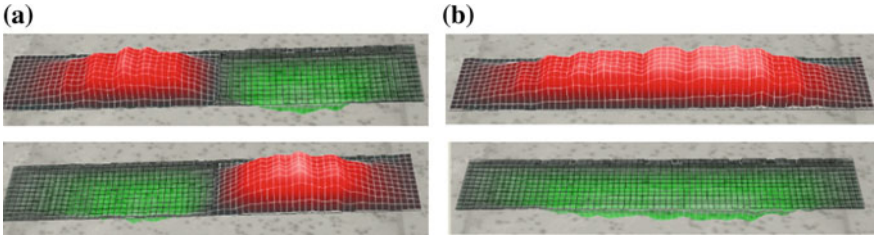

Fig. 16 Experimental mode shapes at **a** $\hat{\Omega}$ = 114.96 kHz (first antisymmetric natural frequency) and **b** $\hat{\Omega}$ = 148.32 kHz (first symmetric natural frequency)

To guarantee a correct attribution of each frequency value to the corresponding mode shape, we have video-recorded the vibration of the microstructure at each frequency. Two examples are reported in Fig. 16. The snapshots at $\hat{\Omega}$ = 114.96 kHz (Fig. 16a) show the first antisymmetric mode, where only the points in the middle of the microbeam are not oscillating (in addition to the points at the boundaries). The snapshots at $\hat{\Omega}$ = 148.32 kHz (Fig. 16b) show the first symmetric mode, where all the points are vibrating (except for the boundaries). Note that the first mode of the experimental microbeam is antisymmetric instead of symmetric, which is likely due to the associated combination of mechanical and geometrical parameters ensuing from the microbeam being curled, i.e., this is another effect of imperfections.

3.2 Experimental Multistability

We experimentally observe the nonlinear phenomena arising in the device response in a neighborhood of the first symmetric resonance, when both the frequency and the electrodynamic voltage are varied. Several experimental frequency sweeps are acquired. They are attained at V_{DC} = 0.7 V, which is close to the electrostatic load previously considered. Two of the resulting frequency response diagrams are reported in Fig. 17, which illustrates the response at V_{AC} = 2 V and V_{AC} = 4 V. Forward and backward sweeps are, respectively, in red stars and blue circles. To compare the sweeps among them, the same experimental conditions are adopted. Specifically, the frequency step is 5 Hz and the pressure is kept (practically) constant at 40 mTorr. All the diagrams are measured at about the same point along the external profile of the microbeam, where the laser is directed. We analyze the obtained experimental data when increasing the V_{AC} voltage excitation.

At V_{AC} = 2 V (Fig. 17a), the frequency response curve exhibits softening bending. This feature provides an interval where both the non-resonant branch (left frequency curve) and the resonant one (right frequency curve) coexist, i.e., two different kinds of oscillations with different characteristics may take place at the same values of (Ω, V_{AC}). The microstructure can respond under safe conditions both with a large motion

المنارة للاستشارات

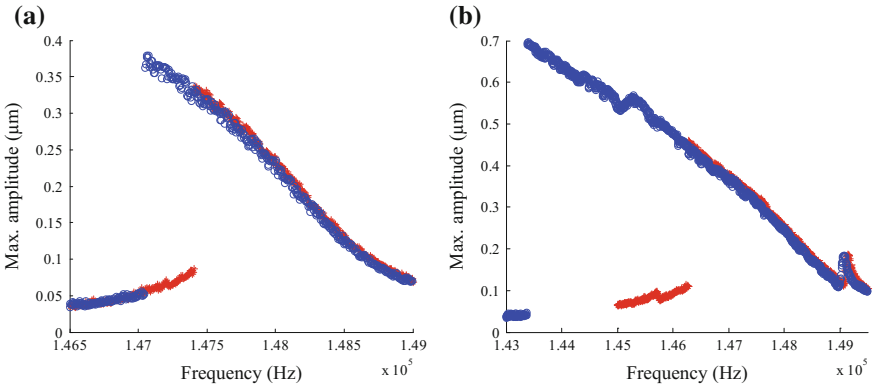

Fig. 17 Experimental frequency sweeps at $V_{DC} = 0.7$ V and **a** $V_{AC} = 2$ V, **b** $V_{AC} = 4$ V. The forward and backward sweep are, respectively, in red stars and blue circles

and with a small one. This equips the device of a certain versatility of behavior, which is valuable in a variety of applications.

At $V_{AC} = 4$ V (Fig. 17b), the resonant branch considerably expands its interval of existence, which provides an interesting widening of the range of multistability. In addition, we can observe the activation of two superharmonic resonances. The presence of superharmonics contributes to make the dynamics even more complex and interesting for practical applications. The ⅓ superharmonic of the second symmetric frequency occurs at $\hat{\Omega} \cong 149.15$ kHz, which is along the resonant branch. The ⅓ superharmonic of the second antisymmetric one occurs at $\hat{\Omega} \cong 145.3$ kHz and concerns both the resonant and the non-resonant attractor. In a neighborhood of these superharmonics, the oscillation amplitude experimentally measured amplifies, though only slightly. In the former, it is clearly visible (albeit small) an incipient bending toward the left.

Technically, in some sweeps there is a blank hole in the non-resonant branch, e.g., at about $\hat{\Omega} = (143.4; 145)$ kHz in Fig. 17b. This is because the frequency sweeps are attained with a small frequency step, which is very time consuming and expensive to be acquired. For this reason, we prefer to perform the sweep in a neighborhood of the critical points, e.g., next to the disappearance of the attractors and next to the superharmonic resonances, whereas we neglect the parts where the sweep is not expected to show particularly relevant phenomena.

We deeply investigate the range $V_{AC} = [0; 5]$ V, after which the microstructure stopped working correctly, probably due to the deterioration of the device.

At disappearance, no one of the attractors undergoes dynamic pull-in (escape). This is because we are examining the device behavior at relatively small V_{AC} excitations, whereas higher voltages are required to trigger the pull-in phenomenon. All the sweeps, instead, exhibit a safe jump, which can be either from lower to higher response or vice versa. Note the relevant difference between the maximum amplitude of the non-resonant branch and the resonant one. At jump, this provides a large stroke,

المنارة للاستشارات

which is desirable in many different applications since enhances the signal-to-noise ratio, i.e., the quality of the signal.

Multistability combined with jumps (with large stroke) offers an interesting behavior from a practical point of view since there is the opportunity to activate a hysteretic loop between the non-resonant and the resonant oscillations. This is appealing for instance in filters, where we are looking for an interval with large oscillations bounded by ranges with small ones, and in detection, where the device is expected to exhibit a certain motion and to switch into a different kind of oscillation upon detection of a physical parameter. Also, the frequency curves achieved in the present case-study refer to moderately low values of electrodynamic excitation, i.e., these phenomena may be triggered at low power consumption, which is even more desirable.

The relevance of all these nonlinear dynamic features in applications underlines the importance of detecting where the disappearance of each attractor effectively occurs under realistic conditions, i.e., where we can count on an effective multistability of the attractors.

3.3 Model Formulation

We introduce a simple model which, despite the inevitable approximations, is able to take into account the main imperfections arising in the characterization. In particular, the device is modeled as a microbeam with length L, fixed–fixed boundary conditions, and constant rectangular cross-section of width b and thickness h. A schematic is shown in Fig. 18.

The imperfections at the boundaries are simulated by assuming an effective length which includes the segments of the pads that are actually vibrating due to undercut. The curled-up configuration is assumed to be derived both from residual stresses and from shape imperfections. Residual stresses are represented by a constant axial load P, which produces the axial displacement w_B at the right end B. Shape imperfections are modeled via a shallow-arched initial configuration, expressed as $y_0(\hat{z}) = (1/2)y_0(1-\cos(2\pi\hat{z}/L))$, where y_0 is the maximum initial rise. The shallow-arched approximation is assumed.

The microbeam is described in the framework of the Euler– Bernoulli theory and a linearly elastic isotropic and homogeneous material is supposed. After "condensing" the axial displacement $w(\hat{z},\hat{t})$ by a classical procedure so that the elongation of the

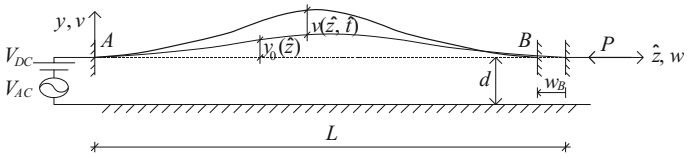

Fig. 18 A schematic of the MEMS device

المنارة للاستشارات

central line of the microbeam does not depend on $\hat{z}$ but only on $\hat{t}$ (Villaggio 1997), the non-dimensional governing equation of the transverse deflection becomes

$$\ddot{v} + \xi \dot{v} + v'''' + \alpha(v'' + y_0'') = -\gamma F_e, \tag{6}$$

where

$$\alpha = n - ka \int_0^1 \left(\frac{1}{2}(v')^2 + v' y_0' \right) dz \tag{7}$$

and

$$F_e = \frac{(V_{DC} + V_{AC}\cos(\Omega t))^2}{(d - v(z,t) + y_0(z))^2} \tag{8}$$

and the boundary conditions are

$$v(0,t) = 0, \quad v(1,t) = 0, \quad v'(0,t) = 0, \quad v'(1,t) = 0. \tag{9}$$

The superimposed dot and prime denote the derivative, respectively with respect to the non-dimensional time t and the space z. The non-dimensional variables are

$$z = \frac{\hat{z}}{L}, \quad t = \frac{\hat{t}}{T}, \tag{10}$$

and we express in microns the remaining variables of length. The resulting parameters become

$$ka = \frac{EA}{EJ}, \quad \gamma = \frac{1}{2}\varepsilon_0 \varepsilon_r A_c \frac{L^3}{EJ}, \quad \xi = c\frac{L^4}{EJT}, \quad T = \sqrt{\frac{\rho A L^4}{EJ}}, \quad \Omega = \hat{\Omega} T, \tag{11}$$

where EA is the axial stiffness, EJ is the bending stiffness, A and J are the area and the moment of inertia of the cross-section, E is the effective Young's modulus, ρ is the material density, d is the gap width between the stationary electrode and the ideal straight configuration, $A_c = bL$ is the overlapped area between the microbeam and the stationary electrode, ε_0 is the dielectric constant in the free space, ε_r is the relative permittivity of the gap space medium with respect to the free space, and c is the viscous damping coefficient.

Equation (6) has both a geometrical nonlinearity (within the operator α), which is due to the mid-plane stretching and an electrical nonlinearity (F_e), which is due to the presence of the electric force.

المنارة للاستشارات

3.4 Identification Process

To identify the unknowns, an identification process is carried (Ruzziconi et al. 2013f). Here, we briefly report the main aspects, since they outline the need of dynamical integrity arguments also for identification purposes.

Since the adopted mechanical model inevitably has various approximations, we cannot expect to identify the unknowns in order that every single experimental result can be theoretically simulated and matched. For this reason, we restrict the identification and focus only on the first symmetric natural frequency, which is the range of interest for the forthcoming analysis. Based on these considerations, the identification process is developed in the frequency-domain, in order to check that all the main linear and nonlinear phenomena in the device experimental response in a neighborhood of the analyzed natural frequency are adequately represented.

Special attention is devoted to identifying the parameters in order to have a correct representation of the extent of each branch. In fact, as highlighted by dynamical integrity concepts, we cannot observe under realistic condition all the theoretical extent of the frequency response curves, since disturbances reduce in practice the range of existence of each attractor. Also, if the frequency sweeps were conducted under smaller disturbances, e.g., with a smaller frequency step, being equal all the other experimental conditions, the experimental extent of each branch would have been slightly longer. Thus, the model is certainly called to realize of all the range of existence of each attractor, which is an essential part of the actual response. However, this is not enough. In fact, the theoretical curves slightly exceed the experimental ones, which is in agreement with the fact that the dynamical integrity analysis allows not only interpreting the available experimental data but also simulating the device under different experimental conditions.

In accordance with the identification process, we refer to the dimensions: $L = 440\ \mu\text{m}$, $b = 55.8\ \mu\text{m}$, $h = 1.873\ \mu\text{m}$, $y_0 = 1.323\ \mu\text{m}$, $n = 64.274$, $E = 1.66 \times 10^{11}\ \text{N/m}^2$ (polysilicon material), $\rho = 2332\ \text{kg/m}^3$ (polysilicon material), $\varepsilon_r = 1$ (air), $\xi = 0.085$, $d = 0.7\ \mu\text{m}$. Note that, regarding the dimensions where we have a nominal reference, the identified value is very close to the nominal one. The resulting parameters are $ka = 3.45285\ \mu\text{m}^{-2}$; $T = 4.26387 \times 10^{-5}$; $\gamma = 1.85135\ \mu\text{m}^3$.

It is worth highlighting that, although the identification is focused only on the first symmetric resonance and its neighborhood, the model is able to match also the second symmetric one, which goes beyond what expected. However, it is not able to catch the antisymmetric frequencies and the related superharmonics. This alerts that the microstructure may have other defects in addition to the principal ones actually considered, i.e., the model may be further improved. This discrepancy confirms the complexity in modeling the analyzed MEMS device and underlines that the imperfections in the microbeam cannot be disregarded and they considerably complicate the investigation.

المنارة للاستشارات

3.5 Galerkin Reduced-Order Model

Assuming the electrostatic contribution as negligible, which is an acceptable approximation since we deal with a small V_{DC}, both the static nonlinear equation and the eigenvalue problem associated to the linear unforced undamped dynamics can be solved in closed form. Consequently, the static deflection is

$$v_s(z) = \frac{1}{2}1.327(1 - \cos(2\pi z)) \tag{12}$$

and the first symmetric mode is

$$\phi(z) = 1.1665sin(7.1172z) + 2.6334\cos(7.1172z)$$

$$-1.4939\sinh(5.5574z) + 1.5055\cosh(5.5574z) - 4.1389\cos(2\pi z). \tag{13}$$

These results are collected to generate a reduced-order model. After approximating the microbeam deflection as $v(z,t) \cong v_s(z) + \Sigma_{i=1}^{M}\phi_i(z)x_i(t)$, where $v_s(z)$ is the static configuration and $\phi_i(z)$ are the corresponding mode shapes, the single first symmetric mode dynamics ($M = 1$) are considered and the Galerkin technique is applied, which yields

$$\ddot{x} + 0.085\dot{x} + 1564.41x - 1033.40x^2 + 209.72x^3$$

$$+1.851(V_{DC} + V_{AC}\cos(\Omega t))^2 \int_0^1 \frac{\phi(z)dz}{(d + v_s(z) + y_0(z) + x\phi(z))^2} = 0. \tag{14}$$

Since the integral term in the electric contribution is not very practical to be computed at each time step, we approximate it via Padé curve fitting. To retain the key aspects of the device response, the Padé coefficients are detected by requiring the fulfillment of the most significant quantitative and qualitative features of both the electric potential and of the potential energy. This is essential to continue ensuring a proper representation of both the in-well and the out-of-well dynamics. A detailed discussion about the small approximations deriving from the performed Padé approximation has been developed by Ruzziconi et al. (2013a).

The single d.o.f. reduced-order model becomes

$$\ddot{x} + 0.085\dot{x} + 1564.41x - 1033.40x^2 + 209.72x^3$$

$$-\frac{1.33949}{(2.05926 - x)^2}(V_{DC} + V_{AC}\cos(\Omega t))^2 = 0 \tag{15}$$

المنارة للاستشارات

where $x(t)$ is the modal coordinate amplitude. Equation (15) is the reduced-order model that we use for the forthcoming simulations.

3.6 Theoretical Predictions Versus Experimental Data

We simulate the experimental dynamics via theoretical frequency response diagrams, which represent the maximum amplitude of the oscillations. Examples are reported in Fig. 19, expressed in dimensional form and overlapped with the experimental data. Since no exact information was recorded about the point of the microbeam where each experimental sweep is acquired, the maximum amplitude is scaled up to reach a proper fitting of the amplitude of the resonant branch. To enhance the readability of the pictures, the exceeding parts of the theoretical resonant attractor are sketched in dashed line.

Theoretical predictions and experimental response nearly coincide, i.e., the theoretical curves show that the model is able to achieve a very good matching. This occurs not only at low electrodynamic voltages (Fig. 19a) but also at higher ones (Fig. 19b). The theoretical model is able to alert the relative difference in the maximum amplitude of oscillations between the two branches, i.e., the jump with large stroke.

However, the comparison between experiments and simulations highlights that the range of existence of each attractor, and consequently the multistability zone, is smaller in practice. In the theoretical curves, both the non-resonant branch and the resonant one lose stability (in classical sense) by saddle-node (SN) bifurcation, after which they vanish. In the experiments, the response directly jumps from one branch to the other one at points different from the bifurcation values predicted in the theoretical curves. On the one hand, the simulations are able to catch all the experimental extent of both the attractors and not only a part of it, which corroborates

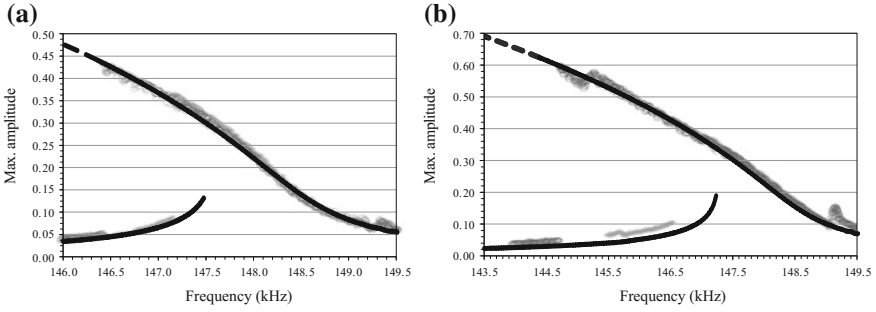

Fig. 19 Frequency response diagram (in dimensional form) at **a** V_{AC} = 2.5 V and **b** V_{AC} = 3.5 V. The theoretical results achieved are in black solid line. The sweeps experimentally acquired are in grey stars (forward sweep) and circles (backward sweep)

المنارة للاستشارات

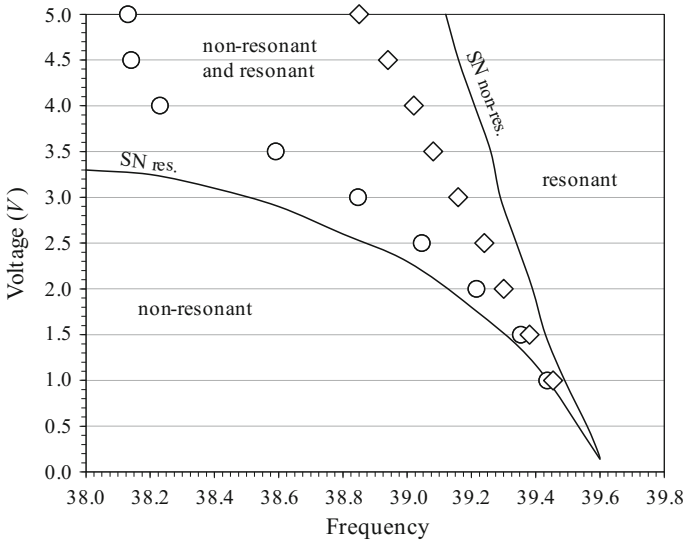

Fig. 20 Frequency-electrodynamic voltage behavior chart of the microbeam-based MEMS device in a neighborhood of the first symmetric resonance. The curves of theoretical appearance and/or disappearance of the attractors are in solid line. The experimental disappearance of the non-resonant branch and of the resonant one are represented, respectively, in diamonds and circles

the reliability of the model. This aspect is essential for any further analysis. On the other hand, this discrepancy emphasizes the need for developing dynamical integrity investigations to be interpreted.

Another discrepancy with the experiments is represented by the superharmonic resonances. Of course, the performed simulations are not able to catch the ⅓ second symmetric superharmonic, which occurs at $\hat{\Omega} \cong 149.5$ kHz, and the ⅓ second anti-symmetric one, which occurs at $\hat{\Omega} \cong 145.3$ kHz, since the model in Eq. (15) includes only the single first symmetric mode dynamics and does not take other modes into account. This issue is addressed by Ruzziconi et al. (2013a), where a two-degree-of-freedom reduced-order model is developed, which is able to represent also the ⅓ second symmetric superharmonic.

To illustrate the overall scenario of the main dynamical events, we develop the frequency-electrodynamic voltage behavior chart, which is reported in Fig. 20 along with the measured experimental data. Qualitatively, this represents a small part of the chart analyzed in the first case-study in Sect. 2, corresponding only to a small portion up to the lower part of the Δ-shaped region, which is characterized by the coexistence of the two attractors.

The degenerate cusp bifurcation point occurs at (Ω, V_{AC}) approximately equal to (39.6, 0.14). The two curves of saddle-node SN delimitate the range of parameters where both the non-resonant and the resonant oscillations coexist. The chart clearly illustrates the considerable enlargement of the present range of theoretical

المنارة للاستشارات

multistability, which gradually characterizes wider and wider frequency values, when increasing V_{AC}. This phenomenon is deeply influenced by the resonant branch since a slight increment of V_{AC} provides a large shift of its SN bifurcation toward lower frequency values, which significantly broadens the range of existence of the attractor. The non-resonant branch, instead, reduces its extent when V_{AC} increases, but this decrement is not substantial.

The experimental data of disappearance are overlapped to the theoretical results. They are denoted with diamonds and circles, respectively for the non-resonant and the resonant branch, and confirm the discrepancies highlighted in the frequency response diagrams.

3.7 The Practical Disappearance of the Attractors

To investigate the device from a global perspective, we perform attractor–basins phase portraits. Some examples are reported in Fig. 21, at $V_{AC} = 3.5$ V. The basins are orange and green, respectively, for the non-resonant and the resonant branch. The white color denotes the escape.

Approaching the resonance, the resonant branch appears. At $\Omega = 38$ (Fig. 21a), its basin is still rather narrow, whereas the other basin is particularly wide. Increasing Ω, this outline rapidly changes. At $\Omega = 38.8$ (Fig. 21b), the two basins are comparable. Each one of them presents a compact area, which is appreciably large and mainly develops around the attractor, and a non-compact one, which is even wider and consists of thin tongues spiraling around the compact part. Further increasing Ω, the basin and the compact part of the resonant branch significantly enlarge at the expense of the basin of the non-resonant one, which considerably shrinks. At $\Omega = 39$ (Fig. 21c) the magnitude of this last basin is still wide. At $\Omega = 39.22$ (Fig. 21d), instead, it becomes nearly residual. The non-resonant branch experimentally disappears at $\Omega = 39.08$ ($\hat{\Omega} = 146.55$ kHz), i.e., between the two last attractor–basins phase portraits, where the compact area of its basin becomes too small to endure the presence of

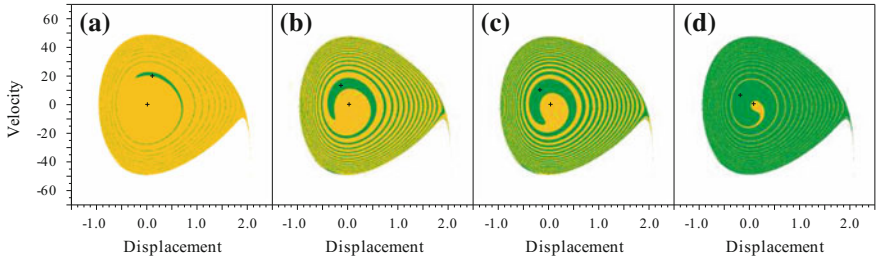

Fig. 21 Attractor–basins phase portrait at $V_{AC} = 3.5$ and (from left to right): **a** $\Omega = 38$; **b** $\Omega = 38.8$; **c** $\Omega = 39$; **d** $\Omega = 39.22$

المنارة للاستشارات

disturbances. Similarly, the experimental disappearance of the resonant branch arises at $\Omega = 38.59$ ($\hat{\Omega} = 144.71$ kHz), which is between Fig. 21a and b.

At the experimental disappearance, note that each attractor and the compact part of its basin are located far from the escape. They are immersed and surrounded by the other basin. This outline guarantees the safe jump between the two branches, as observed in the experimental data. However, further amplifying the electric excitation beyond the analyzed range, the resonant attractor and its basin turn closer and closer to the escape (not shown in the figures) and finally undergoes dynamic pull-in.

We analyze the practical disappearance of each branch by developing dynamical integrity profiles. Operatively, this analysis is similar to the one developed for the capacitive accelerometer in Sect. 2. The same definitions of safe basin and the same dynamical integrity measure (LIM) are considered. The attractor–basins phase portraits are sampled using a grid of $\Omega = 0.1$ Hz (or less). Results are reported in Fig. 22.

We focus on the resonant branch and analyze the range $\Omega = [37.8; 39.3]$, Fig. 22a. As an example, we consider the profile at $V_{AC} = 3.5$ V. At $\Omega = 39.1$, there is LIM $\cong 15\%$, which is not particularly wide, but is still large enough to guarantee that the attractor is experimentally visible. Decreasing Ω, the LIM slowly slides down to smaller values. This fall produces a significant loss of the attractor's dynamical integrity. The smaller integrity enhances the sensitivity of the system to unexpected excitations, and eventually makes the attractor exposed to the experimental disturbances. This is the range where the resonant branch experimentally disappears, precisely at $\Omega = 38.59$, with LIM $\cong 6.64\%$. The last part of the integrity profile is characterized by a minimal dynamical integrity. The LIM keeps decreasing, but slower, up to the disappearance of the attractor (not shown in the figure). Since the dynamical integrity is only residual, the sweeping process cannot catch in practice this remaining theoretical range of existence of the attractor.

Comparing the frequency response (Fig. 19b) to the integrity profile (Fig. 22a) when Ω decreases, the amplitude of the resonant oscillations gradually increases while the dynamical integrity drops. Moderately large vibrations can be experimentally observed since they are equipped with an acceptable integrity. Conversely, larger oscillations are structurally weak and cannot exist from a practical point of view.

Varying the electrodynamic voltage, the main features in Fig. 22a essentially remain unchanged, except for some minor differences. At $V_{AC} = 2.5$ V, the range with negligible LIM is nearly imperceptible, then, it successively broadens. When increasing V_{AC}, the values of LIM corresponding to the experimental disappearance slightly increase but remain confined in a precise and very narrow interval, LIM = 6.2–6.8%. Only exceptions occur at higher V_{AC}, in particular at $V_{AC} = 4.5$ V, where the resonant branch disappears at LIM $\cong 7.5\%$, and at $V_{AC} = 5$ V, where it disappears at LIM $\cong 8.9\%$. These values are slightly higher, but not excessively. This fact may be due to the model. As explained in Sect. 3.3 and underlined by Ruzziconi et al. (2013a, c, f), we are aware that the present model has many approximations since many physical parameters are unknown. Raising V_{AC}, the effects of the nonlinearities increase and the effects of the approximations of the model amplify, which affects the reliability of the results. Nevertheless, it may be related also to deterioration of

المنارة للاستشارات

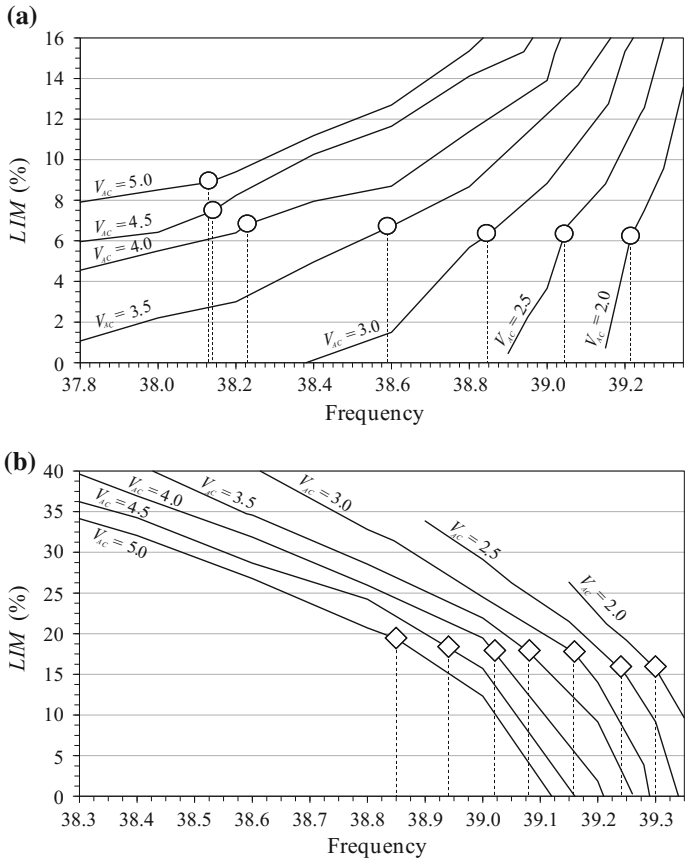

Fig. 22 LIM dynamical integrity profiles to analyze the practical disappearance for **a** the resonant branch and **b** the non-resonant one, at different V_{AC} values

the device, which is due to the multiplicity of the performed experiments. Note that the experimental backward sweep at $V_{AC} = 5$ V was the last sweep that we were able to achieve, after which the microstructure broke.

A similar dynamical integrity analysis is developed for the non-resonant branch. According to the remarks in the attractor–basins phase portraits (Fig. 21), the compact part of its basin strongly reduces very close to the curve of disappearance, which may make the attractor vanish in practice in this neighborhood. On the contrary, slightly far from this curve, this attractor has a basin with a large compact part, since the resonant branch either does not exist or has a small basin. Consequently, in this range the attractor is expected to have a broad dynamical integrity, i.e., to be robust to disturbances. For this reason, in the non-resonant case, we can investigate the dynamical integrity in a smaller interval than in the resonant one. In particular, we

المنارة للاستشارات

consider Ω = [38.3; 39.35], since this is the most critical range where the attractor needs to be analyzed from a dynamical integrity perspective (Fig. 22b).

Considering V_{AC} = 3.5 V at increasing Ω, the integrity profile initially declines slowly, then descends more rapidly, and finally falls within a narrow range, which directly ends with the theoretical SN bifurcation. The experimental disappearance occurs at LIM ≅ 17.7%. This layout does not substantially modify as varying V_{AC}. Similarly to the resonant branch, when V_{AC} increases, the experimental disappearance occurs at a slightly higher LIM. Nevertheless, we can identify a precise range where the attractor experimentally vanishes in all the analyzed frequency sweeps, LIM = 16–19%. Even if this interval is slightly larger than the one observed for the resonant branch, it corresponds to a small band of frequency, where the attractor may practically vanish.

The loss of robustness is very rapid in the non-resonant case. In the resonant one, instead, the fall is slow, and, consequently, a small interval of LIM denotes a broad band of frequency. Hence, accuracy in detecting the LIM is particularly valuable in the resonant branch, more than in the non-resonant one.

The dynamical integrity charts are reported in Fig. 23. We can observe that they succeed in predicting properly the experimental data. In the resonant branch, Fig. 23a, safe conditions are ensured at LIM > 8% (except at V_{AC} = 5 V). Below this percentage, the attractor is practically vulnerable. It is at about LIM = 6–8% that, in practice, the final motion may become different from the theoretical predictions, leading to a jump to the other branch. The last range with LIM < 6% actually does not exist under realistic conditions, with the present expected disturbances. Similarly, the non-resonant attractor, Fig. 23b, can safely operate the device up to LIM > 20%. Then, the LIM drops faster (the lines of constant percentage of LIM are really next to each other) up to the disappearance of the attractor (at SN non-res). At about LIM = 15–20%, which corresponds to a tiny frequency range, the response jumps to the other branch. The final range of existence of the attractor is only theoretical.

These results highlight that, despite numerous uncertainties in the model, dynamical integrity is able to detect a precise range of LIM, which corresponds to a precise range of frequency, where we can expect to observe the experimental disappearance of the analyzed attractor. Below this interval, the branch practically does not exist, although it appears in the theoretical predictions. Therefore, this analysis is able to provide a satisfactory interpretation of the disturbances inevitably encountered in the experimentation. Of course, the more accurate is the model, the more precise will be the dynamical integrity analysis in predicting the threshold of practical disappearance.

Hence, Eq. (15) is able not only to predict the general outline of the frequency sweeps, but also to provide reliable (and not rough) dynamical integrity predictions of the experimental extent of each branch.

Note that, up to V_{AC} = 4.5 V, the practical disappearance occurs within a very small range of LIM. After this V_{AC} value, the range gradually enlarges, both in the non-resonant and in the resonant branch. Thus, the dynamical integrity analysis may be used also as a valuable tool to denote the threshold of applicability of the model, since is able to detect the voltage boundary after which the model slowly starts to

المنارة للاستشارات

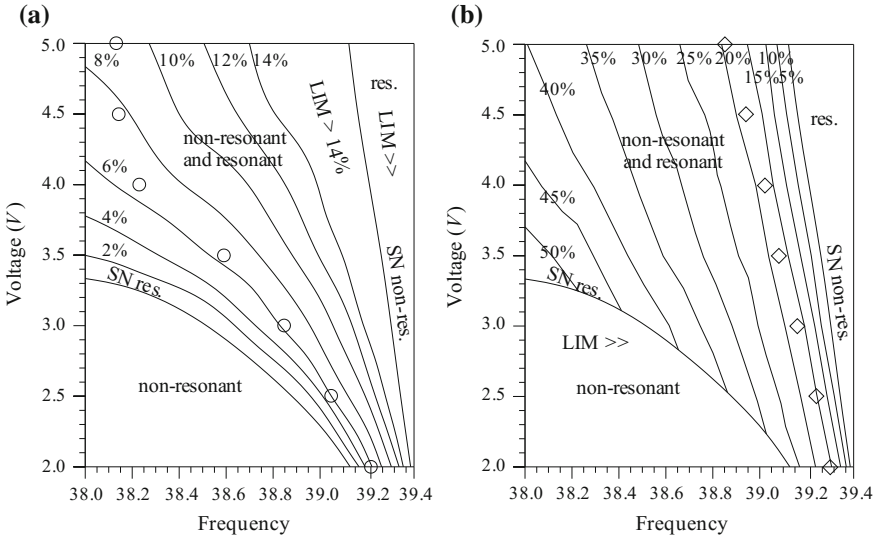

Fig. 23 LIM frequency-electrodynamic voltage dynamical integrity charts for the practical disappearance of **a** the resonant attractor and of **b** the non-resonant attractor

decrease its accuracy. In the present case, this threshold practically covers all the range with available experimental data.

The schematic dynamical integrity chart in Fig. 24 summarizes the overall scenario, namely these are the region where only one branch exists both in theory and in practice (white); the region where only one branch exists in practice, whereas the other one practically disappears (light grey); the region where both the branches practically coexist (dark grey).

4 An Electrically Actuated Single-Walled Slacked Carbon Nanotube

The complexity of the system's nonlinear behavior is the topic of the third case-study. Thanks to the inherent nonlinearities, even simple MEMS and NEMS devices may exhibit very rich dynamics. As an example, we present a theoretical investigation of the nonlinear response of a slacked carbon nanotube (CNT) when actuated by large electrostatic and electrodynamic excitations. The coexistence of several competing attractors with different characteristics is observed, which leads to a considerable versatility in the system's dynamics. This is a realistic case with multiresponse behavior, which may be desirable for many feasible applications.

We analyze the integrity profiles of each one of the principal attractors since they offer valuable information to the designer about the practical range of actuality of

المنارة للاستشارات

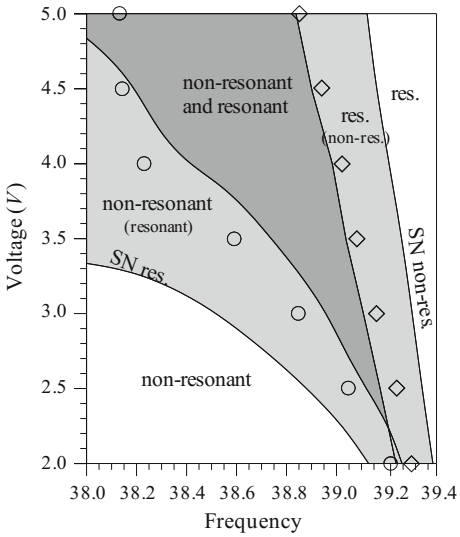

Fig. 24 Schematic dynamical integrity chart. The *white* region represents the parameter range where only one branch (non-resonant or resonant) exists both in theory and in practice. The *light grey* region represents the range where only one branch exists in practice, whereas the other one (expressed in brackets) practically disappears. The region where both the branches practically coexist is *dark grey*

the CNT. Nevertheless, when the response becomes increasingly complex as in the present system, restricting only to the analysis of the practical disappearance of the attractors is typically not sufficient. In fact, to have a comprehensive outline of the final response under realistic conditions, various dynamical integrity aspects need to be considered, e.g., the robustness of the potential well, the final behavior after the disappearance of an attractor, etc. In the following, we raise the need for focusing on different dynamical integrity issues, although we refer to dedicated papers for their detailed discussion.

In the literature, the complexity in a CNT is observed by Xu et al. (2017) and the analysis of the response of a similar device under different complementary dynamical integrity perspectives is developed by Ruzziconi et al. (2013e).

4.1 The Slacked CNT

The analyzed NEMS device consists of a very slender single-walled slacked CNT electrically actuated, which is schematically represented in Fig. 25. The electrode is placed directly underneath the CNT at a certain distance d. Both the electrostatic and the electrodynamic actuations are taken into account, where V_{DC} is the electrostatic voltage and $V_{AC}\cos(\Omega t)$ is the electrodynamic excitation, with voltage V_{AC} and frequency Ω. The nanotube is modeled as a fixed–fixed nanobeam, of length L and a constant circular cross-section with radius R.

The slacked configuration, which simulates the imperfections possibly due to the fabrication process, is expressed as $y_0(z) = y_0 \sin^2(\pi z/L)$, where b_0 is the maximum initial rise. The problem formulation is very similar to the one of a microbeam-based

المنارة للاستشارات

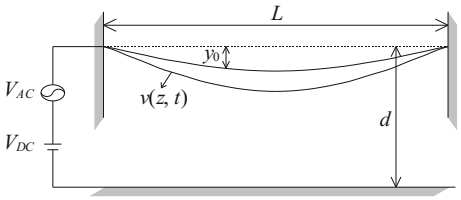

Fig. 25 Schematic of the electrically actuated slacked single-walled carbon nanotube

MEMS device. We briefly recall the main steps, since they are the starting point of the present analysis. The dimensionless governing equation of the transverse deflection of the CNT can be written as

$$\ddot{v} + \xi\dot{v} + v'''' - \alpha(v'' - y_0'') = \gamma F_e \tag{16}$$

with

$$\alpha = ka\int_0^1 \left(\frac{1}{2}(v')^2 - v'y_0'\right)dz \tag{17}$$

and the electric force term F_e is expressed as (Ouakad and Younis 2011, 2012)

$$F_e = \frac{(V_{DC} + V_{AC}\cos(\Omega t))^2}{\sqrt{(1-v-y_0)(1-v-y_0+2R)\left(\cosh^{-1}\left(1+\frac{1-v-y_0}{R}\right)\right)^2}}. \tag{18}$$

The boundary conditions are

$$v(0,t) = 0, \quad v(1,t) = 0, \quad v'(0,t) = 0, \quad v'(1,t) = 0. \tag{19}$$

The level of slack and the geometry of the considered CNT are selected in order to activate two stable configurations. In particular, we consider: L = 1750 nm, R_{out} = 1 nm, R_{in} = 0.5 nm, d = 500 nm, Young modulus E = 1 TPa, mass density ρ = 1.3 g/cm^3, and a slack level of 100 nm.

After applying the Galerkin technique and the Padé approximation, the final single mode reduced-order model becomes

$$\ddot{x} + 0.2237\dot{x} + 19272 \times 10^6 x - 2.2911 \times 10^7 x^2 + 6.0539 \times 10^7 x^3$$

$$= \frac{10.7424 - 22.0783x + 2.8898x^2 + 20.2295x^3}{(0.5574 - x)^2}(V_{DC} + V_{AC}\cos(\Omega t))^2 \tag{20}$$

where $x(t)$ is the modal coordinate amplitude (Xu et al. 2017).

The system has an asymmetric double potential well, with escape direction on the right. A zoom in correspondence of the wells is reported in Fig. 26. The asymmetry

المنارة للاستشارات

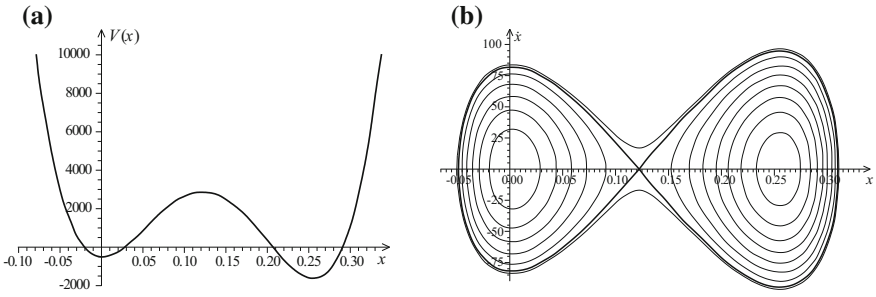

Fig. 26 **a** Double potential well and **b** phase portrait, at V_{DC} = 10 V

is due to the presence of the electric excitation in only one side of the CNT. The well at right is slightly wider and closer to the escape, whereas the well at left is smaller and far from it.

The corresponding phase portrait illustrates the four physical equilibrium points, namely the elliptic center $x_{s1} = 0.0018$, the saddle $x_{s2} = 0.1217$ related to the maximum between the two wells, the elliptic center x_{s3} = 0.2553, and the hill-top saddle x_{s4} = 0.5492 (which exceeds the range shown in the figure). We can clearly observe the small vibrations confined inside each single well surrounding each center, the two homoclinic loops separating the small in-well dynamics from the large cross-well oscillations spanning both the wells, and finally (not shown in the zoom) the homoclinic orbit of the hill-top saddle, separating all the bounded motions from the out-of-well escape. The natural frequency associated with x_{s1} is at $\Omega \cong 1321$, and the natural frequency associated with x_{s3} is at $\Omega \cong 1450$. These two natural frequencies are slightly different from each other. This is another consequence of the asymmetry of the system.

4.2 Multiresponse Behavior

The main aspects of the CNT dynamics are theoretically explored, highlighting the possibility of multiresponse behavior. We report the theoretical frequency response curves at $V_{DC} = V_{AC}$ = 10 V, Fig. 27. Several different attractors may arise. The principal attractors oscillating in the neighborhood of the stable equilibrium x_{s1} (left well) are in black line, the principal attractors oscillating in the neighborhood of the stable equilibrium x_{s3} (right well) are in blue line, and the large cross-well dynamics are in green line.

Focusing on the primary resonances, Fig. 27a, we can observe that attractors A_1 (non-resonant) and A_2 (resonant) in the left well and attractors B_1 (non-resonant) and B_2 (resonant) in the right well coexist for a wide Ω-range. The non-resonant branch disappears by saddle-node bifurcation (SN). The resonant one, instead, performs a period-doubling cascade leading to chaotic motion and finally disappearing

المنارة للاستشارات

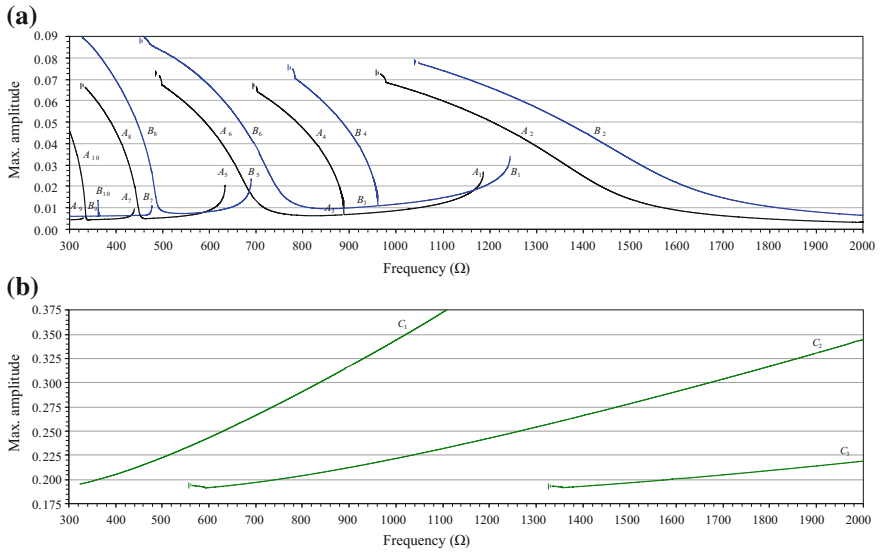

Fig. 27 Frequency response curves of **a** in-well attractors and **b** large cross-well oscillations, at V_{DC} = 10 V and V_{AC} = 10 V. Attractors in the left well, in the right well and large cross-well dynamics are respectively in black, blue, and green lines

by boundary crisis (BC); we can notice the first period-doubling, whereas the other bifurcations affect a very small parameter range and for this reason are only symbolically sketched in the figure. As anticipated in the preliminary investigations, the two resonance zones are shifted a little, due to the asymmetry of the CNT.

We can see parametric resonance. Focusing on the oscillations in the left well (black), this phenomenon occurs at $\Omega \cong 880.6$. Decreasing the frequency, the non-resonant attractor A_1 at primary resonance becomes the resonant branch A_4 at parametric resonance. We can observe the presence of the non-resonant branch (A_3) and of the resonant one (A_4). There is a tiny interval where the non-resonant and the resonant branch separate. The resonant branch immediately increases the amplitude of its oscillations. The non-resonant branch, instead, continues performing very small vibrations. The coexistence of the non-resonant and the resonant attractors endures approximately all along $\Omega \cong [701.8; 880.6]$, which is a rather large Ω-range, although smaller than the one involved at primary resonance. Only close to its disappearance, the resonant branch rapidly undergoes period-doubling cascade and finally vanishes by boundary crisis.

Superharmonics are clearly visible since the voltage excitation is elevated enough to allow detecting them properly. Still investigating the left well dynamics (black), we can see the ½ superharmonic, at $\Omega \cong 660.5$. The scenario is very similar to the one at primary resonance. There are the non-resonant (A_5) and the resonant branch (A_6), which previously was the non-resonant A_3. As expected, the parameter range

المنارة للاستشارات

involved in the ½ superharmonic is smaller than in the primary case, but the amplitude of the resonant peak rises up to about the same oscillation amplitude.

The frequency response diagram plainly illustrates the ⅓ superharmonic at $\Omega \cong 440.3$. Also in this case, bifurcations are very similar to the ones at primary resonance. The range involved by the non-resonant (A_7) and resonant (A_8) attractors is increasingly smaller, although their oscillations achieve elevated amplitudes.

Finally, the ¼ superharmonic at $\Omega \cong 330.3$ can be seen, whose dynamics are analogous to the ones at primary resonance, except that the interval where the non-resonant (A_9) and resonant (A_{10}) oscillations are confined is very narrow, although it slightly continues behind the parameter values examined in the present paper.

All couples of resonant and non-resonant branches exhibit the characteristic bending toward lower frequencies. Although different resonant attractors belonging to the same well are generated and some of these branches are considerably long (e.g., at primary, parametric resonance and ½ resonance), we cannot find them simultaneously, i.e., unfortunately, the CNT under consideration offers no chance to have some of the resonant attractors coexisting.

Similar behavior occurs in a neighborhood of the stable configuration x_{s1} (right well), where in addition to the primary resonance with attractors B_1 and B_2, we can clearly observe the parametric resonance with attractors B_3 and B_4, the ½ superharmonic with attractors B_5 and B_6, the ½ superharmonic with attractors B_7 and B_8, and the ¼ superharmonic with attractors B_9 and B_{10}. Their peaks are slightly higher than the ones in the left well. Small differences are observed with respect to the left well dynamics, as a consequence of the asymmetry of the system. A discrepancy arises in the resonant branch at ⅓ superharmonic, which appears and/or disappears by saddle-node bifurcation and not by boundary crisis. Another discrepancy occurs in the resonant branches at ⅓ and at ½ superharmonics, whose length is notably longer than in the corresponding branches in the left well. Dissimilarity arises at ¼ superharmonic, which is only slightly perceived at this voltage excitation and it does not rise up to elevated values, but its resonant peak remains well below the ones exhibited at the other resonance cases.

In addition to the nonlinear aspects previously examined, we can observe the large cross-well oscillations reported in Fig. 27b, namely C_1, C_2, and C_3, which appear and/or disappear by boundary crisis and increase their maximum amplitude up to reach and exceed the range reported in the figure and finally undergoing dynamic pull-in. Note that the present reduced-order model considers only one natural frequency (since it has only one d.o.f.). However, other resonances can be activated, which further increases the complexity of the system's response.

In Fig. 28, LIM dynamical integrity profiles are reported to investigate the disappearance of the in-well attractors, in order to understand which one of them may be expected to effectively operate the device. We focus on a neighborhood of the ½ superharmonic resonances. Only one normalizing condition is adopted, which permits comparing the robustness of all the attractors among them, namely, we normalize each radius with the analogous radius drawn for B in the unforced dynamics.

The attractors on the left and on the right well share a similar profile, although some discrepancies arise due to the slight asymmetry. The non-resonant branches A_5 and

المنارة للاستشارات

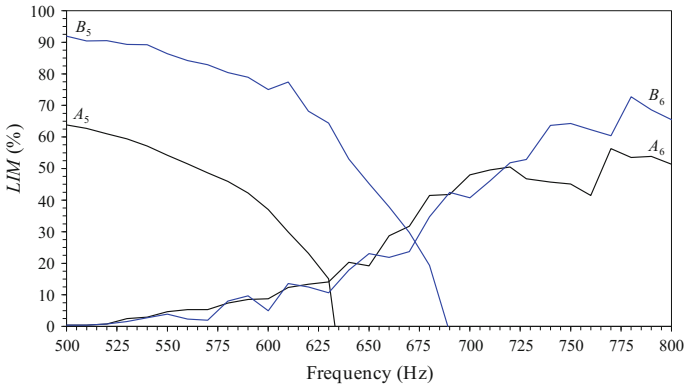

Fig. 28 Dynamical integrity profiles of the principal in-well attractors, at V_{DC} = 10 V and V_{AC} = 10 V. Attractors in the left and right well are respectively in black and blue line

B_5 have an elevated dynamical integrity up to a close vicinity of their corresponding SN; the resonant branches A_6 and B_6, have an elevated integrity only appreciably before their corresponding BC. Note that the profiles present various sharp indented parts. Evident ones occur at $\Omega \cong 760$ in A_6 and $\Omega \cong 770$ in B_6, but other minor drops arise all along the LIM curves. These are the effect of some minor attractors, which successively appear and/or disappear. Although they exist only in small parameter ranges, they are able to noticeably affect and reduce the robustness of the principal branches.

In addition to the practical disappearance of the in-well attractors, other different dynamical integrity aspects may be investigated, in order to have detailed information of the expected behavior under realistic conditions. For example, analyzing the robustness of each potential well allows detecting the parameter ranges where it remains wide enough to tolerate disturbances without undergoing dynamic pull-in; detecting the final behavior after the disappearance of an attractor is a key aspect for practical purposes in view of different kinds of applications; etc. Thus, when the scenario is rather complex, the combined use of different dynamical integrity charts offers the possibility to achieve a deep insight about the expected dynamics under realistic conditions, which is essential for design and applications. A similar analysis has been developed for instance by Ruzziconi et al. (2013e).

المنارة للاستشارات

5 Conclusions

In the present chapter, three different case-studies of engineering application of dynamical integrity concepts have been examined.

In the first case-study, the dynamical integrity analysis has been observed to provide valuable information for interpreting the experimental data and for predicting the expected behavior under different experimental conditions. A capacitive accelerometer has been investigated in a neighborhood of its fundamental natural frequency. To take disturbances into account and explore the practical response under realistic conditions, a dynamical integrity analysis has been performed. The definition of safe basin and the measure of dynamical integrity have been selected in order to establish a continuous parallelism between the dynamical integrity tools and the experimental sweeping process. Each branch experimentally exists in the range where its dynamical integrity is elevated; conversely, it practically disappears where its dynamical integrity is not enough to sustain the experimental disturbances. All these results have been collected in the dynamical integrity charts. The matching is well beyond what expected, remarkably in the resonant branch. The integrity curves have been observed to be able to detect properly and accurately the threshold which separates the area of practical existence, where the attractor can safely operate the device, from the area of practical disappearance, where the attractor becomes too much vulnerable to disturbances and vanishes in practice, although it theoretically exists and is stable. The practical range of existence of each branch is smaller, and sometimes considerably smaller than the theoretical one.

In the second case-study, investigating a microbeam-based MEMS device electrically actuated, attention has been focused on the importance of the dynamical integrity analysis for detecting the parameter range of application of the considered theoretical model. An identification process has been developed, where in addition to the linear and nonlinear aspects of the system response, dynamical integrity concepts have been taken into account. We have stressed that the dynamical integrity study cannot prescind from a good classical modeling, since the more accurate is the mechanical modeling, and the more precise is the dynamical integrity in predicting the system's response in experiments and practice.

In the third case-study, a slacked carbon nanotube has been considered, which presents two stable static configurations. Focusing on the first symmetric natural frequency, the system's dynamical response has been analyzed. This is characterized by a rich nonlinear behavior. To describe the complexity of the CNT under realistic conditions, the dynamical integrity of the principal attractors has been examined and the need of combining information from different dynamical integrity perspectives has been highlighted.

We can conclude that, in the present chapter, starting from particular case-studies, the issue of dynamical integrity investigations in a mechanical system has been addressed and its use in the engineering design has been highlighted in order to operate the structure according to the desired outcome. We have underlined the large

المنارة للاستشارات

applicability of this analysis both in MEMS and, more in general, in any mechanical system.

Acknowledgements The following permissions to reprint are acknowledged: Figs. 14–17 from IOP Publishing Ltd.

References

Abdel-Rahman, E. M., Younis, M. I., & Nayfeh, A. H. (2002). Characterization of the mechanical behavior of an electrically actuated microbeam. *Journal of Micromechanics and Microengineering*, *12*, 759–766.

Alsaleem, F. M., Younis, M. I., & Ouakad, H. M. (2009). On the nonlinear resonances and dynamic pull-in of electrostatically actuated resonators. *Journal of Micromechanics and Microengineering, 19*(4), 045013.

Alsaleem, F. M., Younis, M. I., & Ruzziconi, L. (2010). An experimental and theoretical investigation of dynamic pull-in in MEMS resonators actuated electrostatically. *Journal of Microelectromechanical Systems, 19*(4), 794–806.

Belardinelli, P., Lenci, S., & Brocchini, M. (2014). Modeling and analysis of an electrically actuated microbeam based on nonclassical beam theory. *Journal of Computational and Nonlinear Dynamics*, *9*(3), 031016-1–031016-10.

Cho, H., Jeong, B., Yu, M.-F., Vakakis, A. F., McFarland, D. M., & Bergman, L. A. (2012). Nonlinear hardening and softening resonances in micromechanical cantilever-nanotube systems originated from nanoscale geometric nonlinearities. *International Journal of Solids and Structures, 49*(15–16), 2059–2065.

Cho, H., Yu, M.-F., Vakakis, A. F., Bergman, L. A., & McFarland, D. M. (2010). Tunable, broadband nonlinear nanomechanical resonator. *Nano Letters, 10*(5), 1793–1798.

Castellanos-Gomez, A., Meerwaldt, H. B., Venstra, W. J., van der Zant, H. S. J., & Steele, G. A. (2012). Strong and tunable mode coupling in carbon nanotube resonators. *Physical Review B, 86,* 041402.

Das, K., & Batra, R. C. (2009a). Pull-in and snap-through instabilities in transient deformations of microelectromechanical systems. *Journal of Micromechanics and Microengineering, 19,* 035008.

Das, K., & Batra, R. C. (2009b). Symmetry breaking, snap-through, and pull-in instabilities under dynamic loading of microelectromechanical shallow arch. *Smart Materials and Structures, 18,* 115008.

Gonçalves, P. B., Silva, F. M. A., Rega, G., & Lenci, S. (2011). Global dynamics and integrity of a two-dof model of a parametrically excited cylindrical shell. *Nonlinear Dynamics, 63,* 61–82.

Gottlieb, O., & Champneys, A. (2005). Global bifurcations of nonlinear thermoelastic microbeams subject to electrodynamic actuation. In G. Rega & F. Vestroni (Eds.), *IUTAM Symposium on Chaotic Dynamics and Control of Systems and Processes in Mechanics* (pp. 117–126). Solid Mechanics and Its Applications. Dordrecht: Springer.

Guckenheimer, J., & Holmes, P. J. (1983). *Nonlinear oscillations, dynamical systems and bifurcation of vector fields*. New York: Springer.

Hajjaj, A. Z., Ramini, A. H., Alcheikh, N., & Younis, M. I. (2017). Electrothermally tunable arch resonator. *Journal of Microelectromechanical Systems, 26*(4), 837–845.

Hornstein, S., & Gottlieb, O. (2008). Nonlinear dynamics, stability and control of the scan process in noncontacting atomic force microscopy. *Nonlinear Dynamics, 54*(1), 93–122.

Jeong, B., Cho, H., Keum, H., Kim, S., McFarland, M. D., Bergman, L. A., et al. (2014). Complex nonlinear dynamics in the limit of weak coupling of a system of microcantilevers connected by a geometrically nonlinear tunable nanomembrane. *Nanotechnology, 25,* 465501.

المنارة للاستشارات

Kacem, N., Baguet, S., Hentz, S., & Dufour, R. (2011). Computational and quasi-analytical models for non-linear vibrations of resonant MEMS and NEMS sensors. *International Journal of Non-Linear Mechanics, 46,* 532–542.

Kacem, N., & Hentz, S. (2009). Bifurcation topology tuning of a mixed behavior in nonlinear micromechanical resonators. *Applied Physics Letters, 95*(18), 183104.

Karabalin, R. B., Cross, M. C., & Roukes, M. L. (2009). Nonlinear dynamics and chaos in two coupled nanomechanical resonators. *Physical Review B, 79,* 165309.

Kozinsky, I., Postma, H. W. C., Kogan, O., Husain, A., & Roukes, M. L. (2007). Basins of attraction of a nonlinear nanomechanical resonator. *Physical Review Letters, 99,* 207201.

Krylov, S., & Dick, N. (2010). Dynamic stability of electrostatically actuated initially curved shallow micro beams. *Continuum Mechanics and Thermodynamics, 22*(6–8), 445–468.

Krylov, S., Ilic, B. R., & Lulinsky, S. (2011). Bistability of curved microbeams actuated by fringing electrostatic fields. *Nonlinear Dynamics, 3*(66), 403–426.

Krylov, S., Ilic, B. R., Schreiber, D., Serentensky, S., & Craighead, H. (2008). The pull-in behavior of electrostatically actuated bistable microstructures. *Journal of Micromechanics and Microengineering, 18*(5), 055026.

Lansbury, A. N., Thompson, J. M. T., & Stewart, H. B. (1992). Basin erosion in the twin-well Duffing oscillator: Two distinct bifurcation scenarios. *International Journal of Bifurcation and Chaos, 2,* 505–532.

Lenci, S., & Rega, G. (2003). Optimal control of nonregular dynamics in a Duffing oscillator. *Nonlinear Dynamics, 33,* 71–86.

Lenci, S., & Rega, G. (2004). A unified control framework of the nonregular dynamics of mechanical oscillators. *Journal of Sound and Vibration, 278*(4–5), 1051–1080.

Lenci, S., & Rega, G. (2006). Control of pull-in dynamics in a nonlinear thermoelastic electrically actuated microbeam. *Journal of Micromechanics and Microengineering, 16,* 390–401.

Lenci, S., & Rega, G. (2011a). Experimental versus theoretical robustness of rotating solutions in a parametrically excited pendulum: A dynamical integrity perspective. *Physica D: Nonlinear Phenomena, 240,* 814–824.

Lenci, S., & Rega, G. (2011b). Load carrying capacity of systems within a global safety perspective. Part I. Robustness of stable equilibria under imperfections. *International Journal of Non-Linear Mechanics*, *46*, 1232–1239.

Lenci, S., & Rega, G. (2011c). Load carrying capacity of systems within a global safety perspective. Part II. Attractor/basin integrity under dynamic excitations. *International Journal of Non-Linear Mechanics*, *46*, 1240–1251.

Lenci, S., Rega, G., & Ruzziconi, L. (2013). Dynamical integrity as a conceptual and operating tool for interpreting/predicting experimental behavior. *Philosophical Transactions of the Royal Society of London A*, *371*(1993), 20120423-1–20120423-19.

Mahboob, I., Dupuy, R., Nishiguchi, K., Fujiwara, A., & Yamaguchi, H. (2016). Hopf and period-doubling bifurcations in an electromechanical resonator. *Applied Physics Letters, 109,* 073101.

Medina, L., Gilat, R., Ilic, B., & Krylov, S. (2014). Experimental investigation of the snap-through buckling of electrostatically actuated initially curved pre-stressed micro beams. *Sensors and Actuators, A: Physical, 220,* 323–332.

Medina, L., Gilat, R., & Krylov, S. (2012). Symmetry breaking in an initially curved micro beam loaded by a distributed electrostatic force. *International Journal of Solids and Structures, 49*(13), 1864–1876.

Medina, L., Gilat, R., & Krylov, S. (2016). Bistable behavior of electrostatically actuated initially curved micro plate. *Sensors and Actuators, A: Physical, 248,* 193–198.

Mestrom, R. M. C., Fey, R. H. B., Phan, K. L., & Nijmeijer, H. (2010). Simulations and experiments of hardening and softening resonances in a clamped-clamped beam MEMS resonator. *Sensors and Actuators, A: Physical, 162*(2), 225–234.

Mestrom, R. M. C., Fey, R. H. B., van Beek, J. T. M., Phan, K. L., & Nijmeijer, H. (2008). Modelling the dynamics of a MEMS resonator: Simulations and experiments. *Sensors and Actuators, A: Physical, 142,* 306–315.

المنارة للاستشارات

Nayfeh, A. H., & Balachandran, B. (1995). *Applied nonlinear dynamics*. New York: Wiley.
Nayfeh, A. H., & Younis, M. I. (2005). Dynamics of MEMS resonators under superharmonic and subharmonic excitations. *Journal of Micromechanics and Microengineering, 15,* 1840–1847.
Nayfeh, A. H., Younis, M. I., & Abdel-Rahman, E. M. (2005). Reduced-order models for MEMS applications. *Nonlinear Dynamics, 41,* 211–236.
Nayfeh, A. H., Younis, M. I., & Abdel-Rahman, E. M. (2007). Dynamic pull-in phenomenon in MEMS resonators. *Nonlinear Dynamics, 48*(1–2), 153–163.
Nguyen, V.-N., Baguet, S., Lamarque, C.-H., & Dufour, R. (2015). Bifurcation-based micro/nanoelectromechanical mass detection. *Nonlinear Dynamics, 79,* 647–662.
Nusse, H. E., & Yorke, J. A. (1998). *Dynamics: Numerical explorations*. New York, Heidelberg, Berlin: Springer.
Orlando, D., Gonçalves, P. B., Rega, G., & Lenci, S. (2011). Influence of modal coupling on the nonlinear dynamics of Augusti's model. *ASME Journal of Computational and Nonlinear Dynamics*, *6*, 041014-1–041014-11.
Ouakad, H. M., & Younis, M. I. (2010). The dynamic behavior of MEMS arch resonators actuated electrically. *International Journal of Non-Linear Mechanics, 45*(7), 704–713.
Ouakad, H. M., & Younis, M. I. (2011). Natural frequencies and mode shapes of initially curved carbon nanotube resonators under electric excitation. *Journal of Sound and Vibrations, 330,* 3182–3195.
Ouakad, H. M., & Younis, M. I. (2012). Dynamic response of slacked carbon nanotube resonators. *Nonlinear Dynamics, 67,* 1419–1436.
Ramini, A. H., Bellaredj, M. L. F., Al Hafiz, M. A., & Younis, M. I. (2016a). Experimental investigation of snap-through motion of in-plane MEMS shallow arches under electrostatic excitation. *Journal of Micromechanics and Microengineering*, *26*, 015012.
Ramini, A. H., Hajjaj, A. Z., & Younis, M. I. (2016b). Tunable resonators for nonlinear modal interactions. *Scientific Report, 6,* 34717.
Ramini, A. H., Hennawi, Q. M., & Younis, M. I. (2016c). Theoretical and experimental investigation of the nonlinear behavior of an electrostatically-actuated in-plane MEMS arch. *Journal of Microelectromechanical Systems, 25*(3), 570–578.
Rega, G., & Lenci, S. (2005). Identifying, evaluating, and controlling dynamical integrity measures in nonlinear mechanical oscillators. *Nonlinear Analysis, 63,* 902–914.
Rega, G., & Lenci, S. (2008). Dynamical integrity and control of nonlinear mechanical oscillators. *Journal of Vibration and Control, 14,* 159–179.
Rega, G., & Lenci, S. (2015). A global dynamics perspective for system safety from macro- to nanomechanics: Analysis, control, and design engineering. *Applied Mechanics Reviews*, *67*, 050802-1–050802-19.
Rega, G., & Salvatori, A. (1996). Bifurcation structure at 1/3-subharmonic resonance in an asymmetric nonlinear elastic oscillator. *International Journal of Bifurcation and Chaos, 6*(8), 1529–1546.
Rega, G., Salvatori, A., & Benedettini, F. (1995). Numerical and geometrical analysis of bifurcation and chaos for an asymmetric elastic nonlinear oscillator. *Nonlinear Dynamics, 7,* 259–272.
Rega, G., & Settimi, V. (2013). Bifurcation, response scenarios and dynamic integrity in a single-mode model of noncontact atomic force microscopy. *Nonlinear Dynamics, 73*(1–2), 101–123.
Rega, G., & Troger, H. (2005). Dimension reduction of dynamical systems: Methods, models, applications. *Nonlinear Dynamics, 41*(1–3), 1–15.
Rhoads, J. F., Kumar, V., Shaw, S. W., & Turner, K. L. (2013). The non-linear dynamics of electromagnetically actuated microbeam resonators with purely parametric excitations. *International Journal of Non-Linear Mechanics, 55,* 79–89.
Rhoads, J. F., Shaw, S. W., & Turner, K. L. (2006a). The nonlinear response of resonant microbeam systems with purely-parametric electrostatic actuation. *Journal of Micromechanics and Microengineering, 16*(5), 890–899.
Rhoads, J. F., Shaw, S. W., & Turner, K. L. (2010). Nonlinear dynamics and its applications in micro- and nanoresonators. *Journal of Dynamic Systems, Measurement, and Control, 132*(3), 034001.

المنارة للاستشارات

Rhoads, J. F., Shaw, S. W., Turner, K. L., Moehlis, J., & DeMartini, B. E. (2006b). Generalized parametric resonance in electrostatically actuated microelectromechanical oscillators. *Journal of Sound and Vibration, 296*(4–5), 797–829.

Ruzziconi, L., Bataineh, A. M., Younis, M. I., Cui, W., & Lenci, S. (2013a). Nonlinear dynamics of an electrically actuated imperfect microbeam resonator: Experimental investigation and reduced-order modeling. *Journal of Micromechanics and Microengineering*, *23*(7), 075012-1–075012-14.

Ruzziconi, L., Lenci, S., & Younis, M. I. (2013b). An imperfect microbeam under an axial load and electric excitation: Nonlinear phenomena and dynamical integrity. *International Journal of Bifurcation and Chaos*, *23*(2), 1350026-1–1350026-17.

Ruzziconi, L., Younis, M. I., & Lenci, S. (2012). An efficient reduced-order model to investigate the behavior of an imperfect microbeam under axial load and electric excitation. *ASME Journal of Computational and Nonlinear Dynamics*, *8*, 011014-1–011014-9.

Ruzziconi, L., Younis, M. I., & Lenci, S. (2013c). An electrically actuated imperfect microbeam: Dynamical integrity for interpreting and predicting the device response. *Meccanica, 48*(7), 1761–1775.

Ruzziconi, L., Younis, M. I., & Lenci, S. (2013d). Dynamical integrity for interpreting experimental data and ensuring safety in electrostatic MEMS. In M. Wiercigroch & G. Rega (Eds.), *IUTAM Symposium on Nonlinear Dynamics for Advanced Technologies and Engineering Design* (pp. 249–261). IUTAM Bookseries. Dordrecht: Springer.

Ruzziconi, L., Younis, M. I., & Lenci, S. (2013e). Multistability in an electrically actuated carbon nanotube: A dynamical integrity perspective. *Nonlinear Dynamics, 74*(3), 533–549.

Ruzziconi, L., Younis, M. I., & Lenci, S. (2013f). Parameter identification of an electrically actuated imperfect microbeam. *International Journal of Non-Linear Mechanics, 57,* 208–219.

Sazonova, V., Yaish, Y., Üstünel, H., Roundy, D., Arias, T. A., & McEuen, P. L. (2004). A tunable carbon nanotubes electromechanical oscillator. *Nature, 431,* 284–287.

Seleim, A., Towfighian, S., Delande, E., Abdel-Rahman, E. M., & Heppler, G. (2012). Dynamics of a close-loop controlled MEMS resonator. *Nonlinear Dynamics, 69,* 615–633.

Sensata Technologies. Retrieved August 31, 2017, from http://www.sensata.com.

Senturia, S. D. (2001). *Microsystem design*. Dordrecht: Kluwer Academic Publishers.

Settimi, V., Gottlieb, O., & Rega, G. (2015). Asymptotic analysis of a noncontact AFM microcantilever sensor with external feedback control. *Nonlinear Dynamics, 79*(4), 2675–2698.

Settimi, V., & Rega, G. (2016a). Exploiting global dynamics of a noncontact atomic force microcantilever to enhance its dynamical robustness via numerical control. *International Journal of Bifurcation and Chaos*, *26*, 1630018-1–1630018-17.

Settimi, V., & Rega, G. (2016b). Global dynamics and integrity in noncontacting atomic force microscopy with feedback control. *Nonlinear Dynamics, 86*(4), 2261–2277.

Settimi, V., & Rega, G. (2016c). Influence of a locally-tailored external feedback control on the overall dynamics of a non-contact AFM model. *International Journal of Non-Linear Mechanics, 80,* 144–159.

Soliman, M. S., & Thompson, J. M. T. (1989). Integrity measures quantifying the erosion of smooth and fractal basins of attraction. *Journal of Sound and Vibration, 135,* 453–475.

Soliman, M. S., & Thompson, J. M. T. (1992). Global dynamics underlying sharp basin erosion in nonlinear driven oscillators. *Physical Review A, 45*(6), 3425–3431.

Sumali, H., Younis, M. I., & Abdel-Rahman, E. M. (2008). Special issue on micro- and nano-electromechanical systems. *Nonlinear Dynamics, 54,* 1–2.

Szemplińska-Stupnicka, W. (1992). Cross-well chaos and escape phenomena in driven oscillators. *Nonlinear Dynamics, 3,* 225–243.

Szemplińska-Stupnicka, W., & Tyrkiel, E. (1997). Sequences of global bifurcations and the related outcomes after crisis of the resonant attractor in a nonlinear oscillator. *International Journal of Bifurcation and Chaos, 7,* 2537–2557.

Thompson, J. M. T. (1989). Chaotic phenomena triggering the escape from a potential well. *Proceedings of the Royal Society of London A, 421,* 195–225.

المنارة للاستشارات

Thompson, J. M. T., Rainey, R. C. T., & Soliman, M. S. (1990). Ship stability criteria based on chaotic transients from incursive fractals. *Philosophical Transactions of the Royal Society of London A, 332*(1624), 149–167.

Tusset, A. M., Balthazar, J. M., Bassinello, D. G., Pontes, B. R., Jr., & Felix, J. L. P. (2012). Statements on chaos control designs, including a fractional order dynamical system, applied to a "MEMS" comb-drive actuator. *Nonlinear Dynamics, 69,* 1837–1857.

Üstünel, H., Roundy, D., & Arias, T. A. (2005). Modeling a suspended nanotube oscillator. *Nano Letters, 5*(3), 523–526.

Venstra, W. J., Westra, H. J. R., & van der Zant, H. S. J. (2010). Mechanical stiffening, bistability, and bit operations in a microcantilever. *Applied Physics Letters, 97*(19), 193107.

Villaggio, P. (1997). *Mathematical models for elastic structures*. Cambridge: Cambridge University Press.

Villanueva, L. G., Karabalin, R. B., Matheny, M. H., Chi, D., Sader, J. E., & Roukes, M. L. (2013). Nonlinearity in nanomechanical cantilevers. *Physical Review B, 87*(2), 024304.

Westra, H. J. R., Poot, M., van der Zant, H. S. J., & Venstra, W. J. (2010). Nonlinear modal interactions in clamped-clamped mechanical resonators. *Physical Review Letters, 105,* 117205.

Xu, T., Ruzziconi, L., & Younis, M. I. (2017). Global investigation of the nonlinear dynamics of carbon nanotubes. *Acta Mechanica, 228*(3), 1029–1043.

Younis, M. I. (2011). *MEMS linear and nonlinear statics and dynamics*. New York: Springer.

Younis, M. I., Abdel-Rahman, E. M., & Nayfeh, A. H. (2003). A reduced-order model for electrically actuated microbeam-based MEMS. *Journal of Microelectromechnical Systems, 12*(5), 672–680.

Younis, M. I., & Alsaleem, F. M. (2009). Exploration of new concepts for mass detection in electrostatically-actuated structures based on nonlinear phenomena. *ASME Journal of Computational and Nonlinear Dynamics, 4,* 021010.

Younis, M. I., & Nayfeh, A. H. (2003). A study of the nonlinear response of a resonant microbeam to an electric actuation. *Nonlinear Dynamics, 31*(1), 91–117.

Younis, M. I., Ouakad, H., Alsaleem, F. M., Miles, R., & Cui, W. (2010). Nonlinear dynamics of MEMS arches under harmonic electrostatic actuation. *Journal of Microelectromechanical Systems, 19*(3), 647–656.

Zhang, W., Baskaran, R., & Turner, K. (2002). Tuning the dynamic behavior of parametric resonance in a micromechanical oscillator. *Applied Physics Letters, 82*(1), 130–132.

المنارة للاستشارات

Nonlinear Dynamics, Safety, and Control of Structures Liable to Interactive Unstable Buckling

Paulo B. Gonçalves, Diego Orlando, Frederico M. A. Silva, Stefano Lenci and Giuseppe Rega

Abstract The nonlinear dynamics of two archetypal structural systems exhibiting interactive modal post-buckling behavior is addressed, the discrete Augusti's model and a reduced-order model of the axially loaded cylindrical shell. The uncoupled models exhibit a stable post-buckling response. However, the modal interaction leads to unstable post-buckling paths that entail a complex dynamic behavior and imperfection sensitivity, with a marked influence on the dynamic integrity and safety. Perfect and imperfect Augusti's models are investigated in terms of static buckling, linear vibrations, nonlinear normal modes, local and global nonlinear response to harmonic excitation, dynamic integrity, control of global bifurcations aimed at increasing the load carrying capacity. Then, as an example of a continuous system exhibiting strong modal coupling and interaction, a two-degree-of-freedom model of the thin-walled cylindrical shell is investigated in terms of global behavior and dynamic integrity. The influence of uncertainties on the nonlinear response and dynamic integrity is also shortly addressed. The chapter shows how a judicious use of the tools of nonlinear

P. B. Gonçalves (✉)
Department of Civil Engineering, Pontifical Catholic University, Rio de Janeiro, Brazil
e-mail: paulo@puc-rio.br

D. Orlando
Department of Mechanics and Energy – FAT, University of State of Rio de Janeiro, Resende, Brazil
e-mail: dgorlando@gmail.com

F. M. A. Silva
School of Civil and Environmental Engineering, Federal University of Goiás, Goiânia, Brazil
e-mail: silvafma@gmail.com

S. Lenci
Department of Civil and Building Engineering, and Architecture, Polytechnic University of Marche, Ancona, Italy
e-mail: lenci@univpm.it

G. Rega
Department of Structural and Geotechnical Engineering, Sapienza University of Rome, Rome, Italy
e-mail: giuseppe.rega@uniroma1.it

© CISM International Centre for Mechanical Sciences 2019

S. Lenci and G. Rega (eds.), *Global Nonlinear Dynamics for Engineering Design and System Safety*, CISM International Centre for Mechanical Sciences 588,
https://doi.org/10.1007/978-3-319-99710-0_4

المنارة للاستشارات

dynamics sheds light on the actual safety of structural systems liable to unstable buckling under static and dynamic loads.

Keywords Structural instability · Interactive buckling · Dynamic integrity
Control of global bifurcations · System safety and load carrying capacity

1 Introduction

Stability represents a fundamental research area in theoretical and applied mechanics, which must be fully understood to increase the load carrying capacity of structures and to ensure their safety against collapse in the presence of external disturbances. The theory of stability is of crucial importance in scientific fields as diverse as solid mechanics, electronics, chemistry, cosmology, and ecology. Mathematically, the theory of stability is what is referred to as the bifurcation analysis. Slender civil, space, aerospace, nuclear, offshore, and naval structures have traditionally been designed to work below their critical load, obtained usually through a linear stability analysis, because any instability is normally identified as connected to failure or loss of functionality. However, performing linearization in state space at the critical point of the parameter space does not provide sufficient information to predict what kind of behavior the system may exhibit under finite perturbations. In recent years, the simultaneous use of the theory of elastic stability and the theory of nonlinear dynamical systems has provided more powerful tools to analyze the overall behavior of structural systems liable to buckling and quantify their integrity in a dynamic environment. Also, the stability analysis of structures has received a new impetus due to the use of multi-stable mechanisms, which have an impact on many high-tech applications such as stretchable electronics, nanotube serpentines, snapping surfaces, foldable and deployable structures, morphing structures, nano- and microstructures under electromagnetic forces, as well as on sensors and flexible actuators and vibration absorbers.

Some important references on the theory of elastic stability include Croll and Walker (1972), Thompson and Hunt (1973, 1984) and Bazant and Cedolin (1991). For a good introduction on the basics of local bifurcation analysis, the reader is referred to Guckenheimer and Holmes (1984), Wiggins (1990) and Kuznetsov (2004). For an overview of the theory of nonlinear dynamical systems the reader is referred to the works by Nayfeh and Mook (2008) and Thompson and Stewart (2002) while the numerical aspects are treated in Seydel (1988), Doedel et al. (1991) and Nayfeh and Balachandran (1995), among others.

The developments of the theory of elastic stability in the past century led to the identification of several structures liable to unstable pitchfork or asymmetric bifurcation. Such systems display for load levels lower than the static buckling load more than one equilibrium position and the stable pre-buckling position is sensitive to imperfections and dynamic disturbances which may lead to escape from the safe pre-buckling potential well. The design of such systems is one of the main con-

المنارة للاستشارات

cerns of a structural engineer. A particularly dangerous case is when the structural system displays coincident or nearly coincident buckling loads and the interaction of different stable buckling modes leads to unstable coupled post-buckling branches (Croll and Walker 1972; Thompson and Hunt 1973, 1984; Bazant and Cedolin 1991). Continuous structures displaying coincident or nearly coincident buckling loads are, among others, plates, shells, thin-walled beams, and some frame structures. A particularly notorious case is the cylindrical shell under axial compression, which, as shown by Koiter (Van der Heijden 2008), may display for certain geometries an infinite number of coincident buckling loads. In such cases, the pre-buckling safe solution may be surrounded by several saddles, leading to several local and global bifurcations and, consequently, a complex topology of the phase space.

Simple phenomenological buckling models made up of rigid links and elastic springs have served to illustrate the most important phenomena in the study of elastic buckling. Some of these models are very useful for explaining or understanding the different types of coupled instabilities. Gioncu (1994) presents a general report on the theory of coupled instabilities in the light of extensive developments in the previous century containing over 230 papers. He reviews the principal aspects, phenomena, theories, and methods as well as applications to structural elements and structures. Among these phenomenological models, the well-known discrete two-degree-of-freedom Augusti's model (Augusti 1964; Bazant and Cedolin 1991; Raftoyiannis and Kounadis 2000; Orlando et al. 2011a, b) has become the archetypal model of interactive unstable buckling. Other simplified models displaying the same behavior are found in the literature (Thompson and Hunt 1984; Hunt et al. 1979; Jansen 1977; Sophianopoulos 2007; Thompson and Gaspar 1977; Gioncu 1994; Orlando et al. 2013a, b). Recently, Dubina and Ungureanu (2014) published a review paper summarizing several mode interaction problems, with an emphasis on the relationship between the generalized imperfection and the erosion of theoretical buckling strength of a member undergoing local and global buckling mode interaction.

Here, Augusti´s model is used to understand the influence of interactive buckling and coupled instabilities on the structures' safety and dynamic integrity. Initially, the stability analysis of the perfect models is conducted, including the identification of all pre- and post-critical equilibrium paths, and the effect of imperfections on the load carrying capacity of the structure and stability of the various equilibrium paths. The purpose of this analysis is to understand how the various unstable post-critical solutions and imperfections influence the geometry of the potential energy surface, the contour of the pre-buckling potential well, and the integrity of the structure under the inevitable external disturbances. Then, the behavior of the models in free vibration is investigated, including the identification of the natural frequencies, nonlinear vibration modes, and possible internal resonances. To understand the dynamics of the models, the geometry of the safe region surrounding the pre-buckling equilibrium position and the invariant manifolds of saddle points that define this region are obtained using the tools of Hamiltonian mechanics. Also, as part of the free vibrations analysis, all stable and unstable nonlinear vibration modes and their frequency–amplitude relations are obtained. These nonlinear stable and unstable modes, which arise due to modal coupling and the symmetries of the models, govern and explain

المنارة للاستشارات

the dynamics of the model under forced vibration. Based on these results, we study the behavior of the models subjected to a base excitation through a systematic study of the local and global bifurcations, and the robustness of stable solutions through the evolution and stratification of the basins of attraction and their dynamic integrity measures. Finally, we study how to increase the safety of the structure through the control of global homoclinic and heteroclinic bifurcations. This chapter concludes with a brief analysis of a reduced-order model of an axially excited cylindrical shell, which is one of the most complex examples of a continuous slender structure exhibiting strong modal coupling and interaction, and with some comments on the influence of uncertainties and noise on the dynamic integrity.

This chapter is organized as follows. In Sect. 2, the governing equations describing the dynamics of Augusti's model are obtained, and the main dynamical issues are discussed. The buckling and post-buckling analysis of the perfect and imperfect model is studied in Sect. 3, while in Sect. 4 the linear vibration analysis and the nonlinear normal modes are obtained and the influence of symmetries on the static and dynamic analysis is highlighted. Section 4 shows the forced response of Augusti's model under a harmonic base excitation, including a detailed bifurcation analysis, the stability boundaries in force control space and the evolution of the basins of attraction, including the erosion profiles. Based on these results, Sect. 4 also presents the integrity measures, which report a measure of the system safety versus the increasing load, and presents a control technique developed to increase these integrity measures. A single-degree-of-freedom (s.d.o.f.) model with its Hamiltonian and perturbed dynamics, which are particularly useful in showing the control performances, is described together with the formulation and analysis of the control method. In Sect. 7, a consistent reduced-order model for the analysis of cylindrical shells under axial load is deduced and used to study the global behavior and dynamic integrity of the shell. Section 8 discusses briefly the influence of uncertainties on the nonlinear response and dynamic integrity measures. The chapter ends with some conclusions (Sect. 9).

2 A Discrete Archetypal System for Interactive Unstable Buckling

The authors have in recent years conducted an extensive analysis on the nonlinear dynamics of some archetypal systems for interactive unstable buckling, including Augusti's model and a simplified model of a guyed mast proposed by Thompson and co-workers (Thompson and Hunt 1984). Orlando et al. (2011a, b) investigated in detail the nonlinear dynamics and imperfection sensitivity of Augusti's model with emphasis on the influence of modal coupling on the stability boundaries, bifurcations, and basins evolution due to variation of system parameters, leading to the determination of erosion profiles and integrity measures which enlightened the loss of safety of the structure due to penetration of eroding fractal tongues into the safe basin.

المنارة للاستشارات

Later, Orlando et al. (2013a) investigated, using Augusti's model and the simplified model of a guyed mast, how system symmetries, the symmetry-breaking effect of initial geometric imperfections and energy level influence the number and stability of the nonlinear normal modes and the existence of multimode solutions in structural systems liable to unstable buckling. Lenci et al. (2012a, b) applied a method for controlling the global nonlinear dynamics of Augusti's model and the inverted guyed pendulum to increase the safety of these structures in a dynamic environment. A detailed analysis of the inverted guyed pendulum can be found in Orlando et al. (2013b).

Augusti's model, as shown in Fig. 1a, consists of an inverted spatial pendulum composed of a slender, rigid (but massless) bar of length l, with a tip-mass m in a gravitational field of constant acceleration g, pinned at the base and stabilized laterally by two rotational springs with constant stiffness k_1 and k_2 that are initially located in two perpendicular planes and rotate with the bar. Figure 1b shows the deformed configuration of the geometrically perfect system and the variables used in the derivation of the equations of motion. Let φ_i be the angles between the pendulum rod and the three Cartesian coordinate axes, as shown in Fig. 1b, then the cosines of φ_i must obey the geometrical constraint $\cos^2\varphi_1+\cos^2\varphi_2+\cos^2\varphi_3=1$. Thus, the projection of the pendulum length onto the z-axis is $\Delta=l\cos\varphi_3=l(1-\cos^2\varphi_1-\cos^2\varphi_2)^{1/2}$. The angles $\theta_i=(\pi/2)-\varphi_i$, $(i=1,2)$, are chosen as the two-degree-of-freedom of the inverted pendulum. They measure the spring deformation in Augusti's model.

For the geometrically imperfect column, the initial configuration is defined by the angles ϕ and ψ shown in Fig. 1c, where the two angles φ_{i0} that define the rod position in the Cartesian reference frame are also reported. The deformed configuration of the imperfect model is illustrated in Fig. 1d. The angle ϕ measures the initial inclination of the unloaded bar (a small initial geometric imperfection) and the angle ψ denotes the direction of the projected imperfect bar onto the $x\times y$ plane. Hence, the angles ϕ_i are the magnitudes of the geometric imperfection in the θ_i directions. The angles γ_1 and γ_2 are, respectively, the deformations of the springs in the θ_1 and θ_2 directions ($\theta_1=\phi_1+\gamma_1$, $\theta_2=\phi_2+\gamma_2$). These angular quantities are related by

$$l\cos\varphi_{10}=l\sin\phi_1\cos\psi,\quad \phi_1=(\pi/2)-\varphi_{10} \tag{1a}$$

$$l\cos\varphi_{20}=l\sin\phi_2\sin\psi,\quad \phi_2=(\pi/2)-\varphi_{20}. \tag{1b}$$

When considering the forced dynamics, the system is subjected to a harmonic base excitation, $D_b(t)$, acting at an angle φ with respect to the x-axis (Fig. 1a). $D_b(t)$ is decomposed into two orthogonal components, $u_b(t)=F_b\cos\varphi\sin(\omega_e t)$ in the x-direction and $v_b(t)=F_b\sin\varphi\sin(\omega_e t)$ in the y-direction, where F_b is the excitation base displacement and ω_e the excitation frequency.

The kinetic energy is written in terms of θ_i as (Orlando et al. 2013a)

المنارة للاستشارات

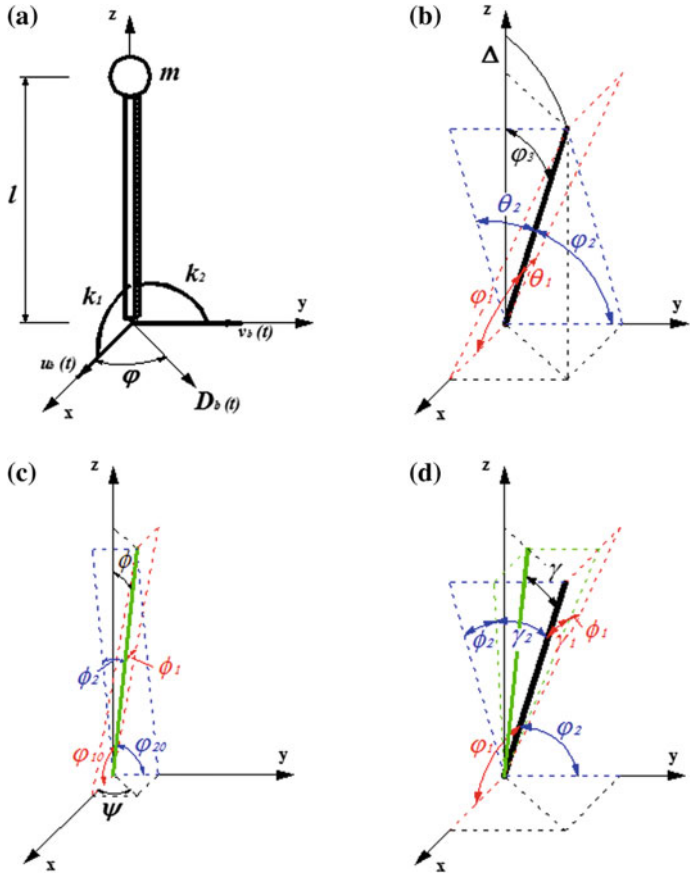

Fig. 1 Augusti's two-degree-of-freedom model. Perfect system: **a** undeformed and **b** deformed configuration. Imperfect system: **c** undeformed and **d** deformed configuration

$$T = \frac{1}{2}m\Big((l\dot{\theta}_1\cos\theta_1 + \dot{u}_b)^2 + (l\dot{\theta}_2\cos\theta_2 + \dot{v}_b)^2 + \frac{l^2\big(\dot{\theta}_1\cos\theta_1\sin\theta_1 + \dot{\theta}_2\cos\theta_2\sin\theta_2\big)^2}{\cos^2\theta_1 + \cos^2\theta_2 - 1}\Big), \tag{2}$$

where the dot indicates differentiation with respect to time t.

The total potential energy of the imperfect system is given by

$$\Pi = U + V = \frac{1}{2}k_1(\theta_1 - \phi_1)^2 + \frac{1}{2}k_2(\theta_2 - \phi_2)^2 - Pl\left(\sqrt{1 - \sin^2\phi_1 - \sin^2\phi_2} - \sqrt{1 - \sin^2\theta_1 - \sin^2\theta_2}\right), \tag{3}$$

المنارة للاستشارات

where U and V are the strain energy and the potential energy of the applied load $P = mg$, respectively.

In order to consider viscous damping with coefficients C_i in the equations of motion, the work of the nonconservative forces is added to the energy functional as

$$E = \frac{1}{2}C_1\dot{\theta}_1^2 + \frac{1}{2}C_2\dot{\theta}_2^2. \tag{4}$$

First, the nonlinear equilibrium equations of the imperfect system are obtained by the use of the stationary energy principle

$$\frac{\partial(\Pi)}{\partial\theta_i} = 0; i = 1, 2.$$

The stable static equilibrium configuration θ_{is} within the safe pre-buckling potential well corresponding to a given load level and imperfection and the nonlinear equilibrium paths are obtained by solving the equilibrium equations by the Newton–Raphson method together with continuation techniques.

Then a dynamic perturbation θ_{id} is added to the static displacement field:

$$\theta_i(t) = \theta_{is} + \theta_{id}(t). \tag{6}$$

The reference for the dynamic response is the static deformed configuration, thus the variation of the total potential energy of the system between the static and perturbed configurations reads $\Pi = (U_t - U_s) + (V_t - V_s)$ and the Lagrange function is defined as

$$L\left(\theta_{id}, \dot{\theta}_{id}\right) = T - [(U_t - U_s) + (V_t - V_s)]. \tag{7}$$

Finally, the equations of undamped motion of the perturbed imperfect pre-loaded system are obtained

$$\frac{d}{dt}\frac{\partial(T)}{\partial\dot{\theta}_{id}} - \frac{\partial(T)}{\partial\theta_{id}} + \frac{\partial\left(\prod\right)}{\partial\theta_{id}} = 0. \tag{8}$$

Through this procedure, the static configuration becomes the origin of the phase space. For the perfect system, the reference static configuration reduces to the trivial solution, $\theta_{is} = 0$. The natural frequencies ω_{0i} of the imperfect pre-loaded system and the corresponding vibration mode shapes Φ_i are obtained by linearizing the equations of motion and solving the resulting eigenvalue problem. The explicit equations of motion for the Augusti's model are given in Orlando et al. (2011b).

For the conservative model, the Hamiltonian, H, is the total energy of the system, that is, $H = T + \Pi$ is constant.

المنارة للاستشارات

3 Static Buckling Analysis

For the perfect Augusti's model, the following homogeneous system of linearized equilibrium equations is obtained:

$$[k_1 - Pl]\theta_1 = 0; \quad [k_2 - Pl]\theta_2 = 0; \tag{9}$$

The linearized equations of motion have no coupling terms and the perfect system has two bifurcation loads given by $P_1 = k_1/l$ and $P_2 = k_2/l$. The respective orthogonal eigenvectors are given by $\{1, 0\}^T$ and $\{0, 1\}^T$. The buckling behavior is a function of the relative stiffness of the springs, $\alpha = k_1/k_2$. For $\alpha = 1$, $P_1 = P_2 = k/l$ and a degenerate eigenvalue problem is obtained where any vector can be an eigenvector of the system. Thus, for $\alpha \approx 1$ the two bifurcation loads are nearly equal leading to possible modal interaction. The influence of the relative stiffness of the springs on the static buckling behavior is now analyzed. Figure 2a shows the post-buckling paths of the perfect models with $\alpha = 1$, where $\lambda = P/P_{cr}$ with $P_{cr} = k/l$, thus $\lambda_{cr} = 1$. The fundamental path is stable up to the static critical load. Four post-buckling paths are identified: two ascending unstable paths, which correspond to the two uncoupled solutions (U2 for $\theta_1 = 0$ and U1 for $\theta_2 = 0$) and the two coupled descending unstable orthogonal paths at 45° (C1 for $\theta_1 = \theta_2$ and C2 for $\theta_1 = -\theta_2$). These four post-critical paths are associated with the four planes of symmetry of the structural system. The uncoupled system with one spring in the θ_1 plane has been traditionally used as an example of stable post-buckling behavior (Croll and Walker 1972). The coupling of two otherwise stable modes leads to the unstable solutions shown in Fig. 2a. Figure 2b shows the potential energy surface for a static load level $\lambda = 0.9 < \lambda_{cr}$ as well as the isoenergetic curves on the $\theta_1 \times \theta_2$ plane. For any value of λ between 0 and 1, there is a minimum corresponding to the stable pre-buckling solution, surrounded by four saddles at the same energy level. These saddles correspond to the unstable post-buckling configurations along the descending unstable paths. As λ increases, the safe basin shrinks and disappears at $\lambda = \lambda_{cr}$ (Gonçalves and Santee 2008; Gonçalves et al. 2011; Silva and Gonçalves 2015). Figure 3 shows two suitable projections of the stable and unstable manifolds of the saddles. Two pairs of heteroclinic orbits, each pair connecting two opposite saddles (S1–S3 and S2–S4) at ±45° are identified, each manifold contained within a plane of symmetry. These manifolds are obtained by integrating the nonlinear equations of motion of the unforced undamped system, with initial conditions in the vicinity of the relevant saddles (Lenci et al. 2012a, b).

Figure 2c and 2d shows the fundamental solution and the post-critical paths for, respectively, $\alpha = 1.05$ and $\alpha = 1.50$ ($k_1 > k_2$). The fundamental equilibrium path ($\theta_1 = \theta_2 = 0$) and the initial uncoupled post-critical path associated with k_2 are stable. The other post-critical paths are unstable. For $\alpha \neq 1$, the coupled unstable descending paths emerge from a secondary subcritical bifurcation along the post-critical path associated with k_2. This secondary bifurcation moves away from the primary bifurcation as α increases and, for sufficiently large values of α, the system behaves as a system of one-degree-of-freedom with a stable symmetric bifurcation. Keeping k_2

المنارة للاستشارات

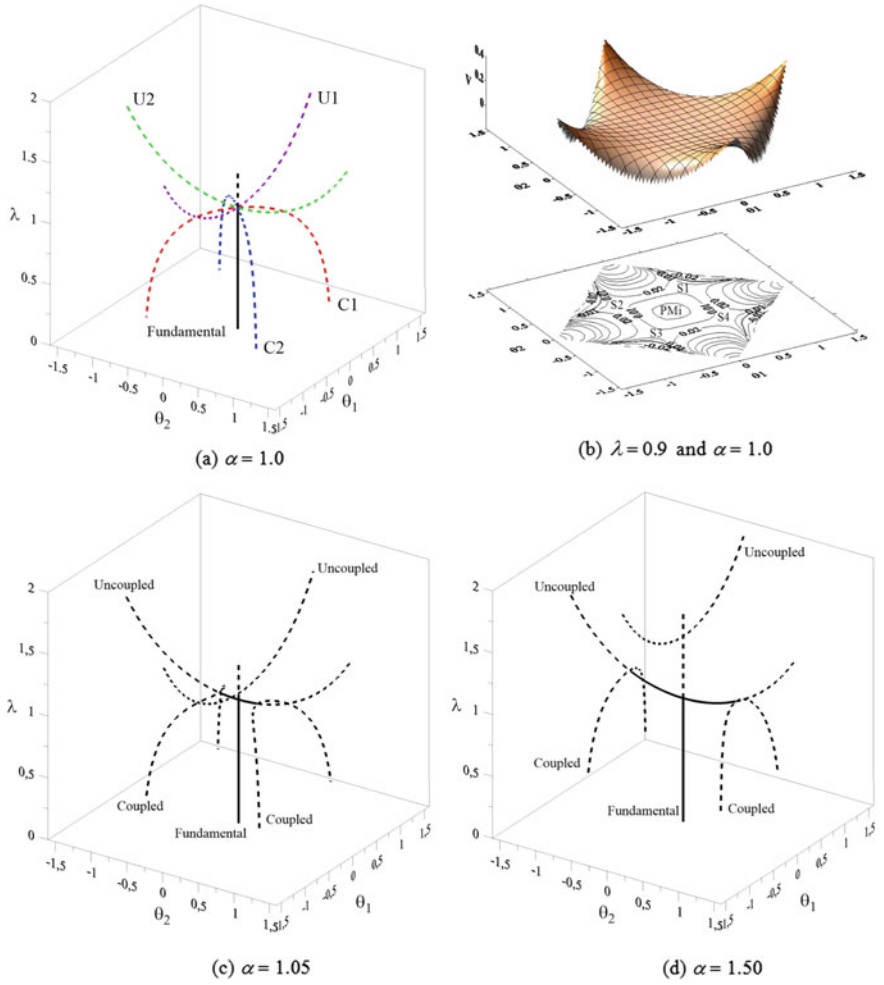

Fig. 2 Fundamental and post-buckling equilibrium paths for three values of the stiffness parameter. In (**b**), S: Saddles, PMi: Stable position corresponding to a local minimum

constant and increasing k_1, α increases and the bifurcation load associated with k_1 increases while the critical load associated with k_2 remains constant, decreasing the possibility of modal interaction. For $\alpha = 1.05$ and $\alpha = 1.50$, the system also displays the four saddle points surrounding the stable pre-buckling position for load levels lower than the critical load. However, they gradually move away from the stable equilibrium position as α increases, thereby increasing the safe region.

The results in Fig. 2 illustrate the main features of interactive buckling: new coupled equilibrium paths appear, coexisting with those of the uncoupled systems and the otherwise stable ascending equilibrium paths become unstable. These features have,

المنارة للاستشارات

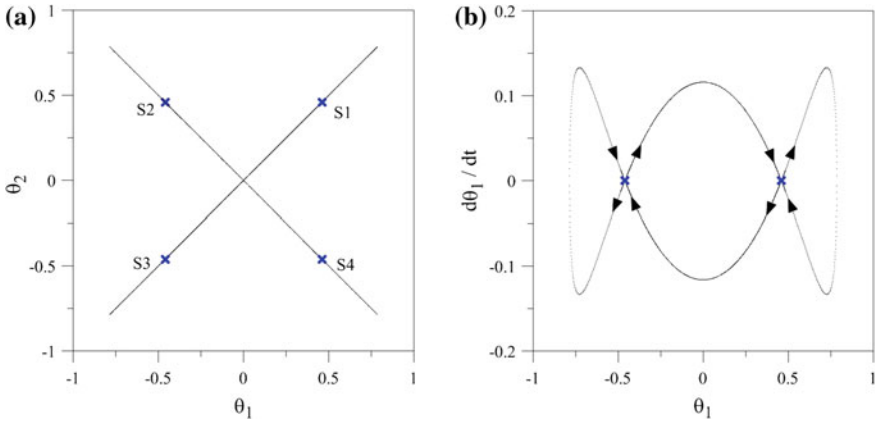

Fig. 3 Two projections of the stable and unstable manifolds of the saddles that define the boundary of the safe pre-buckling region. $\lambda = 0.9$

as shown here, a huge influence on the topology of the potential energy surface and, consequently, on the ensuing nonlinear dynamics. The results also show that a simplified modeling that does not consider the possible modal interactions may lead to the unsafe design and catastrophic failure of the structural system. So, possible modal interaction must be investigated whenever equal or nearly equal bifurcation loads are obtained from the linearized eigenvalue buckling problem. It is also observed that symmetries, often found in structural systems, are closely connected with interactive buckling (Jensen et al. 1999; Orlando et al. 2013a). Thereafter, the results are concentrated on the results for $\alpha = 1$, where the influence of modal interaction can be better observed and discussed.

It is well known that small imperfections influence the response of structural systems liable to buckling, in particular, systems exhibiting unstable symmetric or asymmetric bifurcation (Croll and Walker 1972; Thompson and Hunt 1984; Bazant and Cedolin 1991), where the load carrying capacity is eroded by increasing imperfections (Gonçalves and Santee 2008). In such cases, the structure is said to be imperfection sensitive. The nonlinear equilibrium paths for the imperfect Augusti's model with $\alpha = 1$, $\psi = 0°$, and $\phi = 1°$ are illustrated in Fig. 4a. The point of multiple bifurcations in Fig. 2a is destroyed by the imperfection and the imperfect system under increasing static loading displays a stable nonlinear equilibrium path contained in the $x \times y$ plane (θ_1 plane), since $\psi = 0°$, which becomes unstable due to a subcritical pitchfork bifurcation. This solution is the same as that of the imperfect s.d.o.f. system with stable post-critical behavior up to the bifurcation point where it becomes unstable. The critical load is lower than that of the perfect system, $\lambda_{cr} = 0.955698$, as expected for an imperfection-sensitive system. Four additional unstable coupled paths and three secondary bifurcations corresponding to the perturbed unstable post-buckling paths of Fig. 2a are observed. These paths converge to those of the perfect system as the imperfection magnitude goes to zero. The safe region is defined by

المنارة للاستشارات

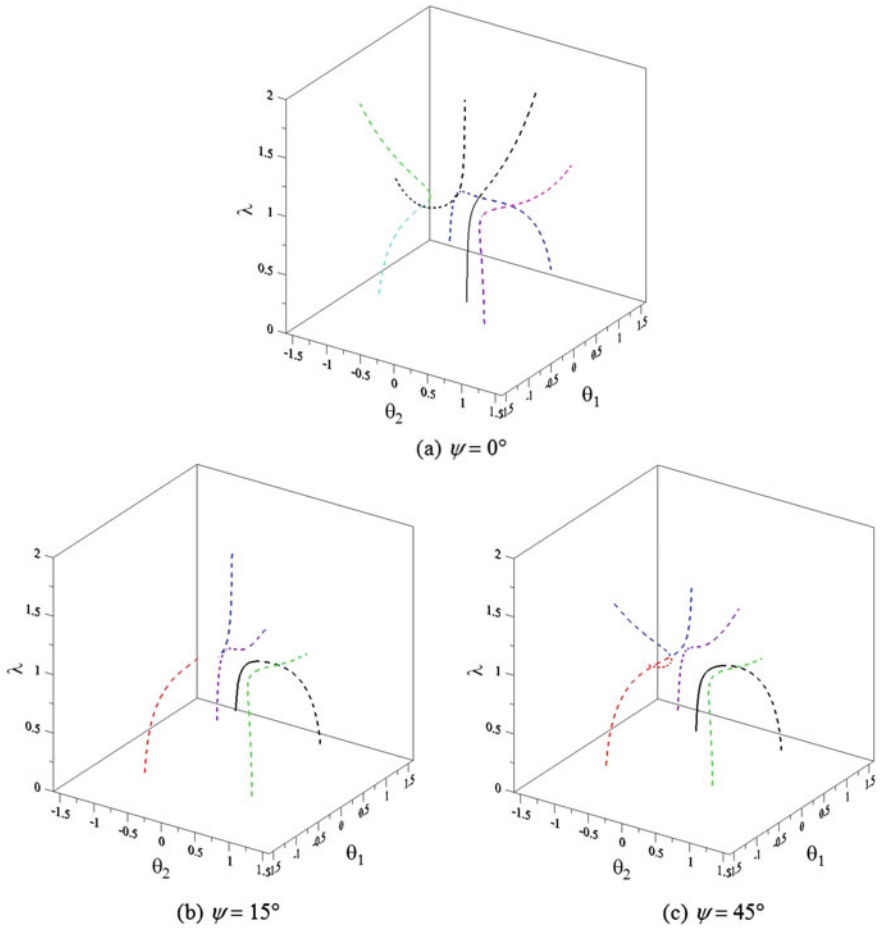

Fig. 4 Nonlinear equilibrium paths for the imperfect model with $\phi = 1°$

the saddles S1 and S4 at the same energy level ($H = 0.006189$), Fig. 5b, associated with the bifurcated unstable solution (saddles S2 and S3 are at a higher energy level, $H = 0.02402$). Each of the saddles S1 and S4 is associated with a homoclinic orbit, arising from the perturbed heteroclinic orbits shown in Fig. 5b. However, they no longer are in a plane manifold, as illustrated in the two projections shown in Fig. 6b.

Now an imperfection in the direction of one of the diagonal symmetry planes, specifically $\psi = 45°$ and $\phi = 1°$, is considered. Figure 4c shows the response of the imperfect system under static loading. In this case, the nonlinear stable path loses stability at a limit point and the maximum load is even lower than in the previous imperfection case, $\lambda_{cr} = 0.928767$. Again, several unstable complementary paths are observed. In the present case, the safe region is bounded by the saddle at the lowest energy level (saddle S1 at $H = 0.003239$), as shown in Fig. 5d, which is associated

المنارة للاستشارات

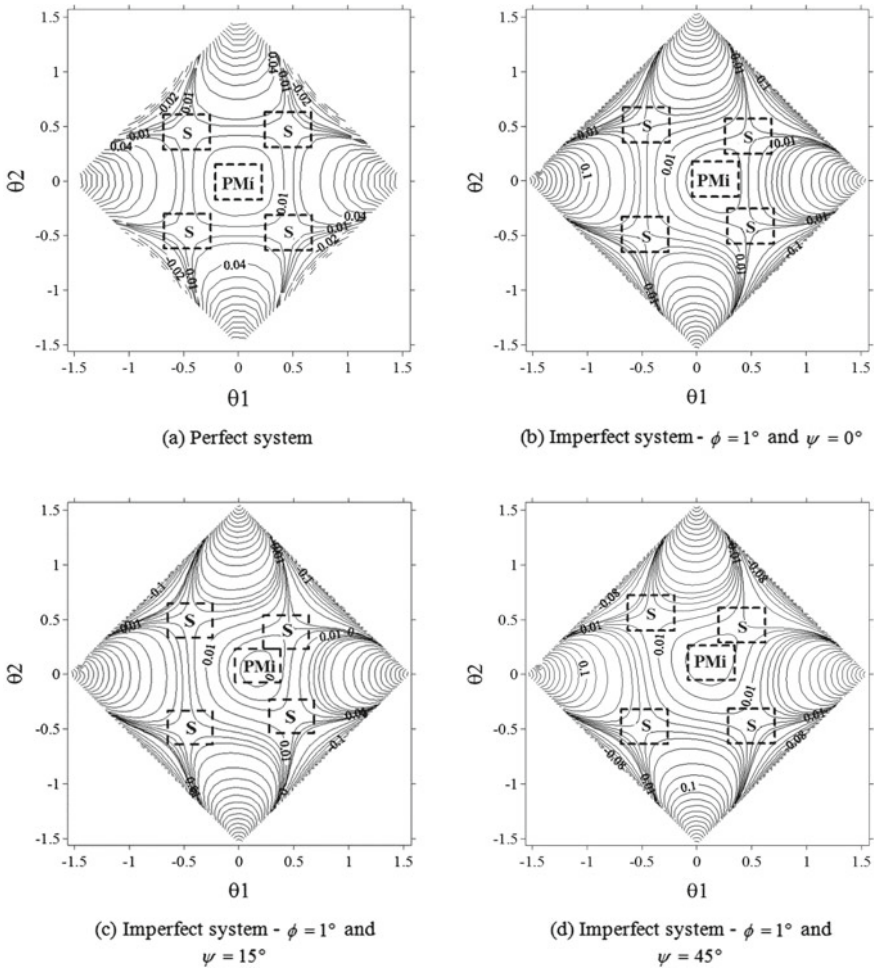

Fig. 5 Curves of equal potential energy for $\lambda = 0.9$. Perfect and imperfect system

with a homoclinic orbit contained in a plane at 45°, Fig. 6c. Saddles S2 and S4 are at the same energy level, $H = 0.014628$, and saddle S3 is at $H = 0.028297$.

Finally, Figs. 4b and 5c show the response for an imperfection defined by $\psi = 15°$ and $\phi = 1°$, where the fundamental path, as in Fig. 4b, loses its stability at a limit point. However, the unstable complementary paths are different from those in Fig. 4c, leading to a different energy landscape.

The conservative safe basin of attraction of the perfect system, Fig. 7a, is clearly delimited by the four saddle points. The presence of several symmetries is observed in this region, reflecting those of the physical model. The geometric imperfections cause various changes in the response. In addition to the symmetry-breaking effects on the topology of the energy landscape, which depends on the type and magnitude of

المنارة للاستشارات

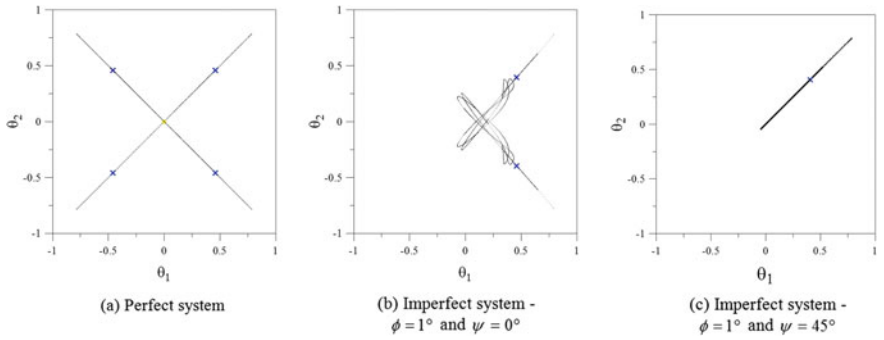

Fig. 6 Manifolds for $\lambda = 0.9$ and $\omega_p = 1.0/s$. Perfect and imperfect system

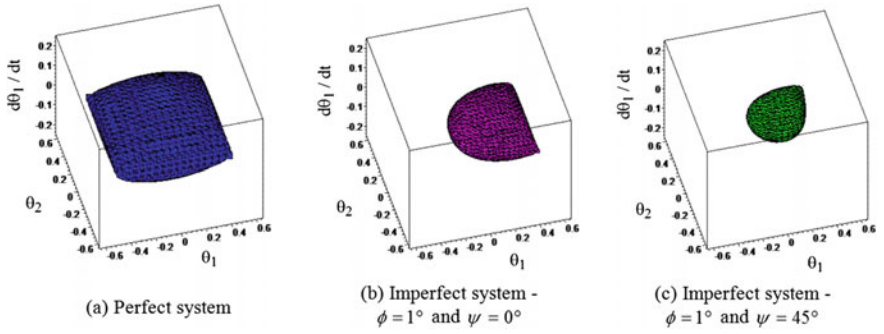

Fig. 7 Three-dimensional sections of safe pre-buckling region for $\lambda = 0.9$ and $\omega_p = 1.0/s$. Perfect and imperfect system

the imperfection, the safe region decreases considerably, significantly reducing the set of initial conditions that lead the system to oscillate around the stable fixed point of the pre-critical solution. Another striking effect is the change in the connections between the saddle points. When $\psi = 0°, 90°, 180°, 270°$ and $\phi \neq 0°$, the safe region is bounded by two saddle points, Fig. 7b. When $\psi \neq 0°, 90°, 180°, 270°$ and $\phi \neq 0°$ (see Fig. 7c for $\psi = 45°$) the safe region is bounded by one saddle point.

These results show how the relative stiffness and initial geometric imperfections change the potential energy landscape, and, therefore, influencing markedly the vibration characteristics and nonlinear dynamics of the model, as it will be shown in the upcoming sections.

4 Linear Vibration Analysis and Nonlinear Normal Modes

Symmetries that lead to interactive buckling can also generate multiple nonlinear vibration modes associated with the same natural frequency. For the perfect Augusti's

المنارة للاستشارات

model, the following homogeneous system of linearized equations of motion is obtained:

$$\begin{bmatrix} 1 & 0 \\ 0 & 1 \end{bmatrix} \begin{Bmatrix} \ddot{\theta}_1 \\ \ddot{\theta}_2 \end{Bmatrix} + (1-\lambda)\frac{\omega_p^2}{\lambda} \begin{bmatrix} 1 & 0 \\ 0 & 1 \end{bmatrix} \begin{Bmatrix} \theta_1 \\ \theta_2 \end{Bmatrix} = \begin{Bmatrix} 0 \\ 0 \end{Bmatrix}. \tag{10}$$

The linearized equations of motion have no coupling terms and the perfect system has two equal natural frequencies, $\omega_1 = \omega_2 = \omega_p\ [(1/\lambda) - 1]^{1/2}$, with $\omega_p = (g/l)^{1/2}$, leading to possible 1:1 internal resonance. Hence, a degenerate eigenvalue problem is again obtained and any pair of linearly independent vectors in the space defined by θ_i can be chosen as eigenvectors (Jordan and Smith 2007). Thus, the linear system is equivalent to two uncoupled oscillators. The coupling is only through the nonlinear terms in the equations of motion. Thus, the kind of possibly coupled nonlinear response depends on the initial conditions and imperfections and on the energy level. However, the system symmetries and internal resonance may lead to a number of nonlinear normal modes (NNMs) greater than the number of degrees of freedom of the discrete model.

NNMs can be regarded as a generalization of linear normal modes. The initial concept was introduced by Rosenberg (1960, 1966), who defined a NNM of a discrete, conservative, nonlinear system as a synchronous periodic oscillation where all material points of the system reach their extreme values or pass through zero simultaneously. In 1991, Shaw and Pierre (1991) introduced a more general concept of NNMs. They define NNMs as motions on invariant manifolds which are tangent to, and of the same dimension as, the linear eigenspaces in the system phase space. A feature of NNMs that has no counterpart in the linear theory is that their number may exceed the number of degrees of freedom (superabundance of modes). Due to mode bifurcations, not all NNMs can be regarded as a nonlinear continuation of the underlying linear modes, and these bifurcating NNMs are essentially nonlinear with no linear counterparts. Modes generated through internal resonances are one example. Another example corresponds to the generation of additional fundamental NNMs due to symmetry (Peeters et al. 2009; Vakakis and Rand 1992). These two features are found in Augusti's model. These modes may be stable or unstable, while in the linear theory they are neutrally stable. Several methods are proposed in the literature for calculating NNMs based on perturbation expansions such as multiple scale analysis (Nayfeh and Nayfeh 1994; Nayfeh et al. 1996) and invariant manifold method (Shaw and Pierre 1991; Boivin et al. 1995; Pesheck et al. 2001; Gavassoni et al. 2014, 2015). They provide analytical expressions of NNMs, but are limited to weak nonlinearities or small amplitudes.

For low-dimensional systems, the application of Poincaré maps is an efficient tool to determine numerically the existence of NNMs. For the conservative model, fixing the energy level of the Hamiltonian $H = T + \Pi$, one can restrict the flow of the dynamical system to a three-dimensional isoenergetic surface. This is achieved by setting $H = h$, where h is the adopted energy level. If the three-dimensional isoenergetic region is cut by a 2D plane and the flow is transverse to this plane

المنارة للاستشارات

(Wiggins 1990), the resulting cross-section Σ is two-dimensional and defines the Poincaré map.

Techniques for obtaining the Poincaré maps of two-dimensional systems are presented in Month and Rand (1980), Orlando (2010). Using this technique, one can determine the overall flow of the dynamical system sufficiently close to each mode, and thus obtain a complete and detailed description of nonlinear modes and their stability. Stationary modes correspond to stationary points in the Poincaré section. They are stable if they are centers (elliptical fixed points) and unstable if they are saddles (hyperbolic points). For an energy level higher than that of one of the saddles that define the boundary of the safe pre-buckling well, $H = h_{sd}$, no stable solution and consequently no stable mode can be found. Thus, this energy level corresponding to the maximum equipotential surface is used as a reference upper bound in the present analysis.

Figure 8 shows two Poincaré sections for 50% of h_{sd} for $\lambda = 0.9$ and $\omega_p = 1.0/s$. These sections show the existence of several stable and unstable nonlinear modes. The centers Pij (point i of section j) shown in Fig. 8 are related to four nonlinear modes. Their modal lines, which correspond to the motion of the top mass in the configuration space, are shown in Fig. 9. In nonlinear systems, the modal lines can be either a straight line (similar mode) or a curve (non-similar mode). Each mode is contained within one of the four symmetry planes of the perfect structure which are also the two-dimensional invariant manifolds of these modes. A number of similar modes greater than the number of d.o.f. are due to the simultaneous effect of symmetry and internal resonance. The modes are characterized as follows: M1 (point P02) by $\theta_2 = 0$, M2 (point P01) by $\theta_1 = 0$, M3 (points P11 and P12) by $\theta_1 = \theta_2 = u/(2)^{1/2}$ (in-phase mode), and M4 (points P21 and P22) by $\theta_1 = -\theta_2 = u/(2)^{1/2}$ (out-of-phase mode), see Figs. 8 and 9a. Hence, modes M1 and M2 correspond to uncoupled modes, while modes M3 and M4 correspond to coupled stationary modes. Figure 10a shows the frequency–amplitude relation of mode M1 which is analogous to that of mode M2. These two modes display a hardening behavior. As shown in Figs. 2b or 5a, the potential energy along the axes is a one well potential (the energy increases with θ). The potential energy profile in these planes has a positive curvature with increasing stiffness (declivity), as observed in Fig. 2b. Figure 10b shows the frequency–amplitude relation for mode M3, which is similar to mode M4 in the perpendicular direction. In this case, the modes show a strong softening behavior and their stability is bounded by the two heteroclinic orbits.

When adding a small geometric imperfection, it will act as a detuning parameter and the singularity disappears leading to two different (but close) natural frequencies and two linearly independent orthogonal eigenvectors (linear normal modes). Figure 9b–d show the modal lines for $\phi = 1°$ and three values of ψ for two given energy levels, where one similar mode M1 (point P02) and one non-similar mode M2 (point P01) are identified. They result from the perturbation of modes M1 and M2 in Fig. 9a due to the small geometric imperfection. Mode M1 ($\theta_2 = 0$) of the perfect system is unaffected since the imperfection direction is just along the symmetry plane $\theta_2 = 0$, thus preserving the symmetry of the structure in the perpendicular direction (i.e., along θ_2); in contrast, the similar mode M2 ($\theta_1 = 0$) of the perfect

المنارة للاستشارات

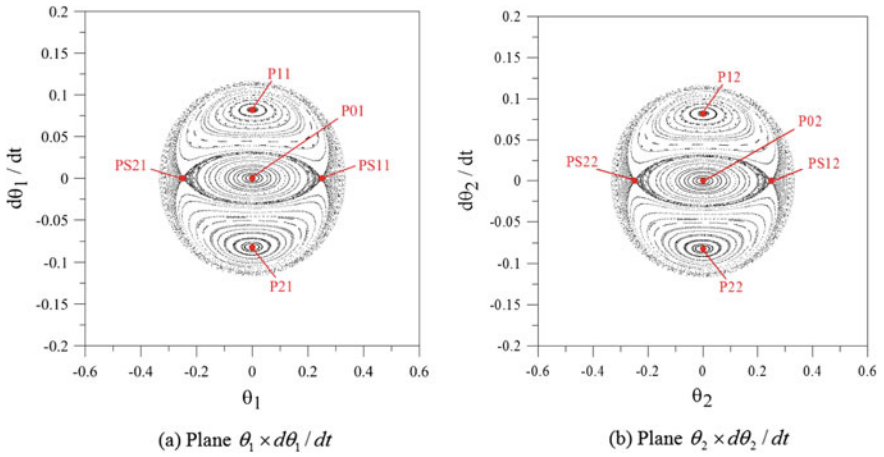

Fig. 8 Poincaré sections for increasing energy level. $\lambda = 0.9$, $\omega_p = 1.0/s$, and 50% h_{sd}

system becomes non-similar due to the symmetry-breaking effect of the imperfection in the perpendicular direction (i.e., along θ_1). The imperfection also destroys the internal resonance and two distinct natural frequencies are now obtained, $\omega_1 = 0.311$ (non-similar mode) and $\omega_2 = 0.353$ (similar mode). However, they remain very close, due to the inherent symmetry of the original system.

Now consider an imperfection in the direction of one of the diagonal symmetry planes, specifically $\psi = 45°$ and $\phi = 1°$ (direction of the mode M3 of the perfect system), Fig. 9a. For a given energy level (50% h_{sd}), two modes (one similar M3 and one non-similar M4) are detected, Fig. 9c. As in the previous imperfection case, they emanate from the modes M3 and M4 of the perfect system, Fig. 9a. For this imperfection case, the nearly commensurate natural frequencies and linear modes are: $\omega_1 = 0.302$, $\{1, 1\}^T$ (similar mode) and $\omega_2 = 0.361$, $\{1, -1\}^T$ (non-similar mode). Now general imperfections that break all symmetries of the original system are considered. Let us consider an imperfection defined by $\psi = 10°$ and $\phi = 1°$, Fig. 9d.

By varying the values of ψ, it is observed that for general imperfections no similar mode can be found, since all symmetries are lost. In general, two non-similar modes emanating from the two independent linear modes are observed.

Figure 11a shows for $\phi = 1°$ and $\psi = 0°$ the bifurcation diagram for the nonlinear mode P01 as a function of the energy level. To illustrate the two observed bifurcations, Fig. 11b–d show the Poincaré sections for three energy levels. At $h = 50\%$ h_{sd} a pitchfork bifurcation of the nonlinear mode is perceived, where the original stable mode (P01) becomes unstable originating two new stable modes (P11 and P21). At $h = 85.5\%$, h_{sd} a period doubling bifurcation of each of the stable modes P11 and P21 is perceived, thus increasing the number of NNMs and the complexity of the system dynamics.

المنارة للاستشارات

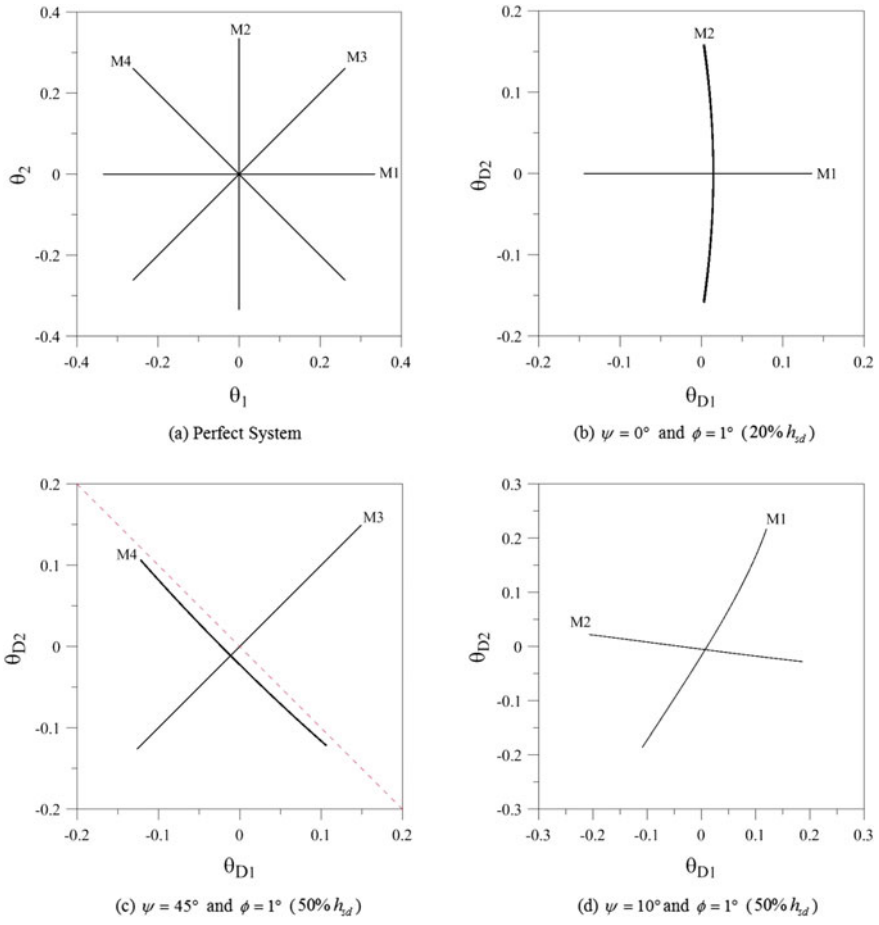

Fig. 9 Modal lines for different imperfections at appropriate energy levels. $\phi = 1°$, $\lambda = 0.9$, and $\omega_p = 1.0/s$

5 Nonlinear Dynamic Analysis of the Forced System

Now the behavior of Augusti's model under harmonic base excitation with dimensionless frequency $\Omega = \omega_e/\omega_p$ is investigated in order to understand the influence of the interactive buckling, symmetries and nonlinear normal modes on the nonlinear dynamics, bifurcations, and instabilities of the system.

First the importance of the multiplicity of NNMs and their nonlinear frequency–amplitude characteristics as to the behavior of the structure under external forcing is investigated. Figure 12a shows for selected values of the forcing direction φ, $F = 0.02$, $\lambda = 0.9$, and $\xi_1 = \xi_2 = 0.01$ (modal damping), the response of the perfect Augusti's model. For $\varphi = 0°$, the resonance curve is governed by the similar mode

المنارة للاستشارات

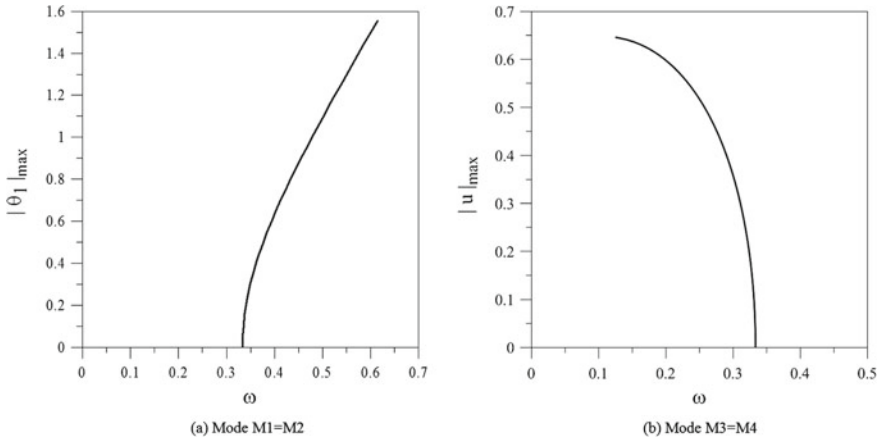

Fig. 10 Projection of frequency–amplitude relation for the modes M1, M2, M3, and M4. $\lambda = 0.9$, $\omega_p = 1.0/s$ and $\omega_1 = \omega_2 = 1/3$

M1, Fig. 9a, which, as shown in Fig. 10a, displays a hardening behavior. On the other hand, for $\varphi = 45°$, the resonance curve is governed by the similar mode M3, Fig. 9a, which, as shown in Fig. 10b, displays a strong softening behavior. In both cases, the forced response can be described by the s.d.o.f. reduced-order model associated with the specific NNM, that is, at any excitation frequency the dynamics of the original system is captured by the reduced-order model if the initial conditions are confined to the specific phase-plane (invariant manifold). For any value of φ different from those that define the four symmetry planes, both nonlinear modes influence the forced response which is necessarily coupled. This can be clearly observed in the results for $\varphi = 30°$ in Fig. 12a, where the resonance curve displays two peaks governed by the two contributing nonlinear modes.

Figure 12b shows the results for the imperfect Augusti's model considering $\psi = 45°$, $F = 0.01$, $\phi = 1°$, $\lambda = 0.9$, and $\xi_1 = \xi_2 = 0.01$. The resonance curves for selected values of the forcing direction φ show how the two nonlinear modes shown in Fig. 12b, in particular, the softening mode associated with the coupled response, influence their resonance curves.

These results show that the concept of NNM can be used to understand and model nonlinear dynamic phenomena that might have no counterparts in linear theory. In particular, the occurrence of superabundant modes, generated by the inherent symmetries of the structure and by bifurcations, leads to the existence of extra-peaks in the frequency response function, possibly associated to new phenomena, such as unexpected resonances, localization, and energy transfer (Vakakis et al. 1996, 2008).

Now the influence of modal interaction on the dynamic buckling (escape from the safe potential well) is analyzed. The escape load, F_{esc}, corresponds to escape of the response from the pre-buckling potential well in a slowly evolving system, which occurs upon the total annihilation of all in-well basins of attraction. In order

المنارة للاستشارات

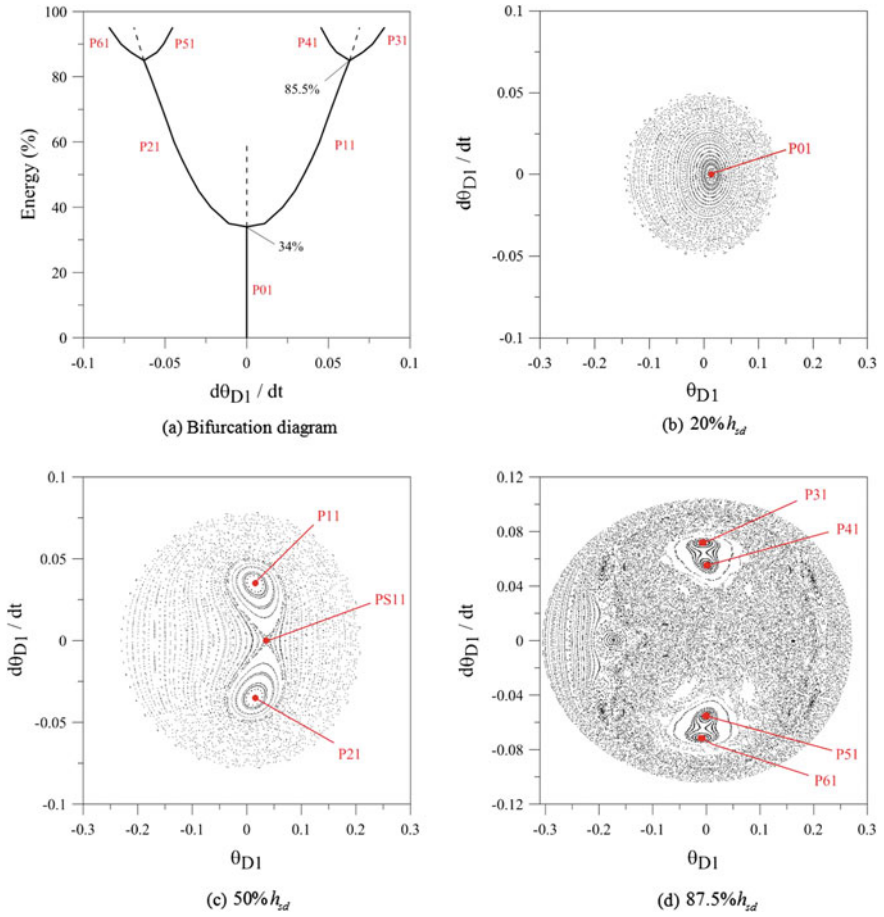

Fig. 11 **a** Bifurcation diagram of the nonlinear mode M2 as a function of the energy level. **b–d** Poincaré sections for increasing energy level. $\psi = 0°$, $\phi = 1°$, $\lambda = 0.9$, and $\omega_p = 1.0/s$

to understand the influence of modal coupling, the solutions using the coupled and uncoupled models are compared. First, the behavior of the perfect system with a forcing direction $\varphi = 0°$ is considered. Figure 13 shows the bifurcation diagrams for $\varphi = 0°$ and $\Omega = 1/3$ having as control parameter the forcing magnitude F. Two cases are considered: in Fig. 13a the uncoupled case, when perturbations only in θ_1 and $d\theta_1/dt$ are considered and only these coordinates are excited, and (b) the coupled case, when very small perturbations in θ_2 and $d\theta_2/dt$ are also considered after each load step ($\theta_2 = d\theta_2/dt = 0.001$), bringing about the coupling of the two modes. Although both diagrams display the same bifurcation sequence, leading to escape from the safe well, for even very small values of θ_2 and $d\theta_2/dt$, which entail coupling of the two modes, a drastic reduction in the escape load is observed, corroborating the importance of modal interaction in Augusti's model (and similar problems).

المنارة للاستشارات

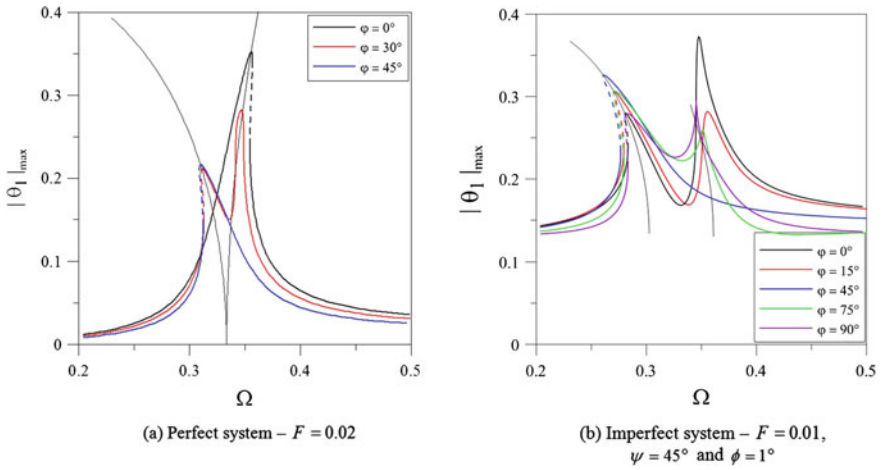

Fig. 12 Resonance curves—maximum vibration amplitude versus excitation frequency. Continuous line: stable, dashed line: unstable. $\lambda = 0.9$ and $\xi_1 = \xi_2 = 0.01$

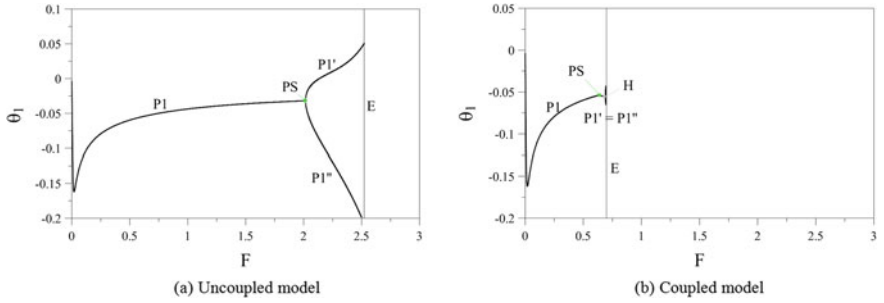

Fig. 13 Bifurcation diagrams for $\varphi = 0°$ and $\Omega = 1/3$. Coupled and uncoupled cases. PS: supercritical pitchfork bifurcation. H: Hopf bifurcation. E: escape

Figure 14 shows the basin of attraction of the bounded solution of the coupled and uncoupled system in the $\theta_1 \times d\theta_1/dt$ plane for a forcing magnitude $F = 0.1$. The black region corresponds to initial conditions that lead to safe motions within the pre-buckling well while white corresponds to solutions that diverge to infinity. The safe, continuous non-fractal basin of attraction of the uncoupled system (Fig. 14) is still relatively large since the considered $F = 0.1$ value is well below the escape threshold. In contrast, for the coupled system, the basin cross-section shows a drastic reduction of the safe basin area, since the forcing magnitude is nearer to the escape load. Thus, the modal interaction leads to a drastic reduction of the dynamic integrity of the system, corroborating the importance of the modal interaction between the buckling modes on its nonlinear dynamics.

By mapping the escape load through a sufficiently large number of bifurcation diagrams obtained by increasing slowly the forcing amplitude while holding the

المنارة للاستشارات

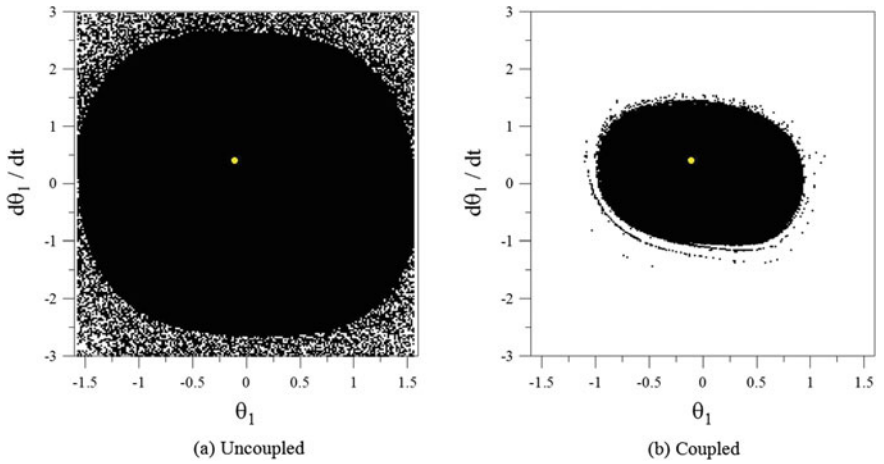

Fig. 14 Comparison of the basin of attraction of the coupled and uncoupled cases for $\varphi = 0°$, $F = 0.1$, and $\Omega = 1/3$

frequency constant in a forcing frequencies range which includes the fundamental parametric resonances ($\omega_e = \omega_i$) of the two modes and their principal, order 1/2 ($\omega_e = 2\omega_i$) or 1/3 (($\omega_e = 3\omega_i$) subharmonic, parametric resonances, the stability boundaries in force control space (load magnitude vs. forcing frequency) are obtained. Figure 15 shows stability boundaries for the forcing direction $\varphi = 0°$, considering the coupled and uncoupled cases. For the uncoupled case, the lowest values of the escape load occur in the neighborhood of the principal resonances ($\Omega = 2/3$ and $\Omega = 1$) of the two coinciding modes, as expected in a condition of parametric excitation. In contrast, quite high F_{esc} values do occur in the region of fundamental resonance ($\Omega = 1/3$). But for even very small values of θ_2 and $d\theta_2/dt$, which entail coupling of the two modes, a drastic reduction in the escape load is observed in the latter region. In fact, there is a marked difference between the relevant stability boundaries in the two cases, an overall reduction of the escape load in the whole excitation frequency range here analyzed is observed for the coupled case. The decrease in the escape load is followed by a significant decrease in the safe non-fractal area of the basin of attraction, as illustrated in Fig. 14b. These results show that to overlook essential interactions in structural modeling may lead to an unsafe design with unexpected and even dangerous consequences.

Figure 16 shows the stability boundaries for different values of the forcing direction φ. As observed, the forcing direction has a strong influence on the escape load due to the relative influence of the NNMs on the resonant behavior. Two different regions are observed. For $\Omega < 0.6$, the escape boundary has two minima in the vicinity of the natural frequency, with the lowest escape load occurring for $\phi = 0°$. For $\Omega > 0.6$, the major reduction occurs for $\varphi = 45°$, when the coupling effect is the highest one.

المنارة للاستشارات

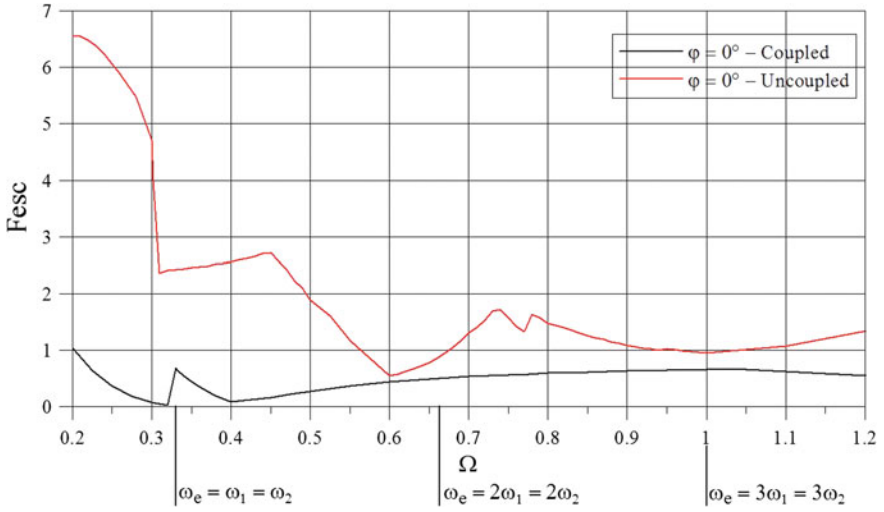

Fig. 15 Stability boundaries in force control space (load vs. forcing frequency) for the forcing direction $\varphi = 0°$, considering the coupled and uncoupled cases. F_{esc}: escape load

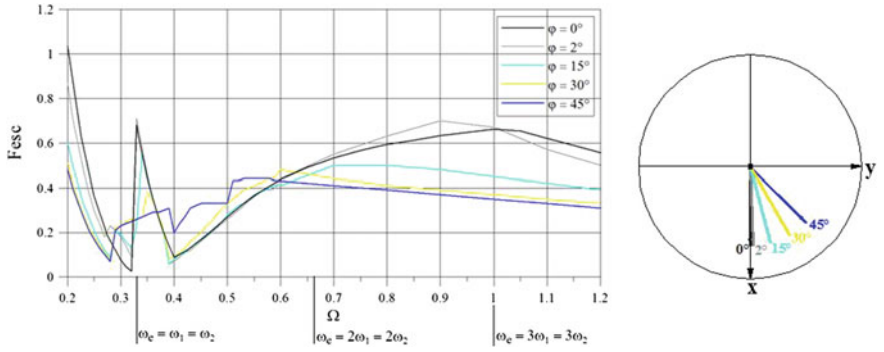

Fig. 16 Stability boundaries in force control space (load vs. forcing frequency) for different values of the forcing direction φ

Now the behavior of the system for $\varphi = 45°$ is analyzed in detail to understand how the sequence of bifurcations leading to escape changes with the forcing frequency. Figure 17 shows the bifurcation diagrams for two excitation frequencies, namely $\Omega = 1/3$ and $\Omega = 0.4$, illustrating in both cases the relevant local bifurcations. Figure 18 shows the loci of the relevant local bifurcations in the fundamental resonance region prior to escape together with the escape boundary. For small values of the forcing frequency, the escape is controlled by the saddle-node bifurcation A (SN A), as illustrated in Fig. 18, leading to a catastrophic bifurcation with a sudden jump to infinity (first descending branch). The following smooth ascending branch of the escape boundary is associated with a supercritical pitchfork bifurcation which is

المنارة للاستشارات

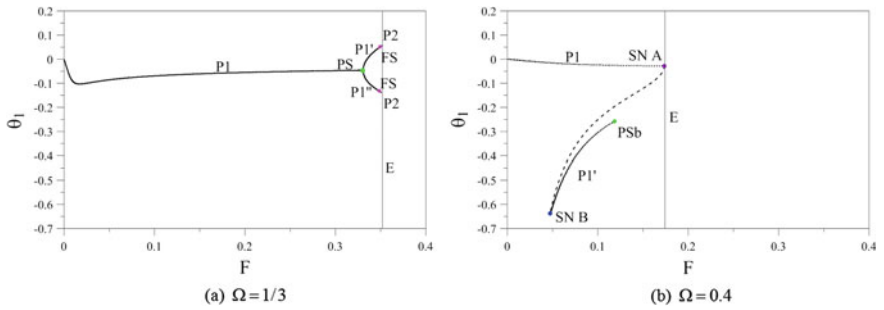

Fig. 17 Bifurcation diagrams for $\varphi = 45°$, illustrating the relevant local bifurcations for two excitation frequencies. SN: saddle-node, PS: supercritical pitchfork, PSb: subcritical pitchfork, FS: supercritical flip, E: escape

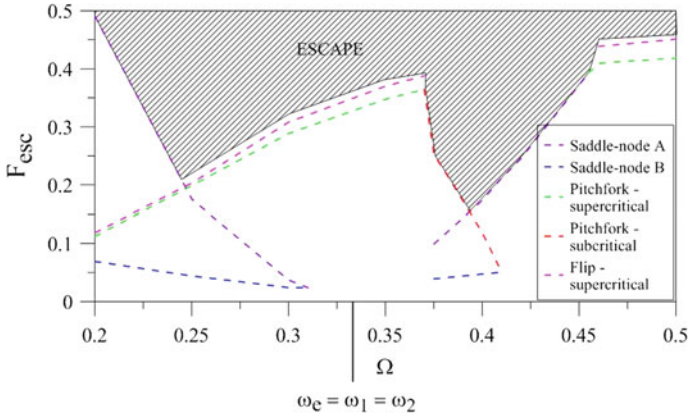

Fig. 18 Mapping of the local bifurcations in the fundamental resonance region prior to escape for $\varphi = 45°$

followed by a flip bifurcation, as illustrated in Fig. 17a. The change between saddle-node and pitchfork bifurcation corresponds to a local minimum of the escape load. The next descending branch of the escape boundary is due to a subcritical pitchfork bifurcation, leading again to a catastrophic jump to infinity. The subsequent ascending branch is connected with a saddle-node bifurcation.

The previous results have shown the significant influence of initial geometric imperfections on the equilibrium paths, load carrying capacity, and NNMs of the model. It is thus expected initial imperfection to have an equally substantial influence on the escape load. Figure 19 compares the stability boundaries for different frequency values for the perfect system and for the imperfect system considering $\phi = 1°$ and $\psi = 45°$. When imperfection is added, a significant decrease of the dynamic buckling load is observed with respect to the perfect system for any value of the forcing frequency Ω.

المنارة للاستشارات

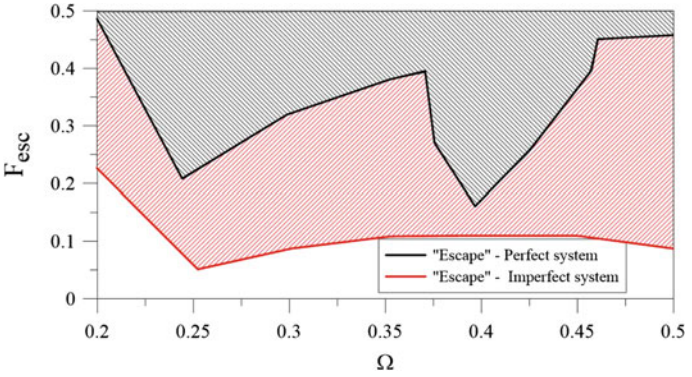

Fig. 19 Comparison of the escape boundary of the coupled perfect and imperfect ($\phi = 1°$ and $\psi = 45°$) system in the main resonance region. $\varphi = 45°$, $\lambda = 0.9$, and $\xi_1 = \xi_2 = 0.01$. Minimum escape load: $F_{esc} = 0.1653$ (perfect) and $F_{esc} = 0.0510$ (imperfect)

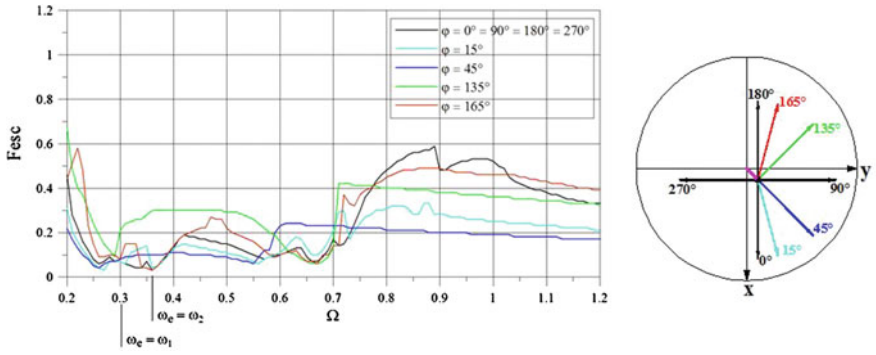

Fig. 20 Stability boundaries in force control space (load vs. forcing frequency) for different values of the forcing direction φ (see polar diagram) for the imperfect systems. $\phi = 1°$ and $\psi = 45°$

Figure 20 shows the stability boundaries for different values of the forcing direction φ, for the imperfect system considering $\phi = 1°$ and $\psi = 45°$. The results show a high imperfection sensitivity for all values of φ. Thus, the escape load depends not only on the imperfection magnitude and direction but also on the forcing direction. The decrease in the escape load is followed by a similar decrease in the safe basin area. Figure 21, where the $\theta_1 \times d\theta_1/dt$ cross-section of the basin of attraction of the perfect (well below the escape threshold, see Fig. 16) and imperfect (slightly below the escape threshold, see Fig. 20) system are compared, shows the influence of the imperfection on the basin of attraction for $\Omega = 1/3$, $F = 0.1$, and $\varphi = 0°$.

Finally, Fig. 22 shows the variation of the escape load with the column initial inclination ϕ for $\psi = 45°$. The escape load reduction already occurring for the perfect system owing to the $\varphi \neq 0°$ excitation direction is clearly visible for $\phi = 0°$. As the initial inclination ϕ increases the escape load smoothly decreases, but at $\phi = 1.2°$ it

المنارة للاستشارات

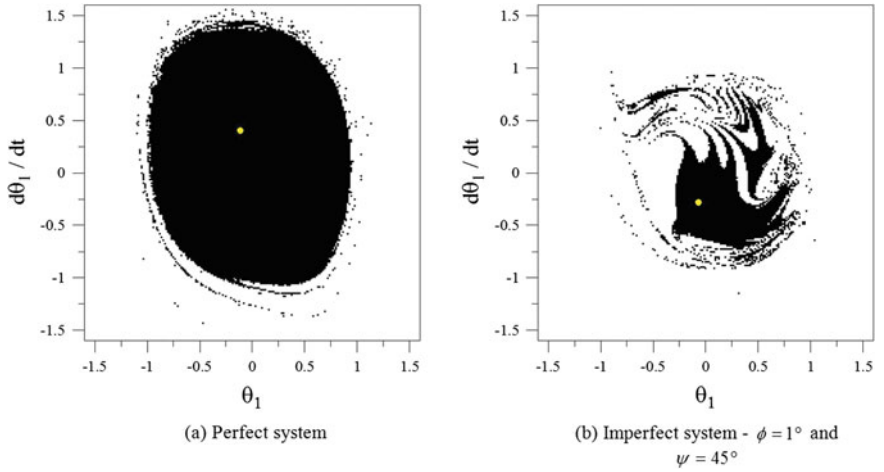

Fig. 21 Variation of the basin of attraction with the geometric imperfection. $\Omega = 1/3$, $F = 0.1$, and $\varphi = 0°$

suddenly falls down to zero, which corresponds to the complete annihilation of the basin of attraction for whatever excitation direction (also for the uncoupled case—$\varphi = 0°$). This shows that even very small imperfections may have a remarkable influence on the stability and safety of the structure and, in particular, that the residual dynamic integrity of the system (Rega and Lenci 2005) associated with the nonvanishing value of the escape load for $\phi = 1°$ actually corresponds to a very dangerous system configuration from the nonlinear dynamics viewpoint.

6 Dynamic Integrity and Control

Usually, the loss of safety is triggered by global (homoclinic or heteroclinic) bifurcations, since the boundary of the safe basin is the stable manifold of the saddles lying on the contour of the safe pre-buckling well. For the undamped case, these are homoclinic or heteroclinic orbits connecting the saddles. For increasing dynamical load, the safety reduction is related to the penetration of eroding fractal tongues into the safe basin, which is driven by the evolution of the stable (and unstable, indeed) manifolds of the saddles on the boundary of the safe region. It may be controlled by the elimination of manifolds intersections. Based on these considerations, Lenci and Rega (1998a) developed a method for controlling nonlinear dynamics and chaos and tested it on various mechanical systems (Lenci and Rega 2004; Rega and Lenci 2010).

The method consists of the optimal elimination of intersection of stable and unstable manifolds (perturbations of homoclinic or heteroclinic orbits) by properly adding

المنارة للاستشارات

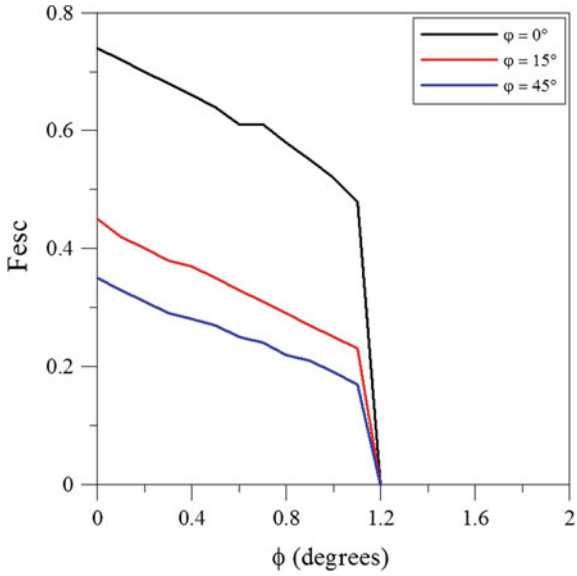

Fig. 22 Variation of the escape load with the column initial inclination ϕ for $\Omega = 1$ and $\psi = 45°$

superharmonic terms to a given harmonic excitation. By means of the solution of an appropriate optimization problem, it is possible to select the amplitudes and the phases of the added superharmonics in such a way that the manifolds distance is as large as possible. The elimination of the manifolds intersections permits to remove from the system dynamics various nonlinear phenomena such as chaotic transients, sensitivity to initial conditions, and fractal basin boundaries.

Single-degree-of-freedom model with its Hamiltonian and perturbed dynamics. Augusti's model reduces to an s.d.o.f. the system when the springs are equal, when it is excited in the symmetry directions $\varphi_s = 0°, 45°, 90°, 135°$, and when the imperfections are in the same plane of the excitation. To illustrate the control strategy, let us consider the Augusti's model excited along $\varphi_s = 45°$. This reduced-order model has some advantages for the control strategy, including easier computation of the integrity measures and identification of homoclinic and heteroclinic unperturbed and perturbed orbits. However, it misses the influence of modal coupling in some forcing regions (see Fig. 24a forward).

The relevant equation of motion could be obtained from the general ones (reported in Orlando 2010; Orlando et al. 2011a, b) of the two-d.o.f. system by properly restricting them to the manifold $\theta_1 = \theta_2 = u/(2)^{1/2}$, with u unique Lagrangian parameter describing the system configuration when excited in a diagonal symmetry direction. More simply, the nondimensional kinetic and potential energies and the work of nonconservative forces can be written directly for the reduced order geometrically imperfect system (with imperfection in the same direction of the excitation) (Orlando 2010):

المنارة للاستشارات

$$\bar{T} = \frac{T}{ml^2\omega_e^2} = \frac{1}{2}\left(\dot{u}\,\cos\left(\frac{u\sqrt{2}}{2}\right) + F\cos(\tau)\right)^2 + \frac{\dot{u}^2\sin^2\left(\frac{u\sqrt{2}}{2}\right)\cos^2\left(\frac{u\sqrt{2}}{2}\right)}{-1+2\,\cos^2\left(\frac{u\sqrt{2}}{2}\right)} \tag{11}$$

$$\bar{V} = \frac{V}{ml^2\omega_e^2} = \frac{(u-u_0)^2}{2\lambda\Omega^2} - \frac{1}{\Omega^2}\left(\sqrt{1-2\sin^2\left(\frac{u_0\sqrt{2}}{2}\right)} - \sqrt{1-2\sin^2\left(\frac{u\sqrt{2}}{2}\right)}\right) \tag{12}$$

$$\bar{E} = \frac{E}{ml^2\omega_e^2} = \frac{\xi}{\Omega}\dot{u}^2, \tag{13}$$

where $\tau = \omega_e\, t$ and the dot indicates differentiation with respect to τ, ending up to the following governing equation via application of the extended Hamilton principle:

$$\left(\frac{1+\cos\left(u\sqrt{2}\right)}{2\,\cos\left(u\sqrt{2}\right)}\right)\ddot{u} + \frac{\sqrt{2}\sin\left(u\sqrt{2}\right)}{2+2\,\cos\left(2u\sqrt{2}\right)}\dot{u}^2 + \frac{u-u_0}{\lambda\Omega^2} - \frac{\sqrt{2}}{\Omega^2}\frac{\sin\left(\frac{u\sqrt{2}}{2}\right)\cos\left(\frac{u\sqrt{2}}{2}\right)}{\sqrt{1-2\,\sin^2\left(\frac{u\sqrt{2}}{2}\right)}}$$
$$+\frac{2\xi}{\Omega}\dot{u} = F\,\cos\left(\frac{u\sqrt{2}}{2}\right)\sin(\tau). \tag{14}$$

The phase portrait of the undamped ($\xi = 0$) unforced ($F = 0$) Eq. (14), which can easily be obtained by the energy equation $\bar{T} + \bar{V} = const.$, is illustrated in Fig. 23a in the perfect case ($u_0 = 0°$), and in Fig. 23b in the imperfect case ($u_0 = 1° = 0.01745329$ rad). The safe potential well of the Augusti's perfect model is bounded by two heteroclinic orbits, while that of the imperfect model is bounded by a homoclinic orbit. A large decrease in the safe area is observed due to the initial imperfection, decreasing the practical stability threshold. This is mainly due to the change of the relevant orbit from heteroclinic to homoclinic.

To determine analytically the illustrated homoclinic and the heteroclinic orbits, the notation $\bar{t}(u)\dot{u}^2 = \bar{T}(u,\dot{u})$, valid in both cases when $F = 0$, is used, so that the total energy can be written as $H = \bar{t}(u)\dot{u}^2 + \bar{V}(u)$. Since these orbits approach the saddles as time tends to plus and minus infinity, they have the same energy $h = \bar{V}(u_{saddle})$ of the saddles, which is a known constant. By equating H with h, the equation that describes the homoclinic or the heteroclinic orbit is obtained. Solving this equation for $\dot{u}_h$ and integrating, one gets

$$\dot{u}_h(u_h) = \pm\sqrt{\frac{h-\bar{V}(u_h)}{\bar{t}(u_h)}}$$
$$\frac{du_h}{d\tau} = \dot{u}_h(u_h) \rightarrow \frac{du_h}{\dot{u}_h(u_h)} = d\tau \rightarrow \tau(u_h) = \int_{\text{limit}}^{u_h}\frac{du}{\dot{u}_h(u)}$$
$$= \pm\int_{\text{limit}}^{u_h}\sqrt{\frac{\bar{t}(u)}{h-\bar{V}(u)}}du, \tag{15}$$

المنارة للاستشارات

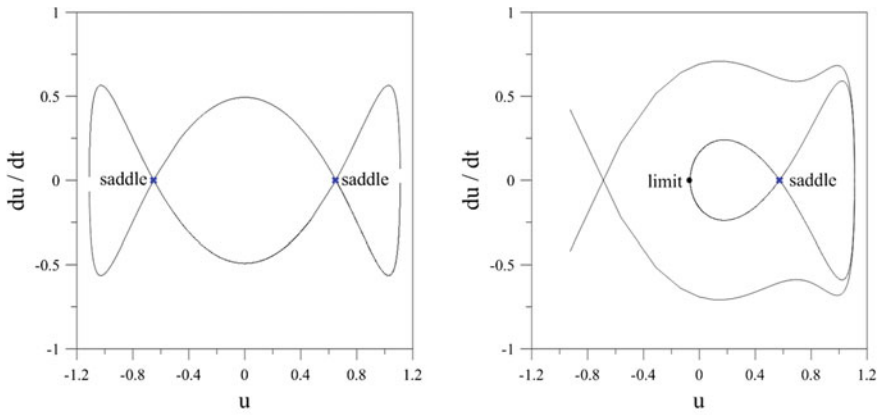

(a) Heteroclinic orbit. Perfect model - $u_0 = 0$

(b) Homoclinic orbit. Imperfect model - $u_0 = 1°$

Fig. 23 Heteroclinic and homoclinic orbits that delimit the safe potential well (bounded solutions) in Augusti's model. $\lambda = 0.9$ and $\Omega = 1/3$

Table 1 Equations of the heteroclinic and homoclinic orbits

Heteroclinic orbits	Homoclinic orbits
$\tau(u_h) = \int_0^{u_h} \sqrt{\frac{\bar{t}(u)}{h-\bar{V}(u)}} du$	$\tau_1(u_h) = -\int_{\text{limit}}^{u_h} \sqrt{\frac{\bar{t}(u)}{h-\bar{V}(u)}} du$, for $-\infty < \tau_1 \leq 0$
	$\tau_2(u_h) = \int_{\text{limit}}^{u_h} \sqrt{\frac{\bar{t}(u)}{h-\bar{V}(u)}} du$, for $0 \leq \tau_2 < \infty$

where "limit" is the point on the orbit corresponding to $\tau = 0$ (by symmetry considerations, for homoclinic orbits it is the maximum u-extent of the orbit in the phase space, which is the non-saddle solution of $h = \bar{V}(u)$, while for heteroclinic orbits it is 0).

Table 1 shows the equation of the heteroclinic orbit and the two equations that describe the lower and upper parts (in-phase space) of the homoclinic orbit.

Equation (14) is a particular case of the more general equation

$$\ddot{u} + \frac{\bar{t}'(u)\dot{u}^2}{2\bar{t}(u)} + \frac{\bar{V}'(u)}{2\bar{t}(u)} + \frac{\varepsilon \bar{C}(\dot{u})}{2\bar{t}(u)} + \frac{\varepsilon \bar{F}(u,\tau)}{2\bar{t}(u)} = 0, \tag{16}$$

where ε is a small nondimensional parameter which measures the magnitude of damping and excitation and has been introduced to stress their smallness. $\bar{t}'(u)$ and $\bar{V}'(u)$ are the derivatives of $\bar{t}(u)$ and $\bar{V}(u)$ with respect to u, $\bar{C}(\dot{u}) = 2\xi\dot{u}/\Omega$ is the damping and $\bar{F}(u,\tau) = -F\text{var}_1 \sin(\tau)$ is the external excitation, where $\text{var}_1 = \cos(u\sqrt{2}/2)$. As it will be useful in the following developments related to control, we consider here the more generic excitation $\bar{F}(u,\tau) = -F\text{var}_1 \sin(j\tau)$, which clearly reduces to the harmonic reference case for $j = 1$.

المنارة للاستشارات

Table 2 Functions α_1, $\alpha_2(j)$, and $\alpha_3(j)$

Heteroclinic orbits	Homoclinic orbits
$\alpha_1 = \int_{-\text{saddle}}^{\text{saddle}} \dot{u}_h(u_h)du_h$	$\alpha_1 = -\int_{\text{saddle}}^{\text{limit}} \dot{u}_h(u_h)du_h + \int_{\text{limit}}^{\text{saddle}} \dot{u}_h(u_h)du_h$
$\alpha_2(j) = \int_{-\text{saddle}}^{\text{saddle}} \text{var}_1 \sin\left(j \int_0^u \frac{du_h}{\dot{u}_h(u_h)}\right)du$	$\alpha_2(j) = \int_{\text{saddle}}^{\text{limit}} \text{var}_1 \sin\left(-j \int_{\text{limit}}^u \frac{du_h}{\dot{u}_h(u_h)}\right)du + \int_{\text{limit}}^{\text{saddle}} \text{var}_1 \sin\left(j \int_{\text{limit}}^u \frac{du_h}{\dot{u}_h(u_h)}\right)du$
$\alpha_3(j) = \int_{-\text{saddle}}^{\text{saddle}} \text{var}_1 \cos\left(j \int_0^u \frac{du_h}{\dot{u}_h(u_h)}\right)du$	$\alpha_3(j) = \int_{\text{saddle}}^{\text{limit}} \text{var}_1 \cos\left(-j \int_{\text{limit}}^u \frac{du_h}{\dot{u}_h(u_h)}\right)du + \int_{\text{limit}}^{\text{saddle}} \text{var}_1 \cos\left(j \int_{\text{limit}}^u \frac{du_h}{\dot{u}_h(u_h)}\right)du$

Using information on the unperturbed system ($\varepsilon = 0$), Melnikov's method (Melnikov 1963) allows us to measure the minimum distance between the perturbed ($\varepsilon \neq 0$) stable and unstable manifolds of the saddle, and, consequently, provides a criterion to determine when the intersection of the two manifolds first occurs (Wiggins 2003). The Melnikov function is (Orlando 2010)

$$M(m) = -\frac{2\xi}{\Omega}\alpha_1 + F[\cos(jm)\alpha_2(j) + \sin(jm)\alpha_3(j)], \tag{17}$$

where the expressions of α_1, $\alpha_2(j)$, and $\alpha_3(j)$ are shown in Table 2. By symmetry considerations, it is possible to show that $\alpha_2(j) = 0$ for heteroclinic orbits and $\alpha_3(j) = 0$ for homoclinic orbits.

The intersection of the manifolds occurs if the Melnikov function has a simple zero. In the reference case of harmonic excitation, $j = 1$, the equation $M(m) = 0$ provides (η is an inessential constant)

$$\frac{2\xi}{\Omega}\alpha_1 = F\sqrt{\alpha_2(1)^2 + \alpha_3(1)^2}\sin(m + \eta), \tag{18}$$

from which we see that the first intersection occurs for

$$F_{cr}^h = \frac{2\xi\alpha_1}{\Omega\sqrt{\alpha_2(1)^2 + \alpha_3(1)^2}}. \tag{19}$$

This critical excitation amplitude corresponds to a global (homoclinic or heteroclinic) bifurcation.

The behavior charts for perfect and imperfect models around the main resonance are reported in Fig. 24, including the thresholds of global bifurcation (heteroclinic or homoclinic bifurcation). Looking at Fig. 24a note that, while allowing to satisfactorily catch the V-escape region at low-frequency values that we are here interested to control (see the following subsection), consideration of the s.d.o.f. perfect model

المنارة للاستشارات

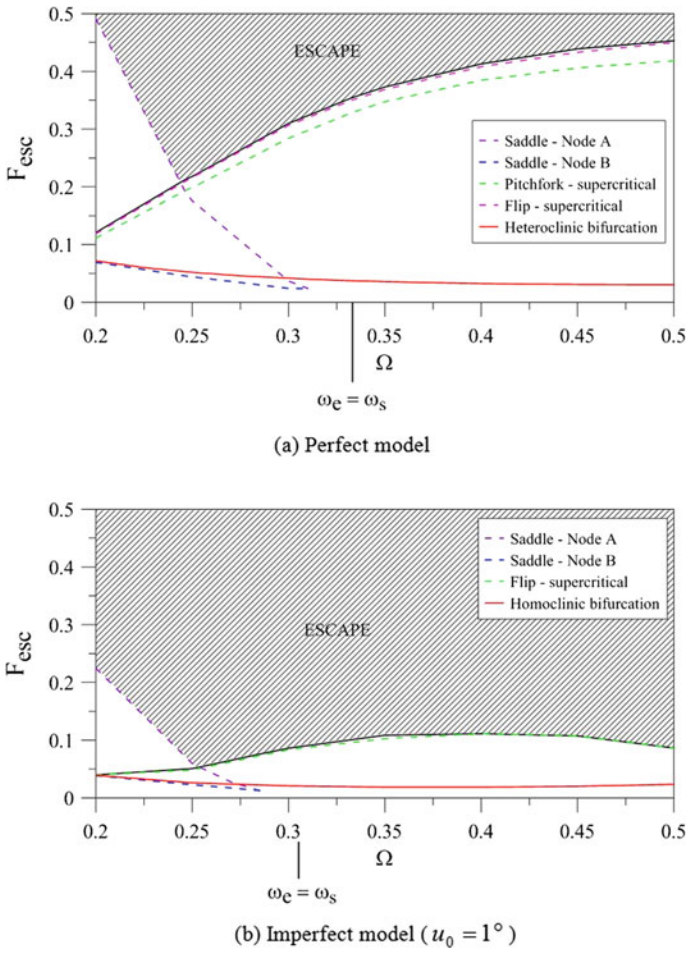

Fig. 24 Behavior charts in the main resonance region. $\lambda = 0.9$ and $\xi = 0.01$

misses the second V-escape region exhibited in Fig. 18 by the corresponding two-d.o.f. coupled model.

Controlling global bifurcations and enhancing system safety. The control method consists of looking for the periodic excitation which avoids, in an optimal manner, the intersection of the stable and unstable perturbed manifolds, and comprises the following steps:

1. determination of the homoclinic or heteroclinic bifurcation (critical excitation amplitude), e.g., by the method of Melnikov; in the present case this has been done for the reference harmonic excitation;
2. analysis of the dependence of homoclinic or heteroclinic bifurcation thresholds on the shape of the excitation, i.e., on the controlling superharmonic terms;

المنارة للاستشارات

3. formulation and solution of the mathematical optimization problem, which consists of determining the theoretical optimal excitation that maximizes the distance between the stable and unstable manifolds for a fixed excitation amplitude or, equivalently, the critical amplitude where the global bifurcation occurs;
4. numerical implementation of the optimal excitation needed to confirm the theoretical predictions and to verify the feasibility and performance of the control technique.

Following this procedure, the excitation is taken in the following form:

$$\bar{F}(u,\tau) = -F\left(\sin(\tau) + \sum_{j=2}^{n} \frac{F_j}{F}\sin(j\tau + \nu_j)\right)\mathrm{var}_1, \tag{20}$$

where F_i and ν_i, $j = 2, 3, \ldots n$, are the amplitudes and phases of the controlling superharmonics, whereas F is the overall excitation amplitude.

The Melnikov function with the excitation (20) is

$$\begin{aligned} M(m) = &-\frac{2\xi}{\Omega}\alpha_1 + F\{\cos(m)\alpha_2(1) + \sin(m)\alpha_3(1) \\ &+ \sum_{j=2}^{n} \frac{F_j}{F}[\cos(jm + \nu_j)\alpha_2(j) + \sin(jm + \nu_j)\alpha_3(j)]\} \end{aligned} \tag{21}$$

and can be rewritten in the form

$$M(m) = -\frac{2\xi}{\Omega}\alpha_1 + F\sqrt{\alpha_2(1)^2 + \alpha_3(1)^2}\gamma(m), \tag{22}$$

where

$$\gamma(m) = \sin(\eta + m) + \sum_{j=2}^{n} h_j \sin(\bar{\eta}_j + jm + \nu_j),\ h_j = \frac{F_j}{F}\frac{\sqrt{\alpha_2(j)^2 + \alpha_3(j)^2}}{\sqrt{\alpha_2(1)^2 + \alpha_3(1)^2}} \tag{23}$$

The critical threshold with control is now

$$F_{cr}^{cont} = \frac{2\xi\alpha_1}{\Omega\sqrt{\alpha_2(1)^2 + \alpha_3(1)^2}}\frac{1}{\max_{m\in[0,2\pi]}\{\gamma(m)\}}. \tag{24}$$

Comparing (19) with (24) to ascertain the effect of control, one obtains the control gain:

$$G = \frac{F_{cr}^{cont}}{F_{cr}^{h}} = \frac{1}{\max_{m\in[0,2\pi]}\{\gamma(m)\}} \stackrel{def}{=} \frac{1}{\bar{m}} \tag{25}$$

The aim of the procedure, as shown in Lenci and Rega (1998b), is to obtain the lowest value of $\bar{m} < 1$ that leads to the largest (optimal) value of F_{cr}^{cont}.

المنارة للاستشارات

For a single unperturbed homoclinic orbit, which is connected to a unique saddle, using the expression (25) is sufficient to avoid the tangency (and the intersection) between the stable and unstable manifolds of the perturbed saddle. For a heteroclinic orbit, this is no longer sufficient because the system has two saddles. It is necessary to control separately the intersection of the upper and lower branches [Fig. 23a, see Lenci and Rega (1998b, 2005)]. In this case, instead of the single expression (25), we have to consider

$$\bar{m}_{\text{inf}} = \max_{m\in[0,2\pi]}\{\gamma(m)\} \rightarrow G_{\text{inf}} = \frac{F^{cont}_{cr,\text{inf}}}{F^{h}_{cr,\text{inf}}} = \frac{1}{\bar{m}_{\text{inf}}} \tag{26}$$

which applies to the lower heteroclinic connection. By symmetry, for the upper heteroclinic connection, we must consider

$$\bar{m}_{\text{sup}} = -\min_{m\in[0,2\pi]}\{\gamma(m)\} \rightarrow G_{\text{sup}} = \frac{F^{cont}_{cr,\text{sup}}}{F^{h}_{cr,\text{sup}}} = \frac{1}{\bar{m}_{\text{sup}}}. \tag{27}$$

Expressions (26) and (27) must be taken into account in the formulation of the control method.

Lenci and Rega (2003a, 2004) proposed two types of control: (a) one-side, and (b) global control. The one-side control is indicated for homoclinic orbits, since it can only control one orbit. When applied to heteroclinic loops, only one orbit is controlled, and the uncontrolled one will bifurcate at a lower load level, which is unwanted. Thus, when only one homoclinic orbit must be controlled, the optimization problem can be written as

$$\max\left\{G^{\text{hom}}\right\} \text{ by varying the Fourier coefficients } h_j \text{ and } \nu_j,\ j = 2, 3, \ldots, \tag{28}$$

where $G^{\text{hom}} = G$ is given by (25).

For the heteroclinic case, both the upper and lower orbits (G_{sup} and G_{inf}) can be simultaneously controlled if the condition $G^{\text{het}} = G_{\text{inf}} = G_{\text{sup}}$, that is, $\max_{m\in[0,\,2\pi]}\{\gamma(m)\} = -\min_{m\in[0,\,2\pi]}\{\gamma(m)\}$, is satisfied. This is the global control approach, which entails solving the following optimization problem:

$$\begin{aligned}&\max\left\{G^{\text{het}}\right\} \text{ by varying the Fourier coefficients } h_j \text{ and } \nu_j,\ j = 2, 3, \ldots,\\ &\text{with the constraint } \max_{m\in[0,2\pi]}\{\gamma(m)\} = -\min_{m\in[0,2\pi]}\{\gamma(m)\}.\end{aligned} \tag{29}$$

The solutions to the optimization problems (28) and (29) give the optimal values of h_i and ν_i. They depend on the type of orbit and the number of superharmonics used in the analysis. Once they are determined, the magnitude of each superharmonic is simply given by

$$F_j = F h_j \frac{\sqrt{\alpha_2(1)^2 + \alpha_3(1)^2}}{\sqrt{\alpha_2(j)^2 + \alpha_3(j)^2}}. \tag{30}$$

المنارة للاستشارات

Table 3 Results of the optimization problems with increasing number of superharmonics considering one-side control

n	G_n^{hom}	h_2, ν_2	h_3, ν_3	h_4, ν_4	h_5, ν_5
2	1.4142	0.353553, π			
3	1.6180	0.552756, π	0.170789, 0		
4	1.7321	0.673525, π	0.333274, 0	0.096175, π	
5	1.8019	0.751654, π	0.462136, 0	0.215156, π	0.059632, 0
…	….	…	…	…	…
∞	2	1, π	1, 0	1, π	1, 0

Table 4 Results of the optimization problems with increasing number of superharmonics considering global control. Even superharmonics h_{2j} vanish

n	G_n^{het}	h_3, ν_3	h_5, ν_5	h_7, ν_7	h_9, ν_9
3	1.1547	−0.166667, π			
5	1.2071	−0.232259, π	0.060987, 0		
7	1.2310	−0.264943, π	0.100220, 0	−0.028897, π	
9	1.2440	−0.284314, π	0.125257, 0	−0.053460, π	0.016365, 0
…	….	…	…	…	…
∞	1.2732	−0.333333, π	0.200000, 0	−0.142857, π	0.111111, 0

Problems (28) and (29) are independent of the system and of the excitation (in fact, they do not depend on F, Ω, and ξ) and can be solved without any reference to the mechanical system under investigation. Despite this simplification, the solution cannot be obtained analytically, and a numerical approximation is required. The numerical solution of the problems (28) and (29) has been studied by Lenci and Rega (2003a, b, 2005). The optimal Fourier coefficients h_i and ν_i for an increasing number of superharmonics n are shown in Tables 3 and 4 for, respectively, one-side and global control.

As shown in Table 4, the global optimal solutions only include odd superharmonics. Thus, the solution of the optimization problem (29) can be written as

$$\gamma(m) = \sin(\eta + m) + \sum_{j=1}^{(n-1)/2} h_{2j+1} \sin(\bar{\eta}_{2j+1} + (2j+1)m + \nu_{2j+1}) \tag{31}$$

i.e., it belongs to the subclass of symmetric excitations, where the condition $\max_{m\epsilon[0,\,2\pi]} \{\gamma(m)\} = -\min_{m\epsilon[0,\,2\pi]} \{\gamma(m)\}$ is automatically satisfied.

The columns of G_n^h in Tables 3 and 4 allow us to observe that, in general, the gains increase with increasing number of superharmonics. However, the gains for global control are lower than those for one-side control. The differences are quantitatively significant. Thus, it can be concluded that the one-side control is much more useful

المنارة للاستشارات

from a theoretical point of view. A shortcoming is that it requires larger amplitudes of the superharmonics. Thus, the one-side control requires more energy expenditure.

The last line of each table presents, for comparison purposes, the values of the optimal coefficients h_i considering an infinite number of superharmonics. These values represent the upper bounds of the optimal solutions.

We start by applying the control to the perfect model. Here, the parameters $\Omega = 0.2465$, $\lambda = 0.9$ and $\xi = 0.01$, corresponding to the lowest escape load and consequently to the most dangerous situation (see Fig. 24a), are considered. In this case, the magnitude of the load at which heteroclinic bifurcation occurs, obtained from expression (19), is $F^h = F^h_{cr,\text{inf}} = F^h_{cr,\text{sup}} = 0.0528979$.

According to theoretical analysis, the global control is applied to this case; to check its performances in the "worst" situation, only a third order superharmonic excitation ($n = 3$) is used, so that we can improve the present results simply by using more superharmonics. The optimal values are $h_3 = 0.166667$ and $\nu_3 = \pi$, as shown in Table 4, and from (30) we get $F_3 = -1.1152799F$. The heteroclinic bifurcation increases to $F^{cont} = F^{cont}_{cr,\text{inf}} = F^{cont}_{cr,\text{sup}} = 0.0610813$, and there is a gain of 15.47% (see Table 4).

Observing the basins of attraction shown in Fig. 25, we can better understand the beneficial effect of the control strategy. For $F = 0.06$, there is practically no erosion in both situations. When the force increases to $F = 0.066$ the basin of the original model already shows some erosion while the basin of the controlled model is still nearly intact. At $F = 0.07$, when the erosion of the basin of the controlled model is still beginning, the safe basin of the original model already presents a considerable erosion which entails a fractal structure.

By building many basins of attractions like those in Fig. 25, it is possible to obtain a synthetic picture of the evolution of the system safety by constructing the so-called erosion profiles (Rega and Lenci 2008), which provide a measure of the basin dynamical integrity (i.e., of the safety of the system) versus increasing excitation amplitude. We consider two different integrity measures (Rega and Lenci 2008): the Global Integrity Measure (GIM), which measures the entire safe area, and the Integrity Factor (IF), whose measure is the radius of the largest circle inscribed in the same safe area. In both cases, the integrity measure is normalized with respect to the corresponding magnitude for $F = 0$.

The integrity profiles for IF are shown in Fig. 26a for both the controlled and the uncontrolled case, while those for GIM are shown in Fig. 26b. Besides highlighting a general shift of the practical starting point of erosion toward higher excitations, with respect to global bifurcation thresholds, these curves clearly highlight that the theoretical control gain of 15.47% is substantially confirmed by numerical simulations. There is an unquestionable gain due to the addition of the single controlling superharmonic to the harmonic excitation: the erosion of the safe basin in the controlled model starts later (see Fig. 25), thus increasing the magnitude of the disturbances that the system can undergo without practically losing its stability and consequently its safety margin in a dynamic environment.

The right control strategy for the imperfect model is the one-side control, which consists of adding a superharmonic of order two to the harmonic excitation. The

المنارة للاستشارات

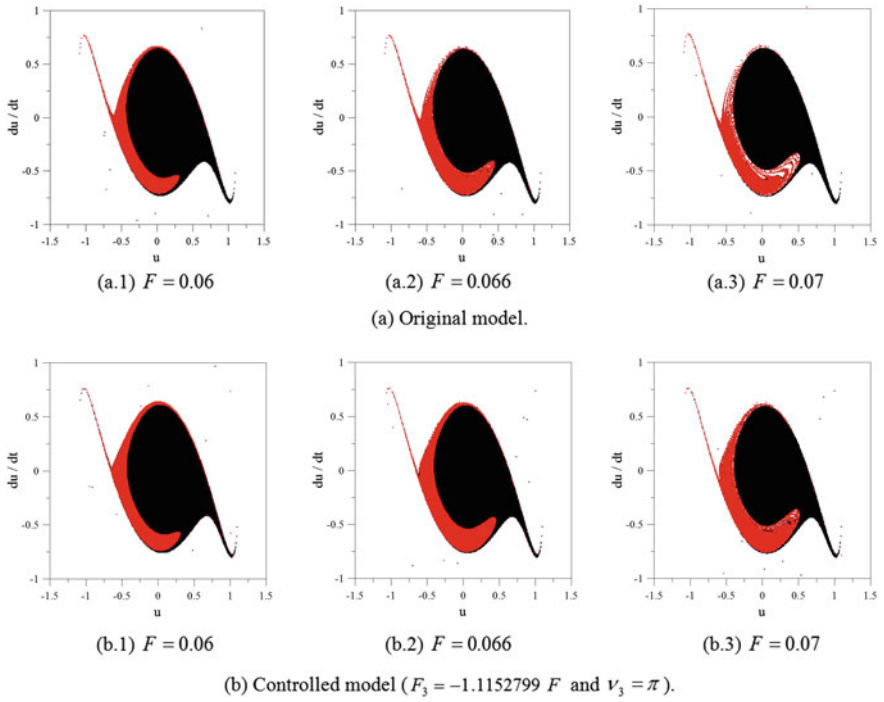

Fig. 25 Evolution of the basins of attraction with the applied load for $\Omega = 0.2465$, $\lambda = 0.9$, and $\xi = 0.01$. Perfect Augusti's model. Red and black basins correspond to resonant and nonresonant in-well periodic attractors

optimal values in this situation are given in Table 3, $h_2 = 0.353553$ and $\nu_2 = \pi$. Thus, from (30), we have $F_2 = 1.337189F$.

Moving to the imperfect system, the effectiveness of control is demonstrated by considering the following parameters: $u_0 = 1°$, $\Omega = 0.2465$, $\lambda = 0.9$ and $\xi = 0.01$, which correspond to the lowest escape load (most dangerous situation), as shown in Fig. 24b. In this case, the homoclinic bifurcation occurs at $F = F_{cr}^{h} = 0.02561$. With the addition of control, the bifurcation occurs at $F = F_{cr}^{cont} = 0.03622$, and the critical load increases of 41.42%.

The effectiveness of one-side control in terms of reducing fractal basin erosion is shown in Fig. 27, in particular, by comparing Fig. 27a.2 with Fig. 27b.2. More generally, the evolution of basins of attraction for increasing load levels shows a remarkable difference in the behavior of the two models. While the erosion of the original model starts at $F = 0.029$, the erosion of the controlled model begins only at about $F = 0.039$, when the basin of the original model is already very eroded.

Figure 28 shows a comparison of the IF and GIM integrity profiles between the original and controlled models. There is a significant increase (according to the fact that now the optimal gain $G = 41.42\%$ is "large") of the load level at which the process

المنارة للاستشارات

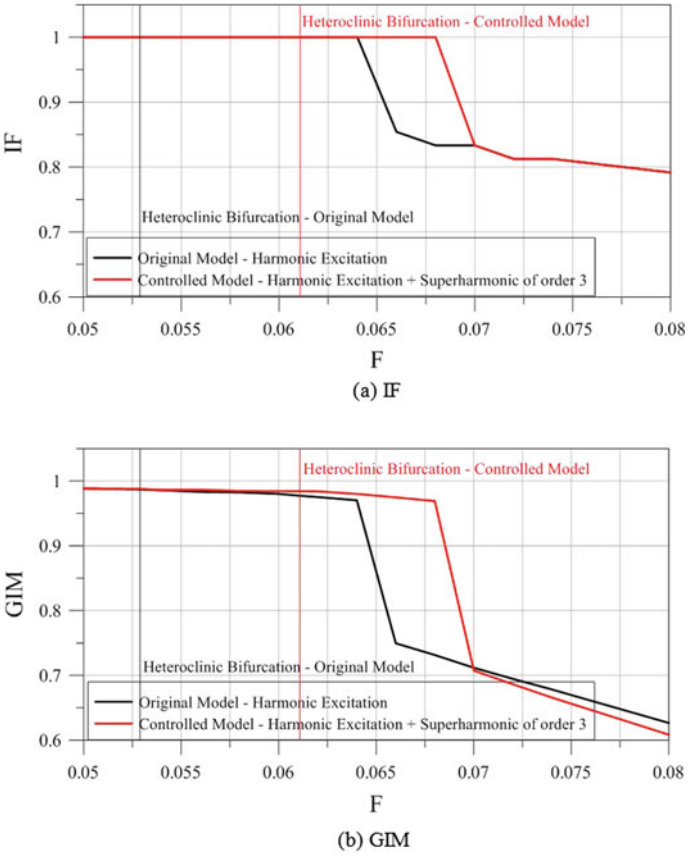

Fig. 26 Integrity profiles for increasing load for $\Omega = 0.2465$, $\lambda = 0.9$ and $\xi = 0.01$, original and controlled ($F_3 = -1.1152799F$ and $\nu_3 = \pi$) cases. Perfect Augusti's model

of erosion begins, and this largely increases the margin of safety of the system. Up to this load level, the integrity measures remain practically constant.

Compared with Fig. 26 holding for the perfect model, the IF and GIM profiles show the marked absolute loss of dynamic integrity due to the geometric imperfection, making its negative effect on the system safety clear. However, the results show that, through the present control strategies, one can increase the safety by increasing the safe region of the basin of attraction. The biggest gain is observed for the imperfect model, which is the expected situation in practical applications as well as the most dangerous one, because the range of involved values of F is much lower and the thresholds of starting erosion and final escape are much closer to each other (see also Fig. 23). The imperfection changes the heteroclinic orbit into a homoclinic one and, consequently, the optimal control changes from global to one-side, which is more efficient. When more superharmonics are considered in the control strategy,

المنارة للاستشارات

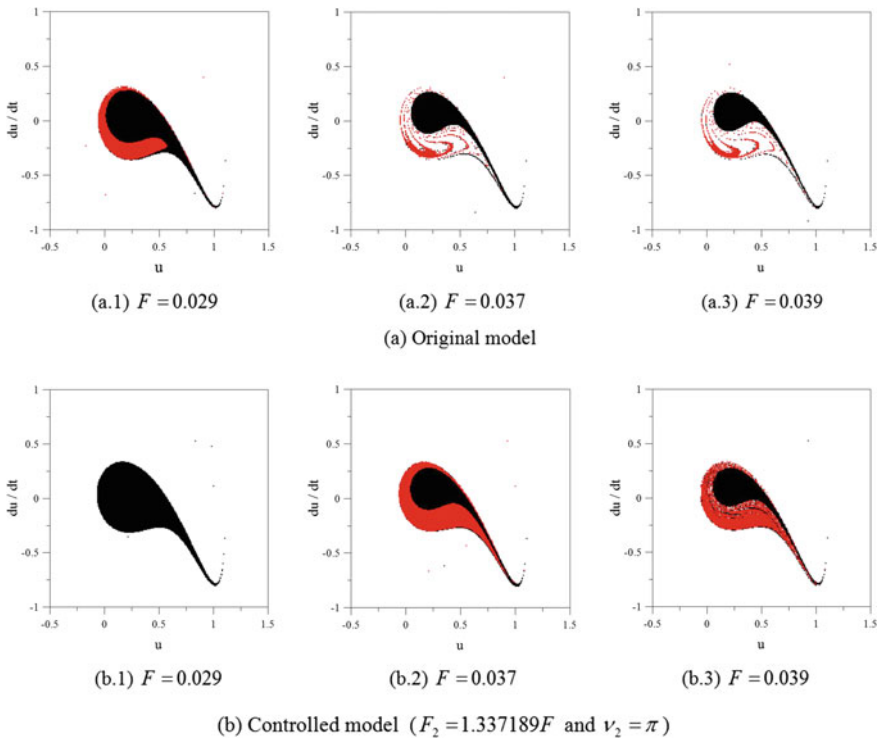

Fig. 27 Evolution of the basin of attraction for $u_0 = 1°$, $\Omega = 0.2465$, $\lambda = 0.9$, and $\xi = 0.01$. Imperfect Augusti's model. Red and black basins correspond to resonant and nonresonant in-well periodic attractors

the theoretical gain increases, as shown in Tables 3 and 4, and so even better results are expected in practice.

7 Cylindrical Shell: Reduced-Order Model, Global Behavior, Dynamic Integrity

The nonlinear dynamic analysis of continuous systems, such as thin plates and shells, is a problem of relevance in many engineering fields. The finite element method is the most used approach for nonlinear dynamic analyses of these structures. However, the computational effort is very high. As an alternative to complex numerical approaches, analytical methods using simplified models can be successfully employed to understand the main nonlinear features of the problem and may constitute efficient tools in the initial design stages. For plates and shells, the derivation of efficient reduced-order models is, in fact, essential due to the complex nonlinear response of these struc-

المنارة للاستشارات

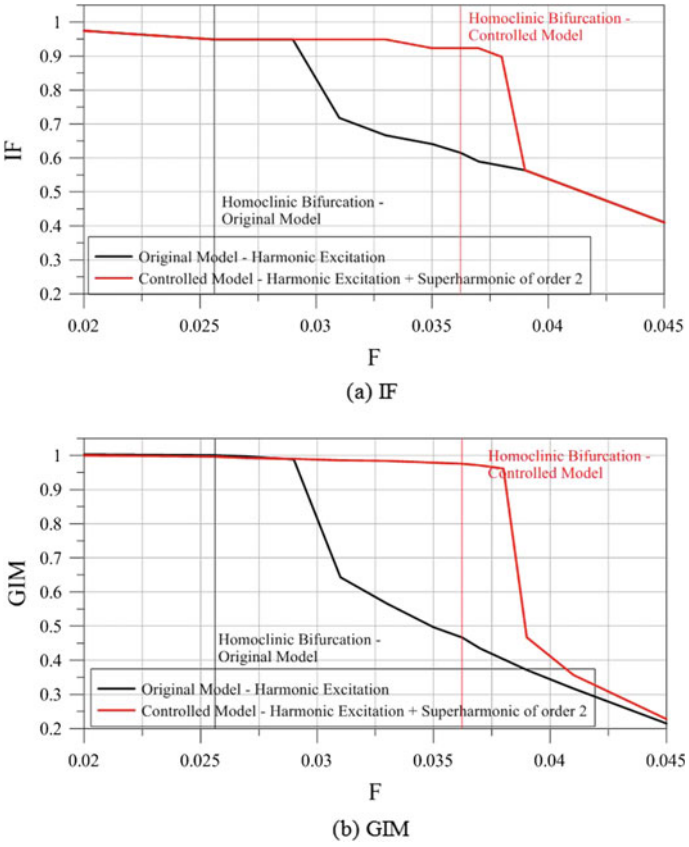

Fig. 28 Integrity profiles for increasing load for $u_0 = 1°$, $\Omega = 0.2465$, $\lambda = 0.9$ and $\xi = 0.01$, original and controlled ($F_2 = 1.337189F$ and $\nu_2 = \pi$) cases. Imperfect Augusti's model

tures. The usual procedure is to reduce the partial differential equations of motion of the continuous system to an approximate system of time-dependent ordinary differential equations of motion, which are in turn solved by numerical methods or, approximately, by perturbation procedures. However, the use of inappropriate modal expansions usually leads to misleading results or may require a rather large number of terms. Consistent nonlinear models can be derived by the use of perturbation techniques, nonlinear normal modes or proper orthogonal decomposition (Gonçalves et al. 2008) which can capture the influence of modal couplings and interactions.

This section is based on an extensive research work on the dynamics of cylindrical shells. The nonlinear vibration analysis of fluid-filled cylindrical shells was initially investigated by Gonçalves and Batista (1988). Based on this seminal work, Gonçalves and Del Prado (2002, 2004), using a reduced-order model, investigated in detail the nonlinear oscillations and stability of parametrically excited cylindrical shells and the influence of nonlinear modal interaction between different nonlinear

المنارة للاستشارات

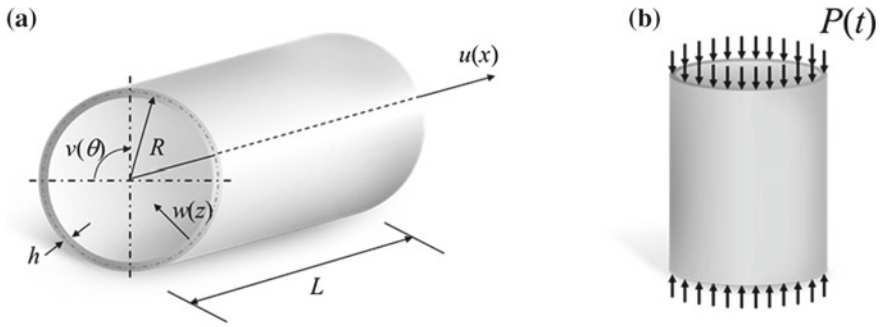

Fig. 29 Circular cylindrical shell: **a** geometry and system and **b** applied axial load

modes on the parametric stability of the shell. Then the effect of modal coupling was further analyzed by Rodrigues et al. (2014). Based on the developed formulation, Gonçalves et al. (2007a, b) studied the transient stability of empty and fluid-filled cylindrical shells and their global stability and dynamic integrity through the evolution of basin boundaries. Later, a general modal expansion for the nonlinear analysis of cylindrical shells was developed by Gonçalves et al. (2008) based on a perturbation procedure and proper orthogonal decomposition. This was generalized for any number of interacting modes in Gonçalves et al. (2016). The potential energy of preloaded cylindrical shells may exhibit several potential wells and several coexisting dynamic solutions. A detailed parametric analysis of the bifurcations, basin evolution and dynamic integrity measures of an axially loaded cylindrical shell, using a reduced 2-d.o.f. model, was further investigated by Gonçalves et al. (2011). Selected results are presented in this section. Recently, Silva et al. (2015) analyzed the influence of physical and geometrical uncertainties in the parametric instability load of an axially excited cylindrical shell.

Parametrically excited thin-walled cylindrical shells are among the several structural components where modal coupling and interaction have a fundamental role in the static and dynamic response. In the remaining part of this chapter, a brief discussion of this problem is presented. Consider a thin-walled, simply supported cylindrical shell of radius R, length L, and thickness h. A cylindrical system is adopted with the center at the lower end of the shell, as illustrated in Fig. 29. The mid-surface displacements in the axial, circumferential and radial directions are denoted, respectively, by u, v, and w. The shell material is considered to be elastic, homogeneous and isotropic with Young's modulus E, Poisson ratio ν, and density ρ. For most shell geometries its dynamics can be accurately described by Donnell's nonlinear shallow shell theory in terms of the transversal displacement w and a stress function f (Brush and Almroth 1975).

Using Donnell's nonlinear shallow shell theory, the equation of motion in the transversal direction is given by

المنارة للاستشارات

$$\rho h w_{,tt} + \beta_1 w_{,t} + \beta_2 \nabla w_{,t} + D\nabla^4 w = \left(P(t) + f_{,yy}\right) w_{,xx} + f_{,xx}\left(w_{,yy} + 1/R\right) - 2 f_{,xy} w_{,xy}, \tag{32}$$

where $D = Eh^3/[12(1-\nu^2)]$ is the flexural stiffness, β_1 and β_2 are, respectively, the linear viscous damping and the viscoelastic material damping coefficients, $P(t) = P_0 + P_1 \cos(\Omega t)$ is the applied axial load, which is the sum of the axial static preload, P_0, plus an harmonic time-dependent axial load, being P_1 the load magnitude and Ω the forcing frequency, and ∇^4 is the bi-harmonic operator, and the associated compatibility equation is written as

$$\frac{1}{Eh}\nabla^4 f = -\frac{1}{R} w_{,xx} - w_{,xx} w_{,yy} + w_{,xy}^2. \tag{33}$$

To obtain a consistent modeling with a limited number of modes, the sum of shape functions for the displacements must express the inherent nonlinear coupling among these modes and the in–out asymmetry of the deformed curved shell surface. Perturbation methods may be used to identify these essential modes and the importance of each mode in the modal expansion can be quantified by computing the relevant contribution to the total energy of the system. Based on these considerations, the lateral deflection w for an infinitely long shell can be generally described as (Rodrigues et al. 2014; Gonçalves et al. 2016)

$$w = \sum_{\mathrm{i}=1,3,5} \sum_{\mathrm{j}=1,3,5} W_{ij} \cos(i\, n\theta) \sin(j\, m\pi\xi) + \sum_{\mathrm{k}=0,2,4} \sum_{\ell=0,2,4} W_{kl} \cos(k\, n\theta) \cos(\ell\, m\pi\xi), \tag{34}$$

where n is the number of waves in the circumferential direction of the basic buckling or vibration mode, m is the number of half-waves in the axial direction, $\theta = y/R$ and $\xi = x/L$.

One must retain in (34) at least two modes to obtain a qualitatively correct description of the nonlinear vibration modes: the basic vibration mode—the seed mode—and the corresponding axisymmetric mode with twice the number of half-waves in the axial direction as the basic mode, that is

$$W(\theta, \xi, \tau) = \zeta(\tau)_{n,m} \cos(n\,\theta) \sin(m\pi\xi) + \zeta(\tau)_{0,2m} \cos(2m\pi\xi), \tag{35}$$

where $\tau = t\omega_0$, ω_0 is the lowest natural frequency of the shell and $\zeta_{ij} = W_{ij}/h$.

The substitution of (35) into the compatibility equation (33) leads to the following solution for the nondimensional stress function:

المنارة للاستشارات

$$\bar{f} = -\frac{1}{4}\frac{\beta^2}{\alpha^2}\frac{\theta^2}{\pi\sqrt{3\left(1-\nu^2\right)}}\Gamma + \frac{m^2}{\pi^2\left(m^2+\gamma^2\right)^2}\zeta_{11}\cos(n\,\theta)\sin(m\,\pi\,\xi)$$
$$+\frac{1}{4}\frac{\zeta_{02}}{m^2\pi^2}\cos(2m\,\pi\,\xi) + 2\frac{\alpha\,m^2n^2}{\pi^2\left(m^2+\gamma^2\right)^2}\zeta_{11}\zeta_{02}\cos(n\,\theta)\sin(m\,\pi\,\xi)$$
$$-2\frac{\alpha\,m^2n^2}{\pi^2\left(9m^2+\gamma^2\right)^2}\zeta_{11}\zeta_{02}\cos(n\theta)\sin(3m\,\pi\,\xi) + \frac{1}{32}\frac{\alpha\,n^2}{m^2\pi^2}\zeta_{11}^2\cos(2m\,\pi\,\xi)$$
$$-\frac{1}{32}\frac{\beta^4 h\,m^2\pi^2}{n^2\alpha^3}\zeta_{11}^2\cos(2n\,\theta), \tag{36}$$

where the following nondimensional quantities were introduced:

$$\alpha = h/R \quad \beta = h/L \quad \gamma = L\,n/\pi R \quad \xi = x/L$$
$$\zeta_{ij} = W_{ij}/h \quad \theta = y/R \quad \Gamma = P/P_{cr} \quad \bar{f} = R\,f/(Eh^2L^2) \tag{37}$$

and $P_{cr} = E\,h^2/\{R\,[3(1-\nu^2)]^{1/2}\}$ is the static critical load of an axially loaded cylinder (Brush and Almroth 1975; Bazant and Cedolin 1991).

By applying the Galerkin method, the following set of two simultaneous nonlinear differential equations of motion is obtained:

$$T_{11}\ddot{\zeta}_{11} + R_{11}\dot{\zeta}_{11} + (V_{11}-\Psi_{11})\zeta_{11} + V_{112}\zeta_{11}\zeta_{02} + \frac{1}{6}V_{1111}\zeta_{11}^3$$
$$+\frac{1}{2}V_{1122}\zeta_{11}\zeta_{02}^2 = 0$$
$$T_{22}\ddot{\zeta}_{02} + R_{22}\ddot{\zeta}_{02} + (V_{22}-\Psi_{22})\zeta_{02} + \frac{1}{2}V_{112}\zeta_{11}^2 + \frac{1}{2}V_{1122}\zeta_{11}^2\zeta_{02} = 0. \tag{38}$$

This low-dimensional model has been compared with more refined modal expansions and shell theories in Gonçalves et al. (2008), where it has been shown to retain the essential nonlinear features of the problem.

Based on the discretized model, the following expressions are obtained for the total potential energy of the statically loaded shell, V, and kinetic energy, T:

$$\Pi = \frac{1}{2}(V_{11}-\Psi_{11})\zeta_{11}^2 + \frac{1}{2}(V_{22}-\Psi_{22})\zeta_{02}^2$$
$$+\frac{1}{2}V_{112}\zeta_{11}^2\zeta_{02} + \frac{1}{24}V_{1111}\zeta_{11}^4 + \frac{1}{4}V_{1122}\zeta_{11}^2\zeta_{02}^2 \tag{39}$$
$$T = \frac{1}{4}T_{11}\dot{\zeta}_{11}^2 + \frac{1}{4}T_{22}\dot{\zeta}_{02}^2. \tag{40}$$

More refined models can be obtained by considering an increasing number of modes in Eq. (35) and by applying the Galerkin method. Figure 30a shows the convergence of the frequency–amplitude relation of the cylindrical shell. It is observed that the inclusion of the first- (02, 20, 22) and second-order modes (31, 13, 33)

المنارة للاستشارات

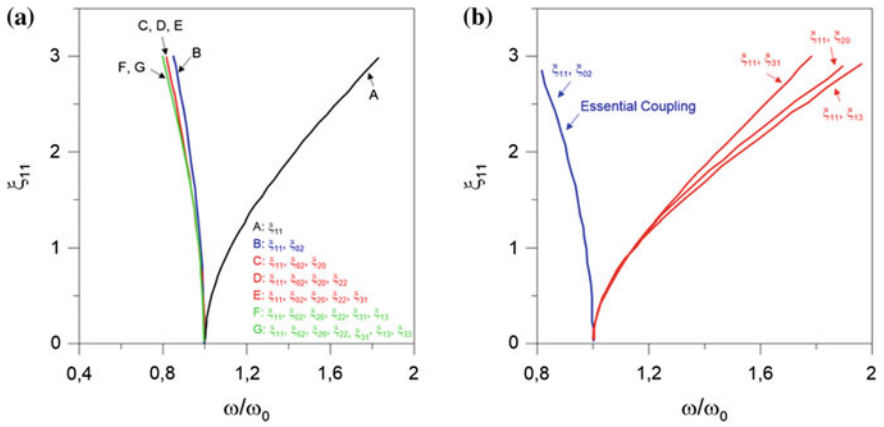

Fig. 30 Influence of first (02, 20, 22) and second order modes (31, 13, 33) obtained by the perturbation procedure on the frequency–amplitude relation of a cylindrical shell. **a** Convergence, **b** coupling effect: seed mode (linear vibration mode) plus selected first- and second-order modes. $m=1$; $n=5$; $R=0.2$ m; $h=0.002$ m; $L=0.40$ m; $E=210$ GPa; $\nu=0.3$; $\rho=7850$ kg/m^3

obtained by the perturbation procedure leads to convergence for vibration amplitudes up to three times the shell thickness (here $\xi_{ij}=W_{ij}/h$). Figure 30b shows the influence of the nonlinear modal coupling between the seed mode (linear vibration or buckling mode) and selected second- and third-order modes. It is observed that, while in most cases the coupling leads to a hardening behavior, the coupling between the seed mode and the axisymmetric mode with twice the number of waves in the axial direction as the seed mode leads to the expected softening behavior for this shell geometry and mode shape. This is the essential modal coupling due to quadratic nonlinearity for cylindrical shells, and is the main responsible for the in–out asymmetry of the shell nonlinear displacement field, as explained in detail by McRobie et al. (1999). The in–out asymmetry is due to the initial shell curvature. This cannot be observed in a linear analysis or in system with only cubic nonlinearity (e.g., perfect nonlinear plate). This axisymmetric mode has been sometimes approximated by a series of axisymmetric linear modes, increasing thus the model order. Gonçalves et al. (2011) have used a 2-d.o.f. model based on this modal expansion to investigate the global dynamics and integrity of a parametrically excited cylindrical shell based on the evolution of the basins of attraction of the several coexisting solution. At present, such analysis cannot be properly conducted using higher dimensional models.

Figure 31a shows the characteristic unstable post-buckling path of the axially loaded shell obtained with the present reduced model. For load levels between the minimum post-critical load, $\Gamma_{\min}$ (saddle-node bifurcation) and the critical load of the shell ($\Gamma_0=P_0/P_{cr}=1.0=\Gamma_{0cr}$, subcritical pitchfork bifurcation) there are five equilibrium positions. Figure 31b shows for a static load level $\Gamma_0=0.4$ the five equilibrium points, the two heteroclinic orbits that connect the two hilltop saddles

المنارة للاستشارات

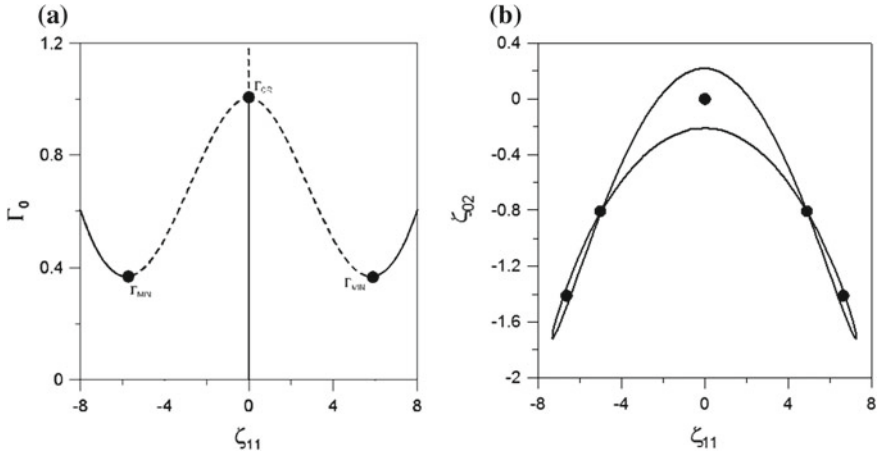

Fig. 31 **a** Post-buckling response of the axially loaded shell. **b** The five equilibrium points (two saddles and three centers) of the shell for a static load level $\Gamma_0 = 0.4$ and the two heteroclinic and two homoclinic orbits connecting the two saddles

and define the contour of the pre-buckling potential well and the two homoclinic orbits that define the contour of the two post-buckling wells.

The stability of the pre-loaded shell ($\Gamma_0 = 0.4$) under harmonic axial load is summarized in Fig. 32, where the main parametric resonance region of the pre-loaded shell around twice the lowest natural frequency of the loaded shell (ω_p) is shown together with the transient and permanent escape boundaries. The definition of transient and permanent escape was introduced by Thompson and co-workers (Thompson 1989; Soliman and Thompson 1989; Lansbury et al. 1992; Soliman and Thompson 1992). Here, the transient escape boundary is obtained considering the response starting from rest after each load increment, at least during the transient stage, the pre-buckling potential well (Gonçalves et al. 2007a). The permanent escape corresponds to the complete annihilation of the basin of attraction of all solutions within the pre-buckling well. The left-hand side of the main instability regions corresponds to subcritical parametric bifurcations, where the trivial solutions become unstable, giving rise to a period-two unstable solution, while the right-hand side of the stability boundary corresponds to supercritical bifurcations, where the trivial solutions become unstable, giving rise to a period-two stable solution. This is typical of softening systems. For a hardening system, the reverse occurs.

First, to understand the global behavior of the shell, a bifurcation diagram containing all stable solutions is shown in Fig. 33 for $\Omega = 1.50$ (subcritical bifurcation). The shell displays periodic, quasi-periodic and chaotic in-well and cross-well solutions of various orders. Five broad classes of periodic solution can be identified: (1) the trivial pre-buckling solution, (2) the nontrivial $2T$ solution within the pre-buckling well, (3) the small-amplitude initial vibrations within each of the post-buckling wells (the two branches are symmetric with respect to the ζ_{11} axis), (4) the long-lasting medium-

المنارة للاستشارات

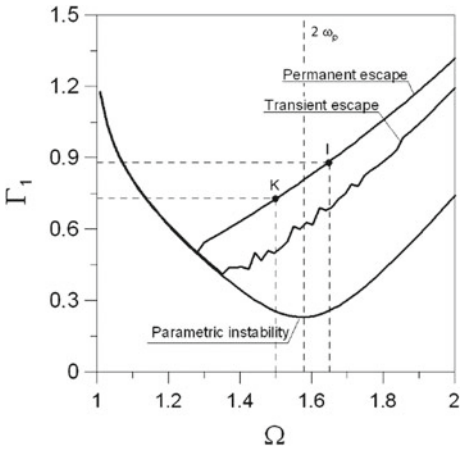

Fig. 32 Main parametric instability region of the pre-loaded shell. Parametric, transient escape (system starting from rest at each load increment), and permanent escape (complete erosion of safe basin) instability boundaries. $\Gamma_0 = 0.4$

amplitude cross-well solutions, and (5) a very large-amplitude cross-well period-3 solution which is robust in the whole excitation amplitude range. All periodic solutions are identified for future reference by the symbol Pj in Fig. 33a for selected values of the forcing amplitude and the projections of their four-dimensional orbits in the plane $\zeta_{11}(\tau) \times d\zeta_{11}(\tau)/d\tau$ are shown in Fig. 34.

Figure 35 shows in black, for small values of the excitation magnitude Γ_1, the cross-sections of the 4D safe basin of the pre-buckling trivial solution by the $\zeta_{11}(\tau) \times d\zeta_{11}(\tau)/d\tau$ plane while the initial conditions that lead to the possibly different out-of-well solutions are depicted with the same white color. The dots denote the relevant attractors which are the centers of the hyper-spheres associated with the definition of the local integrity measure, LIM (Soliman and Thompson 1989). In Fig. 35a for $\Gamma_1 = 0.0$ (static case), the white parallel tongues immersed in the black region are associated with the post-buckling solutions and delimit the radius of the 4D hyper-sphere that defines the integrity measure, LIM. As observed here the hyper-sphere touches in this plane the white region, but it will be shown later for other solutions how the hyper-sphere could also fictitiously intersect a competing basin if drawn on different cross-sections. As the magnitude of the load increases from zero a 1T periodic attractor arises in the post-buckling well (see Fig. 34a) from the stable equilibrium point. This solution experiences a period doubling bifurcation at A (Figs. 33b and 34b).

Figure 35b shows for $\Gamma_1 = 0.04$ the same basin structure with the thin white tongues corresponding to this attractor. These results show that a very small (minor) attractor can significantly modify the integrity of the main one, thus justifying the need to analyze competing profiles of several coexisting solutions, as successively pursued. These thin white tongues decrease as Γ_1 increases and disappear at $\Gamma_1 = 0.050$ (point B in Fig. 33b) when all post-buckling 2T solutions become unstable and the safe basin shows a remarkable increase, as illustrated in Fig. 35c for $\Gamma_1 = 0.10$, where the LIM radius is bounded by the vertical white tongues that correspond

المنارة للاستشارات

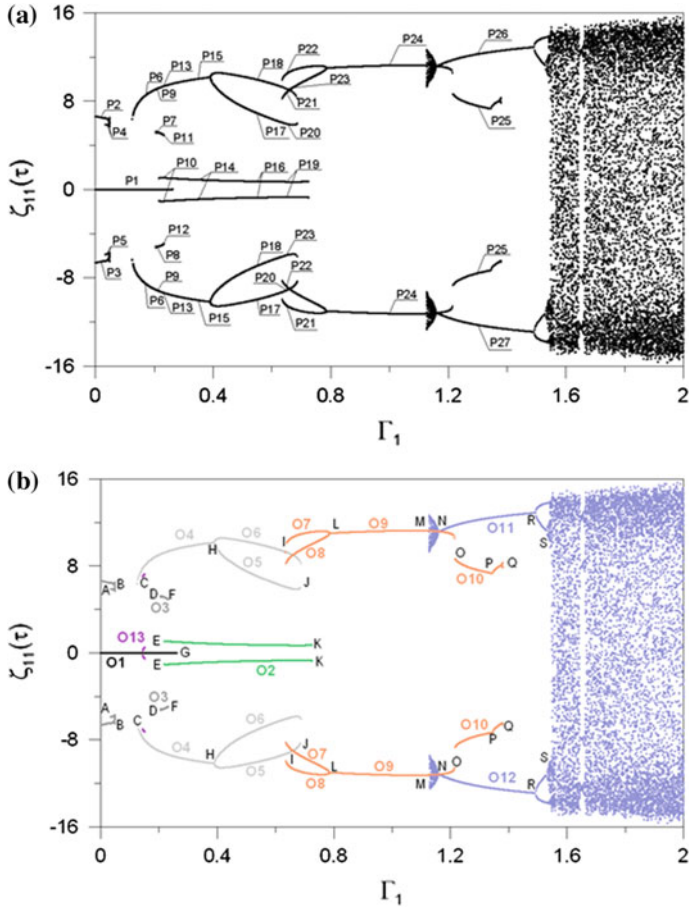

Fig. 33 Bifurcation diagram: **a** identification of different types of stable periodic solutions, **b** bifurcation points and classes of solutions. $\Gamma_0 = 0.40$ and $\Omega = 1.50$

to the large-amplitude cross-well period-3 solution occurring in the whole Γ_1 range. The saddle-node bifurcation occurring at point C and the ensuing 2T stable medium-amplitude cross-well solution (see Fig. 34c) plus a minor 4T cross-well attractor in a very small Γ_1 range, denoted as O13 in Fig. 33b, lead to a sudden decrease in the LIM radius, as shown in Fig. 35d.

Point D in Fig. 33b ($\Gamma_1 = 0.202$) corresponds to the re-stabilization of the post-buckling solution and point E denotes the saddle-node bifurcation giving rise to the 2T stable pre-buckling well solution which competes with the trivial solution up to point G. So, the system exhibits an increasing number of attractors, as illustrated in Fig. 34d and 34e where, respectively, four and five attractors are observed, in addition to the (not shown) 3T large cross-well motion. So, the basins of attraction exhibit an increasing complexity. The competition between the two in-well pre-buckling

المنارة للاستشارات

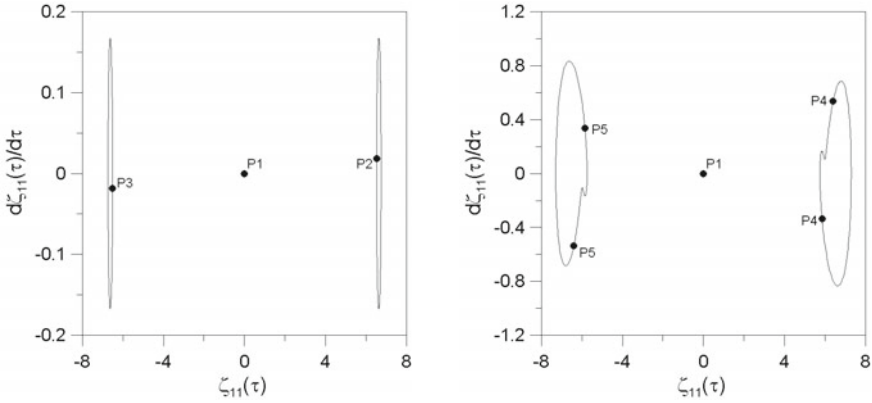

(a) $\Gamma_1 = 0.02$

(b) $\Gamma_1 = 0.04$

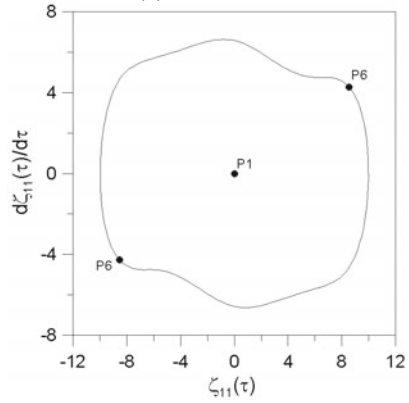

(c) $\Gamma_1 = 0.17$

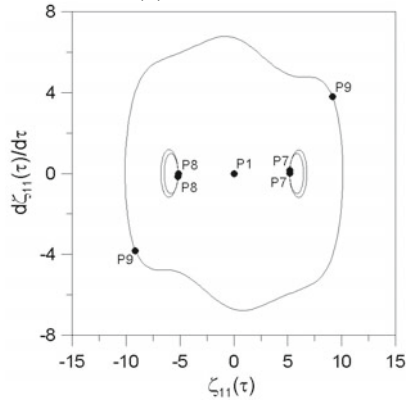

(d) $\Gamma_1 = 0.21$

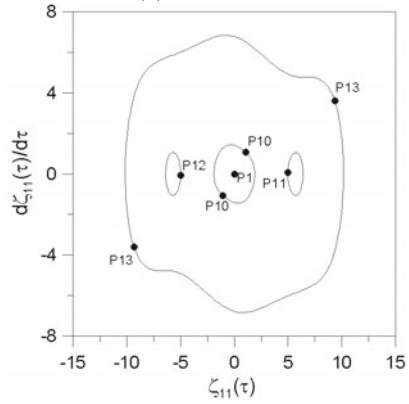

(e) $\Gamma_1 = 0.23$

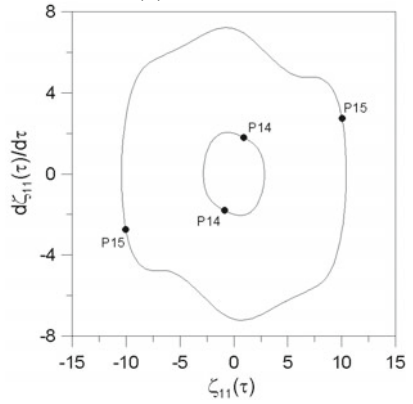

(f) $\Gamma_1 = 0.35$

Fig. 34 Projections of the different solutions on the $\zeta_{11}(\tau)$ versus $d\zeta_{11}(\tau)/d\tau$ plane for selected values of Γ_1. $\Omega = 1.50$ and $\Gamma_0 = 0.40$

المنارة للاستشارات

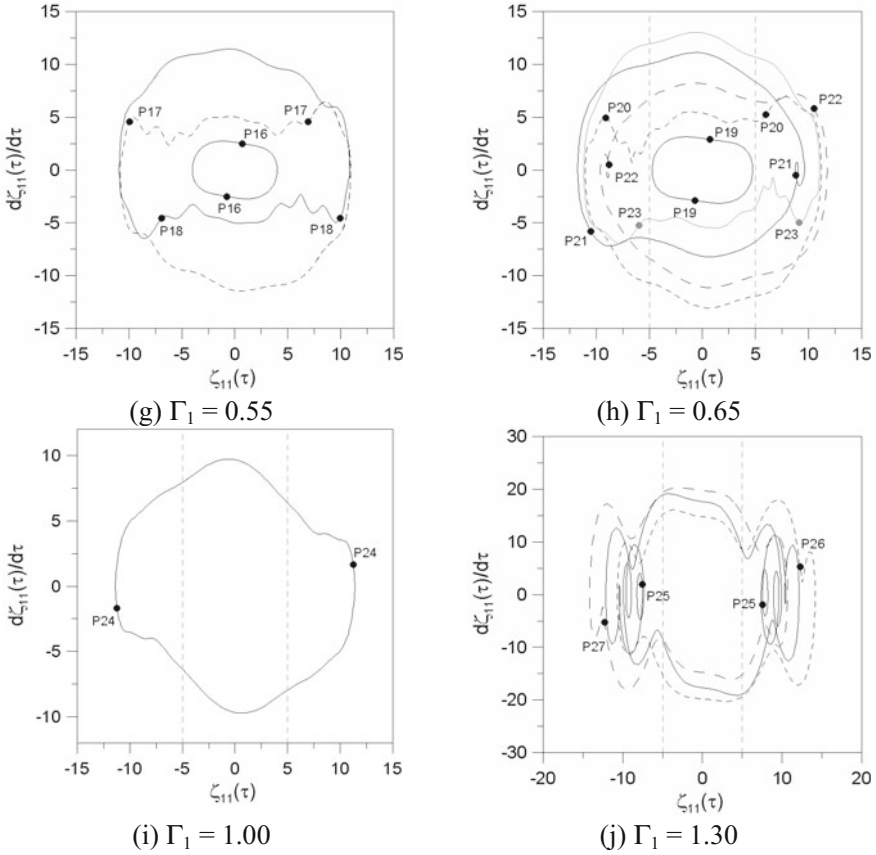

Fig. 34 (continued)

attractors is illustrated in the basin cross-sections shown for increasing values of Γ_1 in Fig. 36 where black corresponds to the trivial solution, white to the escape solutions, and the two blue dark and light shade sub-basins to the 2T pre-buckling solution (P10 in Figs. 33a and 34e). These cross-sections allow us to focus on the competition and evolution of in-well solutions (classes O1 and O2), without being interested in distinguishing between basins of different out-of-well solutions (shown with the same white color). Enlarged versions of these basins containing also the basins of the post-buckled and cross-well solutions are presented in Fig. 37. Note that, being the basins of attraction contained in a 4D hyper-volume, it is not easy in some circumstances to observe when the hyper-sphere centered in a given attractor touches the nearest competing basin. The large window in Fig. 37 is useful to give a general view of the topological complexity of the overall attractors-basins portrait when working in 4D, by also resolving some relevant seemingly odd issues. In particular Fig. 37 properly shows also the two fixed points (Fig. 37a–d) corresponding to the period-2 medium-amplitude cross-well solutions O4 (P6–P9–P13–P15, already visible in the phase

المنارة للاستشارات

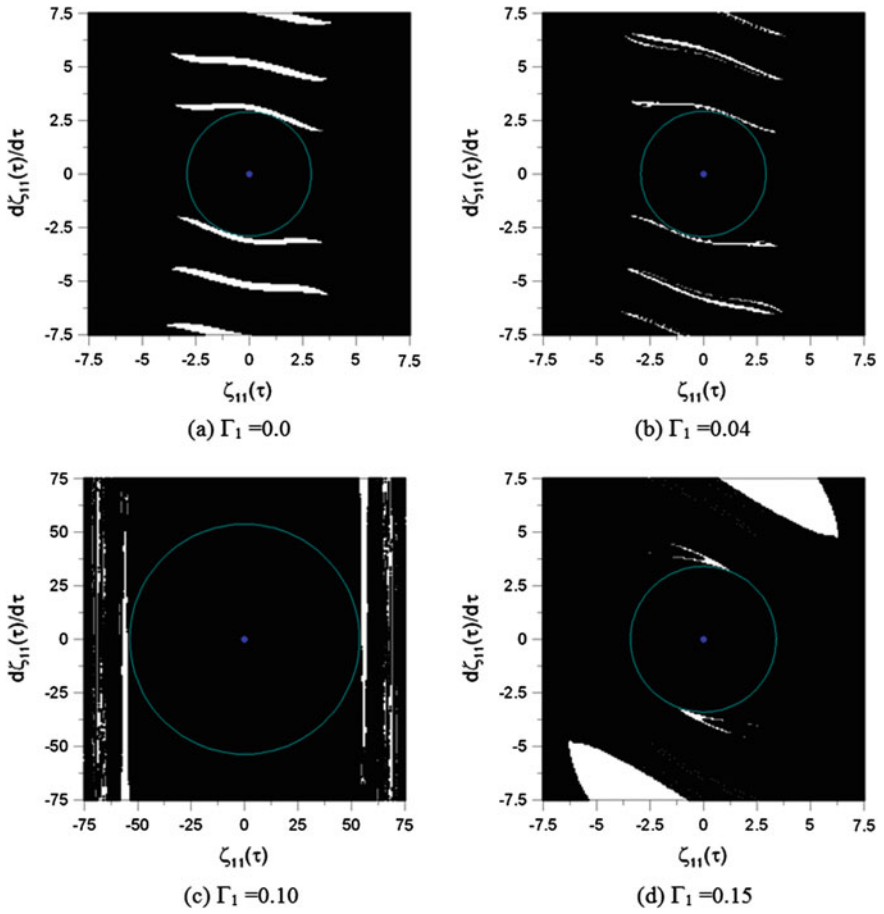

Fig. 35 Cross-sections of the basins of attraction of the in-well pre-buckling trivial solution ($\zeta_{02} = \dot{\zeta}_{02} = 0$) and of the corresponding hyper-sphere. $\Omega = 1.50$ and $\Gamma_0 = 0.40$. Black: trivial solution. White: escaping trajectories

portraits of Fig. 34c–f) as well as their splitting (P17–P18, Figs. 34g and 37e) after the pitchfork bifurcation at H (Fig. 33b). Moreover, it allows to distinguish, again through different colors, between the relevant sub-basins, which, however, due to the considered ($\zeta_{02}(\tau) = d\zeta_{02}(\tau)/d\tau = 0$) cross-section, seem to be totally uncorrelated with the reference attractors (e.g., the right/left external yellow points in Fig. 37a with respect to the relevant up/down light/dark red sub-basins). The issue can, however, be resolved by looking at cross-sections made at suitable ζ_{02}, $d\zeta_{02}(\tau)/d\tau$ values allowing to properly locate the fixed points of the medium-amplitude cross-well solutions into their respective sub-basins (Gonçalves et al. 2011).

To evaluate the system dynamic integrity, different measures can be used, as already shown for the Augusti model (for a more general treatment of the matter, see Rega et al. 2018 in this book). The global integrity measure (GIM), defined

المنارة للاستشارات

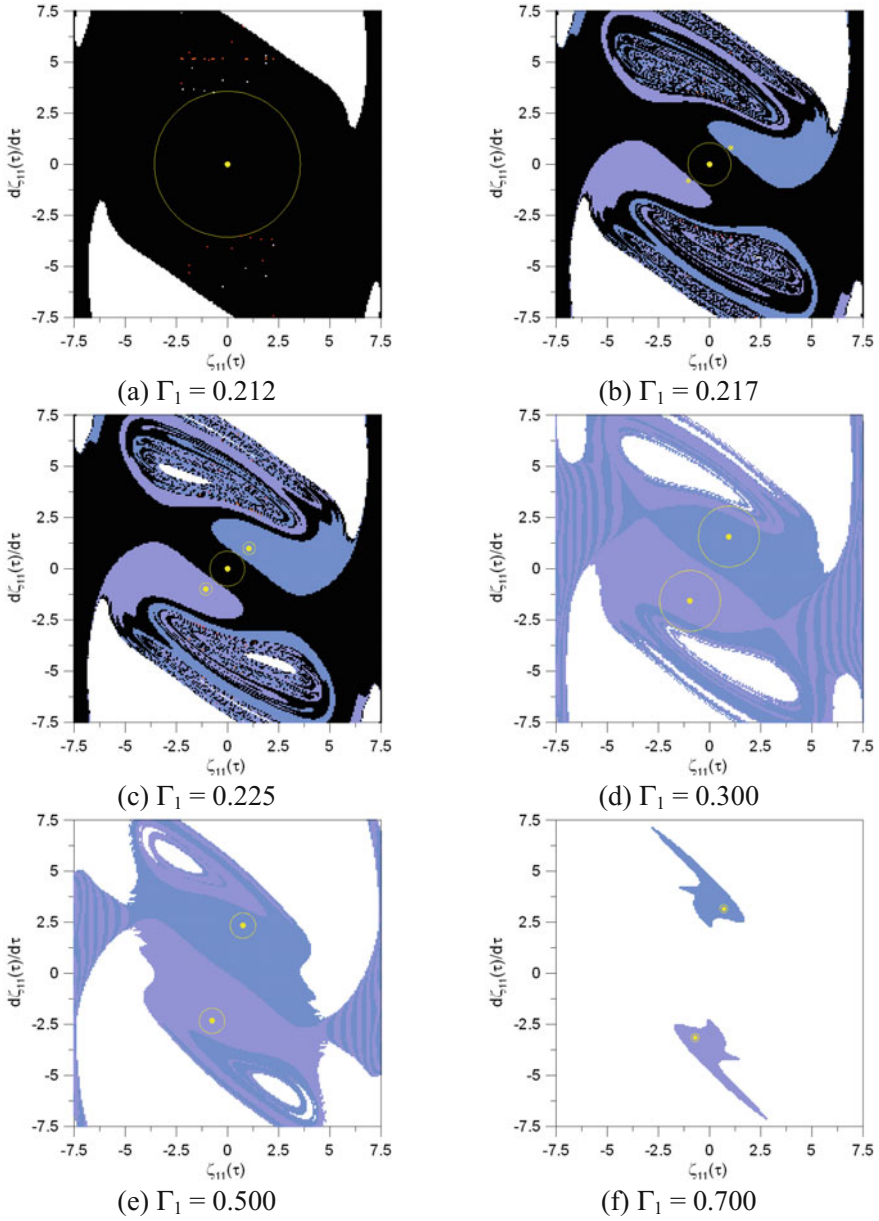

Fig. 36 Basins of attraction of the in-well pre-buckling attractors ($\zeta_{02}(\tau) = d\zeta_{02}(\tau)/d\tau = 0$). $\Omega = 1.50$ and $\Gamma_0 = 0.40$. Black: trivial solution. Light and dark blue: period-two bifurcated solution. White: escaping trajectories

المنارة للاستشارات

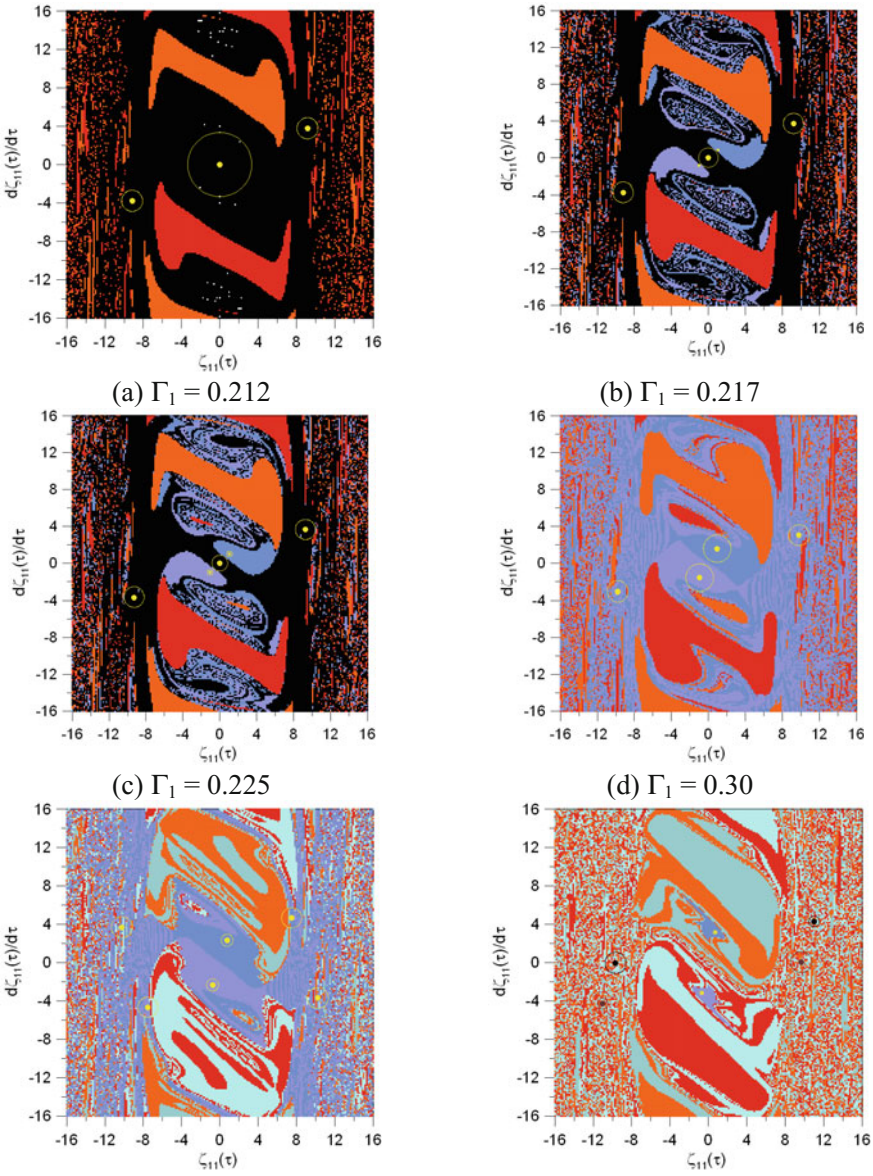

Fig. 37 Enlarged views of basins of attractions containing both in-well and out-of-well attractors ($\zeta_{02}(\tau) = d\zeta_{02}(\tau)/d\tau = 0$). $\Omega = 1.50$ and $\Gamma_0 = 0.40$

المنارة للاستشارات

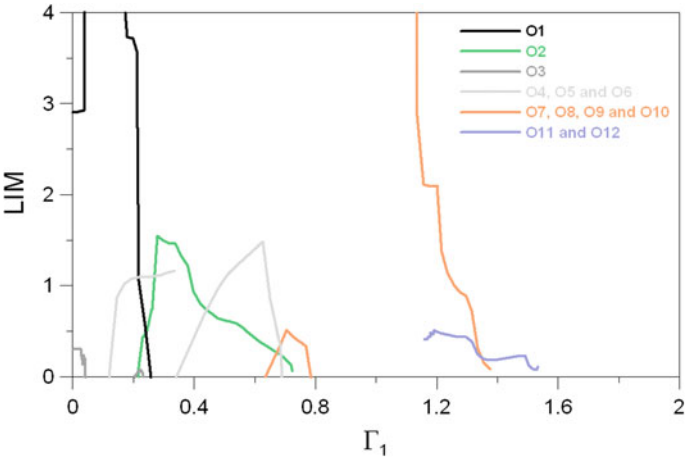

Fig. 38 Variation of the LIM of the solutions for $\Gamma_0 = 0.40$ and $\Omega = 1.50$. Subcritical parametric bifurcation

as the normalized hyper-volume of the safe basin, is the most intuitive and easy measure, but it is not satisfactory in all cases in which the safe basin is strongly fractal or intertwined with other basins. Moreover, although all trajectories with initial conditions in the black area of Fig. 35 converge to the trivial solution, initial conditions away from the pre-buckling well may lead to rather long large-amplitude cross-well involved transients. This is an unacceptable situation in most structural problems, such as the present one, where large-amplitude cross-well motions lead to high stresses and damage of the structure material, leading in most cases to the failure of the structural system. In such a situation, the integrity factor IF is definitely more appropriate than the GIM in the evaluation of the integrity of the structure. As a matter of fact, being the GIM insensitive to the basin compactness, it would lead to a (locally) completely different erosion profile and would dramatically overestimate the dynamic integrity of the reference main solution. As mentioned previously, the local integrity measure (LIM) proposed by Soliman and Thompson (1989) can be defined as the maximum radius of the hyper-sphere entirely belonging to the safe basin and centered at the attractor, and leads to a radius equal or smaller than the IF. This integrity measure is used in the present analysis.

For the reference subcritical case, jointly looking at bifurcation diagram (Fig. 33), phase portraits (Fig. 34), and attractor-basin portraits (zoomed, Figs. 35 and 36; enlarged, Fig. 37), and summarizing the relevant results in terms of integrity profiles (Fig. 38), the competition among various solutions in different Γ_1 ranges is apparent. Hereafter solutions and competition features are discussed in detail.

1. For very low Γ_1 (<0.05), solution classes O1 and O3 do coexist, with the former being in the pre-buckled (central) well and the latter in the post-buckled (lateral) wells (Fig. 33b), and the corresponding LIM being $\cong$3.0 and 0.3, respectively (Fig. 38).

المنارة للاستشارات

2. In the low Γ_1 range (0.05–0.125), there is only the trivial solution O1 with the very large LIM value, which is bounded by the large-amplitude cross-well period-3 solution occurring in the whole Γ_1 range.
3. In a small subsequent Γ_1 range (about 0.125–0.262), a number of nearly coexisting dynamic/topological phenomena do occur, and affect the competing integrity profiles in a relatively clear way. The LIM of solution O1 falls down to about 3.6 due to the onset (point C, $\Gamma_1 = 0.125$) of the 2T cross-well solution O4, whose white basin overall delimits the black one in Fig. 36a and in the following sub-figures. In between D and E (Fig. 33b, $\Gamma_1 = 0.212$), the reestablished (while dying) solution O3, somehow affects the LIM of solution O1; however, this LIM further falls down—up to definitely vanishing at point G—in connection with the meaningful shrinking of its basin (Fig. 36b, c) due to the onset at E of the subcritically bifurcated in-well solution O2, whose LIM increases from zero to about 1.5 in this range.
4. In the low-medium Γ_1 range (about 0.262–0.726), the basin (and the LIM profile) of the pre-buckling in-well period-two solution O2 are smoothly eroded (Figs. 36d–f and 37d–f) by the basin (and profile) of the cross-well solution O4, and of its bifurcated solutions O5 and O6, up to their definite vanishing at point K. At point H the self-antisymmetric solution P15 undergoes a symmetry-breaking (pitchfork) bifurcation giving rise to two antisymmetric (mirrored) 2T solutions P17 and P18 (Fig. 34g). The same occurs in the reverse direction (i.e., with decreasing Γ_1) on passing from the self-antisymmetric P24 (Fig. 34i) to the antisymmetric solutions P21 and P22 (Fig. 34h). The two antisymmetric 2T solutions P17 and P18 (or O5 and O6) coexist with comparable basins (Fig. 37e) and increasing LIMs (see Fig. 38 where just one light gray profile is shown for these cross-well solutions), their influence on the decreasing LIM of the pre-buckling 2T solution O2 being clearly visible in Fig. 38. In between points I ($\Gamma_1 = 0.635$) and J ($\Gamma_1 = 0.685$) the interaction among the five attractors (Fig. 34h)—four in the post-buckling and one in the pre-buckling well—is rather complex, but this is actually a minor (localized) issue.
5. Between points J and L, the orange profiles of the vanishing cross-well antisymmetric solutions O7 and O8 first increase and then decrease due to some increasing intertwining of their basins. The newborn cross-well solution O9 dominates the dynamics in the larger Γ_1 range up to the onset of another couple of mirrored competing cross-well solutions O11 and O12 at point M, with a very large LIM limited again by the large-amplitude 3T cross-well motion.
6. The new cross-well solutions start as a couple of narrow-size quasi-periodic attractors, thereafter evolving to the two competing cross-well solutions P26 and P27, and are responsible for the strong LIM decrease of the orange cross-well solution O9 at $\Gamma_1 \cong 1.2$. The further decrease of the LIM of all three solutions (just one blue profile being shown in Fig. 38 for the cross-well O11 and O12 solutions) is due to the increasing intertwining and fractality of the competing basins. The level of complexity increases as Γ_1 increases, where the fractal structure of the competing basins of the 1T solutions P26 and P27 (Fig. 34j) leads to a practically null LIM.

المنارة للاستشارات

8 The Influence of Uncertainties in Systems Liable to Unstable Buckling

Slender structural systems liable to unstable buckling usually become unstable at load levels much lower than the linear buckling load of the perfect structure. In some cases, experimental buckling loads can be just a small fraction of the theoretical critical load (Batista and Gonçalves 1994). This is mainly due to the imperfections present in real structures. The imperfection sensitivity of structures under static loading is well studied in the literature, but little is known on the sensitivity of these structures under dynamic conditions. In a dynamic environment, not only geometric imperfections but also initial conditions (disturbances), physical and geometrical system parameters uncertainties and excitation noise influence the bifurcation scenario and basins of attraction.

The influence of both random noise and system parameter uncertainties on the dynamic instability of structural systems liable to buckling was discussed in Gonçalves and Santee (2008), Silva and Gonçalves (2015), Gonçalves et al. (2007a), Wiebe and Spottswood (2014). The influence of uncertainties and random noise is particularly important in the vibration control of dynamical systems with multiple coexisting attractors.

The physical parameters (E, υ, and ρ) and the geometrical parameters (L, R, and h) of the shell usually have some reference values, which are defined at the stage of design. However, depending on the allowable tolerances in the fabrication process, small variations of these parameters may occur. Usually, these small variations have a negligible influence on the load capacity of the structure. But in structural systems liable to buckling, due to mainly the inherent nonlinearity of the buckling process, small changes may lead to significant changes in the load capacity and safety of the structure.

For each physical and geometrical parameter, α, the following uniform probability density function, f, is assumed (Gonçalves and Santee 2008):

$$f(\alpha) = \begin{cases} \frac{100}{2\alpha_0 Q}, & if\ \alpha_0 - \frac{\alpha_0 Q}{100} < \alpha < \alpha_0 + \frac{\alpha_0 Q}{100} \\ 0, & otherwise \end{cases} \tag{41}$$

where α is the system parameter (E, υ, ρ, L, R, or h), α_0 is the mean value of the chosen parameter (design value), and Q is a parameter which expresses the quality of the fabrication process as a percentage of the mean value, α_0.

Figure 39 shows the stability boundaries of the buckling load of a system subjected to asymmetric bifurcation considering a slowly applied load (in black) and a suddenly applied load (in red) together with the scatter of buckling loads obtained considering uncertainties in all system parameters for both loading cases, except the external load [$Q = 10$ in Eq. (41)]. The scatter of results illustrates the sensitive dependence of structures liable to unstable buckling to not only geometric imperfections but also any variation of the system parameters. These results are compared with the

المنارة للاستشارات

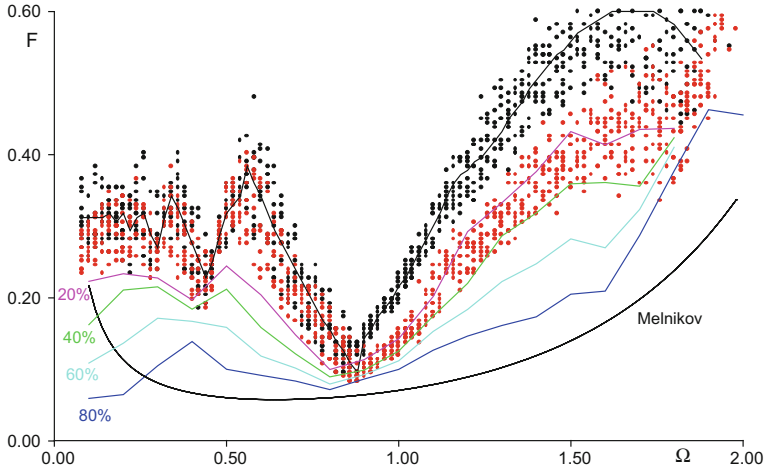

Fig. 39 Buckling load of an imperfection-sensitive structure considering uncertainties in all system material and geometric parameters. Red: suddenly applied load. Black: slowly applied load

curves of constant basin area and the Melnikov load for this structure (Gonçalves and Santee 2008). The results corroborate the lower bound character of the Melnikov load. However, if a good quality control is considered at the fabrication stage, the designer may use a less conservative estimate of the dynamic buckling load based on the safe basin area. In fact, one can observe in Fig. 39 that almost all results in this numerical experiment are above the curve corresponding to a safe basin with an area equal to 40% of the reference basin of the unloaded system A_0.

Consider now the cylindrical shell subjected to a harmonic axial load of the following form:

$$P = P_0 + P_1 \cos(\omega t) + G(P_1, \omega, t) \tag{42}$$

where P_0 is the axial static pre-load, P_1 is the amplitude of the deterministic harmonic load, ω is the deterministic excitation frequency, t is time, and $G(P_1, \omega, t)$ is the random disturbance that depends on the deterministic parameters P_1 and ω.

For the numerical calculations of the present work, the nondeterministic term of the axial load in (42), $G(P_1, \omega, t)$, is considered as a stationary and ergodic continuous stochastic process in time (Gonçalves and Santee 2008). Another hypothesis is that the stochastic process $G(P_1, \omega, t)$ has a zero expected value, that is

$$E[G(P_1, \omega, t)] = 0. \tag{43}$$

The description of a stochastic process is usually made in the frequency domain. Here, it is assumed that the random term $G(P_1, \omega, t)$ has a spectral density function given by

المنارة للاستشارات

$$\Phi_{GG}(\bar{\omega}) = \frac{\sigma_{GG}^2}{2\,\omega_l} \text{ for } \Omega - \frac{\omega_l}{2} < \bar{\omega} < \Omega + \frac{\omega_l}{2}, \tag{44}$$

where σ_{GG}^2 is the variance of the random force amplitude and ω_l is the frequency bandwidth of the excitation frequency.

Additionally, it is considered that the standard deviation of the random force amplitude is proportional to the deterministic force amplitude, P_1, thus

$$\sigma_{GG} = \delta P_1 \tag{45}$$

where δ is the standard deviation parameter of proportionality. So, the random force is a stochastic process that depends on the frequency, ω, and amplitude, P_1, of the deterministic term. The numerical algorithms used in the present work can be found in Gonçalves and Santee (2008).

Figure 40 (Silva et al. 2012) shows the influence of the random portion of the load, $G(P_1, \omega, t)$, described by Eq. (42), on the parametric instability and escape boundaries of the axially loaded cylindrical shell for one bandwidth, ω_l, 0.50 and two values of the standard deviation parameter, δ, 0.05 and 0.10. For this value of ω_l and δ, ten samples are generated and the two critical loads are evaluated, considering the average values of the shell geometry and physical parameters. In Fig. 40, curves in black are the results for a deterministic harmonic force. The dashed gray curves represent the average of the escape load. The presence of noise leads to a dispersion of the results in the right side of the instability region. The continuous gray curves represent the value of the mean load added or subtracted from the value of the standard deviation of ten samples. As the standard deviation parameter, δ, increases, the dispersion of the dynamic buckling loads increases. Also all escape loads of the perturbed system are lower than the permanent escape load of the shell under a deterministic load. So, the shell is sensitive to noise in the excitation and this decreases the safety of the shell in a dynamic environment.

Figure 41 illustrates the influence of random noise on the basin of attraction of the shell considering $\Gamma_0 = 0.40$, $\Gamma_1 = 0.40$, $\Omega = 1.60$. It shows three cross-sections of the 12-dimensional basin of attraction by the $\zeta_{11}(\tau) \times d\zeta_{11}(\tau)/d\tau$ plane. A total of 150×150 cells are considered in the analysis. The black region corresponds to the initial conditions that converge to the period-two attractor within the pre-buckling well while the gray region corresponds to initial conditions that lead to a period-two large-amplitude solution outside the pre-buckling well. Figure 41a corresponds to the deterministic case and Fig. 41b and Fig. 41c are related to perturbed solutions obtained with $\delta = 0.05$ and $\delta = 0.10$, respectively, and $\omega_l = 0.25$. In the deterministic case, each set of initial conditions leads to a specific attractor. In the nondeterministic case, for each set of initial conditions, the equations of motion are integrated using ten different samples of random perturbation. If in all cases all responses converge to the same attractor as in the deterministic case the cell is either marked in black or gray, but if they converge to different attractors or if the attractor is different from the one identified in the deterministic case, this means that the response associated with a given set of initial conditions is sensitive to random noise and the cell is

المنارة للاستشارات

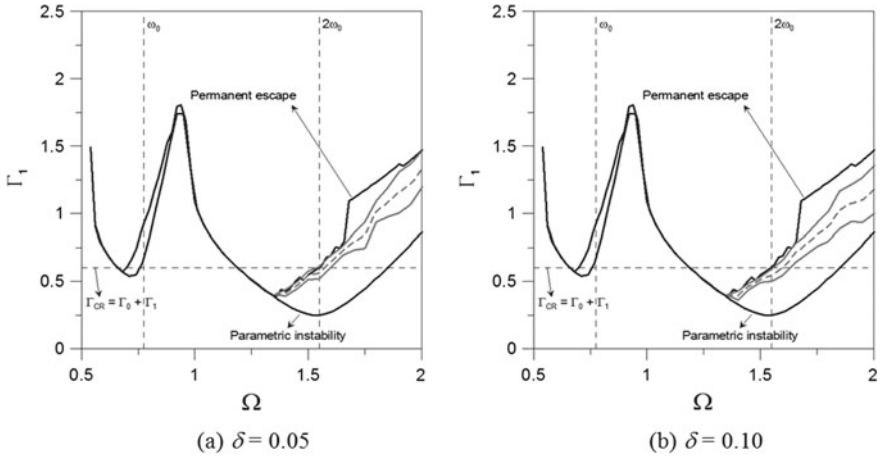

Fig. 40 Instability boundaries in force control space. ($\Gamma_0 = 0.40$, $\omega_l = 0.50$)

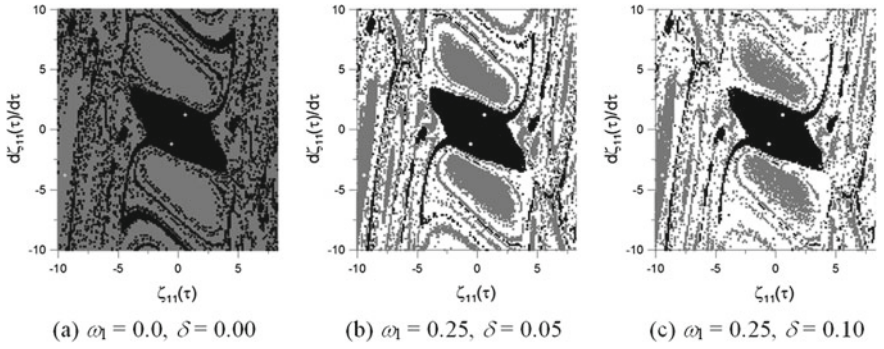

Fig. 41 Cross-sections of the basin of the attraction of the shell submitted to **a** a deterministic and **b**, **c** nondeterministic load. ($\Gamma_0 = 0.40$, $\Gamma_1 = 0.40$, $\Omega = 1.60$)

marked in white in Fig. 41b, c. As the standard deviation parameter δ increases the white region increases, decreasing the safe region associated with a given attractor. Yet, it is worth noting how the black basin compactness (to be suitably measured by a proper integrity measure, e.g., the IF) of the safe period-two attractor within the pre-buckling well in the nondeterministic case is not meaningfully reduced with respect to the corresponding deterministic one.

9 Conclusions

In this chapter, we studied the nonlinear dynamics of two archetypal structural systems exhibiting interactive modal post-buckling behavior, the discrete Augusti's

المنارة للاستشارات

model, and a reduced-order model of an axially loaded cylindrical shell. The uncoupled models exhibit a stable post-buckling response. However, in both cases, the modal interaction leads to unstable post-buckling paths that have a marked influence on the underlying potential energy, which exhibits several saddles at the same energy level surrounding and defining the boundary of the safe pre-buckling well. The resulting topology of the potential energy leads to a complex dynamic behavior and imperfection sensitivity, which has a marked influence on the dynamic integrity and safety of the structure in a dynamic environment. Also, these models present some inherent symmetries which influence the nonlinear static and dynamic response, being closely connected with the observed modal couplings and interactions.

First, we carried out a systematic analysis of the global response of Augusti's model and the mechanisms responsible for escape from a safe potential well. The static buckling analysis of the model stresses the influence of the modal coupling, imperfections, and symmetry on the nonlinear behavior of the system. Strong modal coupling is observed when the two bifurcation loads are equal, or nearly equal, leading to various unstable post-buckling solutions. Safe solutions are defined as the static pre-buckling equilibrium position and periodic oscillations which remain within the pre-buckling potential well. First, the response of the perfect and imperfect conservative system is studied through various cross-sections of the phase space and identification of the heteroclinic orbits of the saddles that define the safe region. This region is swiftly reduced as the static load approaches the critical value. Then we investigate how symmetries and imperfections influence the number, stability, and bifurcations of the nonlinear vibration modes. The analysis of Poincaré sections of the Hamiltonian systems for increasing energy levels shows that the inherent symmetries of the perfect systems lead to a superabundance of modes, including both similar and non-similar modes which influence the nonlinear resonant behavior. Next, the behavior of the model under harmonic base excitation, considering different forcing directions, is analyzed, emphasizing the influence of the modal coupling on the dynamics and stability of the system. The escape boundaries are obtained and the bifurcations connected with these boundaries are identified. Basin cross-sections of the bounded solutions are studied for increasing forcing amplitudes and the integrity factor that measures the size of the compact basin of the safe attractor is evaluated. The resulting integrity profiles clarify the robustness of bounded solutions and show to be a good measure of the safety of the structure in an evolving environment. Finally, a method for controlling nonlinear dynamics and chaos has been applied to a reduced s.d.o.f. Augusti's model with the aim of increasing its load carrying capacity, or the "practical" stability threshold. After having summarized the main features of the control method, it has been applied to the considered mechanical systems, both in the presence and in the absence of geometrical imperfections, in each case by applying the appropriate version of the control method. The methodology leads to an increment of the integrity of the basins of attraction in the excitation ranges where the erosion takes place, thus increasing both (i) the performance of the system in a dynamic environment, and (ii) its "practical" safety and thus its load carrying capacity.

المنارة للاستشارات

As an example of a continuous system exhibiting strong modal coupling and interaction, a low-dimensional, qualitatively consistent two-degree-of-freedom model is used to investigate in detail the global nonlinear behavior and stability of a thin-walled cylindrical shell under axial load. Selecting a practically relevant static load level in the region where the shell displays three potential wells, the complex bifurcation scenario displayed by the pre-loaded shell under harmonic excitation in the main parametric instability region is investigated. Characteristic bifurcation scenarios are investigated and all stable solutions are identified up to large load levels. They include periodic, quasi-periodic, and chaotic solutions. The basins of attraction of the different solutions in the four-dimensional phase space are obtained for increasing load levels. The basin cross-sections show how the basins interact with each other and how their simultaneous evolution influences their integrity and, consequently, the integrity factors that measure the size of the compact basin of each attractor. The resulting integrity profiles clarify the robustness of each solution and show to be a good measure of the safety of the structure in an evolving environment. Besides an intricate pattern of erosion of competing solutions, two different global events, namely the final escape of system response from the safe pre-buckling well and the final onset of a complex cross-well dynamics, are discussed along with their distinct, mechanical vs dynamical, meanings.

As shown by the two examples, for a structure liable to unstable post-buckling response, the critical load of the perfect or imperfect structure is an upper bound of its buckling load, both in the static and dynamic case, since it corresponds to a safe basin with the null area. So, any disturbance, however small, leads to buckling. To preserve the integrity of the structure under finite perturbation, the designer should prescribe a sufficiently large and robust compact basin surrounding the fixed point of the desired solution. So it is worthwhile in such cases to study how system uncertainties and load noise affect the structure safety. Results show that uncertainties in system parameters influence the dynamic buckling loads that are mostly lower than the load of the unperturbed ideal system. The scatter of results varies with the forcing frequency and is governed by the variation of the safe basin of attraction. For a harmonically excited structure, the known results show that small random noise influences the integrity of the basin of attraction, but has a small influence on the local integrity measure and integrity factor. Large perturbations of the harmonic signal only influence these integrity measures at a load level near the critical load.

The present chapter shows how a judicious use of the tools of nonlinear dynamic analysis can be used to access the safety of structural systems liable to unstable buckling under static and dynamic loads. However, most of these tools are rather difficult to employ in the analysis of high-dimensional system, the alternative being in such case to obtain a reduced-order model based, for example, on nonlinear normal modes.

Acknowledgements Figures 14, 15, 16, 17, and 18 are reproduced from (Orlando et al. 2011b) with the permission of ASME. Figures 24, 25, 26, 27 and 28 are reproduced from (Lenci et al. 2012a) with the permission of AIP Publishing.

المنارة للاستشارات

References

Augusti, G. (1964). Stabilità di strutture elastiche elementari in presenza di grandi spostamenti. *Atti dell'Accademia delle Scienze Fisiche e Matematiche di Napoli, 4*(5) (in Italian).

Batista, R. C., & Gonçalves, P. B. (1994). Non-linear lower bounds for shell buckling design. *Journal of Constructional Steel Research, 28*(2), 101–120.

Bazant, Z. P., & Cedolin, L. (1991). *Stability of structures*. Oxford: Oxford Press.

Boivin, N., Pierre, C., & Shaw, S. W. (1995). Nonlinear modal analysis of structural systems featuring internal resonances. *Journal of Sound and Vibration, 182,* 336–341.

Brush, D. O., & Almroth, B. O. (1975). *Buckling of bars, plates and shells*. New York: McGraw-Hill.

Croll, J. G., & Walker, A. C. (1972). *Elements of structural stability* (1st ed.). London: Macmillan.

Doedel, E., Keller, H. B., & Kernevez, J. P. (1991). Numerical analysis and control of bifurcation problems (I): Bifurcation in finite dimensions. *International Journal of Bifurcation and Chaos, 1*(3), 493–520.

Dubina, D., & Ungureanu, V. (2014). Instability mode interaction: From Van Der Neut model to ECBL approach. *Thin-Walled Structures, 81,* 39–49.

Gavassoni, E., Gonçalves, P. B., & Roehl, D. M. (2014). Nonlinear vibration modes and instability of a conceptual model of a spar platform. *Nonlinear Dynamics, 76*(1), 809–826.

Gavassoni, E., Gonçalves, P. B., & Roehl, D. M. (2015). Nonlinear vibration modes of an offshore articulated tower. *Ocean Engineering, 109,* 226–242.

Gioncu, V. (1994). General theory of coupled instabilities. *Thin-Walled Structures, 19*(2–4), 81–127.

Gonçalves, P. B., & Batista, R. C. (1988). Non-linear vibration analysis of fluid-filled cylindrical shells. *Journal of Sound and Vibration, 127*(1), 133–143.

Gonçalves, P. B., & Del Prado, Z. J. G. N. (2002). Non-linear oscillations and stability of parametrically excited cylindrical shells. *Meccanica, 37*(6), 569–597.

Gonçalves, P. B., & Del Prado, Z. J. G. N. (2004). Effect of non-linear modal interaction on the dynamic instability of axially excited cylindrical shells. *Computers & Structures, 82,* 2621–2634.

Gonçalves, P. B., & Santee, D. M. (2008). Influence of uncertainties on the dynamic buckling loads of structures liable to asymmetric post-buckling behavior. *Mathematical Problems in Engineering*, Article ID 490137.

Gonçalves, P. B., Silva, F. M. A., & Del Prado, Z. J. G. N. (2007a). Global stability analysis of parametrically excited cylindrical shells through the evolution of basin boundaries. *Nonlinear Dynamics, 50,* 121–145.

Gonçalves, P. B., Silva, F. M. A., & Del Prado, Z. J. G. N. (2007b). Transient and steady-state stability of cylindrical shells under harmonic axial loads. *International Journal of Non-Linear Mechanics, 42,* 58–70.

Gonçalves, P. B., Silva, F. M. A., & Del Prado, Z. J. G. N. (2008). Low dimensional models for the nonlinear vibration analysis of cylindrical shells based on a perturbation procedure and proper orthogonal decomposition. *Journal of Sound and Vibration, 315,* 641–663.

Gonçalves, P. B., Silva, F. M. A., & Del Prado, Z. J. G. N. (2016). Reduced order models for the nonlinear dynamic analysis of shells. *Procedia IUTAM, 19,* 118–125.

Gonçalves, P. B., Silva, F. M. A., Rega, G., & Lenci, S. (2011). Global dynamics and integrity of a two-dof model of a parametrically excited cylindrical shell. *Nonlinear Dynamics, 63,* 61–82.

Guckenheimer, J., & Holmes, P. (1984). *Nonlinear oscillations, dynamical systems and bifurcations of vector fields*. New York: Springer.

Hunt, G. W., Reay, N. A., & Yoshimura, T. (1979). Local diffeomorphisms in the bifurcational manifestations of the umbilic catastrophes. *Proceedings of the Royal Society of London, A, 369,* 47–65.

Jansen, J. S. (1977). Some two-mode buckling problems and their relation to catastrophe theory. *AIAA Journal, 15,* 1638.

Jensen, C. N., Golubitsky, M., & True, H. (1999). Symmetry, generic bifurcations, and mode interaction in nonlinear railway dynamics. *International Journal of Bifurcation and Chaos, 9,* 1321–1331.

المنارة للاستشارات

Jordan, D., & Smith, P. (2007). *Nonlinear ordinary differential equations*. Oxford: Oxford University Press (1st ed. 1977).

Kuznetsov, Y. A. (2004). *Elements of applied bifurcation theory*. New York: Springer.

Lansbury, A. N., Thompson, J. M. T., & Stewart, H. B. (1992). Basin erosion in the twin-well duffing oscillator: Two distinct bifurcation scenarios. *International Journal of Bifurcation and Chaos, 2,* 505–532.

Lenci, S., Orlando, D., Gonçalves, P. B., & Rega, G. (2012a). Controlling practical stability and safety of mechanical systems by exploiting chaos properties. *Chaos, 22*, Article ID 047502.

Lenci, S., Orlando, D., Rega, G., & Gonçalves, P. B. (2012b). Controlling nonlinear dynamics of systems liable to unstable interactive buckling. *Procedia IUTAM*, *5*, 108–123. https://doi.org/10.1016/j.piutam.2012.06.014, 2012b.

Lenci, S., & Rega, G. (1998a). A procedure for reducing the chaotic response region in an impact mechanical system. *Nonlinear Dynamics, 15,* 391–409.

Lenci, S., & Rega, G. (1998b). Controlling nonlinear dynamics in a two-well impact system. Parts I & II. *International Journal of Bifurcation and Chaos*, *8,* 2387–2424.

Lenci, S., & Rega, G. (2003a). Optimal control of homoclinic bifurcation: Theoretical treatment and practical reduction of safe basin erosion in the Helmholtz oscillator. *Journal of Vibration and Control, 9,* 281–315.

Lenci, S., & Rega, G. (2003b). Optimal control of nonregular dynamics in a Duffing oscillator. *Nonlinear Dynamics, 33,* 71–86.

Lenci, S., & Rega, G. (2004). A unified control framework of the nonregular dynamics of mechanical oscillators. *Journal of Sound and Vibration, 278,* 1051–1080.

Lenci, S., & Rega, G. (2005). Heteroclinic bifurcations and optimal control in the nonlinear rocking dynamics of generic and slender rigid blocks. *International Journal of Bifurcation and Chaos, 15,* 1901–1918.

McRobie, F. A., Popov, A. A., & Thompson, J. M. T. (1999). Auto-parametric resonance in cylindrical shells using geometric averaging. *Journal of Sound and Vibration, 227,* 65–84.

Melnikov, V. K. (1963). On the stability of the center for time-periodic perturbations. *Transactions of the Moscow Mathematical Society, 12,* 1–56.

Month, L. A., & Rand, R. H. (1980). An application of the Poincaré map to the stability of nonlinear normal modes. *Journal of Applied Mechanics, 47,* 645–651.

Nayfeh, A. H., & Balachandran, B. (1995). *Applied nonlinear dynamics*. New York: Wiley.

Nayfeh, A. H., Chin, C., & Nayfeh, S. A. (1996). On nonlinear normal modes of systems with internal resonance. *Journal of Vibration and Acoustics, 118,* 340–346.

Nayfeh, A. H., & Mook, D. T. (2008). *Nonlinear oscillations*. New York: Wiley (1st ed. 1979).

Nayfeh, A. H., & Nayfeh, S. A. (1994). On nonlinear modes of continuous systems. *Journal of Vibration and Acoustics, 116,* 129–136.

Orlando, D. (2010). *Nonlinear dynamics, instability and control of structural systems with modal interaction*. Ph.D. Thesis, Pontifícia Universidade Católica do Rio de Janeiro (in Portuguese).

Orlando, D., Gonçalves, P. B., Rega, G., & Lenci, S. (2011a). Non-linear dynamics and imperfection sensitivity of Augusti's model. *Journal of Mechanics of Materials and Structures, 6*(7–8), 1065–1078.

Orlando, D., Gonçalves, P. B., Rega, G., & Lenci, S. (2011b). Influence of modal coupling on the nonlinear dynamics of Augusti's model. *Journal of Computational Nonlinear Dynamics*, *6*(4), 041014-1–041014-11.

Orlando, D., Gonçalves, P. B., Rega, G., & Lenci, S. (2013a). Influence of symmetries and imperfections on the non-linear vibration modes of archetypal structural systems. *International Journal of Non-Linear Mechanics, 49,* 175–195.

Orlando, D., Gonçalves, P. B., Rega, G., & Lenci, S. (2013b). Nonlinear dynamics and instability as important design concerns for a guyed mast. In M. Wiercigroch & G. Rega (Eds.), *IUTAM Symposium on Nonlinear Dynamics for Advanced Technologies and Engineering Design* (pp. 223–234). Berlin: Springer.

المنارة للاستشارات

Peeters, M., Viguié, R., Sérandour, G., Kerschen, G., & Golinval, J. C. (2009). Nonlinear normal modes, Part II: Toward a practical computation using numerical continuation. *Mechanical Systems and Signal Processing, 23,* 195–216.

Pesheck, E., Boivin, N., Pierre, C., & Shaw, S. W. (2001). Nonlinear modal analysis of structural systems using multi-mode invariant manifolds. *Nonlinear Dynamics, 25,* 183–205.

Raftoyiannis, I. G., & Kounadis, A. N. (2000). Dynamic buckling of 2-DOF systems with mode interaction under step loading. *International Journal of Non-Linear Mechanics, 35,* 531–542.

Rega, G., & Lenci, S. (2005). Identifying, evaluating and controlling dynamical integrity measures in non-linear mechanical oscillators. *Nonlinear Analysis, 63,* 902–914.

Rega, G., & Lenci, S. (2008). Dynamical integrity and control of nonlinear mechanical oscillators. *Journal of Vibration and Control, 14,* 159–179.

Rega, G., & Lenci, S. (2010). Recent advances in control of complex dynamics in mechanical and structural systems. In M. A. F. Sanjuan & C. Grebogi (Eds.), *Recent progress in controlling chaos* (Vol. 16, pp. 189–237). World Scientific.

Rega, G., Lenci, S. & Ruzziconi, L. (2018). Dynamical integrity: A novel paradigm for evaluating load carrying capacity. In S. Lenci & G. Rega (Eds.), *Global nonlinear dynamics for engineering design and system safety* (Vol. 588, pp. 27–112). CISM Courses and Lectures. Cham: Springer.

Rodrigues, L., Silva, F. M. A., Gonçalves, P. B., & Del Prado, Z. J. G. N. (2014). Effects of modal coupling on the dynamics of parametrically and directly excited cylindrical shells. *Thin Walled Structures, 81,* 210–224.

Rosenberg, R. M. (1960). On normal vibrations of a general class of nonlinear dual-mode systems. *Journal of Applied Mechanics, 17,* 164–172.

Rosenberg, R. M. (1966). On nonlinear vibrations of systems with many degrees of freedom. *Advances in Applied Mechanics, 9,* 155–242.

Seydel, R. (1988). *From equilibrium to chaos. Practical bifurcation and stability analysis*. New York: Elsevier Science Publishing.

Shaw, S. W., & Pierre, C. (1991). Nonlinear normal modes and invariant manifolds. *Journal of Sound and Vibration, 150*(1), 170–173.

Silva, F. M. A., Brazão, A. F., Gonçalves, P. B., & Del Prado, Z. J. G. N. (2015). Influence of physical and geometrical uncertainties in the parametric instability load of an axially excited cylindrical shell. *Mathematical Problems in Engineering*, Article ID 758959.

Silva, F. M. A., & Gonçalves, P. B. (2015). The influence of uncertainties and random noise on the dynamic integrity analysis of a system liable to unstable buckling. *Nonlinear Dynamics, 81,* 707–724.

Silva, F. M. A., Gonçalves, P. B., & Del Prado, Z. J. G. N. (2012). Influence of physical and geometrical system parameters uncertainties on the nonlinear oscillations of cylindrical shells. *Journal of the Brazilian Society of Mechanical Sciences and Engineering, 34,* 622–632.

Soliman, M. S., & Thompson, J. M. T. (1989). Integrity measures quantifying the erosion of smooth and fractal basins of attraction. *Journal of Sound and Vibration, 135,* 453–475.

Soliman, M. S., & Thompson, J. M. T. (1992). Global dynamics underlying sharp basin erosion in nonlinear driven oscillators. *Physical Review A, 45,* 3425–3431.

Sophianopoulos, D. S. (2007). Bifurcations and catastrophes of a two-degrees-of-freedom nonlinear model simulation of the buckling and postbuckling of rectangular plates. *Journal of the Franklin Institute, 344,* 463–488.

Thompson, J. M. T. (1989). Chaotic behavior triggering the escape from a potential well. *Proceedings of the Royal Society of London A, 421,* 195–225.

Thompson, J. M. T., & Hunt, G. W. (1973). *A general theory of elastic stability*. London: Wiley.

Thompson, J. M. T., & Hunt, G. W. (1984). *Elastic instability phenomena*. London: Wiley.

Thompson, J. M. T., & Gaspar, Z. (1977). A buckling model for the set of umbilic catastrophes. *Mathematical Proceedings of the Cambridge Philosophical Society, 82,* 497–507.

Thompson, J. M. T., & Stewart, H. B. (2002). *Nonlinear dynamics and chaos*. London: Wiley (1st ed. 1986).

المنارة للاستشارات

Vakakis, A. F., Gendelman, O. V., Bergman, L. A., McFarland, D. M., Kerschen, G., & Lee, Y. S. (2008). *Nonlinear targeted energy transfer in mechanical and structural systems* (Vol. I and II). New York: Springer.

Vakakis, A. F., Manevitch, L., Mikhlin, Y. V., Pilipchuck, V. N., & Zevin, A. A. (1996). *Normal modes and localization in nonlinear systems*. New York: Wiley.

Vakakis, A. F., & Rand, R. H. (1992). Normal modes and global dynamics of a 2-degree-of-freedom nonlinear-system; Part I: Low energies. *International Journal of Non-Linear Mechanics, 27,* 861–874.

Van der Heijden, A. M. A. (2008). *W. T. Koiter's elastic stability of solids and structures*. Cambridge: Cambridge University Press.

Wiebe, R., & Spottswood, S. M. (2014). Co-existing responses and stochastic resonance in post-buckled structures: A combined numerical and experimental study. *Journal of Sound and Vibration, 333,* 4682–4694.

Wiggins, S. (1990). *Introduction to applied nonlinear dynamical systems and chaos*. New York: Springer.

Wiggins, S. (2003). *Introduction to applied nonlinear dynamical systems and chaos* (Vol. 2). New York: Springer.

المنارة للاستشارات

Local Versus Global Dynamics and Control of an AFM Model in a Safety Perspective

Valeria Settimi and Giuseppe Rega

Abstract The role of local and global dynamics to assess a system robustness and actual safety in operating conditions is investigated, by also studying the effect of different local and global control techniques on the nonlinear behavior of a noncontact AFM. First, the nonlinear dynamical behavior of a single-mode model of noncontact AFM is analyzed in terms of stability of the main periodic solutions, as well as attractors robustness and basins integrity. To the same AFM model, an external feedback control is inserted during its nonlinear continuum formulation, with the aim to keep the system response to an operationally suitable one. The dynamical analysis of the controlled system is developed to investigate and verify the effects of control into the system overall behavior, which could be unexpectedly influenced by the local nature of the control technique. A different control technique is finally applied to the AFM model, acting on global bifurcation events to obtain an enlargement of the systems safe region in parameters space. The analytical procedure, based on Melnikov method, is applied to the homoclinic bifurcation involving the system hilltop saddle, and its practical effects as regards possibly increasing the system overall robustness are numerically investigated by means of a dynamical integrity analysis. Then, a fully numerical procedure is implemented to possibly control global bifurcations involving generic saddles. The method proves to succeed in delaying the drop down of the erosion profile, thus increasing the overall robustness of the system during operating conditions.

Keywords Noncontact AFM · Nonlinear dynamics · External feedback control Control of global bifurcations · Dynamical integrity · System safety

V. Settimi (✉) · G. Rega
Department of Structural and Geotechnical Engineering,
Sapienza University of Rome, Rome, Italy
e-mail: valeria.settimi@uniroma1.it

G. Rega
e-mail: giuseppe.rega@uniroma1.it

© CISM International Centre for Mechanical Sciences 2019

S. Lenci and G. Rega (eds.), *Global Nonlinear Dynamics for Engineering Design and System Safety*, CISM International Centre for Mechanical Sciences 588,
https://doi.org/10.1007/978-3-319-99710-0_5

المنارة للاستشارات

1 Introduction

Analyzing the nonlinear dynamical behavior of a mechanical system usually entails the investigation of the stability of its response under variation of some (characterizing and/or controllable) parameter. Bifurcation diagrams and behavior charts in parameters space allow to verify the system robustness to possible changes of the operational parameter setup, and often reveal a wide variety of nonlinear phenomena, such as bifurcations and in-well instability regions which can lead to possible unstable, aperiodic, or chaotic oscillations. However, besides these analyses, possible changes in the system initial conditions due to imperfections have to be taken into account, since it is nowadays ascertained that the safe operation of a nonlinear system depends not only on the local stability of its solutions but also on the global dynamics associated with the uncorrupted basin surrounding each solution. It appears therefore evident that tools and concepts of global dynamics and dynamical integrity represent crucial instruments not only to achieve a complete and accurate description of the system dynamics, but, from a practical viewpoint, to assess the actual safety of a dynamical system (Rega and Lenci 2015). More importantly, they can be proposed as a comprehensive approach to be applied for an in-depth investigation of a nonlinear model, in order not only to theoretically analyze the robustness of competing attractors and the erosion processes that bring to the escape from bounded regions, but also to critically evaluate the effect of different control techniques and, from an operational viewpoint, to furnish hints useful for engineering design. Following these guidelines, this chapter aims to present a general framework for studying local and global dynamics, as well as control, of a sample mechanical system, taking as reference a reduced order model of noncontact Atomic Force Microscope (AFM), which can indeed represent a large number of nonlinear models with some ensuing dynamic phenomena.

AFMs are powerful devices used for surface analysis in nanoelectronics, mechanics of materials and biotechnology, as they permit to topologically characterize surfaces up to micro- and nano-resolution levels (Sarid 1991; Morita et al. 2009; Eaton and West 2010). In a typical AFM, the topography is imaged by scanning a sharp tip, fixed to the free end of a microcantilever vertically bending over the sample surface, and by measuring the tip deflection through a laser technology. The tip–sample interaction modifies the beam dynamics and allows not only to image surfaces but also to measure some physical properties of the sample. As far as the AFM dynamics is concerned, the most common operation modes are the tapping mode, in which the tip operates in both attractive and repulsive force regions and touches the surface only for short time intervals, and the noncontact mode, in which there is absence of contact between the tip and the sample and their interaction is governed by a solely attractive potential. Consequently, for the latter type of AFM, the tip has to maintain a design gap from the sample such to ensure that the beam elastic restoring force is stronger than the atomic attraction. Otherwise, instability of the equilibrium configuration occurs, with the so-called “jump to contact”, or escape (in dynamical systems terms), phenomenon. As the dynamic excitation tends to strongly reduce the

المنارة للاستشارات

equilibrium gap, the study of system stability as a function of a varying excitation amplitude, among other physical parameters, is a very important issue for noncontact AFMs, in order to reliably determine the escape threshold separating the region of bounded (i.e., noncontact) solutions from that of unbounded solutions, the latter corresponding to unwanted contacts between tip and sample.

During the scan operation, moreover, the sample roughness can modify the distance between the microcantilever tip and the sample to be scanned, and thus, the nonlinear atomic force interaction which is used to obtain the topography can lead to unstable dangerous motions. To prevent these undesirable motions and improve the microscope performances, several control techniques have been proposed in the field of AFMs during the last two decades, primarily based on the feedback control methods that work by keeping the microcantilever vibration to a selected reference one and allowing to simultaneously and reliably measure the sample surface. However, since these procedures are focused on controlling the system local dynamics, their impact on the system overall dynamics is generally unknown. Nevertheless, analyzing the latter is of great importance, especially for micro/nanomechanical systems like AFMs for which slight changes of the initial position and/or velocity at the nanoscale level, or modifications of the operational parameter setup, can produce dramatic modifications of the overall dynamics.

From a global dynamics perspective, it is thus of interest to clearly detect in the state plane the basins of attraction of the periodic (acceptable) solutions and that of the (undesirable) unbounded response compromising the device operation. Furthermore, the relevant erosion process due to variations of some system parameter can be followed and quantified by means of the construction of the so-called erosion profiles. As a practical consequence of such analyses, which belong to the field of dynamical integrity, the sensitivity of a system to variations of both operational parameters and initial conditions can be discussed, and some hints useful to define thresholds able to ensure acceptable safety targets can be achieved. The concept of dynamical integrity can be also referred to for developing a different control technique based on the global properties of the dynamical system, which acts on the homo/heteroclinic bifurcations involving the stable and unstable manifolds of the system saddles responsible for the erosion of the basins. It operates by properly shifting them thanks to the addition of some controlling superharmonics to the reference harmonic excitation, thus increasing the system overall robustness.

The chapter is organized as follows. Nonlinear local and global dynamics of a reduced order model of noncontact AFM are presented in Sect. 2, while Sect. 3 investigates the dynamical effects of an external feedback control on the overall response of the AFM model. Section 4 deals with the implementation, into the same model, of a global control technique, whose effects are analyzed and critically discussed also in terms of safer AFM operation. Finally, in Sect. 5, some general conclusions are drawn.

المنارة للاستشارات

2 Nonlinear Dynamics of a Reduced Order Model of Noncontact AFM

2.1 Equations of Motion, Reduced Order Model, and Unperturbed System

The physical model under consideration is a fixed-free atomic force microscope (AFM) microcantilever, which is assumed to be planar, inextensible, and horizontal, with length L and a sharp tip of height h_T close to its free end, and with a distance g between its fixed side and the sample (Fig. 1a) (Hornstein and Gottlieb 2008). The beam material is considered linearly elastic, homogeneous, and isotropic, with Young modulus E. Reference is made to the general formulation based on the classical inextensional beam model of Crespo da Silva and Glynn (1978). Accordingly, the set of two coupled partial differential equations (PDEs) for the beam horizontal and vertical transverse vibrations is

$$\begin{aligned} m\bar{u}_{tt} - [EI\bar{v}_{rrr}\bar{v}_r - J_z\bar{v}_{ttr}\bar{v}_r + \Lambda(1+\bar{u}_r)]_r &= \bar{Q}_u \\ m\bar{v}_{tt} - [EI(\bar{v}_{rrr} + \bar{v}_r\bar{v}_{rr}^2) + J_z(\bar{v}_{ttr} + \bar{v}_{tr}^2\bar{v}_r) + \Lambda\bar{v}_r]_r &= \bar{Q}_v \end{aligned} \tag{1}$$

where $\bar{u}(r,t)$ and $\bar{v}(r,t)$ are the horizontal and vertical displacements and subscript letters denote partial differentiation with respect to arc length r and time t. Coefficients EI, J_z, and m are beam stiffness, principal moment of inertia, and mass per unit length, respectively, and Λ is a Lagrangian multiplier accounting for the inextensibility condition $(1+\bar{u}_r)^2 + \bar{v}_r^2 = 1$. Generalized forces in horizontal and vertical direction are represented by $\bar{Q}_u$, $\bar{Q}_v$, the former corresponding to a feedback control force depending on the horizontal displacement and the latter also accounting for the localized (at $r = a_T$, see Fig. 1a) transverse atomic force interaction derived from a Lennard Jones potential for a sphere-plane system (Israelachvili 1992; Sarid et al. 1996), localized at the tip and representing the interaction between the tip and the sample. Since the AFM under analysis operates in noncontact regime, the most important atomic force interaction is the attractive one and the repulsion interaction can be neglected. The set of nonhomogeneous boundary conditions

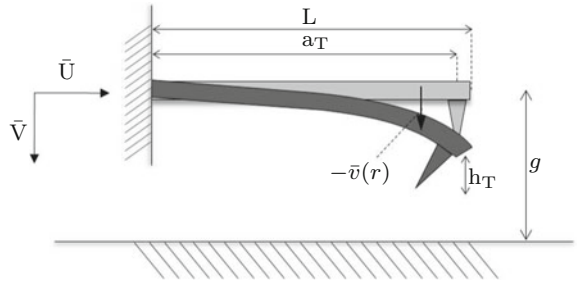

Fig. 1 Microcantilever model

المنارة للاستشارات

$$\begin{aligned} &\bar{v}(0,t) = \bar{V}(t), \qquad \bar{v}_r(0,t) = 0, \qquad \bar{u}(0,t) = \bar{U}(t), \\ &\bar{v}_{rr}(L,t) = 0, \qquad \bar{v}_{rrr}(L,t) = 0, \qquad \bar{u}_r(L,t) = 0 \end{aligned} \tag{2}$$

completes the formulation of the problem, with $\bar{V}(t)$ and $\bar{U}(t)$ being the prescribed vertical transverse and horizontal scan displacement, respectively.

The incorporation of the holonomic constraint, which allows to express the horizontal displacement in terms of the vertical one, the isolation and expansion of the Lagrange multiplier, and the nondimensionalization and use of a moving reference frame ($v(s,\tau) = w(s,\tau) + V(\tau)$) lead to the formulation of an initial-boundary value problem (IBVP) with a homogeneous set of boundary conditions for the transverse vibrating motion. A single-mode assumption ($w(s,\tau) = q_1(\tau)\phi_1(s)$) and a Galerkin approximation (the basis function being that of a clamped-spring beam) reduce the IBVP to the second-order ordinary differential equation (ODE), which has the following nondimensional form:

$$\begin{aligned} \left(1+\alpha_2 x^2\right)\ddot{x} + \left(\alpha_1 + \alpha_2 \dot{x}^2 + \alpha_3 x^2\right) x = &-\frac{\Gamma_1}{\left(1+x+V_g\right)^2} - \left(\rho_1 + \rho_2 x^2\right)\dot{x} \\ &- \nu_2\left(\ddot{V}_g + \nu_1 \dot{V}_g\right) + \left(\mu_1 x + \mu_2 x^3\right)\left(\ddot{U}_g + \eta_1 \dot{U}_g + \eta_2 U_g\right) \end{aligned} \tag{3}$$

where $x(\tau) = q_1(\tau)\phi_1(\alpha)/\gamma$ and $t_N = \omega_1 \tau$; α and γ are the nondimensional tip distances from the microbeam fixed end and the sample, respectively; ρ_1 is the damping coefficient; Γ_1 is the atomic attraction parameter; α_1, α_2 and α_3 are coefficients of the linear and nonlinear terms; $U_g = U/\gamma$ and $V_g = V/\gamma$ represent the horizontal and vertical excitations; η_1, η_2 and ρ_2 are internal feedback control parameters, the first two related to the time dependent horizontal scan and the latter to the cubic damping term. For the nondimensionalizations and detailed expressions of all coefficients, see Hornstein and Gottlieb (2008).

It is worth underlining that the choice to refer to a single-degree-of-freedom model is here justified by the operating conditions dealt with in the following. In fact, even if it has been shown that for tapping AFMs a multimode Galerkin approximation is needed to detect nonlinear phenomena (e.g., grazing bifurcations) that a single-mode analysis does not match, however, in the noncontact operation range, a multimode discretization does not enrich the system response, and a single-mode approximation is sufficient to detect the main nonlinear aspects (Bahrami and Nayfeh 2012). Moreover, the investigated frequency range spans around primary and secondary resonances of the first mode, where the contribution of the higher modes is substantially negligible (Hornstein and Gottlieb 2012).

Accounting for the orders of magnitude of various coefficients in commercial AFMs, feedback controls and the nonlinear terms related to α_2 can be neglected, to obtain

$$\ddot{x} + \alpha_1 x + \alpha_3 x^3 = -\frac{\Gamma_1}{\left(1+x+V_g\right)^2} - \rho_1 \dot{x} - \nu_2\left(\ddot{V}_g + \nu_1 \dot{V}_g\right) + \mu_1 x \ddot{U}_g \tag{4}$$

المنارة للاستشارات

Note that the AFM scan process is performed by means of both vertical and horizontal excitations, the former allowing to quantify the interaction forces and the latter being necessary to obtain the three-dimensional map of the sample. Yet, in existing commercial AFMs the horizontal scan (parametric) frequency is much smaller than the vertical (external) one, so that it appears reasonable to study the two forced cases in the neighborhood of resonances separately. The results presented in this chapter will thus refer to the sole parametric horizontal scan, which is supposed to be harmonic ($U_g = U\sin(\omega_u t)$), even if few considerations will be drawn about the role played by the vertical external excitation, as well.

The operation domain of noncontact AFMs must be such to avoid jump to contact with the scanned sample. In dynamical system terms, this is ascertained by considering the undamped, unforced version of Eq. (4)

$$\ddot{x} + \alpha_1 x + \alpha_3 x^3 + \frac{\Gamma_1}{(1+x)^2} = 0 \tag{5}$$

with the relevant Hamiltonian, where $y = \dot{x}$, being

$$\begin{cases} \dot{x} = \dfrac{\partial H}{\partial y} \\ \dot{y} = -\dfrac{\partial H}{\partial x} \end{cases} \qquad H(x,y) = \frac{y^2}{2} + V(x) = \frac{y^2}{2} + \frac{\alpha_1 x^2}{2} + \frac{\alpha_3 x^4}{4} - \frac{\Gamma_1}{1+x} \tag{6}$$

with the associated single, asymmetric, potential well with left (i.e., towards the sample position $x = -1$) contact direction (Fig. 2a). The unperturbed state space is depicted in Fig. 2b, where the two fixed points of the time-independent problem, i.e., the stable equilibrium (E) of the cantilever tip under elastic (α_1, α_3) and atomic interaction (Γ_1) forces and the corresponding hilltop saddle (S_H), are reported for a given set of values of the governing parameters. The homoclinic orbit $y_h(t)$ of the saddle is also plotted in Fig. 2b: it separates the inner region of bounded periodic solutions from the outer region of unbounded solutions, the former representing the safe domain for noncontact AFM operation. The study of the fixed points as a function of the atomic interaction coefficient Γ_1 is reported in Fig. 2c for $\alpha_1 = 1$ and $\alpha_3 = 0.1$, and provides the upper boundary for the stable equilibrium E existence at the limit value $\Gamma_1 = 4/27$ where a saddle-node bifurcation leads to the birth of the unstable branch. The lower stable equilibrium E_1 settles under the limit value $x = -1$, which corresponds to the position of the sample with respect to the cantilever tip, thus having no physical meaning. This entails that for Γ_1 values higher than that of the saddle-node, the microbeam jumps to contact with the sampled surface. This phenomenon, associated with the escape of the response from the single potential well of Fig. 2a, is precluded in noncontact AFMs: so, there is a great interest in analyzing the conditions for its impending occurrence in different ranges of frequency around parametric (and/or external) resonances, along with the features through which they

المنارة للاستشارات

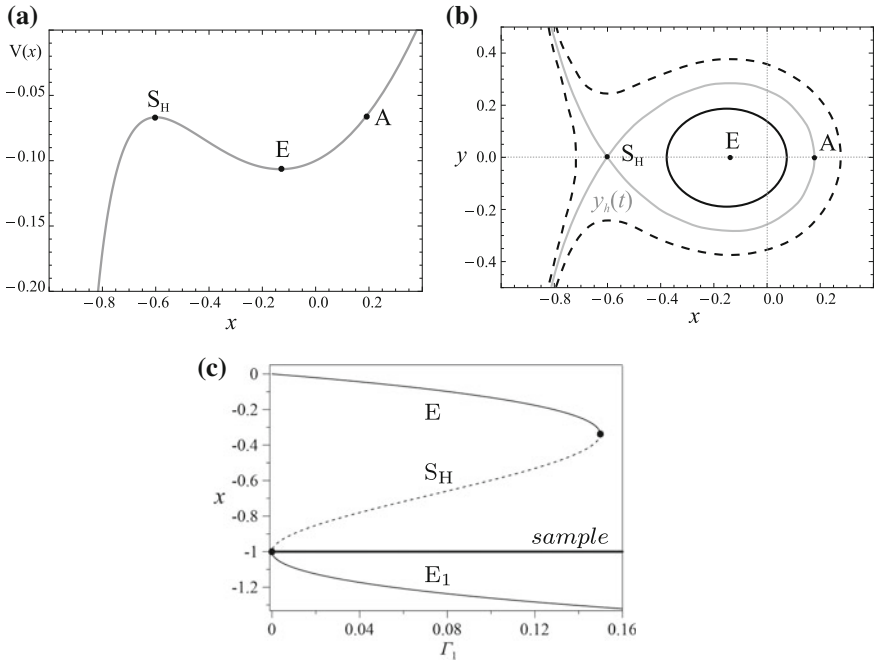

Fig. 2 Potential $V(x)$ (**a**), and unperturbed phase space (**b**) for $\alpha_1 = 1, \alpha_3 = 0.1, \Gamma_1 = 0.1$. Gray line: homoclinic orbit; solid black line: periodic orbit; dashed black line: unbounded orbit. System equilibria as a function of the atomic attraction Γ_1 (**c**). E, E_1: stable equilibria; S_H: hilltop saddle

are realized when varying a control parameter, typically an excitation amplitude characteristic of the system.

2.2 *Bifurcation Scenarios, Response Charts, and Escape Threshold*

The nonlinear response of the parametrically excited single-mode model is analyzed via continuation techniques and numerical simulation (Doedel and Oldeman 2012), for the following set of parameter values (Rega and Settimi 2013):

$$\alpha_1 = 1, \quad \alpha_3 = 0.1, \quad \rho_1 = 0.001, \quad \Gamma_1 = 0.1, \quad \mu_1 = 1.5708 \tag{7}$$

The calculated natural frequency for these values is $\omega_1 = 0.835$. Several bifurcation diagrams as a function of the forcing amplitude U have been obtained in a large range of frequencies including the fundamental ($\omega_u = \omega_1$) and principal ($\omega_u = 2\omega_1$) parametric resonances, and the main periodic solutions and local bifurcations have been

المنارة للاستشارات

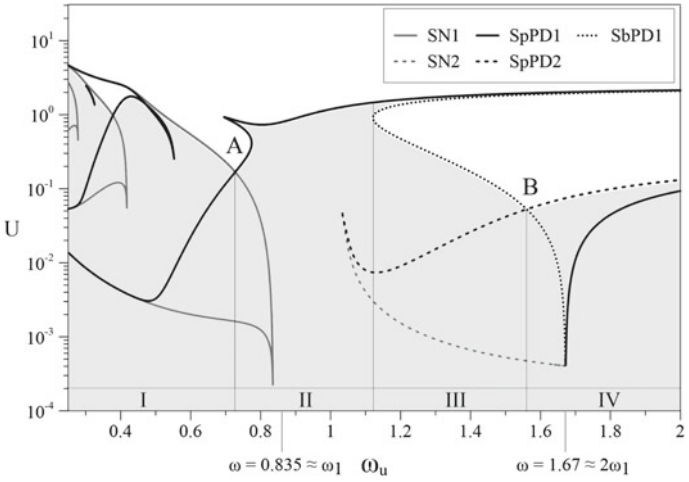

Fig. 3 Local bifurcations map and overall escape threshold in the frequency-amplitude space of parametric excitation. Gray area: region of stable response; SN1: saddle-node of the 1-period solution; SN2: saddle-node of the 2-period solution; SpPD1: supercritical period doubling of the 1-period solution; SpPD2: supercritical period doubling of the 2-period solution; SbPD1: subcritical period doubling of the 1-period solution. Numbers I to IV correspond to four main regions of distinct response scenarios

detected. These diagrams exhibit a variety of response scenarios. The local bifurcation loci in the excitation parameter control space (forcing frequency vs. forcing amplitude) are summarized in the semilogarithmic chart of Fig. 3. The system overall escape threshold separates the bounded solutions (below the curve) from the unbounded solutions (above the curve) and is obtained as the envelope of local bifurcation escape thresholds in different parameter ranges. From a physical viewpoint, it represents the (unacceptable) amplitude value that would bring the beam tip oscillation beyond the location of the sample (at $x = -1$); from the dynamical viewpoint it corresponds to the total annihilation of all basins of attraction (see Sect. 2.3 forward). Changes in the escape threshold slope correspond to changes in the kind of bifurcation event leading to escape and, apart from a localized exchange of the governing one in the frequency range between 0.4 and 0.5, four main different regions can be identified in the parameter control space (Fig. 3), from the escape viewpoint.

Region I includes low frequencies set on the left ($\omega_u = 0.5-0.72$) of the downward vertex A of the overall escape threshold corresponding to nonlinear fundamental resonance. Here, the system displays coexistence, for low values of the forcing amplitude, of two stable 1-period solutions, with the initial low-amplitude (nonresonant) P1L solution being connected to the (resonant) P1H solution of high amplitude through the classical unstable branch in between a couple of saddle-node bifurcations. In this range, the nonresonant solution governs the escape from the bounded region, which thus is determined by the occurrence of the relevant saddle-node bifurcation, while the resonant response exists in a limited range of forcing amplitude

المنارة للاستشارات

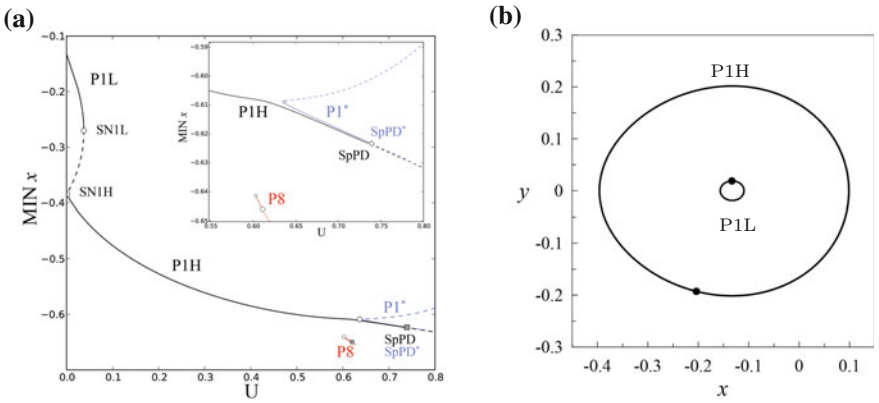

Fig. 4 Bifurcation diagram, and enlargement, as a function of the forcing amplitude U at $\omega_u = 0.8$ (**a**) and phase portrait of the P1L (gray line) and P1H (black line) periodic solutions at $U = 0.01$ (**b**). P1L: low-amplitude (nonresonant) 1-period solution; P1H: high-amplitude (resonant) 1-period solution; P8: 8-period solution; P1*: 1-period solution; SN: saddle-node bifurcation; SpPD: supercritical period doubling bifurcation

and becomes unstable through a supercritical period doubling. As the frequency approaches the nonlinear resonance ($\omega_u = 0.72$, A-vertex), the latter bifurcation moves to growing amplitude values, until at the right of the nonlinear resonance (region II, $\omega_u = 0.72-1.12$), it becomes the local event triggering escape, as shown in the sample bifurcation diagram reported in Fig. 4. Escape occurs after a sequence of period doublings ending up to chaos and disappearing through a successive boundary crisis, all of this being not represented in Fig. 3 because of occurring in very narrow ranges of the control parameter. The III and IV regions are characterized by the presence of a 2-period solution, typical of the dynamical behavior around the subharmonic resonance, which arises through a subcritical period doubling of the 1-period response (SbPD1) and disappears by means of a supercritical period doubling. In this respect, thus, the role played by the saddle-node bifurcation of the low-amplitude 1-period solution at left of the A-vertex is herein replaced by this subcritical period doubling bifurcation. The 2-period solution becomes stable via saddle-node (SN2) bifurcation at low values of forcing amplitude; the response pattern is now similar to the one in region I, apart from replacing P1H with P2. As in that case, the range of coexistence of stable P1 and P2 solutions grows up with increasing forcing frequency, up to entailing (at $\omega_u \cong 1.56$, B-vertex) the exchange of the local event triggering overall escape from SbPD1 to the supercritical period doubling bifurcation (SpPD2) of P2. This is substantially the same pattern as the one on the right of the nonlinear fundamental resonance and, indeed, the cascade of period doubling bifurcations arising from SpPD2 keeps governing the system escape in the whole region IV, which includes the principal resonance range ($\omega_u = 1.56-1.8$, see the bifurcation diagram of Fig. 5).

المنارة للاستشارات

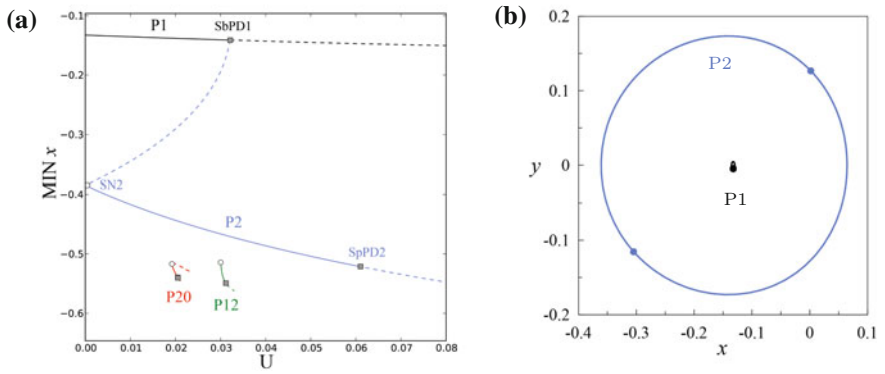

Fig. 5 Bifurcation diagram as a function of the forcing amplitude U at $\omega_u = 1.6$ (**a**) and phase portrait of the P1 (gray line) and P2 (black line) periodic solutions at $U = 0.01$ (**b**). P1: 1-period solution; P2: 2-period solution; P12: 12-period solution; P20: 20-period solution; SN2: saddle-node bifurcation of P2; SbPD1: subcritical period doubling bifurcation of P1; SpPD2: supercritical period doubling bifurcation of P2

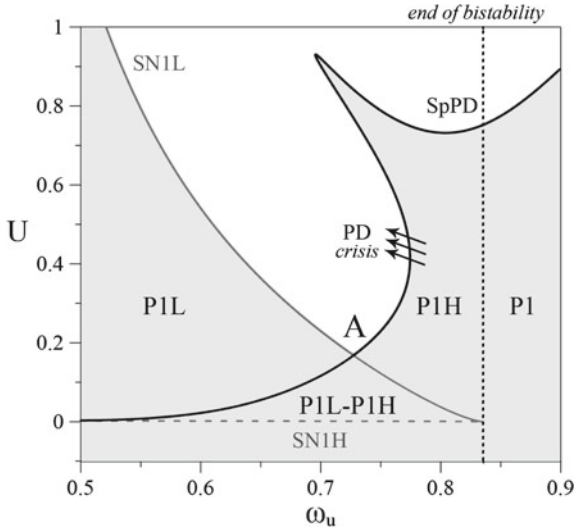

Fig. 6 Behavior chart in the ω_u-U plane close to fundamental resonance ω_1. Gray area: region of stable response; P1L/P1H: nonresonant/resonant 1-period solutions; SN1L/SN1H: saddle-node of the P1L/P1H solution; SpPD: supercritical period doubling

The bifurcation diagrams of Figs. 4 and 5 show also the short-range coexistence with the main periodic solutions of variable solutions of higher periodicity, which arise from saddle-node bifurcations and end up with local chaotic responses via series of period doublings occurring in very narrow ranges of amplitude values. These solutions are indeed of minor interest.

Focusing around the fundamental resonance (Fig. 6), the system shows the same qualitative behavior of a number of softening oscillators subjected to primary external excitation, such as the Helmholtz oscillator (Szemplinska-Stupnicka 1992) and

المنارة للاستشارات

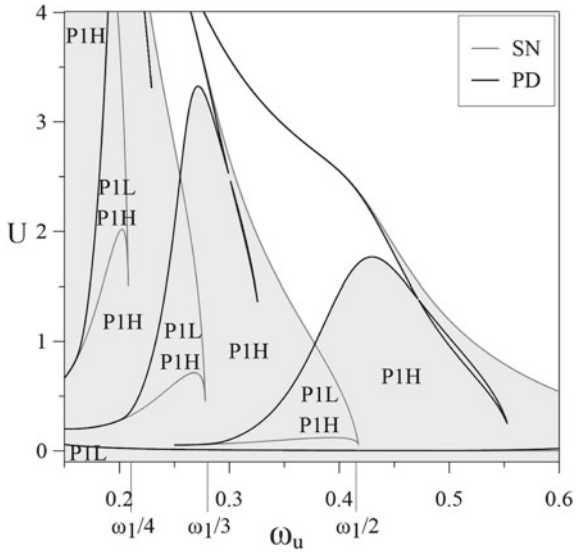

Fig. 7 Behavior chart in the ω_u-U plane at low frequency values. Gray area: region of stable response; P1L/P1H: nonresonant/resonant 1-period solutons; SN: saddle-node bifurcation; PD: supercritical period doubling

single-mode models of MEMs (Lenci and Rega 2006; Alsaleem et al. 2010), especially for what concerns the V-shaped region of escape, its limiting boundaries, and the underlying triangle region with the two coexisting 1-period solutions. Figure 6 shows that such a coexistence in the region in between the two SN loci occurs up to $\omega_u = 0.835 = \omega_1$, where they collapse with each other. Right of this value, and above the corresponding value of forcing amplitude, the sole period-1 solution previously associated with P1H occurs (now called P1 solution) and its annihilation through SpPD (and the following series of period doublings) characterizes the smooth transition to escape for increasing amplitude. Note again that no loci of supercritical period doubling of higher periodicity solutions are reported in Fig. 6, left of (and above) the SpPD threshold, nor the ensuing locus of boundary crisis leading to escape, since these events occur in a very narrow range of control parameter values. Note also that, in contrast, transition to escape from the left side occurs via the typical sudden SN bifurcation.

For the sake of completeness, it is worth noting that the inspection of the bifurcation/response scenarios at low values of the forcing frequency (Fig. 7) points out some interesting features of the system dynamical behavior. The global escape threshold, in fact, displays local minima at frequencies values corresponding to superharmonic resonances $\omega_u \cong 0.41 = \omega_1/2$ (also visible in Fig. 3), $\omega_u \cong 0.27 = \omega_1/3$ and $\omega_u \cong 0.21 = \omega_1/4$, where, as already seen at fundamental resonance, the dynamical response is characterized by a recurrent triangle region of coexistence of nonresonant P1L and resonant P1H solutions, and, according to the resonance frequency value, such solutions are now periodic responses with two harmonics of frequency ω and 2ω (3ω, 4ω). Soon after and to the right of these triangle regions, the system displays the presence of two thresholds of period doubling which delimit a nar-

المنارة للاستشارات

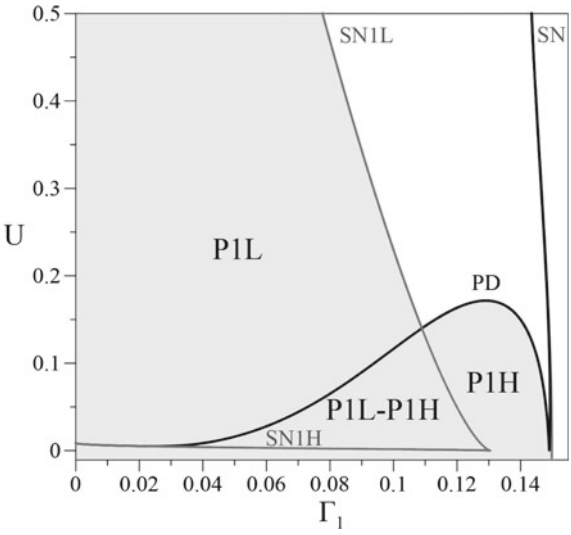

Fig. 8 Behavior chart in the Γ_1-U plane close to fundamental resonance ω_1. Gray area: region of stable response; P1L/P1H: nonresonant/resonant 1-period solutons; SN1L/SN1H: saddle-node of the P1L/P1H solution; PD: period doubling

row region around ultrasuperharmonic frequencies at $\omega_u = 0.218 - 0.229 \cong 2\omega_1/7$, $\omega_u = 0.301 - 0.326 \cong 2\omega_1/5$ and $\omega_u = 0.47 - 0.55 \cong 2\omega_1/3$. Inside these ranges, the sole P1 solution becomes unstable via a subcritical period doubling which leads to the birth of a P2 solution, whose frequency components include, besides the $\omega/2$ frequency characterizing the period-doubled solutions, the superharmonic frequency and its higher harmonics. Thus, summarizing the general dynamical behavior of the model, it can be stated that at fundamental and superharmonic resonance frequencies (i.e., $\omega_u = \omega_1/n$, $n = 1, 2, 3, 4, \ldots$), the system response is characterized by coexistence of resonant and nonresonant 1-period solutions, while at principal resonance and ultrasuperharmonic resonance frequencies (i.e., $\omega_u = 2\omega_1/n$, $n = 1, 3, 5, 7, \ldots$), the main and partially coexisting periodic responses are 1-period and 2-period solutions.

Finally, it is of interest to analyze the influence of the nonlinear interaction parameter variation Γ_1 on the system dynamical response; such parameter, which depends on the kind of tip and sample materials and their distance at nanoscale level, is in fact the characterizing ingredient of an AFM model, and introduces a nonlinear term of order-2 into the system (see Eq. (4)). The behavior chart in the Γ_1-U plane reported in Fig. 8 for a forcing frequency $\omega_u = 0.7$ near the fundamental resonance shows that as the nonlinear interaction increases, with respect to the reference value $\Gamma_1 = 0.1$ used for the previous numerical analyses, the amplitude escape value for the P1L solution rapidly decreases, up to the disappearance of such periodic solution and consequently of the region of coexistence of resonant P1H and nonresonant P1L solutions (at $\Gamma_1 \cong 0.13$); after that, for higher values of the interaction parameter the sole P1H solution remains as system stable periodic solution, and its escape boundary represented by the supercritical period doubling threshold PD1H moves to higher values of the forcing amplitude U, enlarging the stability region up to $\Gamma_1 \cong 0.14$,

المنارة للاستشارات

when it drastically falls down causing the annihilation of the P1H stability region. The outcomes of Fig. 8 can be exploited for design purposes by referring to a dual reading key: on the one hand, in fact, they point out the crucial role played by the tip–sample nonlinear interaction on the response of the AFM cantilever, furnishing practical information about the limiting values of forcing amplitude to be used depending on the sample constitutive properties (i.e., with a given value of Γ_1), while on the other hand, they can be used to calibrate the tip–sample interaction (e.g., tip material choice, or material of the sample to be possibly scanned) depending on the AFM operation settings (e.g., excitation amplitude). Both aspects are of considerable interest in the design stage.

2.3 Global Dynamics and Integrity

The previous investigations highlight that the lowest escape values of forcing amplitude occur at the two main resonance regions, and provide the escape profile as the envelope of forcing amplitude values at which bounded solutions disappear. Yet, such a global stability boundary does not furnish any information about the erosion process of the basins of attraction of the various solutions, which is indeed a critical issue corresponding to system impending jump to contact; therefore, it has no practical utility from the viewpoint of AFM safe operation mode. In this respect, the fundamental concept is the dynamical integrity of the system (see Rega et al. 2018 in this book), which depends on the extent of the erosion of its safe basin represented by the region of the phase space bounded by the homoclinic orbit in the underlying unperturbed system of Fig. 2a.

Tools for investigating the complete basin evolution under a control parameter variation up to escape are the erosion profiles, which allow us to quantify the varying level of basin erosion. Their construction is carried out by means of specific computational tools, based on the safe basin definition and the integrity measure concept. In this work, the safe basin is considered as the union of all classical basins of attraction of the bounded solutions belonging to the system potential well, without taking care of possible transient dynamics out of the safe basin. This means that, in the case of coexistence of more in-well attractors, the safe basin comprises two, or more, competing basins. However, safe basins in the more classical meaning of basins of attraction of given solutions will also be considered when being interested in evaluating the robustness of competing attractors, too, along with the respective roles in the erosion process. The integrity indicators used to build the erosion profiles are the global integrity measure (GIM), which represents the normalized hyper-volume (area in 2D) of the safe basin, and the integrity factor (IF), which is the normalized radius of the largest hypersphere (circle in 2D) entirely belonging to the safe basin, and represents a measure of the sole compact part of the safe basin. In this last respect, note that IF is used instead of the local integrity measure (LIM) also accounting for the sole compact part, because the safe basin of interest here is the whole potential well. The phase space window $x \in [-0.3, 0.3]$, $y \in [-0.65, 0.25]$

المنارة للاستشارات

has been considered in the numerical simulations, since it contains the compact part of the basin of each of the main attractors involved in the erosion/escape process.

Focusing around the fundamental resonance, which from what obtained in Sect. 2.2 results to be an important critical region as regards the system stability, Fig. 9 displays the evolution for increasing forcing amplitude of the basins of attraction before ($\omega_u = 0.7$, Fig. 9a), in the close neighborhood of ($\omega_u = 0.8 \cong \omega_1$, Fig. 9b), and after ($\omega_u = 0.9$, Fig. 9c) the resonance, representing different features of the erosion process leading to escape. Before the resonance (Fig. 9a), a weak competing (purple) basin corresponding to the resonant P1H solution appears within the in-well safe basin initially coinciding with the (green) basin of attraction of the nonresonant P1L response, close to its boundary. However, as the amplitude slightly increases, the two basins are separated by erosion tongues of the unbounded solution (white) basin surrounding the well (third panel of Fig. 9a), and the small basin of the resonant solution is rapidly eroded up to its complete disappearance. After that, the erosion of the main nonresonant basin processes up to the escape with smooth, i.e., uncorrupted, basin boundary.

When moving closer to the resonance condition, in between nonlinear and linear resonances (Fig. 9b), the competition between nonresonant and resonant basins, whose robustness is now comparable, becomes definitively stronger with the newly born P1H basin which grows up swiftly, and with smooth boundary, within the in-well safe basin (second panel of Fig. 9b) up to full replacement of the original P1L basin. For increasing amplitude, it is then raggedly eroded from the unbounded solution basin (fourth panel of Fig. 9b).

Finally, after the resonance (Fig. 9c), the erosion scenario exhibits a sequence of competing basins corresponding to higher periodicity solutions, each one of them lasting for a limited forcing amplitude range. Their distributed small subbasins are located close to the boundary of the sole 1-period basin, a circumstance that entails an overall ragged aspect of the latter along the erosion process. The subsequent onset of the new competing 1-period P1* solution, seen also in the final part of the bifurcation diagram of Fig. 4, for high values of the forcing amplitude (above $U = 0.604$), brings to an inside-the-well, secondary, seemingly double-well potential structure of the competing basins (third panel of Fig. 9c), which then split from each other with strongly fractal edges in between (fourth panel of Fig. 9c).

المنارة للاستشارات

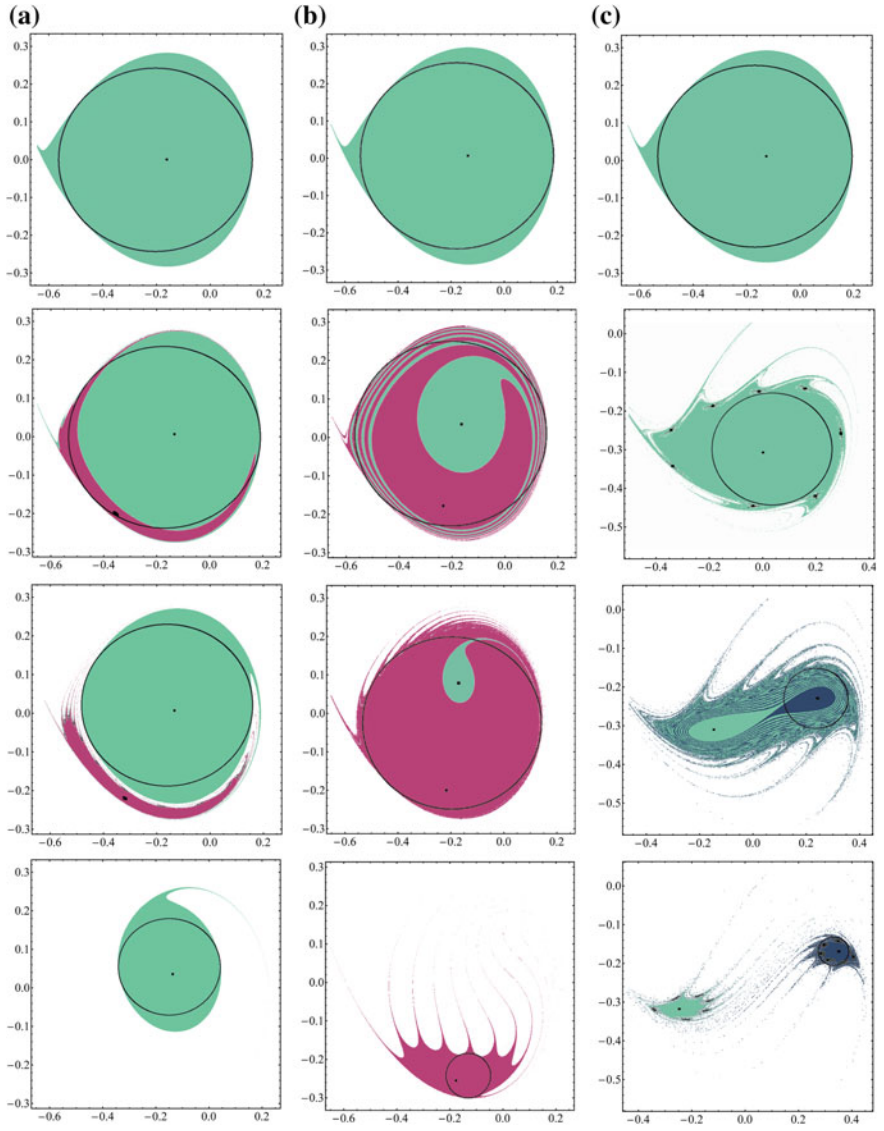

Fig. 9 Basins of attraction and relevant attractors in the (x, y) plane at $\omega_u = 0.7$ and $U = 0/0.006/0.01/0.1$ (**a**), at $\omega_u = 0.8$ and $U = 0/0.01/0.03/0.1$ (**b**), at $\omega_u = 0.9$ and $U = 0/0.5/0.65/0.75$ (**c**). Green basin: P1L (P1 at $\omega_u = 0.9$) solution; purple basin: P1H solution; blue basin: P1* solution at $\omega_u = 0.9$; black basin: high-period solutions; white basin: unbounded solution. The reported circles represent the IF measures for the in-well safe basin

المنارة للاستشارات

The richness of erosion patterns underlying escape is also reflected on the erosion profiles obtained by calculating IF and GIM integrity measures from the basins evolution of Fig. 9. In Fig. 10, reference is made both to the individual basins of main periodic solutions (light gray and black curves) and to the total in-well safe basin (thick black lines). GIM and IF profiles are plotted in solid and dashed lines, respectively, and are nondimensionalized with respect to the safe basin of the unforced system (i.e., for $U = 0$), to obtain dimensionless numbers.

At $\omega_u = 0.7$ (Fig. 10a), the safe basin profile exhibits a sharp, though relatively limited, fall down at low amplitude values when the resonant and nonresonant basins separate inside the well (at around $U = 0.0067$). After that, its evolution, which now coincides with that of the P1L basin, evolves with a long and smooth decrease down to zero. Differently, close to the resonance (Fig. 10b), the strong competition between the basins is highlighted by the crossing between the decreasing P1L (light gray) profile and the increasing (black) one related to the new growing up P1H solution. The internal competition occurs up to nearly complete substitution of the original P1L basin with the new P1H one, which is immediately followed by an ever sharper erosion of the in-well safe basin (thick black, now coinciding with the P1H one), due to the surrounding escape tongues. For frequencies higher than the resonance one, the safe basin profile coincides with that of the main 1-period solution, since the size of the other high-period basins is negligible compared to the well. Its evolution develops smoothly for a wide range of forcing amplitude, up to the separation of the two 1-period basins inside the well which causes a sharp fall down to zero coinciding with the loss of safety of the system.

The integrity curves highlight also a different behavior of the two integrity measures, ensuing from their respective definitions and related to the different features of the erosion process. In fact, when the erosion develops smoothly and from the outer edge of the safe basin or, more generally, in case of weak competition between the basins, the volume (GIM) of the basin is affected in a major way than its compact core (IF), thus entailing a lower value (i.e., in design terms, a major conservativeness) of the GIM measure. In contrast, when the competing basins undergo a strong rolled up evolution, or in presence of very marked fractal eroding tongues, the compact part of the basins is reduced more than its entire volume, and the IF measure becomes more conservative (or even much more conservative, if looking at the single attractors' profiles) than the GIM one, from the safety/robustness viewpoint.

It is worth looking at a summary diagram of GIM profiles of the in-well safe basin for different forcing frequencies: Figure 11 shows an erosion surface in the range $\omega_u = 0.5-1.8$, with several iso-integrity curves obtained by expressing the erosion profiles in terms of remaining safe basin percentage. The profiles have the classical qualitative behavior of the so-called "Dover cliff" erosion curve (Thompson and Stewart 2002), which is characterized by a slow decrease of the uneroded volume of the safe compact region, followed by a sudden fall down to zero. Near the two main resonance frequencies, the surface shows two evident depressions, with the lowest percentage values of residual integrity before the V peak and the sharpest decrease of the profiles just after the peak, thus confirming what already noticed about the differences between the profiles of Fig. 10a and b.

المنارة للاستشارات

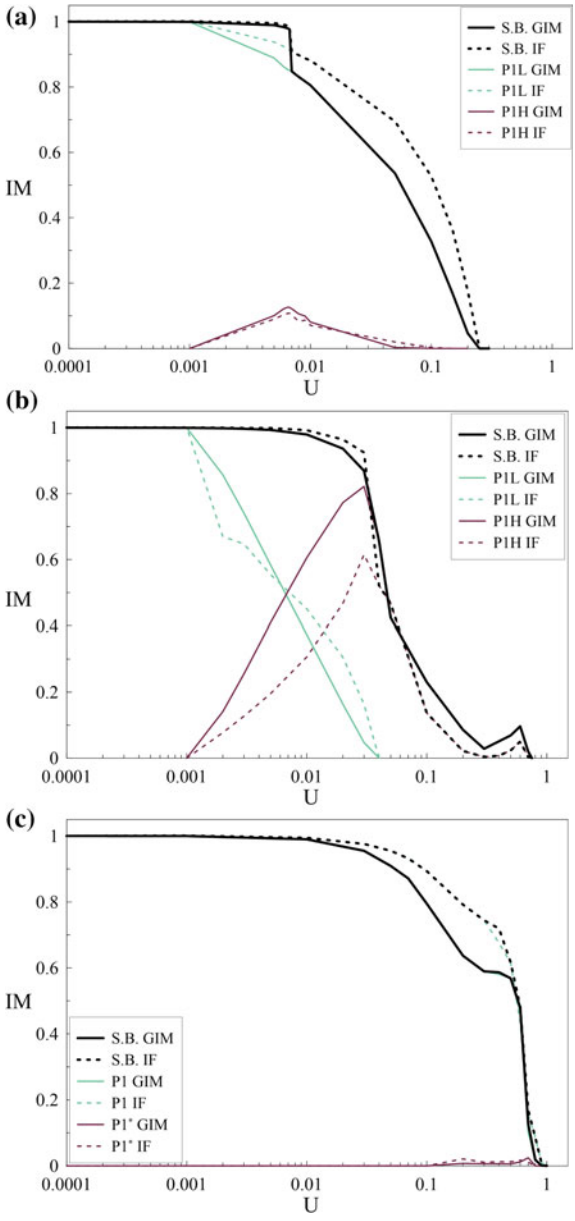

Fig. 10 Erosion profiles at $\omega_u = 0.7$ (**a**), at $\omega_u = 0.8$ (**b**) and at $\omega_u = 0.9$ (**c**). IM: integrity measures

As a practical comment, it is important to point out that slight discrepancies between the escape threshold of Fig. 11a and that of Fig. 3 are due to different numerical procedures used in their realization. Thresholds of Fig. 3 are the result of a continuation analysis, for very small variations of the control parameters, applied

المنارة للاستشارات

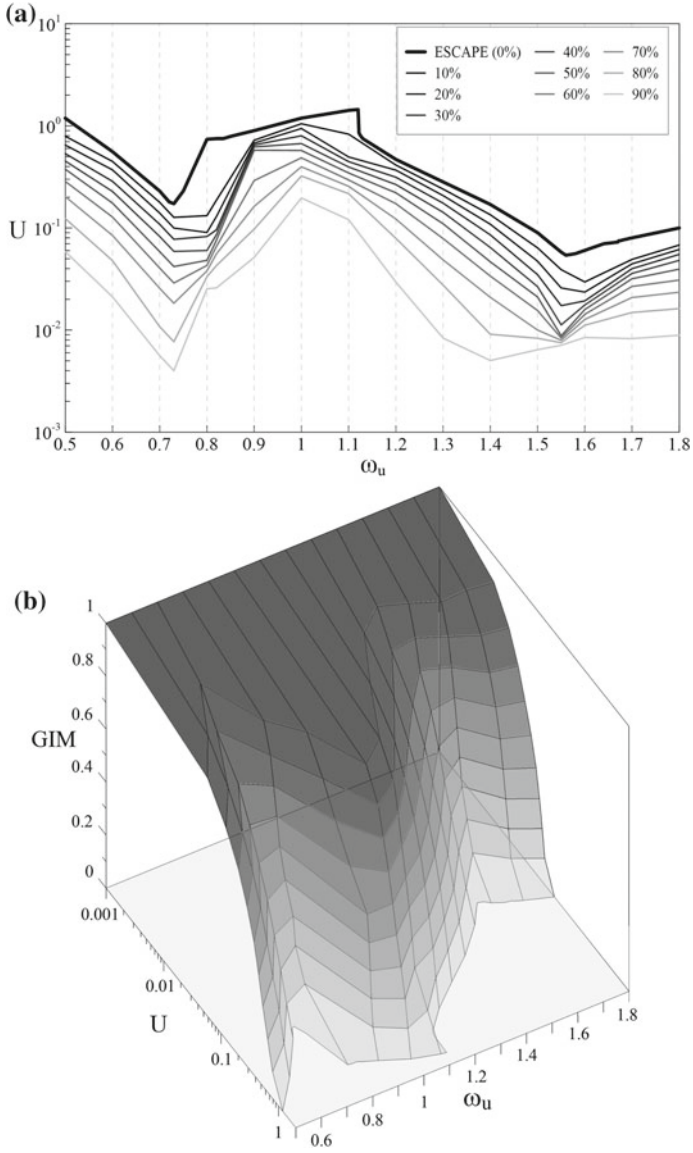

Fig. 11 Iso-integrity curves (**a**, **b**) and overall erosion surface (**b**)

to several local bifurcation points, which is able to catch small changes in the curves trend thus furnishing quite accurate and reliable outcomes. Differently, thresholds of Fig. 11a are obtained as envelope of the (discretized) integrity values deduced from the construction of the erosion profiles. The latter, which are computationally

المنارة للاستشارات

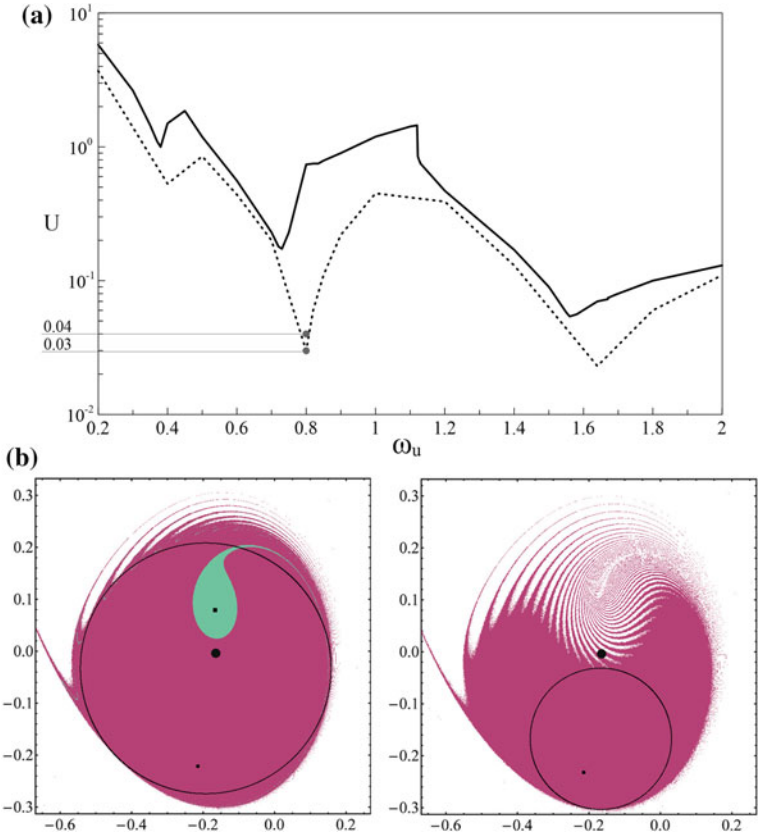

Fig. 12 Comparison between local *ni* (dotted line) and global *bd* (continuous line) escape thresholds in the ω_u-U plane (**a**) and state-space (x, y) basin evolution at $\omega_u = 0.8$ for $U = 0.03$ and $U = 0.04$ (**b**)

burdensome to build, have been realized at frequencies steps which are much wider than the previous case, thus furnishing less refined, though reliable, results.

From the viewpoint of AFM safe operation mode, some matters are of considerable interest as regards the evaluation of system theoretical and practical stability. The first one is concerned with the comparison of the overall escape threshold considered up to now and carried out by mapping the bifurcation diagrams (*bd*), to be considered as a *global* stability boundary, with the escape threshold obtained by looking at the response under numerical integration (*ni*) with fixed initial conditions (i.c.), to be considered as a *local* stability boundary. The comparison is reported in Fig. 12a, where the dashed threshold, related to numerical simulation, represents the forcing amplitude values U, for several forcing frequencies, at which divergence of a specific system response does occur. Of course, the *ni* escape values strongly depend on the particular selection of the i.c. pair; here, values corresponding to the equilibrium

المنارة للاستشارات

position of the unperturbed system have been chosen. With respect to all of the *local ni* boundaries to be possibly constructed by considering divergence from different pairs of i.c. inside the safe basin, the *global bd* boundary represents the upper bound, since it corresponds to safe basin annihilation. For the considered selection of i.c., the figure highlights significant differences between the two boundaries, the *local* one lying below the *global*, with a gap of up to 25 times the *ni* absolute value. Moreover, *ni* local minima occur at primary and secondary resonance frequencies, while *bd* minima are shifted towards left (i.e., to nonlinear resonances) due to the softening behavior of the system. The apparent underestimation of system stability with *ni* ensues from the particular selection of the i.c. pair against the basin erosion scenario. Focusing on fundamental resonance and looking, e.g., at $\omega_u = 0.8$, a slight increase in the excitation amplitude (around the local escape vertex value $U = 0.03$) is seen to cause a basin boundary erosion which swiftly expands up to including the initial position (black point in Fig. 12b), while leaving more than 50% of residual integrity of the safe basin. In contrast, the actual basin annihilation (*bd* threshold) occurs only at $U = 0.74$. This clearly highlights how, in terms of overall system safety with respect to escape, consideration of the outcome of a single trajectory may furnish misleading and too conservative information, unless being specifically interested in the response ensuing from that particular set of i.c.

Anyway, even correctly referring to the *global* stability boundary in terms of overall escape, the major problem in a safety assessment perspective ensues from the associated total lack of information about the features of the underlying basin erosion. Hence, in practical applications, it is particularly important to refer to integrity evaluations in order to determine acceptable frequency-dependent thresholds associated with a priori safe design targets. Figure 13 shows four iso-integrity curves corresponding to increasing target values in the fundamental resonance region. Selecting

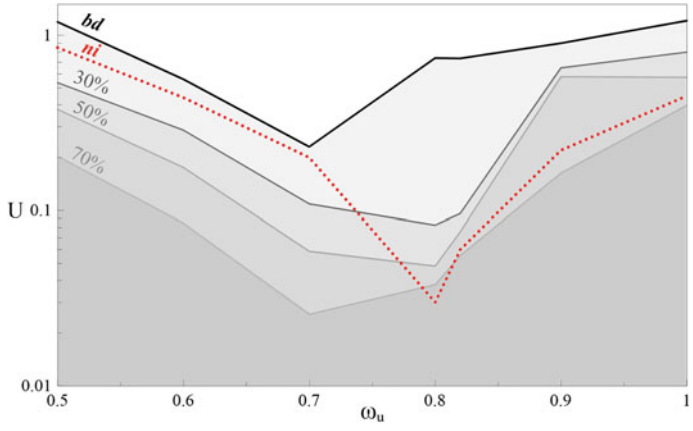

Fig. 13 Comparison between theoretical (*ni* (dotted red line) and *bd* (continuous black line)) and practical (residual integrity, gray lines) boundaries close to fundamental resonance, with detection of some increasingly residual iso-integrity curves

المنارة للاستشارات

for instance the 30% residual safety target, the corresponding threshold allows us to critically discuss the results furnished by numerical simulations (dotted red threshold). Away from the nonlinear resonances (left of them, for the principal resonance see Fig. 12a), though the *ni* thresholds underestimate system safety with respect to the *bd* threshold, they are definitely unacceptable because of corresponding to very low values of residual integrity (0−30%). Yet, the even more questionable point is that *ni* thresholds correspond to a residual integrity which is strongly variable over the control parameter range (see, e.g., the frequency range in between 0.7 and 0.8 in Fig. 13)—and thus unreliable in overall terms—even though the associated threshold may become more and more over conservative (thus corresponding to a higher residual integrity) just where this is more needed. The above comparison highlights the importance of a global analysis which solely accounts for the features of the progressive decrease of the system practical safety due to the erosion up to its final ending to the unwanted escape.

As a final remark, it is worth reporting here that the same analyses have been developed for the system under the sole vertical, harmonic, excitation V_g (see Rega and Settimi 2013). The results concerning the basin erosion process and the local escape thresholds exhibit the same qualitative behavior as the one obtained under parametric excitation, even if the absolute minimum of the total escape threshold is shifted from the subharmonic resonance range to the primary one, consistent with the well-known higher response amplitudes occurring at the latter for an externally driven system.

Furthermore, the influence of combined horizontal scan excitation and vertical beam excitation (which coexist in the noncontact AFM operation mode) on the overall dynamics has been investigated, highlighting a negligible difference of results with those obtained from the sole parametric excitation case, therefore confirming that, for the chosen set of parameters values, the dual excitation analysis is not even necessary in the primary resonance region in which the vertical excitation produces the major effects.

3 AFM with External Feedback Control

The results presented in the previous section have highlighted that slight changes of parameters and/or initial conditions of the AFM model can produce dramatic modifications of its dynamical response, leading to possible unstable oscillations which restrict the operating range of the device. AFMs working in noncontact regime, specifically, can undergo the unwanted "jump-to-contact" phenomenon, or escape in dynamical terms, due to the atomic attraction between the cantilever tip and the sample to be scanned, which can become stronger than the beam restoring elastic force making the equilibrium configuration unstable and producing contacts between tip and sample responsible for errors in the topography process. To avoid these undesirable effects and improve the microscope performances, several control techniques have been proposed and successfully implemented in the last decades, mostly based

المنارة للاستشارات

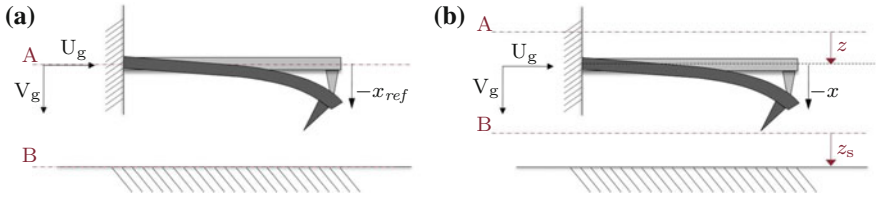

Fig. 14 Microcantilever at reference position (**a**) and in a generic configuration (**b**); lines A and B represent the reference positions of the microcantilever and the sample surface, respectively

on feedback control methods (Yamasue and Hikihara 2006; Arjmand et al. 2008; Payton et al. 2011). Among them, a simple external feedback control can be implemented in the continuum formulation of the noncontact AFM model presented in Sect. 2. Thanks to the control of the cantilever base position (Fig. 14b), the procedure works by keeping the system response (which can change due to the ensuing variations in the sample surface position) to a reference one (Fig. 14a), which represents a stable periodic motion of the uncontrolled system under the same setting of operating parameters. Following the model formulation reported in Settimi et al. (2015), the continuum equations for the controlled system read

$$\begin{aligned} &m\bar{u}_{tt} - [EI\bar{v}_{rrr}\bar{v}_r - J_z\bar{v}_{ttr}\bar{v}_r + \Lambda(1+\bar{u}_r)]_r = \bar{Q}_u \\ &m\bar{v}_{tt} - [EI(\bar{v}_{rrr} + \bar{v}_r\bar{v}_{rr}^2) + J_z(\bar{v}_{ttr} + \bar{v}_{tr}^2\bar{v}_r) + \Lambda\bar{v}_r]_r = \bar{Q}_v \\ &\bar{\xi}_t = \bar{k}(\bar{v}_{ref} - \bar{v}) \end{aligned} \tag{8}$$

where $\bar{\xi}(t)$ is the new control variable representing the distance of the fixed side of the microcantilever from the horizontal reference axis (see Fig. 14b, which refers to the nondimensional system), $\bar{v}_{ref}(r,t)$ is the reference vertical displacement, obtained from the uncontrolled system ($\bar{\xi} = 0$, Eq. (1)), and $\bar{k}$ is a feedback constant. As done for the uncontrolled model, the initial-boundary value problem of the distributed parameter system is reduced to a system of two ODEs with one and a half degrees of freedom through a Galerkin procedure. After neglecting some terms related to internal feedback control and nonlinear geometry, and by considering the presence of the sole horizontal parametric scan excitation (which is assumed to be harmonic), the nondimensional reduced order system results

$$\begin{aligned} &\ddot{x} + \alpha_1 x + \alpha_3 x^3 = -\frac{\Gamma_1}{(1+x+z-z_s)^2} - \rho_1\dot{x} - \mu_1 x U\omega_u^2 \sin\omega_u t \\ &\dot{z} = k_g\left(x_{ref} - x\right) \end{aligned} \tag{9}$$

where $x(t)$ and $z(t)$ are the tip transverse displacement and control variable, respectively, and k_g is the external feedback control parameter. Obviously, the system (9) has to be completed by the addition of Eq. (4) (with $V_g = 0$ and $U_g = U\sin\omega_u t$) relevant to the uncontrolled system, which furnishes the reference response x_{ref} essential

المنارة للاستشارات

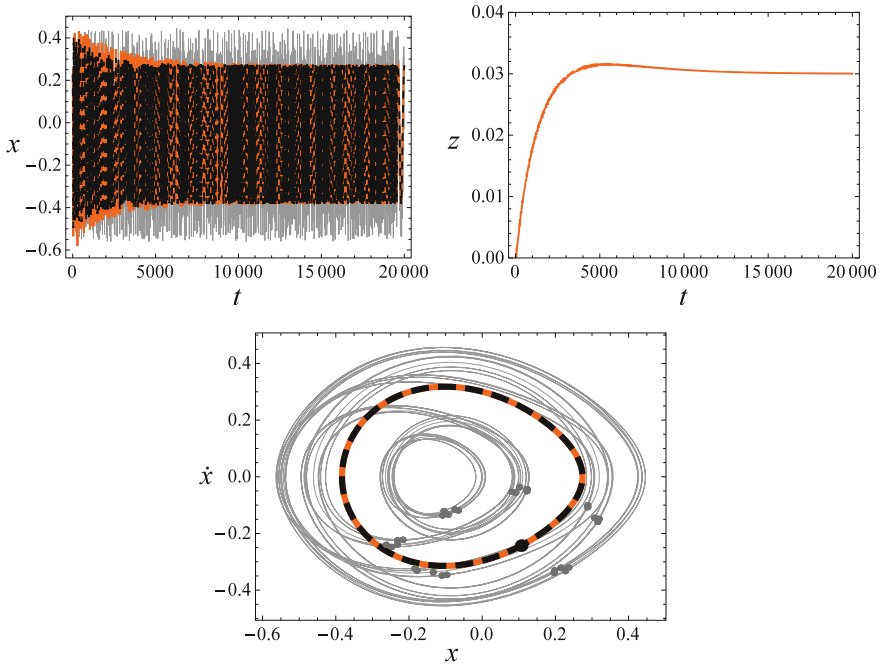

Fig. 15 Time histories and trajectories in the phase plane of the uncontrolled (reference) system with $z_s = 0$ (dashed thick black line), of the uncontrolled system at $z_s = 0.03$ (gray thin continuous line) and of the system at $z_s = 0.03$ with feedback control (continuous orange thick line), at $\omega_u = 0.9$ and $U = 0.5$

for the control application. The control works when the response settles onto the reference one, i.e., when z is equal to the expected value z_s, as shown in the sample case of Fig. 15. Here, the change of 3% in the tip–sample distance, represented by the increase of the z_s parameter with respect to the reference configuration $z_s = 0.0$, causes a modification in the system dynamical response, which passes from the reference 1-period solution (dashed thick black line in figure) to a high-period one (gray thin line in figure). Starting from the latter configuration, the addition of the external feedback control is able to change the system dynamics by avoiding the occurrence of the highly periodic behavior; the controlled model, in fact, manages to properly reproduce the reference 1-period solution (orange thick line in figure), and to set the control variable z to the desired z_s value, $z = z_s = 0.03$.

The study of the system equilibria points out that they are not influenced by the feedback control, as they result to be the same of the reference uncontrolled system. However, due to the presence of control, the arise of a Hopf bifurcation locus reduces the range of stability of the only acceptable stable equilibrium (the upper one in Fig. 2b uncontrolled) also for very low values of the feedback parameter k_g. For the parameters choice (7), the asymptotic stability of the equilibrium solution occurs only for $0 < k_g < 0.00223$ (Settimi et al. 2015).

المنارة للاستشارات

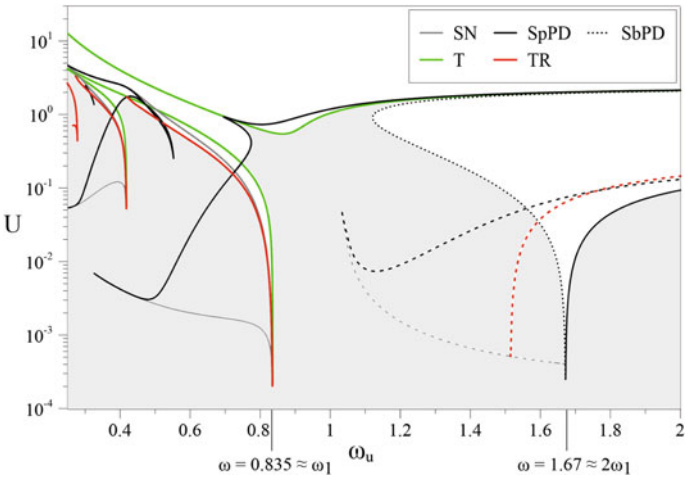

Fig. 16 Local bifurcations map and overall escape threshold in the frequency-amplitude plane of parametric scan excitation for $k_g = 0.001$. Gray area: region of stable reference response of the controlled system; SN (gray lines): saddle-node bifurcation; T (thick green lines): transcritical bifurcation; TR (thick red lines): torus bifurcation; SpPD (black lines): supercritical period doubling; SbPD (black dotted lines): subcritical period doubling. Continuous lines: bifurcations referred to P1 solutions; dashed lines: bifurcations referred to P2 solutions

3.1 Local Bifurcations and Response Scenarios

In order to investigate and verify the overall effects of the control introduction on the system behavior, a comprehensive analysis of its dynamical response is carried out and compared with the results already obtained for the uncontrolled system in Sect. 2.2 (Settimi and Rega 2016c). For the set of parameters values reported in (7), Fig. 16 summarizes the system dynamics under variation of the forcing amplitude U, with identification of the different local bifurcation thresholds. The local bifurcation loci which represent the escape thresholds for the underlying uncontrolled system (i.e., saddle-node (gray) and period doubling (black) thresholds in Fig. 16) are present also in the controlled case, but they do not correspond to the overall stability boundaries anymore. The control introduction in the model, in fact, causes the birth of new thresholds of torus (or Neimark-Sacker) bifurcation (TR) and of transcritical bifurcation (T)—the latter always appearing at much higher amplitudes than the former—which considerably modify the system stability region. In the lower frequencies range up to the fundamental resonance ($\omega_u = 0.835 = \omega_1$), the system escape threshold is governed by the torus bifurcation of the nonresonant 1-period (P1L, i.e., low-amplitude) solution which occurs before the saddle-node governing the onset of escape in the uncontrolled case, while the transcritical bifurcation of the resonant 1-period (P1H, i.e., high amplitude) solution occurs before the period doubling sequence which instabilizes the response of the uncontrolled case. For higher frequencies which include the principal resonance ($\omega_u = 1.67 = 2\omega_1$), the system

المنارة للاستشارات

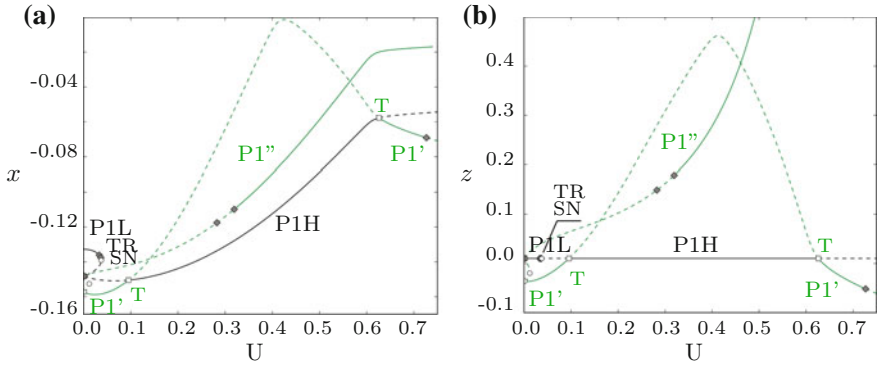

Fig. 17 Bifurcation diagrams at $\omega_u = 0.8$ for increasing forcing amplitude U for the controlled system with $z_s = 0.01$ and $k_g = 0.001$. Black curves: 1-period solutions corresponding to those of the reference system; green curves: new 1-period solutions. P1L: nonresonant 1-period solution; P1H: resonant 1-period solution; P1′/P1″: new 1-period solutions; T: transcritical bifurcation; TR: torus bifurcation; SN: saddle-node bifurcation

shows the coexistence of 1-period and 2-period solutions—the latter governing the nonlinear response in the neighborhood of the 1/2-subharmonic resonance, as for the reference system—which become unstable via a couple of period doublings and a torus bifurcation substituting the period doubling, respectively.

It is worth underlining that the stable region of Fig. 16 refers to system solutions for which the feedback control works properly, i.e., stable 1-period responses of the type (x_{ref}, z_s), such as the nonresonant one (P1L) obtained for the forcing frequency $\omega_u = 0.8$ before the torus bifurcation (TR) and the P1H solution delimited by two transcritical bifurcations (T points) marked in the sample bifurcation diagram of Fig. 17. However, the latter becomes stable only after the system has experienced a region of instability characterized by unbounded responses (white tongues inside the stable region in Fig. 16), a fact that makes it unsafe with respect to possible variations of the operational parameters. According with the control efficiency, stable motions exhibited by the system that do not settle onto the reference one are considered as unwanted outcomes and thus out of the stability region. This is the case, for example, of the new 1-period solution P1′ born from the transcritical bifurcations T (represented with green lines in Figs. 17 and 18), which is a high-amplitude response coexisting with the main ones and displaying a rich scenario of local bifurcations. Indeed, bifurcation diagrams of the control variable z show that for these additional solutions the system fails to reach the reference position (i.e., $z = z_s = 0.01$, see the right panel of Fig. 18a), actually making the z response periodic, so that they appear as unwanted responses. The reported bifurcation diagram highlights also the presence of stable quasiperiodic solutions arisen from the torus bifurcations (Fig. 17), which can be numerically detected and for which the control variable z does not actually reach the expected position $z_s = 0.01$ (see Poincaré map of the z variable of Fig. 18b). Note that the quasiperiodic solution exists up to the occurrence of the saddle-node

المنارة للاستشارات

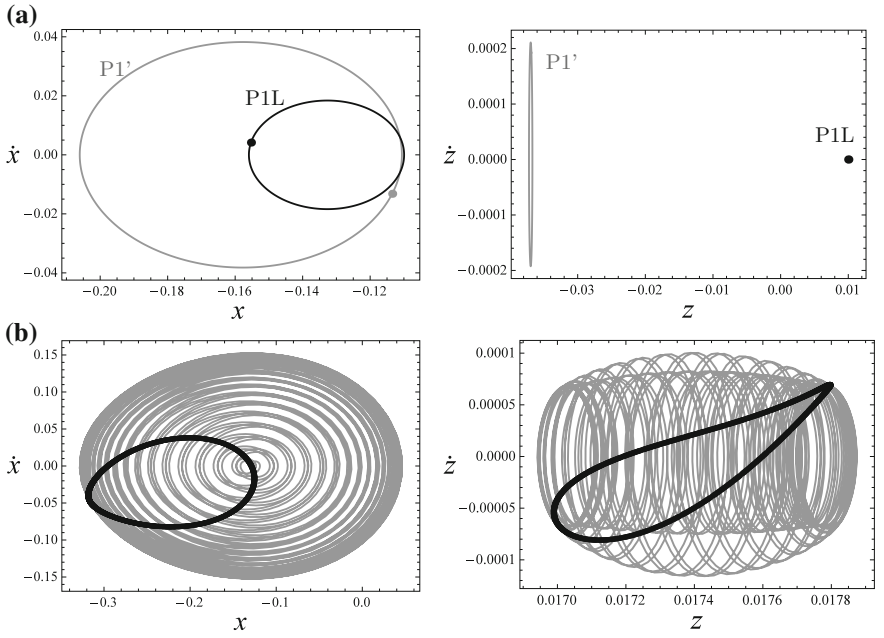

Fig. 18 Phase portraits and Poincaré maps of 1-period solutions at $U = 0.01$, $k_g = 0.001$ and $\omega_u = 0.8$: stable P1L solution (black), new stable P1$'$ solution (gray) (**a**). Phase portraits and Poincaré map of stable quasiperiodic solution at $U = 0.036$ and $\omega_u = 0.8$ after the torus bifurcation (**b**)

bifurcation that makes the reference solution disappear; since it represents the input for the numerical solution of the controlled system, this local bifurcation marks also the death of the stable quasiperiodic response.

Figures 16 and 17 are obtained for low values of the feedback control k_g; indeed, it is interesting to investigate the influence of the increasing feedback control parameter on the stability of the main periodic solutions, since it is known that changes in such parameter can strongly modify the system response. Obviously, it must be taken into account that its maximum acceptable value corresponds to the one instabilizing the system equilibrium, i.e., $k_g = 0.00223$. Thus, focusing around fundamental resonance, several behavior charts for increasing k_g are reported in Fig. 19, to be compared with the one obtained for the uncontrolled system (i.e., $k_g = 0$, Fig. 19a). Figure 19b shows the appearance of an unstable tongue delimited by the new torus and transcritical bifurcation thresholds which occur for low values of the forcing amplitude U, and even for weakly controlled systems. With the control introduction, in fact, the stability of the nonresonant P1L solution is reduced by the torus threshold, while the resonant P1H response loses its stability for low values of the forcing amplitude U, returning stable only after the transcritical bifurcation (Fig. 17). As a consequence, the typical triangle region below the V vertex displayed by the uncontrolled system with the coexistence of stable P1L and P1H solutions is not only

المنارة للاستشارات

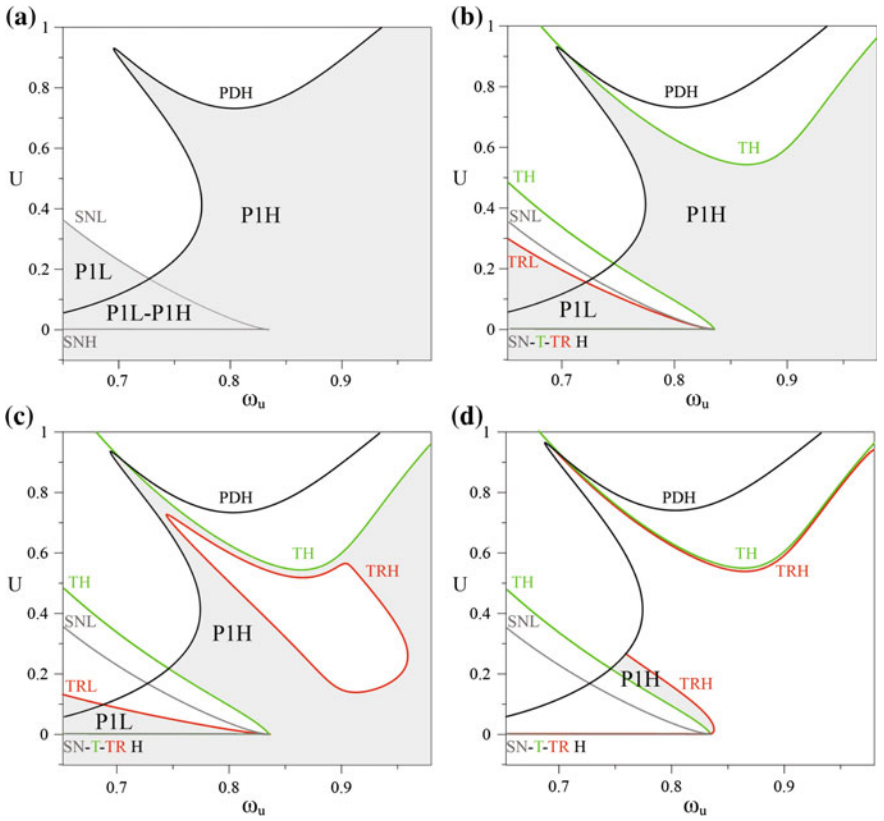

Fig. 19 Behavior charts in the ω_u-U plane around fundamental resonance for $k_g = 0$ (**a**), $k_g = 0.001$ (**b**), $k_g = 0.002$ (**c**) and $k_g = 0.01$ (**d**)

reduced by the torus curve, but displays the presence of the sole nonresonant solution, up to its complete disappearance for higher k_g values. For higher values of the feedback control parameter (Fig. 19c), an unstable region confined by a torus bifurcation (TRH) arises below the upper transcritical threshold, and expands as the control increases. Simultaneously, the torus bifurcation which unstabilizes the P1L solution occurs for decreasing values of U. After that, stability regions reduce to narrow strips of existence of stable P1H solution, associated with very limited ranges of forcing amplitude U (see behavior chart at $k_g = 0.01$ of Fig. 19d). All over Fig. 19, note that the frequency value $\omega_u = 0.8358$ marks the disappearance of the P1L solution, hence for higher frequencies, the P1H solution becomes the sole 1-period solution for the system and its "high-amplitude" connotation becomes unnecessary (as for the reference system, see Fig. 6 and relevant comments); nevertheless, for the sake of readability of the charts its label has been kept unchanged.

To summarize the results concerning the controlled system, and in view of easily comparing them with the outcomes of the uncontrolled one (Sect. 2.2), the behav-

المنارة للاستشارات

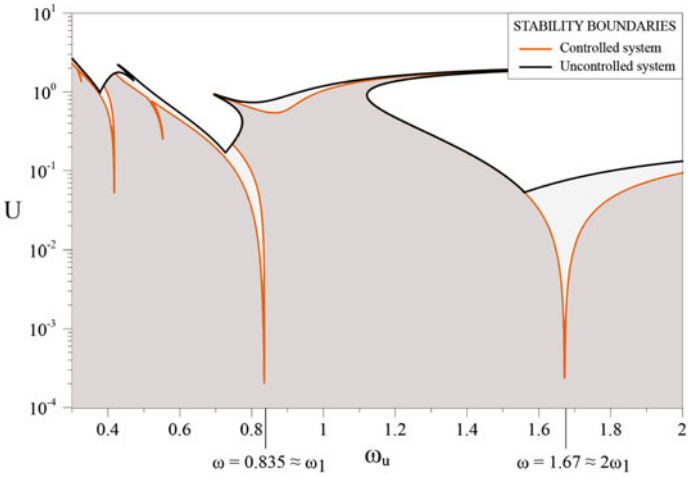

Fig. 20 Behavior chart in the ω_u-U plane with detection of the overall escape thresholds for the controlled ($k_g = 0.001$, orange line) and uncontrolled ($k_g = 0$, black line) systems under parametric excitation. Dark gray area represents the stability region of the controlled and uncontrolled systems and light gray area represents the stability region of the sole uncontrolled system

ior chart in the frequency-amplitude plane is shown in Fig. 20, where the overall escape thresholds of the two systems (controlled and uncontrolled) together with the detection of the corresponding stability regions are reported. The most evident effect concerns the reduction of the dynamical stability of the system entailed by the external feedback control, mostly around the main resonance frequencies, i.e., ω_1, $2\omega_1$ and $\omega_1/2$.

In the close neighborhood of these values, in fact, the feedback control causes the onset of instability tongues which dramatically decrease the escape value of the forcing amplitude, with reductions of about 99.9% around the fundamental (primary) resonance, of 99.4% around the principal (subharmonic) resonance and of about 94% around the superharmonic resonance frequency. This effect can be explained with the fact that the close proximity to the resonance frequencies leads to a substantial increase of the response amplitude of the resonant periodic solutions, that the feedback control is unable to dominate. In these regions, therefore, the escape threshold of the controlled system is governed by the nonresonant responses, which become unstable for considerably lower values of the forcing amplitude. Furthermore, the escape threshold minima of the controlled system are shifted towards frequency values related to the system natural frequency ω_1 (i.e., $\omega_1/2$, ω_1, $2\omega_1$), since the nonresonant periodic solutions are not affected by the softening effect of the nonlinear resonance (as, in contrast, happens for the resonant solutions which govern the escape profile of the uncontrolled system).

It is important to remember also that for the controlled system the stability region does not include all the stable periodic responses, but only those associated with the reference periodic solution of the uncontrolled system, on which the control

المنارة للاستشارات

works properly. This causes an additional reduction of the limiting values of forcing amplitude. In terms of extent, this is evident particularly around the $2\omega_1$ frequency, where the escape boundary of the uncontrolled system is governed by the 2-period response representing the main reference periodic solution for the whole range of high-frequency values which, however, the control fails to correctly reproduce.

It is worth noting that the aforementioned response features are equally present both in the parametrically forced system herein summarized and in the externally forced one which could be considered, in the uncontrolled (see Eq. (4)) or controlled case, under vertical excitation of the microcantilever support. Furthermore, the qualitative behavior of the escape threshold is not modified by the control activation, and therefore maintains the typical features of systems under parametric (external) excitations, with V-shaped profiles around resonance regions and the absolute minimum at principal (fundamental) resonance, thus confirming that the applied control acts on the system irrespective of the forcing type. From a practical point of view, the highlighted behaviors have detrimental implications for AFM operation, as they entail limiting the range of both the forcing amplitude and the feedback control parameter to low values to ensure the effectiveness of control. Moreover, they suggest to select the low-amplitude solution as the reference one, since the control of the high-amplitude solution is effective only in limited regions of the parameter space, so that it would imply a very careful choice of the operational settings.

Finally, the detrimental effect of control on the system stability can be highlighted also when investigating the dynamical behavior as a function of system intrinsic parameters, e.g., the atomic interaction parameter Γ_1 governing the order -2 term of the equation of motion and representing the most significant system nonlinearity. The results, reported in Fig. 21a to be compared with those of Fig. 8, show that the addition of control into the model ($k_g = 0.001$, Fig. 21), also in the Γ_1-U plane, as already seen in the ω_u-U plane, causes the disappearance of the region of coexistence of the P1 solutions with the lowering of the escape boundary of the P1L response due to the birth of a new torus TRL threshold. However, the control presence affects mostly the P1H solution, which in the uncontrolled system was confined by the period doubling threshold PDH; the onset of a new transcritical locus (TH) and of a new torus one (TRH) significantly reduces its stability range which passes from $\Gamma_1 \in [0.127, 0.149]$ to $\Gamma_1 \in [0.1305, 0.1313]$ at a forcing amplitude of $U = 0.0005$. Notwithstanding the small value of the feedback control gain ($k_g = 0.001$), this prevents from operating the AFM for atomic interaction values (e.g., tip material choice, material of the sample to be possibly scanned) slightly higher than the reference one ($\Gamma_1 = 0.1$, see the comparison between the uncontrolled and controlled responses of Fig. 21b for $\Gamma_1 = 0.12$), also with nearly vanishing excitation amplitudes, thus furnishing further practical information of design interest as regards proper AFM operation settings.

المنارة للاستشارات

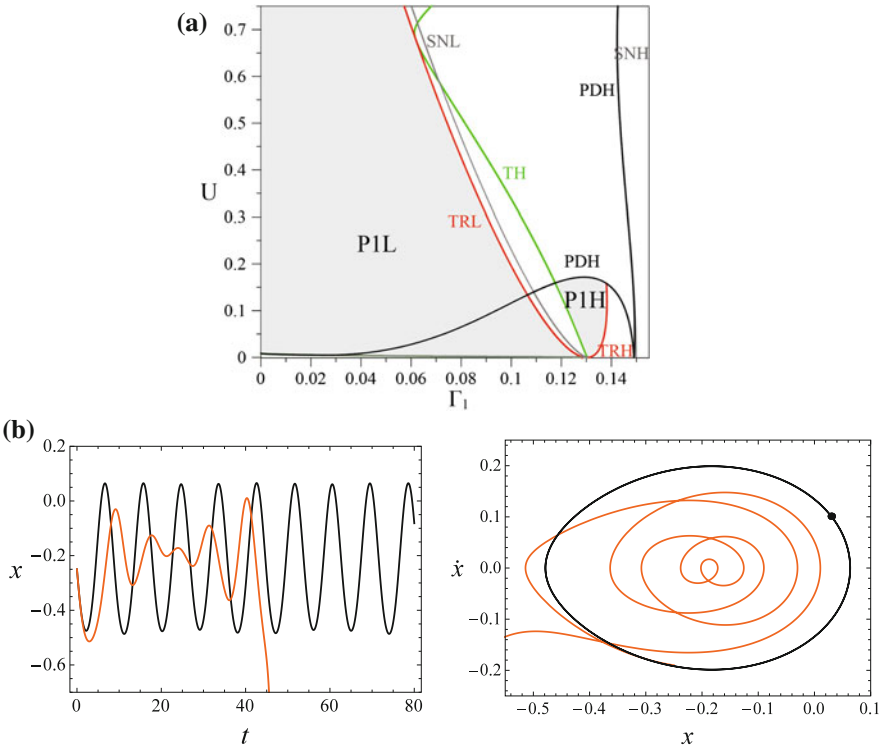

Fig. 21 Behavior chart in the Γ_1-U plane for $\omega_u = 0.7$ and $k_g = 0.001$ (**a**); time histories and trajectories in the phase plane of the uncontrolled (reference) system (black line) and of the controlled system (orange line) at $\Gamma_1 = 0.12$ and $U = 0.12$ (**b**)

3.2 Global Dynamics and Integrity

As previously stated, the investigation of the dynamical integrity of a system when varying some control parameter is strictly related to the definition and choice of specific concepts and tools, namely the safe basin and the integrity measure. From what said in the former Sect. 3.1, it follows that the safe basin for the AFM system with external feedback control must include the sole solutions for which the control procedure works properly, namely the nonresonant (i.e., low-amplitude) 1-period solution around the fundamental frequency. If compared with the reference system (Sect. 2.3), in which the safe basin coincides with the potential well, the system safe basin results to be strongly reduced by the control presence into the model, as it will be described in detail hereinafter.

Notwithstanding the considered minimal (single-mode) approximation of the microcantilever dynamics, the controlled system is five-dimensional in the state space, as it is defined by Eqs. (9) and (4), so that understanding and representing the relevant attractor-basin portraits becomes rather difficult. Therefore, to obtain read-

المنارة للاستشارات

able and interpretable results, analyses are accomplished by systematically assuming that the initial conditions of the displacement variables of the controlled system are the same of the uncontrolled one, i.e., $x(0) = x_{ref}(0)$, $y(0) = y_{ref}(0)$—which also corresponds to considering situations for which the control is more likely to work—thus reducing the basin to three dimensions. Based on this, the erosion evolution is investigated constructing 2D cross sections of the five-dimensional basins of attraction with fixed initial conditions of the control variable z.

In a comparison perspective, the tools selected to build the erosion profiles are the same already used to analyze the dynamical integrity of the uncontrolled system, i.e., the global integrity measure (GIM) and the integrity factor (IF) as integrity indicators, and $x \in [-0.3, 0.3]$, $y \in [-0.65, 0.25]$ as phase space window.

Also in this case, normalization has been performed with respect to the integrity measure calculated for the reference safe basin of the unforced system (i.e., for $U = 0$), so that GIM and IF are dimensionless numbers.

The evolution of the system safe basin is analyzed for increasing forcing amplitude U, with fixed control parameter z_s (equal to 0.01), which is related to the distance between microcantilever tip and sample surface, and with fixed initial condition of the control variable $z(0) = 0$. Several cross sections of basins of attraction in the $(x = x_{ref}, y = y_{ref})$ plane are built for different forcing frequencies around the fundamental resonance ($\omega_u = \omega_1$) region, and the results are compared with those already obtained for the uncontrolled system presented in Sect. 2.3 to evaluate the influence of control on the dynamical safety of the system (Settimi and Rega 2016b). As in Fig. 9, in Fig. 22 the basins of attraction of the controlled system in the $(x = x_{ref}, y = y_{ref}, z = 0)$ plane are reported for increasing values of the forcing amplitude and for three forcing frequencies exemplifying the system behavior around the fundamental resonance, i.e., $\omega_u = 0.7$, $\omega_u \cong \omega_1 = 0.8$ and $\omega_u = 0.9$. The projection of the relevant attractors is marked and the z value at which each attractor settles is indicated. To better frame the following global results refer also to Fig. 19b.

The most evident consequence of the control presence is the generalized increasing of the erosion due to the enlargement of the basin of the unbounded solution (white basin in Fig. 22), which develops at the main detriment of the nondominant responses. In particular, with respect to the uncontrolled case (Fig. 9) for frequencies lower than the resonant one (Fig. 22a), the basin of the resonant solution disappears, as well as the basins of the high-period solutions for ω_u values higher than ω_1 (Fig. 22c). At this frequency, moreover, the feedback control is able to properly reproduce the 1-period solution only in a confined range of the forcing amplitude, after which the periodic responses depicted by the system cannot be considered acceptable anymore. This is highlighted by the z values reported in each basin section of Fig. 22c, indicating the z planes which the attractors belong to; after the critical value $U = 0.598$ (corresponding to a transcritical bifurcation) the stable solutions do not coincide with the reference ones (i.e., $z \neq z_s = 0.01$), confirming the bad control operation. Near the fundamental resonance (Fig. 22b), the control causes the onset of tongues of the unbounded solution basin (white) inside the potential well, whose penetration causes the separation of the resonant/nonresonant basins for low values of the forcing amplitude, and whose development occurs to the detriment of the

المنارة للاستشارات

nonresonant basin, which is strongly and swiftly reduced. Such behavior is peculiar of the system with feedback control and modifies the topological scenario of the basins erosion in the close proximity of the resonance frequency; for the controlled system, in fact, the disappearance of the nonresonant basin is caused by the erosion produced by the unbounded basin, while in the reference case (Fig. 9b) it occurs by replacement with the resonant basin later on eroded by the unbounded one, without penetration of the latter, which enlarges starting from the outer edge of the potential well.

Remembering the bifurcation diagrams of Fig. 17, which indeed well samples the general behavior of the system, it is evident that the basin of attraction of the resonant solution corresponds to different solutions if referred to the controlled system or to the uncontrolled one. In particular, in the controlled case, it represents the new P1′ solution basin for low values of the forcing amplitude U (less than 0.1, i.e., for all red basins in Fig. 22b, at $\omega_u = 0.8$), while it corresponds to the same P1H solution of the reference system, with a proper operation of the control technique, for high values of U where, however, the basin has been already meaningfully eroded.

This can be understood by referring to the 3D ($x = x_{ref}$, $y = y_{ref}$, z) phase space; here, the basins reported in Fig. 22b correspond to ($x = x_{ref}$, $y = y_{ref}$) sections of the five-dimensional basin at $z = 0$. While for the nonresonant basin the attractor belongs to a parallel section at $z = z_s = 0.01$, as expected, the attractor of the resonant basin fails to reach the same section, and settles onto a plane with different (and often negative, see Fig. 22) z, as shown in Fig. 23, which refers to the case $U = 0.01$. Note that the $z = z_s = 0.01$ plane in the figure corresponds to the phase plane of the uncontrolled reference system, so that the cross section of the 5D controlled basin of attraction in this plane coincides with the second picture of Fig. 9b (Sect. 2.3).

To quantify the erosion process of the system safe basin illustrated in Fig. 22, the relevant erosion profiles obtained by means of GIM and IF measures are reported in Fig. 24 and compared to those of the uncontrolled system (black curves). The reduction of the safe basin to the sole 1-period dominant basin causes a lowering of the profiles in the whole range of forcing amplitude, and for all the frequencies analyzed, however with meaningful differences. At $\omega_u = 0.7$ (orange profiles of Fig. 24a), the erosion develops smoothly as in the reference case, with not even the initial sudden fall due to the escape tongue therein separating the outer resonant basin from the nonresonant one. This feature is worthily kept, at this frequency, also at higher excitation amplitudes, as highlighted by the nearly constant intervals in between the successive (orange) iso-GIM curves of Fig. 25. In this sense, despite its slightly lower integrity level, the system with feedback control turns out to be more robust than the uncontrolled one with respect to possible perturbations. Looking at the behavior at $\omega = 0.9$, (orange profiles of Fig. 24c), on the contrary, the limit value $U = 0.598$, responsible for the birth of improper new solutions, causes the collapse of the profiles from 50 to 0% (consistent with the strong packing of the corresponding iso-GIM curves of Fig. 25), making the feedback controlled system particularly dangerous when working around these high-amplitude values. Around the resonance, conversely, due to the fact that the safe basin of the controlled system is reduced to the sole, swiftly reduced, nonresonant one, the fall down of the erosion

المنارة للاستشارات

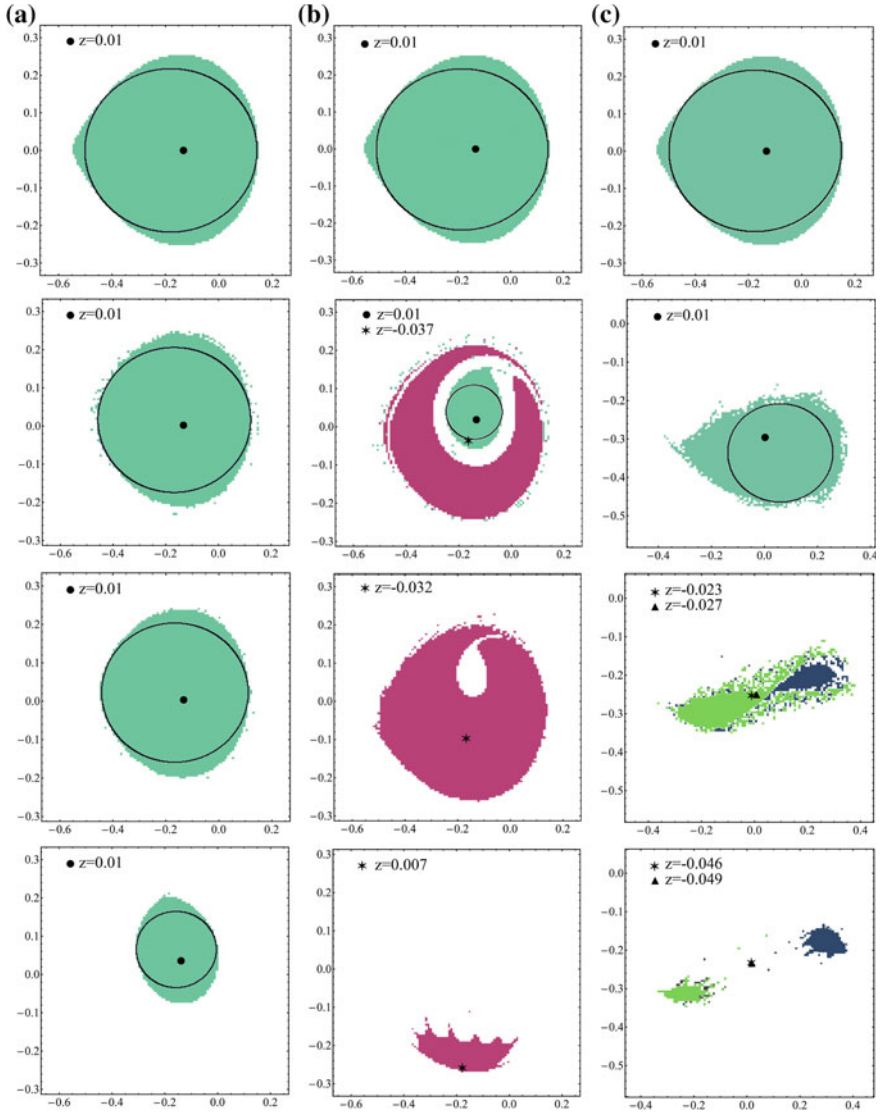

Fig. 22 Basins cross sections with projection of the relevant attractors in the $(x = x_{ref}, y = y_{ref})$ plane for the controlled system $(z = 0, z_s = 0.01, k_g = 0.001)$, at $\omega_u = 0.7$ and $U = 0/0.006/0.01/0.1$ (**a**), at $\omega_u = 0.8$ and $U = 0/0.01/0.03/0.1$ (**b**), at $\omega_u = 0.9$ and $U = 0/0.5/0.65/0.75$ (**c**). Green basin: P1L (P1 at $\omega_u = 0.9$) solution; purple basin: P1′ solution; light green basin: P1′ solution at $\omega_u = 0.9$; blue basin: P1* solution at $\omega_u = 0.9$; black basin: quasiperiodic solutions; white basin: unbounded solution. The reported circles represent the IF measures for the in-well safe basin

المنارة للاستشارات

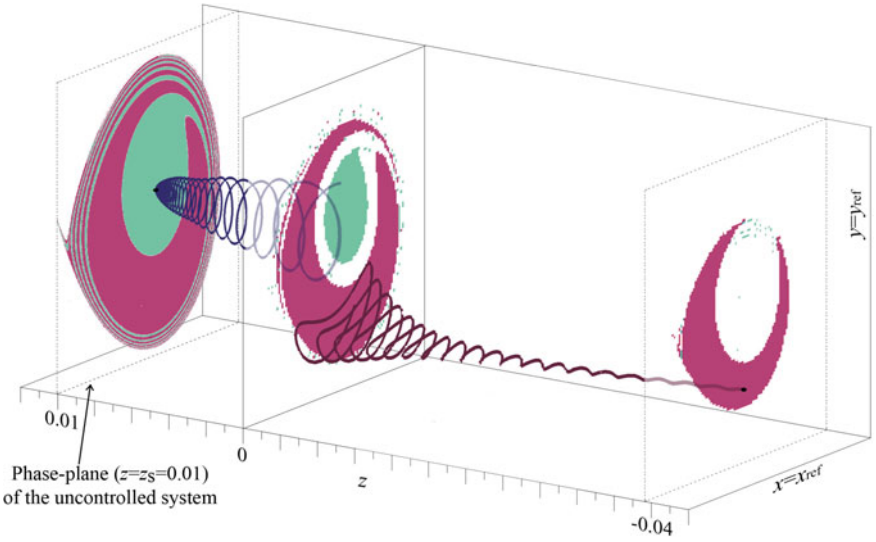

Fig. 23 Basins of attraction and trajectories ending up to the two attractors in the ($x = x_{ref}$, $y = y_{ref}$, z) space at $\omega_u = 0.8$ and $U = 0.01$. Green basin/blue trajectory: nonresonant P1L solution; purple basin/trajectory: new resonant P1′ solution

profiles relevant to the system with feedback control occurs for very low values of the forcing amplitude, and the controlled system results to be much more dangerous than the uncontrolled one. A further contribution to the robustness reduction is furnished by the way the erosion develops as the amplitude increases. In fact, it involves mostly the formerly rolled part of the nonresonant basin, which becomes very fractal, thus causing a sharp decrease of the GIM profile, while affecting the basin compact part (quantified by the IF measure) in a minor way.

As a summary of the obtained results, the iso-integrity curves in the ω_u-U plane are shown in Fig. 25, i.e., frequency-dependent thresholds with constant residual integrity which actually govern the system practical safety, to be compared with those obtained for the system in the absence of control.

The overall outcomes highlight that around the resonance frequency the controlled system undergoes a severe worsening of its practical stability, with the residual integrity being reduced from 90 to 10% in a very narrow range of forcing amplitude values ($\Delta U = 3.6 \times 10^{-3}$ at $\omega_u = 0.82 \approx \omega_1$). Moreover, analyzing the evolution of the iso-integrity curves a shift in their lowest peak can be recognized, with the minimum value moving right from the nonlinear resonance frequency to the natural one, as already observed for the escape threshold of Fig. 20. Both effects are associated with the system softening behavior that prevents the response from attaining the higher amplitude resonant solution, which is characterized by too low values of residual integrity. This is similar to what observed also in other softening systems, e.g., the MEMS capacitor (Alsaleem et al. 2010), where it has been shown also

المنارة للاستشارات

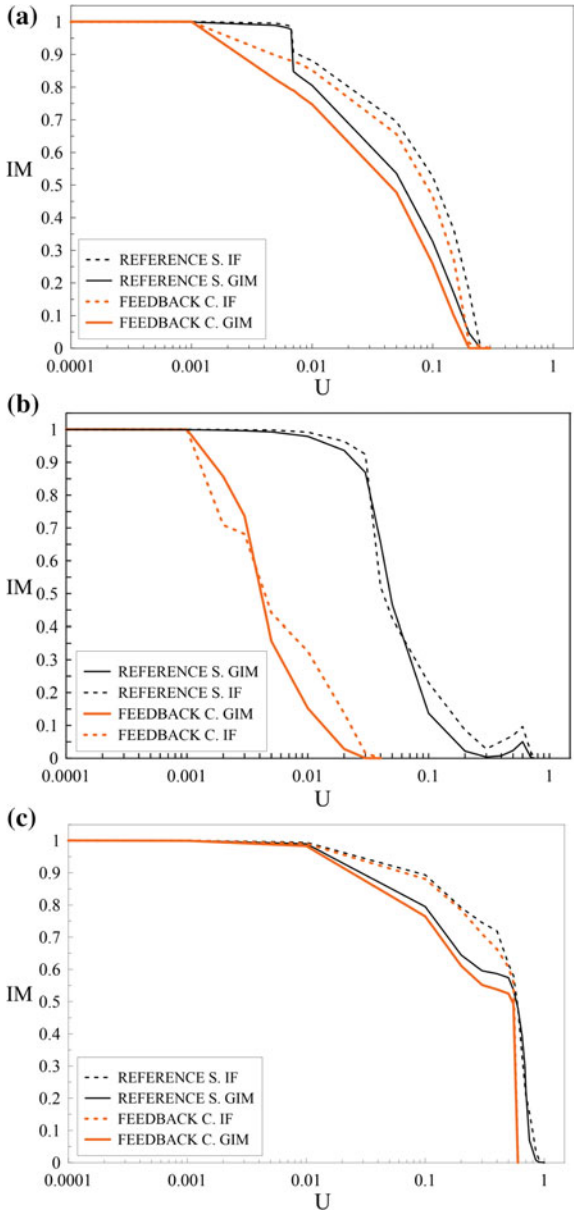

Fig. 24 Erosion profiles at $z_s = 0.01$ of the safe basin of the controlled system (thick orange, corresponding to nonresonant solution) and of the uncontrolled one (black, corresponding to union of solutions), obtained evaluating GIM (solid lines) and IF (dashed lines) measures, at $\omega_u = 0.7$ (**a**), $\omega_u = 0.8$ (**b**) and $\omega_u = 0.9$ (**c**)

المنارة للاستشارات

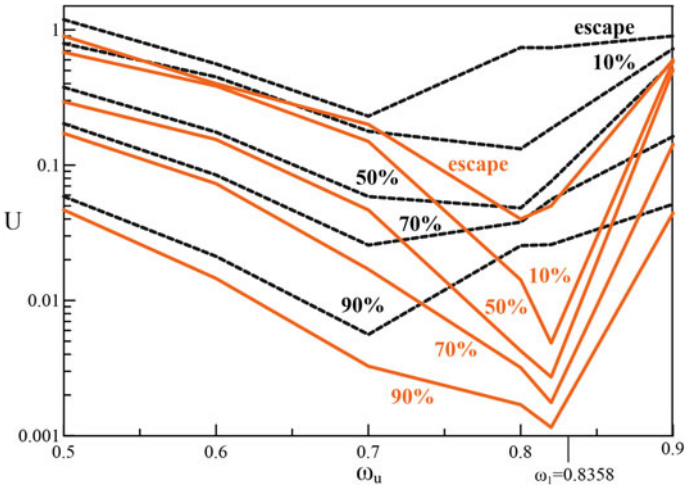

Fig. 25 Residual iso-integrity curves of the system safe basin for the controlled ($z = 0$, $z_s = 0.01$, orange solid lines) and reference ($z = z_s = 0.01$, black dashed lines) systems

responsible for the occurrence of practical escape (therein corresponding to the pull-in phenomenon) at much lower excitation amplitudes and higher forcing frequencies in experimental conditions than in theoretical conditions (see also Rega and Lenci 2015).

Note that the loss of stability due to the control presence is narrower in the left side of the chart and wider in the right, due to the fact that the P1H solution governing the system response in the latter range is no longer acceptable for the system.

Until now, the attractors robustness and the basin erosion of the system with external feedback control has been investigated with respect to variation of external action parameters (i.e., horizontal scan excitation and frequency). Yet, it is also important to verify the practical integrity of the system when varying some intrinsic parameter, like the distance between microcantilever tip and sample surface represented by the control parameter z_s. Due to its dependence on the roughness of the sample to be scanned, this parameter is highly variable during the AFM scanning operation, and the analysis of its effect on the global behavior of the system is particularly important to assess the actual safety in operating conditions.

For this reason, several bidimensional sections of the system basins of attraction in the $(x = x_{ref}, y = y_{ref})$ plane are constructed for increasing values of z_s, fixing the initial condition of the control variable $z = 0$ and the forcing amplitude at $U = 0.01$, which is indeed a low value, and for different forcing frequencies near the fundamental resonance. Note that varying z_s in the theoretical model corresponds to implicitly accounting for the actual time-varying distance during the scan operation.

As a remark, it can be noted that in this case, the phase plane corresponding to the reference uncontrolled system is set to $z = z_s = 0$, differently from what done in the previous Figs. 22, 23, 24, and 25 where the uncontrolled plane is defined

المنارة للاستشارات

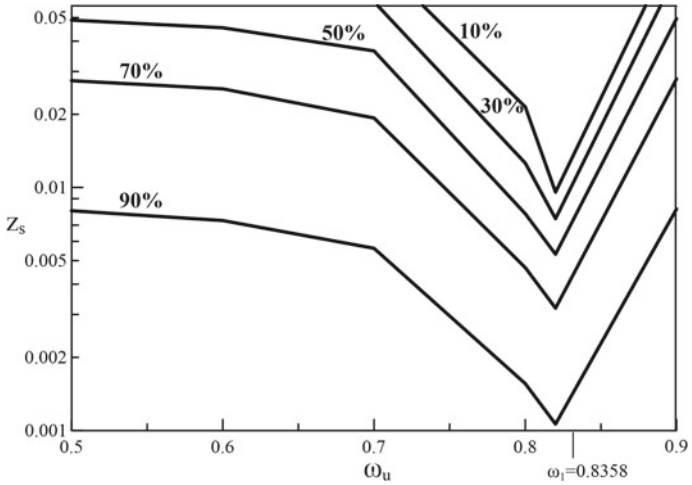

Fig. 26 Residual iso-integrity curves for the controlled system, at $U = 0.01$

as $z = z_s = 0.01$. Since the reference system is obtained from the controlled one when Eqs. (9) and (4) decouple, i.e., when $z = z_s$ for each value of z_s, the different choice between the two integrity analyses is due to reasons of consistency. Indeed, while previously z_s was a fixed parameter, equal to $z_s = 0.01$, here its variation is investigated, so that it is natural to determine the reference plane as the one for which z_s equals the fixed value of the variable z initial condition, i.e., $z_s = z = 0$.

The outcomes highlight that when the tip–sample distance increases (i.e., for increasing z_s) the basin of the unbounded solution enlarges inside the potential well, to the main detriment of the (solely controllable) nonresonant solution, whose basin of attraction is dramatically reduced up to vanishing. The negative effect of the increasing tip–sample gap on the dynamical safety of the system is summarized by the iso-integrity curves reported in Fig. 26, where the resonance region proves to be critical also with respect to variation of the tip–sample distance. Around ω_1, in fact, the dynamical integrity of the controlled solution is drastically reduced as the gap increases, decreasing up to $\approx$10% for $z_s = 0.01$.

Finally, it is of interest to analyze the combined effect of the two main system intrinsic parameters, i.e., the z_s parameter and the atomic interaction parameter represented by Γ_1.

Analyzing and quantifying the basin evolution as a function of z_s at different values of the atomic interaction parameter provides the erosion profiles of the safe basin in Fig. 27. They confirm that an increase of either parameters has an evident negative effect on the system robustness. This information has an important practical consequence, as indicates that a rough sample surface and/or a strong atomic interaction between tip and sample represent dangerous situations for the application of the external feedback control to an AFM, which could lead to errors in the topography. Moreover, for a given acceptable value of residual integrity, the z_s value available

المنارة للاستشارات

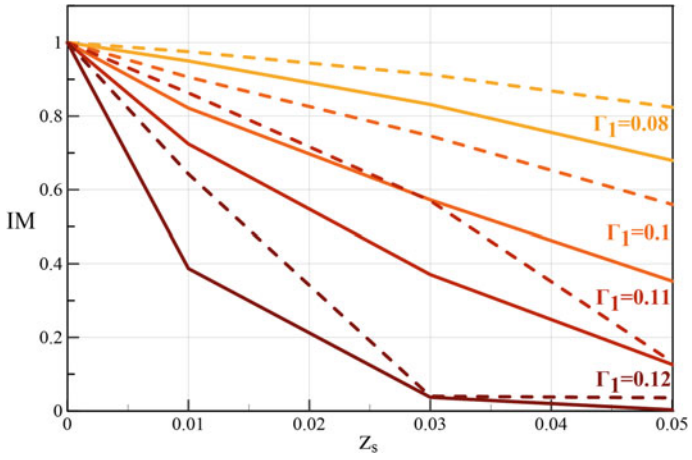

Fig. 27 Erosion profiles of the safe basin as a function of z_s at $U = 0.01$ and $\omega_u = 0.7$, for increasing values of Γ_1: $\Gamma_1 = 0.08$ (yellow lines), $\Gamma_1 = 0.1$ (orange lines), $\Gamma_1 = 0.11$ (red lines), $\Gamma_1 = 0.12$ (dark red lines). Dashed lines: IF measure; continuous lines: GIM measure

for control in safe operating conditions becomes smaller as the atomic interaction increases. Overall, in a design perspective, useful hints are obtained to calibrate the tip–sample interaction (e.g., tip material choice) depending on the sample characteristics and roughness, in order to guarantee a proper safety level during the scan operation.

4 AFM with Global Control

The results presented in the previous Sect. 3 have shown that, while being generally effective in realizing the specific aim for which it is designed, the insertion of an external feedback control in a noncontact AFM model causes a generalized reduction of the stability region and a dangerous decrease of system safety with respect to the unwanted jump-to-contact phenomenon. Yet, from a practical stability perspective, an acceptable system-dependent residual integrity is needed to guarantee secure AFM operation since it is nowadays well known that the safety of a nonlinear system depends not only on stability of its solutions but also on the uncorrupted basins of attraction surrounding them.

Following this assumption, and focusing on the preservation of dynamical integrity, it is worth analyzing whether a non-feedback control technique, specifically aimed at favorably affecting a global bifurcation event which triggers basins erosion, can also work for the AFM system and reduce the basin erosion which leads to the loss of safety. The method (Lenci and Rega 2004) is based on the optimal modification of the shape of the reference harmonic excitation in order to shift the

المنارة للاستشارات

occurrence of the global event (i.e., homo/heteroclinic bifurcation of some saddle) responsible for the sudden fall down of the dynamical integrity profiles, thus obtaining an overall control of the dynamics and an enlargement of the system safe region in parameters space. When the global bifurcation triggering erosion involves the manifolds of the sole hilltop saddle of the system, then its (approximate) occurrence can be determined by means of the Melnikov method, based on the interpretation of the nonlinear system as perturbation of the relevant Hamiltonian one, and the subsequent determination of the amplitude and phase of the controlling superharmonics by solving an optimization problem. This analytical control procedure has demonstrated its effectiveness in increasing the system safety of several different mechanical systems, such as the Helmholtz oscillator (Lenci and Rega 2003a), the Duffing oscillator (Lenci and Rega 2003b), the rigid block (Lenci and Rega 2005) and a reduced model of MEMS microbeam (Lenci and Rega 2006), which have allowed to verify the influence on the erosion of some main mechanical features, like smoothness, stiffness, and symmetry. With reference to the latter, two different approaches have been proposed, the "one-side" control, which is very effective but acts on a single global (homoclinic) bifurcation thus being particularly useful for asymmetric systems, and the "global" control, which is able to increase simultaneously two homo/heteroclinic bifurcations in case of two (or more) potential wells or heteroclinic loop involving two saddles. In the examined cases, the analytical procedure has demonstrated its ability in delaying the erosion also in cases where the loss of safety is likely due to the presence of secondary global bifurcations involving other internal saddles. However, when other secondary saddles play a major role in the development of the basins erosion, and when the profile fall down occurs away from the hilltop bifurcation, the control technique has to be applied by developing a purely numerical procedure to define the optimal shape of the controlling superharmonics.

4.1 Analytical Control of Homoclinic Bifurcation of Hilltop Saddle

In order to apply the analytical procedure, reference has to be made to the underlying Hamiltonian system (see Eq. (6) and Fig. 2 of Sect. 2.1), from which the expression of the homoclinic orbit $y_h(t)$ of the hilltop saddle S_H, reported also in Fig. 28, can be derived (Settimi et al. 2016):

$$y_h(x) = \frac{dx_h}{dt} = \pm\sqrt{2(V(x_{S_H}) - V(x))} \tag{10}$$

where x_{S_H} is the coordinate of the hilltop saddle. The integral (10) cannot be solved in closed form but has to be computed numerically. The curve borders the single potential well, which includes the bounded periodic solutions and represents the safe domain for noncontact AFM operation, separating it from the outer region of unbounded solutions leading to the jump-to-contact phenomenon.

المنارة للاستشارات

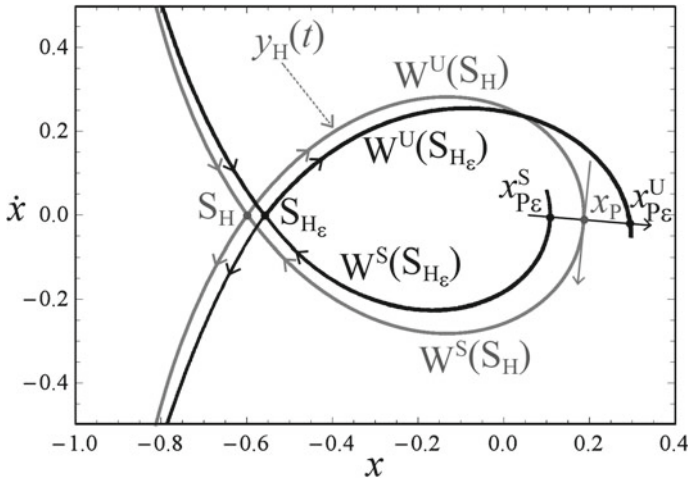

Fig. 28 Qualitative behavior of the stable (W^S) and unstable (W^U) manifolds of the hilltop saddle for the Hamiltonian system (gray) and the ε-perturbed, forced, damped system (black)

Due to the unperturbed nature of the Hamiltonian system, the homoclinic orbit represents also the coinciding right unstable ($W^u(S_H)$) and stable ($W^s(S_H)$) manifolds of the hilltop saddle. When damping and excitation are added into the system (6), the separation of the stable and unstable manifolds of the Hamiltonian system occurs (see Fig. 28, where the (gray) homoclinic orbit is also plotted, for comparison), and their evolution can lead them to intersect or to remain disjoint depending on the value of the excitation parameters. The critical situation of manifolds tangency corresponds to the occurrence of a global homoclinic bifurcation, which can be analytically detected by the classical Melnikov method. The control procedure aims at shifting such bifurcation by optimally modifying the excitation shape, i.e., by adding controlling superharmonics to the harmonic excitation of the system (4) with $V_g = 0$ and $U_g = U \sin \omega_u t$:

$$\ddot{x} + \alpha_1 x + \alpha_3 x^3 + \frac{\Gamma_1}{(1+x)^2} = -\rho_1 \dot{x} - x\mu_1 \omega_u^2 U_1 \sum_{j=1}^{N} \frac{U_j}{U_1} \sin(j\omega_u t + \Psi_j) \quad (11)$$

where U_1 is the horizontal parametric-like reference excitation while U_j and Ψ_j are the amplitudes and phases of the controlling superharmonics. In presence of weak excitation and damping, the system (11) can be expressed as an ε-perturbation of the Hamiltonian system (6):

المنارة للاستشارات

$$\begin{cases} \dot{x} = y \\ \dot{y} = -\alpha_1 x - \alpha_3 x^3 - \frac{\Gamma_1}{(1+x)^2} \\ \quad\quad +\varepsilon\Big(-\rho_1 y - x\mu_1\omega_u^2 U_1 \sum_{j=1}^{N} \frac{U_j}{U_1}\sin(j\omega_u t + \Psi_j)\Big) \end{cases} \tag{12}$$

where ε is a smallness parameter. To the first order, the distance between the stable ($W^s(S_{H\epsilon})$) and unstable ($W^u(S_{H\epsilon})$) manifolds of the perturbed system is furnished by the Melnikov integral:

$$\begin{aligned} \mathcal{M}(t_0) &= \int_{-\infty}^{+\infty} y_h(t)\Big(-\rho_1 y_h(t) - x_h(t)\mu_1\omega_u^2 U_1 \sum_{j=1}^{N}\frac{U_j}{U_1}\sin(j\omega_u(t+t_0)+\Psi_j)\Big)dt \\ &= 2\rho_1 I_1 - 2\mu_1\omega_u^2 U_1 I_2(\omega_u) h(m) \end{aligned} \tag{13}$$

where

$$I_1 = -\int_{x_A}^{x_{S_H}} y_h(x)dx, \quad I_2(j\omega_u) = \int_{x_A}^{x_{S_H}} x\sin\Big(j\omega_u\int_{x_A}^{x}\frac{dr}{y_h(r)}\Big)dx$$

are integrals to be numerically computed, and

$$h(m) = \sum_{j=1}^{N} h_j\cos(j\omega_u t_0 + \Psi_j), \quad h_j = \frac{U_j I_2(j\omega_u)}{U_1 I_2(\omega_u)}$$

is 2π-periodic with zero mean value ($m = \omega_u t_0$). The tangency of the stable and unstable manifolds, i.e., the occurrence of the homoclinic bifurcation, corresponds to a simple zero of the Melnikov integral $\mathcal{M}(t_0) = 0$ for some t_0:

$$\begin{aligned} &U_{1,cr} = \frac{\rho_1 I_1}{\mu_1\omega_u^2|I_2(\omega_u)|M}, \\ &\text{with} \quad \begin{cases} M = M^+ = \max_{m\in[0,2\pi]}\{h(m)\}, & I_2(\omega_u) > 0 \\ M = M^- = -\min_{m\in[0,2\pi]}\{h(m)\}, & I_2(\omega_u) < 0 \end{cases} \end{aligned} \tag{14}$$

Note that in the presence of the sole reference harmonic excitation ($j = 1$) $h_1 = 1$ and $M = 1$. To achieve the best control effect, the homoclinic tangency has to be shifted to the highest possible value of the forcing amplitude, which corresponds to the following optimization problem (Lenci and Rega 2003a):

$$\begin{aligned} &\text{Maximize} \min_{m\in[0,2\pi]}\{h(m)\}, \quad I_2(\omega_u) < 0 \\ &\text{Minimize} \max_{m\in[0,2\pi]}\{h(m)\}, \quad I_2(\omega_u) > 0 \end{aligned} \tag{15}$$

المنارة للاستشارات

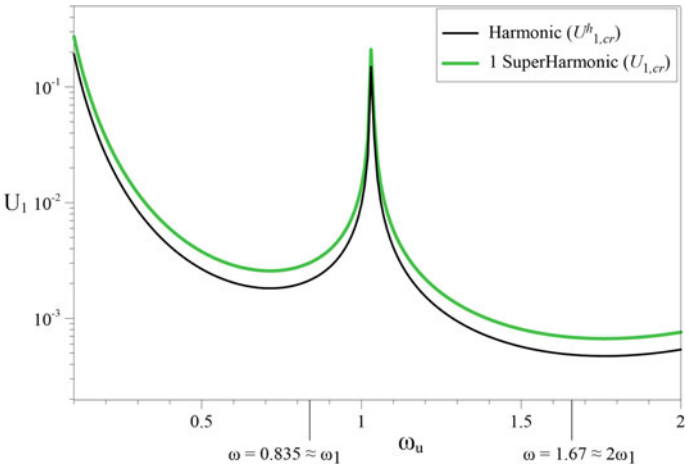

Fig. 29 Analytical bifurcation thresholds in the ω_u-U_1 plane. Black curve: reference harmonic system; green thick curve: system with superharmonic $h_2 = 0.353553$ (optimal)

The optimization can be achieved by properly choosing h_j and Ψ_j, where $j = 1, 2, 3, .., N$ is the number of superharmonics to be added to the system. To measure the improvement obtainable with respect to the reference harmonic excitation, the gain G is introduced: $G = U_{1,cr}/U^h_{1,cr} = 1/M$, where $U^h_{1,cr}$ represents the critical amplitude for the reference harmonic system. Setting $\Psi_j = 0$, focus is paid to the addition of one even superharmonic, i.e., $j = 2$, due to the asymmetric feature of the system which calls for the application of the so-called "one-side" control. The solution of the optimization problem (15) furnishes the value $h_2 = 0.353553$, as its minimum reaches the maximum value in $h(m) = -0.707107$, corresponding to the maximal theoretical gain $G = 1.4142$ (Lenci and Rega 2004). The homoclinic bifurcation thresholds detected by means of the Melnikov method are reported in Fig. 29 in the excitation parameters plane (ω_u, U_1), for the reference harmonically forced system (black curve), and for the system with one optimal controlling superharmonic (green curve). The outcomes confirm that the control manages to shift the bifurcation threshold to higher values of the forcing amplitude with respect to the harmonic case, apart from the region around the "antiresonant" frequency $\omega_u \approx 1.03$ at which the threshold goes to infinity due to the first order nature of the Melnikov approximation.

The numerical detection of the hilltop manifolds validates the analytical results, highlighting the ability of the optimal superharmonic in separating the stable (gray) and unstable (green) hilltop manifolds, as shown in Fig. 30 at frequency values before and after the fundamental resonance $\omega_1 = 0.8357$. It is worth noting that the increase of the bifurcation threshold occurs for negative values of the amplitude of the controlling superharmonic (see Fig. 34 forward), while positive amplitudes produce a worsening effect of the global dynamical behavior. From an operational point of view, the same result can be achieved by applying positive superharmonics with a phase shift $\Psi_2 = \pi$.

المنارة للاستشارات

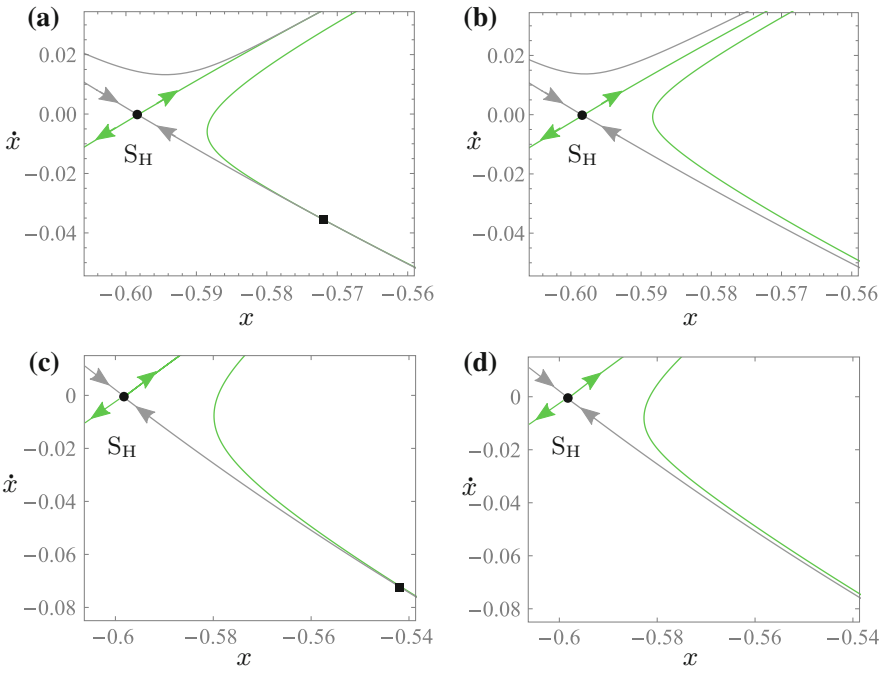

Fig. 30 Stable (gray) and unstable (green) manifolds of the hilltop saddle S_H for the reference harmonic system (**a**, **c**) and for the system with optimal superharmonic $h_2 = 0.353553$ (**b**, **d**) at $U^h_{1,cr} = 0.001823$ and $\omega_u = 0.7$ (**a**, **b**) and at $U^h_{1,cr} = 0.0027652$ and $\omega_u = 0.9$ (**c**, **d**). Square point identifies one of the manifolds tangency points

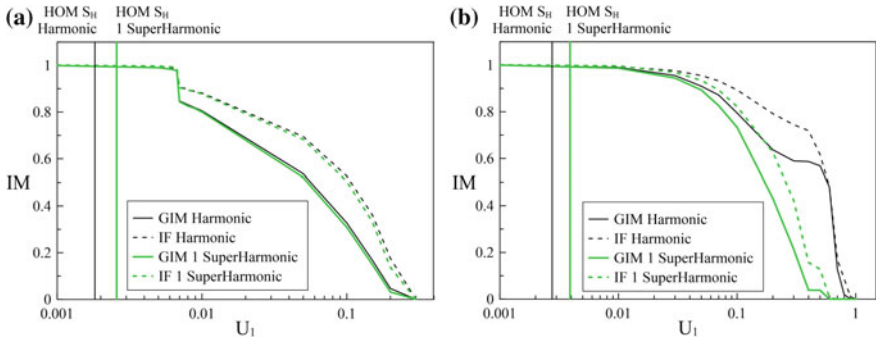

Fig. 31 Erosion profiles as a function of the forcing amplitude U_1 for the reference harmonic system (black) and for the system with optimal superharmonic (thick green), at $\omega_u = 0.7$ (**a**) and at $\omega_u = 0.9$ (**b**). Dashed lines: profiles obtained with integrity factor (IF); continuous lines: profiles obtained with global integrity measure (GIM)

المنارة للاستشارات

With reference to the main practical objective of the applied control, i.e., the overall enlargement of the system safe region, the verification of the homoclinic hilltop bifurcation shift has to be complemented by the investigation of the safe basin evolution, the latter being carried out by the analysis of the system dynamical integrity. In this respect, the safe basin is defined as the union of the classical basins of attraction inside the potential well, and the integrity measures used to quantify the erosion are the Global integrity measure (GIM) and the integrity factor (IF) which work both well in this respect. Once the basins of attraction are numerically obtained for increasing values of the forcing amplitude, and after quantification of the basins integrity, the erosion profiles of Fig. 31 are built, for the system with harmonic excitation (black curves) and for the one with optimal superharmonic (green curves). The results highlight that the controlling superharmonic is not able to improve the system integrity, i.e., to shift the profiles fall down to higher values of the forcing amplitude, different from what observed in several other systems with escape (Rega and Lenci 2008). Moreover, right of the fundamental resonance, the controlled profiles result to be sharper than the harmonic ones in their final part (see Fig. 31b), meaning that for high values of the forcing amplitude, the control worsens the system robustness (this is anyway a well-known behavior, detected in other literature systems (Rega and Lenci 2008)). The causes of this behavior are to be sought in the significant distance, in terms of values of the forcing amplitude, between the occurrence of the homoclinic bifurcation and the profile fall down, as can be seen in Fig. 31. Focusing on the case $\omega_u = 0.7$ and observing the basins evolution (not reported), in fact, it can be noted that, once the manifolds intersect, the unbounded solution basin which surrounds the potential well starts penetrating inside the well through fractal tongues from the outer edge. However, the safe basin erosion develops very slowly and, when the amplitude approaches the value $U_1 = 0.0067$ (numerically detected) corresponding to the profiles fall down, the positive effects of the homoclinic bifurcation shift have been exhausted; in fact, at this value, the stable and unstable manifolds of the hilltop saddle clearly intersect each other. Of course, the same considerations hold at frequencies higher than the fundamental resonance one, as well as, for both cases, the arise of competing basins of attraction before the profiles fall down. Their appearance suggests the presence of other internal saddles whose manifolds are responsible for the basins behavior inside the well, which, however, has to be investigated with solely numerical procedures.

4.2 Numerical Control of Bifurcations of Secondary Saddles

4.2.1 Before the Fundamental Resonance Frequency

An accurate numerical investigation of the global bifurcation scenario of the AFM model at $\omega_u = 0.7$ is required to properly identify the global event responsible for the reduction of system integrity. The results reported in Table 1 display the occurrence of four different global bifurcations, involving stable and unstable manifolds of a

المنارة للاستشارات

secondary saddle internal to the potential well, in addition to the hilltop manifolds. In particular, the arise of such secondary saddle S_1 is related to the appearance, at $U = U_{S_1} = 0.001697$, of the basin of attraction of the 1-period (resonant) solution inside the former (nonresonant) basin, and its stable manifolds represent the smooth edges in between the two basins. This event occurs just before the homoclinic bifurcation of the hilltop saddle at $U = U_{hom1} = 0.001823$, already detected and controlled in the previous Sect. 4.1, and corresponding, from a phenomenological viewpoint, to the beginning of the fractalization of the safe basin outer edge. At considerably higher values of the forcing amplitude, at $U = U_{hom2} = 0.006375$, the tangency between the unstable left manifold $W_l^u(S_1)$ and the stable left manifold $W_l^s(S_1)$ of the in-well saddle points out the occurrence of the left-side homoclinic bifurcation of the saddle S_1, which marks the beginning of the disruption of the smooth separation between the basins inside the well, representing the starting point for the fractalization of the resonant basin boundary inside the nonresonant one. As the amplitude slightly increases, the left unstable manifold of the in-well saddle crosses the left stable one and approaches the right stable manifolds of both the in-well saddle (purple line in the following Fig. 32) and the hilltop one (gray line), whose evolutions have developed keeping them very close to each other.

At $U = 0.006676$, the two mixed-side tangencies ($W_l^u(S_1) \cap W_r^s(S_1)$ and $W_l^u(S_1) \cap W_r^s(S_H)$) occur almost simultaneously, corresponding to a homoclinic bifurcation of the in-well saddle and to a heteroclinic bifurcation between the in-well and hilltop saddles, respectively, reported in Fig. 32. They lead to the penetration of tongues of the unbounded solution basin inside the potential well, which causes the separation of the resonant and nonresonant basins (right panels of Fig. 32), and consequently the strong reduction of the safe basin integrity highlighted by the sharp fall down of the erosion profile. The described global bifurcations are marked on the erosion profiles of the system safe basin in Fig. 33, confirming that the two last bifurcations occur just before the profile sharp decrease, thus suggesting they are the global events to be controlled for increasing the system safety.

To this aim, a fully numerical procedure is developed (Settimi and Rega 2016a), starting from the numerical detection of the saddles and of the relevant stable and

Table 1 Main global events at $\omega_u = 0.7$

Harmonic amplitude	Global event	Saddle involved
$0.001697 = U_{S_1}$	Onset of in-well saddle	S_1
$0.001823 = U_{hom1}$	Homoclinic bif. $W_r^s(S_H) \cap W_r^u(S_H)$	S_H
$0.006375 = U_{hom2}$	Homoclinic bif. $W_l^u(S_1) \cap W_l^s(S_1)$	S_1
$0.006676 = U_{hom3}$	Homoclinic bif. $W_l^u(S_1) \cap W_r^s(S_1)$	S_1
$0.006676 = U_{het}$	Heteroclinic bif. $W_l^u(S_1) \cap W_r^s(S_H)$	S_1, S_H

المنارة للاستشارات

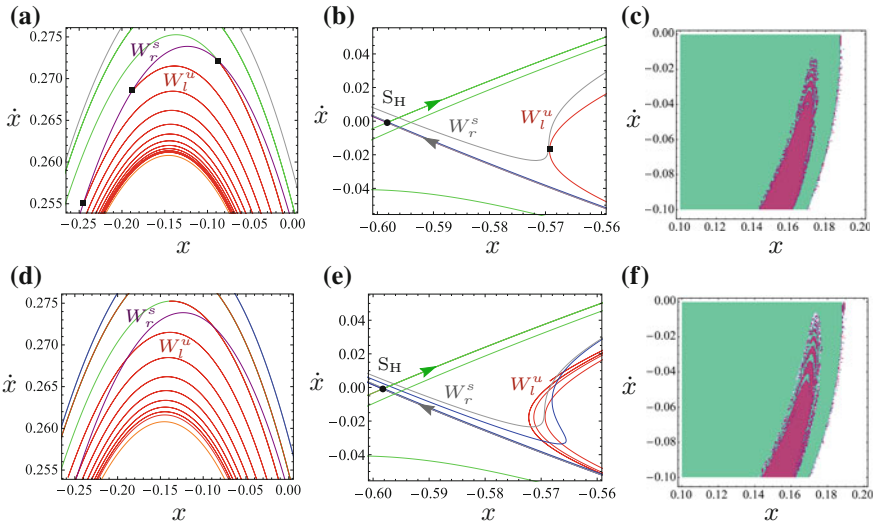

Fig. 32 Manifolds and basins at $U = U_{hom3} \cong U_{het} = 0.006676$: enlargements during ($U = 0.006676$) (**a**–**c**) and after ($U = 0.0068$) (**d**–**f**) the bifurcation events. Left panels (**a**, **d**): $hom3$, Middle panels (**b**, **e**): het. Gray line: stable manifold of S_H saddle; green line: unstable manifold of S_H saddle; purple line: stable right manifold of S_1 saddle; orange line: unstable right manifold of S_1 saddle; blue line: stable left manifold of S_1 saddle; red line: unstable left manifold of S_1 saddle; square dot: bifurcation point

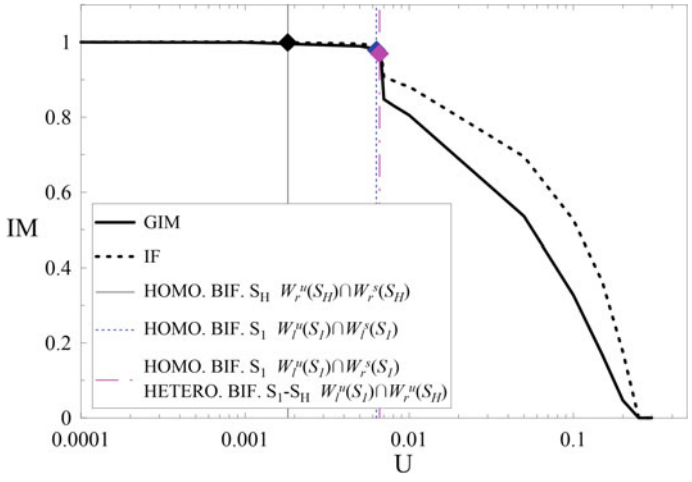

Fig. 33 Erosion profiles at $\omega_u = 0.7$, with detection of the main global bifurcations

المنارة للاستشارات

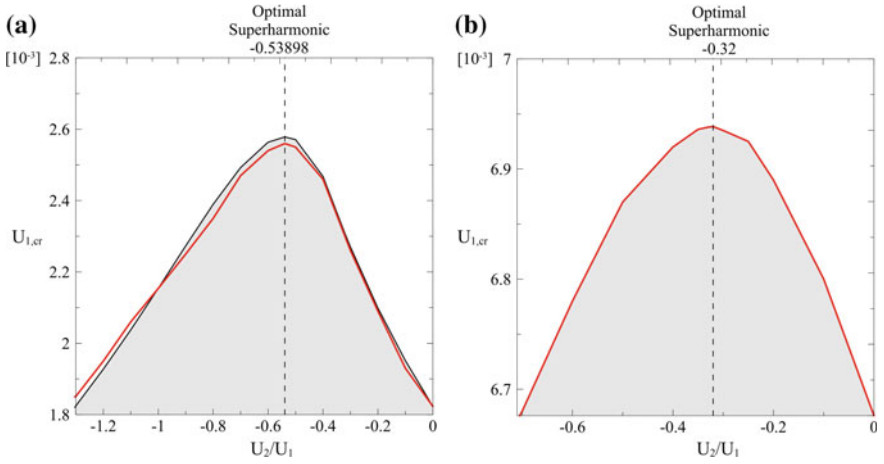

Fig. 34 Analytical (black line) and numerical (thick red line) thresholds of the homoclinic bifurcation $hom1$ ($W_r^s(S_H) \cap W_r^u(S_H)$) as a function of the superharmonic amplitude U_2/U_1 (**a**); Numerical threshold of the homoclinic bifurcation $hom3$ ($W_l^u(S_1) \cap W_r^s(S_1)$) as a function of the superharmonic amplitude U_2/U_1 (**b**)

unstable manifolds involved in the bifurcation to be controlled. Then, a proper region in the state plane including candidate, and graphically handy, bifurcation points is identified, and the computation of the manifolds distance along a proper (i.e., nonparallel to one of the manifolds) direction is carried out via the arclength method. Once one manifold has been numerically discretized, distances are computed starting from each point of it and the minimum value is selected. The direction for calculating the distance is chosen to be that of the unstable eigenvalue of the hilltop saddle, although distances along other (rotated) directions have been also calculated to check the consistency of the obtained results. Apart from obvious quantitative differences, the outcomes have shown the same trend, thus validating the adopted choice. The procedure is repeatedly implemented by varying the amplitude of the harmonic excitation U_1, until the calculated distance becomes equal to zero, warning that the tangency of the manifolds (thus the global bifurcation) occurs. The application of the same process is then carried out for different amplitudes of the controlling superharmonic, i.e., various U_2/U_1 ratios in Eq. (11), assuming $\Psi_j = 0$ and $j = 2$, as done in the analytical case illustrated in Sect. 4.1, thus considering the presence of one even superharmonic ($2\omega_u$). The subsequent detection of the bifurcation threshold in the $U_2/U_1, U_{1,cr}$ plane allows to finally determine the optimal superharmonic able to shift the bifurcation to the highest value of the forcing amplitude.

To test the numerical control, the homoclinic bifurcation of the hilltop saddle occurring at $U_1 = U_{hom1} = 0.001823$ has been investigated, since for it, the Melnikov method already allowed to identify the value of the optimal controlling superharmonic (Sect. 4.1). The good agreement between the analytical and numerical results shown in Fig. 34a confirms the ability of the numerical procedure in detect-

المنارة للاستشارات

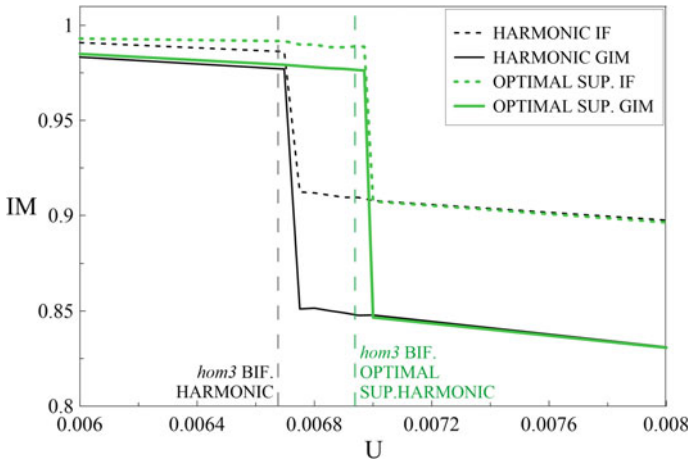

Fig. 35 Erosion profiles for the uncontrolled system (black line) and for the system with optimal superharmonic $U_2/U_1 = -0.32$ (thick green line)

ing the value of the superharmonic to be added to the system for maximizing the delay of the global bifurcation.

Thus, the technique is applied to the bifurcations occurring just before the erosion profile fall down, focusing the attention on the *hom*3 bifurcation, since it requires the detection of the position and of the relevant manifolds of the sole internal saddle, simplifying the implementation of the numerical procedure. The selected region in the state plane is chosen to be $x \in [-0.2, 0.2]$, $\dot{x} \in [-0.3, 0.3]$, since it includes a significant number of tangency points. The obtained bifurcation threshold for varying amplitude of the controlling superharmonic is reported in Fig. 34b, and allows to determine the new value of the optimal superharmonic, which corresponds to the peak of the threshold occurring at $U_2/U_1 = -0.32$. It is worth noting that, in this case, the whole bell of increased bifurcation thresholds is contained in a range of amplitude values of the added superharmonic which are meaningfully lower than the value of the reference harmonic amplitude, thus corresponding to a control suitability also in terms of relatively low cost.

Once the optimal amplitude of the controlling superharmonic is detected, the erosion profiles of the controlled system are realized and compared with those of the uncontrolled one, to verify the effectiveness of the control in delaying the sharp decrease of the dynamical integrity. Figure 35 confirms that, beyond delaying the occurrence of the targeted homoclinic bifurcation, the numerical control is able also to move the profiles fall down to higher values of the forcing amplitude, in this case increasing the system safety of about 4%. This beneficial effect can be easily justified by observing the influence of the control on the behavior of the basins of attraction. With reference to the uncontrolled system (Fig. 32d, f), the optimal superharmonic manages to avoid the manifolds intersection (see comparison between Fig. 32d, e without control and Fig. 36a, b with optimal superharmonic), and entails the reduction

المنارة للاستشارات

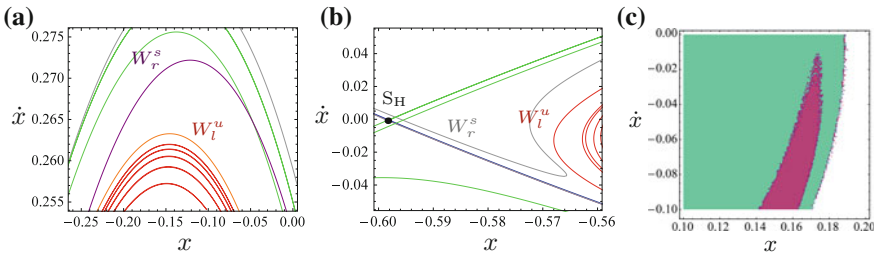

Fig. 36 Manifolds and basins at $U = 0.0068$ for the system with optimal superharmonic $U_2/U_1 = -0.32$ (**a**–**c**): left panel (**a**): $hom3$, middle panel (**b**): het. gray line: stable manifold of S_H saddle; green line: unstable manifold of S_H saddle; purple line: stable right manifold of S_1 saddle; orange line: unstable right manifold of S_1 saddle; blue line: stable left manifold of S_1 saddle; red line: unstable left manifold of S_1 saddle

of the basins fractalization and the postponement of the penetration of the white tongues of the unbounded basin inside the potential well, as highlighted comparing Figs. 32f and 36c. As a consequence, the safe basin, i.e., the union of the resonant and nonresonant basins taken into account by the IF measure, maintains its compactness for a wider range of forcing amplitudes.

With reference to the outcomes presented in literature concerning different dynamical systems, it is worth observing that the presented analysis furnishes coherent and acceptable results. In fact, for the AFM system investigated here, the improvement of about 4% of the dynamical robustness is obtained with relatively low cost in terms of controlling amplitude ($U_2/U_1 = 0.32$). Other literature systems are in line with these values: for an archetypal Duffing equation, the addition of one odd superharmonic has demonstrated to succeed in reducing the scattered chaotic region of about 1% (with $U_2/U_1 = 0.8$) (Lenci and Rega 2003c), while one even superharmonic has been able to increase the saved region of about 5% (with $U_2/U_1 = 0.4$); moreover, in a micro-electromechanical system (Lenci and Rega 2006) one controlling superharmonic has proved to shift the relevant erosion profile of about 8% for $U_2/U_1 = 1.6591$ (which is indeed a major costing amplitude), and of about 4% with $U_2/U_1 = 0.5$.

4.2.2 After the Fundamental Resonance Frequency

The numerical procedure previously described has a very general nature, and can be applied to any kind of global bifurcation with the addition of any number of superharmonics. To verify its versatility, the numerical control has been applied also at $\omega_u = 0.9$, a sample case of the system behavior after the fundamental resonance, for which the analytical control has shown to even deteriorate the safe basin robustness by shifting the smoother part of the relevant erosion backward (see Fig. 31b of Sect. 4.1).

Observing the erosion profiles at this frequency, reported in Fig. 37 for the sake of clarity, it is evident that the sharp loss of robustness occurs for quite high values of the

المنارة للاستشارات

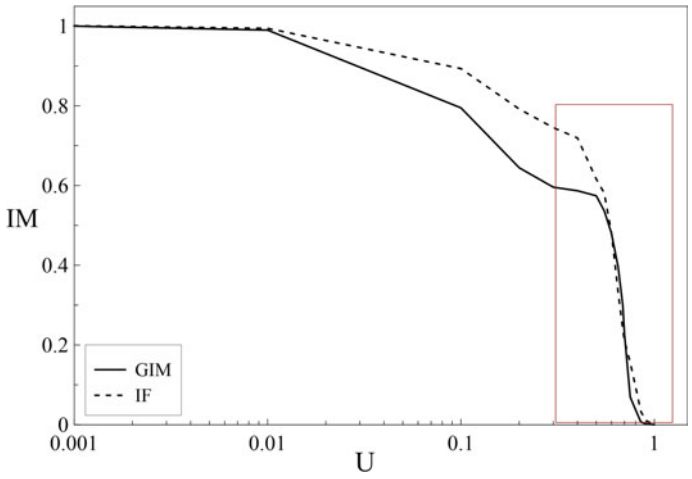

Fig. 37 Erosion profiles of the reference system at $\omega_u = 0.9$

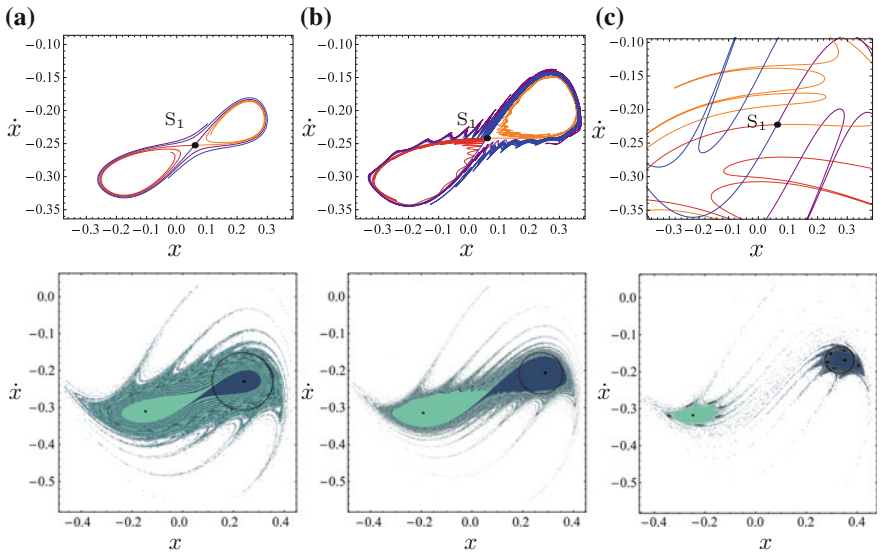

Fig. 38 Manifolds and basins at $\omega_u = 0.9$ for $U = 0.65$ (**a**), $U = U_{hom} = 0.686$ (**b**), $U = 0.75$ (**c**). Purple line: stable right manifold of S_1 saddle; orange line: unstable right manifold of S_1 saddle; blue line: stable left manifold of S_1 saddle; red line: unstable left manifold of S_1 saddle

harmonic forcing amplitude, highlighted by the red box in figure, after a long smooth decrease, and the final fall down of the profile is definitely stronger than the one detected at $\omega_u = 0.7$ (Fig. 31a) swiftly leading to the zeroing of the system dynamical integrity. Also in this case, attention has to be focused on the sharp part of the profiles, which marks the loss of safety for the system, so that the global bifurcation to be

المنارة للاستشارات

controlled has to be sought for amplitude values much higher than that associated with the homoclinic bifurcation of the hilltop saddle analytically determined (i.e., $U^h_{1,cr} = 0.0027652$). A thorough investigation of the system global behavior allows to detect the arise of an internal saddle, coinciding with the birth of a new basin related to a competing 1-period solution, at a very large excitation amplitude ($U = 0.604$). At this value, the manifolds of the hilltop saddle are already fully intersected (not reported in the next figures for readability reasons), suggesting a crucial role of the internal saddle in the loss of robustness of the system. In fact, the relevant left manifolds $W^u_l(S_1)$ and $W^s_l(S_1)$ undergo a homoclinic bifurcation at $U \cong 0.686$, that from a phenomenological viewpoint corresponds to the basins separation inside the potential well, leading to a strong decrease of the system dynamical integrity. The overall behavior can be recognized in Fig. 38, where manifolds and basins of attraction are reported before, during, and after the homoclinic bifurcation $W^u_l(S_1) \cap W^s_l(S_1)$. Figure 39a is a zoom of the upper panel of Fig. 38b around S_1. By applying the same procedure of the case $\omega_u = 0.7$, one even superharmonic is applied to the model. However, this time the ability of control in preventing the homoclinic bifurcation, which is apparent in the separation of the left manifolds of the S_1 saddle shown in Fig. 39b for a very low value of the controlling amplitude, is accompanied by a critical modification of the behavior of the corresponding right manifolds. As highlighted by the purple and orange lines in Fig. 39b, in fact, they intersect each other causing the occurrence of another homoclinic bifurcation $W^u_r(S_1) \cap W^s_r(S_1)$, which obviously neutralizes the beneficial effect achieved on the left manifolds. This result can be easily explained by observing that in this case, as already noticed in commenting Fig. 9c, despite the overall asymmetric one-well potential of the system, the in-well basins of attraction for high values of the forcing amplitude are organized in the state plane so as to assume a local topology similar to that of a symmetric two-well potential, which is now playing the role of safe basin to be optimally controlled by adding odd superharmonics (so-called "global" or, herein better, "two-side" control (Lenci and Rega 2004)). For this reason, to apply the global control at $\omega = 0.9$, one odd superharmonic ($3\omega_u$) is added to the harmonic forcing, unlike what done at $\omega = 0.7$. The implementation of the numerical procedure furnishes the bifurcation threshold of the homoclinic bifurcation for different values of the amplitude ratio U_3/U_1 (Fig. 40), whose peak occurs for $U_3/U_1 = -0.45$ and represents the optimal value of the controlling amplitude to be applied (Settimi and Rega 2017).

The effects of the control application on the basins evolution are reported in Fig. 41, to be compared with those of the reference system in Fig. 38; the evolution of the manifolds is significantly smoother, for both the right and left manifolds of the internal saddle S_1, confirming the ability of the "two-side" control in modifying the behavior of both the wells (basins in this case) governed by the considered saddle. Moreover, the robustness of the (green) dominant basin is increased by considerably delaying the arise of the competing 1-period solution (blue basin), and consequently the basin separation. As a consequence, the fall down of the "new" safe basin profile is shifted to higher values of the harmonic forcing amplitude, enlarging the range of U values in which the system safety is guaranteed, while leaving the qualitative trend of the profiles substantially unchanged, as can be observed by comparing the green

المنارة للاستشارات

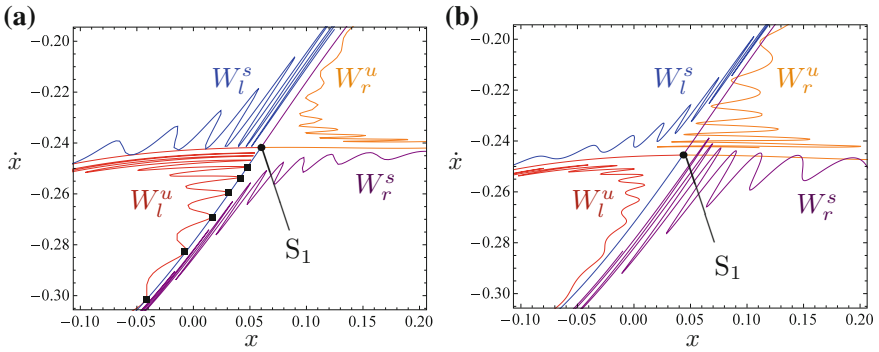

Fig. 39 Manifolds enlargement at $\omega_u = 0.9$, $U = U_{hom} = 0.686$ for the reference system (**a**) and for the system with one even superharmonic of amplitude $U_2/U_1 = -0.005$ (**b**). Purple line: stable right manifold of S_1 saddle; orange line: unstable right manifold of S_1 saddle; blue line: stable left manifold of S_1 saddle; red line: unstable left manifold of S_1 saddle; square dot: bifurcation point

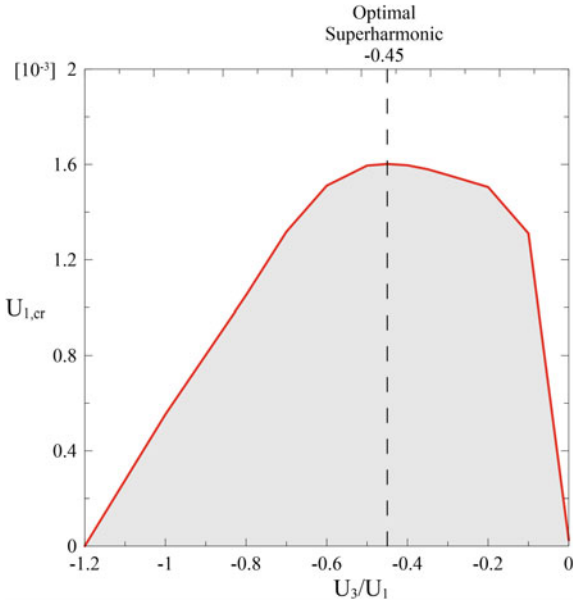

Fig. 40 Numerical threshold of the homoclinic bifurcation *hom* $(W_l^u(S_1) \cap W_l^s(S_1))$ as a function of the superharmonic amplitude U_3/U_1

and black profiles in Fig. 42. From the results, furthermore, it appears that at $\omega = 0.9$ the global control is even more effective than at $\omega = 0.7$, likely due to being farther away from the left-shifted nonlinear resonance (A-vertex of Fig. 6), thus being less influenced by its amplifying effect.

المنارة للاستشارات

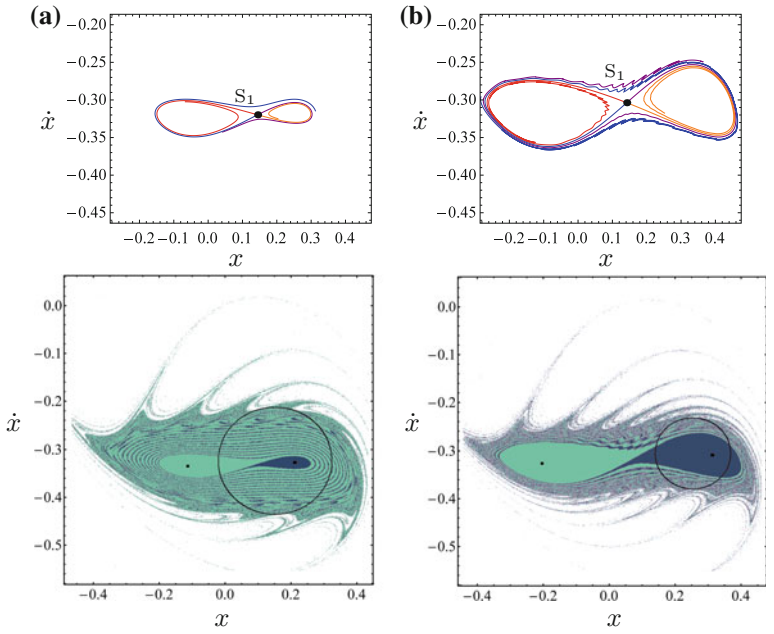

Fig. 41 Manifolds and basins at $\omega_u = 0.9$ for the system with optimal superharmonic $U_3/U_1 = -0.45$, for $U = 0.686$ (**a**) and $U = 0.75$ (**b**). Purple line: stable right manifold of S_1 saddle; orange line: unstable right manifold of S_1 saddle; blue line: stable left manifold of S_1 saddle; red line: unstable left manifold of S_1 saddle

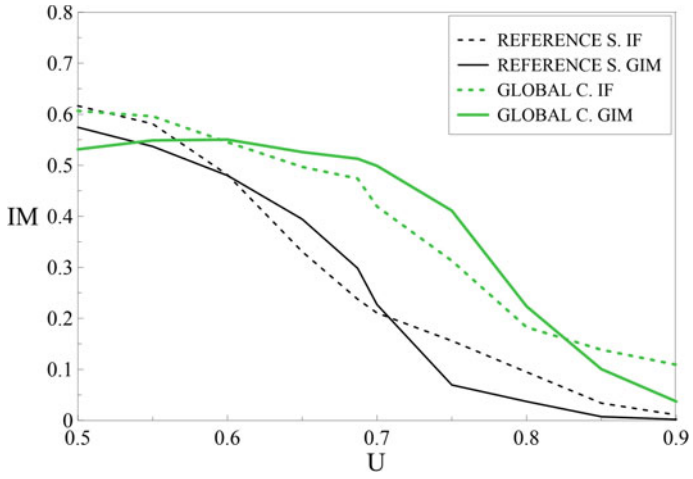

Fig. 42 Erosion profiles for the uncontrolled system (black line) and for the system with optimal superharmonic $U_3/U_1 = -0.45$ (thick green line)

المنارة للاستشارات

5 Conclusions

Local and global dynamics of a reduced order model of noncontact atomic force microscope have been addressed in this chapter, by considering also the possible presence of two different control techniques, in order to comparatively point out their effects on the overall dynamical behavior of the system. The presented results allow to draw some general comments:

- The analysis of the basin of attraction evolution, and the quantitative description of the relevant erosion through the evaluation of different integrity measures, prove to be fundamental tools to obtain a comprehensive characterization of the system dynamics. In particular, the definition of residual integrity levels associated with the system global dynamics has highlighted a marked variability of the classical stability boundary obtained via numerical integration with prescribed initial conditions and, mostly, a meaningful lack of homogeneous safeness of the latter as regards robustness of the system periodic solutions. In contrast, resorting to the tools of dynamical integrity permits to detect thresholds of residual integrity able to ensure acceptable safety targets established a priori according to the required system performances.
- The addition of a simple external feedback control into the model, aimed at keeping the single *local* response of the AFM cantilever to a suitable reference one and representing a simple and efficient procedure for reliably measuring the sample surface, causes a significant modification of both the local and global dynamics. Due to the increased number of degrees of freedom, in fact, the controlled model shows a richer bifurcation scenario than in the original (uncontrolled) system, with elimination of the region of coexistence of resonant and nonresonant solutions and extremely dangerous reduction of the domain of stability of system bounded responses just in the resonance regions where the system behavior has to be taken more strictly under control in practical applications. In these regions, moreover, the analysis of the basins dynamical integrity highlights a generalized detrimental effect of the control on the robustness of the basins of attraction, with small perturbations of parameters which can cause dramatic changes in the system safety.
- In a practical perspective, the suppression of the region of coexistence of resonant/nonresonant responses (known as bistability, and investigated mainly in the tapping AFMs literature) can be also considered as a positive effect of control, as it avoids possible discontinuous transitions from low-amplitude to high-amplitude responses which could lead to distortions in the sample scan. However, such a potentially positive effect of control is vanished in parameter space by the arise of an instability region just near the resonance frequency and in phase space, even more dangerous from an operational point of view, by the penetration of tongues of unbounded response inside the potential well which cause a strong reduction in the system safety for very low values of the excitation amplitude. In this sense, charts with constant integrity obtained for several varying parameters represent useful tools not only to assess the effect of a parameter (or a combination of them)

المنارة للاستشارات

on the system robustness, but also to select an appropriate operating setting able to ensure the functionality of the control and thus the success of the AFM scan process.

- It is worth underlining that, while dynamical integrity is reasonably easy to investigate in single-degree-of-freedom systems, basins of attraction of dimension larger than two are computationally onerous to implement, and interpreting the results becomes anyway a considerably difficult task. That's the case of the system with feedback control, for which, to achieve readable results, the investigation is carried out by analyzing suitable bidimensional sections of the five-dimensional basins of attraction. Of course, this implies making assumptions about some of the system initial conditions, thus restricting the analysis to selected (although reasonable) cases. An alternative approach is to resort to parallel computing, which anyway requires the implementation of ad hoc routines and the possibility to use powerful digital devices (Kreuzer and Lagemann 1996; Xiong et al. 2015; Belardinelli and Lenci 2016).
- The second control method applied to the AFM model, which is specifically based on exploiting the *global* properties of the dynamical system, demonstrates to be able to preserve the system dynamical integrity by reducing the safe basin erosion. The results of Sect. 4 show that the addition of one controlling superharmonic entails a shift of the selected global bifurcation and simultaneously a delay of the fall down of the erosion profiles, thus increasing the system overall safety. Of course, the main challenge in the application of such technique concerns the identification of the global event actual triggering the loss of safety for the system, which calls for the detection of the main saddles with the relevant manifolds. This step of the control procedure is certainly the most computationally onerous, especially in systems (like the one discussed here) with a quite involved topological scenario characterized by tightly rolling manifolds. This is mainly due to the low considered value of the damping parameter ($\rho_1 = 10^{-3}$) typical of the vacuum operating conditions which the analyses refer to. Nevertheless, the control technique has proved to be effective also in such tricky cases, confirming the robustness and the wide applicability of the method.
- As a further aspect of the *global* control application, the behavior of the various manifolds in the state plane reveals to be crucial for the proper selection of controlling superharmonic to be added into the model, i.e., for the choice between "one-side" and "two-side" control. In fact, the system behavior after the resonance highlights the inadequacy of looking only at the Hamiltonian system as selector benchmark, suggesting to carefully investigate the in-well basins organization as the system parameters change.
- From a methodological viewpoint, analysis of dynamical integrity can be used as a general framework for evaluating the effects of control techniques to be possibly employed for securing AFM response robustness and safety against jump to contact in different dynamic conditions. In this sense, some general observations can be pointed out:

المنارة للاستشارات

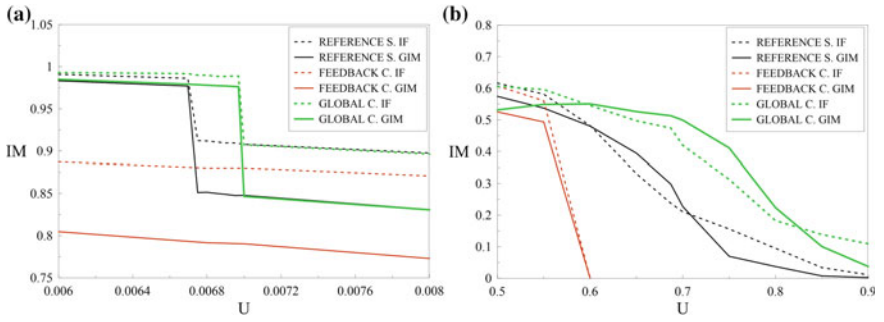

Fig. 43 Erosion profiles for the uncontrolled system (black line), for the system with feedback control (orange line) and for the system with optimal superharmonic (thick green line), before the resonance ($\omega_u = 0.7$) (**a**) and after the resonance ($\omega_u = 0.9$) (**b**)

- Unlike the feedback control, which can be considered as a *local* control technique, the *global* one has the explicit objective to increase the overall robustness of the system, an issue which is successfully accomplished with also beneficial effects on the main solutions displayed by the system, whose basins of attraction are either made less fractal (before the resonance) or actually enlarged (after the resonance).
- However, although the feedback control has some detrimental effect on the behavior of the system with respect to the response robustness, it is able, when properly working, to exactly reproduce the reference response. Conversely, in the *global* control, the addition of the superharmonic slightly modifies the amplitude and the shape of the system responses.
- Finally, some comments can be drawn comparing the IF (dashed) and GIM (continuous) profiles of the safe basins relevant to the reference, locally controlled, and globally controlled systems, respectively, reported in Fig. 43. At the left of the resonance frequency, the erosion develops from the outer edge of the basins, reducing their volume while preserving their compact core. As a consequence, IF is always greater than GIM for all three systems (Fig. 43a). At the right of the resonance, the erosion has the aforementioned development for low values of the forcing amplitude (IF $>$ GIM), whereas in the dangerous initial part of the sharper profiles of both the reference and the globally controlled systems, the safe basin develops by stretching its overall shape, as previously shown in Figs. 38b and 41b, thus maintaining the volume almost unchanged while reducing its core (IF $<$ GIM) (Fig. 43b). It is thus apparent that the choice of the integrity measure to be used for the analyses is of great importance, and it must be made on the basis of the system properties, of the features of the erosion involving the basins and of the level of safety to be guaranteed.

Acknowledgements Financial support from PRIN 2015 (no. 2105JW9NJT) is gratefully acknowledged.

المنارة للاستشارات

References

Alsaleem, F. M., Younis, M. I., & Ruzziconi, L. (2010). An experimental and theoretical investigation of dynamic pull-in in MEMS resonators actuated electrostatically. *Journal of Microelectromechanical Systems*, *19*(4), 794–806.

Arjmand, M. T., Sadeghian, H., Salarieh, H., & Alasty, A. (2008). Chaos control in AFM systems using nonlinear delayed feedback via sliding mode control. *Nonlinear Analysis: Hybrid Systems*, *2*, 993–1001.

Bahrami, A., & Nayfeh, A. H. (2012). On the dynamics of tapping mode atomic force microscope probes. *Nonlinear Dynamics*, *70*, 1605–1617.

Belardinelli, P., & Lenci, S. (2016). A first parallel programming approach in basins of attraction computation. *International Journal of Non-Linear Mechanics*, *80*, 76–81.

Crespo da Silva, M. R. M., & Glynn, C. C. (1978). Nonlinear flexural-flexural-torsional dynamics of inextensional beams. I. Equations of motion. *Journal of Structural Mechanics*, *6*(4), 437–448.

Doedel, E. J., & Oldeman, B. E. (2012). *AUTO-07p: Continuation and bifurcation software for ordinary differential equations*. Montreal: Concordia University.

Eaton, P., & West, P. (2010). *Atomic force microscopy*. Oxford: Oxford University Press.

Hornstein, S., & Gottlieb, O. (2008). Nonlinear dynamics, stability and control of the scan process in noncontacting atomic force microscopy. *Nonlinear Dynamics*, *54*, 93–122.

Hornstein, S., & Gottlieb, O. (2012). Nonlinear multimode dynamics and internal resonances of the scan process in noncontacting atomic force microscopy. *Journal of Applied Physics*, *112*, 074314.

Israelachvili, J. (1992). *Intermolecular and surface forces*. London: Academic Press.

Kreuzer, E., & Lagemann, B. (1996). Cell mappings for multi-degree-of-freedom-systems—Parallel computing in nonlinear dynamics. *Chaos, Solitons & Fractals*, *7*(10), 1683–1691.

Lenci, S., & Rega, G. (2003a). Optimal control of homoclinic bifurcation: Theoretical treatment and practical reduction of safe basin erosion in the Helmholtz oscillator. *Journal of Vibration and Control*, *9*, 281–315.

Lenci, S., & Rega, G. (2003b). Optimal control of nonregular dynamics in a Duffing oscillator. *Nonlinear Dynamics*, *33*, 71–86.

Lenci, S., & Rega, G. (2003c). Optimal numerical control of single-well to cross-well chaos transition in mechanical systems. *Chaos, Solitons & Fractals*, *15*, 173–186.

Lenci, S., & Rega, G. (2004). A unified control framework of the nonregular dynamics of mechanical oscillators. *Journal of Sound and Vibration*, *278*, 1051–1080.

Lenci, S., & Rega, G. (2005). Heteroclinic bifurcations and optimal control in the nonlinear rocking dynamics of generic and slender rigid blocks. *International Journal of Bifurcation and Chaos*, *15*(6), 1901–1918.

Lenci, S., & Rega, G. (2006). Control of pull-in dynamics in a nonlinear thermoelastic electrically actuated microbeam. *Journal of Micromechanics and Microengineering*, *16*, 390–401.

Morita, S., Giessibl, F. J., & Wiesendanger, R. (2009). *Noncontact atomic force microscopy*. Berlin: Springer.

Payton, O., Champneys, A. R., Homer, M. E., Picco, L., & Miles, M. J. (2011). Feedback-induced instability in tapping mode atomic force microscopy: Theory and experiment. *Proceedings of the Royal Society A*, *467*(2130), 1801–1822.

Rega, G., & Lenci, S. (2008). Dynamical integrity and control of nonlinear mechanical oscillators. *Journal of Vibration and Control*, *14*(1–2), 159–179.

Rega, G., & Lenci, S. (2015). A global dynamics perspective for system safety from macro- to nano-mechanics: Analysis, control, and design engineering. *Applied Mechanics Reviews*, *67*(5), 050802.

Rega, G., Lenci, S. & Ruzziconi, L. (2018). Dynamical integrity: A novel paradigm for evaluating load carrying capacity. In S. Lenci & G. Rega (Eds.), *Global nonlinear dynamics for engineering design and system safety* (Vol. 588, pp. 27–112). CISM Courses and Lectures. Cham: Springer.

المنارة للاستشارات

Rega, G., & Settimi, V. (2013). Bifurcation, response scenarios and dynamic integrity in a single-mode model of noncontact atomic force microscopy. *Nonlinear Dynamics*, *73*, 101–123.

Sarid, D. (1991). *Scanning force microscopy: With applications to electric, magnetic, and atomic forces*. New York: Oxford University Press.

Sarid, D., Ruskell, T. G., Workman, R. K., & Chen, D. (1996). Driven nonlinear atomic force microscopy cantilevers: From noncontact to tapping modes of operation. *Journal of Vacuum Science & Technology B*, *14*(2), 864–867.

Settimi, V., Gottlieb, O., & Rega, G. (2015). Asymptotic analysis of a noncontact AFM microcantilever sensor with external feedback control. *Nonlinear Dynamics*, *79*(4), 2675–2698.

Settimi, V., & Rega, G. (2016a). Exploiting global dynamics of a noncontact atomic force microcantilever to enhance its dynamical robustness via numerical control. *International Journal of Bifurcation and Chaos*, *26*(7), 1630018.

Settimi, V., & Rega, G. (2016b). Global dynamics and integrity in noncontacting atomic force microscopy with feedback control. *Nonlinear Dynamics*, *86*(4), 2261–2277.

Settimi, V., & Rega, G. (2016c). Influence of a locally-tailored external feedback control on the overall dynamics of a noncontact AFM model. *International Journal of Non-Linear Mechanics*, *80*, 144–159.

Settimi, V., & Rega, G. (2017). Response robustness and safety against jump to contact in AFMs controlled via different techniques. *Procedia IUTAM, 22*, 184–191.

Settimi, V., Rega, G., & Lenci, S. (2016). Analytical control of homoclinic bifurcation of the hilltop saddle in a noncontact atomic force microcantilever. *Procedia IUTAM*, *19*, 19–26.

Szemplinska-Stupnicka, W. (1992). Cross-well chaos and escape phenomena in driven oscillators. *Nonlinear Dynamics*, *3*, 225–243.

Thompson, J. M. T., & Stewart, H. B. (2002). *Nonlinear dynamics and chaos*. New York: Wiley.

Xiong, F.-R., Qin, Z.-C., Ding, C., Hernández, Q., Fernandez, J., Schütze, O., et al. (2015). Parallel cell mapping method for global analysis of high-dimensional nonlinear dynamical systems. *Journal of Applied Mechanics*, *82*(11), 111010.

Yamasue, K., & Hikihara, T. (2006). Control of microcantilevers in dynamic force microscopy using time delayed feedback. *Review of Scientific Instruments*, *77*, 053703.

المنارة للاستشارات

Global Analysis of Nonlinear Dynamical Systems

Fu-Rui Xiong, Qun Han, Ling Hong and Jian-Qiao Sun

Abstract This chapter discusses recent applications and algorithm developments of the cell mapping methods, which were created by C. S. Hsu in 1980s for global analysis of nonlinear dynamical systems. Such systems can have multiple steady-state responses including equilibrium states, periodic motions, chaotic attractors as well as domains of attraction of these steady-state responses. Without the cell mapping methods, these dynamical responses would have been far more difficult to obtain. Since the creation of them, the cell mapping methods have enjoyed attention from the research communities. New extensions of the methods and new algorithms including parallel computing have been developed in the past few decades. The cell mapping methods have also been applied to global analysis and control design of deterministic, stochastic and fuzzy dynamical systems. Representative examples of new applications are presented in this chapter.

Keywords Cell mapping methods · Global analysis · Applications to deterministic nonlinear systems · Stochastic systems · Fuzzy dynamic systems

F.-R. Xiong
Nuclear Power Institute of China, Chengdu 610041, China
e-mail: xfr90311@gmail.com

Q. Han
Northwestern Polytechnical University, Xi'an 710072, China
e-mail: hanqun@mail.hzau.edu.cn

L. Hong
State Key Laboratory for Strength & Vibration,
Xi'an Jiaotong University, Xi'an 710049, China
e-mail: hongling@mail.xjtu.edu.cn

J.-Q. Sun (✉)
School of Engineering, University of California, Merced, CA 95343, USA
e-mail: jsun3@ucmerced.edu

© CISM International Centre for Mechanical Sciences 2019

S. Lenci and G. Rega (eds.), *Global Nonlinear Dynamics for Engineering Design and System Safety*, CISM International Centre for Mechanical Sciences 588,
https://doi.org/10.1007/978-3-319-99710-0_6

المنارة للاستشارات

1 Introduction

The cell mapping methods were created by Hsu in 1980s for global analysis of nonlinear dynamical systems that can have multiple steady-state responses including equilibrium states, periodic motions, chaotic attractors as well as domains of attraction of these steady-state responses. The cell mapping methods have been applied to global analysis and control design of deterministic, stochastic and fuzzy dynamical systems. There have been several survey articles that present thorough discussions of the literature on the cell mapping methods and their applications (Sun and Luo 2012b; Hong and Sun 2006b; Xu et al. 2013). A comprehensive review of the global analysis with the cell mapping method in Sun and Luo (2012a) provides rich content on engineering applications and algorithm development. A thorough review of the progress in global analysis of nonlinear dynamics and its influence on the analysis, control, and design of mechanical and structural systems is presented in Rega and Lenci (2015). This chapter presents a discussion of the literature of applications and algorithm developments of the cell mapping methods.

Two important extensions of the cell mapping methods have been developed to improve the accuracy of the solutions obtained in the cell state space. The first is the interpolated cell mapping which uses the cell mappings as a foundation to calculate point-wise solutions without further numerical integrations of differential equations. The second is the sub-division technique of the set-oriented method for improving the accuracy of the invariant solutions obtained with the cell mapping methods. For a long time, the cell mapping methods have been applied to dynamical systems with low dimension until now. With the advent of inexpensive computer memories and massively parallel computing technologies such as the graphical processing units (GPUs), global analysis of moderate- to high-dimensional nonlinear dynamical systems becomes feasible.

The cell mapping methods propose to discretize the continuum state space and the time. The discrete space consists of a finite collection of cells. The dynamical systems that originally obey ordinary or partial differential equations are now represented by the mappings in the cell state space, called the cell-to-cell mapping, or cell mapping for short. The cell mappings describe the system evolution over a short time in a finite region of interest in the cell state space. More importantly, long-term system responses such as periodic motion, equilibrium points, limit cycle, chaotic motion, domains of attraction, and stable and unstable manifolds of saddle points can all be obtained from the cell mappings.

This chapter reviews the cell mapping methods applied to deterministic, stochastic and fuzzy dynamical systems and presents several examples of recent applications.

المنارة للاستشارات

2 Cell Mapping Methods

There are two versions of the cell mapping methods: the simple cell mapping (SCM) and the generalized cell mapping (GCM). This section presents a brief introduction of both the SCM and GCM methods.

2.1 Simple Cell Mapping

We assume that the nonlinear dynamical system is described by a point mapping given by

$$\mathbf{x}_{k+1} = \mathbf{G}(\mathbf{x}_k),\ 0 \le k < \infty,\ \mathbf{x}_k \in \mathbf{R}^n, \tag{1}$$

where k is the iteration step, $\mathbf{x}_k$ is the n-dimensional state vector at the kth step. Consider a finite region $\mathbf{U} \subset \mathbf{R}^n$ where a sufficiently rich dynamics of the system resides. We discretize $\mathbf{U}$ into a collection of small, finite size boxes, known as the cells. Since the region $\mathbf{U}$ is finite, there will be a finite number of cells in the discretized region. Hence, each cell in the collection can be numbered by one integer, denoted as z.

The SCM accepts only one image cell for a given pre-image cell, or domain cell. In other words, in SCM, the dynamics of the system starting from one cell with a small but finite volume is represented by that starting from a point in the cell, usually the center of the cell, leading to an integer-valued mapping

$$z_{k+1} = C(z_k),\ 0 \le k < \infty, \tag{2}$$

where $C(\cdot)$ is a symbolical notation of the integer mapping, and z_k is an integer representing the cell where the system resides at the kth step. Usually, $C(\cdot)$ has to be constructed numerically. The region out of the domain $\mathbf{U}$ is called the *sink cell*. If the image of a cell is out of the domain of interest, we say that it is mapped to the sink cell. The sink cell always maps to itself.

Properties of SCM

Because there are only a finite number of cells in $\mathbf{U}$, the integer mapping in Eq. (2) eventually will revisit the cells in the path. The revisited cells hence form closed groups called periodic groups. The minimum period of these groups is one, while the maximum possible period is equal to the total number of cells in $\mathbf{U}$. For the group with period one, we have

$$z = C(z), \tag{3}$$

for the cell z in the group.

The simple cell mappings $z_{k+1} = C(z_k)$ are stored in a single array of length N_t where N_t is the total number of cells in $\mathbf{U}$. For example, let $C(i)$ denote the image array. If $C(i) = j$, then cell $z = j$ is the image of cell $z = i$. This array can be

المنارة للاستشارات

viewed as the storage of a sparse matrix representing the simple cell mappings over $\mathcal{N}$ where $\mathcal{N}$ denotes the set of integers indexing the cells in $\mathbf{U}$ including the sink cell. The sparse matrix reads

$$p_{ji} = \begin{cases} 1 & \text{if } C(i) = j \\ 0 & \text{if } C(i) \neq j \end{cases} \quad i, j \in \mathcal{N} \tag{4}$$

The array $C(i)$ contains the forward dynamics of the system in time. The stable steady-state responses of the system including equilibrium points, periodic orbits and chaotic motion form periodic groups in $C(i)$.

We can also store the pre-image information of an image cell in an array, denoted as $C^{-1}(j)$. That is, $i = C^{-1}(j)$. In terms of the matrix p_{ji}, the sparse matrix of the backward dynamics is simply the transpose of the forward dynamics matrix.

$$p_{ij}^{-1} = p_{ji}, \quad i, j \in \mathcal{N} \tag{5}$$

The backward dynamics provides an important role in the global analysis of nonlinear dynamical systems. In the backward dynamics, the unstable responses appear to be stable. Consider a search starting from the stable steady-state responses, i.e. the identified periodic groups. If we search along the backward dynamics using $C^{-1}(j)$, we would identify the domains of attraction of the stable responses. The backward search, on the other hand, reveals the boundaries of the domains of attraction, which are usually outlined by the unstable manifolds in the saddles.

2.2 Generalized Cell Mapping

The GCM accepts multiple images for a pre-image cell. This is consistent with the fact that the cell with a finite volume will evolve to cover multiple cells under the system dynamics over a finite time. For deterministic and stochastic systems, the GCM leads to a Markov chain representation of the dynamical system with the transition of probabilities given by

$$\mathbf{p}(k+1) = \mathbf{P}(k)\mathbf{p}(k), \ 0 \leq k < \infty, \tag{6}$$

or in the component form

$$p_i(k+1) = \sum_{j=1}^{N_t} P_{ij}(k)\, p_j(k), \tag{7}$$

where $\mathbf{p}(k) = \{p_i(k)\}$ denotes the probability that the system resides in the ith cell at the kth step, and $\mathbf{P}(k) = \{P_{ij}(k)\}$ is the one step transition probability from the jth cell to ith cell at the kth step. N_t is the total number of cells in the computational

المنارة للاستشارات

domain. When the matrix $\mathbf{P}(k)$ is independent of k, the Markov chain is said to be stationary. Otherwise, it is non-stationary.

The rich literature on Markov chains and later the graph theory has provided us highly effective algorithms for analyzing the GCM (Hsu 1982, 1995). The analysis of the GCM leads to the discovery of invariant sets, stable and unstable manifolds of saddle-like equilibrium states, domains of attraction and their boundaries. The invariant sets represent stable equilibrium states, periodic or chaotic motions. The invariant sets are called the *persistent groups* in the Markov chain literature (Chung 1967).

The stable and unstable manifolds of saddle-like equilibrium states, domains of attraction and their boundaries are represented by the so-called transient cells.

The stationary transition probability matrix $\mathbf{P}$ can be partitioned into the following canonical form, also known as the normal form.

$$\mathbf{P} = \begin{bmatrix} \mathbf{P}_1 & & & \mathbf{T}_{11} & \cdots & \mathbf{T}_{1l} \\ & \ddots & & \vdots & \ddots & \vdots \\ & & \mathbf{P}_m & \mathbf{T}_{m1} & \cdots & \mathbf{T}_{ml} \\ & & & \mathbf{Q}_1 & \cdots & \mathbf{R}_{1l} \\ & & & & \ddots & \vdots \\ & & & & & \mathbf{Q}_l \end{bmatrix}, \tag{8}$$

where $\mathbf{P}_i$ is a square matrix representing the transition probability matrix among the cells in the ith persistent group, $\mathbf{Q}_i$ is associated with the ith open communicating group. The cells in the group $\mathbf{Q}_i$ are transient. $\mathbf{T}_{ij}$ and $\mathbf{R}_{ij}$ represent the evolution paths from transient cells to stable and unstable attractors, respectively. $\mathbf{Q}_i$ often contains the saddle like attractors, unstable equilibrium points and unstable periodic orbits.

The ability of the GCM method to conduct global analysis of nonlinear dynamics is fully illustrated by the topological structure of the transition probability matrix $\mathbf{P}$ in the normal form. We can use the GCM method to discover invariant sets, stable and unstable manifolds of saddles, unstable solutions and domains of attraction of invariant sets of nonlinear dynamical systems. The unstable solutions as well as stable manifolds of saddles can be found by the backward cell mapping (Dellnitz and Hohmann 1997; Dellnitz and Junge 2002; Sun and Luo 2012a).

Consider the transition probability sub-matrix $\mathbf{P}_k$ associated with the kth persistent group. If this group of cells represents the period-K motion of the system, it can be partitioned into the following form.

$$\mathbf{P}_k = \begin{bmatrix} & & \mathbf{P}_{k,K} \\ \mathbf{P}_{k,1} & & \\ & \ddots & \\ & \mathbf{P}_{k,K-1} & \end{bmatrix}, \tag{9}$$

المنارة للاستشارات

where $\mathbf{P}_{k,j}$ $(1 \leq j \leq K)$ is a sub-matrix of a certain dimension. When $\mathbf{P}_k$ has at least one non-zero diagonal element, the period of the persistent group is one. It is called an aperiodic group.

3 Set-Oriented Method

As an extension of cell mapping, Dellnitz and colleagues introduced the set-oriented method with the sub-division technique that is capable of obtaining the invariant sets of nonlinear dynamical systems with high accuracy (Dellnitz and Hohmann 1997). The set-oriented method starts with relatively large cells and removes the cells that don't contain part of the invariant set by sampling a number of initial conditions from each cell. The sub-division is then applied to the retained cells. This is how the set-oriented method gains computational efficiency. The set-oriented method is effectively a mixed application of SCM and GCM with the sub-division applied to the covering set of invariant solutions.

There have been many studies of the set-oriented method. An adaptive sub-division algorithm was developed (Dellnitz and Junge 1998) that allows the existence of multiple different cell sizes to cover the solution. A study of non-smooth mechanical system was carried out by Neumann et al. with the set-oriented method to find global attractors (Neumann et al. 2007). The algorithm for extracting unstable manifold and saddle solutions was introduced in Dellnitz and Junge (2002). The set-oriented method is also a robust tool for designing optimal controls (Junge and Osinga 2004; Grune and Junge 2005), especially for multi-objective optimal controls (Schütze et al. 2013; Blesken et al. 2009).

The set-oriented method with sub-division has not been applied to investigate the transient dynamics of the system such as the domains of attraction and basin boundary. On the other hand, the cell mapping methods were developed for comprehensive global analyses of nonlinear dynamical systems including the discovery of invariant sets and transient dynamics.

4 Interpolated Cell Mapping

The sub-division technique leads to smaller and smaller cells, and therefore, the accuracy of the solution for invariant sets improves. At some point, the sub-division has to stop. This is when another important extension of the cell mapping methods comes in: the interpolated cell mapping (ICM) method (Tongue 1987; Tongue and Gu 1988b, c). The ICM uses the simple cell mappings to interpolate the image of a point without integrating the differential equation using this point as an initial condition. The simple cell mappings in the refined cells provide a database for interpolation. The ICM method is able to construct very fine solutions of invariant sets, which

المنارة للاستشارات

assumes that the simple cell mappings are on a sufficiently small grid and that the underlying dynamics of the system is smooth enough for interpolation.

The local interpolation error of ICM is of order $O(h^2)$ with the linear interpolation, where h is the cell size, whereas the accuracy of SCM is of order $O(h)$ (Lee and Hsu 1994). More adjacent cells around the point of interest can be used to construct high order interpolations to further improve the accuracy (Tongue and Gu 1988a). A modified ICM by introducing the sampling idea of GCM was proposed to further increase the capability of ICM to capture the boundaries of domains of attraction (Ge and Lee 1997). Several typical nonlinear systems have been studied with the ICM method including the Lorenz system (White and Tongue 1995), a forced beam with cubic nonlinearity (Lee and Ghang 1994) and a spring-pendulum system (Lee and Hsu 1994). The nonlinear system identification approach using the method of interpolated cell mapping is proposed in Bursal and Tongue (1992).

Previous studies of the ICM have dealt with low dimensional state spaces. Extension of the interpolation scheme to much higher dimensional state space is non-trivial. A recent study by Xiong and colleagues (Xiong et al. 2015) has developed an interpolation scheme for high dimensional state space with the accuracy of order $O(h^2)$.

Let $\mathbf{x} \in \mathbf{R}^N$ as an arbitrary point in cell z which is part of an attractor obtained by the cell mapping method. Let $\mathbf{x}^{(k)}$ $(k = 2, 3, \ldots, 2N + 1)$ denote the centers of the neighboring cells of cell z in the orthogonal coordinate directions, and $\mathbf{x}^{(1)}$ denotes the center of cell z. It can be shown that $\mathbf{x}$ is always contained within the polyhedron with vertices at $\mathbf{x}^{(k)}$ $(k = 2, 3, \ldots, 2N + 1)$. Let $\mathbf{u} \in \mathbf{R}^N$ be the image point of $\mathbf{x}$ to be computed by interpolation using $(2N + 1)$ points $\mathbf{x}^{(k)}$ $(k = 1, 2, \ldots, 2N + 1)$. We propose an interpolation scheme as,

$$u_j = \sum_{i=1}^{N} a_{ji} x_i + \sum_{i=1}^{N} b_{ji} x_i^2 + c_j, \quad j = 1, 2, \ldots, N \tag{10}$$

where u_j is the jth component of $\mathbf{u}$ and x_i the ith component of $\mathbf{x}$. For a given j, Eq. (10) has $(2N + 1)$ coefficients to determine, which matches the number of points for interpolation. Recall that the SCM uses the mapping of the center of a cell to represent its dynamics. The point mappings of $\mathbf{x}^{(k)}$ $(k = 1, 2, \ldots, 2N + 1)$ are saved in the last iteration of sub-division, and are denoted as $\mathbf{u}^{(k)} = \mathbf{F}(\mathbf{x}^{(k)})$, where $\mathbf{F}$ is the underlying function of the mapping. The local error of the interpolation scheme in Eq. (10) is of order $O(\|\mathbf{h}\|_2^2)$.

If we put the set-oriented method with sub-division and the ICM method in the framework of the cell mapping methods, it becomes apparent that the ICM method represents a post-processing step to extract point mappings from the cell mappings on a refined partition of the cell state space.

A Note

Both the set-oriented method and ICM method represent efforts to increase the computational efficiency for finding invariant sets of nonlinear dynamical systems with much improved accuracy. The accuracy of the solutions obtained by the cell mapping method was compared with the accuracy of the point-wise solutions obtained

المنارة للاستشارات

by numerical integration. Such a comparison and pursuit of point-wise accuracy are beyond the original purpose of the cell mapping methods.

As discussed by Professor Hsu on several occasions, the goal of the cell mapping methods is to quickly discover the general global structure of the responses of nonlinear dynamical systems with sufficient accuracy. In other words, the cell mapping methods can answer these questions with high efficiency: How many stable and unstable responses of a nonlinear dynamical system exist in a certain region of the state space? Where are they and how are they connected?

The cell mapping methods cannot deliver the fine structure of fractal dimensional objects such as basin boundaries and strange attractors, because highly accurate numerical integrations must be done to find the fine structure of fractal dimensional geometry. Nevertheless, the GCM can tell where in the state space fractal dimensional objects may exist and can outline their shape.

5 Fuzzy Generalized Cell Mapping

Engineering systems are often subjected to uncertainties that are associated with the lack of precise knowledge of system parameters and operating conditions and that are originated from variability in manufacturing processes. The uncertainties can have significant influence on the dynamic response and the reliability of the system, and are often modeled as random variables or fuzzy sets. Consider a dynamical system with fuzzy uncertainty.

$$\dot{\mathbf{x}} = \mathbf{f}(\mathbf{x}, t, S), \quad \mathbf{x} \in \mathbf{D}, \tag{11}$$

where $\mathbf{x}$ is the state vector, t the time variable, S a fuzzy set with a membership function $\mu_S(s) \in (0, 1]$ where $s \in S$, and $\mathbf{f}$ is a vector-valued nonlinear function of its arguments. When the system parameter S is a fuzzy number. Equation (11) is a fuzzy differential equation.

Considering all possible pre-images of cell i, we have the membership grade of the system being in cell i at the $(n+1)$th step as

$$p_i\,(n+1) = \max_j \min\left[p_{ij},\, p_j\,(n)\right]. \tag{12}$$

Let $\mathbf{p}\,(n)$ be a vector with components $p_i\,(n)$, and $\mathbf{P}$ a matrix with components p_{ij}. Equation (12) can be written in a compact matrix notation

$$\mathbf{p}\,(n+1) = \mathbf{P} \circ \mathbf{p}\,(n)\,, \quad \mathbf{p}\,(n) = \mathbf{P}^n \circ \mathbf{p}\,(0)\,, \tag{13}$$

where $\mathbf{P}^{n+1} = \mathbf{P} \circ \mathbf{P}^n$ and $\mathbf{P}^0 = \mathbf{I}$. $\circ$ denotes the min-max operation. The matrix $\mathbf{P}$ denotes the one-step transition membership matrix. $\mathbf{P}^n$ denotes the n-step transition possibility matrix. The vector $\mathbf{p}\,(n)$ is called the n-step membership distribution

المنارة للاستشارات

vector, and $\mathbf{p}(0)$ the initial membership distribution vector. The (i, j)th element p_{ij} of the matrix $\mathbf{P}$ is called the one-step transition membership from cell j to cell i.

Equation (13) is called a fuzzy generalized cell mapping (FGCM) system, which describes the evolution of the fuzzy solution process $\mathbf{x}(t)$ and its MDFs $p(\mathbf{x}, t)$, and is a finite approximation to the fuzzy dynamical system (11) in $\mathbf{D}$.

Equation (12) of the FGCM can be viewed as a discrete representation of the master equation. The FGCM offers a very effective method for solutions to this equation, particularly, for fuzzy nonlinear dynamical systems.

The whole algorithm of the FGCM method is divided into four major parts (Hong and Sun 2006a; Hong and Xu 1999; Hsu 1995) as follows:

Part 1. Construction of a FGCM system and formation of the one-step transition possibility matrix P.
Part 2. Determination of stable and unstable invariant sets including attractors and unstable solutions.
Part 3. Determination of domains of attraction and boundary regions.
Part 4. Evaluation of quantitative evolution of the MDFs.

Parts 1–3 deal with the analysis of qualitative properties while Part 4 evaluates the quantitative properties such as the MDFs. The qualitative and quantitative properties lead to a dichotomy in the computation treatment of the FGCM, and ensure the accuracy and efficiency of the FGCM. Boolean operations are only used in the qualitative analysis of the FGCM, while the min-max operations are only involved in the quantitative analysis of FGCM. As a result, the transient and steady-state MDFs of a fuzzy response process can be effectively determined in a new way.

Parallel Computing

For a long time, the cell mapping methods have been applied to dynamical systems with low dimension until now. With the advent of cheap dynamic memory and massively parallel computing technologies, such as the graphical processing units (GPUs), global analysis of moderate-to high-dimensional nonlinear dynamical systems becomes feasible. Recent application of parallel computing with cell mapping technique has been reported in Eason and Dick (2014) where multi-core CPU architecture is used to speed up global analysis of nonlinear systems. In another study (Xiong et al. 2015), the simple cell mapping (SCM) and generalized cell mapping (GCM) are implemented in a hybrid manner combined with the subdivision technique to enhance the accuracy of the steady-state responses. The ICM is used as a post-processing step to generate the point-wise approximation of the solutions without additional numerical integrations of differential equations. The cell mapping methods is applied to a nonlinear dynamical system with six-dimensional state space in this work.

المنارة للاستشارات

6 Examples of Deterministic Systems

6.1 Impact Model

We first consider a two dimensional dynamical system defined by the following implicit algebraic equations,

$$x_1^{(k+1)} = x_1^{(k)} + \frac{\Phi}{x_2^{(k)}}, \tag{14}$$

$$x_2^{(k+1)} = \alpha_1\alpha_2 x_2^{(k)} - (1+\alpha_1)\left(\Omega u_0 \sin \Omega x_1^{(k+1)} - \Omega_1 u_1 \cos \Omega_1 x_1^{(k+1)}\right), \tag{15}$$

where

$$\Phi = h\left(1+\frac{1}{\alpha_2}\right) - u_0\left(\cos \Omega x_1^{(k)} - \frac{\cos \Omega x_1^{(k+1)}}{\alpha_2}\right) - u_1\left(\sin \Omega_1 x_1^{(k)} - \frac{\sin \Omega_1 x_1^{(k+1)}}{\alpha_2}\right), \tag{16}$$

and

$$\alpha_1 = 0.8, \alpha_2 = 0.95, u_0 = 0.0125, \Omega = \pi/2, \quad h = 0.15, \Omega_1 = \pi/2, u_1 = -0.05. \tag{17}$$

Equation (14) describes the impact process between a free mass and an oscillator of a vibro-impact drilling device (Neumann et al. 2007). If there are multiple impacts, Eq. (14) is replaced by the following equation,

$$x_1^{(k+1)} = x_1^{(k)} + \frac{u_0}{x_2^{(k)}}\left(\cos \Omega x_1^{(k+1)} - \cos \Omega x_1^{(k)}\right) + \frac{u_1}{x_2^{(k)}}\left(\sin \Omega_1 x_1^{(k+1)} - \sin \Omega_1 x_1^{(k)}\right). \tag{18}$$

For each simulation from step k to $k+1$, Eq. (18) is first examined. If there exists a root $x_1^{(k+1)}$ such that $x_1^{(k+1)} > x_1^{(k)}$, Eq. (15) is applied to solve for $x_2^{(k+1)}$. Otherwise, Eqs. (14) and (15) are numerically solved for $x_1^{(k+1)}$ and $x_2^{(k+1)}$.

Figure 1 shows the sub-division process with four different cell space resolutions. The initial partition is 7×7. The region of interest is defined as $[0, 2\pi/\min\{\Omega, \Omega_1\}] \times [-0.1, 0.6]$. The final cell space resolution reaches 189×189 with 3935 cells representing the global invariant set. The sequential computing takes 64.9844 s, while the parallel computing only takes 4.5573 s. Note that this example requires

المنارة للاستشارات

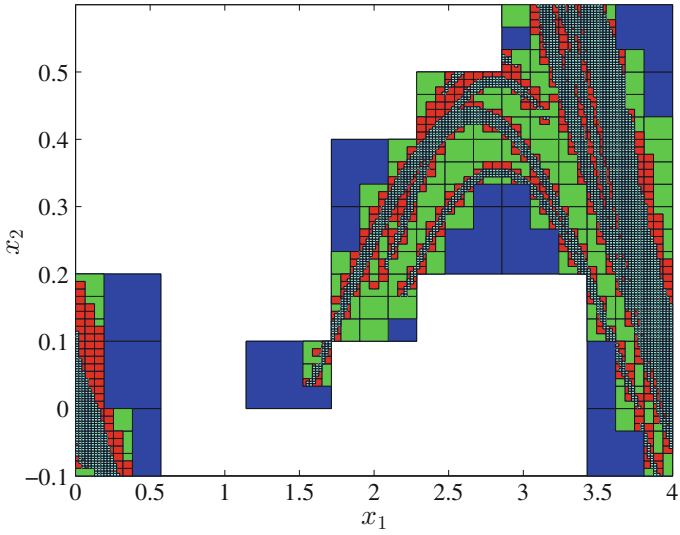

Fig. 1 Global invariant set found of the impact model. The subdivision processes in four different cellular space resolutions are presented to show the improvement of solution accuracy. Initial cell space partition is 7×7. Final cell space resolution reaches 189×189 with 3935 cells found as solutions. Computational time is 64.9844 s for sequential computing and 4.5573 s for parallel computing

careful numerical treatment of a nonlinear zero finding problem. Hence, it is a harder problem compared with those with explicit dynamics.

Figure 2 shows the global properties of the impact model in a 189×189 cell space. In the figure, blue cells represent the chaotic attractor consisting of several disjoint branches. Black cells represent the unstable manifolds connecting the disjoint branches of the attractor. Recall that the unstable manifolds can be only found through the backward mapping (Dellnitz and Hohmann 1997). Therefore, the invariant set found with the backward selection shown in Fig. 1 coincides with the attractor and unstable manifold in Fig. 2. For the global analysis, the sequential computing takes 263.1347 s, while the parallel computing takes 29.9928 s.

To further illustrate the speed up of parallel algorithm for invariant set and global analysis, we perform the computing of this low dimensional example with different configurations. Tables 1 and 2 give the execution time of the same algorithm on CPU (sequential) and GPU (parallel) for invariant set and global analysis respectively. The maximum acceleration for this example can reach more than 40 times, which corresponds to the cell number at a magnitude of 10^4.

المنارة للاستشارات

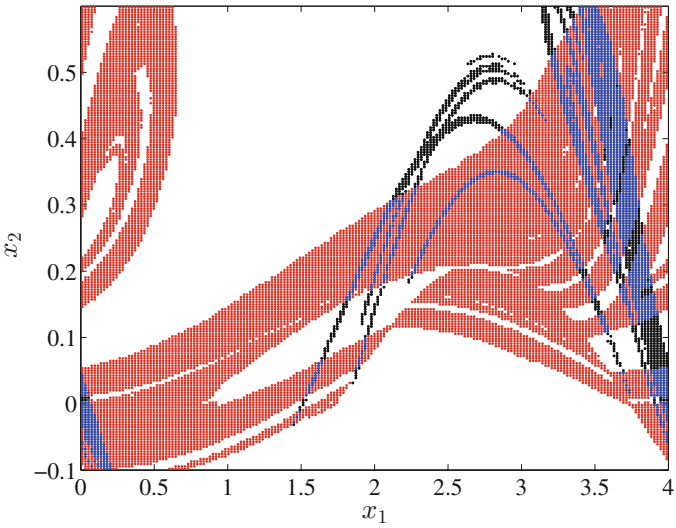

Fig. 2 Global properties of the impact model solved by the modified GCM analysis flow. Cell space partition is 189 × 189. Blue cells are the chaotic attractor, black are the unstable manifold and red are the domain of attraction. Note the attractor and unstable manifold coincides with the invariant set shown in Fig. 1. Sequential computing takes 263.1347 s while parallel computing takes 29.9928 s

Table 1 Comparison between sequential and parallel SCM-GCM hybrid for invariant set finding, eight subdivisions are conducted for all computing

	$N_{init} = [5, 5]$	$N_{init} = [10, 10]$	$N_{init} = [20, 20]$
Sequential SCM-GCM	67.0220 s	170.5987 s	424.3463 s
Parallel SCM-GCM	21.2403 s	22.1674 s	24.8091 s
Speed up	3.1554x	7.6959x	17.1045x
	$N_{init} = [50, 50]$	$N_{init} = [100, 100]$	
Sequential SCM-GCM	1259.8449 s	3362.4154 s	
Parallel SCM-GCM	37.9964 s	82.3980 s	
Speed up	33.1570x	40.8070x	

6.2 *Lorenz System*

The Lorenz system is derived from a partial differential equation governing the convection of fluid. In Musielak and Musielak (2009), the Lorenz systems from low to high dimensions are discussed comprehensively from the modelling perspective. In our work, we pick a $6D$ Lorenz model from Musielak and Musielak (2009) as an example to test the invariant set searching algorithm. Details of the physical interpretation and mathematical treatment can be found in Musielak and Musielak (2009). The $6D$ Lorenz system reads,

المنارة للاستشارات

Table 2 Comparison between sequential and parallel SCM-GCM hybrid for global analysis

	$N = [50, 50]$	$N = [100, 100]$	$N = [150, 150]$
Sequential SCM-GCM	134.6844 s	214.8391 s	1222.3 s
Parallel SCM-GCM	1.3504 s	4.2 s	21.3719 s
Speed up	99.73x	51.15x	57.20x
	$N = [200, 200]$	$N = [250, 250]$	
Sequential SCM-GCM	2200.1 s	3342.1 s	
Parallel SCM-GCM	61.6188 s	135.0587 s	
Speed up	35.70x	24.75x	

$$
\begin{aligned}
\dot{x}_1 &= -\sigma x_1 + \sigma x_2, \\
\dot{x}_2 &= -x_1 x_3 + r x_1 - x_2 + x_3 x_6 - 2 x_5 x_6, \\
\dot{x}_3 &= x_1 x_2 - b x_3 - x_1 x_4 - x_2 x_6, \\
\dot{x}_4 &= x_1 x_3 - 2 x_1 x_5 + r x_6 - c x_4, \\
\dot{x}_5 &= 2 x_1 x_4 + 2 x_2 x_6 - 4 b x_5, \\
\dot{x}_6 &= \sigma / c x_4 - c \sigma x_6,
\end{aligned}
\tag{19}
$$

where $b = \frac{4}{1+a^2}$, $c = \frac{9+a^2}{1+a^2}$, $a = 1/\sqrt{2}$, $r = 45$, and $\sigma = 10$.

The domain of interest is $[-35, 35] \times [-50, 50] \times [0, 100] \times [-20, 20] \times [0, 50] \times [-2, 2]$. The initial coarse cell space partition is taken as $2 \times 2 \times 2 \times 2 \times 4 \times 4$. The integration time to compute point mappings is 1.5 s, and the time increment for a fixed step Runge-Kutta scheme is 0.015 s. 500 randomly sampled points out of each cell are used for the GCM construction. 16 iterations of sub-division are taken to refine the cells. The final cell space resolution is $54 \times 54 \times 54 \times 54 \times 36 \times 36$ with 6325 cells found in the invariant set. The entire computation with SCM-GCM hybrid takes 256.094 s.

Figure 3 shows the growing trend of the number of cells with the iteration of sub-divisions. The "rolling cut" effectively suppressed the exponential increase of the number of cells. This is quite beneficial to high dimensional applications. When the number of cells starts to decrease after a certain number of iterations, it is an indication that the discretization error of the cell mapping with a relatively small number of sampled points begins to show the impact on the accuracy of the solution. The decreasing trend is caused by the removal of certain cells from further consideration in the backward selection, although some portions of the removed cell volume may be part of the invariant set. Such a cell is often located near the boundary of the attractors.

If we put the random sampling to construct cell mappings in the context of estimating the transition probabilities from one cell to its images, the convergence of the sampling is of order $O(m^{-\frac{1}{n}})$, where m is the sampling number and $n = 6$ is the dimension of the state space (Sun and Hsu 1988b, 1990). With $m = 500$, $O(m^{-\frac{1}{n}}) \sim 0.125$. Apparently, a substantially large number of points need to be sampled for the six dimensional problem. This represents a challenge in carrying out

المنارة للاستشارات

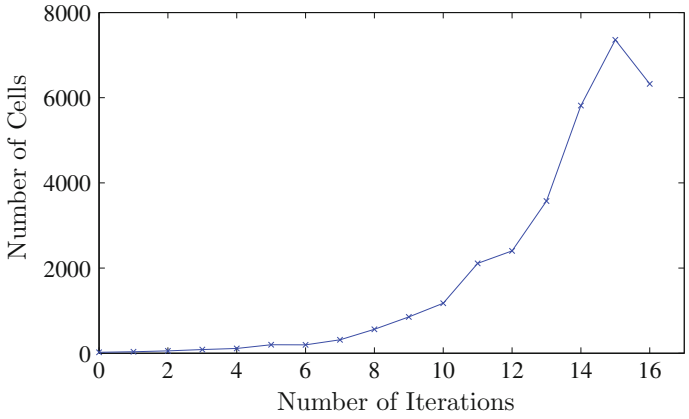

Fig. 3 Number of cells to be processed at each iteration of "rolling cut" sub-division of one dimension at a time. We chose to stop the sub-division when the number starts to decrease at the 16th iteration

global analyses for high dimensional nonlinear dynamical systems, and will be our future effort with supercomputing. Nevertheless, the reduction of the number of cells is an indication to stop the sub-division with the limited number of sampled points.

This is when the post-processing with interpolation comes in. Figure shows the $3D$ projection of the global attractor and solutions from the interpolation scheme. It is seen that the well-known butterfly shape of the strange attractor also lives in the high dimensional state space. Figure 4 gives more information about how the attractor looks like in different projections. The results show that the interpolation scheme can indeed recover the detail of the fine structure in the attractors.

To further examine the quantitative performance of the interpolation scheme for high dimensional problems, we introduce the Hausdorff distance between two sets as a metric. Let $u, v \in \mathbf{R}^n$ be two vectors and $A, B \subset \mathbf{R}^n$ two sets of vectors. The maximum norm distance d_∞, the semi-distance $dist(\cdot, \cdot)$ and the Hausdorff distance $d_H(\cdot, \cdot)$ are defined as follows (Schütze et al. 2010):

1. $d_\infty = \max_{i=1,\ldots,n} |u_i - v_i|$
2. $\text{dist}(u, A) = \inf_{v \in A} d_\infty(u, v)$
3. $\text{dist}(B, A) = \sup_{u \in B} d_\infty(u, A)$
4. $d_H(A, B) = \max\{\text{dist}(A, B), \text{dist}(B, A)\}$

The Hausdorff distance is commonly used in multi-objective optimization community to measure the solution quality of benchmark problems (Schütze et al. 2010). In this study, we numerically integrate the differential equations with the Runge-Kutta method to create point mappings starting from a number of points sampled in the cells obtained previously. The set of the sampled points is denoted as S. The point mappings of the set S is considered as the reference solution, denoted as $D(S)$.

المنارة للاستشارات

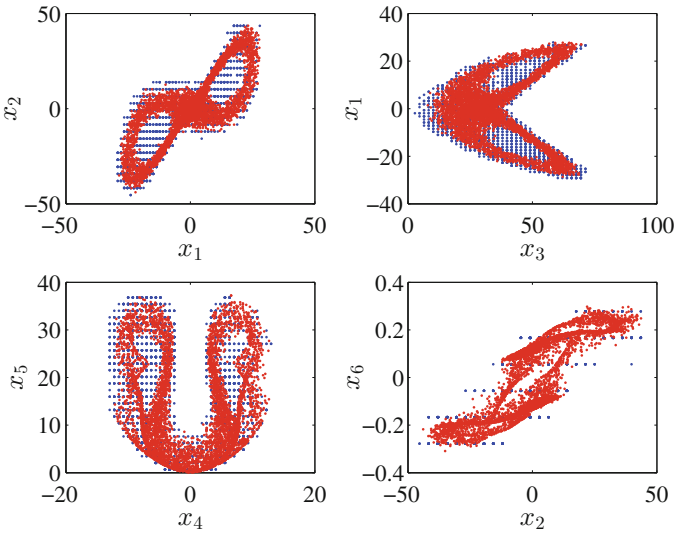

Fig. 4 $2D$ projections of the attractor of the $6D$ Lorenz system. Blue dots are the centers of the cells in the invariant set. Red dots showing the fine structure of the attractor are generated with interpolation

We compute the Hausdorff distance $d_H(I(S), D(S))$ between the reference solution $D(S)$ and the interpolated point mappings of the set S, denoted as $I(S)$. The results shown in Fig. 5 seems to suggest that the Hausdorff distance $d_H(I(S), D(S))$ is insensitive to the size of S.

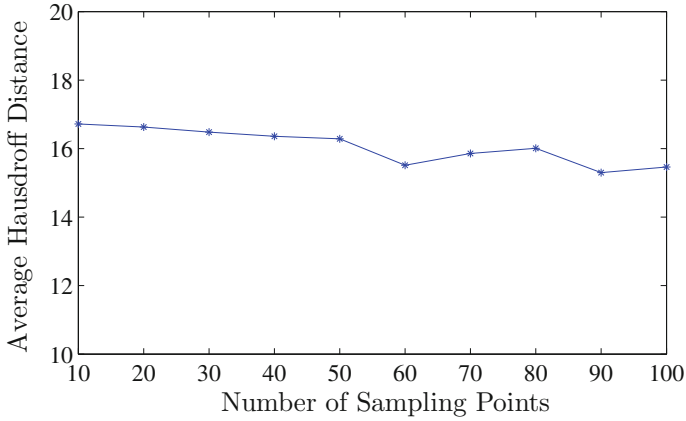

Fig. 5 The relationship between the number of sampled points and the Hausdorff distance of the invariant set of the $6D$ Lorenz system obtained by the interpolation scheme to the reference set. The interpolation scheme appears to be insensitive to the number of sampled points

المنارة للاستشارات

Recall that the local error of the interpolation scheme is proportional to the Hessian matrix $\left.\frac{\partial^2 \mathbf{F}}{\partial \mathbf{x}^2}\right|_{\mathbf{x}=\mathbf{x}_0}$. Hence, the Hausdorff distance actually reflects the topological behavior of the invariant set in terms of the curvature.

6.3 A Summary

We have presented the parallel SCM-GCM hybrid method for searching the invariant set of nonlinear dynamical systems, and a modified GCM implementation for global analysis. Parts of the algorithm are implemented in parallel computing with GPU. The invariant set searching algorithm takes the advantage of the fact that attractors and steady state solutions of nonlinear systems usually occupy a small portion of the state space. The sub-division technique is quite effective to find the invariant set. At some point we must stop the sub-division, and treat the cell mappings as the database for further refinement of the invariant set with the interpolation scheme. We have proposed an interpolation scheme for high dimensional state space and proven its accuracy as a function of the cell size. Furthermore, we have introduced the Hausdorff distance to measure the quality of the interpolated results. We have found that neither the sub-division technique nor the interpolation scheme can replace the GCM method for the global analysis of nonlinear dynamical systems including the domains of attraction and their boundaries. We have presented the modified GCM method and its parallel implementation. Two examples including an impact model governed by implicit mappings and a six dimensional Lorenz system are presented to show the effectiveness of the proposed methods.

The speed up via parallel computing reported in this chapter is hardware dependent. For the low dimensional examples, the laptop with a GPU having 384 cores has delivered 40 times speed up. Higher speed up can be achieved on more advanced machines. Finally, it should be noted that for high dimensional systems, there are still many open computing problems to be addressed, because the compromise between computing demand and information loss may greatly influence the solution accuracy.

7 Examples of Stochastic Systems

We consider nonlinear dynamical systems subject to periodical and Gaussian white noise excitations.

The stochastic response analysis has been a classic and significant research topic in nonlinear dynamical systems (Anh et al. 2014; Hawes and Langley 2015; Zhu and Guo 2015). In particular, when a nonlinear oscillator is driven by periodic and random excitations, it exhibits complex stochastic response phenomena including multiple steady-state responses (Rong et al. 2004), chaotic responses (Gan 2006) and stochastic bifurcations such as P-bifurcation (Huang et al. 2000). As an important

المنارة للاستشارات

characterization of the stochastic response, the PDF always attracts the attention from many researchers. The PDF of a Markov response process is governed by the Fokker-Planck-Kolmogorov (FPK) equation (Risken 1989; Sun 2006). However, the exact solutions of FPK equations are available only in a few special classes of lower order nonlinear stochastic systems. For the nonlinear systems driven by periodic and random excitations, the FPK equation is even more difficult to deal with. We apply the generalized cell mapping (GCM) method based on the short-time Gaussian approximation (STGA) scheme to attack this problem.

The GCM/STGA method can be viewed as an extension of the path integral solution method (Wehner and Wolfer 1983; Naess and Johnsen 1993). The path integral solution method aims to evolve the PDF from an initial distribution by repeatedly using a short-time transition probability density function (TPDF), which is based upon a Taylor expansion of the solution to the first order approximation. While the short-time TPDF in the GCM/STGA method is constructed with the mean and covariance obtained by integrating the moment equations with Gaussian closure.

We study the periodically driven smooth and discontinuous (SD) oscillator originally proposed by Cao and coworkers (2006). The deterministic SD oscillator has been studied extensively in recent years, including the response of discontinuous case (Cao et al. 2008a), codimension-two bifurcation (Tian et al. 2010), piecewise linear approximation (Cao et al. 2008b), resonant behaviors in discontinuous case (Cao et al. 2011), and interior crisis (Wang et al. 2011). Since the SD oscillator is inevitably affected by various random disturbances, Yue et al. (2013) studied the global analysis of stochastic bifurcation in a SD oscillator under bounded noise excitations. The stochastic analysis of the SD oscillator under periodic and random excitations has been seldom reported in the literature.

7.1 The Short-Time Solution

The first-order and second-order moments of the response of a stochastic system $d\mathbf{X}(t) = \mathbf{f}(\mathbf{X}, t)dt + d\mathbf{B}(t)$ read as,

$$\begin{aligned} \mathbf{m}(t) &= E\left[\mathbf{X}(t)\right], \\ \mathbf{C}(t) &= E\left[(\mathbf{X}-\mathbf{m})(\mathbf{X}-\mathbf{m})^T\right], \end{aligned} \tag{20}$$

where $\mathbf{m}(t)$ is the mean value vector, $\mathbf{C}(t)$ is the covariance matrix of the response process $\mathbf{X}(t)$, and $\mathbf{B}(t)$ is the Weiner process of strength $\boldsymbol{\sigma}(\mathbf{X})$. By applying the Itô's lemma, we can derive the differential equations governing the moments as follows

$$\begin{aligned} \dot{\mathbf{m}}(t) &= E\left[\mathbf{f}(\mathbf{X}, t)\right], \\ \dot{\mathbf{C}}(t) &= E\left[(\mathbf{X}-\mathbf{m})\mathbf{f}^T(\mathbf{X}, t) + \mathbf{f}(\mathbf{X}, t)(\mathbf{X}-\mathbf{m})^T + \boldsymbol{\sigma}(\mathbf{X})\boldsymbol{\sigma}^T(\mathbf{X})\right]. \end{aligned} \tag{21}$$

المنارة للاستشارات

Note that some higher-order moments appear on the right hand of the moment equations because of the nonlinearities in $\mathbf{f}(\mathbf{X}, t)$ and $\boldsymbol{\sigma}(\mathbf{X})$. From the FPK equation, we can show that the conditional probability density function $q(\mathbf{x}, \tau|\mathbf{x}_0, 0)$ is approximately Gaussian when τ is sufficiently small. So the higher-order moments can be expressed in terms of the first- and second-order ones (Sun and Hsu 1987; Wu and Lin 1984), resulting in a closed set of nonlinear ordinary differential equations for the first- and second-order moments

$$\begin{aligned} \dot{\mathbf{m}}(t) &= \mathbf{h}\,(\mathbf{m}, \mathbf{C}, t)\,, \\ \dot{\mathbf{C}}(t) &= \mathbf{g}\,(\mathbf{m}, \mathbf{C}, t)\,, \end{aligned} \tag{22}$$

where $\mathbf{h}\,(\mathbf{m}, \mathbf{C}, t)$ and $\mathbf{g}\,(\mathbf{m}, \mathbf{C}, t)$ are nonlinear functions of their arguments.

Since we need the conditional probability density $q(\mathbf{x}, T|\mathbf{x}_0, 0)$ over one period, we divide the period into M segments. Let $\tau = T/M$. τ can be small enough so that the conditional probability density $q(\mathbf{x}, k\tau|\mathbf{x}_0, (k-1)\tau)$ $(k = 1, 2, \ldots, M)$ for each k is approximately Gaussian, which is given by

$$\begin{aligned} q(\mathbf{x}, k\tau|\mathbf{x}_0, (k-1)\tau) = &\frac{1}{(2\pi)^{N/2}\,|\mathbf{C}(k\tau)|^{1/2}} \\ &\times \exp\left\{-\frac{1}{2}[\mathbf{x} - \mathbf{m}(k\tau)]^T\mathbf{C}(k\tau)^{-1}[\mathbf{x} - \mathbf{m}(k\tau)]\right\}, \end{aligned} \tag{23}$$

where $\mathbf{m}(k\tau)$ and $\mathbf{C}(k\tau)$ are the short-time solutions of Eq. (22) subject to the initial conditions $\mathbf{m}[(k-1)\tau] = \mathbf{x}_0$ and $\mathbf{C}[(k-1)\tau] = \mathbf{0}$.

The transition probability from regular cell i to cell j over the time interval $[(k-1)\tau, k\tau]$ in the period reads

$$q_{ji}^{(k)} = \int_{C_j} q(\mathbf{x}, k\tau|\bar{\mathbf{x}}_i, (k-1)\tau)d\mathbf{x}, \tag{24}$$

where $\bar{\mathbf{x}}_i$ is the center of cell i, C_j is the domain of cell j, and $C_j \subset \mathbf{D}_i^{(k)}$, where the region $\mathbf{D}_i^{(k)}$ is defined as

$$\mathbf{D}_i^{(k)} = \{\mathbf{x} \in R^N \mid \int_{\mathbf{D}_i^{(k)}} q(\mathbf{x}, k\tau|\bar{\mathbf{x}}_i, (k-1)\tau)d\mathbf{x} \geq p_{trunc}\}. \tag{25}$$

In this equation, we choose the truncation of the integration domain such that $p_{trunc} = 0.99$ because this can maintain a very high accuracy and an acceptable computational efficiency. We should point out that the truncation level affects the precision of the solution. According to our experience, p_{trunc} should not be less than 0.95. Nevertheless, a quantitative assessment of the effect of truncation of the domain $\mathbf{D}_i^{(k)}$ on the accuracy of the steady-state solutions is not available for nonlinear systems.

المنارة للاستشارات

We should point out that the Gauss-Legendre quadrature rule (Stroud 1974; Yu et al. 1997) is employed to compute $q_{ji}^{(k)}$ from the numerical integration over domain C_j

$$q_{ji}^{(k)} = \sum_{r=1}^{S_j} c_{jr} q(\mathbf{x}_{jr}, k\tau | \bar{\mathbf{x}}_i, (k-1)\tau), \tag{26}$$

where S_j is the number of representative Gauss quadrature points chosen in cell j, and $\mathbf{x}_{jr}$ is the rth Gauss point with the matching weight c_{jr}. Let $\mathbf{Q}^{(k)} = \{q_{ji}^{(k)}\}$ denote the matrix. The mapping over one period reads,

$$\mathbf{p}(n+1) = \mathbf{Q}^{(M)}\mathbf{Q}^{(M-1)} \cdots \mathbf{Q}^{(1)}\mathbf{p}(n), \ n = 0, 1, 2, \ldots \tag{27}$$

It should be noted that the above solution approach to create the mapping over one period is known as the path integral. The present approach is more accurate since the mean and covariance are computed from the moment equations (Sun 2006). We consider the steady-state solution with respect to the periodical mapping (27), which is referred to as the steady-state PDF in the sense of the GCM method. The termination condition for computing the steady-state response PDF from Eq. (27) is taken as

$$|\mathbf{p}(n+1) - \mathbf{p}(n)| < \varepsilon, \tag{28}$$

where ε is a given small positive number. In this example, it is taken to be 0.03.

7.2 Computational Consideration

Here, we discuss some computational issues and quantitative assessment of the GCM/STGA method. The first issue is how to choose the period division parameter M or the mapping time step τ. M is chosen such that the amplitude and phase of the periodic response are accurately represented by the sampled signals. From the point of view of reconstructing a periodic signal, $M = 16$ is enough.

The domain $\mathbf{D}_i^{(k)}$ is an N-dimensional ellipsoid with the center at $\mathbf{m}(k\tau)$ and the length of the rth radius being the rth eigenvalue of the covariance matrix $\mathbf{C}(k\tau)$. The directions of the principal radii of the ellipsoid are determined by the eigenvectors of $\mathbf{C}(k\tau)$. The radii of the ellipsoid provide a guideline to select the proper cell size (Sun and Hsu 1988a, 1990). Because the domain $\mathbf{D}_i^{(k)}$ contains more than 99% of the probabilities of the one-step conditional probabilities, only cells in $\mathbf{D}_i^{(k)}$ are considered as the images of cell i. The cells outside the ellipsoid are neglected. This is an important approach to maintain high computational efficiency of the GCM/STGA method.

المنارة للاستشارات

$\mathbf{m}(k\tau)$ and $\mathbf{C}(k\tau)$ are integrated from the moment equations (22) starting from the initial conditions $\mathbf{m}[(k-1)\tau] = \bar{\mathbf{x}}_i$ and $\mathbf{C}[(k-1)\tau] = \mathbf{0}$. As long as the one-step PDF over the duration τ is nearly Gaussian, its approximation based on $\mathbf{m}(k\tau)$ and $\mathbf{C}(k\tau)$ obtained in the current approach is more accurate than the short-time solution of the FPK equation based on the Taylor expansion over the time interval τ (Risken 1989; Sun 2006). The current approach allows a slightly larger τ while maintaining a comparable accuracy.

In order to assess the accuracy of the GCM/STGA method, we compare the results with direct Monte Carlo simulations. We define the integrated absolute error (IAE) as

$$e_{IAE} = \int_{\Omega} |p_{GCM}(\mathbf{x}, t) - p_{MC}(\mathbf{x}, t)| \, d\mathbf{x}, \tag{29}$$

where $p_{GCM}(\mathbf{x}, t)$ denotes the PDF computed by the GCM/STGA method, and $p_{MC}(\mathbf{x}, t)$ represents the PDF by direct Monte Carlo simulations.

7.3 SD Oscillator

The dimensionless stochastic differential equations of the SD oscillator driven by both periodic force and Gaussian white noise in the Itô sense are given by

$$\begin{aligned} dX_1(t) &= X_2 dt, \\ dX_2(t) &= [-2\xi X_2 - \omega_0^2 X_1 + \omega_0^2 g(X_1) + f\cos(\omega t)]dt + \sqrt{2D}dB(t), \end{aligned} \tag{30}$$

where $X_1(t)$ and $X_2(t)$ are the displacement and velocity response processes, the nonlinear function $g(x_1) = \frac{x_1}{\sqrt{x_1^2+a^2}}$, ξ is the viscous damping coefficient, ω_0 is the natural frequency of the system, f and ω are the amplitude and frequency of the harmonic force. The period of the force is $T = 2\pi/\omega$. a is the so-called smoothness parameter. The system exhibits smooth dynamics behavior when $a > 0$, while the dynamics is discontinuous when $a = 0$ (Cao et al. 2006). $B(t)$ is the unit Weiner process such that

$$E[dB(t)] = 0, \;\; E[dB(t)dB(t')] = \begin{cases} dt, t = t', \\ 0, t \neq t'. \end{cases} \tag{31}$$

Let $m_i = E[X_i]$, $v_i = E[(X_i - m_i)^2]$ $(i = 1, 2)$ and $c_{12} = E[(X_1 - m_1)(X_2 - m_2)]$. The moment equations for m_i, v_i and c_{12} can be derived from Eq. (30) with the help of Itô's lemma.

المنارة للاستشارات

$$
\begin{aligned}
\dot{m}_1 &= m_2, \\
\dot{m}_2 &= -2\xi m_2 - \omega_0^2 m_1 + \omega_0^2 E[g(X_1)] + f\cos(\omega t), \\
\dot{v}_1 &= 2c_{12}, \\
\dot{v}_2 &= -4\xi v_2 - 2\omega_0^2 c_{12} + 2\omega_0^2 E[(X_2 - m_2)g(X_1)] + 2D, \\
\dot{c}_{12} &= v_2 - 2\xi c_{12} - \omega_0^2 v_1 + \omega_0^2 E[(X_1 - m_2)g(X_1)].
\end{aligned} \tag{32}
$$

The initial conditions for the moment equations are

$$
\begin{aligned}
m_1(0) = \bar{x}_{10}, \quad m_2(0) = \bar{x}_{20}, \\
v_1(0) = v_2(0) = c_{12}(0) = 0,
\end{aligned} \tag{33}
$$

where $(\bar{x}_{10}, \bar{x}_{20})$ denotes the center of the cell under consideration.

7.4 *Smooth Case*

When $a > 0$, $g(x_1)$ is a rational function. It is not straightforward to apply the Gaussian closure method to compute the expectation of this function. However, the probability distribution of the system over a short time τ starting from an initial probability density being Dirac delta function will remain highly concentrated in a small region near the initial location. Hence, the function $g(x_1)$ can be approximated by using the Taylor expansion at the initial location. Consider a three-order Taylor expansion of function as

$$
g(x_1) = \beta_0 + \beta_1 x_1 + \beta_2 x_1^2 + \beta_3 x_1^3 + O(x_1^4), \tag{34}
$$

where the coefficients β_j $(j = 0, 1, 2, 3)$ are given by

$$
\begin{aligned}
\beta_0 &= g(\bar{x}_{10}) - \beta_3 \bar{x}_{10}^3 - \beta_2 \bar{x}_{10}^2 - \beta_1 \bar{x}_{10}, \\
\beta_1 &= g'(\bar{x}_{10}) - 3\beta_3 \bar{x}_{10}^2 - 2\beta_2 \bar{x}_{10}, \\
\beta_2 &= \frac{1}{2}[g''(\bar{x}_{10}) - 6\beta_3 \bar{x}_{10}], \\
\beta_3 &= \frac{1}{6} g'''(\bar{x}_{10}).
\end{aligned} \tag{35}
$$

With the Taylor expansion and Gaussian closure, we obtain a closed set of differential equations for the first- and second-order moments

المنارة للاستشارات

$$
\begin{aligned}
\dot{m}_1 &= m_2, \\
\dot{m}_2 &= -2\xi m_2 - \omega_0^2 m_1 + \omega_0^2[\beta_0 + \beta_1 m_1 + \beta_2(m_1^2 + v_1) \\
&\quad + \beta_3(m_1^3 + 3m_1 v_1)] + f\cos(\omega t), \\
\dot{v}_1 &= 2c_{12}, \\
\dot{v}_2 &= -4\xi v_2 - 2\omega_0^2 c_{12} + 2\omega_0^2[\beta_1 c_{12} + 2\beta_2 m_1 c_{12} \\
&\quad + 3\beta_3 c_{12}(m_1^2 + v_1)] + 2D, \\
\dot{c}_{12} &= v_2 - 2\xi c_{12} - \omega_0^2 v_1 + \omega_0^2[\beta_1 v_1 + 2\beta_2 m_1 v_1 + 3\beta_3 v_1(m_1^2 + v_1)].
\end{aligned} \tag{36}
$$

7.5 *Discontinuous Case*

When $a = 0$, $g(x_1)$ is reduced to the sign function $\mathrm{sgn}(x_1)$. The closed set of moment equations after the application of the Gaussian closure can be obtained as

$$
\begin{aligned}
\dot{m}_1 &= m_2, \\
\dot{m}_2 &= -2\xi m_2 - \omega_0^2 m_1 + \omega_0^2 \mathrm{sgn}(m_1)\,\mathrm{erf}\left(\frac{|m_1|}{\sqrt{2v_1}}\right) + f\cos(\omega t), \\
\dot{v}_1 &= 2c_{12}, \\
\dot{v}_2 &= -4\xi v_2 - 2\omega_0^2 c_{12} + 2\omega_0^2\sqrt{\frac{2}{\pi v_1}}\, c_{12}\exp\left(-\frac{m_1^2}{2v_1}\right) + 2D, \\
\dot{c}_{12} &= v_2 - 2\xi c_{12} - \omega_0^2 v_1 + \omega_0^2\sqrt{\frac{2v_1}{\pi}}\exp\left(-\frac{m_1^2}{2v_1}\right).
\end{aligned} \tag{37}
$$

We have used the following expectations of Gaussian processes in the derivation (Sun 1995)

$$
\begin{aligned}
E[\mathrm{sgn}(X_1)] &= \mathrm{sgn}\left(\tfrac{m_1}{\sqrt{2}\sigma_1}\right)\mathrm{erf}\left(\tfrac{|m_1|}{\sqrt{2}\sigma_1}\right), \\
E[(X_2 - m_2)\mathrm{sgn}(X_1)] &= \tfrac{2c_{12}}{\sqrt{2\pi}\sigma_1}\exp\left(-\tfrac{m_1^2}{2\sigma_1^2}\right), \\
E[(X_1 - m_1)\mathrm{sgn}(X_1)] &= \tfrac{2\sigma_1}{\sqrt{2\pi}}\exp\left(-\tfrac{m_1^2}{2\sigma_1^2}\right),
\end{aligned} \tag{38}
$$

where $\sigma_1 = \sqrt{v_1}$ and $\mathrm{erf}(\cdot)$ denotes the error function.

We are now ready to apply the GCM/STGA method to study the stochastic response PDFs of the SD oscillator (30). In this work, the moment equations (36) and (37) are numerically integrated with the fourth order Runge-Kutta algorithm. The short-time Gaussian PDFs of the system over the short time interval τ are constructed with the first- and second-order moments. We have taken M to be 16 and kept the

المنارة للاستشارات

cell size to be 0.05×0.05 for all the reported cases. The 2×2 Gauss quadrature points are used in each cell to compute the integrals for $q_{ji}^{(k)}$ in Eq. (26).

7.6 Transient Response

First, we study the transient response PDFs when $a = 0.6$. We have taken $\xi = 0.04$, $\omega_0 = 1.0$, $f = 0.83$, $\omega = 1.0606$ and $D = 0.01$. $\tau = T/M \approx 0.370$. Moreover, the domain of interest is taken to be $\Omega = [-5, 3] \times [-4, 4]$. The underlying noise-free system (30) also has only one period-1 attractor A located at the point $(x_1, x_2) = (-0.575, 0.025)$ on the Poincaré section. Before reaching the attractor, the system goes through a transient chaos that is represented by a chaotic saddle S. The initial distribution $\mathbf{p}(0)$ is taken as

$$p_{c_A}(0) = 1, \text{ and } p_i(0) = 0, \ i \neq c_A, \tag{39}$$

where c_A is the cell that contains attractor A.

The evolution of the PDFs seems quite complex. The contours of the transient joint PDFs are shown in Fig. 6. It can be seen that the shape of the transient joint PDF gradually evolves to look like the chaotic saddle in figure. The chaotic response

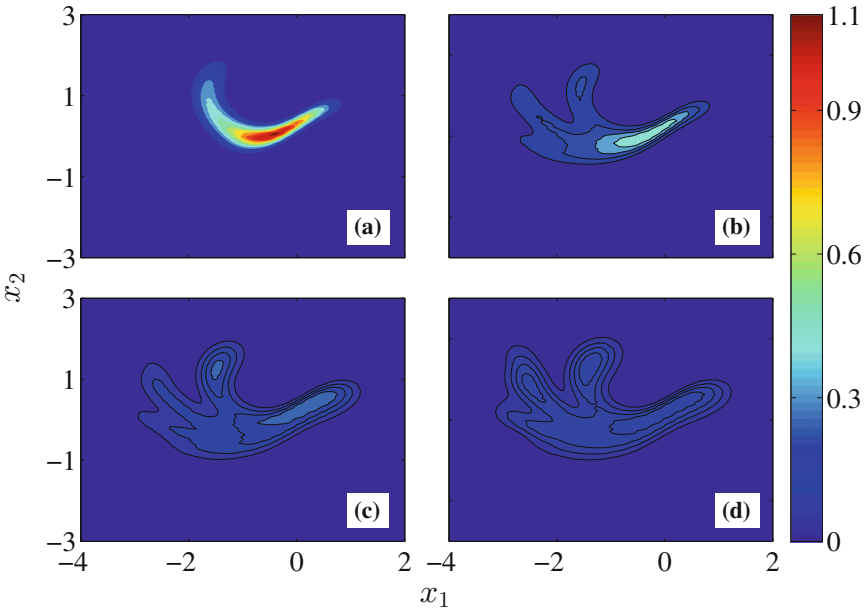

Fig. 6 The contours of the transient joint PDFs of the system (30). **a** $t = 1T$. **b** $t = 2T$. **c** $t = 3T$. **d** $t = 4T$

المنارة للاستشارات

is confirmed with the largest Lyapunov exponent $\lambda_1 = 0.09$ (Benettin et al. 1980). The PDF reaches the steady-state in about four periods.

7.7 Steady-State Response Analysis

We now consider the steady-state response of the SD oscillator. We have taken the parameters $\xi = 0.2$, $\omega_0 = 1.0$, $f = 0.25$, $\omega = 1.0$ and $D = 0.01$. $\tau = 0.393$. The domain Ω is chosen to be $[-3, 3] \times [-3, 3]$. We apply the GCM/STGA method to study the steady-state response PDFs for different smoothness parameters a.

When a decreases to 0, the dynamics of the SD oscillator suddenly becomes discontinuous. In the deterministic system, the velocity flow goes through a jump when the system crosses from one well to another because of the loss of local hyperbolicity (Cao et al. 2006). Figure 7 shows the contours of the steady-state joint PDFs obtained with the GCM/STGA method for different a. The sharp peak of the steady-state PDFs due to the sign function $\mathrm{sgn}(x_1)$ and the stochastic P-bifurcation can be clearly observed.

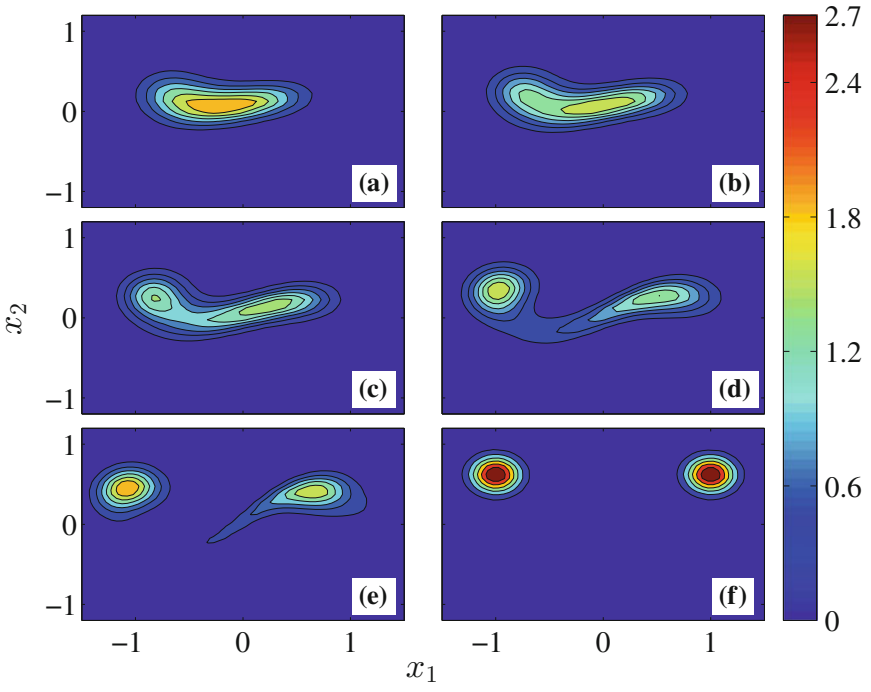

Fig. 7 The contours of the steady-state PDFs of the system (30) for different values of a. **a** $a = 1.0$. **b** $a = 0.9$. **c** $a = 0.8$. **d** $a = 0.6$. **e** $a = 0.4$. **f** $a = 0$

المنارة للاستشارات

7.8 A Summary

The GCM/STGA method offers an effective tool for computing and analyzing the stochastic response of periodically driven nonlinear systems under Gaussian white nose excitations.

8 Examples of Fuzzy Systems

For fuzzy nonlinear dynamical systems, a response process is difficult to analyze because the evolution of the MDFs of the fuzzy response process cannot be readily obtained analytically. Many studies dealt with fuzzy dynamical systems governed by linear ordinary differential equations (Buckley and Feuring 2000; Park and Han 2000; Yoshida 2000). Chaotic sequences of fuzzy nonlinear maps were studied (Buckley and Hayashi 1998). A master equation was derived for the evolution of MDFs of fuzzy processes (Friedman and Sandler 1996, 1999). However, the solution to the fuzzy master equation is rare, particularly for nonlinear dynamical systems.

Fuzzy response is naturally global in the sense that it is represented by a fuzzy set of a finite possibility measure in the state space. It is computationally intensive and ineffective to study such a solution by using numerical simulations (Ma et al. 1999; Zhang et al. 1998). The cell mapping method represents a major advancement in this regard. Here, we present examples of fuzzy dynamical systems with the help of the FGCM method.

8.1 Triple-Well Potential System

Consider the forced Duffing oscillator

$$\ddot{x} + \delta\dot{x} + \frac{dV(x)}{dt} = f\cos\omega t \tag{40}$$

with a triple-well potential $V(x) = \frac{1}{2}\alpha x^2 + \frac{1}{4}\beta x^4 + \frac{1}{6}\gamma x^6$ when $\alpha > 0, \beta < 0, \gamma > 0$. δ is damping coefficient. f and ω are forcing magnitude and frequency. α, β, γ are constant parameters of the potential. A triple-well potential system has attracted much attention, due to the fact that it is a universal nonlinear differential equation, and that many nonlinear oscillators in physics, engineering and biological problems can be described by the model or analogous ones.

We take $\delta = 0.35$, $\alpha = 1.0$, $\beta = -0.5$, $\gamma = 0.05$, $f = 0.2$ and $\omega = 1.0$ where the system has three coexistent period-one attractors A_1, A_2 and A_3. Figure 8 shows the global properties of Eq. (40) by means of point mapping under cell reference (PMUCR), a two-scaled numerical method of global analysis (Jiang and Xu 1994;

المنارة للاستشارات

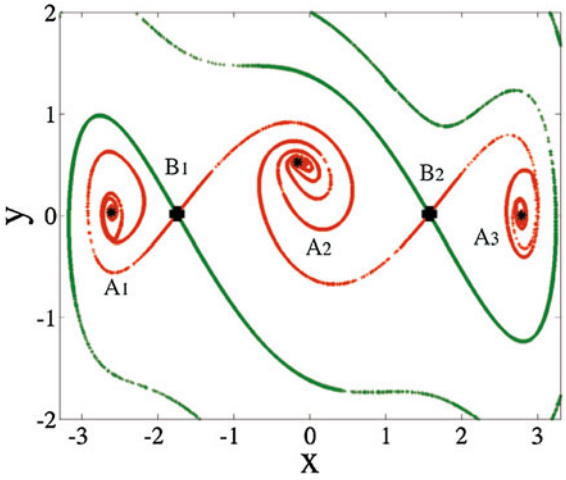

Fig. 8 Global phase portrait of the deterministic Duffing (40). A_1 A_2 and A_3 (black dots) denote three period-one attractors. On basin boundary lie the saddles denoted by B_1 and B_2 (black dots). The basin boundary denoted by a green line is the stable manifold of the saddle B_1 and B_2. The unstable manifolds of the saddle B_1 and B_2 denoted by a red line are directed to A_1, A_2 and A_3 respectively

Jiang 2012). The basin boundary (green) is the stable manifolds of unstable saddles B_1 and B_2. The branches (red) of the unstable manifolds of B_1 and B_2 are directed to the three attractors A_1, A_2 and A_3 respectively. B_1 and B_2 are the unstable invariant sets of the Duffing system (40). A_1, A_2 and A_3 the stable invariant sets.

In the following, we will study escape bifurcations and transient and steady-state MDFs of a fuzzy response for the forced Duffing oscillator with fuzzy uncertainty.

8.2 *Additive Fuzzy Noise*

Consider now the Duffing equation with additive fuzzy noise

$$\begin{aligned} \dot{x} &= y \\ \dot{y} &= -\delta y - \alpha x - \beta x^3 - \gamma x^5 + f\cos\omega t + S. \end{aligned} \tag{41}$$

where S is a fuzzy parameter with a triangular membership function,

$$\mu_S(s) = \begin{cases} [s-(s_0-\varepsilon)]/\varepsilon, & s_0-\varepsilon \leqslant s < s_0 \\ -[s-(s_0+\varepsilon)]/\varepsilon, & s_0 \leqslant s < s_0+\varepsilon \\ 0, & \text{otherwise} \end{cases} \tag{42}$$

$\varepsilon > 0$ is a parameter characterizing the intensity of fuzziness of S and is called a fuzzy noise intensity. s_0 is the nominal value of S with membership grade $\mu_S(s_0) = 1$. In the computation, we take $s_0 = 0$.

The domain $\mathbf{D} = (-3.5 \leq x \leq 3.5) \times (-2.0 \leq y \leq 2.0)$ is discretized into 141×141 cells. The 5×5 sampling points are used within each cell. S is discretized

المنارة للاستشارات

into 401 segments. Hence, out of each cell, there are 10,025 trajectories with varying membership grades to determine the one-step transition possibility with the time length $\triangle T = T = 2\pi/\omega$. T is called one mapping step. The FGCM is used to analyze the escape bifurcations and the transient and steady-state MDFs of the fuzzy response of the system.

In the computation of the two examples, 199,307,025 sample trajectories in total are calculated to generate a FGCM system by using the adaptive method of

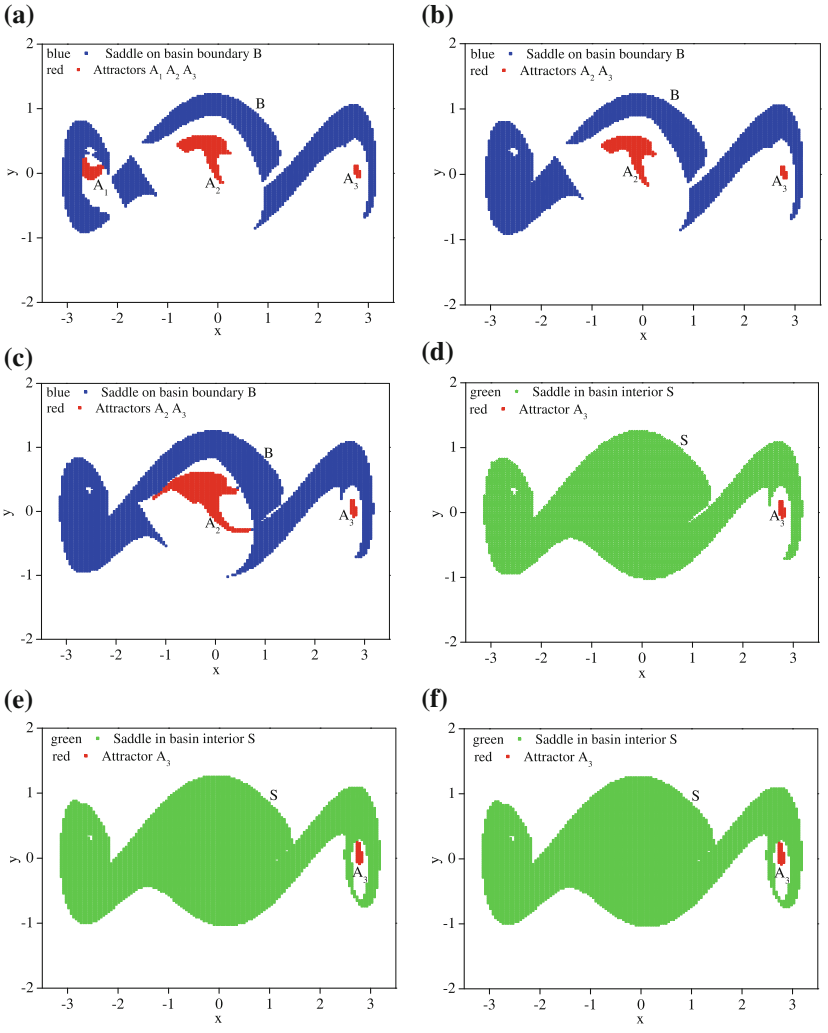

Fig. 9 Escape bifurcations of the fuzzy Duffing system (41) with respect to the intensity of fuzzy noise ε. **a** and **b** catastrophic bifurcation in the interval $(0.256, 0.257)$; **c** and **d** catastrophic bifurcation in the interval $(0.281, 0.282)$; **e** and **f** explosive bifurcation in the interval $(0.297, 0.298)$. Letter 'A' denotes the attractor and 'S' denotes the saddle

المنارة للاستشارات

Runge-Kutta simulations. An estimation error is taken 1.0e−6 to control the step size of integrations. The CPU runtime is 4 h in average for a run of the whole FGCM algorithm with a desktop PC of CPU6600/2.4 GHz.

Here we concentrate on noise-induced escape from each of potential wells with an increase of the intensity of fuzzy noise ε. It involves the two kinds of catastrophic and explosive bifurcations (Thompson et al. 1994; Grebogi et al. 1983), a sudden change in the topology of fuzzy attractors. We propose an understanding of these bifurcations through a phase portrait diagram involving three types of fuzzy sets: an attractor A, a saddle in a basin boundary B or a saddle in the interior of a basin S.

As the intensity of fuzzy noise ε increases from 0.0 to 0.256, the fuzzy attractor A_1, shown in Fig. 9a moves towards to the fuzzy saddle in the basin boundary. The catastrophic bifurcation occurs when the attractor touches the saddle at $\varepsilon = 0.256$. After the collision at $\varepsilon = 0.257$, shown in Fig. 9b, the attractor A_1 together with its basin of attraction disappears, and is converted into the saddle in the boundary B.

As ε increases further from 0.257 to 0.281, the fuzzy attractor A_2 in Fig. 9c and the fuzzy saddle in the basin boundary grow bigger and bigger. The catastrophic bifurcation occurs when the saddle and the attractor collide at $\varepsilon = 0.281$, leaving behind a saddle in the basin interior of A_3 after the collision $\varepsilon = 0.282$. This escape bifurcation with respect to the parameter ε is graphically illustrated in Fig. 9c, d.

The last escape from a potential well is due to an explosive bifurcation when $\varepsilon \in (0.297, 0.298)$ shown in Fig. 9e, f. In this case the attractor A_3 collides with the saddle in the basin interior to form a large attractor A_{large}.

8.3 A Summary

The fuzzy generalized cell mapping (FGCM) method is demonstrated to be an effective tool for analyzing dynamics and bifurcations of complex nonlinear dynamical systems with fuzzy uncertainties. A mathematical foundation of the FGCM is established as a discrete representation of the fuzzy master equation for the possibility transition of continuous fuzzy processes.

Acknowledgements The material in this chapter is based on work supported by grants (11672218, 11172197, 11332008 and 11572215) from the National Natural Science Foundation of China, and a grant from the University of California Institute for Mexico and the United States (UC MEXUS) and the Consejo Nacional de Ciencia y Tecnología de México (CONACyT) through the project "Hybridizing Set Oriented Methods and Evolutionary Strategies to Obtain Fast and Reliable Multi-objective Optimization Algorithms". Figures 1, 2, 3, 4 and 5 are reproduced from Xiong et al. (2015) with the permission of ASME. Figures 6 and 7 are reproduced from Han et al. (2016) with the permission of Elsevier. Figures 8 and 9 are reproduced from Hong et al. (2015) with the permission of World Scientific Publishing Company.

المنارة للاستشارات

References

Anh, N., Zakovorotny, V., & Hao, D. (2014). Response analysis of Van der Pol oscillator subjected to harmonic and random excitations. *Probabilistic Engineering Mechanics*, *37*, 51–59.

Benettin, G., Galgani, L., Giorgilli, A., & Strelcyn, J.-M. (1980). Lyapunov characteristic exponents for smooth dynamical systems and for Hamiltonian systems; A method for computing all of them. Part 2: Numerical application. *Meccanica*, *15*(1), 21–30.

Blesken, M., Ruckert, U., Steenken, D., Witting, K., & Dellnitz, M. (2009). Multiobjective optimization for transistor sizing of CMOS logic standard cells using set-oriented numerical techniques. In *Proceedings of 2009 NORCHIP*, Piscataway, New Jersey (pp. 1–4).

Buckley, J. J., & Feuring, T. (2000). Fuzzy differential equations. *Fuzzy Sets and Systems*, *110*, 43–54.

Buckley, J. J., & Hayashi, Y. (1998). Applications of fuzzy chaos to fuzzy simulation. *Fuzzy Sets and Systems*, *99*, 151–157.

Bursal, F. H., & Tongue, B. H. (1992). A new method of nonlinear system identification using interpolated cell mapping. In *Proceedings of American Control Conference* (pp. 3160–3164).

Cao, Q., Wiercigroch, M., Pavlovskaia, E. E., Grebogi, C., & Thompson, J. M. T. (2006). Archetypal oscillator for smooth and discontinuous dynamics. *Physical Review E*, *74*(4), 046218.

Cao, Q., Wiercigroch, M., Pavlovskaia, E. E., Grebogi, C., & Thompson, J. M. T. (2008a). The limit case response of the archetypal oscillator for smooth and discontinuous dynamics. *International Journal of Non-Linear Mechanics*, *43*(6), 462–473.

Cao, Q., Wiercigroch, M., Pavlovskaia, E. E., Thompson, J. M. T., & Grebogi, C. (2008b). Piecewise linear approach to an archetypal oscillator for smooth and discontinuous dynamics. *Philosophical Transactions of the Royal Society of London A: Mathematical, Physical and Engineering Sciences*, *366*(1865), 635–652.

Cao, Q., Xiong, Y., & Wiercigroch, M. (2011). Resonances of the SD oscillator due to the discontinuous phase. *Journal of Applied Analysis and Computation*, *1*(2), 183–191.

Chung, K. L. (1967). *Markov chains with stationary transition probabilities*. New York: Springer.

Dellnitz, M., & Hohmann, A. (1997). A subdivision algorithm for the computation of unstable manifolds and global attractors. *Numerische Mathematik*, *75*(3), 293–317.

Dellnitz, M., & Junge, O. (1998). An adaptive subdivision technique for the approximation of attractors and invariant measures. *Computing and Visualization in Science*, *1*(2), 63–68.

Dellnitz, M., & Junge, O. (2002). Set oriented numerical methods for dynamical systems. *Handbook of Dynamical Systems*, *2*, 221–264.

Eason, R. P., & Dick, A. J. (2014). A parallelized multi-degrees-of-freedom cell mapping method. *Nonlinear Dynamics*, *77*(3), 467–479.

Friedman, Y., & Sandler, U. (1996). Evolution of systems under fuzzy dynamic laws. *Fuzzy Sets and Systems*, *84*, 61–74.

Friedman, Y., & Sandler, U. (1999). Fuzzy dynamics as an altemative to statistical mechanics. *Fuzzy Sets and Systems*, *106*, 61–74.

Gan, C. (2006). Noise-induced chaos in Duffing oscillator with double wells. *Nonlinear Dynamics*, *45*(3–4), 305–317.

Ge, Z. M., & Lee, S. C. (1997). A modified interpolated cell mapping method. *Journal of Sound and Vibration*, *199*(2), 189–206.

Grebogi, C., Ott, E., & Yorke, J. A. (1983). Crises, sudden changes in chaotic attractors, and transient chaos. *Physica D*, *7*(1–3), 181–200.

Grune, L., & Junge, H. (2005). A set oriented approach to optimal feedback stabilization. *Systems & Control Letters*, *54*(2), 169–180.

Han, Q., Xu, W., & Yue, X. (2014). Global bifurcation analysis of a Duffing-Van der Pol oscillator with parametric excitation. *International Journal of Bifurcation and Chaos*, *24*(04), 1450051.

Han, Q., Xu, W., & Sun, J. Q. (2016). Stochastic response and bifurcation of periodically driven nonlinear oscillators by the generalized cell mapping method. *Physica A—Statistical Mechanics and Its Applications*, *458*, 115–125.

المنارة للاستشارات

Hawes, D. H., & Langley, R. S. (2015). Numerical methods for calculating the response of a deterministic and stochastically excited Duffing oscillator. *Proceedings of the Institution of Mechanical Engineers, Part C: Journal of Mechanical Engineering Science*. https://doi.org/10.1177/0954406215607544.

Hong, L., & Sun, J. Q. (2006a). Codimension two bifurcations of nonlinear systems driven by fuzzy noise. *Physica D-Nonlinear Phenomena*, *213*(2), 181–189.

Hong, L., & Sun, J. Q. (2006b). Global bifurcations of complex nonlinear dynamical systems with cell mapping methods. In J. Q. Sun & A. C. J. Luo (Eds.), *Bifurcation and chaos in complex systems* (Vol. 1, pp. 191–298). Oxford, UK: Elsevier Science Ltd.

Hong, L., & Xu, J. X. (1999). Crises and chaotic transients studied by the generalized cell mapping digraph method. *Physics Letters A*, *262*, 361–375.

Hong, L., Jiang, J., & Sun, J.-Q. (2015). Fuzzy responses and bifurcations of a forced duffing oscillator with a triple-well potential. *International Journal of Bifurcation and Chaos*, *25*(1). https://doi.org/10.1142/S0218127415500054.

Hsu, C. S. (1982). A probabilistic theory of nonlinear dynamical systems based on the cell state space concept. *Journal of Applied Mechanics*, *49*, 895–902.

Hsu, C. S. (1995). Global analysis of dynamical systems using posets and digraphs. *International Journal of Bifurcation and Chaos*, *5*(4), 1085–1118.

Huang, Z., Zhu, W., & Suzuki, Y. (2000). Stochastic averaging of strongly non-linear oscillators under combined harmonic and white-noise excitations. *Journal of Sound and Vibration*, *238*(2), 233–256.

Jiang, J. (2012). An effective numerical procedure to determine saddle-type unstable invariant limit sets in nonlinear systems. *Chinese Physics Letters*, *29*(5), 050503.

Jiang, J., & Xu, J. X. (1994). A method of point mapping under cell reference for global analysis of nonlinear dynamical systems. *Physics Letters A*, *188*, 137–145.

Junge, O., & Osinga, H. M. (2004). A set oriented approach to global optimal control. *ESAIM. Control, Optimisation and Calculus of Variations*, *10*, 259–270.

Lee, W. K., & Ghang, M. R. (1994). Domains of attraction of a forced beam by interpolated mapping. *Journal of Applied Mechanics*, *61*(1), 144–151.

Lee, W. K., & Hsu, C. S. (1994). A global analysis of an harmonically excited spring-pendulum system with internal resonance. *Journal of Sound and Vibration*, *171*(3), 335–359.

Ma, M., Friedman, M., & Kandel, A. (1999). Numerical solutions of fuzzy differential equations. *Fuzzy Sets and Systems*, *105*, 133–138.

Musielak, Z. E., & Musielak, D. E. (2009). High-dimensional chaos in dissipative and driven dynamical systems. *International Journal of Bifurcation and Chaos*, *19*(9), 2823–2869.

Naess, A., & Johnsen, J. M. (1993). Response statistics of nonlinear, compliant offshore structures by the path integral solution method. *Probabilistic Engineering Mechanics*, *8*(2), 91–106.

Neumann, N., Sattel, T., & Wallaschek, J. (2007). On set-oriented numerical methods for global analysis of non-smooth mechanical systems. *Journal of Vibration and Control*, *13*(9–10), 1393–1405.

Park, J. Y., & Han, H. K. (2000). Fuzzy differential equations. *Fuzzy Sets and Systems*, *110*, 69–77.

Rega, G., & Lenci, S. (2015). A global dynamics perspective for system safety from macro- to nanomechanics: Analysis, control, and design engineering. *Applied Mechanics Reviews*, *67*(5).

Risken, H. (1989). *The Fokker-Planck equation, methods of solution and application* (2nd ed.). Berlin, Heidelberg: Springer.

Rong, H., Meng, G., Wang, X., Xu, W., & Fang, T. (2004). Response statistic of strongly non-linear oscillator to combined deterministic and random excitation. *International Journal of Non-Linear Mechanics*, *39*(6), 871–878.

Schütze, O., Laumanns, M., Tantar, E., Coello Coello, C. A., & Talbi, E.-G. (2010). Computing gap free Pareto front approximations with stochastic search algorithms. *Evolutionary Computation*, *18*(1), 65–96.

المنارة للاستشارات

Schütze, O., Witting, K., Ober-Blöbaum, S., & Dellnitz, M. (2013). Set oriented methods for the numerical treatment of multiobjective optimization problems. In *EVOLVE—A bridge between probability, set oriented numerics and evolutionary computation* (Vol. 447, pp. 187–219). Springer.

Stroud, A. H. (1974). *Numerical quadrature and solution of ordinary differential equations*. New York: Springer.

Sun, J. Q. (1995). Random vibration analysis of a non-linear system with dry friction damping by the short-time gaussian cell mapping method. *Journal of Sound and Vibration*, *180*(5), 785–795.

Sun, J.-Q. (2006). *Stochastic dynamics and control*. Elsevier.

Sun, J.-Q., & Hsu, C. (1988a). A statistical study of generalized cell mapping. *Journal of Applied Mechanics*, *55*(3), 694–701.

Sun, J.-Q., & Hsu, C. S. (1987). Cumulant-neglect closure method for nonlinear systems under random excitations. *Journal of Applied Mechanics*, *54*(3), 649–655.

Sun, J.-Q., & Hsu, C. S. (1988b). A statistical study of generalized cell mapping. *Journal of Applied Mechanics*, *55*(3), 694–701.

Sun, J. Q., & Hsu, C. S. (1990). The generalized cell mapping method in nonlinear random vibration based upon short-time Gaussian approximation. *Journal of Applied Mechanics*, *57*(4), 1018–1025.

Sun, J.-Q., & Luo, A. C. J. (2012a). *Global analysis of nonlinear dynamics*. New York: Springer.

Sun, J. Q., & Luo, A. C. J. (2012b). *Global analysis of nonlinear dynamics*. New York: Springer.

Thompson, J. M. T., Stewart, H. B., & Ueda, Y. (1994). Safe, explosive, and dangerous bifurcations in dissipative dynamical systems. *Physical Review E*, *49*(2), 1019–1027.

Tian, R., Cao, Q., & Yang, S. (2010). The codimension-two bifurcation for the recent proposed SD oscillator. *Nonlinear Dynamics*, *59*(1–2), 19–27.

Tongue, B., & Gu, K. (1988a). A higher order method of interpolated cell mapping. *Journal of Sound and Vibration*, *125*(1), 169–179.

Tongue, B. H. (1987). On obtaining global nonlinear system characteristics through interpolated cell mapping. *Physica D: Nonlinear Phenomena*, *28*(3), 401–408.

Tongue, B. H., & Gu, K. (1988b). A theoretical basis for interpolated cell mapping. *SIAM Journal on Applied Mathematics*, *48*(5), 1206–1214.

Tongue, B. H., & Gu, K. (1988c). Interpolated cell mapping of dynamical systems. *Journal of Applied Mechanics*, *55*, 461–466.

Wang, J., Zhang, X., & Hong, L. (2011). Study of the interior crisis in SD oscillator. *Journal of Dynamics and Control*, *4*, 331–336.

Wehner, M. F., & Wolfer, W. G. (1983). Numerical evaluation of path-integral solutions to Fokker-Planck equations. *Physical Review A*, *27*(5), 2663–2670.

White, M., & Tongue, B. (1995). Application of interpolated cell mapping to an analysis of the Lorenz equations. *Journal of Sound and Vibration*, *188*(2), 209–226.

Wu, W. F., & Lin, Y. K. (1984). Cumulant-neglect closure for non-linear oscillators under random parametric and external excitations. *International Journal of Non-Linear Mechanics*, *19*(4), 349–362.

Xiong, F. R., Qin, Z. C., Ding, Q., Hernández, C., Fernandez, J., Schütze, O., & Sun, J. Q. (2015). Parallel cell mapping method for global analysis of high-dimensional nonlinear dynamical systems. *Journal of Applied Mechanics*, *82*(11).

Xu, W., Sun, C., Sun, J.-Q., & He, Q. (2013). Development and study on cell mapping methods. *Advances in Mechanics*, *43*(1), 91–100.

Yoshida, Y. (2000). A continuous-time dynamic fuzzy system. (I) A limit theorem. *Fuzzy Sets and Systems*, *113*, 453–460.

Yu, J., Cai, G., & Lin, Y. (1997). A new path integration procedure based on Gauss-Legendre scheme. *International Journal of Non-Linear Mechanics*, *32*(4), 759–768.

Yue, X., Xu, W., & Wang, L. (2013). Stochastic bifurcations in the SD (smooth and discontinuous) oscillator under bounded noise excitation. *Science China Physics, Mechanics and Astronomy*, *56*(5), 1010–1016.

المنارة للاستشارات

Zhang, Y., Qiao, Z., & Wang, G. (1998). Solving processes for a system of first-order fuzzy differential equations. *Fuzzy Sets and Systems*, *95*, 333–347.
Zhu, H.-T., & Guo, S.-S. (2015). Periodic response of a Duffing oscillator under combined harmonic and random excitations. *Journal of Vibration and Acoustics*, *137*(4), 041015.

المنارة للاستشارات